Integration of multiple outlets' operation and sediment management options in the reservoir for increasing efficiency of turbidity current venting and clear water storage

Chen Peng-An

Acknowledgments

I would like to express my highest gratitude to Prof. Dr. Tetsuya Sumi (角　哲也 教授), professor of Socio and Eco Environment Risk Management laboratory, Water Resource Research Center, Disaster Prevention Research Institute, Kyoto University, for offering me an opportunity to join the Sumi laboratory and become a PhD student. Sumi sensei's suggestions and critical reviews always encourage my consistent efforts in the field. I enjoy a lot about the field survey for understanding the Japanese river systems and reservoir management. I also appreciate Sumi sensei providing many opportunities for attending the national and international conferences and workshops that cultivate my international and interdisciplinary thinking.

I am very grateful for the support and encouragement from my direct supervisor, Assoc. Prof. Dr. Sameh Ahmed Kantoush, associate professor of Socio and Eco Environment Risk Management laboratory, Kyoto University. Sameh sensei's endless knowledge with systematic cogitation, patient discussions, and massive and extensive brainstorming improved my academic thinking and gained my knowledge. Sameh sensei's wide international networks with international groups, famous scientists, and engineers help me overcome academic difficulties and expand my thinking. Though I will make some mistakes and lose the way during my PhD, Sameh sensei always be enthusiastic about supporting and guiding me back to the right and efficient way.

I would like to thank Assoc. Prof. Dr. Yasuhiro Takemon (竹門康弘　准教授), associate professor of Socio and Eco Environment Risk Management laboratory, Kyoto University. I got impressive experience in the ecological and biological field survey. I am just a rookie in the biological field, but Takemon sensei always patient instructs me his broad knowledge about biological sampling, seigyu, and river environment. I also enjoy

the coffee time in Takemon sensei's office and have a good time fishing together.

I wish to acknowledge the help of Asst. Prof. Dr. Nohara (野原大督), Asst. Prof. Dr. Kobayashi (小林草平), Asst. Prof. Dr. Saber for filling in my knowledge blind spot. I would like to acknowledge to Asst. Prof. Dr. Koshiba (小柴孝太) for supporting me the programming skill and solving the mathematic and statistic problems. I would like to thank Dr. Binh for guiding me in building the numerical model and understanding the knowledge of sediment transportation. I appreciate the support from Dr. Lai (賴進松), Dr. Lee (李豐佐), Dr. Wu (吳慶現) for helping me understand the Shihmen Reservoir and data collection. I thank Asst. Prof. Dr. Taymaz, Dr. Sebastien, Dr. Kubota, Dr. Riadh Ata for their godsend support in solving the technical problem about Telemac, numerical modelling, and Tecplot.

I would like to acknowledge Mrs. Ibaraki (茨木純子), Mrs. Obara (小原久恵), and Mrs. Morimoto (森本慎子), secretary of Sumi laboratory, for their supports regarding my research, traveling, daily life during my PhD. My thanks are to all members of Sumi laboratory: Mr. Mahmoud, Mrs. Tahani, Mss. Yamasaki (山﨑弘美), Mr. Ishizuka (石塚淳也), Mss. Sabah, Mss. Miura (三浦　爽), Mss. Iwamoto (岩本麻紀), Mr. Tamagawa (玉川一晃), Mr. Nishimura (西村昂輝), Mr. Oonishi (大西左海), Mr. Ahmed. Mss. Thao, Mr. Okamoto (岡本悠希), Mss. Goto (後藤ひかる), Mr. Mouhanned.

Special thanks are to Dr. Xiao (肖恩邦), Dr. Dina, Eng. Karim, Mr. Lin (林佳奇), Mss. Wang (王珏). All their support not only in academic but daily life and mental. I am really enjoying the time hanging out with them and having life experiences sharing. My PhD life would not have been complete without the befriend of Dr. Xiao (肖恩邦) and his wife, Mrs. Lin (林伊雯). I am pleased by having parties, hanging out, playing basketball, and fishing with them. I also thank my first friend in Japan, Mss. Hsieh (謝佩儒) supports my language problems and helps me pass through the gloomy time. My

sincere thanks are also to the Taiwanese Student Association, Kyoto University, for supporting me in successfully settling down in Japan.

I would like to express my special gratitude to my girlfriend, Wan Shanbin (万杉彬), for being with me, sticking together, helping me release my pressure, and staying with me through the gloomy time. It is impossible to pass through the tough time and finish my PhD without her accompany.

Last but not least, my sincere gratitude to my family for their selfless dedication. It is impossible to study PhD at Kyoto University and live with peace of mind without their unreasonable support, sacrifice, encouragement, and contribution. Therefore, I would like to dedicate this thesis to

My father

Chen A-Nan (陳阿南)

My mother

Tsai Shu-Yuan (蔡淑媛)

陳鵬安

Chen Peng-An

2022.01.01

Abstract

The intense monsoon and typhoon rains and frequent earthquakes lead to rapid sedimentation rates in Taiwan's reservoir. With its high sediment yield, about one-third of the total reservoir capacity has been lost. To mitigate the sediment deposition and prolong the reservoir life, various desilting strategies, including hydraulic desiltation and mechanical removal, have been implemented in Shihmen Reservoir. Among those techniques, turbidity current venting has the ability to release half of the inflowing sediment load and deliver suspended sediment without drawdown water level. Therefore, the turbidity current venting operation is critical for low-cost sediment desilting.

The numerical models are the most appropriate tool for profoundly understanding the turbidity current characteristics and venting operation. It could avoid scale effects and provide numerous results, enhancing the understanding of the process. This study implemented the powerful and flexible Telemac system to solve complex geometry domains with fine mesh and adapted equations and theories for specific scenarios. Meanwhile, for investigating the turbidity current plunging mechanism, stratification, and multiple outlets' operation from different elevations, the fully three-dimensional numerical model (Telemac-3D) is considered a suitable tool. Through comprehensive sensitivity analysis, which considers the computational time and accuracy simultaneously, the applicable scope of the dimensionless numerical model setting is determined. The results reveal that the reliable three-dimensional numerical modelling setup could reference different scale numerical building.

Using the fully three-dimensional numerical model, the turbidity flow converted from sediment-laden flow to turbidity current could be clearly understood. The vertical profiles of sediment-laden flow reveal that the flow regime and sediment distribution are

similar to the open-channel flow. Under certain hydraulic conditions, the high sediment concentration flow plunges and concentrates to turbidity current. With the plane and longitudinal view, the turbidity current plunging and stratification phenomenon was investigated, and it emphasized the importance of the fully three-dimensional numerical model application. The turbidity current process from different generated hydrographs is assessed to study the governing terms for turbidity current. After that, the corresponding historical event could be used to evaluate the feasibility of turbidity current estimation. Based on the understanding above, the shortcomings of the existing venting methods could be found, and potential improving methods are proposed in this study. Moreover, additional measurements to monitor the deficiencies are crucial to obtain comprehensive assessments of turbidity current interaction at tributaries and beds.

Based on the understanding of the turbidity current transportation from the plunging location to each sediment venting outlet, the effective improving methods are discussed in this study. The proposed improving scenarios could be divided into soft and engineering methods to assess the potential improving methods. In soft methods, two significant parts were discussed: (1) The operation sequence of each outlet, which is sorted by sediment venting ability, was evaluated to determine the appropriate multiple outlets' operation. (2) Assess the impact of operating timing on turbidity current venting efficiency and clear water resources. Moreover, according to the findings from numerical simulations and the physical model results, the additional structures and facilities are considered potential, improving engineering methods for guiding the turbidity current movement. To increase the venting efficiency and concentrate the turbidity current: (1) Build the blockade structures to avoid the turbidity current spread flow into the tributaries. (2) Evaluate the impact of extended pipes' location and additional extended pipes on turbidity current venting through sediment bypass tunnels. (3) Apply the proposed

dredging channel for guiding and concentrating the turbidity current vent through the extended pipes. The results indicated that the turbidity current venting efficiency increasing the percentage by adopting soft and engineering methods instead of the existing method is 81% and 160%, respectively. Meanwhile, the released water ratios rose from 42.3% (existing method) to 61.8% (soft method) and 92.2% (engineering method). Based on the aforementioned results, the proposed engineering method could effectively increase the turbidity current venting efficiency under the abundant water resources.

To simplify the discussion procedure and reduce the computational time, the experiment-scale numerical model is adopted to investigate the optimal strategies. However, the hydrological conditions and geological are more complicated in realistic situations. Thus, assessing the feasibility of proposed improving methods under the complex field hydrological and geological conditions is essential. The results indicated that the proposed soft methods also provide a reliable improvement in realistic situations. But the outlets' operation sequence under using dredging channel is different from the experiment due to the inflow sediment concentration being hydrograph instead of fixed values. The effectiveness of turbidity current venting is reduced after peak sediment concentration. Then it converts to release muddy lake instead of the turbidity current.

By adopting the proposed soft and modified engineering methods, the increasing percentage of total released sediment is 35.1% and 50.59%, respectively. The prediction of deposition rate could be obtained by the probability of the events and improvement percentage from each cluster, which was classified by inflow discharge. The results showed that if without any improvement, the Shihmen Reservoir will lose most of its function due to the severe sedimentation (83.4% storage lost) in 2100. However, the application of the proposed soft and engineering methods can remain 32.7% and 40.4% storage capacity in 2100. The proposed improving methods could be a reference for

reservoir managers to mitigate the sediment deposition and prolong the reservoir life.

Keywords: Turbidity current characteristics, Three-dimensional numerical model, Multiple outlets' operation, sediment management options, turbidity current venting, clear water storage, reservoir usage life.

Table of contents

Acknowledgments ..... **i**

Abstract ..... **iv**

Table of contents ..... **viii**

List of figures ..... **xv**

List of tables ..... **xxxv**

List of symbols ..... **xxxviii**

Abbreviations ..... **xliii**

Chapter 1: Introduction and research processes **1**

1.1 Water resource shortage due to severe sedimentation within the reservoir 1

1.2 Research objectives 6

1.3 Thesis structure 8

1.4 Outline of the thesis 9

Chapter 2: Literature review and theoretical basis **12**

2.1 Suitable desilting methods for reservoir sedimentation removal 12

2.1.1 Historical alteration of reservoir sedimentation 12

2.1.2 Hydraulic desiltation and mechanical removal strategies 15

A. Sediment bypassing 16

B. Sediment sluicing 17

C. Turbidity current venting 17

D. Sediment flushing 18

E. Dredging and mechanical removal 18

2.1.3 Importance and advantage of turbidity current venting 19

2.2 Turbidity current characteristics and processes 20

2.2.1 Turbidity current plunging mechanism and flow regime 20
2.2.2 Turbidity current body structure and head velocity 22
2.2.3 Investigation of efficient turbidity current venting operation 22
A. Outflow discharge 23
B. Turbidity current venting operating timing 23
C. Outlet height 24
2.3 Numerical studies 25
2.3.1 One-dimensional numerical model 25
2.3.2 Two-dimensional numerical model 26
2.3.3 Three-dimensional numerical model 27
2.3.4 Turbidity current simulation by using three-dimensional numerical model 27
2.4 Research gaps 30
Chapter 3: Field and physical model measurements 31
3.1 Description of Shihmen Reservoir 31
3.1.1 Construction and facilities within Shihmen Reservoir 31
A. Facilities at the dam site 31
B. Facilities within reservoir 33
C. Planned and under constructed facilities 35
3.1.2 Measurements data from field survey and sampling 36
A. Reservoir bathymetry 38
B. Sediment material 40
3.1.3 Hydrological measurement under Typhoon events 42
3.1.4 Relationship of hydrological factors in Shihmen Reservoir 46
A. Relationship between rainfall and inflow discharge 46
B. Relationship between inflow discharge and sediment 49

C. H-A-V curve 52
3.2 The 1/100 down-scaling distorted physical model 54
3.2.1 Physical model building and initial and boundary condition setting 55
3.2.2 Investigating the effectiveness of venting facilities improvement 56
Chapter 4: Three-dimensional numerical modelling setup and sensitivity analysis 58
4.1 Introduction 58
4.2 Background of Telemac-3D and Gaia 59
4.2.1 Telemac-3D 59
4.2.2 Gaia 60
4.3 Performance criteria for model evaluation 61
4.4 Investigation of numerical modelling under experiment-scale 62
4.4.1 Initial and boundary condition 62
4.4.2 Sensitivity analysis of domain discretization 63
A. Horizontal discretization 63
B. Vertical discretization 67
C. Time step 70
4.4.3 Sensitivity analysis of turbulence scheme 73
A. Investigating the same scheme for horizontal and vertical aspects 76
B. Investigating the mixing scheme for horizontal and vertical aspects 76
4.4.4 Sensitivity analysis of morphodynamic aspect 78
A. Bed roughness 78
B. Settling velocity 79
4.4.5 Calibration and validation results by adopting optimal numerical aspects and equations 81

4.5 Investigation of numerical modelling setup under field-scale 83
4.5.1 Initial and boundary condition 83
4.5.2 Three-dimensional numerical modeling for field-scale simulation 84
A. Calibration and validation by using Soudelor and Dujuan Typhoon data.... 85
B. Assess the feasibility of validated model for future events..... 90
4.6 Conclusion 92
Chapter 5: Understanding of the turbidity current characteristics and processes under variable inflow 93
5.1 Introduction..... 93
5.2 Understanding of turbidity current processes 95
5.3 Investigation of governing terms for turbidity current processes 101
5.3.1 Influence of different scenarios of inflow boundary on turbidity current process 102
5.3.2 Plunging mechanism investigation and location estimation 109
5.3.3 Vertical profile of velocity and sediment concentration estimation.....114
5.3.4 Turbidity current arrival time and the muddy lake formed evaluation 121
5.4 Evaluation of the potential improving methods for solving the shortcomings of the existing venting methods 129
5.4.1 Estimation of turbidity current arrival time with the empirical formula.... 129
5.4.2 Investigation of the turbidity current venting ability of each outlet from different locations 130
5.4.3 Influence of the tributaries on turbidity current transportation 131
5.5 Assessment of the necessity of additional measurements to monitor the deficiencies for turbidity current simulation 133
5.5.1 Impact of the deficient observations from the tributary..... 133

5.5.2 Influence of the deficient observations of the active deposition layer 137
5.5.3 Solution for solving the deficient observations within the reservoir to increase the simulation accuracy 140
A. Build the monitoring facilities within tributaries 140
B. Apply the Soil drilling for investigating the sediment materials 140
5.6 Conclusion 142
Chapter 6: Investigating the impacts of sediment management options on efficiency of turbidity current venting 144
6.1 Introduction 144
6.2 Investigation of the turbidity current venting operation from multiple existing and constructing outlets 148
6.2.1 Operation sequence of each outlet for multiple outlets' operation 149
6.2.2 Upstream outlet operation influence on turbidity current transportation and the muddy lake formed 152
6.2.3 Impact of muddy lake evolution on clear water supply 154
6.3 Investigation of the influence of the optimal outlets' operating timing on turbidity current venting 156
6.4 Blockade structure for avoiding the spread flow into tributary 159
6.4.1 Height of blockade structure 159
6.4.2 Length of blockade structure 164
6.4.3 Shape of blockade structure 166
6.5 Application of extended pipe from SBTs for attracting turbidity current to vent through outlets effectively 168
6.5.1 Evaluation of the influence of the elevation of the ELEP on venting efficiency 168

6.5.2 Assess the feasibility of extended pipe from Amu_SBT 170
6.6 Application of dredging channel for guiding turbidity current movement 172
6.6.1 Width of dredging channel 172
6.6.2 Depth of dredging channel 175
6.6.3 Entrance and exit section of dredging channel 176
6.7 Conclusion 180
Chapter 7: Assessing the turbidity current venting and reservoir storage in future 183
7.1 Introduction 183
7.2 Assessment of the feasibility of proposed improving methods 184
7.2.1 Evaluate the proposed improving methods under the realistic situations .. 184
7.2.2 Investigate the sediment deposition after events under using improving methods 194
7.2.3 Application of proposed improving methods under different inflow hydrological events 196
7.3 Prediction of the reservoir usage life extension by adopting the proposed improving methods 198
7.4 Conclusion 201
Chapter 8: Conclusions and Recommendations 202
8.1 Conclusions 202
8.2 Recommendations 204
References 206
Appendix A: Background of Telemac-3D and Gaia 215
A.1 Background of Telemac-3D 215
A.1.1 Governing equations 215

A.1.2 The inputs and outputs 216
A.2 Background of Gaia 217
A.2.1 Suspended sediment transport 218
A.2.2 Bedload transport 219
Appendix B: Turbidity current processes from different inflow scenarios 220
Appendix C: Turbidity current processes and deposition in the reservoir under different venting strategies 230
C.1 Existing method 230
C.2 Soft methods 249
C.3 Engineering methods 268

List of figures

Figure 1.1 Shihmen Reservoir and Baoshan No. 2 Reservoir depleted view at the end of May in 2021 (source from Shihmen Reservoir Live Cam and BBC News). . 2

Figure 1.2 (a) Concept of the turbidity current process within the reservoir; (b) the process of turbidity current transportation and the muddy lake formed..... 3

Figure 1.3 The proposed plan for solving the shortcomings of the existing method for turbidity current venting. 5

Figure 1.4 Overview of the research structure and objectives. 8

Figure 2.1 Deposition within Jen-San-Pei reservoir in Taiwan with and without sediment management (Kondolf et al., 2014). 15

Figure 2.2 List of integrated reservoir desiltation strategies. (WRA, Taiwan, 2020)..... 16

Figure 2.3 Concept diagram of sediment bypassing. 16

Figure 2.4 Concept diagram of sediment sluicing..... 17

Figure 2.5 Concept diagram of sediment sluicing..... 17

Figure 2.6 Concept diagram of sediment flushing 18

Figure 2.7 Concept diagram of dredging and mechanical removal..... 18

Figure 2.8 Cluster of reservoir desilting techniques based on CSR and CIR (WRA, Taiwan, 2020). 19

Figure 2.9 Prior researches were investigating turbidity current characteristics..... 20

Figure 2.10 Reservoir flow pattern after plunging (Farrell & Stefan, 1986)..... 21

Figure 2.11 Concept of the height of aspiration principal (Chamoun et al., 2016). 24

Figure 3.1 Locations of outlets, floating platform of TDR, rainfall stations and hydrological stations in the Shihmen Reservoir catchment. 32

Figure 3.2 Sediment concentration measurement by using (a) TDR sensor was settled on

the (b) observation pile at Lofu station and (c) floating platform at the middle of the Shihmen Reservoir. 34
Figure 3.3 Sediment bypass tunnel planning alternatives in Shihmen Reservoir..... 35
Figure 3.4 Historical alteration of deposition and reservoir storage capacity. 36
Figure 3.5 The (a) reservoir bathymetry and (b) bed evolution from 2013 to 2016. 39
Figure 3.6 Longitudinal bed elevation and outlets' elevation of Shihmen Reservoir..... 39
Figure 3.7 (a) The grain size distribution of suspended sediment from the upstream boundary and each outlet (black line means average value), and (b) the box plot of D_{50} from several sediment sampling at each location (number means average D_{50}). 41
Figure 3.8 (a) the measurement of suspended sediment concentration from TDR, (b) the configuration of the TDR measurement station, and (c) the raw data from T7. 43
Figure 3.9 Taking the turbidity flow sample and measuring the turbidity and sediment concentration by using turbidity meter and gravimetric analysis. 45
Figure 3.10 The rainfall and inflow discharge from ten rainfall stations and Lofu station in Soudelor Typhoon..... 45
Figure 3.11 The correlation coefficient of inflow discharge and rainfall in different lag times from each typhoon event. 47
Figure 3.12 The rainfall and inflow discharge of major flood typhoon events with shifting 5 hours from considering the time of concentration. 48
Figure 3.13 The relationship between rainfall and inflow discharge. 48
Figure 3.14 The relationship between inflow discharge and sediment with (a) historical data from 1963 to 2004 and (b) add major flood typhoon data. 50
Figure 3.15 The comparison of observed and estimated sediment concentration. 51

Figure 3.16 The inflow discharge and sediment concentration of major flood typhoon events. 51
Figure 3.17 The H-A-V curves from 1963 to 2020 in Shihmen Reservoir. 52
Figure 3.18 The segments in Shihmen Reservoir according to the relationship between water level and reservoir storage area. 53
Figure 3.19 The configuration of Shihmen Reservoir physical model..... 54
Figure 3.20 The Shihmen Reservoir physical model construction uses (a) brick for contour setup and (b) cement mortar and gravel for reservoir bed and terrain construct. (c) the completion of the physical model..... 55
Figure 4.1 The upstream (inflow discharge and suspended sediment) and downstream (water level) boundary conditions for model calibration and validation..... 62
Figure 4.2 The sensitivity tests of mesh size for investigating the (a) RMSE of CS4 and outlets and computational time; (b) relationship between element number and performance and computational time. 65
Figure 4.3 The (a) turbidity current movement within the reservoir; (b) configuration of integration of finer mesh in the middle of the channel and coarser mesh at the banksides; (c) results from improved mesh setting and the improvement percentage from $b_0/6$ and $b_0/3$. 66
Figure 4.4 The (a) configuration of layer setting style; (b) vertical profile of CS4 from each scenario; (c) RMSE from each layer setting style and improvement percentage of performance at bottom reach (shown as numbers in the figure). 68
Figure 4.5 The RMSE values of CS4 and outlets and computational time from different layer numbers. 69
Figure 4.6 The sensitivity tests of time step for investigating the RMSE of CS4 and outlets

and computational time. 70
Figure 4.7 The comparison of turbidity current simulation within reservoir between 4 and 0.5 s time step at (a) 2160 s and (b) 3600 s. 71
Figure 4.8 The relationship between averaged Courant number and performance and computational time. 72
Figure 4.9 Comparison between the numerical and the experimental results of cross sections, outlets, and water level in calibration and validation cases. 82
Figure 4.10 The hydrological and sediment concentration measurement for model calibration and validation. 83
Figure 4.11 The critical shear stresses for erosion as a function of particle size and dry sediment density. 84
Figure 4.12 Comparison between the simulation and the observation of each venting outlet in Soudelor Typhoon for model calibration. 86
Figure 4.13 Cross sectional performance comparison between the simulation and the TDR 20-1 observation of (a) top, (b) middle, (c) bottom reach, and (d) vertical profile from Soudelor Typhoon for model calibration. 87
Figure 4.14 Comparison between the simulation and the observation of each venting outlet in Dujuan Typhoon for model validation. 88
Figure 4.15 Cross sectional performance comparison between the simulation and the TDR 12-2 observation of (a) top, (b) middle, (c) bottom reach, and (d) vertical profile from Dujuan Typhoon for model validation. 89
Figure 4.16 Turbidity current arrival time at each cross section. 91
Figure 5.1 The experimental-scale simulation of turbidity current process in the reservoir by using validated Telemac-3D: (a) the head velocity and arrival time at CS24; (b) the wider width and tributary lead to the velocity and thickness decrease;

(c) the configuration of turbidity current from plunging to arrive at dam site; (d) the muddy lake formed after the turbidity current arrives dam. 94

Figure 5.2 The streamline within the Shihmen Reservoir under the flooding event and the configuration of the turbidity current processes: (1) the sediment-laden flow region; (2) the turbidity current plunges; (3) the turbidity current transportation is divided into mainstream and tributary direction; (4) the turbidity current spread flow into the tributary lead to the circulation; (5) the turbidity current region. 95

Figure 5.3 The plane view of sediment concentration and velocity vector at (a) surface, (b) middle, and (c) bottom. 97

Figure 5.4 The longitudinal view of sediment concentration at (a) left side, (b) middle and (c) right side of mainstream, and (d) tributary. 98

Figure 5.5 The cross sectional view and vertical profile of sediment concentration and velocity at (a) CS28, (b) CS20, and (c) CS12. 99

Figure 5.6 The bed elevation before and after event and deposition at (a) left side, (b) middle and (c) right side of mainstream, and (d) tributary. 100

Figure 5.7 The configuration of the turbidity current process. 102

Figure 5.8 Generated inflow boundaries based on different amounts of inflow discharge and sediment concentration 103

Figure 5.9 The turbidity current simulation with a small amount of inflow discharge and different amounts of inflow sediment concentration. 105

Figure 5.10 The turbidity current simulation with the middle amount of inflow discharge and different amounts of inflow sediment concentration. 106

Figure 5.11 The turbidity current simulation with a large amount of inflow discharge and different amounts of inflow sediment concentration. 107

Figure 5.12 The comparison between turbidity current simulation with the (a) same amount of inflow discharge and (b) same amount of inflow sediment concentration (black and red line point out the plunging location and turbidity current head, respectively). 108
Figure 5.13 The flow regime near the plunging location. 109
Figure 5.14 The plunging location and corresponding Fr_d with different inflow conditions at (a) 7.5 and (b) 15 hours. 110
Figure 5.15 The relationship between inflow conditions and Fr_p'.....111
Figure 5.16 Turbidity current plunging location estimation in Shihmen Reservoir with inflow sediment concentration and discharge ratio. 112
Figure 5.17 The averaged turbidity current plunging location from different inflow sediment concentrations and inflow discharge (unit: distance from CS30 (m)). 113
Figure 5.18 The turbidity current thickness at CS20 from different inflow sediment concentrations and discharges. 114
Figure 5.19 The sketch of TDR equipment and vertical profile of sediment concentration and velocity. 115
Figure 5.20 The sediment concentration and velocity profile in (a) concept and under (b) large, (c) middle, (c) small amount of inflow discharge.....116
Figure 5.21 The dimensionless sediment concentration and velocity profile from proposed equations for (a) large, (b) middle, and (c) small amount of inflow discharge. 118
Figure 5.22 Assessment of the parameter of turbidity current head velocity. 119
Figure 5.23 The flowchart for obtaining the pattern of turbidity current transportation. 120

Figure 5.24 The turbidity current transportation (including velocity, travel time, and arrival time) and muddy lake evolution investigation in this section. 121
Figure 5.25 The turbidity current (a) travel time and (b) arrival time at the dam from different inflow sediment concentrations and discharges (unit: hours). 121
Figure 5.26 The averaged turbidity current velocity from different inflow sediment concentrations and inflow discharges (unit: m/s) 122
Figure 5.27 The relationship between inflow conditions and turbidity current velocity. 123
Figure 5.28 The muddy lake formed with a small amount of inflow discharge and different amounts of inflow sediment concentration. 124
Figure 5.29 The muddy lake formed with a middle amount of inflow discharge and different amounts of inflow sediment concentration. 125
Figure 5.30 The muddy lake formed with a large amount of inflow discharge and different amounts of inflow sediment concentration. 126
Figure 5.31 The configuration of muddy lake evolution and the influence of water supply intake. 127
Figure 5.32 The muddy lake reach time at the water supply intake from different inflow sediment concentrations and inflow discharges (unit: hours). (Note: - means the muddy lake does not affect the water supply facilities.) 128
Figure 5.33 The turbidity current arrival time estimation by using the proposed empirical formulas. 129
Figure 5.34 The location of each outlet within Shihmen Reservoir. 131
Figure 5.35 The concept diagram of (a) blockade structure and (b) dredging channel. 132
Figure 5.36 The (a) hypothesis of inflow discharge ratio for mainstream and tributaries (numbers in brackets represent proportions), and the upstream boundary

conditions (b) without, and (c) with considering the tributaries' inflow. ... 134
Figure 5.37 The relationship between inflow discharge and sediment with modified mainstream inflow discharge. ... 134
Figure 5.38 The turbidity current flow regime (a) without and (b) with inflow from the tributaries. ... 135
Figure 5.39 The longitudinal view of sediment concentration without ((a) and (c)) and with ((b) and (d)) tributaries' inflow at mainstream and tributaries. ... 136
Figure 5.40 Comparison between the simulations, with and without deposition layer, and the observation of each venting outlet. ... 137
Figure 5.41 Cross-sectional performance comparison between the simulation with and without deposition layer and the TDR 20-1 observation of (a) top, (b) middle, (c) bottom reach, and (d) vertical profile ... 138
Figure 5.42 The bed elevation of simulation with and without deposition layer between before and after the turbidity current arrival. ... 139
Figure 5.43 The planned underwater terrain measurement area and camera install sites. ... 141
Figure 6.1 The proposed soft and engineering methods for investigating the optimal improvement scenario. ... 144
Figure 6.2 The proposed scenarios for investigating the optimal soft methods. ... 146
Figure 6.3 The proposed structures for determining the optimal engineering methods. ... 147
Figure 6.4 The location of venting facilities and the vertical profile of turbidity current body along longitudinal from upstream to (a) dam and (b) intake facility. 148
Figure 6.5 The comparison of (a) released sediment concentration and (b) accumulated released sediment from each single outlet operation. ... 150

Figure 6.6 Comparison of each outlet's released sediment performance from (a) Multi_1-B, (b) Multi_2-B, (c) Multi_3-B, (d) Multi_4-B. 151
Figure 6.7 Comparison of simulation (a) with ELEP operation and (b) without any outlets operation: (c) difference of sediment concentration and turbidity current thickness from upstream (CS14) and downstream (CS8) of ELEP and (d) the ELEP operation causes head velocity decrease. 153
Figure 6.8 The muddy lake evolution from different multiple outlets' operations..... 155
Figure 6.9 The muddy lake reach time at water supply facilities from multiple outlets' operation. 155
Figure 6.10 The comparison of released sediment and water at (a) dam outlets and (b) ELEP from different operating timing. 156
Figure 6.11 The (a) influence of the different operating timing on the accumulated released sediment and water and (b) concept of the dragged released sediment by aspiration force in early operation. 157
Figure 6.12 The configuration of the blockade structure within the reservoir. 160
Figure 6.13 The turbidity current (shown in 3 g/l) transportation around the tributary area under (a) without and (b) with 0.1 m blockade structure; (c) the high sediment concentration turbidity flow (shown in 30 g/l) is trapped by blockage structure. 161
Figure 6.14 The blockade effect from (a) 0.1 m and (b) 0.2 m blockade structure and the flow field around (c) 0.1 m and (s) 0.2 m blockade structure. 162
Figure 6.15 The other muddy lake formed at tributary due to the (a) 0.1 m and (b) 0.2 m blockade structure; the sediment deposition difference between without blockade structure and (c) 0.1 m, and (d) 0.2 m blockade structure. 162
Figure 6.16 The difference of the V_e between without blockade structure and with 0.05,

0.1, and 0.2 m blockade structure from before and after turbidity current arrival. 163
Figure 6.17 The configuration of the three quarters length blockade structure. 164
Figure 6.18 The turbidity current (shown in 3 g/l) transportation around the tributary area under Blockade_L_3/4 at (a) 1044 s and (b) 1764 s; (c) the flow regime of high sediment concentration turbidity flow (shown in 30 g/l) around blockade structure. 165
Figure 6.19 The configuration of the curve shape blockade structure. 166
Figure 6.20 The influence of the (a) straight and (b) curve shape of the blockade structure on flow direction change. 167
Figure 6.21 The location of the ELEP_Y04 and ELEP_Y15. 169
Figure 6.22 The locations of Amu_SBT and Daw_SBT and their extended pipes in a horizontal and vertical perspective. 171
Figure 6.23 The released sediment concentration from ELEP_A with different widths of the dredging channel. 173
Figure 6.24 The configuration of the different widths of the dredging channel. 174
Figure 6.25 The turbidity current transportation (shown in 30 g/l) under (a) 1.2 m, (b) 0.8 m and (c) 0.4 m width of dredging channel. 174
Figure 6.26 The turbidity current transportation under (a) 0.15 m, (b) 0.1 m and (c) 0.05 m depth of dredging channel. 176
Figure 6.27 The configuration of the entrance section for (a) Channel_D_0.05 and (b) Channel_Enter_C. 177
Figure 6.28 The flow regime of turbidity current at the entrance section in (a) Channel_D_0.05 and (b) Channel_Enter_C. 178
Figure 6.29 The configuration of the entrance section, dredging channel and exit section

from (a) Channel_Enter_C and (b) Channel_Exit_S..... 179
Figure 6.30 The released sediment and water ratios of existing, soft, and engineering methods..... 181
Figure 6.31 The deposition within Shihmen Reservoir by using (a) existing, (b) soft, and (c) engineering methods. 182
Figure 7.1 The details of (a) operating duration, (b) released water percentage, (c) released sediment percentage and (b) averaged released sediment concentration of each operated outlet under the existing method..... 185
Figure 7.2 The details of (a) operating duration, (b) released water percentage, (c) released sediment percentage and (b) averaged released sediment concentration of each operated outlet under the soft methods..... 186
Figure 7.3 The details of (a) operating duration, (b) released water percentage, (c) released sediment percentage and (b) averaged released sediment concentration of each operated outlet under the engineering methods (with additional extended pipe). 187
Figure 7.4 The details of (a) operating duration, (b) released water percentage, (c) released sediment percentage and (b) averaged released sediment concentration of each operated outlet under the engineering methods (with dredging channel). . 188
Figure 7.5 Comparison of proposed improving method under experimental-scale and field-scale..... 189
Figure 7.6 The released sediment concentration from ELEP and ELEP_A and the longitudinal view of (a) turbidity current arrival and (b) muddy lake..... 191
Figure 7.7 The details of (a) operating duration, (b) released water percentage, (c) released sediment percentage and (b) averaged released sediment concentration of each operated outlet under the engineering methods (modified operating sequence).

..... 192
Figure 7.8 The turbidity current venting performance from existing method and improving methods. 193
Figure 7.9 The longitudinal view of the bed elevation change after the flooding event. 194
Figure 7.10 The deposition at (a) left, (b) middle and (c) right side of mainstream, and (d) tributary under existing, soft, and engineering methods. 195
Figure 7.11 The turbidity current venting efficiency by using (a) existing, (b) soft, and (c) engineering methods from different inflow hydrological conditions (unit: %) and improvement percentage by adopting improving methods..... 196
Figure 7.12 The muddy lake reach time by using (a) existing, (b) soft, and (c) engineering methods from different inflow hydrological conditions (unit: hours)..... 197
Figure 7.13 Prediction of remaining storage capacity by using existing, soft, and engineering methods. 200
Figure A.1 Sketch of the sediment transport mechanisms. Above, D and E are deposition and erosion rates (Audouin et al., 2020). 217
Figure B.1 The configuration of the Shihmen Reservoir and the longitudinal line. 220
Figure B.2 Generated inflow discharge and sediment concentration. 220
Figure B.3 The turbidity current processes from arrival at CS20, dam, and the muddy lake formed in (a) longitudinal and (b) plane view under Sc# Q_LS_L. 221
Figure B.4 The turbidity current processes from arrival at CS20, dam, and the muddy lake formed in (a) longitudinal and (b) plane view under Sc# Q_LS_M..... 222
Figure B.5 The turbidity current processes from arrival at CS20, dam, and the muddy lake formed in (a) longitudinal and (b) plane view under Sc# Q_LS_S..... 223
Figure B.6 The turbidity current processes from arrival at CS20, dam, and the muddy lake

formed in (a) longitudinal and (b) plane view under Sc# Q_MS_L..... 224
Figure B.7 The turbidity current processes from arrival at CS20, dam, and the muddy lake formed in (a) longitudinal and (b) plane view under Sc# Q_MS_M..... 225
Figure B.8 The turbidity current processes from arrival at CS20, dam, and the muddy lake formed in (a) longitudinal and (b) plane view under Sc# Q_MS_S..... 226
Figure B.9 The turbidity current processes from arrival at CS20, dam, and the muddy lake formed in (a) longitudinal and (b) plane view under Sc# Q_SS_L..... 227
Figure B.10 The turbidity current processes from arrival at CS20, dam, and the muddy lake formed in (a) longitudinal and (b) plane view under Sc# Q_SS_M..... 228
Figure B.11 The turbidity current processes from arrival at CS20, dam, and the muddy lake formed in (a) longitudinal and (b) plane view under Sc# Q_SS_S..... 229
Figure C.1 Operated outlets and the operating sequence under existing method. 230
Figure C.2 The turbidity current processes from arrival at CS20, dam, and the muddy lake formed in (a) longitudinal and (b) plane view under Sc# Q_LS_L with existing method. 231
Figure C.3 The bed elevation before and after event, and deposition at (a) left, (b) middle and (c) right side of mainstream, and (d) tributary under Sc# Q_LS_L with existing method. 232
Figure C.4 The turbidity current processes from arrival at CS20, dam, and the muddy lake formed in (a) longitudinal and (b) plane view under Sc# Q_LS_M with existing method. 233
Figure C.5 The bed elevation before and after event, and deposition at (a) left, (b) middle and (c) right side of mainstream, and (d) tributary under Sc# Q_LS_M with existing method. 234
Figure C.6 The turbidity current processes from arrival at CS20, dam, and the muddy lake

formed in (a) longitudinal and (b) plane view under Sc# Q_LS_S with existing method. 235
Figure C.7 The bed elevation before and after event, and deposition at (a) left, (b) middle and (c) right side of mainstream, and (d) tributary under Sc# Q_LS_S with existing method. 236
Figure C.8 The turbidity current processes from arrival at CS20, dam, and the muddy lake formed in (a) longitudinal and (b) plane view under Sc# Q_MS_L with existing method. 237
Figure C.9 The bed elevation before and after event, and deposition at (a) left, (b) middle and (c) right side of mainstream, and (d) tributary under Sc# Q_MS_L with existing method. 238
Figure C.10 The turbidity current processes from arrival at CS20, dam, and the muddy lake formed in (a) longitudinal and (b) plane view under Sc# Q_MS_M with existing method. 239
Figure C.11 The bed elevation before and after event, and deposition at (a) left, (b) middle and (c) right side of mainstream, and (d) tributary under Sc# Q_MS_M with existing method. 240
Figure C.12 The turbidity current processes from arrival at CS20, dam, and the muddy lake formed in (a) longitudinal and (b) plane view under Sc# Q_MS_S with existing method. 241
Figure C.13 The bed elevation before and after event, and deposition at (a) left, (b) middle and (c) right side of mainstream, and (d) tributary under Sc# Q_MS_S with existing method. 242
Figure C.14 The turbidity current processes from arrival at CS20, dam, and the muddy lake formed in (a) longitudinal and (b) plane view under Sc# Q_SS_L with

existing method. 243
Figure C.15 The bed elevation before and after event, and deposition at (a) left, (b) middle and (c) right side of mainstream, and (d) tributary under Sc# Q_SS_L with existing method. 244
Figure C.16 The turbidity current processes from arrival at CS20, dam, and the muddy lake formed in (a) longitudinal and (b) plane view under Sc# Q_SS_M with existing method. 245
Figure C.17 The bed elevation before and after event, and deposition at (a) left, (b) middle and (c) right side of mainstream, and (d) tributary under Sc# Q_SS_M with existing method. 246
Figure C.18 The turbidity current processes from arrival at CS20, dam, and the muddy lake formed in (a) longitudinal and (b) plane view under Sc# Q_SS_S with existing method. 247
Figure C.19 The bed elevation before and after event, and deposition at (a) left, (b) middle and (c) right side of mainstream, and (d) tributary under Sc# Q_SS_S with existing method. 248
Figure C.20 Operated outlets and the operating sequence under soft methods. 249
Figure C.21 The turbidity current processes from arrival at CS20, dam, and the muddy lake formed in (a) longitudinal and (b) plane view under Sc# Q_LS_L with soft methods. 250
Figure C.22 The bed elevation before and after event, and deposition at (a) left, (b) middle and (c) right side of mainstream, and (d) tributary under Sc# Q_LS_L with soft methods. 251
Figure C.23 The turbidity current processes from arrival at CS20, dam, and the muddy lake formed in (a) longitudinal and (b) plane view under Sc# Q_LS_M with soft

methods..... 252
Figure C.24 The bed elevation before and after event, and deposition at (a) left, (b) middle and (c) right side of mainstream, and (d) tributary under Sc# Q_LS_M with soft methods..... 253
Figure C.25 The turbidity current processes from arrival at CS20, dam, and the muddy lake formed in (a) longitudinal and (b) plane view under Sc# Q_LS_S with soft methods..... 254
Figure C.26 The bed elevation before and after event, and deposition at (a) left, (b) middle and (c) right side of mainstream, and (d) tributary under Sc# Q_LS_S with soft methods..... 255
Figure C.27 The turbidity current processes from arrival at CS20, dam, and the muddy lake formed in (a) longitudinal and (b) plane view under Sc# Q_MS_L with soft methods..... 256
Figure C.28 The bed elevation before and after event, and deposition at (a) left, (b) middle and (c) right side of mainstream, and (d) tributary under Sc# Q_MS_L with soft methods..... 257
Figure C.29 The turbidity current processes from arrival at CS20, dam, and the muddy lake formed in (a) longitudinal and (b) plane view under Sc# Q_MS_M with soft methods..... 258
Figure C.30 The bed elevation before and after event, and deposition at (a) left, (b) middle and (c) right side of mainstream, and (d) tributary under Sc# Q_MS_M with soft methods..... 259
Figure C.31 The turbidity current processes from arrival at CS20, dam, and the muddy lake formed in (a) longitudinal and (b) plane view under Sc# Q_MS_S with soft methods..... 260

Figure C.32 The bed elevation before and after event, and deposition at (a) left, (b) middle and (c) right side of mainstream, and (d) tributary under Sc# Q_MS_S with soft methods..... 261
Figure C.33 The turbidity current processes from arrival at CS20, dam, and the muddy lake formed in (a) longitudinal and (b) plane view under Sc# Q_SS_L with soft methods..... 262
Figure C.34 The bed elevation before and after event, and deposition at (a) left, (b) middle and (c) right side of mainstream, and (d) tributary under Sc# Q_SS_L with soft methods..... 263
Figure C.35 The turbidity current processes from arrival at CS20, dam, and the muddy lake formed in (a) longitudinal and (b) plane view under Sc# Q_SS_M with soft methods..... 264
Figure C.36 The bed elevation before and after event, and deposition at (a) left, (b) middle and (c) right side of mainstream, and (d) tributary under Sc# Q_SS_M with soft methods..... 265
Figure C.37 The turbidity current processes from arrival at CS20, dam, and the muddy lake formed in (a) longitudinal and (b) plane view under Sc# Q_SS_S with soft methods..... 266
Figure C.38 The bed elevation before and after event, and deposition at (a) left, (b) middle and (c) right side of mainstream, and (d) tributary under Sc# Q_SS_S with soft methods..... 267
Figure C.39 Operated outlets and the operating sequence under engineering methods. 268
Figure C.40 The turbidity current processes from arrival at CS20, dam, and the muddy lake formed in (a) longitudinal and (b) plane view under Sc# Q_LS_L with

engineering methods. 269
Figure C.41 The bed elevation before and after event, and deposition at (a) left, (b) middle and (c) right side of mainstream, and (d) tributary under Sc# Q_LS_L with engineering methods. 270
Figure C.42 The turbidity current processes from arrival at CS20, dam, and the muddy lake formed in (a) longitudinal and (b) plane view under Sc# Q_LS_M with engineering methods. 271
Figure C.43 The bed elevation before and after event, and deposition at (a) left, (b) middle and (c) right side of mainstream, and (d) tributary under Sc# Q_LS_M with engineering methods. 272
Figure C.44 The turbidity current processes from arrival at CS20, dam, and the muddy lake formed in (a) longitudinal and (b) plane view under Sc# Q_LS_S with engineering methods. 273
Figure C.45 The bed elevation before and after event, and deposition at (a) left, (b) middle and (c) right side of mainstream, and (d) tributary under Sc# Q_LS_S with engineering methods. 274
Figure C.46 The turbidity current processes from arrival at CS20, dam, and the muddy lake formed in (a) longitudinal and (b) plane view under Sc# Q_MS_L with engineering methods. 275
Figure C.47 The bed elevation before and after event, and deposition at (a) left, (b) middle and (c) right side of mainstream, and (d) tributary under Sc# Q_MS_L with engineering methods. 276
Figure C.48 The turbidity current processes from arrival at CS20, dam, and the muddy lake formed in (a) longitudinal and (b) plane view under Sc# Q_MS_M with engineering methods. 277

Figure C.49 The bed elevation before and after event, and deposition at (a) left, (b) middle and (c) right side of mainstream, and (d) tributary under Sc# Q_MS_M with engineering methods. 278
Figure C.50 The turbidity current processes from arrival at CS20, dam, and the muddy lake formed in (a) longitudinal and (b) plane view under Sc# Q_MS_S with engineering methods. 279
Figure C.51 The bed elevation before and after event, and deposition at (a) left, (b) middle and (c) right side of mainstream, and (d) tributary under Sc# Q_MS_S with engineering methods. 280
Figure C.52 The turbidity current processes from arrival at CS20, dam, and the muddy lake formed in (a) longitudinal and (b) plane view under Sc# Q_SS_L with engineering methods. 281
Figure C.53 The bed elevation before and after event, and deposition at (a) left, (b) middle and (c) right side of mainstream, and (d) tributary under Sc# Q_SS_L with engineering methods. 282
Figure C.54 The turbidity current processes from arrival at CS20, dam, and the muddy lake formed in (a) longitudinal and (b) plane view under Sc# Q_SS_M with engineering methods. 283
Figure C.55 The bed elevation before and after event, and deposition at (a) left, (b) middle and (c) right side of mainstream, and (d) tributary under Sc# Q_SS_M with engineering methods. 284
Figure C.56 The turbidity current processes from arrival at CS20, dam, and the muddy lake formed in (a) longitudinal and (b) plane view under Sc# Q_SS_S with engineering methods. 285
Figure C.57 The bed elevation before and after event, and deposition at (a) left, (b) middle

and (c) right side of mainstream, and (d) tributary under Sc# $Q_S S_S$ with engineering methods. 286

List of tables

Table 2.1 The annual sedimentation for reservoirs in different regions. 13

Table 2.2 Prior researches investigating the plunging densimetric Froude number..... 21

Table 2.3 Summarizes the prior research on turbidity current using a three-dimensional numerical model. 29

Table 3.1 The information of each outlet in Shihmen Reservoir. 33

Table 3.2 Hydrological data in the Shihmen Reservoir from major flood typhoon events since 2004. 37

Table 3.3 The Thiessen coefficient of each rainfall station and the time of concentration from those to Lofu station in Soudelor Typhoon. 46

Table 3.4 Test results of each turbidity current venting scenario in Shihmen Reservoir from physical model simulation. 57

Table 4.1 The information of time step setting in each considered sensitivity test. 64

Table 4.2 The information of layer number and Δz in each of sensitivity tests. 69

Table 4.3 The averaged and maximum Courant number at the upstream boundary from different time step settings. 71

Table 4.4 The constants of the κ-ε 74

Table 4.5 The limitation of each candidate turbulence scheme. 75

Table 4.6 The sensitivity tests of turbulence scheme for horizontal and vertical aspects. 77

Table 4.7 Compares cross sectional and outlet performance between Nikuradse, Chezy, and Manning bed roughness equation. 79

Table 4.8 Compares cross sectional and outlet performance between Rubey, Van Rijn, Zhu&Cheng settling velocity formula. 80

Table 4.9 Optimal numerical aspects and equations for turbidity current simulation. ... 81
Table 4.10 The RMSE and CC values of cross sections, outlets, and water level in calibration and validation cases. 82
Table 4.11 The numerical setting for field-scale simulation. 85
Table 4.12 RMSE and CC values of venting outlets in calibration and validation cases. 90
Table 5.1 Classification of each typhoon event 104
Table 6.1 The sediment venting and water releasing performance of each outlet operation for determining the operating order. 150
Table 6.2 The improvement percentage of the muddy lake reach time at water supply intake from each multiple outlets' operation instead of without operation. 154
Table 6.3 The improvement percentage of total released sediment and water from multiple outlets' operation in in-time operation instead of operating from beginning. 158
Table 6.4 Comparison of the V_e from different height of the blockade structure. 163
Table 6.5 Comparison of the V_e from different lengths of the blockade structure. 165
Table 6.6 Comparison of the V_e from different shapes of the blockade structure. 167
Table 6.7 Comparison of V_e and released sediment and water from ELEP_Y04 and ELEP_Y15. 169
Table 6.8 Comparison of V_e and muddy lake reach time at water supply intake from Multi_4-B with different elevations of ELEP 169
Table 6.9 Comparison of the venting ability between Single_7-B and Single_8-B. 171
Table 6.10 The venting abilities from adopting ELEP_A. 171
Table 6.11 Comparison of the V_e from different width of the dredging channel. 172
Table 6.12 Comparison of the V_e from different depths of the dredging channel. 175

Table 6.13 Improvement of the modified entrance and exit section of the dredging channel. 177
Table 6.14 The updated operating order of each outlet using the dredging channel. ... 179
Table 7.1 The performance of existing, soft, and engineering methods and improvement percentage of improving methods instead of the existing method. 193
Table 7.2 The historical major flood typhoon events since 1963 and clusters. 198
Table 7.3 The events' probability and improvement percentage for each cluster and prediction for future events. 199

List of symbols

(F_x, F_y) are source terms denoting the wind, Coriolis force, and bottom friction

(U, V, W) is velocity component in x-, y-, and z-direction

u_i' is the turbulent fluctuation of velocity

C_{eq} is the equilibrium near-bed concentration

C_f is Chézy coefficient

$C_{in,i}$ is inflow concentration at time *i*

$C_{out,i}$ is outflow concentration at time *i*

C_s is a dimensionless coefficient

C_{zref} is the near-bed concentration

C_μ means the empirical constant

D_{ij} is the strain rate tensor of average motion

L_m means the mixing length parameter

N_l is the total number of layers

P_{atm} is atmospheric pressure

$Perf'$ is the performance of the improved model

P_s is water surface pressure

Q_b is the bedload transport rate per unit width

$Q_{in,i}$ is inflow discharge at time *i*

Q_{in} is inflow discharge

Q_{mb} is the vector of the mass transport rate per unit width without pores

$Q_{out,i}$ is outflow discharge at time *i*

Q_{out} is outflow discharge

$Q_{s,in}$ is inflow sediment at time *i*

Q_t is tracer source of the sink

R_h is hydraulic radius

SSC_{in} is inflow sediment concentration

U_d is the depth-averaged velocity

U_{tc} is averaged turbidity current velocity

n_l is the layer number

t_c is outlet closing time

t_o is outlet opening time

u_{*mud}^{cr} is the critical shear velocity for mud deposition

y_i and $\hat{y}_i$ are presented the measured and simulated data at *N* values

$\overline{y_i}$ and $\overline{\hat{y}_i}$ is the averaged measurement and simulation

α_c, β_c and γ_c are coefficients for sediment concentration profile.

α_u, β_u and γ_u are coefficients for velocity profile.

ν_t is diffusion coefficient

ρ_a is the density of the ambient water

ρ_s is sediment density

ρ_t is the density of the turbidity flow

τ_b is the bed shear stress

τ_{ce} is the critical bed shear stress

$\forall$ means reservoir storage capacity

Δt represents time step

Δx means mesh size

Δz is vertical layer spacing

$\Delta\rho$ is a variation of density around the reference density.

b_0 is the width of inflow boundary

C_m is sediment concentration at H_m

C_{tc} is averaged sediment concentration of turbidity current

C_{tc} is averaged sediment concentration of turbidity current.

D is deposition

D_{50} is median sediment diameter

D_r is relative distance of turbidity current plunging location

E is erosion

Fr_d is densimetric Froude number

Fr_p is densimetric Froude number for turbidity current plunging

g means gravity

G value is a term according to the forces of gravity in the case of temperature gradients

H is water level (m)

H_0 is elevation of bottom (m)

H_b is height of the backflow zone (m)

H_m is height of the maximum velocity (m)

H_s is elevation of water surface (m)

H_{tc} is turbidity current thickness (m)

k is Strickler coefficient

K is turbulent kinetic energy

k_s means the asperity size

n is Manning coefficient

N is the number of data

P is the term for the production of turbulent energy

Prt being the Prandtl number

Q_L is large amount of inflow discharge

Q_M is middle amount of inflow discharge

Q_S is small amount of inflow discharge

R is rainfall

S_L is large amount of inflow sediment concentration

S_M is middle amount of inflow sediment concentration

S_S is small amount of inflow sediment concentration

u is the magnitude of the velocity

U_f is the turbidity current head velocity

U_m is maximum velocity (m/s)

V_e is venting efficiency

w_s is settling velocity

ε is dissipation

θ is Shield number

ω is specific dissipation ($= \frac{\varepsilon}{\kappa}$)

Φ is the diameter

C is the depth-averaged concentration in % volume ($= C(x, y, z)$)

D is total water depth

M is Krone-Partheniades erosion constant

$Perf$ is the performance of the original model

S means reservoir storage

T is tracer

$c(z)$ is the sediment concentration at distance z above bed.

s is the relative density ($= \rho_s/\rho_a$)

$u(z)$ is the velocity at distance z above bed.

β means fractional density

κ is von Karman constant

κy is the von Karman constant at distance y from the wall

λ is the bed porosity

μ is the skin friction's correction factor

ν is molecular diffusion

Abbreviations

% IMP: improvement percentage

3D: three dimensional

Amu_SBT: Amuping sediment bypass tunnel

CAP: reservoir capacity

CIR: capacity-inflow ratio

CPU time: computational time

CS: cross section

CSR: capacity-sediment ration

Cst: constant viscosity

Daw_SBT: Dawangping sediment bypass tunnel

EDF: National Hydraulics and Environment Laboratory of Electricité de France

ELEP: elephant trunk steel pipe from Dawangping sediment bypass tunnel

ELEP_A: elephant trunk steel pipe from Amuping sediment bypass tunnel

hr: hour

LS: layer style

LSPIV: Large-Scale Particle Image Velocimetry

MAR: mean annual runoff

MAS: mean annual sediment

PPI: power plant intake

PRO: permanent river outlet

R^2: coefficient of determination

RMSE: root mean square error

RMSE: root mean square error

SBT: sediment bypass tunnel

Sc: scenario

SCI: Shihmen canal intake

SIR: sediment-inflow ratio

Smag: Smagorinsky

SP: spillway

ST: spillway tunnel

TDR: time-domain reflectometry

VT: venting tunnel

WRA: Water Resources Agency

Chapter 1: Introduction and research processes

1.1 Water resource shortage due to severe sedimentation within the reservoir

Turbidity current venting has the ability to release a massive amount of the inflowing sediment load and deliver suspended sediment without drawdown water level. The turbidity current venting is gaining more importance for mitigating the sediment deposition and prolonging the reservoir life. Although annual rainfall in Taiwan is 2510 mm/year, 2.6 times the global average, only 20 percent of rainfall can be used as water resources. It means that Taiwan is in 18th place in global rankings and stated as a "water resource-poor region" by United Nations. Moreover, ample reasons for intense monsoon and typhoon rains and frequent earthquakes lead to rapid sedimentation rates in Taiwan's reservoir, which is the highest globally. With its highly high sediment yield, about one-third of the total reservoir capacity from 61 major reservoirs, impounded 2.2 billion m^3 freshwater, is occupied by sediment depositions. As climate changes and extreme hydro-meteorological events increase, sustainable water resources from reservoirs are essential not only for human use and agriculture but also for manufacturing and the global economy.

Typhoon rain is the critical freshwater income for reservoirs in Taiwan. On average, there are three to four typhoons landfall Taiwan per year. However, 2020 is an unusual year under which no typhoon hits Taiwan. That has plunged into Taiwan's worst drought in 56 years. Most reservoirs have less than 20% of the present capacity left at the end of May in 2021. Figure 1.1 shows that the Shihmen Reservoir and Baoshan No. 2 Reservoir almost dries up with only 7.63 and 3.1% storage capacity left. If these reservoirs dry up, it could be detrimental for local irrigation, even the global electronics sector, because around 90% of advanced microchips are manufactured in Taiwan. Integrated the reservoir

storage capacity decrease and rainfall uncertainty increase, implementation of effective sediment management has become a contemporary problem to solve.

Figure 1.1 Shihmen Reservoir and Baoshan No. 2 Reservoir depleted view at the end of May in 2021 (source from Shihmen Reservoir Live Cam and BBC News).

The turbidity current venting approach requires a reservoir with bottom venting facilities and sufficient velocity and turbulence for turbidity current traveling to the dam. As illustrated in Figure 1.2 (a), the turbidity current process is divided into the sediment-laden flow and turbidity current region by plunging occurrence. According to the sediment management experience in Shihmen Reservoir, the turbidity current occurring and can arrive at dam conditions are (1) peak inflow sediment concentration above 20000 ppm; (2) peak inflow discharge should be higher than 1800 m^3/s; (3) over 300 m^3/s inflow discharge continue at least 35 hours within a flooding event. Based on the above conditions, turbidity current is prone to occur under strong typhoon events due to the intense rainfall causing extremely high inflow discharge and sediment concentration.

In Shihmen Reservoir, over ten turbidity current venting operations have been implemented in the past two decades. To increase the venting efficiency, one of the power plant penstocks, located at the bottom of Shihmen Reservoir, is modified to focus on turbidity current venting from 2013. Figure 1.2 (a) illustrates that the modified power plant penstock could efficiently vent through the high sediment concentration turbidity

current. However, the venting efficiency is still only around 35%, and over 3.4 million m^3 sediment is trapped within the reservoir per year. Therefore, the additional two sediment bypass tunnels (SBTs), Dawanping and Amuping SBT, are constructed for turbidity current venting from upstream and avoiding muddy lake formed impact to the water supply facilities (Figure 1.2 (b)).

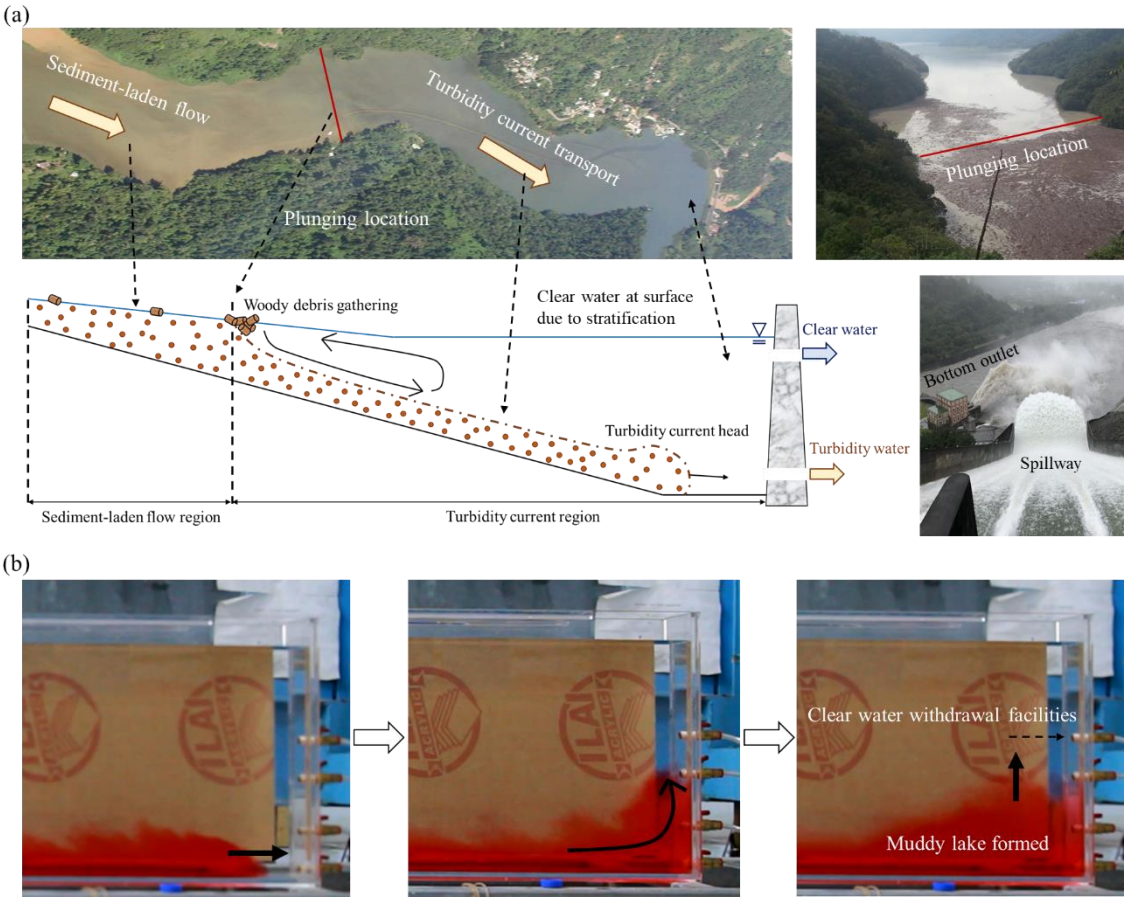

Figure 1.2 (a) Concept of the turbidity current process within the reservoir; (b) the process of turbidity current transportation and the muddy lake formed.

Turbidity current venting operation under multiple reservoir outlets is a challenging decision-making process balancing the releases of turbidity currents with the maintenance of clear water circulation within the reservoir. Due to the incorrect outlets' operation, after the typhoon events, the water supply shut down for 15 and 3 days in 2004 and 2015 due to the high concentration turbidity flow at the withdrawal outlet. Based on the historical

typhoon measurements, the limitation of the turbidity current venting efficiency in the existing method is around 38%. For increasing the turbidity current venting efficiency, the Taiwan water resources planning institute proposed two SBTs (Plan A). The experiment results indicated that the limited improvement from using additional SBTs due to the elevation of the outlets of SBTs are higher than the thickness of turbidity current. The Taiwan water resources planning institute built an extended elephant trunk pipe from Dawanping SBT and received a practical improvement to solve these problems. Therefore, the feasibility of implementing extended elephant trunk pipes from SBTs is assessed in this study (Plan B).

Moreover, we found that the turbidity current spread flows into tributaries harm continuous turbidity current transportation and turbidity current venting efficiency. Thus, the guiding construction, including blockade structure and dredging channel (Figure 1.3), is proposed in this study (Plan C). Overall, the improvement of the proposed turbidity current venting facilities and guiding structure is investigated in this study (Figure 1.3).

It still exists some research gap of the turbidity current simulation in the Shihmen Reservoir. There are three tributaries within the Shihmen Reservoir (Figure 1.3), but without discharge, and sediment concentration data are measured from them. Also, all of the researches ignore the impact of the tributaries. As previously mentioned, it should be considered to investigate the turbidity current movement. Moreover, most researchers did without thinking about the accumulated sedimentation for the turbidity current simulation in Shihmen Reservoir. The lack of erosion of the accumulated sedimentation causes the underestimated simulation at the bottom outlets. Therefore, the necessity of additional measurements to monitor the inflow from tributaries and the sediment material of the active deposition is evaluated for solving the limitation of turbidity current simulation.

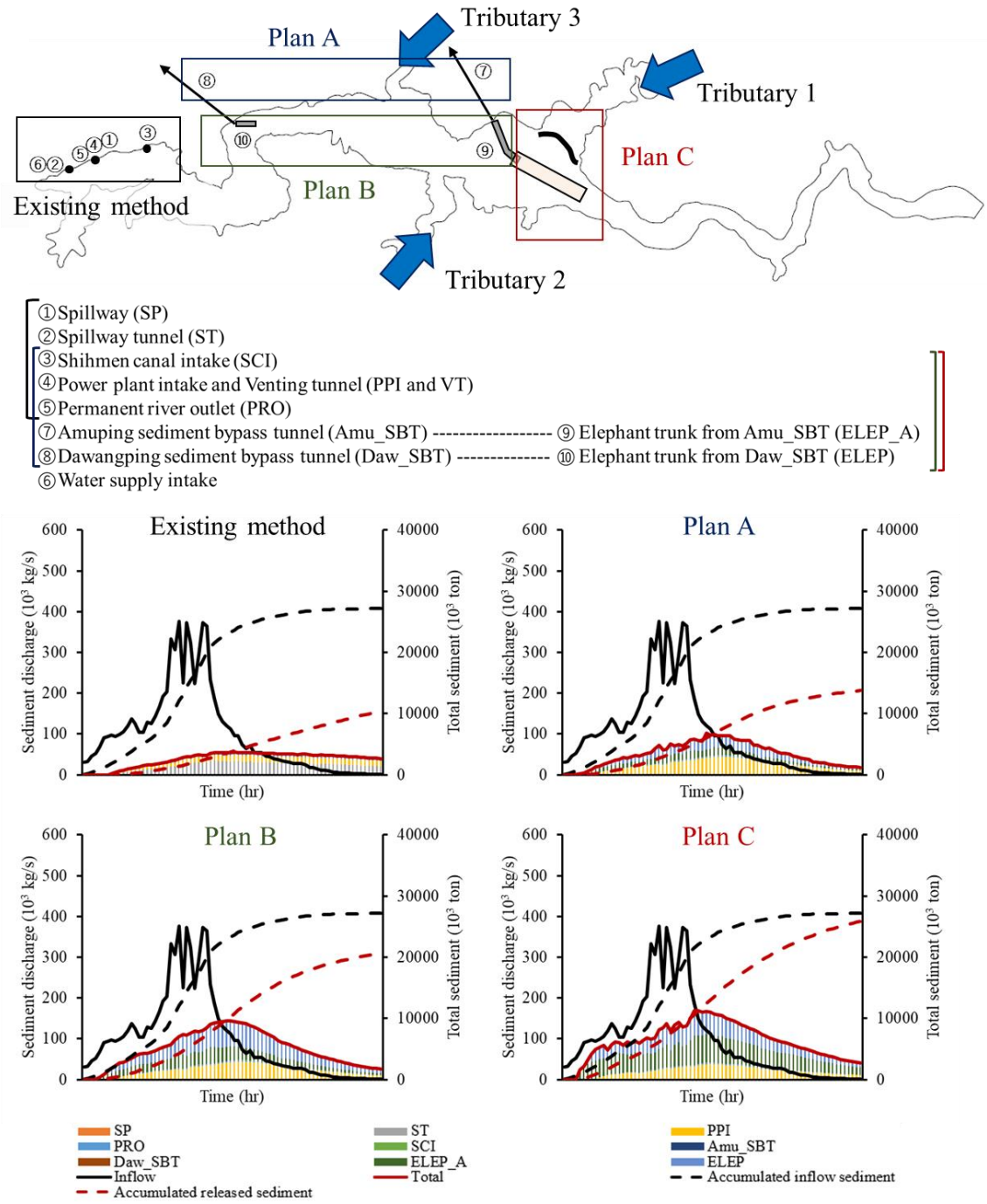

Figure 1.3 The proposed plan for solving the shortcomings of the existing method for turbidity current venting.

1.2 Research objectives

Taking into account the research was stemmed from a series of scientific questions regarding the optimization of reservoir turbidity current venting and clear water storage under multiple outlet facilities and sediment management options:

Determining the effective and reliable three-dimensional numerical modelling setup for turbidity current simulation

1. Analyze and filter the field survey data to ensure the input data quality for building the numerical model.
2. Consider the computational time and accuracy simultaneously, the applicable scope of numerical parameters is investigated.
3. Assess the feasibility of proposed dimensionless numerical model setting guidelines for different scale cases.

Understanding of the turbidity current characteristics and processes under variable flow and sediment conditions

1. Emphasize the importance of the fully three-dimensional numerical model application for investigating the flow regime and turbidity current transportation.
2. Investigate the governing terms for turbidity current processes. How to evaluate the turbidity current plunging location? Why is the vertical profile of sediment concentration and velocity essential for transporting estimation? When are turbidity current arrival time at the dam and muddy lake reach time at water supply facilities under different hydrological conditions?
3. Evaluate the shortcomings of the existing venting methods and figure out the potential improving methods.
4. Assess the impact of deficient observations from tributaries and active deposition on turbidity current simulation.

Investigating the impacts of sediment management options on efficiency of turbidity current venting

1. How to determine the optimal turbidity current venting operation from multiple outlets?
2. Why do operating timing impact turbidity current venting efficiency and clear water resources?
3. Could blockade structures avoid the turbidity current spread flow into the tributaries?
4. Evaluate the application of extended pipe from SBTs for attracting turbidity current to effectively vent through outlets.
5. How is the efficiency of the dredging channel for guiding and concentrating the turbidity current vent through the extended pipe from SBTs?

Assessing the turbidity current venting and reservoir storage in future

1. Investigate the improvement of the turbidity current venting efficiency by adopting the proposed soft methods.
2. Evaluate the necessities and efficiency of the proposed engineering methods.
3. Estimate the reservoir usage life extension by adopting the proposed improving methods.

1.3 Thesis structure

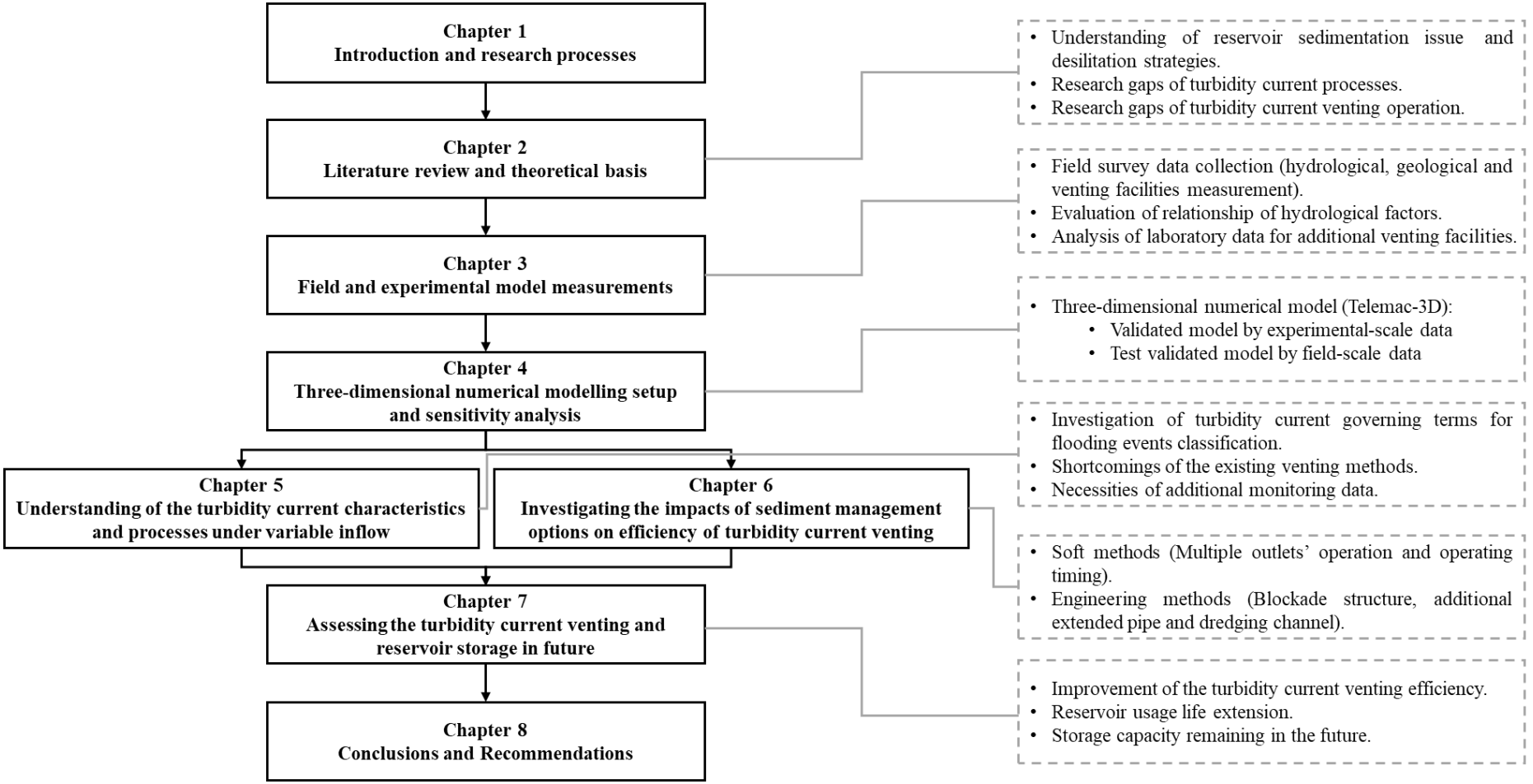

Figure 1.4 Overview of the research structure and objectives.

1.4 Outline of the thesis

This thesis consists of six main components: (1) research motivation, objectives and processes (chapter 1), and theoretical background understanding through literature review (chapter 2); (2) Measurement and monitoring data analysis (chapter 3); (3) three-dimensional numerical model simulation and turbidity current characteristics understanding (chapter 4 and 5); (4) optimal scenario for improving the water resources management (chapter 6); (5) The application of proposed improving methods for reservoir management (chapter 7), and (6) conclusions and recommendations (chapter 8). This research is divided into eight chapters summarized as follows:

Chapter 1 presents a brief introduction about the importance of reservoir desiltation to clear water storage and prolong the reservoirs' usage life. How to adopt suitable desilting techniques in a specific reservoir? What is the missing knowledge for reservoir water resource management? To fill the research gap, the necessity and objectives of this research are addressed in this chapter. The overall research structure and processes are shown in chapter 1.

Chapter 2 describes the essential background of the reservoir sedimentation issue and desilting methods. What is the suitable desilting technique by analyzing the advantages and disadvantages of each approach? Understanding the turbidity current characteristics and process is essential for investigating the optimal turbidity current venting operation. The necessity of the fully three-dimensional numerical model for a comprehensive assessment of turbidity current process within in reservoir is explored in this chapter.

Chapter 3 introduces the background of Shihmen Reservoir and the 1/100 down-scaling distorted Shihmen Reservoir physical model. This chapter shows and analyzes the details of the measured rainfall and hydrological data from measuring facilities within the

reservoir. Based on historical measurements, the relationship between each hydrological factor is evaluated and considered helpful information for the missing data addendum and future flooding events prediction. Also, the efficiency of the additional sediment bypass tunnels is assessed by analyzing the laboratory data.

Chapter 4 describes the background of Telemac-3D and Gaia, including the governing equations, applicable scope, and influential points for turbidity current simulation. This chapter addresses the importance of comprehensive sensitivity analysis. The influence of various numerical parameters and equations that involve the sensitivity testing processes are quantified by considering the computational time and accuracy. The general numerical modeling setup is regarded as a good reference for experience- and field-scale model settings. The results of the determined numerical parameters are capable of simulating to understand the turbidity current process and investigate the efficient scenario for increasing the turbidity current venting efficiency.

Chapter 5 analyzes the turbidity current process, including plunging mechanism, flow regime near plunging location, the thickness of turbidity current body and head, transport velocity, transporting process from plunging location to the dam, and the muddy lake formed. Based on the previous understanding, the shortcomings of the existing venting methods are investigated in this chapter. Moreover, the necessity of additional measurements to monitor the inflow from tributaries and the sediment material of the active deposition for solving the limitation of field-scale simulation is evaluated.

Chapter 6 proposes the various improving methods for increasing the turbidity current venting efficiency based on the shortcomings of the existing method. The optimal venting operation from multiple outlets, gate operating timing, and additional venting facilities and constructures is adopted to estimate the reservoir usage life extension.

Chapter 7 assesses the feasibility of proposed improving methods for future flooding

events. How is the efficiency of the proposed soft and engineering methods for turbidity current venting? Considering the balance between economic benefits and the improvement of additional constructures, the necessity of the proposed engineering methods is evaluated. Finally, the estimation of the reservoir usage life extension by adopting the proposed improving methods is the central core of this study.

Chapter 8 summarizes new findings and understanding of the reservoir's turbidity current process and proposes a new conception for maximum turbidity current venting efficiency. It also draws critical recommendations to prolong the reservoir usage life by adopting an appropriate improving method for reservoir managers.

Chapter 2: Literature review and theoretical basis

2.1 Suitable desilting methods for reservoir sedimentation removal

2.1.1 Historical alteration of reservoir sedimentation

With global concerns over water resources, the United Nations proposed sustainable development goal 6 to ensure water availability and sustainable management. Although three-fourths of the Earth is covered with water (1386 million km^3), only around 1/15000 of the total water (93,100 km^3) is available for people's daily use (Shiklomanov, 1993). For sustainable development of water resources, reservoirs provide a large portion of freshwater. The reservoir storage capacity is crucial for multiple purposes such as irrigation, power generation, water supply, and flood control. However, dams interrupt the natural continuity of sediment transport through rivers, which results in sediment deposition in the reservoir behind the dam (Kondolf et al., 2014). The reservoir sedimentation reduces the reservoir storage capacity (Alemu, 2016; Lai & Shen, 1996; Oehy & Schleiss, 2007; Pandey et al., 2016) and the capacity for flooding regulation which is crucial for assuring the reservoir functions of multiple purposes (Schleiss & De Cesare, 2010; White, 2001).

The majority of reservoir sedimentation researches has been investigated since 1980 (De Cesare & Lafitte, 2007). According to the available worldwide survey data, the global reservoir storage capacity loss rate was estimated at 0.5 to 1% (ICOLD, 2009; Mahmood, 1987; Wisser et al., 2013). The averaged sedimentation rates in the worldwide reservoir are listed in Table 2.1. Due to the variability of hydrological conditions and basin geological, the discrepancy of annual sedimentation from 1987 (0.22%) to 2009 (0.36%) could vary with sediment yield and desiltation strategies. According to the survey data of global reservoirs, 0.94% of the worldwide reservoir storage capacity is lost annually due

to sedimentation (ICOLD, 2009). It causes the estimated usage life of existing reservoirs to be only around 30 to 40 years (Schleiss et al., 2016). Overall, reservoir storage capacity preservation is an urgent task for sustainable water resources worldwide.

Table 2.1 The annual sedimentation for reservoirs in different regions.

Continent	Region	Annual sedimentation (%)	Source
Australia and Oceania		0.94	
Europe*		0.73	
Middle East		1.02	Basson, 2009
South America		0.75	
Central America		0.74	
North America		0.68	
	USA	0.22	Crowder, 1987
Africa		0.85	Basson, 2009
	Zimbabwe	0.5	Van den Wall Bake, 1986
	Morocco	0.7	Abdelhadi, 1995
	Tunisia	2.3	Abdelhadi, 1995
Asia		0.79	Basson, 2009
	Turkey	1.2	Gogus & Yalcinkaya, 1992
	India	1.41	Patra et al., 2019
	China	2.3	Morris & Fan, 1998
	Taiwan	**0.87**	WRA, Taiwan, 2018

*Note: including Russia

Dadson et al. (2003) demonstrated that Taiwan supplies abundant suspended sediment into the ocean, around 1.9% of the world's total, from only 0.024% of the world's land area. Ample reasons for intense monsoon and typhoon rains and frequent earthquakes lead to rapid sedimentation rates in Taiwan's reservoir, the highest in the world. With its high sediment yield, about one-third of the total reservoir capacity from 61 major reservoirs, impounded 2.2 billion m^3 freshwater, is occupied by sediment depositions. Due to its high sediment yields, the efficient management of various desiltation strategies associated with Taiwan's reservoirs is essential (Wang et al., 2018). Also, Kondolf et al. (2014) revealed the influence of with and without sediment management on reservoir sedimentation (Figure 2.1).

Although the annual rainfall in Taiwan is around 2510 mm/year, most of them bring from monsoon and typhoons, which means rainfall is concentrated from May to September. Due to the high wet-dry season rainfall ratio (1.5 and 9 in northern and southern Taiwan, respectively), the large reservoir storage capacity is crucial to store water resources for the dry season using as much as possible. In addition, as climate changes and extreme hydro-meteorological events increase, sustainable water resources from reservoirs are essential not only for human use and agriculture but also for manufacturing and the global economy. On average, there are three to four typhoons landfall Taiwan per year. However, 2020 is an unusual year under which no typhoon hits Taiwan, and monsoon rainfall is also lower than average. That has plunged into Taiwan's worst drought in 56 years. It caused the global electronics sector to be intense due to the 90% of the advanced microchips are manufactured by Taiwanese companies. Overall, integrated the reservoir storage capacity decrease and rainfall uncertainty increase, implementation of effective sediment management has become a contemporary problem to solve.

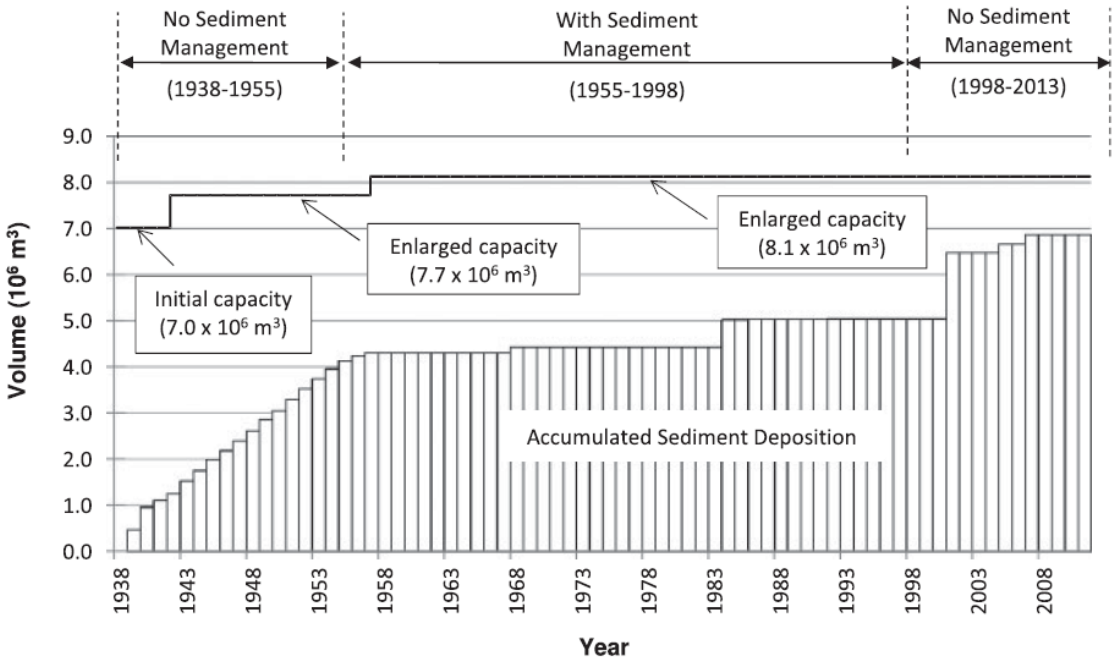

Figure 2.1 Deposition within Jen-San-Pei reservoir in Taiwan with and without sediment management (Kondolf et al., 2014).

2.1.2 Hydraulic desiltation and mechanical removal strategies

Efficient water and soil conservation and desilting management from upstream catchment to downstream of a reservoir are essential for sustainable reservoirs. As illustrated in Figure 2.2, integrated sediment management strategies have been applied to existing reservoirs. Reducing sediment inflow, minimizing and removing deposition are three main categories for recovering the reservoir storage capacities. Due to most of Taiwan's reservoir catchment tectonically shattered geology, steep terrain, frequent earthquakes, and intense rainfall, severe erosion and landslide inevitably occur and flow into the reservoir. Therefore, researchers and engineers pay more attention to minimizing the reservoir sedimentation and maximizing the desilting ratio. To mitigate the sediment deposition and prolong the reservoir life, various desilting strategies, including hydraulic desiltation and mechanical removal, have been implemented (Kondolf et al., 2014):

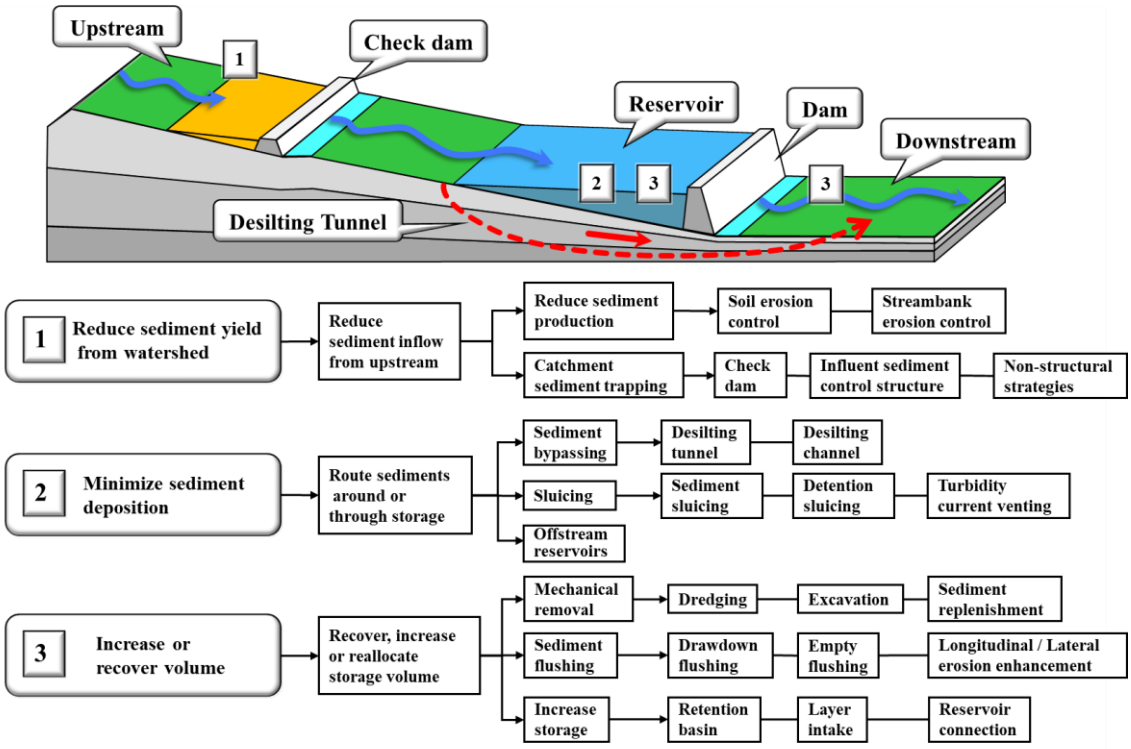

Figure 2.2 List of integrated reservoir desiltation strategies. (WRA, Taiwan, 2020)

A. Sediment bypassing

Sediment bypass tunnels (SBTs) within the middle of the reservoir advantage to divert part of the incoming sediment-laden waters (Figure 2.3). The sediment bypassing approach suites mountain reservoirs by contributing to prolonging reservoir life and downstream river restoration (Sumi et al., 2015).

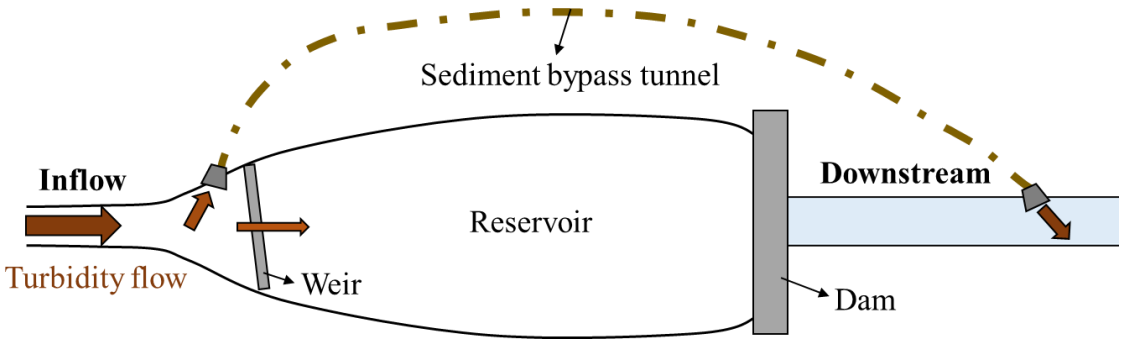

Figure 2.3 Concept diagram of sediment bypassing.

B. Sediment sluicing

The concept of the sluicing strategy is permitting sediment to be transported through the dam structures with outlets operation during high inflows to the reservoirs (Figure 2.4). The sluicing approach is beneficial for keeping natural continuous fine sediment transportation and minimizing the reservoir's deposition.

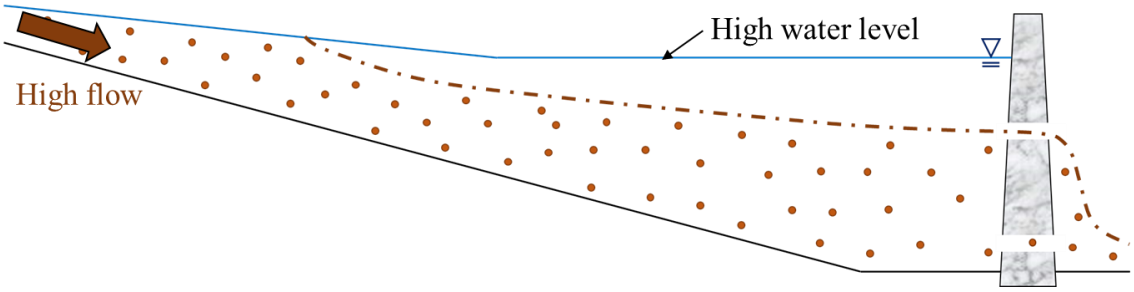

Figure 2.4 Concept diagram of sediment sluicing

C. Turbidity current venting

Similar to the sediment sluicing approach, but turbidity current venting approach requires a reservoir with bottom venting facilities and sufficient velocity and turbulence for turbidity current traveling to the dam (Figure 2.5). Advantages of turbidity current venting are that the suspended sediment delivers downstream without drawdown water level and can release half of the inflowing sediment load (Morris and Fan, 1998).

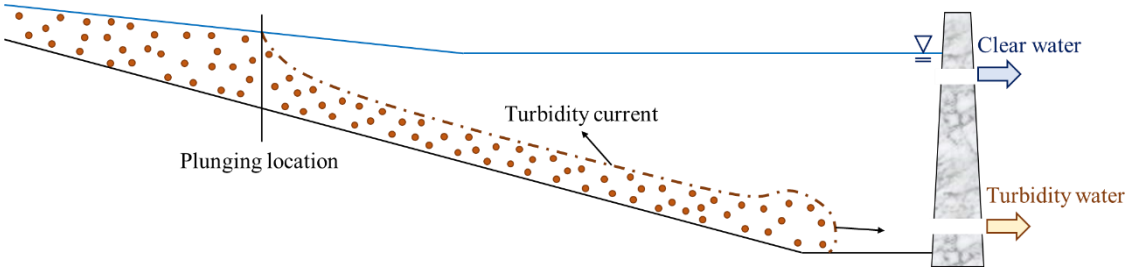

Figure 2.5 Concept diagram of sediment sluicing

D. Sediment flushing

In contrast to the sluicing approach, the flushing approach benefits scouring and re-suspending sedimentation under the drawdown water level. With continuously lowering water level until river-like flow conditions, the increasing flow velocity and bed shear stress lead to agitating the sedimentation within the reservoir and freely passing through the bottom outlets. (Figure 2.6).

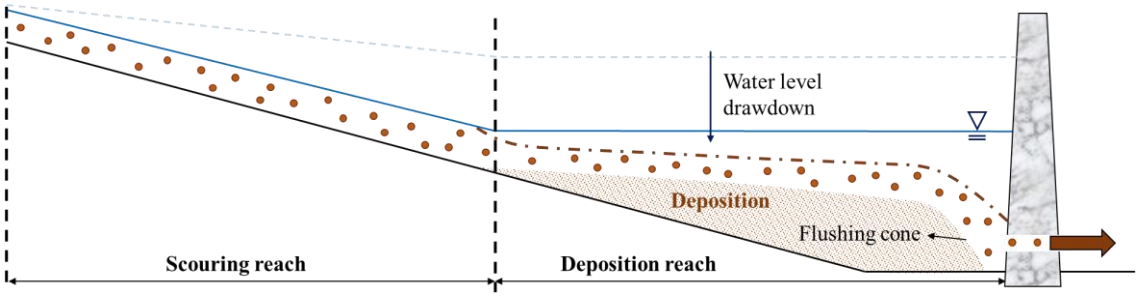

Figure 2.6 Concept diagram of sediment flushing

E. Dredging and mechanical removal

To remove the sediment from a specific area near the power plant and water supply intake, the dredging approach by suction using hydraulic pumps is applied (Figure 2.7). Moreover, the mechanical removal approach could be implemented by using scrapers and dump trucks to remove accumulated sediments in the completely drawn-down areas. Though these techniques are costly and inefficient, they provide continuous reservoir sedimentation removal.

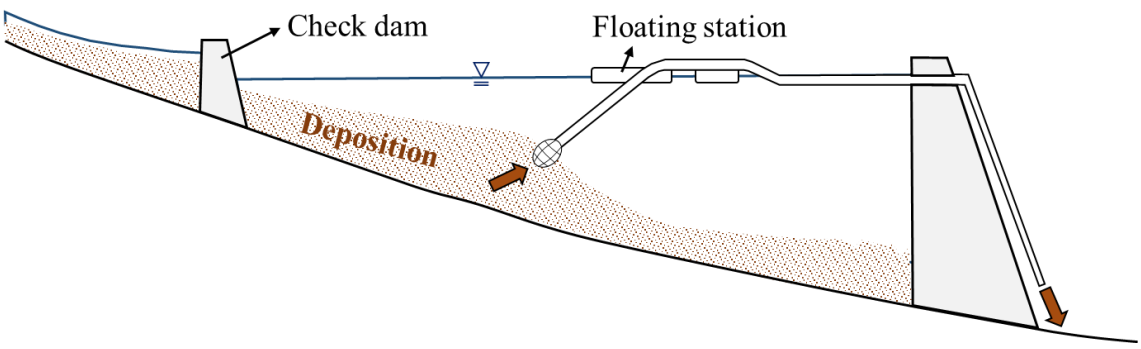

Figure 2.7 Concept diagram of dredging and mechanical removal

2.1.3 Importance and advantage of turbidity current venting

Assessment of the suitable desilting techniques in a specific reservoir is crucial. Basson (1997) indicated that the relationship between the capacity-inflow ratio (CIR), reservoir capacity (CAP) divided by mean annual runoff (MAR), and capacity-sediment ration (CSR), CAP divided by mean annual sediment (MAS), is essential for analyzing the appropriate desilting approach. Based on two critical indexes (CIR and CSR) and sediment management experience, sluicing, turbidity current venting, and sediment bypassing are suitable desilting techniques for the major reservoirs in Taiwan (Figure 2.8). Among them, due to the turbidity current venting has the ability to release half of the inflowing sediment load and deliver suspended sediment without drawdown water level (Morris and Fan, 1998), the turbidity current venting is gaining more importance for low-cost sediment desilting.

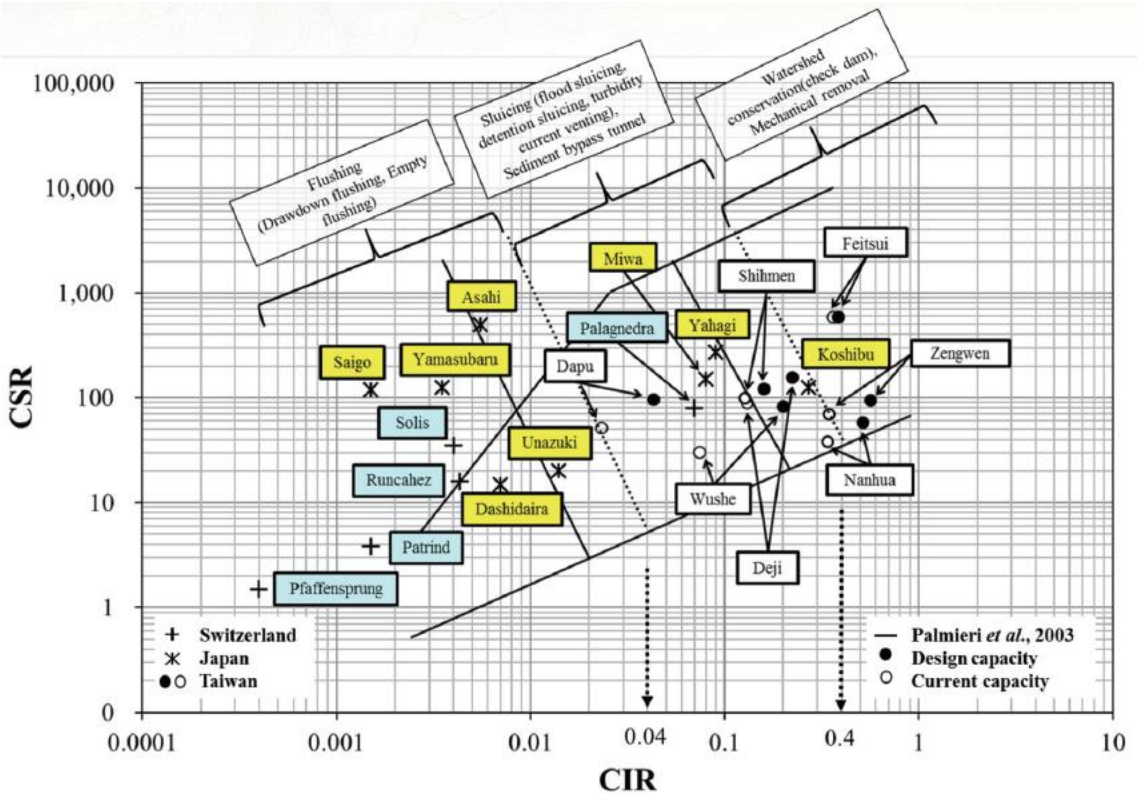

Figure 2.8 Cluster of reservoir desilting techniques based on CSR and CIR (WRA, Taiwan, 2020).

2.2 Turbidity current characteristics and processes

The studies on turbidity current have been researched for more than 60 years. Numerous studies have addressed the dynamics and formation of turbidity currents (Altinakar et al., 1996; Ashida & Egashira, 1975; Ellison & Turner, 1959; Mulder et al., 1997). The turbidity current transport processes have been well known and could be divided into three research-worthy parts: (1) plunging phenomenon, (2) body structure, and (3) venting operation (Figure 2.9).

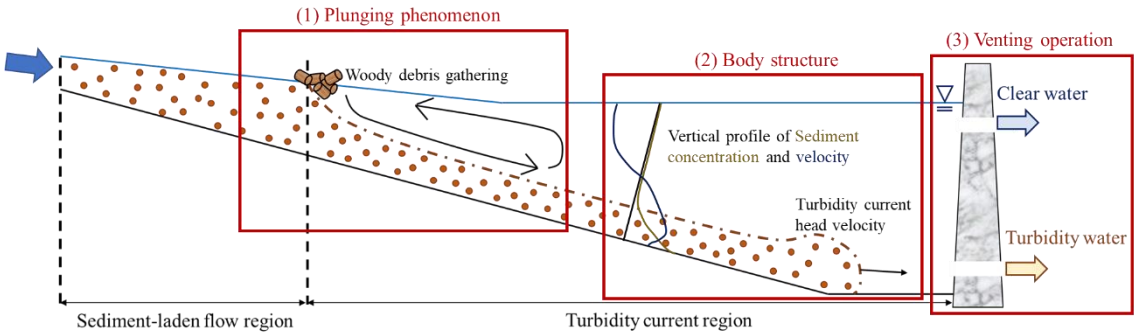

Figure 2.9 Prior researches were investigating turbidity current characteristics.

2.2.1 Turbidity current plunging mechanism and flow regime

Based on the field survey and laboratory measurements of turbidity current processes, the sediment-laden flow plunges and concentrates to turbidity current under certain conditions related to flow velocity, water depth, and differential fluid density (Graf, 1983). The densimetric Froude number has been identified as a critical characteristic for the turbidity current plunging location (Fan, 1960; Jain, 1981; Wunderlich & Elder, 1973). Parker & Toniolo (2007) proposed that the single parameter characterizes, which considers the densimetric Froude number before and after plunging, investigate the turbidity current venting location. Using the two-control-volume theory, the plunging flow and clarifies the plunging condition could be more general circumstances (Dai & Garcia, 2009). Based on measurements from flume and field, the range of densimetric

Froude number for turbidity current plunging was investigated (Table 2.2).

As illustrated in Figure 2.10, the flow regimes before and after turbidity current plunging were different. Due to the turbidity current plunging, the circulation occurred at the surface ambient water area, and the water temperature has high related to turbidity current pattern (Bournet et al., 1999; Farrell & Stefan, 1986). Based on this phenomenon, the plunging location could be observed by flow direction, watercolor, and woody debris gathering area.

Table 2.2 Prior researches investigating the plunging densimetric Froude number

Authors	Year	Plunging densimetric Froude number
Singh & Shah	1971	0.3-0.8
Savage & Brimberg	1975	0.3-0.8
Hebbert et al.	1979	0.18-0.26
Itakura & Kishi	1980	0.54-0.69
Ford & Johnson	1981	0.1-0.7
Fukuoka et al.	1980	0.37-0.68
Akiyama & Stefan	1984	0.1-0.55
Farrell & Stefan	1986	0.69
Lee & Yu	1997	0.6-0.1
Chen	2017	0.36-0.76
Lee et al.	2017	0.45-0.1
Chang et al.	2020	0.34-0.67

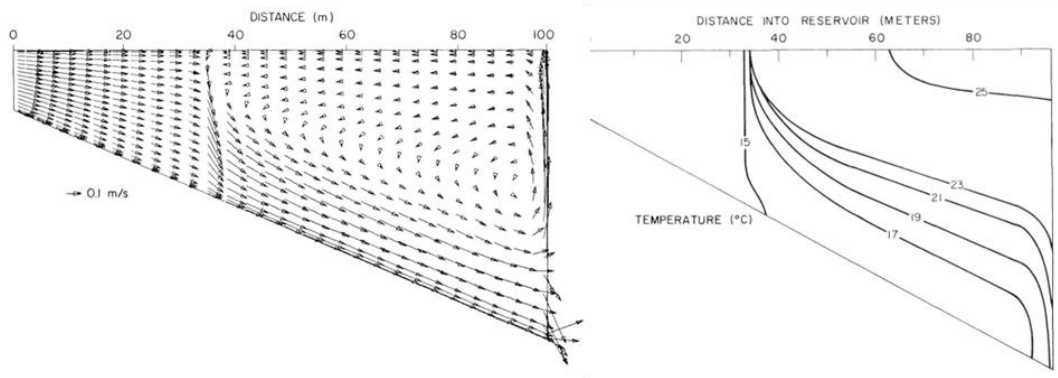

Figure 2.10 Reservoir flow pattern after plunging (Farrell & Stefan, 1986).

2.2.2 Turbidity current body structure and head velocity

It is difficult to measure the turbidity current body during flooding events. Understanding the flow regime and turbidity current transportation within Shihmen Reservoir was useful for making operating decisions. The general characteristics of the velocity profiles (Altinakar et al., 1996; Kneller & Buckee, 2000; Kneller et al., 1999) and sediment concentration profiles (Altinakar et al., 1996; Garcia, 1994; Kneller & Buckee, 2000) have been described. Hosseini et al. (2006) established the near-Gaussian and empirical power relation equations to successfully estimate the velocity and sediment concentration profiles. It could help understand the flow regime in turbidity current and assess the turbidity current characteristics, including thickness, head velocity, and sediment distribution.

Turner (1979) proposed the turbidity current head velocity equation under quasi-uniform width flume without considering the effects of bottom friction and the mixing process. Chang et al. (2020) demonstrated that the turbidity current head velocity is related to a water depth of plunging location, turbidity current thickness, and density of turbidity current flow. Therefore, integration of vertical sediment concentration and velocity profile, and turbidity current head velocity equation could effectively estimate the turbidity current travel time.

2.2.3 Investigation of efficient turbidity current venting operation

Based on a good understanding of the dynamics of the turbidity current, the adequate outlet's operation could be evaluated and brings a tremendous amount of turbidity current venting. Though the data of the turbidity current released from the reservoir was recorded in 1919 at the Elephant Butte Reservoir (Lee et al., 2014), the systematical application still does not exist yet. To increase the turbidity current venting efficiency, Basson (1997)

mentioned that the outflow discharge, venting timing, outlet height, morphological and topographical are the main parameters for affecting venting efficiency:

A. Outflow discharge

The measurements of turbidity current venting within the reservoir showed decreased turbidity current venting efficiency with increasing reservoir length and decreasing ratio of outflow to inflow discharge (Morris & Fan, 1998). Yu et al. (2004) presented that the outflow sediment concentration could be estimated by simple mass conservation when inflow and outflow discharge are the same values. However, Lee et al. (2014) demonstrated that applying the half value of inflow discharge instead of the same value for outflow discharge could increase the turbidity current venting efficiency at the bottom outlet from 0.49 to 0.6. Overall, the capacity of outlets plays a critical role in optimizing the turbidity current venting.

B. Turbidity current venting operating timing

The outlets' operating timing is essential to increase the venting efficiency and reduce the water resources waste (Annandale, 1987). The late operation caused small amounts of sediments to be released, and a muddy lake was easily formed. In contrast, the early operation will lose valuable water (Chamoun et al., 2016). Chamoun et al. (2018) revealed that the slightly early operation to make sure the evacuation is synchronized with the turbidity current arrival at the outlets was the optimal operating timing on the efficiency of turbidity current venting. Moreover, Wan et al. (2010) demonstrated that the correct operating timing could save 7.31% water resources and increase 8.77% sediment releasing in the Sanmenxia Reservoir. Therefore, the outlets' operating timing is the critical parameter to be determined in this study.

C. Outlet height

The height of outlets is the critical factor in terms of turbidity current venting. As illustrated in Figure 2.11, the outlets' sediment releasing ability directly links to the limit of height of aspiration. Based on the height aspiration concept, the bottom outlets, where includes all of the turbidity currents, always bring the high venting efficiency. The results of Lee et al. (2014) revealed that compared to the middle outlet, the bottom outlet's outflow sediment concentration is approximately 4.5 times higher. Overall, the appropriate location of outlets is essential to increase the turbidity current venting efficiency and reduce the clear water waste.

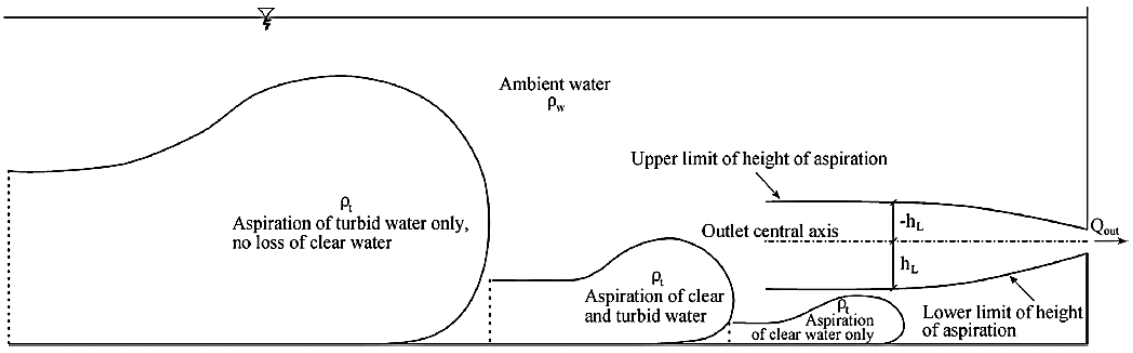

Figure 2.11 Concept of the height of aspiration principal (Chamoun et al., 2016).

To investigate the optimal turbidity current venting operation, the field measurements could be challenging given the flood conditions in which turbidity currents occur, and venting is performed (Morris and Fan 1998, Lee et al., 2014). The experimental models were widely used to study turbidity current venting (Chamoun et al., 2018; Lee et al., 2014; Perez, 2010). To avoid the scale effects and keep flexibility for investigating different scenarios, many researchers opted for the numerical modeling in the past to study venting in reservoirs (Amini et al., 2017; Chamoun et al., 2018; Esmaeili et al., 2017; Huang et al., 2019; Lee et al., 2014; Perez, 2010).

2.3 Numerical studies

The possibility of reducing the deposition and removing the sedimentation increases the turbidity current venting efficiency. However, the physical and numerical models have been strong tools for turbidity current simulation due to the complex mechanisms. When it comes to case studies, numerical models are the most appropriate tool, avoiding scale effects and providing numerous results, enhancing the understanding of the process (Amini et al., 2017).

2.3.1 One-dimensional numerical model

The unstable condition of sediment transportation could be reflected by using the one-dimensional numerical model for bed and suspended loads separately. The HEC-RAS, SRH-1D, and NETSTARS are commonly used one-dimensional hydraulic and sediment transport models. The HEC-RAS, free and easy to run, was used to simulate the sediment flushing in the Kabeli Reservoir in Nepal (Maskey & Ruther, 2019). The NETSTARS model was developed by Lee in 1997 and is widely utilized for one-dimensional sediment transportation simulation in Taiwan. Lee (2018) applied the NETSTARS for longitudinal bed changes simulation in the Shihmen Reservoir after the typhoon event. However, due to the oversimplified assumption, the one-dimensional numerical models do not apply to meandering channels, and they cannot reflect the horizontal and vertical concentration and velocity distributions. Moreover, the variations of the sediment concentration of turbidity current were unavailable to simulate due to the depth-averaged values are used in one-dimensional numerical models.

2.3.2 Two-dimensional numerical model

To consider more complicated hydraulic aspects, including unsteady flow, backflow and bend flow, and sediment transportation aspect, involved migration pattern of sediment and non-uniform sedimentation, the two- and three-dimensional numerical models are appropriated to be applied for turbidity current simulation. However, two-dimensional numerical models are more developed and feasible than three-dimensional, and the computational time is unrestricted. Due to the relatively short computational time, two-dimensional numerical models are suitable for long-term predictions of variations in reservoirs. The two-dimensional numerical models could be divided into (1) horizontal models: they can provide lateral distributions of flow regime and sediment transportation but lack vertical profile information, and (2) vertical models: in contrast to horizontal and gives good contributions on vertical flow and concentration distributions.

Amini et al. (2014) investigated the Peruvian Reservoir's (Peru) sedimentation, complete drawdown flushing, and sediment concentration in power intakes by comparing the one-dimensional, horizontal and vertical two-dimensional numerical models. Numerous two-dimensional simulation studies for Taiwan's reservoirs have existed. Hung et al. (2009) developed the unsteady two-dimensional depth-averaged model for simulating the nonequilibrium sediment transportation and showed its applicability to assess the desilting efficiency for the Agongdian Reservoir. The SRH-2D was applied to simulate the turbidity current transportation in the Shihmen Reservoir during typhoon events (Huang et al., 2019). The midstream simulations could provide valuable information to machine learning techniques for real-time forecasting (Huang et al., 2021).

2.3.3 Three-dimensional numerical model

Due to the two-dimensional models still cannot represent the x-, y- and z-directional flow field and trends of turbidity flow, the three-dimensional numerical models, including ANSYS-CFX, FLOW-3D, Delft-3D, SSIM-3D, and Telemac-3D, was considered to grasp the complex flow regime and sediment migration behavior effectively. The SSIM-3D was utilized to simulate the sediment flushing efficiency of Dashidaira Reservoir (Esmaeili et al., 2017) and Unazuki Reservoir (Esmaeili et al., 2018) in Japan. The ANSYS-CFX and FLOW-3D are the most commonly used commercial software to solve the hydraulic engineering problems in Taiwan. Lee et al. (2014) applied the ANSYS-CFX for evaluating the turbidity current venting efficiency in the Zengwen Reservoir. Sixth District Management Office (2017) revealed that the application of FLOW-3D provides valuable solutions for turbidity current plunging location, vertical profile of sediment concentration, turbidity current movement, and muddy lake generation simulations. Based on the literature review, the three-dimensional numerical model was considered the appropriate tool to understand better the turbidity current physical phenomenon, including plunging, transportation, and venting mechanism.

2.3.4 Turbidity current simulation by using three-dimensional numerical model

As illustrated in Table 2.3, various researchers opted for numerical modeling in the past to study turbidity issues in reservoirs. Moreover, three-dimensional numerical modelling allows in-depth analysis of the turbidity current characteristics and processes in multiple outlets operation from different elevations. Based on the literature review, we found that various studies selected commercial software, especially ANSYS-CFX, to simulate turbidity current. Due to the ANSYS-CFX being considered the robust, reliable, and user-friendly numerical model, many researchers used it to study turbidity current

transportation and venting simulation. Amini et al. (2017) indicate that outlet opening timing and discharge, optimizing venting operations, allows venting the more significant number of sediments while minimizing the water release. De Cesare et al. (2001, 2006) used ANSYS-CFX for simulating turbidity current movement at Luzzone Reservoir and Lake Lugano. Oehy & Schleiss (2007) employed an ANSYS-CFX to simulate the effects of solid and permeable obstacles in the turbidity current movement.

Jodeau et al. (2018) reveal that the ANSYS-CFX and Telemac-3D are both in good agreement. However, Telemac-3D is open source and can be easily modified, and allows to add the additional formula and module. Pérez-Díaz et al. (2019) simulate the density current in the coastal area with Telemac-3D and reveal that the comprehensive sensitivity analysis is crucial to determine the optimal model setting. Peteuil et al. (2018) show that Telemac-1D, -2D, and -3D can accurately simulate sediment transport (and the evolution of sediment deposits) in reservoirs for various processes and configurations. Based on the reviews mentioned above, the Telemac-3D was considered the appropriate model for turbidity current simulation in this study.

Table 2.3 Summarizes the prior research on turbidity current using a three-dimensional numerical model.

Author	Year	Numerical model	Model type	Study area	Objective
Heimsund et al.	2002	FLOW-3D	Commercial	Flume	TC
Janocko et al.	2013	FLOW-3D	Commercial	Flume	TC
Lai & Wu	2019	SRH-3D	Not released yet	Flume	TC
Perez	2010	SSIM-3D	Open-source	Flume	TC
Haun et al.	2013	SSIM-3D	Open-source	Angostura reservoir	TC
Ota et al.	2017	OpenFOAM	Open-source	Experiment	TC
Amini et al.	2017	ANASYS-CFX	Commercial	Rudbar-Lorestan reservoir	TC
Lee et al.	2014	ANASYS-CFX	Commercial	Zengwen reservoir	TC
De Cesare et al.	2006	ANASYS-CFX	Commercial	Lake Lugano	TC
De Cesare et al.	2001	ANASYS-CFX	Commercial	Luzzone reservoir	TC
Jodeau et al.	2018	ANASYS-CFX Telemac-3D	Open-source Commercial	Flume	TC
Peteuil et al.	2018	Telemac-1& -2& -3D	Open-source	St Egrève reservoir, Kapichira reservoir& Longefan reservoir	TC
Pérez-Díaz et al.	2019	Telemac-3D	Open-source	Flume	DC

*Note: TC means turbidity current; DC means density current.

2.4 Research gaps

The comprehensive reviews found that turbidity current venting is the suitable desilting method for the Shihmen Reservoir. To optimize the turbidity current venting operation, integrating three-dimensional simulations and the well-known dynamic and formation of turbidity currents are essential. Numerous studies have proposed various methods to increase turbidity current venting efficiency. Still, some research gaps exist:

In turbidity current understanding:

1. The systematical turbidity current venting operation still does not exist yet. How to arrange the multiple outlets' operation from different elevations?
2. The sediment bypass tunnel in the middle of the reservoir could provide a good ability to release sediment from midstream. However, no studies focus on the influence of sediment bypass tunnels operation on turbidity current arrival time at dam.
3. Numerous experiments and numerical simulations investigate the turbidity current in straight and meandering channels. However, most studies only consider the turbidity current transportation in the main channels and ignore the tributaries effect.

In numerical modelling:

1. The sensitivity analysis is essential for numerical model establishment. However, most of the studies only focus on the accuracy without considering the computational time simultaneously. The balance between computational time and accuracy is vital to the simulation of future events.
2. There are still no rules on systematical setup for three-dimensional numerical models. The reliable dimensionless numerical model setting guidelines for different scale cases will play a role in effectively building the numerical models.

Chapter 3: Field and physical model measurements

3.1 Description of Shihmen Reservoir

The Shihmen Reservoir is located in the middle reach of the Dahan River in northern Taiwan with a catchment area of 763.4 km^2 (Figure 3.1). The 133 m height embankment dam was completed in 1963. Under the normal water level of EL. 245 m, the original design storage capacity, reservoir impounding area, and water surface area are 309 million m^3, 16.5 km in length, and 8.15 km^2, respectively. Due to extensive reservoir sedimentation, almost 34% of storage capacity has been reduced. It will seriously affect the function of the multipurpose Shihmen Reservoir, which includes hydroelectric power, flooding control, water supply for people's livelihood and irrigation, and recreation.

3.1.1 Construction and facilities within Shihmen Reservoir

The locations of the rainfall stations and hydrological stations are shown in Figure 3.1. The inflow sediment concentration was measured in the Lofu hydrological station, the Shihmen Reservoir's upstream boundary. It is located at the cross section 32, named CS32 (Figure 3.1). Meanwhile, the time domain reflectometry (TDR) is adopted to detect the sediment concentration from the different levels in the reservoir. There are several water releasing facilities, including spillway (SP), spillway tunnel (ST), Shihmen canal intake (SCI), power plant intake (PPI), venting tunnel (VT), permanent river outlet (PRO), sediment bypass tunnels (SBTs) and water supply intake, for different purposes (Figure 3.1). The detailed information is expressed below:

A. Facilities at the dam site

The information of each sediment venting (PRO and VT), flooding control (SP and ST), hydroelectric power (PPI), and water supply (SCI and water supply intake) outlet is listed in Table 3.1. To increase the desilting efficiency, one of the power plant penstocks

(named VT) is modified to focus on turbidity current venting from 2013. During the typhoon events, the withdrawal of high turbidity water from low elevation outlets could not be treated by the water purification plant. Thus, the additional water supply intake with three different elevation outlets, Intake_Bot (220 m), Intake_Mid (228 m), and Intake_Top (236 m), were built to withdraw the clear water from the surface of the reservoir and maintain the supply of clear water for people's livelihood.

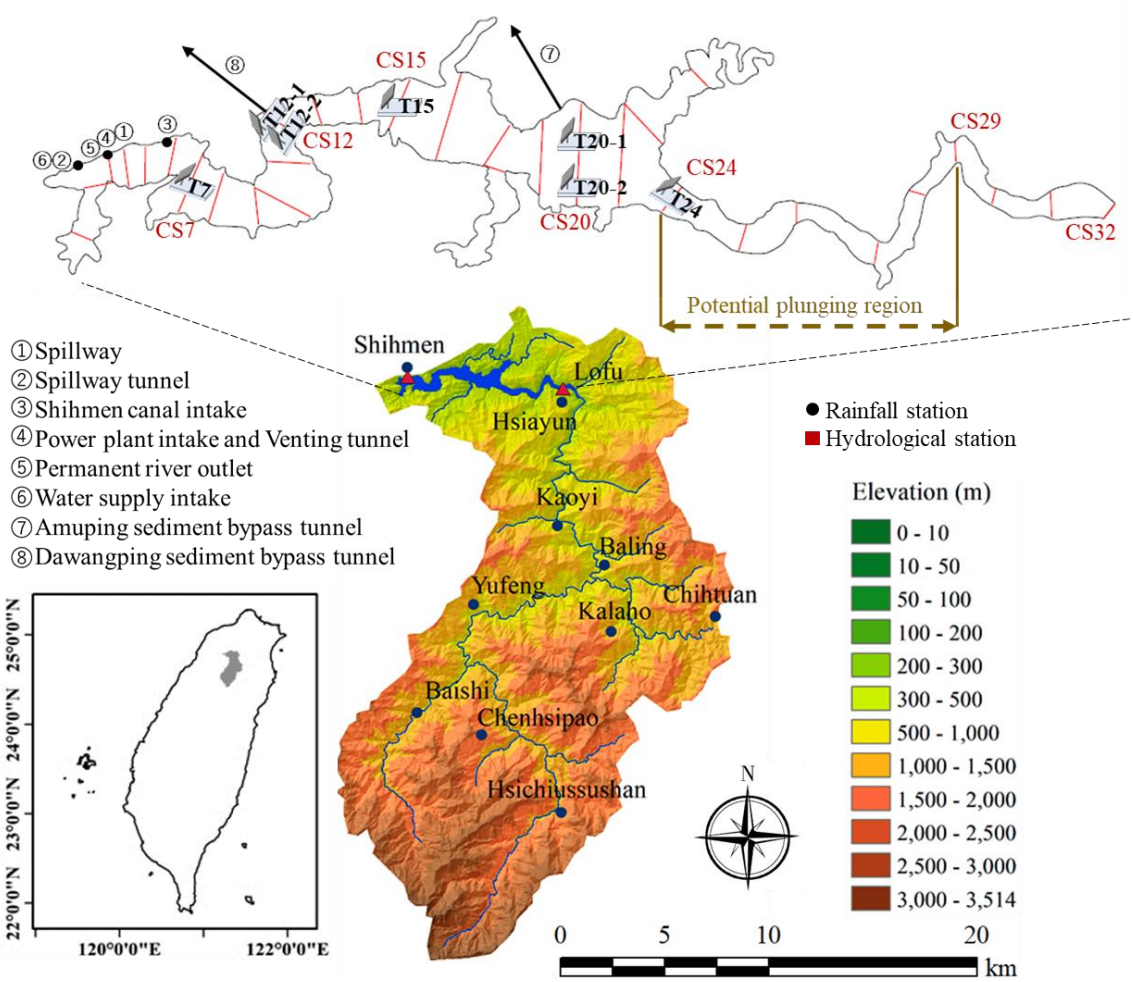

Figure 3.1 Locations of outlets, floating platform of TDR, rainfall stations and hydrological stations in the Shihmen Reservoir catchment.

Table 3.1 The information of each outlet in Shihmen Reservoir.

Outlets	Size (m)	Elevation (m)	Designed discharge (m^3/s)
Spillway	10×14	235	11400
Spillway tunnel	Φ= 9	220	2400
Shihmen canal intake	Φ= 2.5	193.5	18.4
Power plant intake	Φ= 4.5	173	68.6
Venting tunnel			300
Permanent river outlet	Φ= 1.37	169.5	34
Water supply intake	Φ= 2.5	Top: 236 Middle: 228 Bottom: 220	16.2
Amuping sediment bypass tunnel	Φ= 8	235	800
Dawangping sediment bypass tunnel	Φ= 10	220	1400

B. Facilities within reservoir

The TDR was applied to measure the sediment transportation process and vertical distribution. TDR used a similar one-dimensional radar's electromagnetic wave sensing technology. The principal concepts were analysis of the attenuation of the propagation speed and propagation constant, influenced by the permittivity and electrical conductivity in the transmission line. By analyzing a bunch of information from the reflected signal, the electric conductivity of the target object could be obtained. Due to the dielectric difference between water (80) and soil particles (3 to 8), the sediment concentration could be obtained by the travel time of the electromagnetic wave to the sensor. The lower dielectric constant leads to higher electric conductivity and shorter travel time with higher sediment concentration. Therefore, the working concept of TDR is based on the relationship between transmission time and sediment concentration. Moreover, the TDR is feasible for various grain sizes due to the electric conductivity does not be affected by the particle sizes. The TDR is a suitable automatic measuring device for high suspended sediment concentration with multiple sediment materials based on the introduction above.

As illustrated in Figure 3.1, the TDR has been established an inflow measuring location (CS32) and several reservoir measuring locations (CS24, 20, 15, 12, and 7). Due to the Amuping SBT (Amu_SBT) and Dawangping SBT (Daw_SBT) being located slightly downstream of CS20 and CS12, respectively, two TDR were established at left and right side of CS20 (TDR20-1 and TDR20-2) and CS12 (TDR12-1 and TDR12-2) for clearly understand the sediment distribution around the SBT. As illustrated in Figure 3.2, the TDR was settled on the floating platform within the reservoir. The observation pile was built at CS32. Eight TDR sensors were distributed from the water surface to the reservoir bottom to detect the vertical sediment profile.

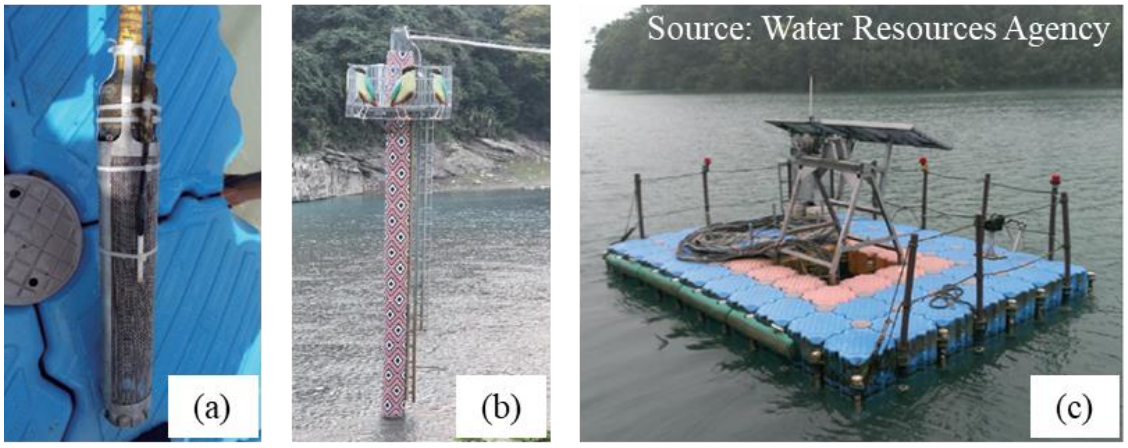

Figure 3.2 Sediment concentration measurement by using (a) TDR sensor was settled on the (b) observation pile at Lofu station and (c) floating platform at the middle of the Shihmen Reservoir.

C. Planned and under constructed facilities

To determine the optimal constructing project of the SBTs, the balance between geological topography, engineering funds, construction period, and desilting efficiency was evaluated. Water Resources Planning Institute proposed a preliminary project planning of various schemes, including cases A1, A2, B, C1, C2, D1, and D2 (Figure 3.3). Based on the field investigation and physical model simulation, the feasible schemes selected cases A2, C1, and D2. With the careful consideration of entrance, route, topography, geomorphology, geology, length of each SBT, the Daw_SBT (case C1) and Amu_SBT (case D2) are under construction. The details of the physical model construction and comparison of desiltation schemes are discussed in **Chapter 3.2**.

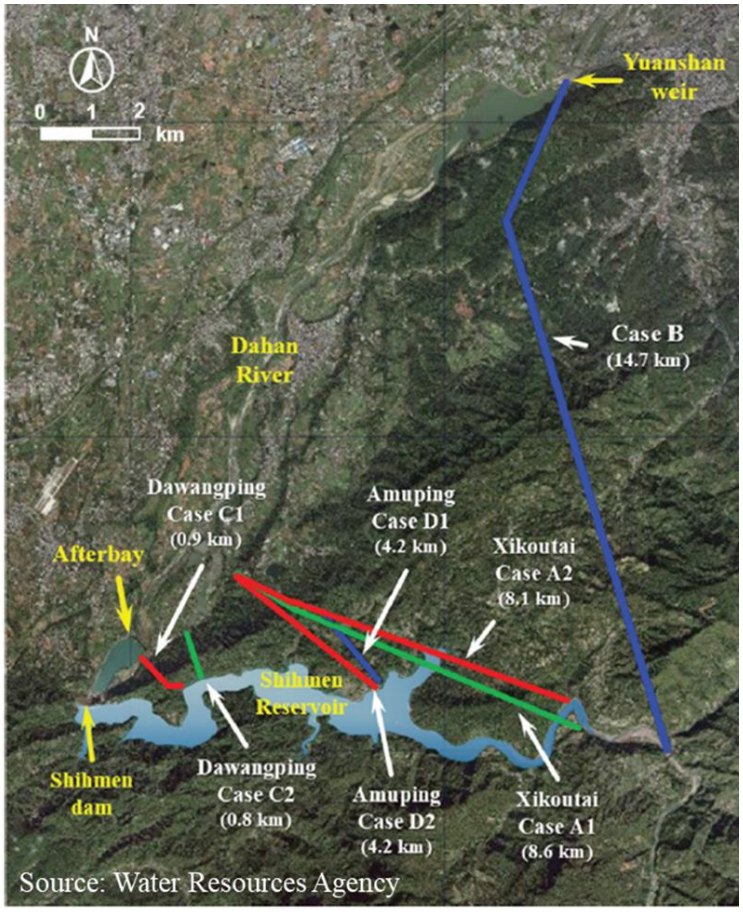

Figure 3.3 Sediment bypass tunnel planning alternatives in Shihmen Reservoir.

3.1.2 Measurements data from field survey and sampling

The Shihmen Reservoir has been implemented for over 50 years. As illustrated in Figure 3.4 and Table 3.2, strong typhoon events always cause severe deposition, and 33.97% of storage capacity has been lost. The typhoons bring heavy rainfall in the mountainous catchment of the Shihmen Reservoir. It leads to the soil's drastic weakness and the massive amount of sediments, such as landslides and severe slope erosion, flow into the reservoir. As Table 3.2 showed, the trapped sediment volume from each year's Typhoon event is close to the annual deposited sediment volume. Based on the aforementioned information, effective sediment venting strategies during Typhon events are crucial. This section discusses the bed evolution and inflow sediment materials to investigate the historical alteration of reservoir geometry.

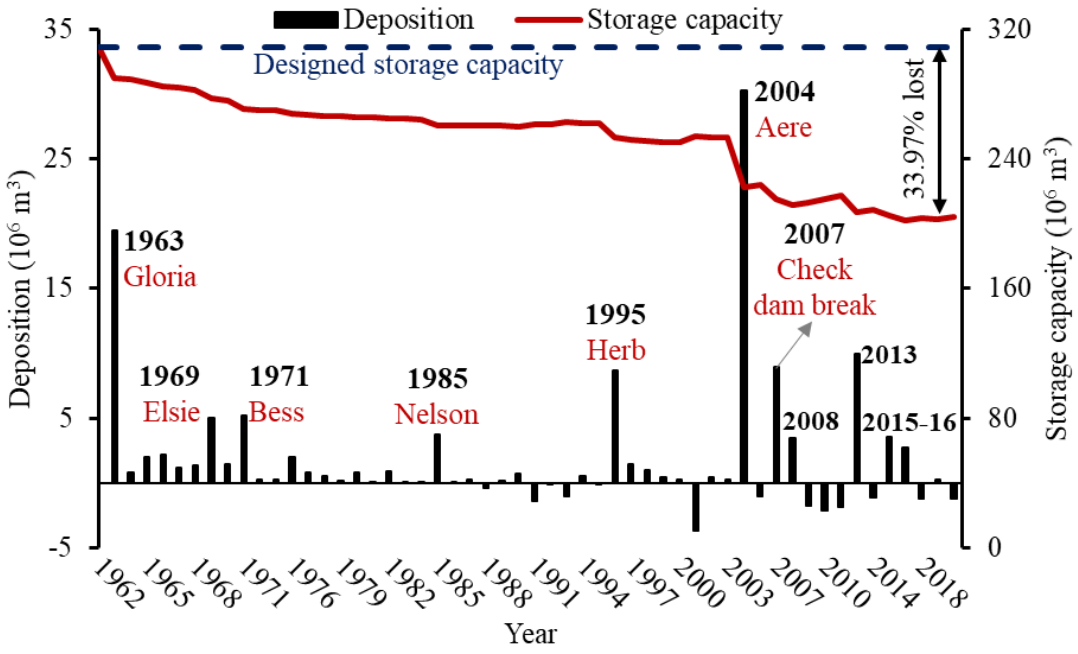

Figure 3.4 Historical alteration of deposition and reservoir storage capacity.

Table 3.2 Hydrological data in the Shihmen Reservoir from major flood typhoon events since 2004.

Event	Date	Peak inflow		Total volume			Desilting efficiency (%)	The continuous duration of inflow discharge over 300 m^3/s
		Discharge (m^3/s)	Sediment concentration (ppm)	Inflow Discharge (10^6 m^3)	Inflow sediment (10^4 ton)	Trapped sediment (10^4 ton)		
*Aere	2004/8/23	8594.0	57921	713.87	2912.00	1942.30	33.30	-
Fungwong	2008/7/26	2039.8	28235	157.15	164.70	143.74	12.73	35
Sinlaku	2008/9/11	3446.9	33270	626.38	1094.80	826.40	24.52	173
Jangmi	2008/9/26	3292.0	33195	265.79	408.60	353.90	13.39	70
Morakot	2009/8/5	1837.5	23864	227.99	184.00	158.80	13.70	84
Saola	2012/7/30	5385.1	39100	492.30	763.18	648.07	15.08	101
Soulik	2013/7/11	5457.9	94900	250.82	921.90	635.00	**31.12**	48
Trami	2013/8/20	2412.5	72594	165.31	320.50	201.30	**37.19**	44
Soudelor	2015/8/6	5634.1	18287	247.15	254.20	163.80	**35.56**	49
Dujuan	2015/9/29	3802.5	16177	188.60	184.00	122.60	**33.37**	46
Megi	2016/9/25	4268.0	23221	248.60	351.00	277.90	**20.83**	53

* Note: The hydrological data of Aere Typhoon is estimated, and the implementation of the venting tunnel started in 2013.

A. Reservoir bathymetry

For investigating the alterations in the Shihmen Reservoir bathymetry, the marine echo sounder equipment was used to measure the bed elevation. The reservoir bathymetry from 2013 to 2016 and the bed evolution from each year are shown in Figure 3.5. Because no major flood typhoon hit northern Taiwan, the sedimentation slightly decreased in 2014. Based on the comparison between 2013 and 2016, the severe sedimentation deposits at midstream and downstream of Shihmen Reservoir due to four major flood typhoon events bring a massive amount of sediment flow into the reservoir. To reveal the alteration in bed evolution, the longitudinal bed elevation is shown in Figure 3.6. The bed elevation significantly increases with increasing time, especially between 2004 and 2005. The severe deposition raised around 3.07 m bed elevation in 2004 due to the massive amount of sediment inflow from Typhoon Aere. Moreover, with the bottom outlets (i.e., PPI and PRO) operation and dredging and mechanical removal near the dam, the bed elevation close to the dam site is lower.

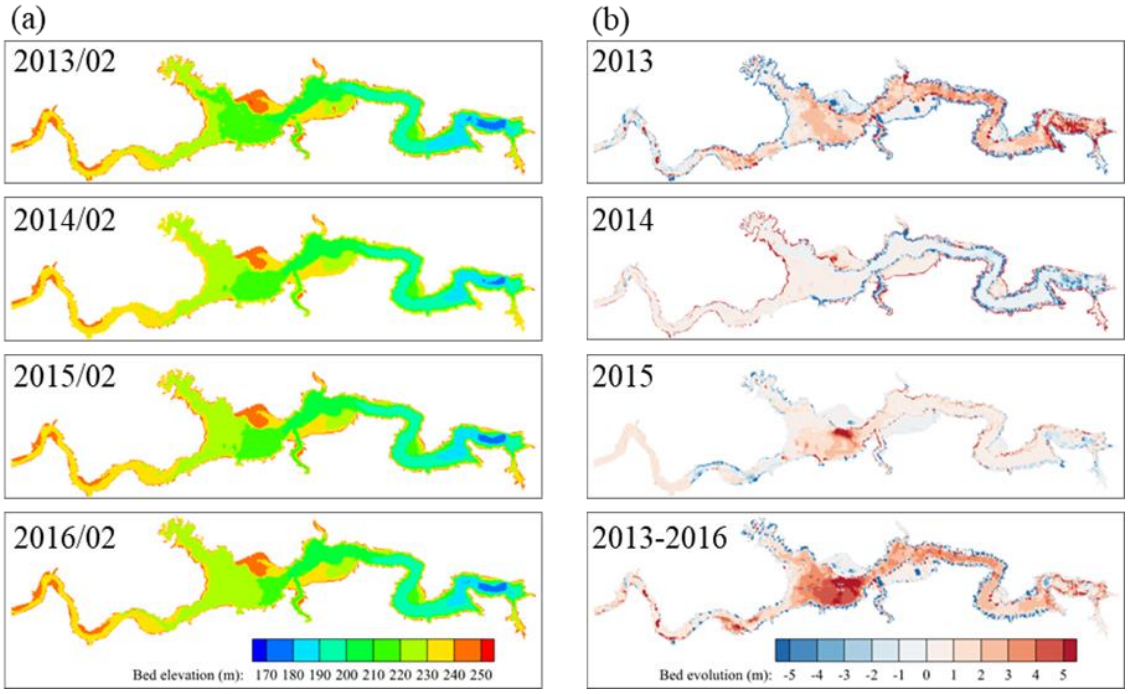

Figure 3.5 The (a) reservoir bathymetry and (b) bed evolution from 2013 to 2016.

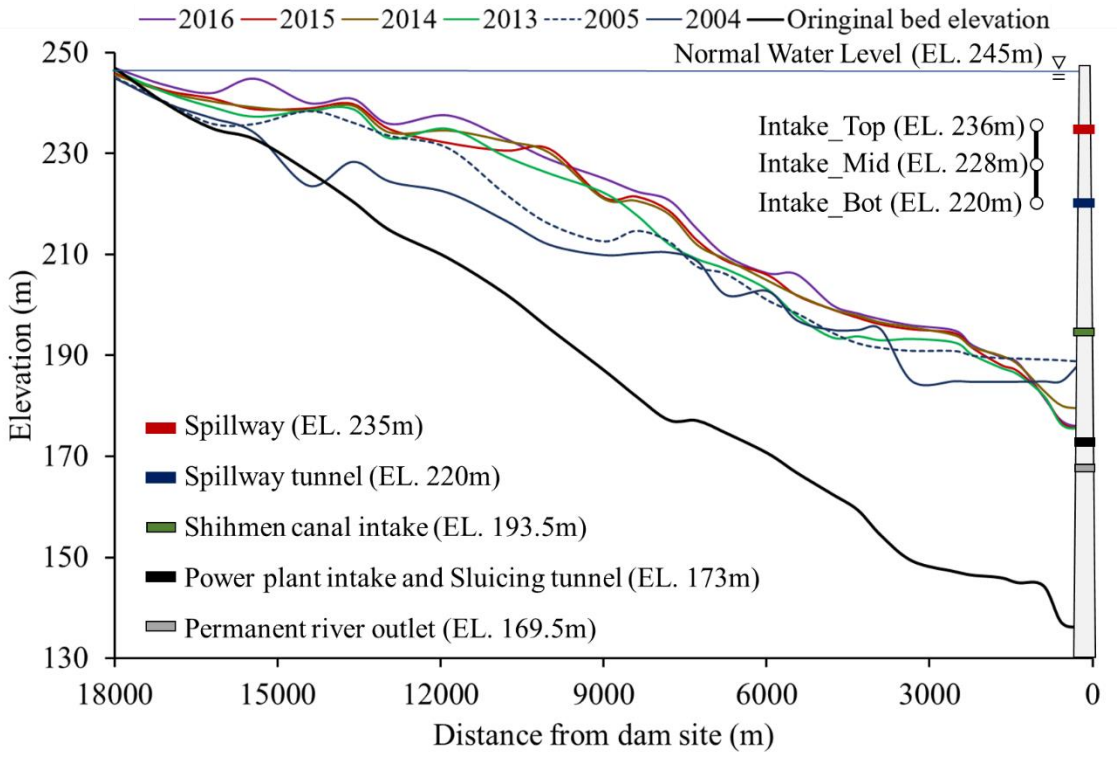

Figure 3.6 Longitudinal bed elevation and outlets' elevation of Shihmen Reservoir.

B. Sediment material

As illustrated in Figure 3.7, the grain size distribution was obtained by several sediment sampling from Lofu station, PPI, VT, SCI, ST, and SP. The measurement significantly indicates that the grain size distribution at the upstream boundary has higher dispersibility. It means that with the sediment transporting, the sediment is sorted, and only fine suspended sediment could transport to the dam site and be released from downstream outlets. As Figure 3.7 (b) showed, due to the outlier (i.e., 70 and 78 μm) D_{50} values at Lofu station, the average D_{50} value was considered overestimated. To solve this problem, the average D_{50} of Lofu station is calculated by averaging the 25^{th} percentile value (6.51 μm) and 75^{th} percentile value (24.38 μm). Based on the aforementioned results, the inflow sediment material is cohesive sediment, which diameter is much less than 62.5 μm.

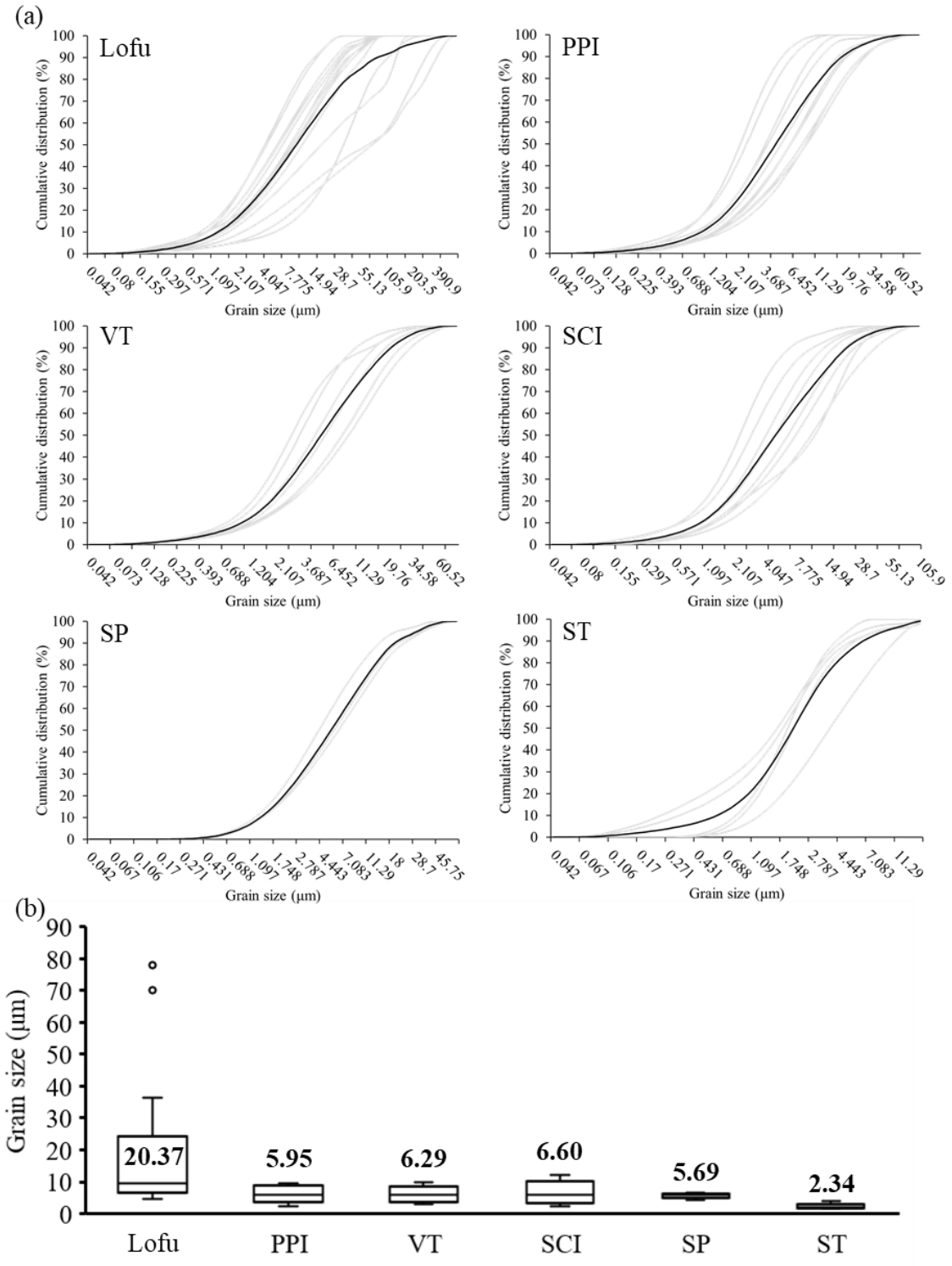

Figure 3.7 (a) The grain size distribution of suspended sediment from the upstream boundary and each outlet (black line means average value), and (b) the box plot of D_{50} from several sediment sampling at each location (number means average D_{50}).

3.1.3 Hydrological measurement under Typhoon events

Effective desiltation during typhoon events is essential for extending the usage life of reservoirs. To achieve these goals, detailed hydrological data, including rainfall, inflow discharge, sediment concentration, water level, outflow sediment concentration from each venting facility, and rain within the Shihmen Reservoir basin, are critical. Table 3.2 presents the summary of hydrological data in major flood typhoon events from 2004 to 2016. The essential hydrological information for generating turbidity current, including peak inflow discharge, sediment concentration, and continuous duration of high discharge, is listed in Table 3.2. Although the peak inflow sediment concentration from Typhoon Soudelor and Dujuan is lower than the experienced turbidity current occurring condition, the measurements from TDR and outlets still prove that the turbidity current is generated and could arrive dam site.

The TDR equipment was implemented in 2013 to clearly understand the turbidity current process and arrival time at each cross section. Due to the extremely high sediment concentration, woody debris, and fish interference, the obtained low-quality measurement is difficult to analyze. After the TDR data processing, the unreasonable data, such as extremely high and negative values, were removed, the available vertical sediment concentration measurement from Megi Typhoon was shown in Figure 3.8. To reduce the uncertainty, the top two, middle three, and bottom three TDR equipment were divided into top, middle, and bottom reach, respectively (Figure 3.8 (b)). The average sediment concentration from the top, middle, and bottom reach was named TDR_Top, TDR_Mid, and TDR_Bot, respectively. Figure 3.8 (c) showed that the clustered data could be easier to understand the sediment transportation process and validate the model.

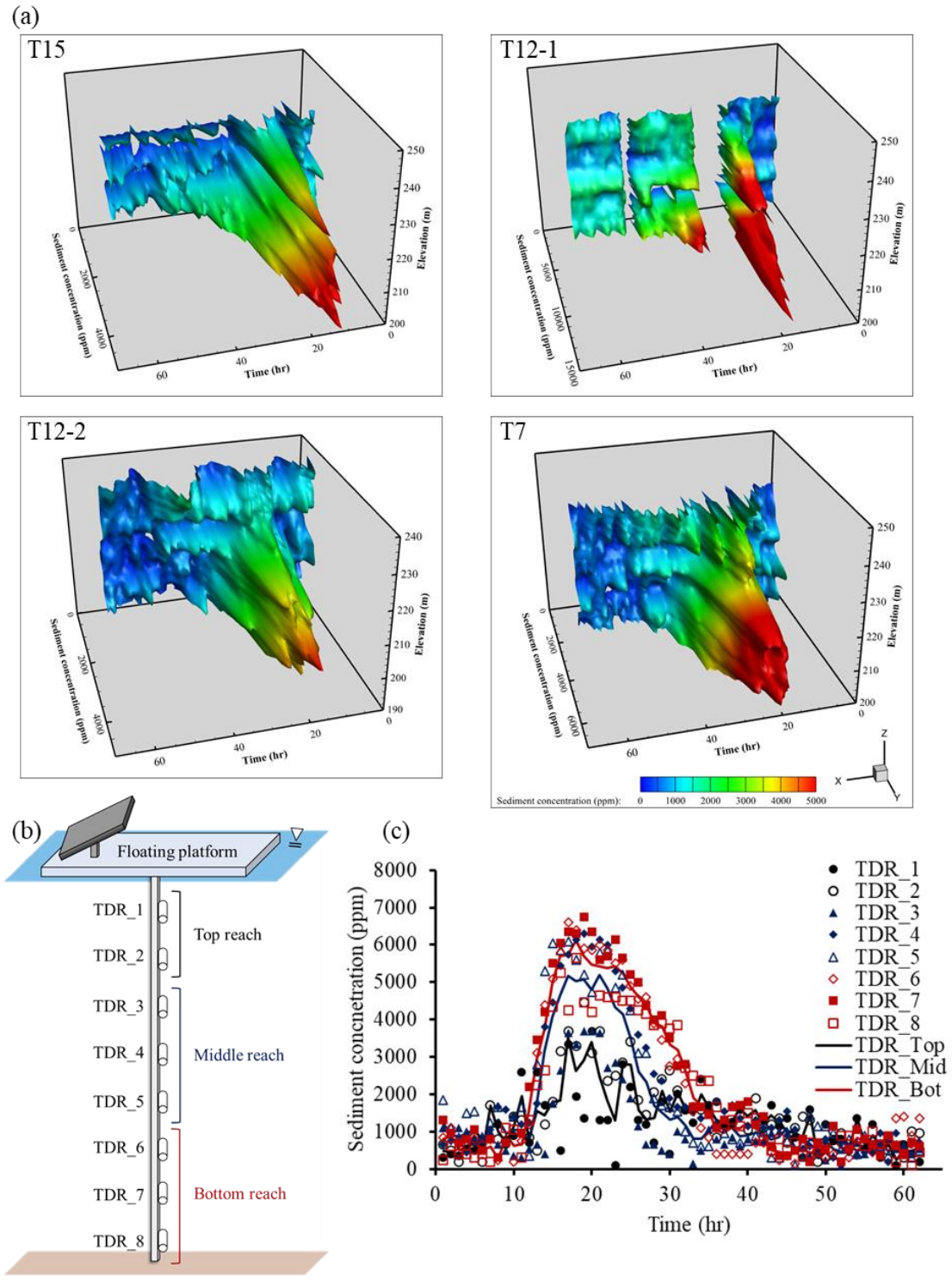

Figure 3.8 (a) the measurement of suspended sediment concentration from TDR, (b) the configuration of the TDR measurement station, and (c) the raw data from T7.

As illustrated in Table 3.2, the desilting efficiency significantly increased from 17% to 34.6% due to the application of the VT. However, it still reveals that most sediment is trapped within the reservoir. Compared to the annual deposition volume, we found that the trapped sediment from typhoon events is the main reason for severe reservoir sedimentation. Thus, increasing the turbidity current venting efficiency is essential for extending the reservoir's useful life. To provide the references for outlets operation, the real-time sediment concentration is vital to detect by using a turbidity meter (Figure 3.9). Compared to the sediment concentration from gravimetric analysis, the turbidity from the turbidity meter is similar and reliable for reservoir managers to decide the gate closing timing.

There are ten rainfall stations within the Shihmen Reservoir basin (Figure 3.1). The rainfall data from each station in Soudelor Typhoon is shown in Figure 3.10. The average rainfall in the Shihmen Reservoir was calculated using Thiessen's polygon method. Thiessen's coefficient of each rainfall station was listed in Table 3.3. As illustrated in Figure 3.10, the time difference between peak rainfall and discharge could estimate the time of concentration from each rainfall station. The time of concentration from Hsichiussushan, Chenhsipao, and Baishi station is around 4 hours due to the long distance from those stations to Shihmen Reservoir. In contrast, the time of concentration from Hsiayun and Kaoyi station is about 1 and 2 hours. The time of concentration is essential for the inflow discharge estimation from rainfall. Thus, the time of concentration from each rainfall station is listed in Table 3.3. Due to the Shihmen rainfall station is located downstream of Lofu station, the time of concentration from the Shihmen rainfall station is unavailable.

Figure 3.9 Taking the turbidity flow sample and measuring the turbidity and sediment concentration by using turbidity meter and gravimetric analysis.

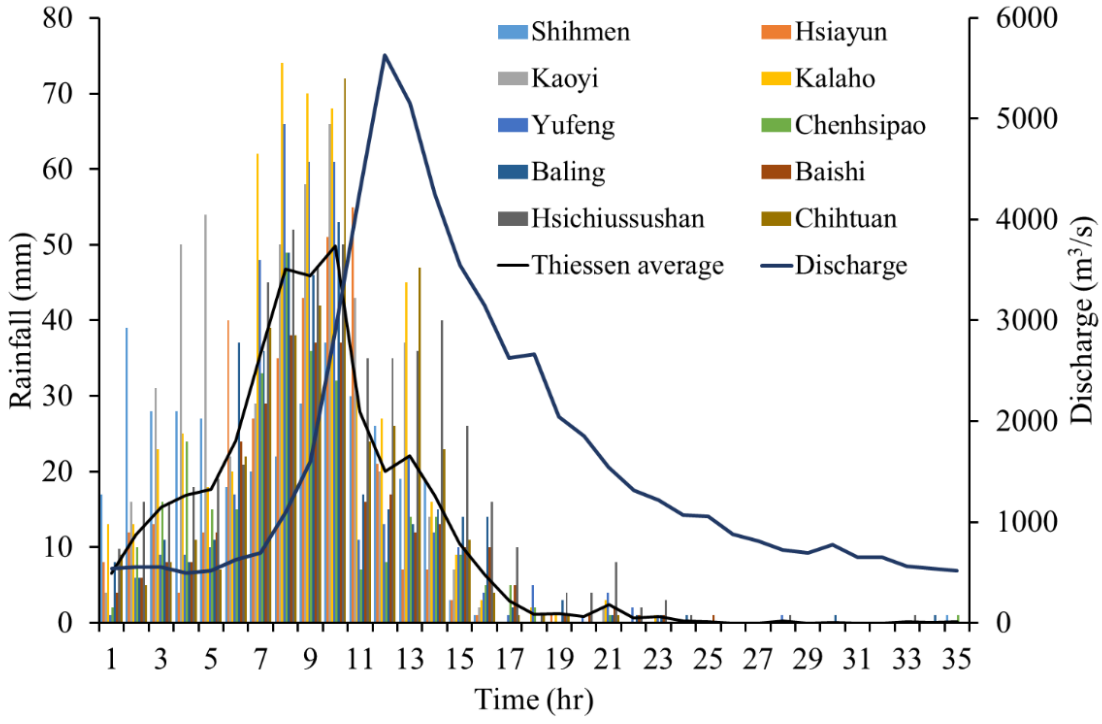

Figure 3.10 The rainfall and inflow discharge from ten rainfall stations and Lofu station in Soudelor Typhoon.

Table 3.3 The Thiessen coefficient of each rainfall station and the time of concentration from those to Lofu station in Soudelor Typhoon.

Rainfall station	Thiessen coefficient	Time of concentration (hr)
Shihmen	4.32	-
Hsiayun	17.03	1
Kaoyi	9.29	2
Kalaho	7.31	4
Yufeng	10.02	4
Chenhsipao	12.74	4
Baling	7.31	2
Baishi	11.52	4
Hsichiussushan	14.46	4
Chihtuan	3.97	2

* Note: - means unavailable data.

3.1.4 Relationship of hydrological factors in Shihmen Reservoir

Based on the measured historical typhoon data, the relationship between each hydrological element could be analyzed. As the obtained measurement shows, there are some low-qualities and missing data. The calculated rating curves are helpful for the unreasonable data correlation and the missing data addendum.

A. Relationship between rainfall and inflow discharge

Thiessen's averaged rainfall is used to simplify the analysis process in this step. Based on the previous introduction, there is a lag time for rainfall water from rainfall stations to flow into the reservoir. The correlation analysis evaluated the lag time between rainfall and inflow discharge. As illustrated in Figure 3.11, the highest correlation coefficient could be obtained with five hours lag time. It reveals that the time of concentration in Shihmen Reservoir is around five hours. Therefore, Figure 3.12 presents that after shifting five hours later for rainfall, a pretty well agreement between rainfall and inflow discharge is obtained. Based on the high correlation between rainfall and

inflow discharge, the rating curve of rainfall and inflow discharge was obtained:

$$Q_{in} = 93.214R + 554.02 \quad (3\text{-}1)$$

where Q_{in} is inflow discharge (m^3/s), and R is rainfall (mm/hr). As shown in Figure 3.13, the linear regression is not suitable for the discharge estimation. However, the results reveal that it still can give a proper assessment with good agreement in high discharge.

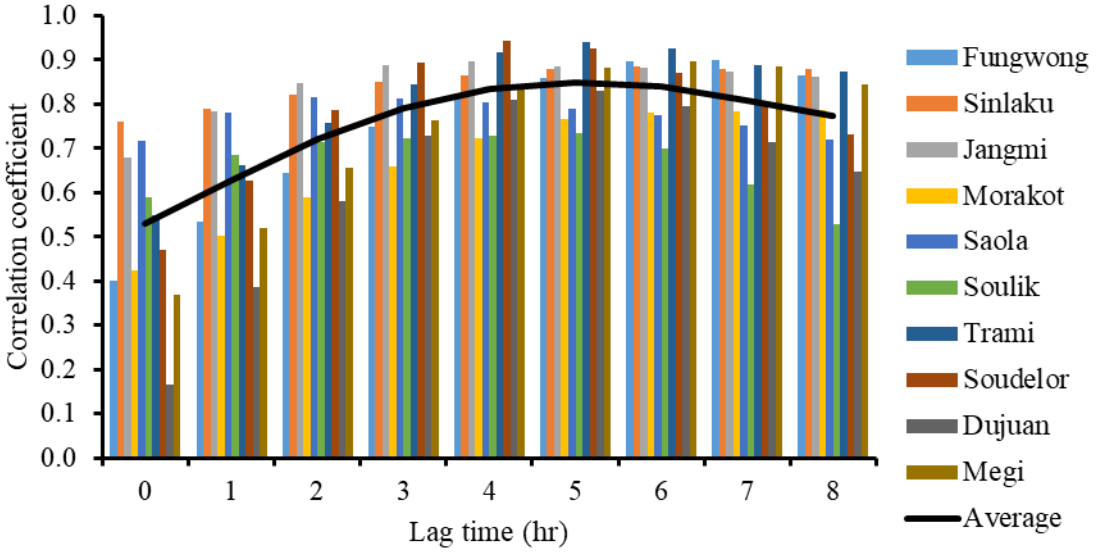

Figure 3.11 The correlation coefficient of inflow discharge and rainfall in different lag times from each typhoon event.

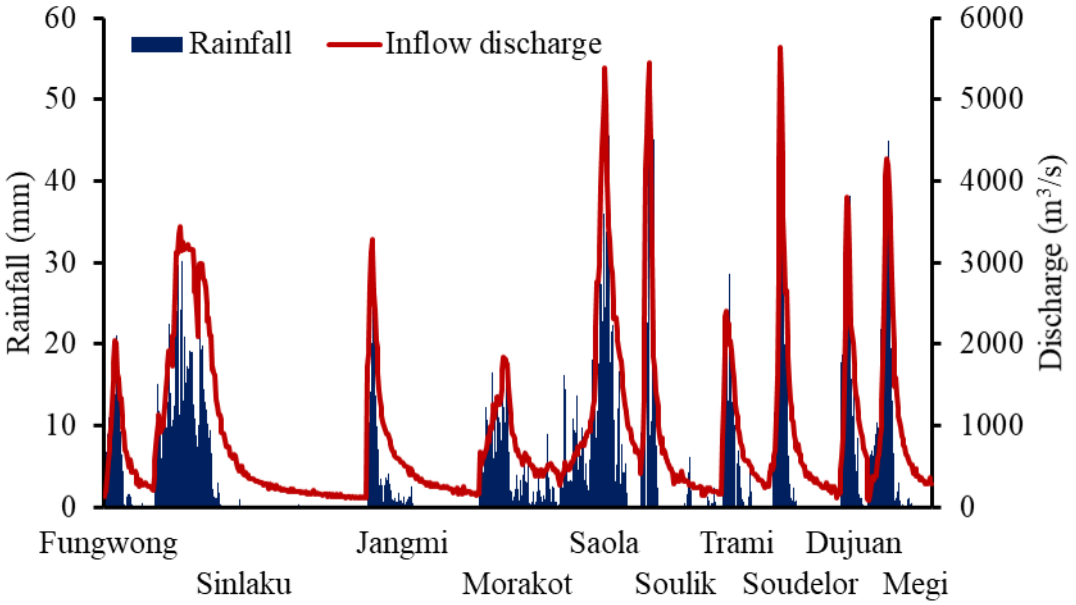

Figure 3.12 The rainfall and inflow discharge of major flood typhoon events with shifting 5 hours from considering the time of concentration.

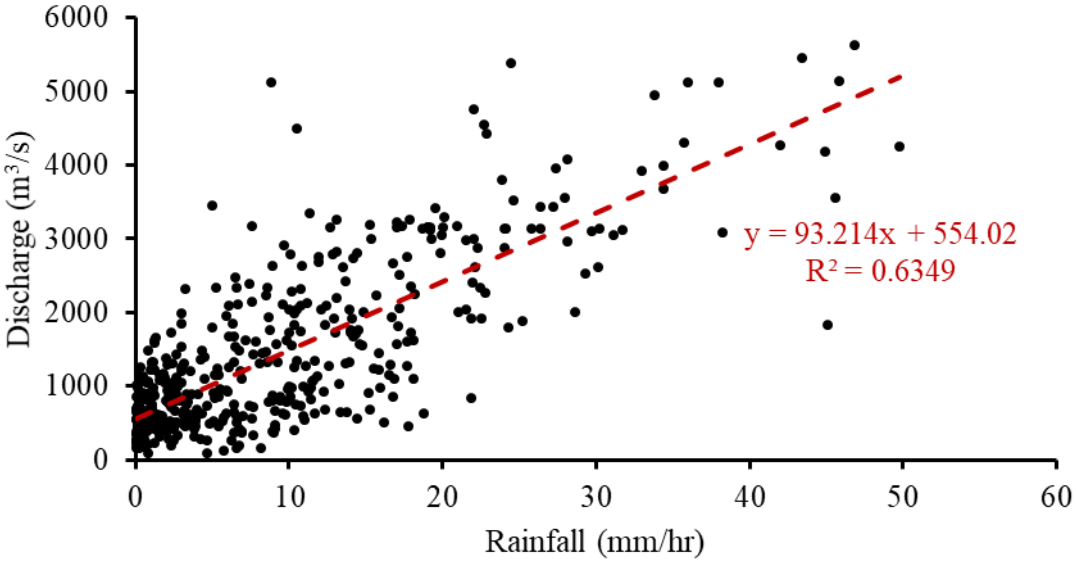

Figure 3.13 The relationship between rainfall and inflow discharge.

B. Relationship between inflow discharge and sediment

As illustrated in Figure 3.14 (a), the relationship between inflow discharge and sediment concentration with historical data from 1963 to 2004 was commonly used for Shihmen Reservoir inflow sediment estimation. Most of the sampling was taken under low discharge conditions (1000 m^3/s). However, the typhoon events' inflow discharge is much higher than 1000 m^3/s. It could cause the underestimated inflow sediment concentration estimation. Therefore, the ten major flood typhoon events data (listed in Table 3.2 Hydrological data in the Shihmen Reservoir from major flood typhoon events since 2004.) were added to solve the above problem (Figure 3.14 (b)). The calculated rating curves of inflow discharge and sediment from two data sets are expressed:

Rating curves with 1963 to 2004 data set:

$$Q_{s,in} = 0.0047 {Q_{in}}^{1.979} \quad (3\text{-}2)$$

Rating curves with 1963 to 2004 data set and ten typhoon events:

$$Q_{s,in} = 0.0039 {Q_{in}}^{2.1093} \quad (3\text{-}3)$$

where $Q_{s,in}$ is inflow sediment (kg/s). To evaluate the performance of the inflow sediment estimation, the comparison between observation and estimated values by using two equations is shown in Figure 3.15. The results reveal that the estimated sediment concentration with equation (3-2) is underestimated at peak values due to the lack of considering the high inflow events. In contrast, the strong influence of extreme typhoon events (i.e., Soulik Typhoon) on calculating the rating curve of inflow discharge and sediment leads to a significant overestimation. Based on the aforementioned results, we understood that the inflow sediment is related to inflow discharge and lacks considering factors (such as accumulated sedimentation erosion, landslide, etc.). Furthermore, climate change is one of the not considered factors. As Figure 3.16 showed, the high inflow

discharge not always brings the high inflow sediment, especially shown in Soudelor, Dujuan, and Megi Typhoon. More factors and complicated techniques should be adopted for accurate inflow sediment concentration estimation.

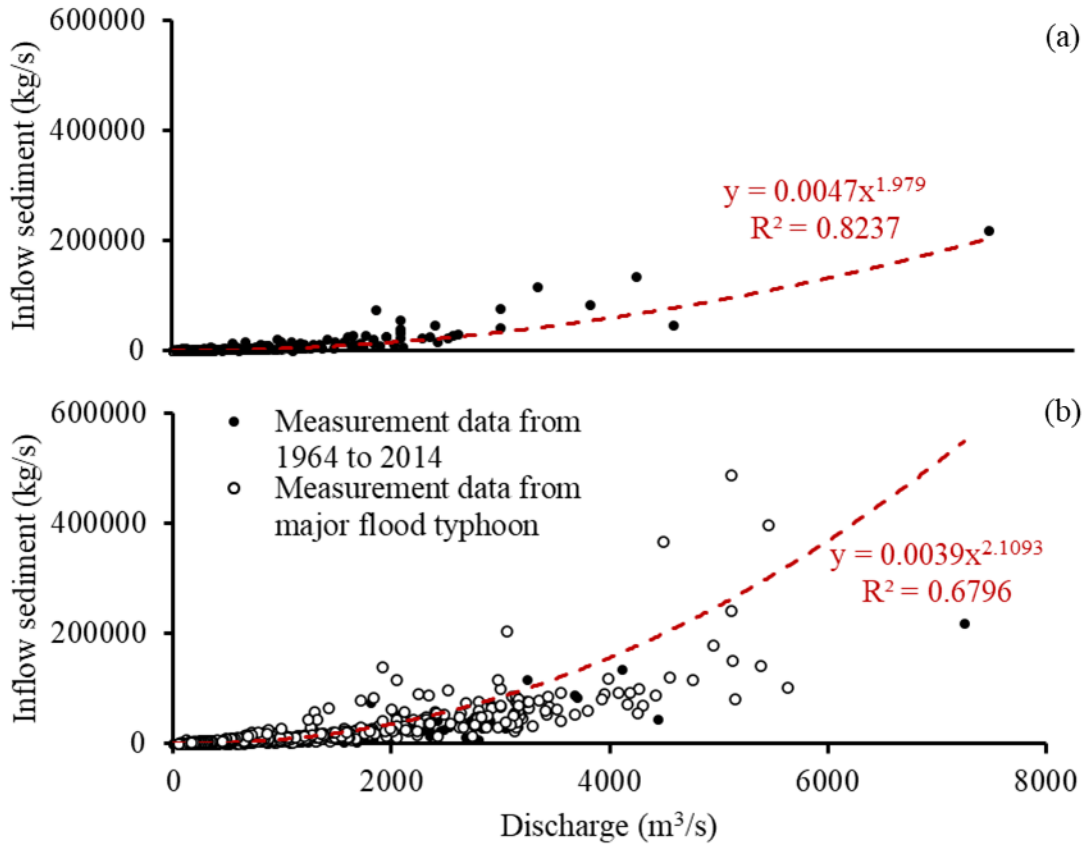

Figure 3.14 The relationship between inflow discharge and sediment with (a) historical data from 1963 to 2004 and (b) add major flood typhoon data.

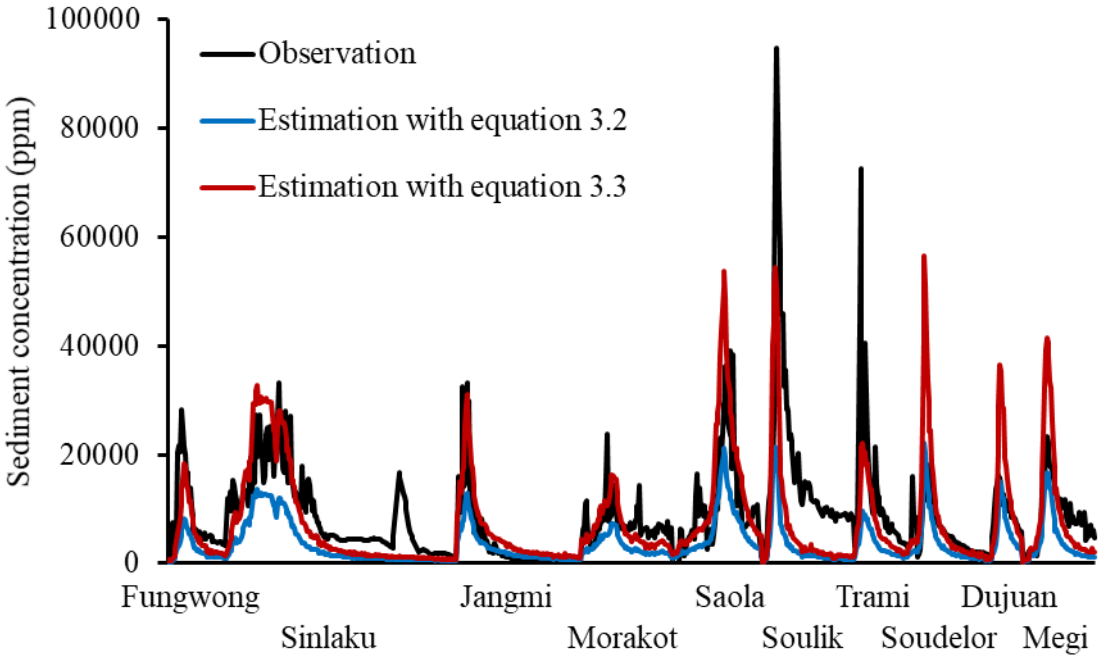

Figure 3.15 The comparison of observed and estimated sediment concentration.

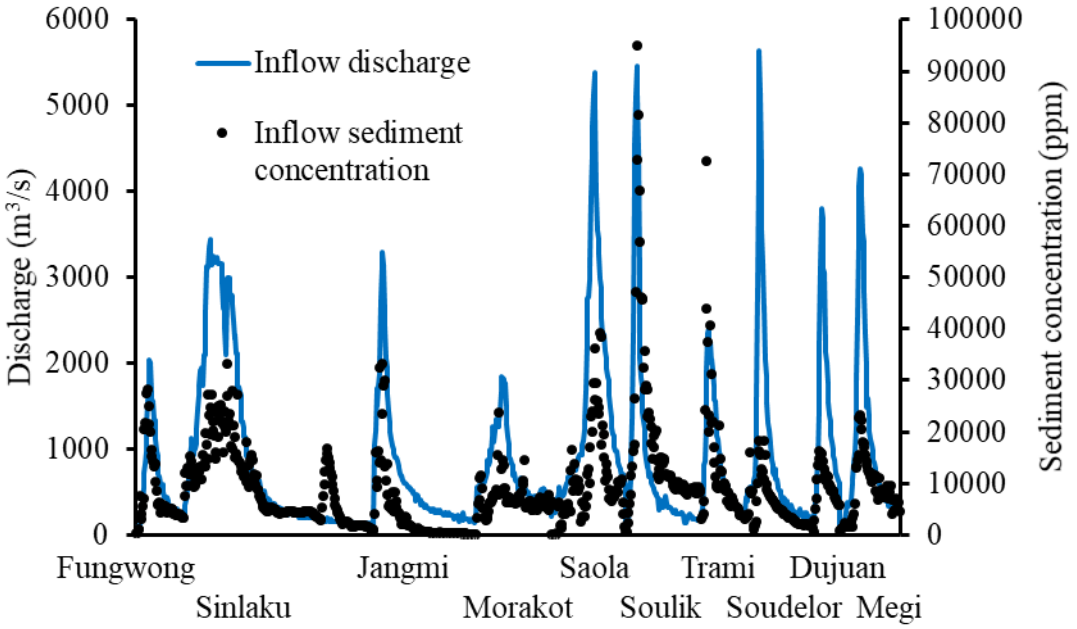

Figure 3.16 The inflow discharge and sediment concentration of major flood typhoon events.

C. H-A-V curve

The reservoir storage area and capacity could be calculated by water level based on the H-A-V curve. Figure 3.4, Figure 3.6, and Figure 3.17 significantly indicate that the reservoir storage capacity gradually decreases with increasing time. As illustrated in Figure 3.18, the Shihmen Reservoir could be divided into three segments according to the relationship between water level and reservoir storage area: (1) the water level below 190 m, which only store the water close to the Shihmen dam, is regarded as segment 1. (2) In segment 2, the stored water between 190 and 220 m could be distributed from the dam to the middle stream, which closes to the biggest tributary. (3) As the water level exceeds 220 m, it could be stored within the Shihmen Reservoir. Based on the previous introduction, the rating curve of water level and reservoir storage capacity is obtained:

$$\begin{cases} H = 181.89\forall^{0.0133} & H < 190\ m \\ H = 176.99\forall^{0.0518} & 190\ m \le H \le 220\ m \\ H = 158.21\forall^{0.0821} & H > 220\ m \end{cases} \quad (3\text{-}4)$$

where, H is water level (m) and $\forall$ means reservoir storage capacity (10^6 m^3).

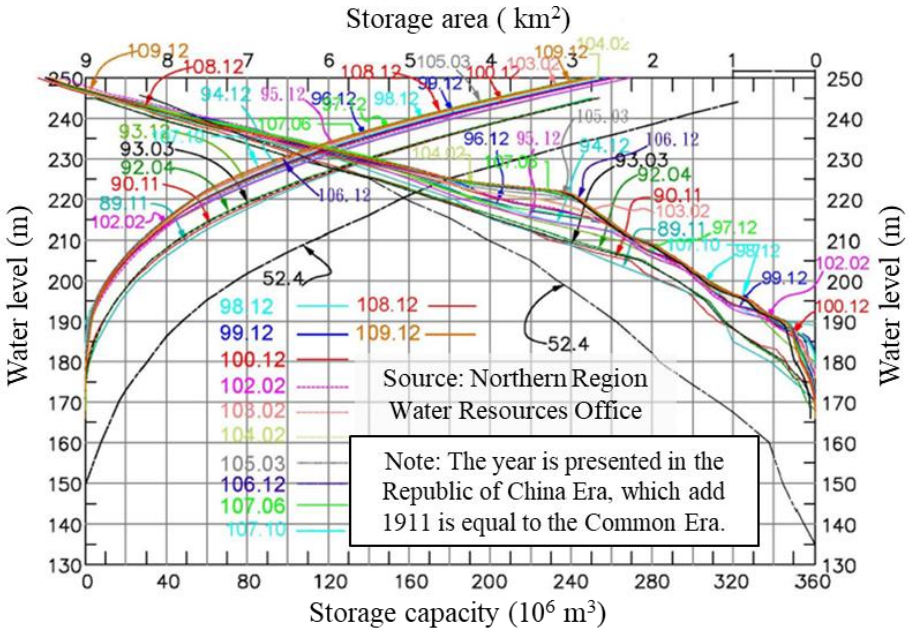

Figure 3.17 The H-A-V curves from 1963 to 2020 in Shihmen Reservoir.

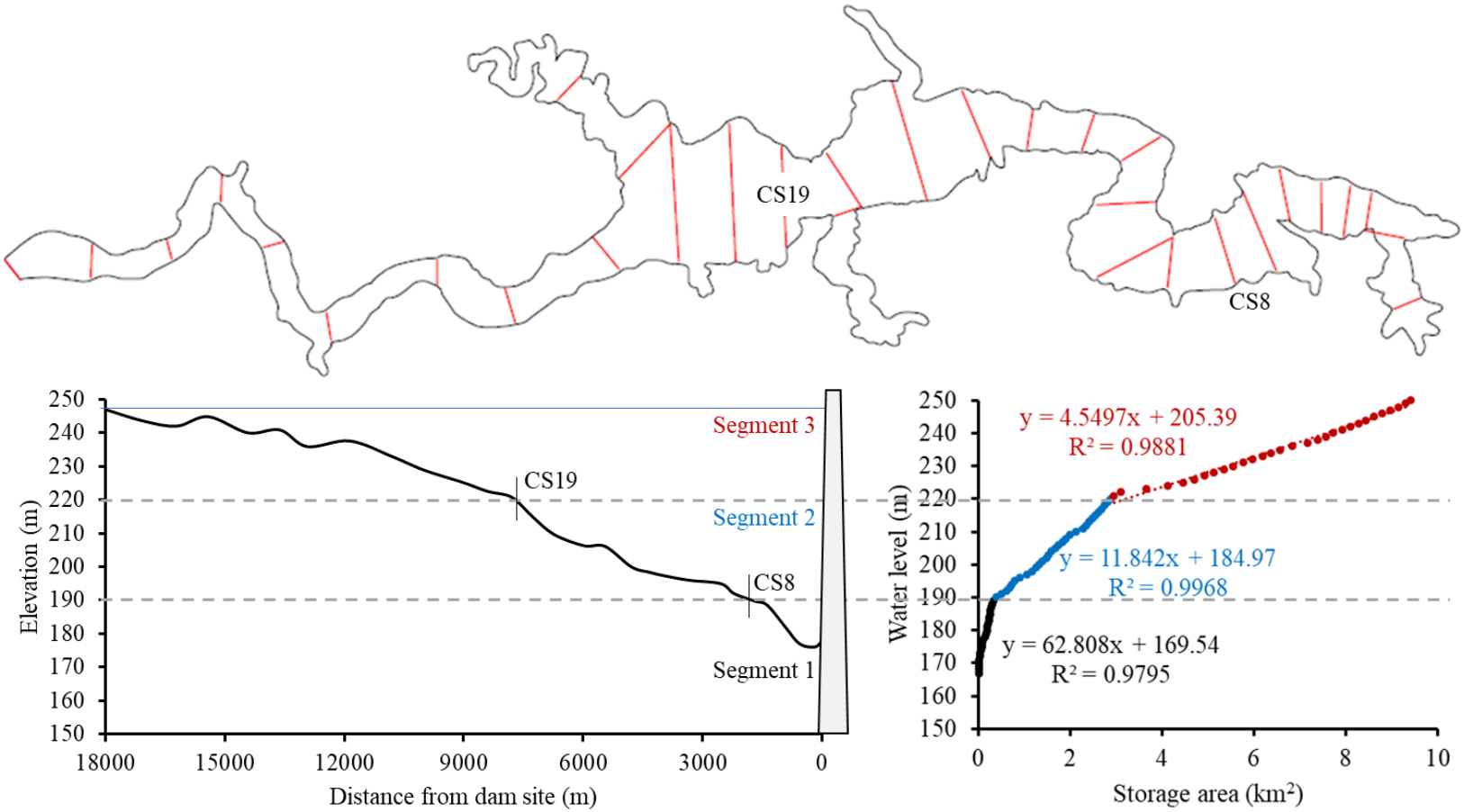

Figure 3.18 The segments in Shihmen Reservoir according to the relationship between water level and reservoir storage area.

3.2 The 1/100 down-scaling distorted physical model

The serious sedimentation issue is getting worse in Shihmen Reservoirs. To decrease the risk of water shortage due to reservoir siltation, SBTs and water supply intake were built by the water resources planning institute for increasing the venting efficiency and clear water supply. A 1/100 down-scaling distorted physical model was built to determine the location of SBTs and investigate the venting efficiency of multiple outlets operation, including the ST, SCI, PPI, PRO, Daw_SBT, and Amu_SBT (Figure 3.19). With the law of similarity, the model scale of critical terms in physical model are expressed: velocity scale= 1/10; time scale= 1/10; discharge scale= 1/100000; sediment concentration scale= 1. As illustrated in Figure 3.20, the brick, plastic plate, and plank were used for reservoir terrain layout, and the three-dimensional reservoir terrain was formed by cement mortar with waterproof coating.

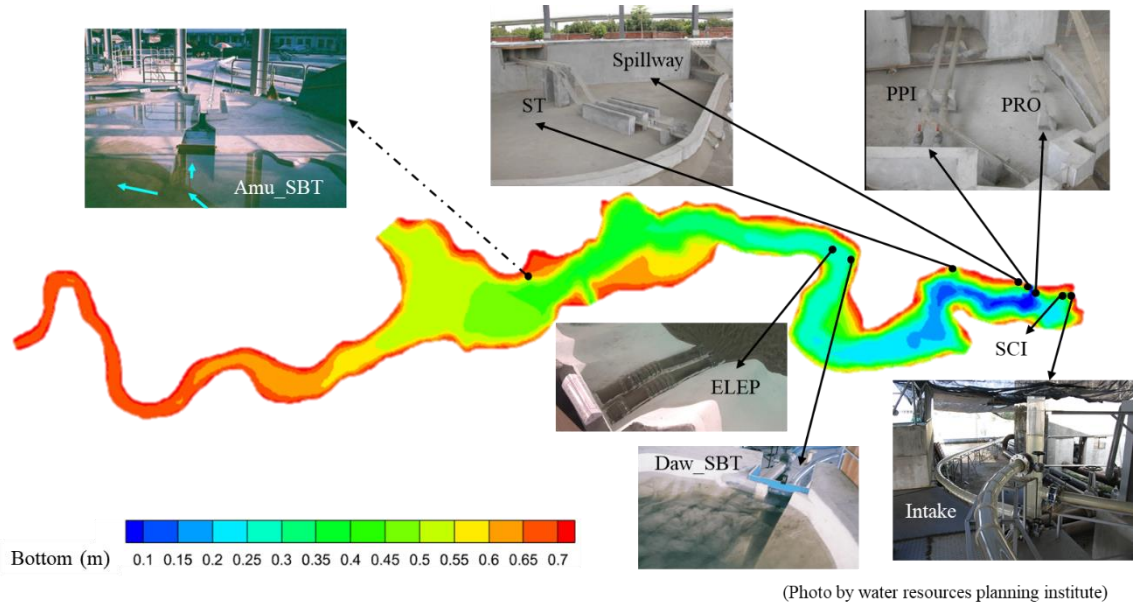

Figure 3.19 The configuration of Shihmen Reservoir physical model.

Source: Water Resources Agency

Figure 3.20 The Shihmen Reservoir physical model construction uses (a) brick for contour setup and (b) cement mortar and gravel for reservoir bed and terrain construct. (c) the completion of the physical model.

3.2.1 Physical model building and initial and boundary condition setting

Based on the above model construction, the inflow discharge and sediment concentration from Aere Typhoon, which causes severe sedimentation in the Shihmen Reservoir, are used in the physical model. Due to the lack of the measurement sediment concentration data in Aere Typhoon, the total inflow sediment amount was calculated to be 29.44 million tons. Considering the upstream tributaries effect, 29.12 million tons of sediment was used in this model. Meanwhile, the average inflow sediment concentration (43.8 g/l) was calculated by the total amount of inflow sediment and accumulated water volume. Moreover, the sediment used in the physical model was materials dredged in front of the Shihmen dam. In model scaling, the grain size scale down from 8 μm is difficult, and the extremely fine is dominated by viscosity and van der Waals force. Therefore, with the preparation works, including cutting, removing impurities, grinding, crushing, and pulverizing, the sampled sediment in the Shihmen Reservoir was used.

3.2.2 Investigating the effectiveness of venting facilities improvement

As illustrated in Figure 3.3, the feasible SBT construction was evaluated by adopting the experiment model. To investigate the turbidity current venting efficiency, the four scenarios are constructed. Scenario Sc# 0 represents that it only applies to the existing outlets. Then, three alternative structures that combine operation with Xikoutai SBT, Daw_SBT, and Amu_SBT, are named Sc# A2, C1, and D2, respectively. The released sediment amount of each outlet from each scenario is shown in Table 3.4. Based on the results of Sc# C1, the poor venting performance at Daw_SBT due to the elevation of the outlet being higher than the height of the turbidity current body, which led to the turbidity current could not be smoothly released through the SBT. To solve this problem, the elephant trunk steel pipe (ELEP), extending from Daw_SBT, was installed at the middle and bottom of the channel (named Sc# ELEP). As Table 3.4 showed, the application of the ELEP could effectively increase the venting efficiency. The sequence of average sediment concentrations in each scenario is expressed as Sc# A2, Sc# ELEP, Sc# D2, and Sc# C1. We found that the unsuitable outlet elevation is one of the main reasons for the poor performance of Sc# D2 and Sc# C1. Also, the turbidity flow spread into tributary cause the low releasing sediment concentration through Amu_SBT. The balance between engineering cost and venting efficiency is essential for the government to decide. The results reveal that Sc# A2 can bring 62.3% venting efficiency, but the construction fee of Xikoutai SBT is around 4.5 billion USD. Based on the aforementioned comprehensive considerations, the ELEP is the worthiest solution. In addition, the Amu_SBT is considered as the flooding control facility due to the high flood releasing ability.

Table 3.4 Test results of each turbidity current venting scenario in Shihmen Reservoir from physical model simulation.

	Sc# 0	Sc# A2	Sc# C1	Sc# D2	Sc# ELEP
Additional venting facility	-	Xikoutai SBT	Dawangping SBT	Amuping SBT	Elephant trunk pipe from Dawangping
Length of sediment bypass tunnel (km)	-	8.1	0.9	4.2	-
Flood discharge capacity (10^6 m^3)	93	262	341	275	278
Flood discharge ratio (%)	13.4	37.5	48.1	40.6	38.8
Peak releasing sediment concentration from additional venting facility (ppm)	-	45500	23600	26900	68200
The total amount of sediment venting through an additional venting facility (10^6 tons)	-	9.18	2.38	2.27	9.2
The total amount of sediment venting through all reservoir outlets (10^6 tons)	9.7	18.18	15.98	18.42	16.17
Total venting efficiency (%)	33.3	62.3	55.1	63.5	55.2
Construction cost (billion USD)	-	4.5	0.85	2.35	-

*Note: - means no information; all values are converted to real scale.

Chapter 4: Three-dimensional numerical modelling setup and sensitivity analysis

4.1 Introduction

The measurements could briefly understand the turbidity current transportation from measuring facilities within the reservoir. However, as mentioned in **chapter 3.1.1**, the data quality is not stable, and the continuous transit of turbidity current is impossible to detect under the flooding events. To solve these problems, numerical models are the most appropriate tool, avoiding scale effects and providing numerous results to enhance understanding of the process (Amini et al., 2017). For building a reliable numerical model, the good quality input data for boundary and initial condition was filtered and analyzed in **chapter 3.** The 1/100 down-scaling experimental-scale model is built to do the sensitivity analysis to reduce the computational time and simplify the conditions. Numerical models have been widely applied in many research areas and purposes, including the turbidity current investigation in the reservoir. However, each researcher has to analyze the sensitivities of all numerical parameters and governing equations. In this study, based on the bathymetry of the research area, hydrological information, and investigating target, the general guideline of modeling setup was proposed to avoid the repeating and time-consuming sensitivity analysis process.

This chapter aims to establish the three-dimensional model that is applicable to simulate the turbidity current process and the hydro-sediment-morphodynamics in the reservoir. The 3D Numerical modeling procedure was divided into four steps: (1) The general numerical parameters setting was determined by the sensitivity testing with 1/100 down-scaling experimental-scale numerical model. (2) The numerical model with the proposed optimal model setting is calibrated and validated by the results of the 1/100

down-scaling physical model. (3) The proposed guideline of the numerical modeling setup gives a reference to the field-scale numerical model setting. (4) To assess the validated three-dimensional numerical model's stability for future flooding events, the testing model was built by different years from calibrated and validated cases.

Overall, this chapter presents a 3D numerical modeling setup in establishing the experimental- and field-scale model. The reliable numerical model was adopted to analyze the holistic understanding of turbidity current process and complicated flow regime during extreme flooding events in **Chapter 5**. Also, it provides a capable tool to investigate the appropriate scenario for increasing turbidity current venting efficiency and extending the reservoir usage life in **Chapter 6** and **Chapter 7**.

4.2 Background of Telemac-3D and Gaia

4.2.1 Telemac-3D

The open-source numerical model Telemac-3D was developed by the National Hydraulics and Environment Laboratory of Electricité de France (EDF). The Telemac-3D code is solved by following the assumptions of three dimensional Navier-Stokes equation with a free surface in time, incompressible fluid, hydrostatic pressure hypothesis, and Boussinesq approximation for the momentum. At each node of the computation in 3D, the main results are the velocity in x-, y- and z-direction (longitudinal, transversal, and vertical directions, respectively). Telemac-3D's prominent applications can be implemented in riverine and maritime hydraulics. It can take the various processes into account, including the influence of temperature and salinity on density, bottom friction, Coriolis force effect, Influence of weather elements, consideration of the sources and sinks within the flow domain, complex or straightforward turbulence models effect, dry areas in the tidal flats and floodplains, and the current drift and diffusion of a tracer. The

Telemac-3D is applicable to many fields by coupling with sediment transport modules (Gaia or Sisyphe), wave propagation module (Tomawac), and water quality module (Waqtel). Due to all the simulation modules being written in Fortran 90, they can be run on personal computers and workstations under Windows, Linux, and Unix operating systems. The advantages of the Telemac system are able to run in parallel and allow users to modify the subroutines. Based on the powerful and flexible Telemac system, the complex geometry domains with fine mesh and adapted equations and theories for specific scenarios can be considered. More details of governing equations, and input and output files of Telemac-3D are presented in **Appendix A**.

4.2.2 Gaia

Gaia is a sediment transport and bed evolution module of the Telemac Mascaret system. Gaia is the brand new open-source module, building upon the historical sediment transport module Sisyphe. Audouin et al. (2020) reveal that Gaia can model the complex sediment and morphodynamic process for various watersheds (e.g., rivers, lakes, reservoirs, and coastal regions). Moreover, Gaia can efficiently manage the cohesive sediment (diameter $\leq$ 62.5 μm), non-cohesive sediment (diameter > 62.5 μm), and sand-mud mixtures. The two- and three-dimensional spatial and temporal variability of sediment size classes and sediment transport modes (including suspended, bedload, and both simultaneously) has been implemented. In contrast to Sisyphe, the application of dry mass instead of volume minimizes roundoff errors for evaluating the quantity of each sediment class in the bed. Furthermore, in Gaia, the adoption of a simultaneous paradigm allows erosion and deposition occurrence simultaneously. Details of Gaia are introduced in **Appendix A**.

4.3 Performance criteria for model evaluation

To evaluate the performance of the numerical model, various performance criteria are employed to indicate the discrepancy between the measured and simulated values:

The coefficient of determination (R^2) is calculated as follow:

$$R^2 = \left(\frac{N \sum_{i=1}^{N} (y_i \times \hat{y}_i - \sum_{t=1}^{N} y_i \sum_{t=1}^{N} \hat{y}_i)}{\sqrt{N \sum_{t=1}^{N} {y_i}^2 - (\sum_{t=1}^{N} y_i)^2} \sqrt{N \sum_{t=1}^{N} {\hat{y}_i}^2 - (\sum_{t=1}^{N} \hat{y}_i)^2}} \right)^2 \quad (4\text{-}1)$$

where N is the number of data, y_i and $\hat{y}_i$ are presented the measured and simulated data at N values, respectively. The higher R^2 values (approaching 1) indicate better agreement between the measured and simulated values.

The Pearson correlation coefficient (CC) is commonly used to assess the relationship between the relative movements of two variables.

$$CC = \frac{\sum_{i=1}^{N} (y_i - \overline{y_i})(\hat{y}_i - \overline{\hat{y}_i})}{\sqrt{\sum_{t=1}^{N} (y_i - \overline{y_i})^2} \sqrt{\sum_{t=1}^{N} (\hat{y}_i - \overline{\hat{y}_i})^2}} \quad (4\text{-}2)$$

where $\overline{y_i}$ and $\overline{\hat{y}_i}$ is the averaged measurement and simulation.

The root mean square error (RMSE) is a reliable performance criterion for comparing the errors between measured and simulated values. The smaller RMSE values (close to 0) represent the better-established simulation.

$$RMSE = \sqrt{\frac{1}{N} \sum_{i=1}^{N} (y_i - \hat{y}_i)^2} \quad (4\text{-}3)$$

The improvement percentage (% IMP) is computed as follow:

$$\% \text{ IMP} = \frac{Perf' - Perf}{Perf} \times 100\% \quad (4\text{-}4)$$

where $Perf'$ is the performance of the improved model, and $Perf$ is the performance of the original model.

4.4 Investigation of numerical modelling under experiment-scale

4.4.1 Initial and boundary condition

There are two liquid boundaries within the study domain. The prescribed time series inflow discharge and sediment concentration are used for an upstream boundary. The water level control and free outflow are adopted in the downstream boundary. Moreover, the sinks are regarded as the turbidity current venting facilities' outlets. Due to the bed material of the experimental model being cement and without accumulated sedimentation, the smoothy bed roughness (Nikuradse coefficient= 0.001385) and the non-erodible bed are adopted. The cohesive sediment with fine grain size (D_{50}= 8 μm) and sediment density (2650 kg/m^3) is adopted for inflow sediment material. The upstream and downstream boundary conditions for model calibration and validation are shown in Figure 4.1.

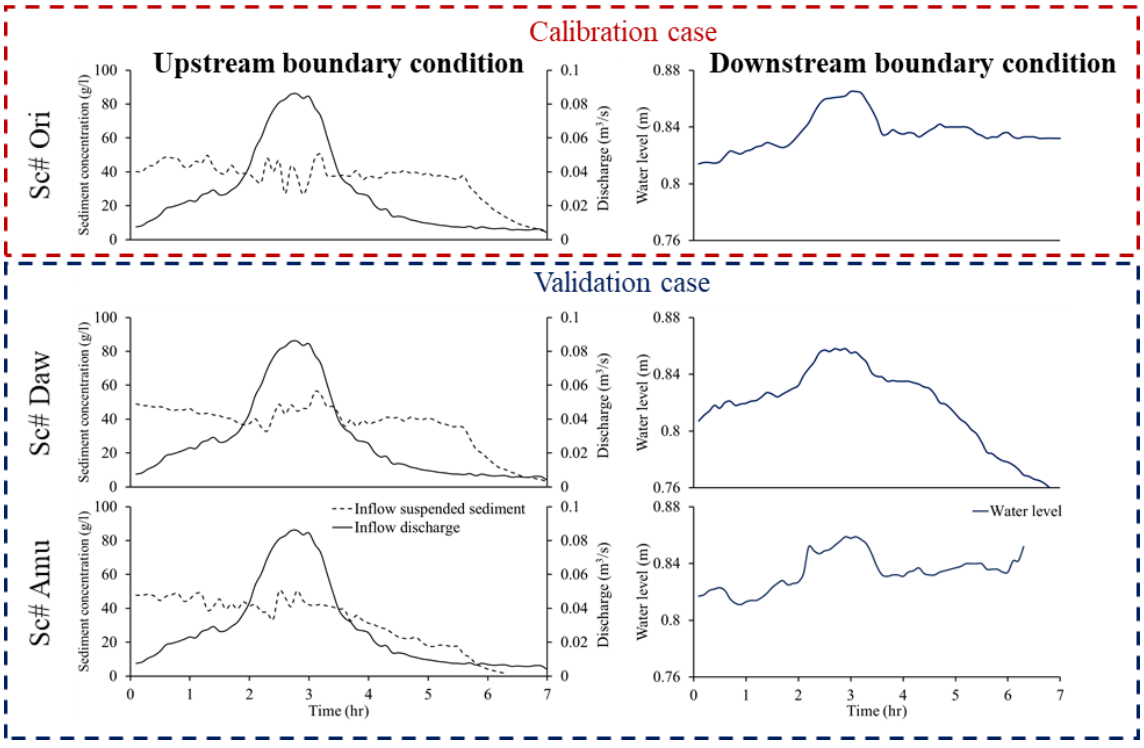

Figure 4.1 The upstream (inflow discharge and suspended sediment) and downstream (water level) boundary conditions for model calibration and validation.

The details of the measurements of the physical model from each scenario have been introduced in **chapter 3.2**. Based on the settled initial and boundary condition, the sensitivity analysis of domain discretization, turbulence scheme, and morphodynamic are essential to calibrate the model by testing various equations and parameters.

4.4.2 Sensitivity analysis of domain discretization

The determination of modelling setup by using sensitivity analysis for turbidity current simulation is essential (Pérez-Díaz et al., 2019). To consider the computational time and accuracy simultaneously, the applicable scope of mesh size and time step are governing terms. A finer mesh domain discretization is beneficial to the high spatial-temporal gradients of the variables modeled. Meanwhile, a finer mesh size leads to a longer computational time. A dimensionless quantity, the Courant number, is commonly adopted to link spatial and temporal scales and stated as follows:

$$u\frac{\Delta t}{\Delta x} \qquad (4\text{-}5)$$

where, u is the magnitude of the velocity, Δt represents time step, and Δx means mesh size. Generally, the value of c must be equal to or smaller than 1 for the model's stability and avoid negative numerical viscosity. However, based on Telemac's guideline, the Courant number smaller than ten is still acceptable. Overall, the brief descriptions of the sensitivity analysis for domain discretization are introduced here below:

A. Horizontal discretization

The horizontal discretization (i.e., mesh size) is critical to the accuracy of simulations. To achieve a balance between computational time and accuracy, the various mesh size components were tested. For the sensitivity analysis of horizontal discretization, the fixed vertical discretization was set for all scenarios in this step. A total of 20 layers for vertical discretization was established, following the recommendations of Kulis & Hodges (2006).

Due to the turbidity current transport at the bottom, the finer layer close to bed ($\Delta z = 0.03H$) and courser layers for the middle ($\Delta z = 0.06H$) and surface ($\Delta z = 0.08H$) reaches were adopted. Moreover, based on the Courant number, the time step is related to mesh size. To stay in stability, the $\Delta t/\Delta x$ was set as 5 (i.e., average Courant number < 1 in this case). Moreover, the commonly used turbulence scheme, *k*-*ε*, was adopted for both horizontal and vertical aspects.

As shown in Table 4.1, five cases with mesh sizes, related to the width of inflow boundary (b_0), from 0.1 m to 0.5 m were adopted to determine the optimal horizontal discretization. The results indicate that with Δx increase, the performance in both cross sectional and outlets get worse, but less computational time was required (Figure 4.2 (a)). As illustrated in Figure 4.2 (b), the regression formula can estimate the computational time and accuracy with an element number. It indicates that a total element number around 25000 was regarded as the appropriate amount. Hence, the 0.25 m (total element is 23400) was set, and the simulated performance had good agreements with the estimated performance (the triangle symbols in Figure 4.2 (b)).

Table 4.1 The information of time step setting in each considered sensitivity test.

Horizontal domain	Δx (m)	Element number (10^3)	Δt (s)
Sensitivity analysis for horizontal discretization			
$b_0/12$	0.1	147.97	0.5
$b_0/6$	0.2	36.68	1
$b_0/4$	0.3	16.16	1.5
$b_0/3$	0.4	9.00	2
$5b_0/12$	0.5	5.72	2.5
Estimated appropriate mesh size for horizontal discretization			
$5b_0/24$	0.25	23.40	1.25
Integration of different mesh sizes for horizontal discretization			
[$b_0/6$; $b_0/3$]	[0.2; 0.4]	24.33	1

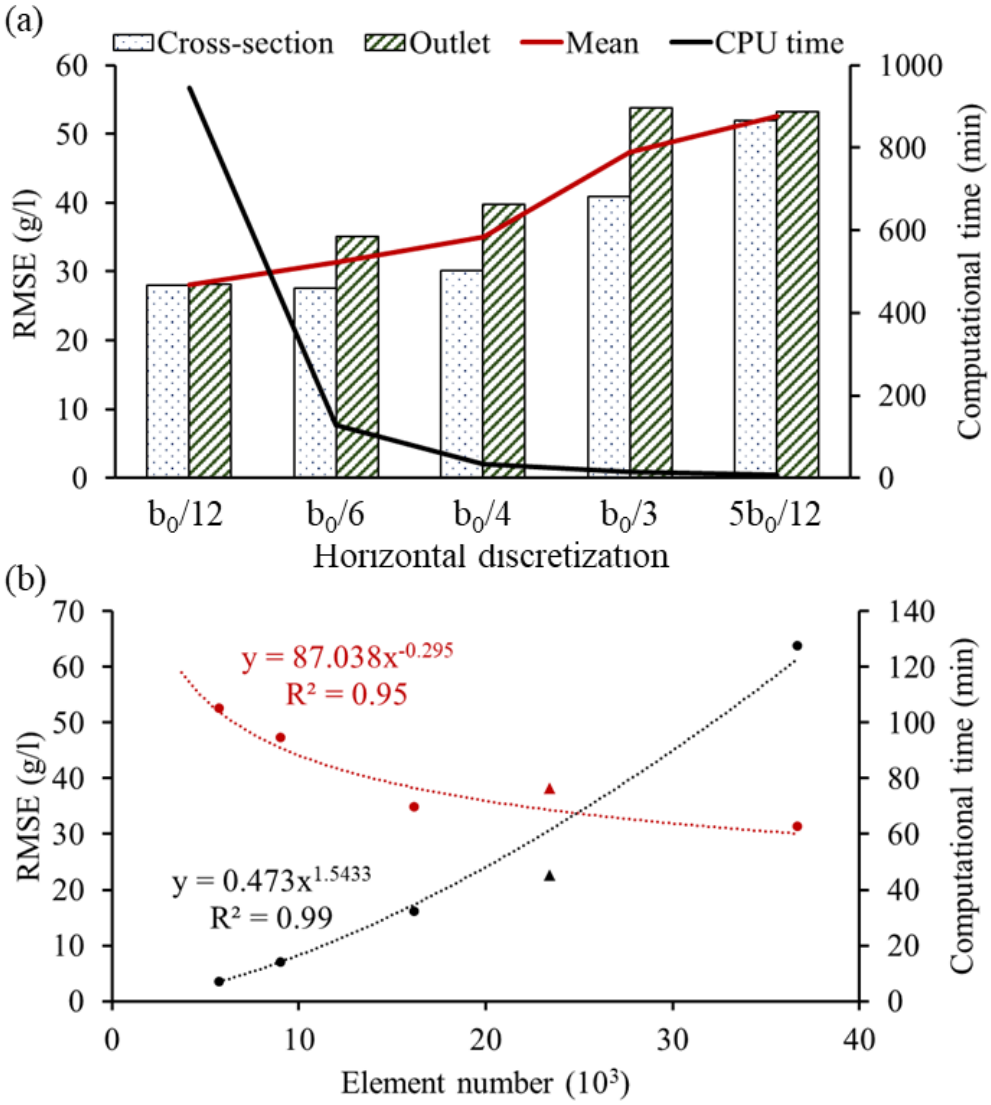

Figure 4.2 The sensitivity tests of mesh size for investigating the (a) RMSE of CS4 and outlets and computational time; (b) relationship between element number and performance and computational time.

Moreover, Figure 4.3 (a) reveals the turbidity current transport at thalweg, which is at the bottom and middle stream. Integrated the two different mesh sizes, finer mesh in the middle of the channel and coarser mesh at the banksides were proposed (Figure 4.3 (b)). To keep the model stable, the Δt was determined by Courant number with finer Δx. As illustrated in Figure 4.3 (c), the turbidity current was simulated under a finer mesh size domain. The results confirm that compared to the single mesh size setting ($\Delta x =$

0.25 m), the 34% more computational time it took but the accuracy improve 37%, especially the 46% improvement for the performance of outlets. Therefore, the integrated two different mesh sizes with $\Delta x = [b_0/6;\ b_0/4]$ was determined as the applicable scope of horizontal discretization in this study.

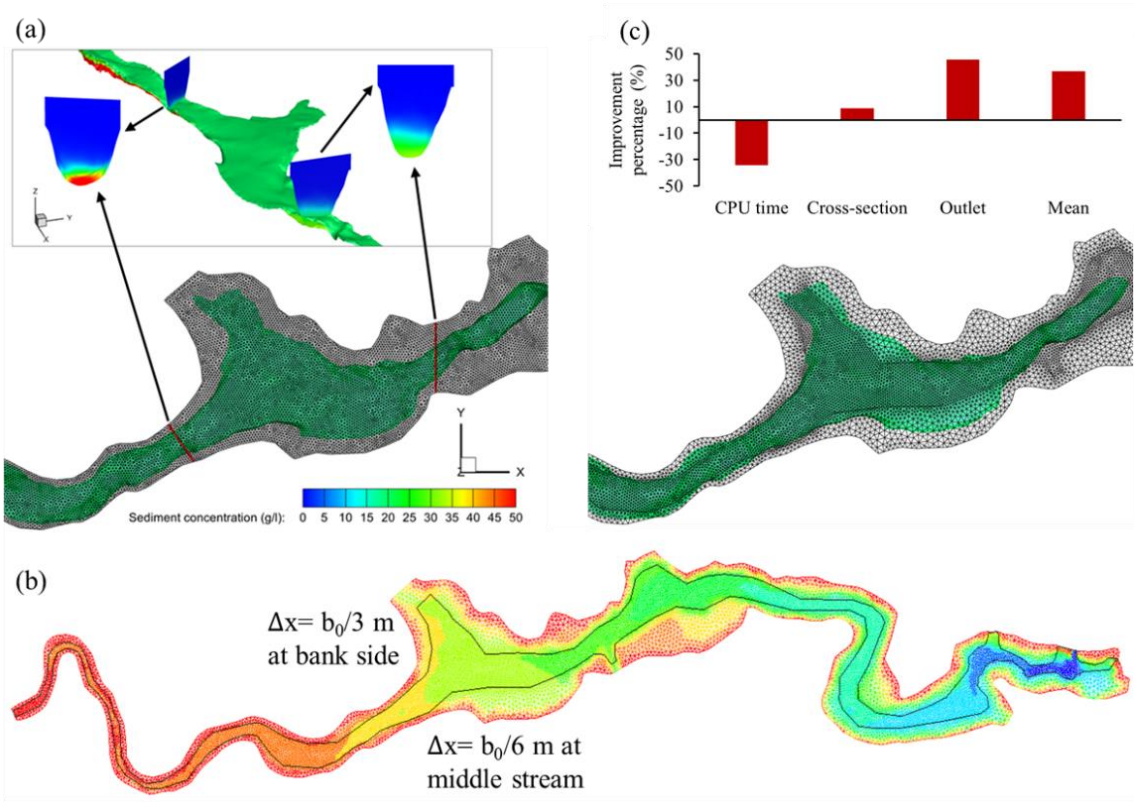

Figure 4.3 The (a) turbidity current movement within the reservoir; (b) configuration of integration of finer mesh in the middle of the channel and coarser mesh at the banksides; (c) results from improved mesh setting and the improvement percentage from $b_0/6$ and $b_0/3$.

B. Vertical discretization

The vertical discretization (i.e., layer) is critical to the turbidity current simulation, which has strong interaction in the vertical aspect. The layer distribution and number are essential to turbidity current simulation. Due to the stratification of clear surface water and bottom turbidity current, the dense layers must be implemented for accurate simulation. Moreover, Kulis & Hodges (2006) presented that the low vertical grid resolution leads to the poor performance of turbidity current at the vertical aspect. For the sensitivity analysis of vertical discretization, the determined mesh size ($\Delta x = [b_0/6; b_0/4]$) was adopted and several tests were conducted for layer style and layer number.

Firstly, sensitivity to the layer style was studied. For this purpose, a sigma coordinate layers (LS1) and two non-homogenized layer styles (LS2 and LS3) were conducted. The vertical layer spacing (Δz) is specified as a fraction of the total water depth (D). The Δz values in each layer style are express:

LS1:
$$\Delta z = D/N_l \quad (4\text{-}6)$$

LS2:
$$\Delta z_{n_l} = 2n_l D/N_l(N_l + 1) \quad (4\text{-}7)$$

LS3:
$$\Delta z = \begin{cases} 1.6D/N_l & \text{Surface reach} \\ 1.2D/N_l & \text{Middle reach} \\ 0.6D/N_l & \text{Bottom reach} \end{cases} \quad (4\text{-}8)$$

where N_l is the total number of layers and n_l is the layer number. The bottom layer is located at the bed, and the height of the top layer (H) should be the same as D. As shown in Figure 4.4 (a), the Δz gradually increases from bottom to surface in LS2. Compared to LS3, the layer number at each reach is the same, but the denser layer setting at the bottom was adopted in LS2 instead of the homogenized Δz was used within each reach. As illustrated in Figure 4.4 (b), the results reveal that the dense layer was setting at the bottom yields better agreement of vertical sediment concentration profile, especially at

the bottom reach. Due to the insufficient layers close to the bottom, the underestimated results at bottom reach, critical for turbidity current transportation, were obtained. By using the appropriated layer distribution (i.e., LS2), the accuracy at the bottom reach can improve 39% and 21.2% from LS1 and LS2, respectively (Figure 4.4 (c)).

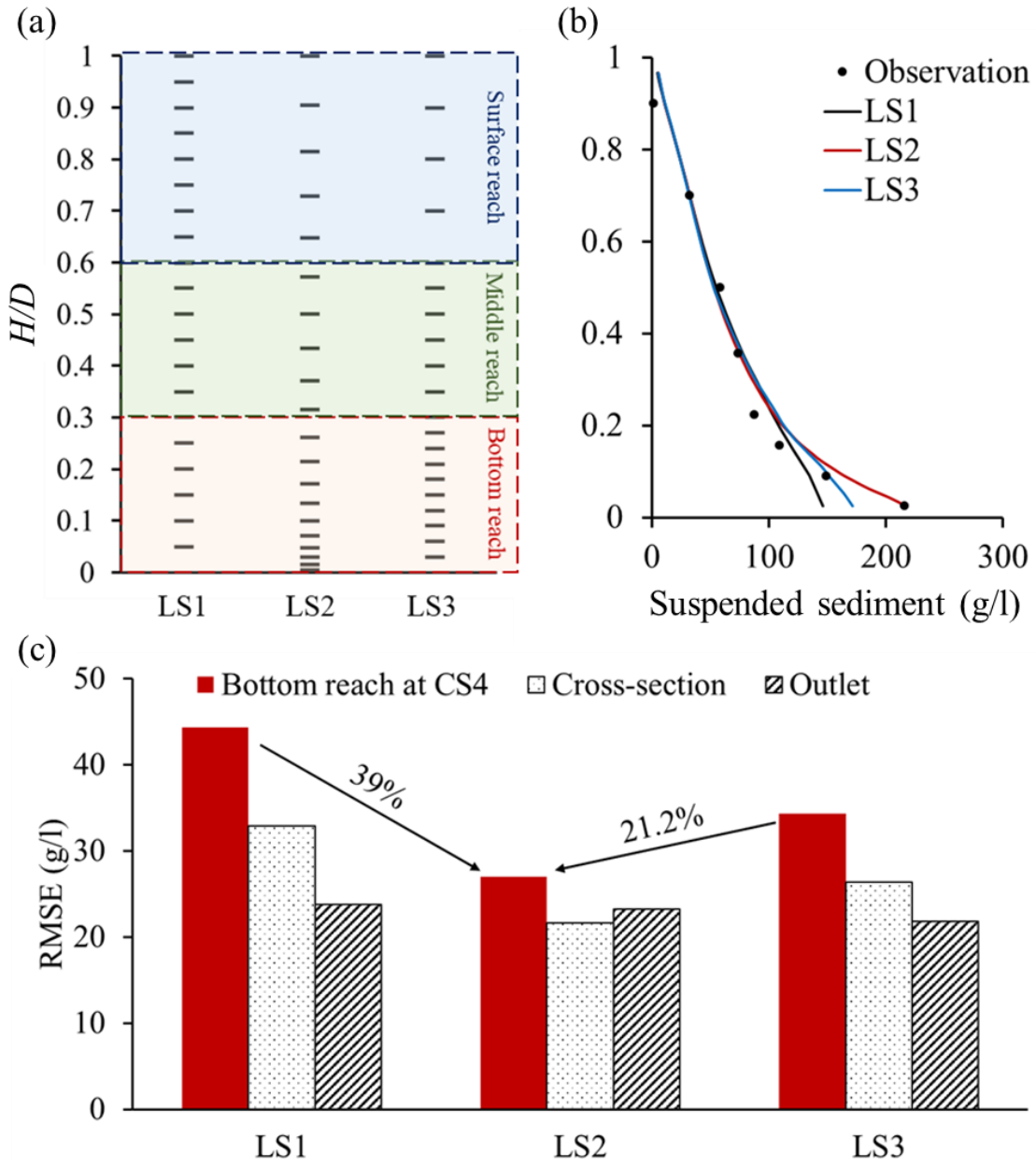

Figure 4.4 The (a) configuration of layer setting style; (b) vertical profile of CS4 from each scenario; (c) RMSE from each layer setting style and improvement percentage of performance at bottom reach (shown as numbers in the figure).

Second, sensitivity to the layer number was analyzed. To consider the horizontal and vertical discretization simultaneously, the layer number (N_l) is determined by Δx and D (Table 4.2). By adopting determined non-homogenized LS2, five cases, with layer numbers from 10 to 30, were used to determine the optimal vertical discretization. As shown in Figure 4.5, with layer number increased, the RMSE value decreased (i.e., better performance), and computational time increased. However, the results indicate a similar simulation performance with layer numbers above 15 layers. The accuracy improvement from 15 to 30 layers was only 4%, but it took twice the computational time. Overall, the 15 layers with LS2 layer setting style is the appropriate vertical domain setting.

Table 4.2 The information of layer number and Δz in each of sensitivity tests.

Vertical domain	Layer number	Upstream boundary		Downstream boundary	
		Δz_{min} (cm)	Δz_{Max} (cm)	Δz_{min} (cm)	Δz_{Max} (cm)
$N_l = 40\Delta x/D$	10	0.22	2.18	1.45	14.55
$N_l = 60\Delta x/D$	15	0.10	1.50	0.67	10.00
$N_l = 80\Delta x/D$	20	0.06	1.14	0.38	7.62
$N_l = 100\Delta x/D$	25	0.04	0.92	0.25	6.15
$N_l = 120\Delta x/D$	30	0.03	0.77	0.17	5.16

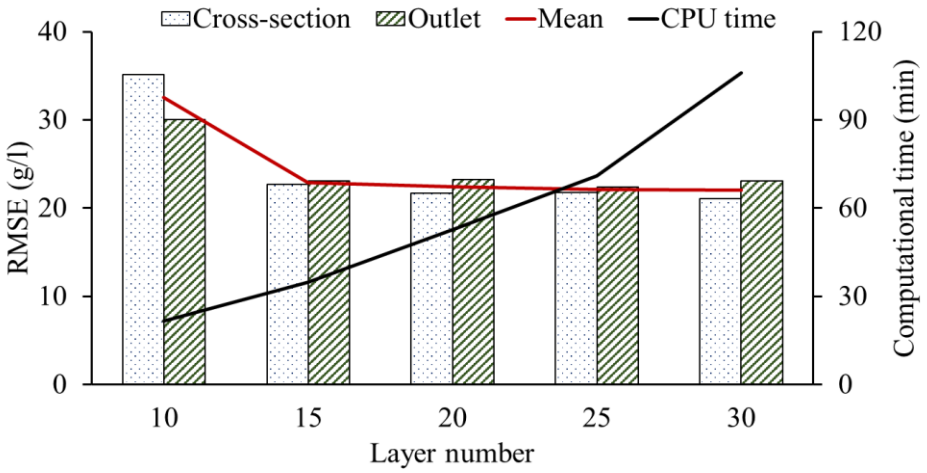

Figure 4.5 The RMSE values of CS4 and outlets and computational time from different layer numbers.

C. Time step

The time step selection is essential for the numerical model stability. The Courant number is adopted to determine the time step by considering Δx and velocity. Based on the inflow average (0.164 m/s) and maximum velocity (0.45 m/s), five cases with Δt from 0.2 to 4 s were used to determine the appropriate time step (Table 4.3). As illustrated in Figure 4.6, the results reveal that the too large time step leads to inaccuracy and unstable simulation. Compared to the simulation with Δt= 0.5, turbidity current plunging and transportation processes are similar to those with Δt= 4. However, the unstable flow pattern leads to high diffusion at the plunging region and a spike within the reservoir (Figure 4.7). Meanwhile, the simulation with too large Δt causes the extremely underestimated sediment concentration at the bottom. Figure 4.6 shows that the accuracy from Δt= 0.5 and 1s are similar, only 7% difference, but 74.6% more computational time is required with smaller time steps.

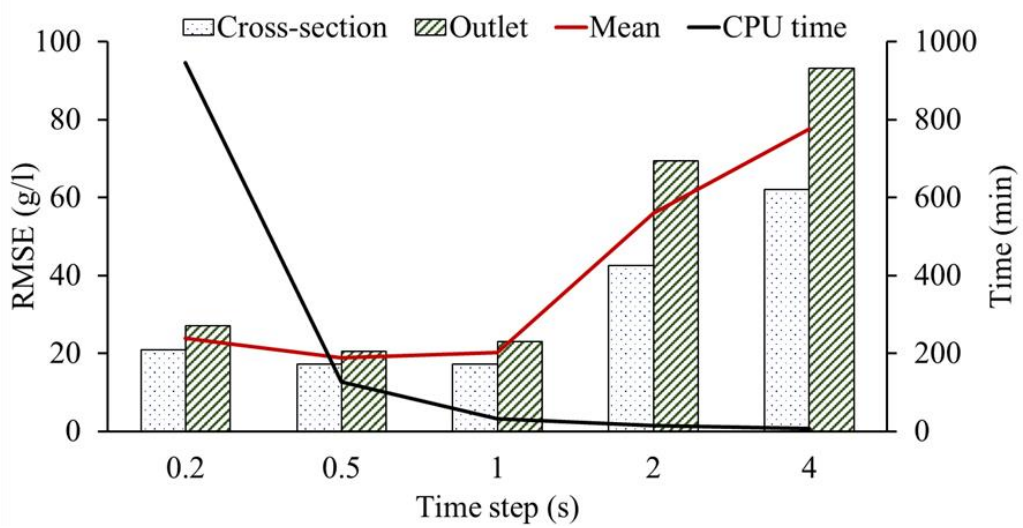

Figure 4.6 The sensitivity tests of time step for investigating the RMSE of CS4 and outlets and computational time.

Table 4.3 The averaged and maximum Courant number at the upstream boundary from different time step settings.

Time step (s)	$\Delta t/\Delta x$	Courant number	
		Average	Maximum
0.2	1	0.16	0.45
0.5	2.5	0.41	1.13
1	5	0.82	2.25
2	10	1.64	4.50
4	20	3.28	9.00

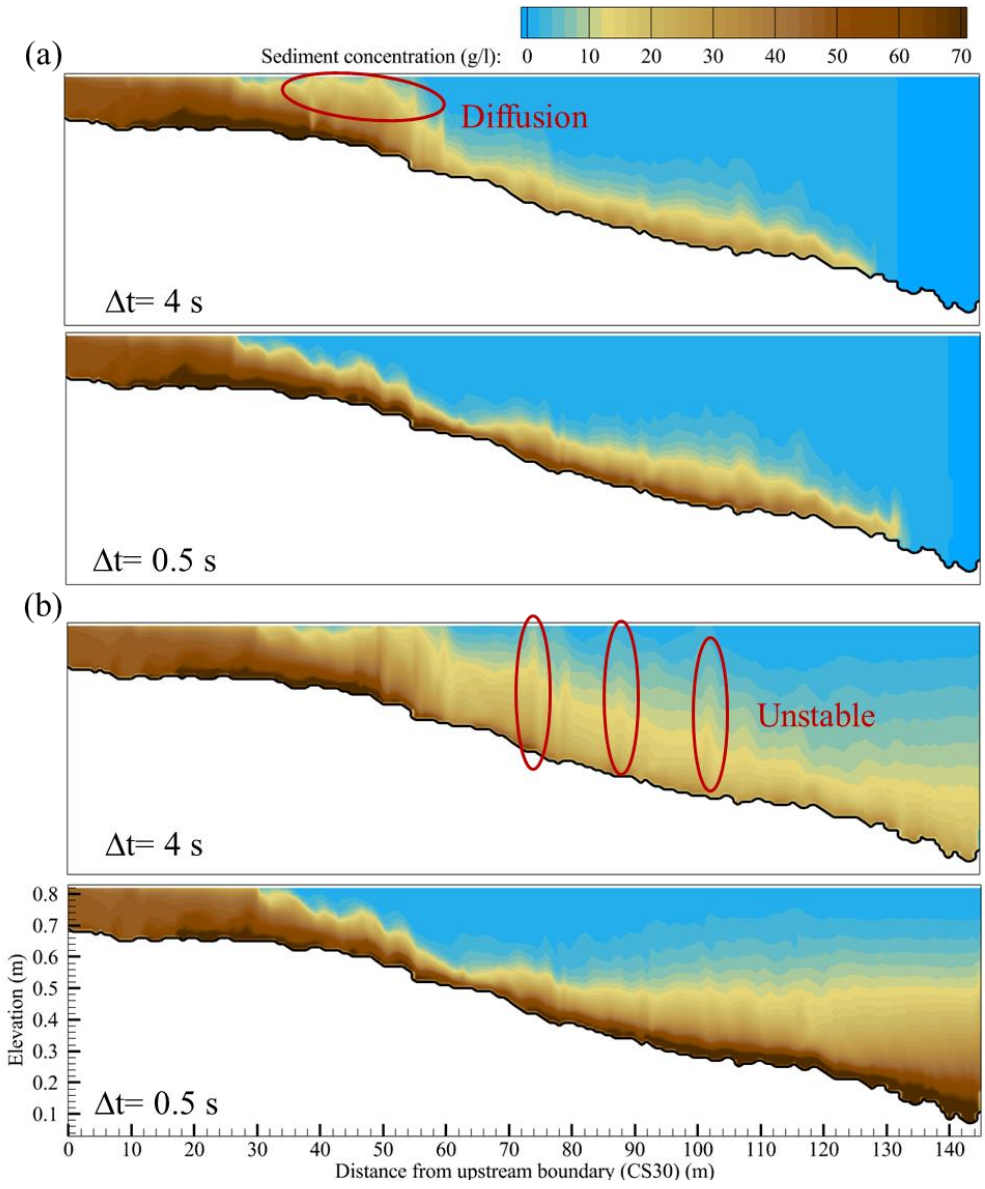

Figure 4.7 The comparison of turbidity current simulation within reservoir between 4 and 0.5 s time step at (a) 2160 s and (b) 3600 s.

Based on the relationship between Courant number and performance and computational time, the Courant number close to 1 accounts for the appropriate value for achieving the balance between computational time and accuracy (Figure 4.8). Overall, the Δt= 0.5 s is regarded as the suitable temporal gradients for experiment-scale turbidity current simulation.

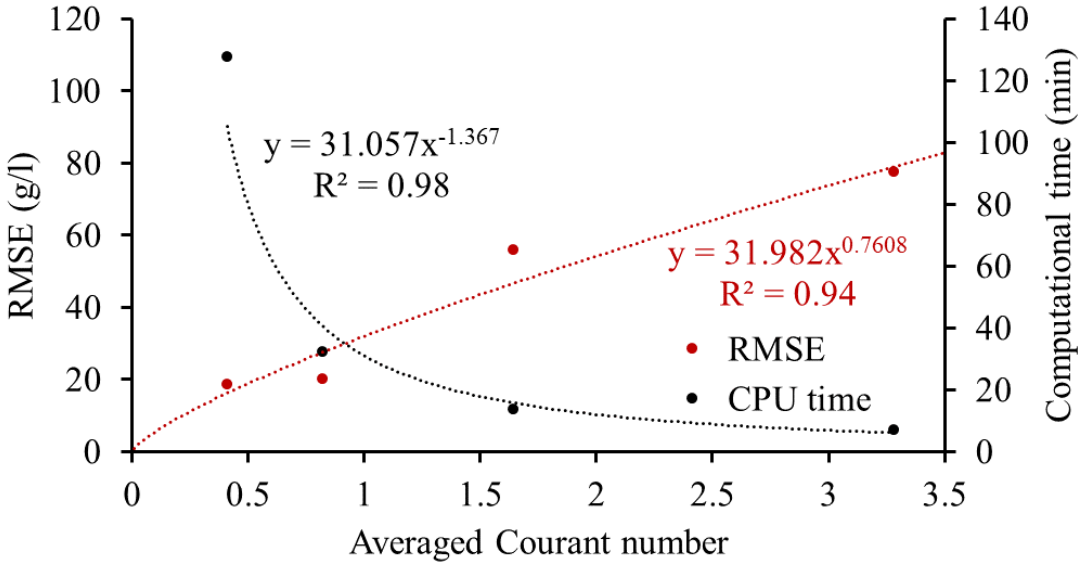

Figure 4.8 The relationship between averaged Courant number and performance and computational time.

4.4.3 Sensitivity analysis of turbulence scheme

Based on the previous domain discretization sensitivity tests, this section investigates the appropriate turbulence formula crucial to hydrodynamic simulation. The sensitivity tests of zero-equation models (including constant viscosity, Smagorinsky, and Mixing-length models) and two-equation models (including k-epsilon and k–omega models) were analyzed in this section. The candidate turbulence schemes for horizontal and vertical aspects are briefly described as follows:

Constant viscosity (Cst): The simplest turbulence model consists. It is sufficient when the flow is governed by pressure gradient and advection.

Mixing-length model (ML): The ML presents the turbulent viscosity (i.e., diffusion coefficient) (ν_t) as a function:

$$\nu_t = {L_m}^2 \sqrt{2D_{ij}D_{ij}} \qquad (4\text{-}9)$$

where L_m means the mixing length parameter, which is equal to κy at a distance y from the wall with von Karman constant is 0.41. L_m remains constant while the size of eddies is no longer influenced by walls; indices i and j vary from 1 to 3 represented to the direction involved; D_{ij} is the strain rate tensor of average motion:

$$D_{ij} = \frac{1}{2}\left(\frac{\partial \bar{u}_i}{\partial x_j} + \frac{\partial \bar{u}_j}{\partial x_i}\right) \qquad (4\text{-}10)$$

Smagorinsky model (Smag): The Smag is proposed based on ML and belongs to the sub-grid turbulence model. The principal concept is to add a turbulent viscosity deduced from ML into the molecular viscosity.

$$\nu_t = {C_s}^2 \Delta x^2 \sqrt{2D_{ij}D_{ij}} \qquad (4\text{-}11)$$

where C_s is a dimensionless coefficient, ranging from 0.1 (canal flow) to 0.2 (isotropic turbulence).

k-epsilon model (*k*-ε): The ν_t from *k*-ε is deduced from turbulent kinetic energy (*K*) and dissipation (ε):

$$\nu_t = C_\mu \frac{k^2}{\varepsilon} \quad (4\text{-}12)$$

where:

$$k = \frac{1}{2}\overline{u_\iota{}' u_\iota{}'} \quad (4\text{-}13)$$

$$\varepsilon = \nu \overline{\frac{\partial u_\iota{}'}{\partial x_j}\frac{\partial u_\iota{}'}{\partial x_j}} \quad (4\text{-}14)$$

where C_μ means the empirical constant; $u_i{}'$ is the turbulent fluctuation of velocity; bar represents averaging; ν is molecular diffusion (i.e., kinematic viscosity). In three dimensions, the quantities κ and ε are solved by the following two equations:

$$\frac{\partial k}{\partial t} + \overline{U}_i \frac{\partial k}{\partial x_i} = \frac{\partial}{\partial x_i}\left(\frac{\nu_t}{\sigma_k}\frac{\partial k}{\partial x_i}\right) + P - G - \varepsilon \quad (4\text{-}15)$$

$$\frac{\partial \varepsilon}{\partial t} + \overline{U}_i \frac{\partial \varepsilon}{\partial x_i} = \frac{\partial}{\partial x_i}\left(\frac{\nu_t}{\sigma_\varepsilon}\frac{\partial \varepsilon}{\partial x_i}\right) + C_{1\varepsilon}[P + (1 - C_{3\varepsilon})G] - C_{2\varepsilon}\frac{\varepsilon^2}{k} \quad (4\text{-}16)$$

where:

Shear *P* value is the term for the production of turbulent energy:

$$P = \nu_t\left(\frac{\partial \overline{U}_i}{\partial x_i} + \frac{\partial \overline{U}_i}{\partial x_i}\right)\frac{\partial \overline{U}_i}{\partial x_i} = 2\nu_t D_{ij} D_{ij} \quad (4\text{-}17)$$

Buoyancy *G* value is a term according to the forces of gravity in the case of temperature gradients:

$$G = \beta \frac{\nu_t}{Prt} g \frac{\partial T}{\partial z} \quad (4\text{-}18)$$

where β means fractional density (i.e., volume expansion); *Prt* being the Prandtl number. Several empirical constants have been determined by comparison with a broad range of turbulent flow situations (Table 4.4).

Table 4.4 The constants of the κ -ε

C_μ	*Prt*	$C_{1\varepsilon}$	$C_{2\varepsilon}$	$C_{3\varepsilon}$	σ_k	σ_ε
0.09	1	1.44	1.92	0 if G > 0; 1 if G < 0	1	1.3

k–omega model (*k-ω*): The concept of *k-ω* is similar to *k-ε*. The main difference between *k-ω* and *k-ε* is that adopting the specific dissipation ω instead of ε. The relationship between ω and ε is $\omega = \frac{\varepsilon}{\kappa}$. Vostruha & Pelant (2013) reveals that compared to *k-ε*, *k-ω* is suitable in the case of boundary conditions due to the friction velocity. Also, the complex wall functions could be solved by *k-ω*, which means that the better performance close to the bed and solid wall boundary could be obtained by adopting *k-ω*. As illustrated in Table 4.5, the limitations of each turbulence scheme setting must be paid attention to in the sensitivity analysis of turbulence schemes.

Table 4.5 The limitation of each candidate turbulence scheme.

Turbulence schemes		Cautions
Horizontal	Vertical	
Cst		✓ In Cst, the global (molecular and turbulent) viscosity should be provided by the user (In this study: 10^{-6} m^2/s). ✓ In other turbulence models, molecular viscosity is prescribed by users, and turbulent viscosity is calculated by models.
Smag		✓ If Smag is used for the vertical turbulence model, the horizontal aspect is automatically set as Smag. ✓ On the contrary, Smag in the horizontal aspect can be used with every possible turbulence for the vertical aspects.
k-ε		✓ It is impossible to mix *k-ε* and *k-ω* in horizontal and vertical aspects.
k-ω		
ML		✓ The ML is only available for vertical diffusivity of velocities calculation.

A. Investigating the same scheme for horizontal and vertical aspects

To simplify the sensitivity testing of turbulence schemes, the tests with the same scheme for horizontal and vertical aspects were first analyzed (Table 4.6). The results indicate that the least computational time was needed by using Cst because the turbulent viscosity calculation is unnecessary. Because the turbidity current is the complex flow situation at the bottom reach and around constructures, as mentioned above, the *k-ω* is suitable in these conditions. The results show that compared to simulation with Cst, the better performance at bottom reach was yielded using *k-ω*. Moreover, we found that terrible results were generated by using Smag due to the size of the vortices being larger than the mixing length. Based on the aforementioned results, the Cst, *k-ω,* and *k-ω* can bring acceptable results for cross sectional and outlets.

B. Investigating the mixing scheme for horizontal and vertical aspects

This section discussed the mixing scheme for horizontal and vertical aspects to achieve the balance of computational time and accuracy. Based on the conclusion from the previous section, the feasibility of the mixing Cst (i.e., less computational time) and *k-ω* (i.e., better performance) were evaluated. As shown in Table 4.6, we found that the application of mixing two different turbulence schemes leads to better performance, but computational time slightly increases. In addition, similar to Smag, the ML is inappropriate for turbidity current simulation. The results indicate that the overall better performance from case 6, using Cst and *k-ω* for horizontal and vertical aspect, respectively, was obtained. The turbidity current transportation in the horizontal direction is stable and complex interaction in the vertical direction (e.g., plunging effect and turbulent wake at stratification interface). Therefore, it is reliable to adopt Cst for horizontal aspect and *k-ω* for vertical aspect in the turbidity current simulation.

Table 4.6 The sensitivity tests of turbulence scheme for horizontal and vertical aspects.

Cases	Horizontal aspect	Vertical aspect	CPU time (min)	RMSE (g/l)			
				Bottom reach	Cross section	Outlet	**Mean**
Same scheme for horizontal and vertical aspects							
1	Cst	Cst	***27.82***	29.50	23.51	20.71	22.11
2	*k-ε*	*k-ε*	34.82	28.27	22.71	23.08	22.89
3	*k-ω*	*k-ω*	38.83	***26.61***	***21.82***	22.31	22.07
4	Smag	Smag	30.28	112.82	82.53	84.97	83.75
Mixing scheme for horizontal and vertical aspects							
5	*k-ω*	Cst	40.42	27.08	22.09	22.04	22.07
6	Cst	*k-ω*	38.90	26.86	21.89	***19.12***	***20.50***
7	Cst	ML	28.20	129.76	95.05	94.67	94.86

*Note: the bold character means better performance

4.4.4 Sensitivity analysis of morphodynamic aspect

The GAIA is coupled with Telemac-3D to simulate sediment transport and bed evolution. To accurately simulate the turbidity current in the reservoir, the sediment material, bed roughness, and settling velocity (w_s) are critical in this study. The turbidity current is composed of fine particles (e.g., silt and clay). Based on the deposition sampling from the reservoir bed around the dam site, the diameter of suspended sediment is smaller than 62.5 μm. Therefore, the cohesive phenomenon is considered in this study. This section discusses the sensitivity tests for evaluating the applicable scope of bed roughness and settling velocity formula for the turbidity current simulation in the reservoir.

A. Bed roughness

The bed roughness setting is essential to determine the appropriate bottom friction, which is highly related to flow velocity and bed shear stress. To select the suitable bed roughness, the sensitivity tests of Chézy, Manning, and Nikuradse laws were analyzed.

Chézy law:

$$\begin{cases} F_x = -\dfrac{u}{\cos\alpha}\dfrac{g}{DC_f{}^2}\sqrt{u^2+v^2} \\ F_y = -\dfrac{v}{\cos\alpha}\dfrac{g}{DC_f{}^2}\sqrt{u^2+v^2} \end{cases} ;\ C_f = kR_h{}^{1/6} \qquad (4\text{-}19)$$

Manning law:

$$\begin{cases} F_x = -\dfrac{u}{\cos\alpha}\dfrac{gn^2}{D^{4/3}}\sqrt{u^2+v^2} \\ F_y = -\dfrac{v}{\cos\alpha}\dfrac{gn^2}{D^{4/3}}\sqrt{u^2+v^2} \end{cases} ;\ n = \frac{1}{k} \qquad (4\text{-}20)$$

Nikuradse law:

$$\begin{cases} F_x = -\dfrac{u}{\cos\alpha}\dfrac{g}{DC_f{}^2}\sqrt{u^2+v^2} \\ F_y = -\dfrac{v}{\cos\alpha}\dfrac{g}{DC_f{}^2}\sqrt{u^2+v^2} \end{cases} ;\ C_f = 7.83\ln\left(12\frac{D}{k_s}\right) \qquad (4\text{-}21)$$

where R_h is the hydraulic radius, which can be equal to D under the condition of the very large canals; k is the Strickler coefficient, and k_s means the asperity size. Based on the empirical coefficient of cement mortar, the Chézy (75) and Manning (0.013) coefficients were obtained. Moreover, the k_s could be calculated by using the Ramette formula with k:

$$k = 8.2\sqrt{g}/k_s^{1/6} \quad (4\text{-}22)$$

In Telemac-3D, the bottom friction from Chézy and Manning law is computed from friction velocity and its relation to the coefficient (C_f and n, which the user prescribes). For the Nikuradse law, the velocity profile within the logarithmic layer is considered. It means that the bed roughness could be changeable according to water depth. As illustrated in Table 4.7, the performance form using the Nikuradse law was much better than using Chézy and Manning law. It significantly reveals that the uniform bed roughness for the whole domain is inappropriate in this study.

Table 4.7 Compares cross sectional and outlet performance between Nikuradse, Chezy, and Manning bed roughness equation.

	Nikuradse	Chezy	Manning
Bottom reach at CS4	26.86	42.73	40.29
Cross section	21.89	33.02	31.24
Outlet	19.12	40.68	34.04
Mean	20.50	36.85	32.64

B. Settling velocity

Huang et al. (2019) indicate that the settling velocity is crucial for the plunge phenome and turbidity current transport estimation. Due to most of the suspended sediment within Shihmen Reservoir being silt and clay, the applicable settling velocity formula is expressed:

Rubey:

$$w_s = \frac{[1.636(s-1)d_{50}^3 + 9v^2]^{0.5} - 3v}{500d} \quad (4\text{-}23)$$

Van Rijn:

$$w_s = \frac{(s-1)gd_{50}^2}{18v} \quad (4\text{-}24)$$

Zhu&Cheng:

$$w_s = \frac{v}{9d}\{-24 + [576 + 18d\left(\frac{g(s-1)}{v^2}\right)^{1/3}]^{0.5}\} \quad (4\text{-}25)$$

where $s = \rho_s/\rho_a$ is the relative density; ρ_s is sediment density (2650 kg/m^3); ρ_a is water density (1000 kg/m^3). Table 4.8shows that the Rubey and Van Rijn settling velocity formula yields similar results, but the Rubey still has a slightly better performance than the Van Rijn. Based on the aforementioned results, the Nikuradse law with k_s equal to 0.001385 and Rubey settling velocity formula was regarded as the appropriate governing terms for the morphodynamic aspect.

Table 4.8 Compares cross sectional and outlet performance between Rubey, Van Rijn, Zhu&Cheng settling velocity formula.

	Rubey	Van Rijn	Zhu&Cheng
Bottom reach at CS4	26.86	26.81	45.88
Cross section	21.89	21.86	35.17
Outlet	19.12	19.40	29.70
Mean	20.50	20.63	32.43

4.4.5 Calibration and validation results by adopting optimal numerical aspects and equations

According to the previous comprehensive sensitivity analysis, the optimal numerical aspects and equations were determined (Table 4.9). With the optimal modelling setup, the results from the calibration case (i.e., Sc# Ori) have a good agreement with the measurements (Figure 4.9). Moreover, the same modelling setup for validation cases (Sc# Daw and Sc# Amu) also brings good agreements with measures from the cross section, outlets, and water level. We found that the simulations at CS24 bottom from both Sc# Daw and Sc# Amu are underestimated, but the overall performances are acceptable. As illustrated in Table 4.10, the RMSE and CC values of cross sections, outlets, and water level were obtained, revealing that the simulations yield accurate results. The aforementioned results proved that the Telemac-3D with determined modelling setups could give the precise and reliable turbidity current simulation to investigate optimal reservoir management.

Table 4.9 Optimal numerical aspects and equations for turbidity current simulation.

Numerical aspect	Options
Mesh size	$[b_0/6, b_0/3]$
Time step	$\Delta t/\Delta x = 5$
Layer style	LS2
Layer number	15
Horizontal turbulence model	Cst
Vertical turbulence model	κ-ω
Bed roughness fromula	Nikuradse
Settling velocity	Rubey

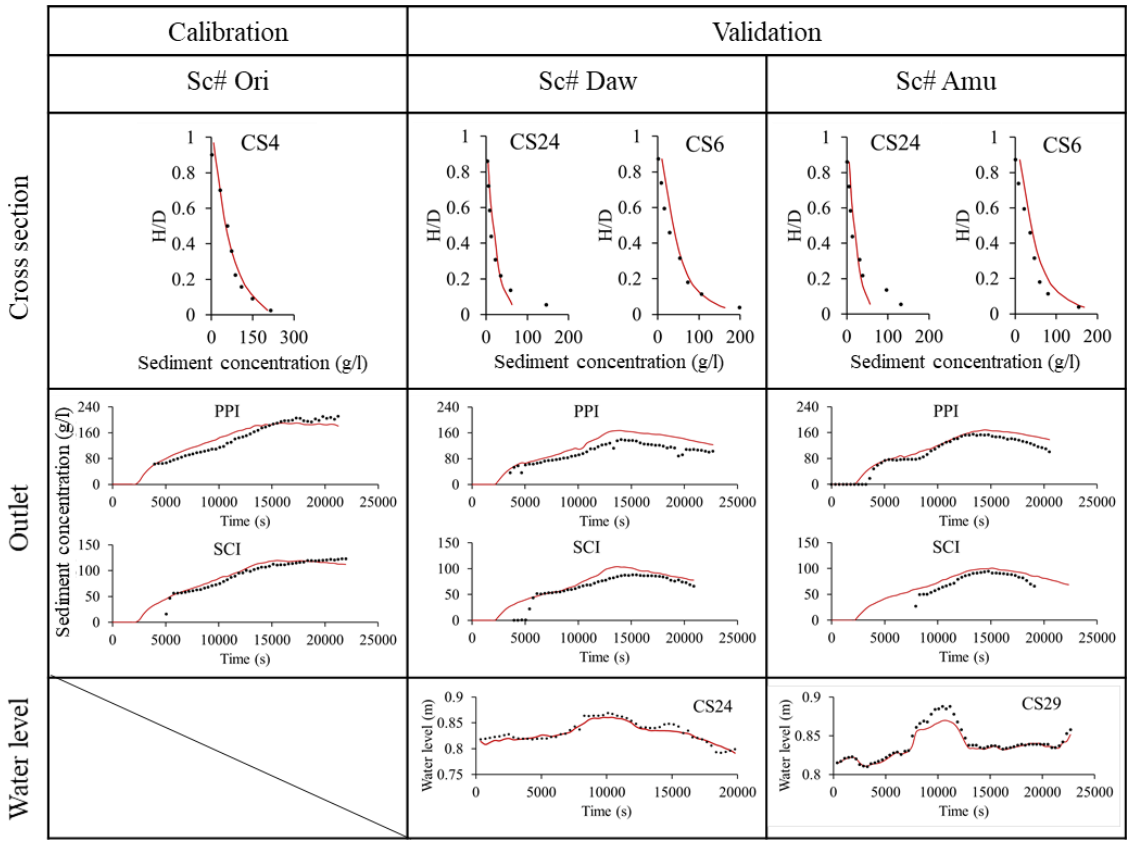

Figure 4.9 Comparison between the numerical and the experimental results of cross sections, outlets, and water level in calibration and validation cases.

Table 4.10 The RMSE and CC values of cross sections, outlets, and water level in calibration and validation cases.

	Calibration		Validation			
	Sc# Ori		Sc# Daw		Sc# Amu	
	RMSE	CC	RMSE	CC	RMSE	CC
Cross section (g/l)						
CS24	-	-	30.26	0.969	33.26	0.978
CS6	-	-	15.36	0.996	15.92	0.993
CS4	21.89	0.994	-	-	-	-
Outlet (g/l)						
PPI	25.39	0.957	27.47	0.982	16.58	0.991
SCI	12.84	0.950	10.72	0.957	12.37	0.987
SBT	-	-	20.98	0.836	8.30	0.850
Water level (m)	-	-	0.0067	0.979	0.0068	0.993

4.5 Investigation of numerical modelling setup under field-scale

4.5.1 Initial and boundary condition

As illustrated in Table 3.2, the 2015 typhoon events, Soudelor and Dujuan Typhoon, are selected to calibrate and validate the numerical model due to the complete available field data. Moreover, the Megi Typhoon was used to test the validated model's stability for future flooding events. The upstream and downstream boundary conditions for model calibration and validation are shown in Figure 4.10. According to the empirical coefficient, the Nikuradse coefficient of the natural channel is around 0.042. As illustrated in Figure 3.7, the inflow sediment material is cohesive sediment with 15 μm size, calculated by averaging the 25th (6.51 μm) and 75th percentile value (24.38 μm).

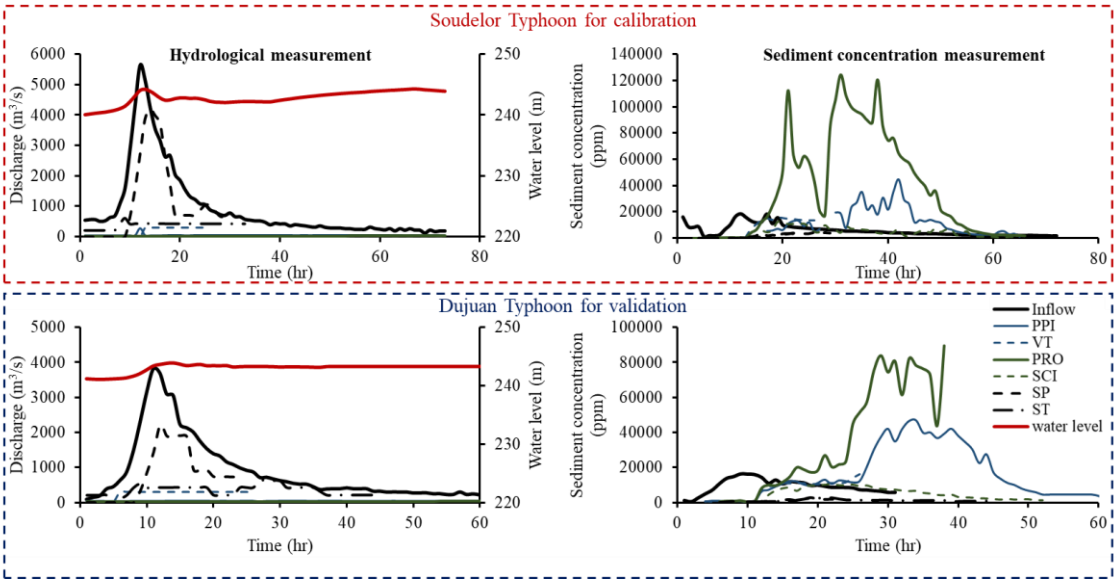

Figure 4.10 The hydrological and sediment concentration measurement for model calibration and validation.

Based on the sediment sampling, the dry and wet sediment density (1800 and 2650 kg/m^3) is adopted for inflow sediment material. As shown in Figure 4.11, the critical shear stress for the erosion of the Shihmen Reservoir sediment is around 0.5 N/m^2. With the

settled initial and boundary condition, the modeling setup for the field-scale numerical model was evaluated based on the experimental-scale setting.

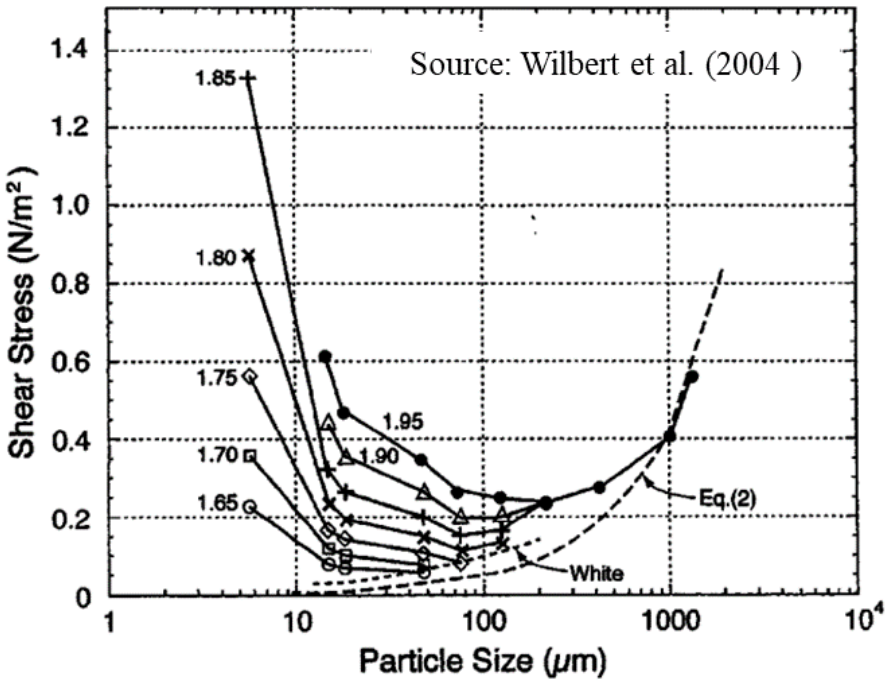

Figure 4.11 The critical shear stresses for erosion as a function of particle size and dry sediment density.

4.5.2 Three-dimensional numerical modeling for field-scale simulation

According to the guidelines from experimental-scale sensitivity analysis, the numerical modelling of numerical aspects and governing equations for the field-scale model was listed in Table 4.11. The generated mesh based on the 2015 Shihmen Reservoir bathymetry was used for the turbidity current simulation in Soudelor and Dujuan Typhoon. As mentioned in **Chapter 4.4.2**, the finer mesh was used in the middle stream, and two times of mesh size was applied for the bankside. Moreover, according to the measurements from TDR facilities, the initial suspended sediment concentration is around 1000 ppm. Based on the aforementioned numerical modelling, the calibrated and validated results by using Soudelor and Dujuan Typhoon are expressed:

Table 4.11 The numerical setting for field-scale simulation.

Numerical aspect	Options
Mesh size	[20, 40] m
Time step	4 s
Layer style	LS2
Layer number	15
Horizontal turbulence model	Cst
Vertical turbulence model	κ-ω
Bed roughness formula	Nikuradse
Settling velocity	Rubey

A. Calibration and validation by using Soudelor and Dujuan Typhoon data

As illustrated in Figure 4.12, the results showed that the released sediment concentration at the beginning of the bottom outlets (i.e., PRO, PPI, and VT) have good agreements, and the released sediment concentration from the upper outlets (i.e., SCI, ST, and SP) have good performance during the whole typhoon event. Moreover, Figure 4.13 clearly showed that the cross sectional simulations have good agreement with observation in not only the time series but vertical profile. However, we found that the extremely underestimated simulation was obtained at PRO and PPI's peak released sediment concentration. The underestimation might be caused by the lack of accumulated sedimentation setting in front of the dam. But it is difficult to do the sensitivity analysis for the initially deposited sediment layer due to the lack of bottom material measurements. Moreover, the same modelling setup was adopted for the numerical model validation by using the turbidity current simulation in Dujuan Typhoon. As shown in Figure 4.14 and Figure 4.15, the validated case got a similar performance to the calibrated case. Overall, the numerical modelling setup based on the experimental-scale model for the field-scale model is suitable for obtaining the acceptable turbidity current simulations.

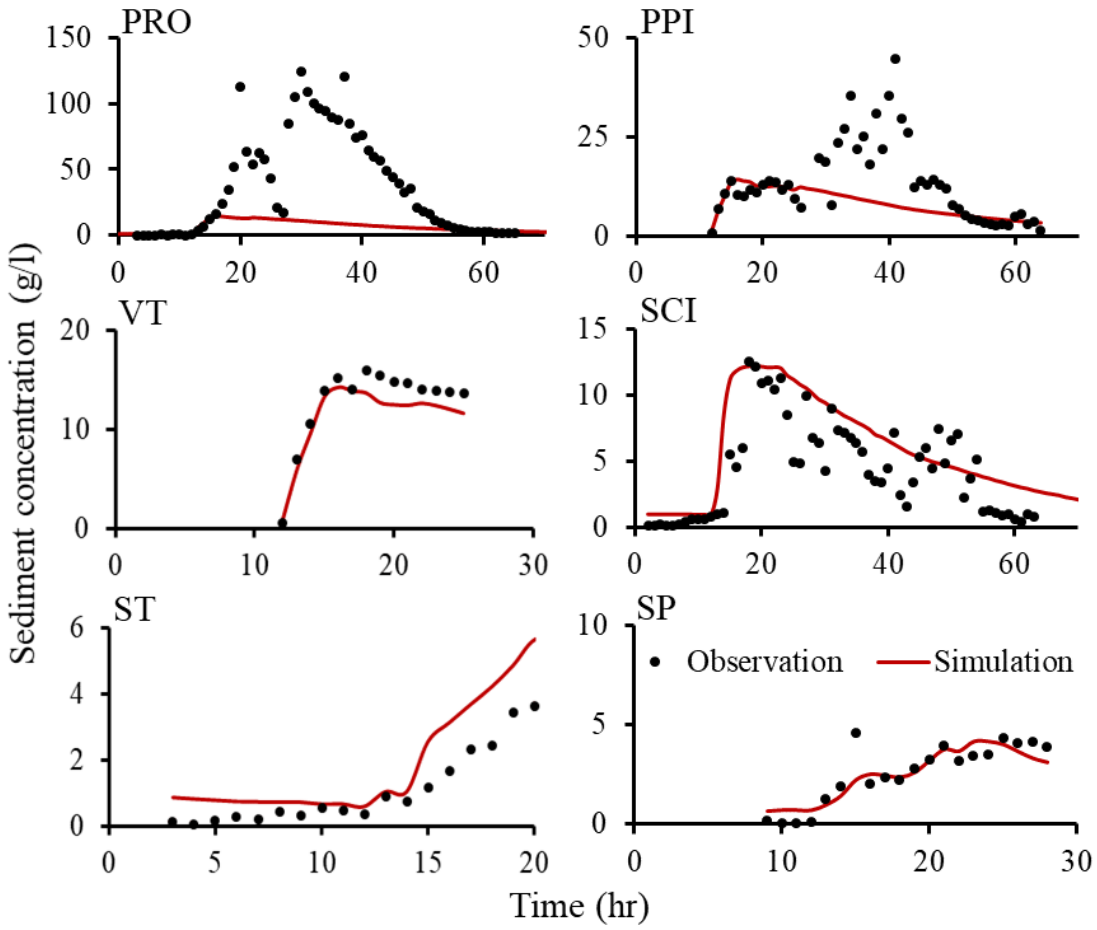

Figure 4.12 Comparison between the simulation and the observation of each venting outlet in Soudelor Typhoon for model calibration.

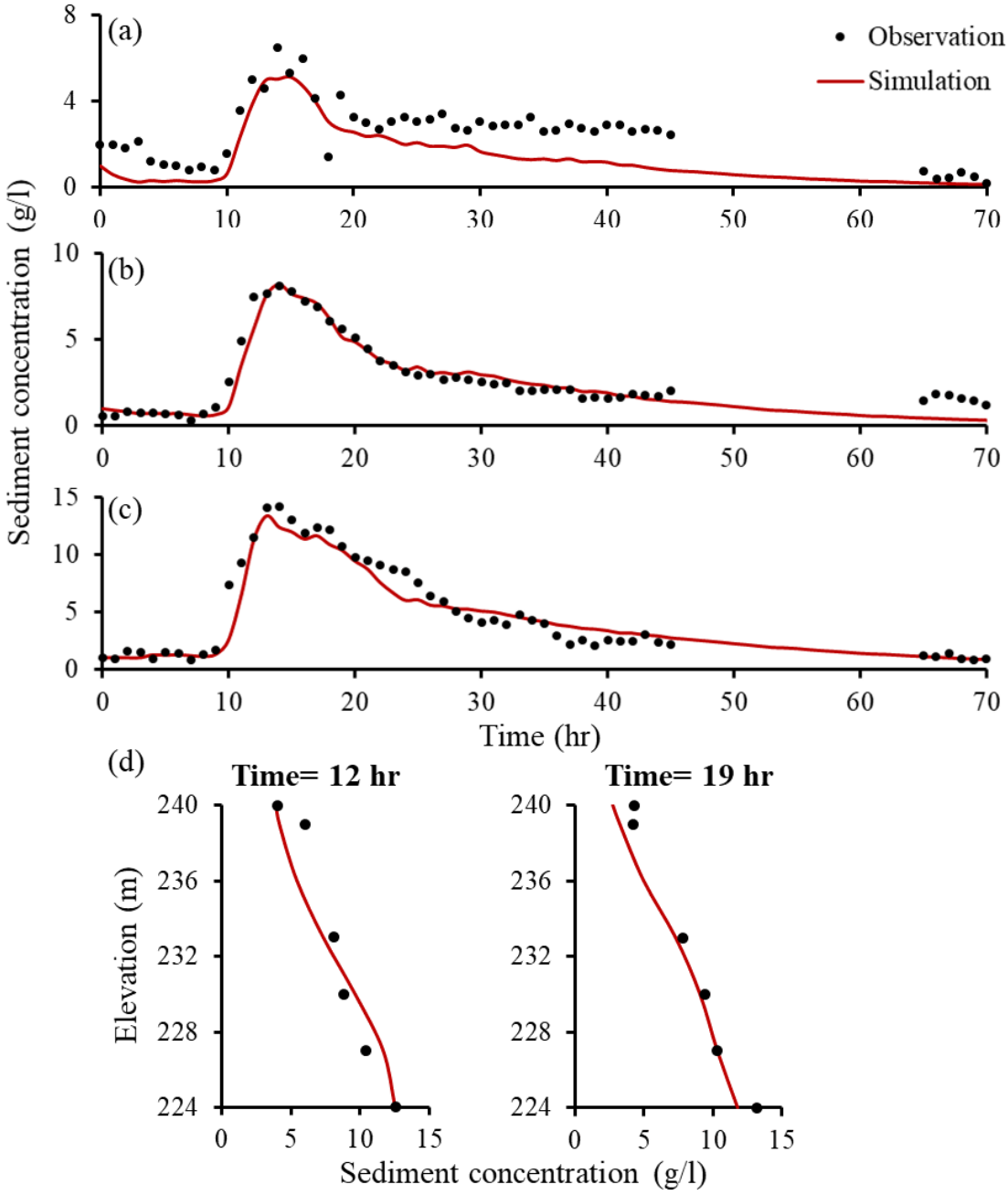

Figure 4.13 Cross sectional performance comparison between the simulation and the TDR 20-1 observation of (a) top, (b) middle, (c) bottom reach, and (d) vertical profile from Soudelor Typhoon for model calibration.

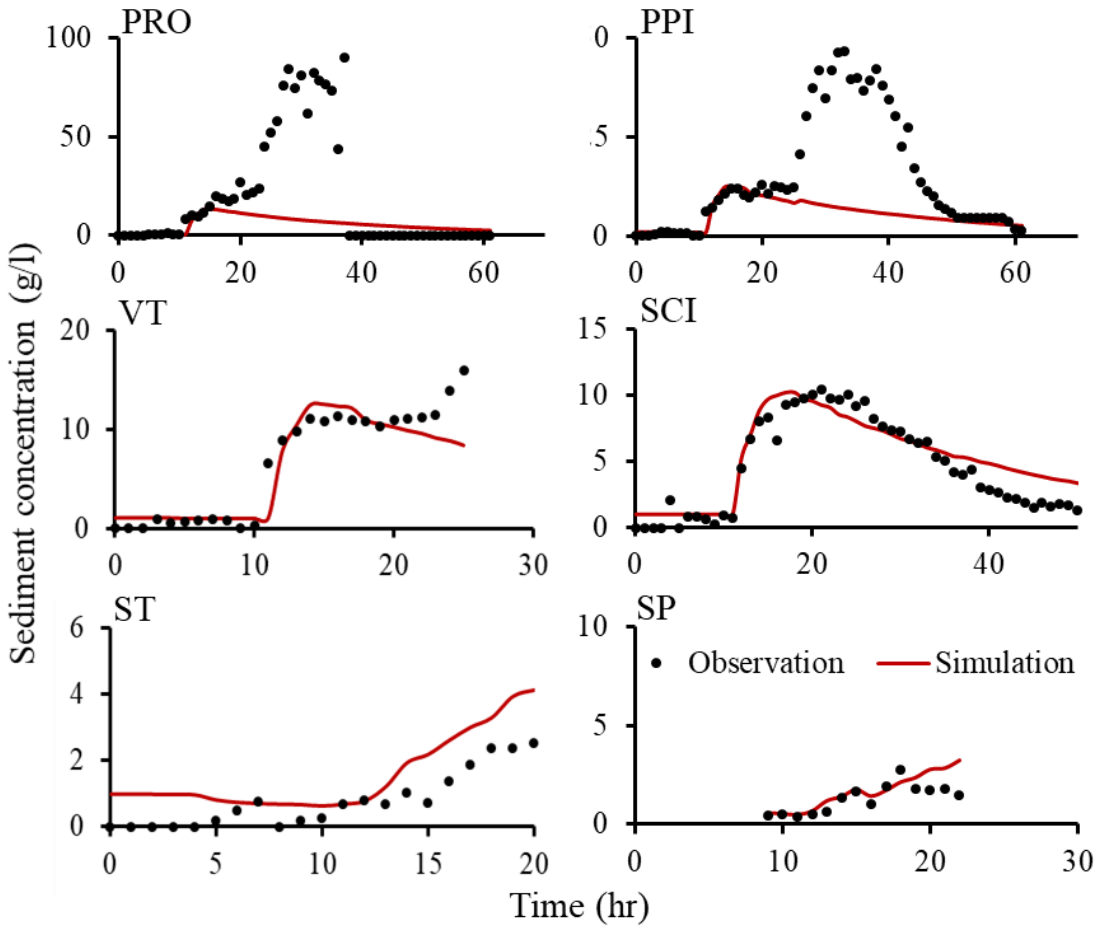

Figure 4.14 Comparison between the simulation and the observation of each venting outlet in Dujuan Typhoon for model validation.

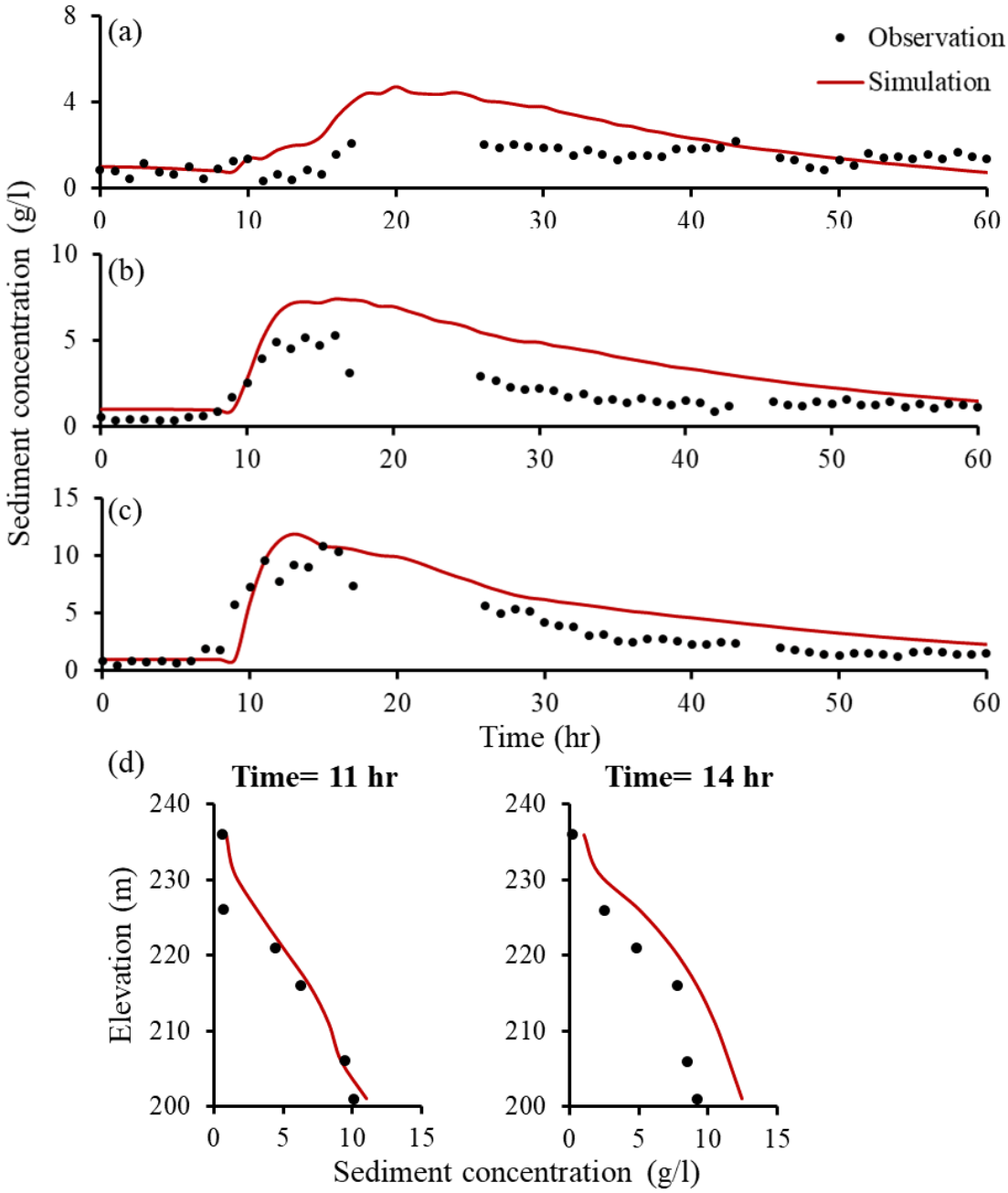

Figure 4.15 Cross sectional performance comparison between the simulation and the TDR 12-2 observation of (a) top, (b) middle, (c) bottom reach, and (d) vertical profile from Dujuan Typhoon for model validation.

B. Assess the feasibility of validated model for future events

To assess the stability of the validated three-dimensional numerical model for future flooding events, the model was built for turbidity current simulation in Megi Typhoon. As illustrated in Table 4.12, the RMSE and CC values reveal that the simulated sediment venting has similar performance in 2015 and 2016 typhoon events. Moreover, the accurate turbidity current arrival time from the plunging location to the dam was obtained (Figure 4.16). Based on the aforementioned results, the validated numerical model is provided to be appropriate for the turbidity current simulation in any condition. Overall, according to the guideline of numerical aspects and equations setting, the efficient and accurate turbidity current simulation in both experimental- and field-scale could be obtained.

Table 4.12 RMSE and CC values of venting outlets in calibration and validation cases.

Outlets	Soudelor (2015)		Dujuan (2015)		Megi (2016)	
	RMSE (g/l)	CC	RMSE (g/l)	CC	RMSE (g/l)	CC
PPI	10.00	0.36	16.21	0.43	6.13	0.83
PRO	42.90	0.62	30.39	0.46	16.94	0.79
SCI	2.74	0.83	1.25	0.95	6.95	0.58
SP	0.73	0.88	0.57	0.76	1.43	0.79
ST	1.08	0.98	0.98	0.86	-	-
VT	1.62	0.98	2.70	0.91	4.06	0.87
Average	**9.84**	**0.77**	**8.68**	**0.73**	**7.10**	**0.77**

*Note: - means no available data.

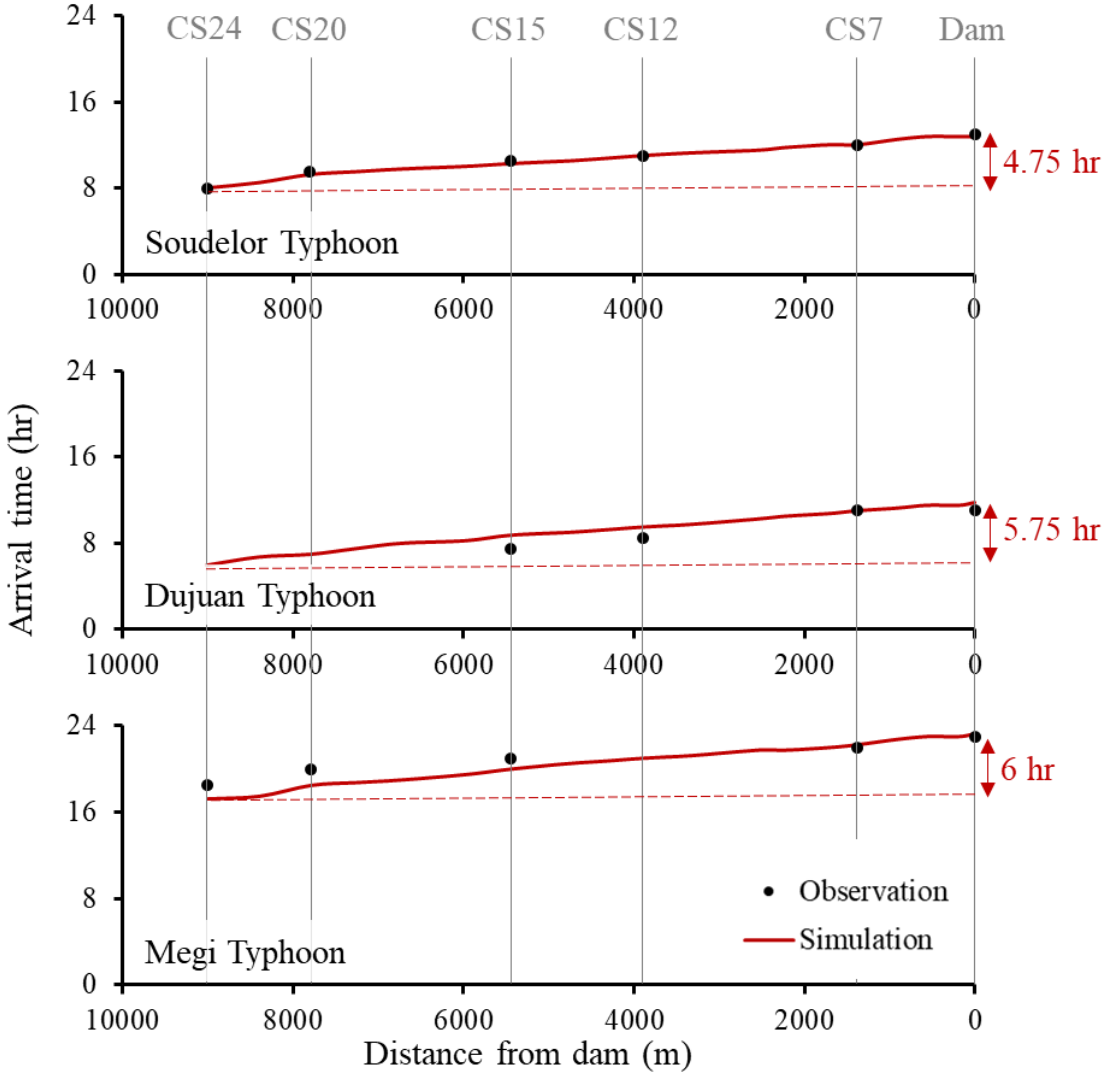

Figure 4.16 Turbidity current arrival time at each cross section.

4.6 Conclusion

The numerical model was the most appropriate tool to deeply understand the turbidity current characteristics and venting operation because it could avoid scale effects and provide numerous results enhancing the understanding of the process. For investigating the turbidity current plunging mechanism, stratification, and multiple outlets' operation from different elevations, the fully three-dimensional numerical model (Telemac-3D) was considered suitable in this study. To evaluate the performance of the numerical modelling setup, the coefficient of determination, root mean square error, and improvement percentage were employed to indicate the discrepancy between the measured and simulated values.

Through comprehensive sensitivity analysis, which considers the computational time and accuracy simultaneously, the applicable scope of the dimensionless numerical model setting, including domain discretization, turbulence scheme, and morphodynamic aspect, was determined. According to the numerical aspects and equations setting guideline, the efficient and accurate turbidity current simulation in both experimental- and field-scale could be obtained. Overall, the reliable three-dimensional numerical modelling setup could provide a reference for different scale numerical building.

Chapter 5: Understanding of the turbidity current characteristics and processes under variable inflow

5.1 Introduction

The turbidity current plunging mechanism, head velocity, and thickness are the critical factors for understanding the turbidity current process in the reservoir. As illustrated in Figure 5.1, the turbidity current process could be investigated by the obtained three-dimensional simulation. The head velocity and arrival time at each cross section and outlet can be detected to estimate the in-time operation timing. Due to the wider width of the cross section between CS24 and CS19, the velocity slows down. Also, the turbidity flow spreading into the tributary leads to the thickness decrease (Figure 5.1 (b)). Based on the plunging mechanism (Morris and Fan, 1998), the ambient water circulation induced by the plunging turbidity current is associated with an opposite surface velocity. The plunging location is between CS29 and CS24.

Meanwhile, it seemed impossible to release all of the turbidity currents through the outlets within the Shihmen Reservoir. The muddy lake is formed as the remaining turbidity flow is stranded in the reservoir (Figure 5.1 (d)). Predicting the high turbidity muddy lake reaching water supply intake is essential to manage the withdrawal of clear water. In this section, the critical terms for governing the turbidity current plunging, transportation are investigated.

Moreover, based on the conclusion in **Chapter 4.5**, the deficient data from tributaries and accumulated deposition material could lead to the limitation of the field-scale numerical model. Thus, the necessity of additional measurements to monitor the inflow from tributaries and the sediment material of the active deposition for solving the limitation of field-scale simulation is evaluated in this section. After that, the acquired

data conduce to accurate field-scale simulation is essential for assessing the efficiency of proposed improvement strategies in **Chapter 6**.

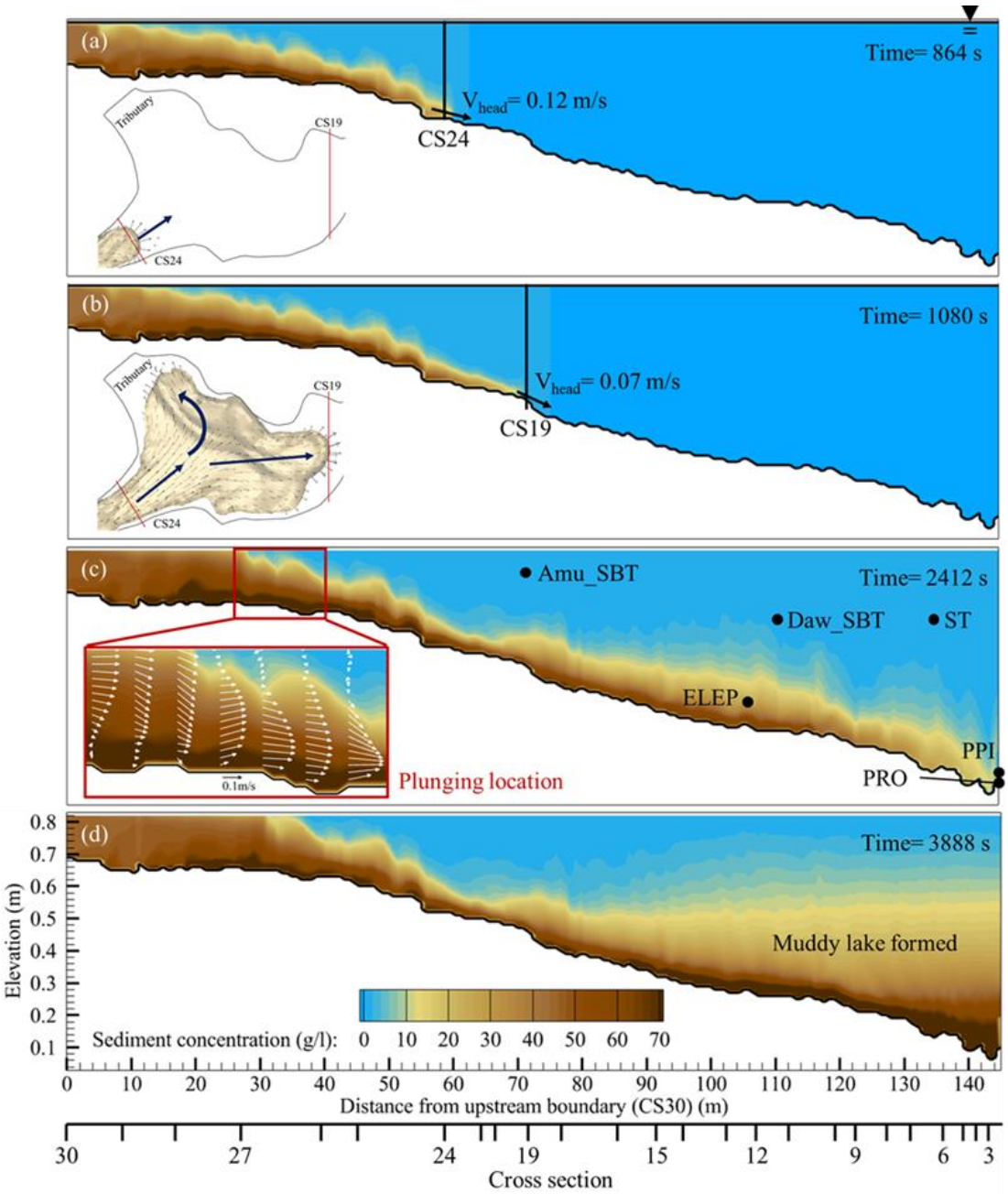

Figure 5.1 The experimental-scale simulation of turbidity current process in the reservoir by using validated Telemac-3D: (a) the head velocity and arrival time at CS24; (b) the wider width and tributary lead to the velocity and thickness decrease; (c) the configuration of turbidity current from plunging to arrive at dam site; (d) the muddy lake formed after the turbidity current arrives dam.

5.2 Understanding of turbidity current processes

A three-dimensional simulation is essential to understand the turbidity current processes within the reservoir. Using the fully three-dimensional numerical model, the turbidity flow converted from sediment-laden flow to turbidity current could be clearly understood (Figure 5.2). The results showed that the velocity of sediment-laden flow is higher due to the shallow water upstream of the reservoir. Under certain conditions, the high sediment concentration flow plunges and concentrates to turbidity current. After turbidity current plunging, the turbidity current is transported to the bottom of the reservoir. The huge tributary within the middle of the reservoir leads to turbidity current transportation is divided into mainstream and tributary directions. Meanwhile, the circulating flow occurs due to the turbidity current spreading flow into the tributary.

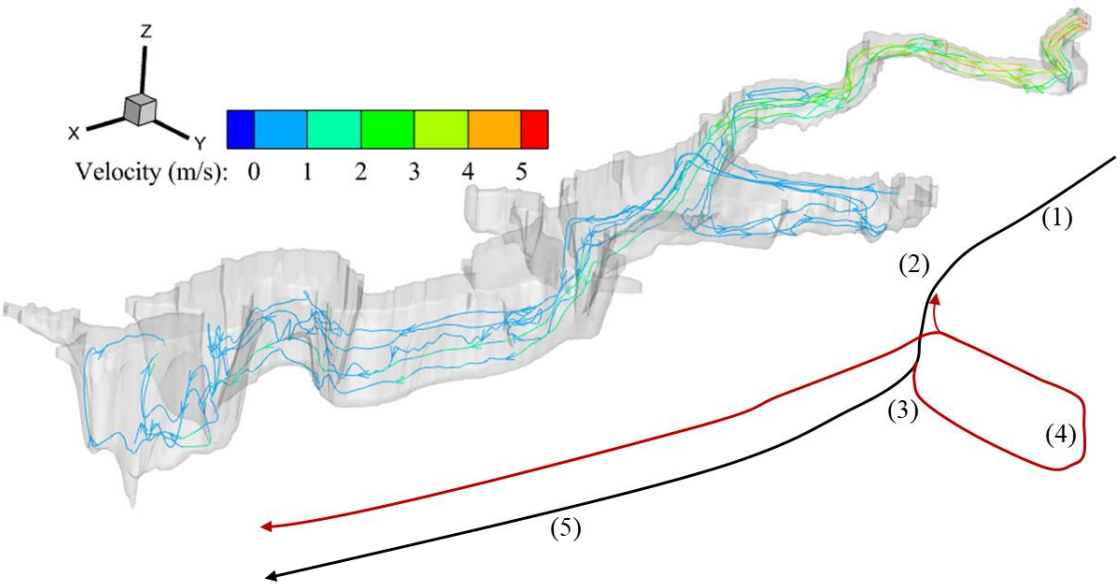

Figure 5.2 The streamline within the Shihmen Reservoir under the flooding event and the configuration of the turbidity current processes: (1) the sediment-laden flow region; (2) the turbidity current plunges; (3) the turbidity current transportation is divided into mainstream and tributary direction; (4) the turbidity current spread flow into the tributary lead to the circulation; (5) the turbidity current region.

As illustrated in Figure 5.3, the plunging location is significantly revealed by the interface of turbidity flow and ambient water. After the turbidity current plunging, the surface plane is still ambient water and high sediment concentration flow at the bottom plane due to the stratification. Moreover, due to the turbidity current plunging force causing the vortex near the plunging location, the plunging location also could be pointed out by the interface of positive and negative surface flow direction. Meanwhile, the stratification is clearly shown in the longitudinal view at mainstream (Figure 5.4). The results reveal that the bed elevation of the right and left side of the mainstream is higher and turbidity current transport at the bottom. Therefore, we understood that if it is necessary to build additional venting facilities, the location of outlets should be settled along the middle of the mainstream. Moreover, the circulation within the tributary due to the turbidity current spread flow into the tributary could be investigated (Figure 5.4). The result indicated that the turbidity current flows at the bottom from mainstream to tributary. Meanwhile, the ambient water at the surface flows in the opposite.

The vertical profile of sediment concentration and velocity at the sediment-laden flow region (CS28) and turbidity current region (CS20 and CS12) is shown in Figure 5.5. The results showed that the vertical profiles differed before and after the turbidity current plunging. The sediment concentration difference between surface (H) and bottom (H_0) is only 0.34 g/l at the sediment-laden flow region, almost uniform distribution. The sediment-laden region's flow regime and sediment distribution are similar to the open-channel flow. On the contrary, the sediment concentration difference is around 15 g/l, and surface water is ambient due to the stratification. As shown in Figure 5.5 (b) and (c), the velocity of turbidity current is much faster than the surface ambient water. Also, due to the turbidity current plunging, the negative flow could be observed at the surface of CS20, where close to the plunging location.

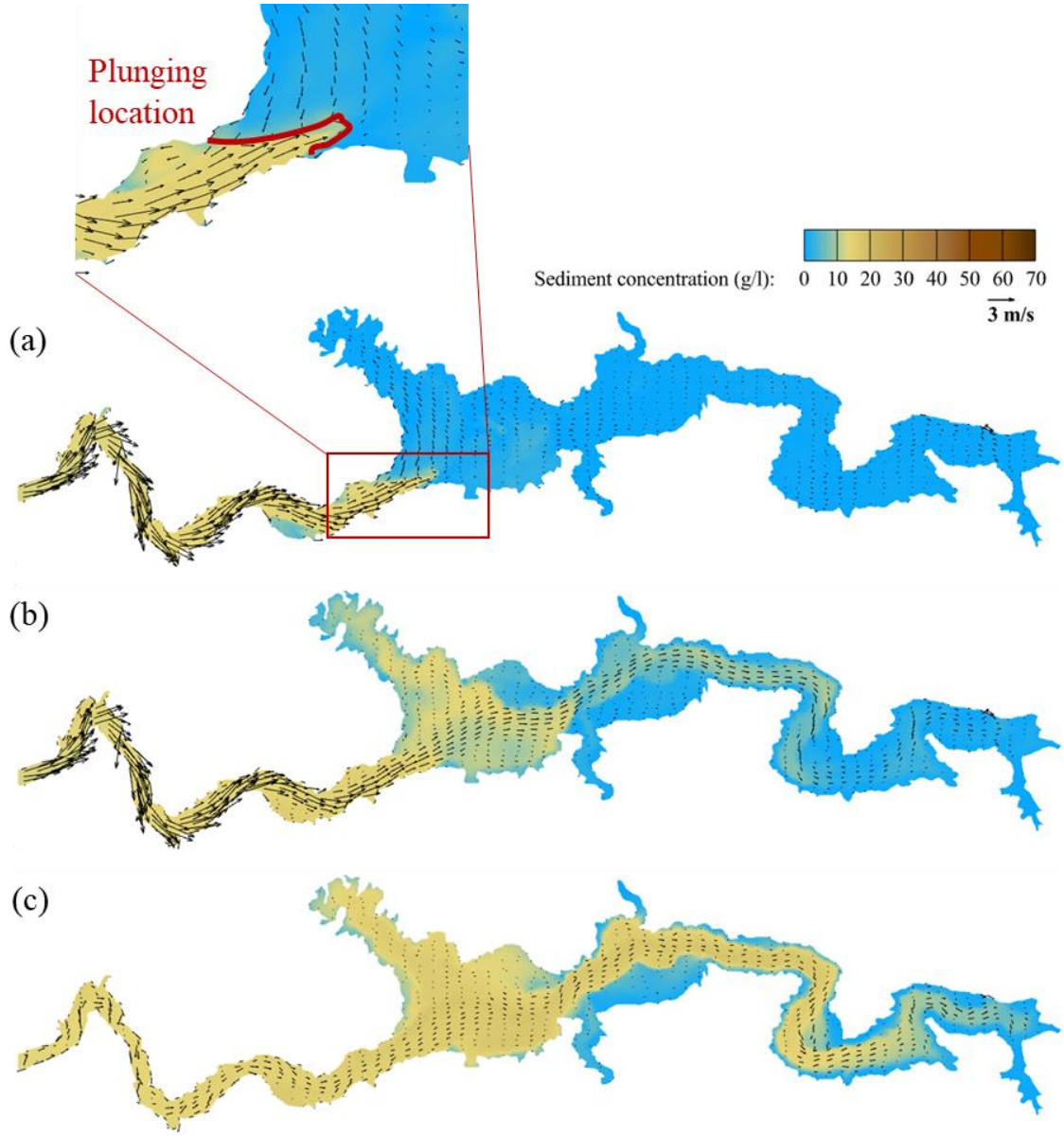

Figure 5.3 The plane view of sediment concentration and velocity vector at (a) surface, (b) middle, and (c) bottom.

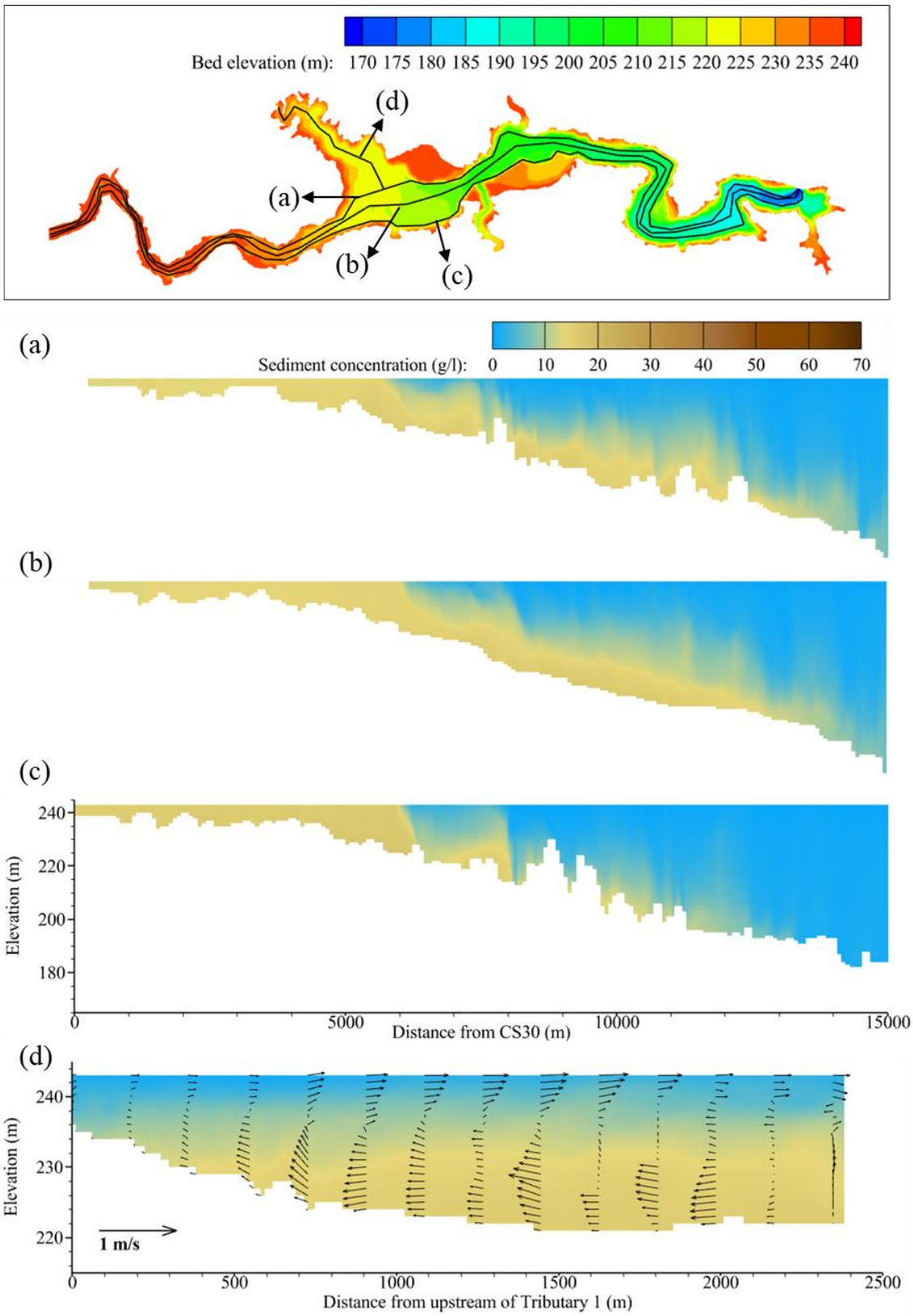

Figure 5.4 The longitudinal view of sediment concentration at (a) left side, (b) middle and (c) right side of mainstream, and (d) tributary.

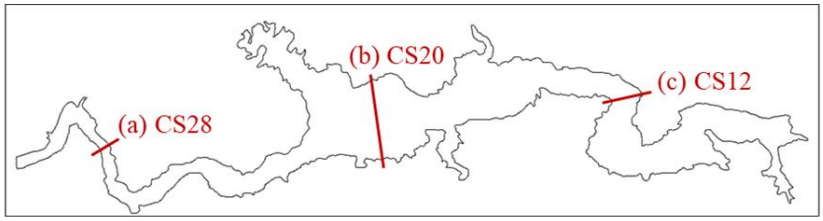

(a)

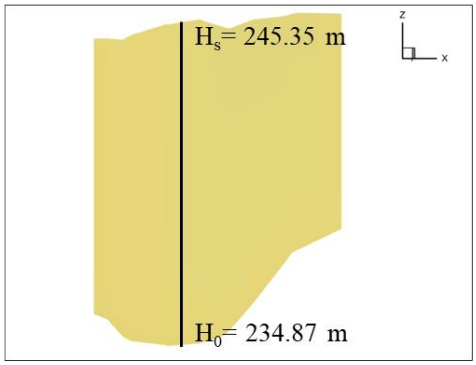

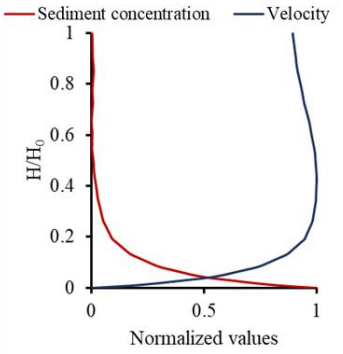

	Sediment concentration (g/l)	Velocity (m/s)
Maximum	13.7	4.04
Minimum	13.36	1.34

(b)

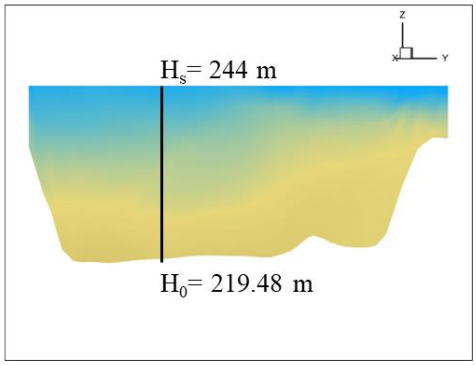

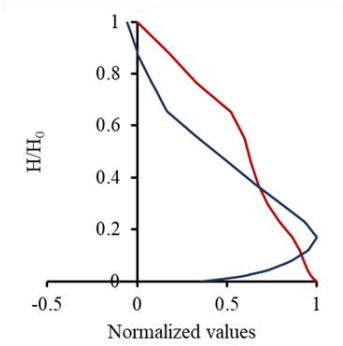

	Sediment concentration (g/l)	Velocity (m/s)
Maximum	16.27	1.04
Minimum	1.82	0.076

(c)

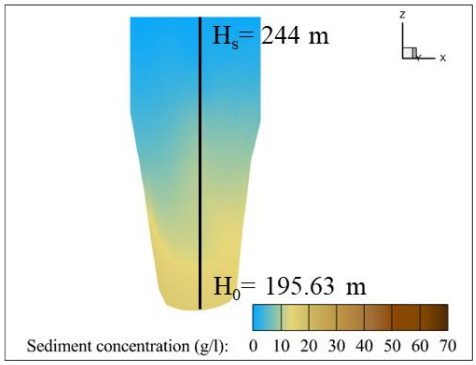

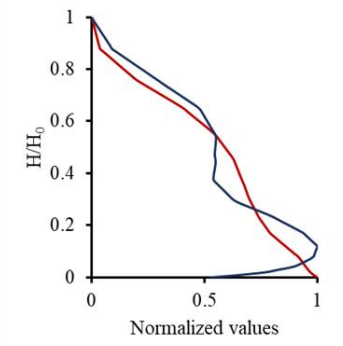

	Sediment concentration (g/l)	Velocity (m/s)
Maximum	16.03	0.85
Minimum	0.614	0.057

Figure 5.5 The cross sectional view and vertical profile of sediment concentration and velocity at (a) CS28, (b) CS20, and (c) CS12.

As illustrated in Figure 5.6, the bed difference after the flooding event is clearly shown in the plane view and longitudinal view. The serious deposition location has been pointed out in Figure 5.6. The result indicated that the sediment is deposited in the outside curve area. Moreover, due to the muddy lake formed at reservoir downstream, the severe deposition is settled by the muddy lake. Meanwhile, we found that considerable sediment is deposited in the tributaries. Overall, based on the previous understanding, the appropriate improving scenarios could be proposed in this study.

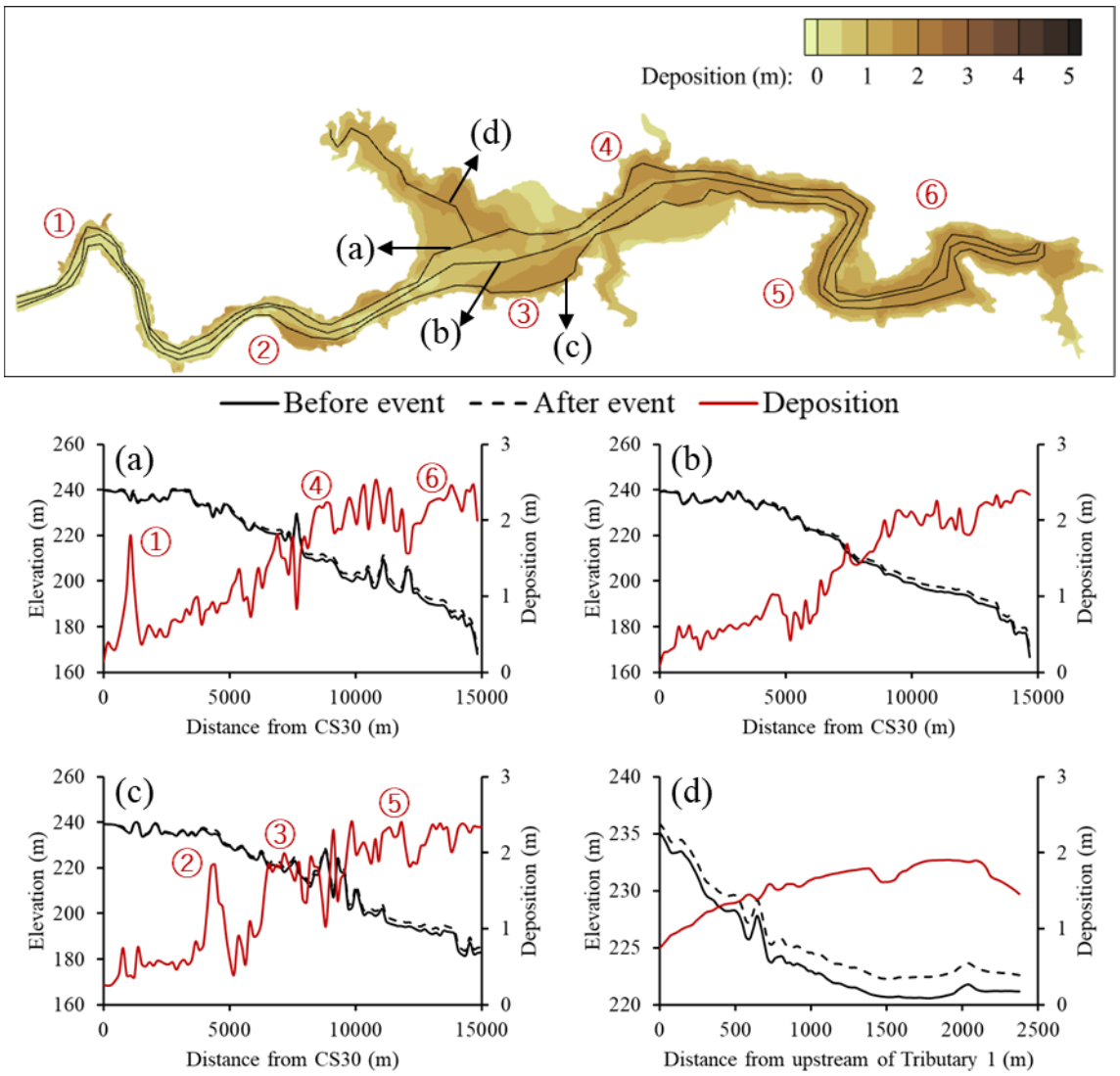

Figure 5.6 The bed elevation before and after event and deposition at (a) left side, (b) middle and (c) right side of mainstream, and (d) tributary.

5.3 Investigation of governing terms for turbidity current processes

As illustrated in Figure 5.7, the turbidity current process could be divided into two parts based on plunging location: sediment-laden flow region and turbidity current region. The main difference between those two regions is the significant stratification occurs in the turbidity current region. Due to the density difference of clear water and turbidity flow, the turbidity current transport at the bottom and the transport mechanism is different from the sediment-laden flow region. Therefore, the plunging location investigation is critical to understanding the turbidity current process introduced in **Chapter 5.3.2**. As Figure 5.7 showed, the force of turbidity flow plunging leads to the vortex near the plunging location, and the surface velocity direction is negative (i.e., flow to upstream). Although TDR equipment is in the Shihmen Reservoir, the continuous sediment concentration profile is difficult to obtain. Moreover, understanding the vertical profile of velocity is essential for investigating the turbidity current velocity and vortex effect. Therefore, **Chapter 5.3.3** describes the vertical profile of velocity and sediment concentration estimation in this thesis. Moreover, the turbidity current arrival time is crucial for determining the appropriate outlets' operating timing. The muddy lake reach time at the clear water supply intake is essential for the clear water supply instead of the turbidity water using and stop supplying. The details of the turbidity current arrival time and the muddy lake formed evaluation are presented in **Chapter 5.3.4**. To investigate the turbidity current process under different inflow conditions, the nine scenarios based on different amounts of inflow discharge and sediment concentration were generated and evaluated in **Chapter 5.3.1**.

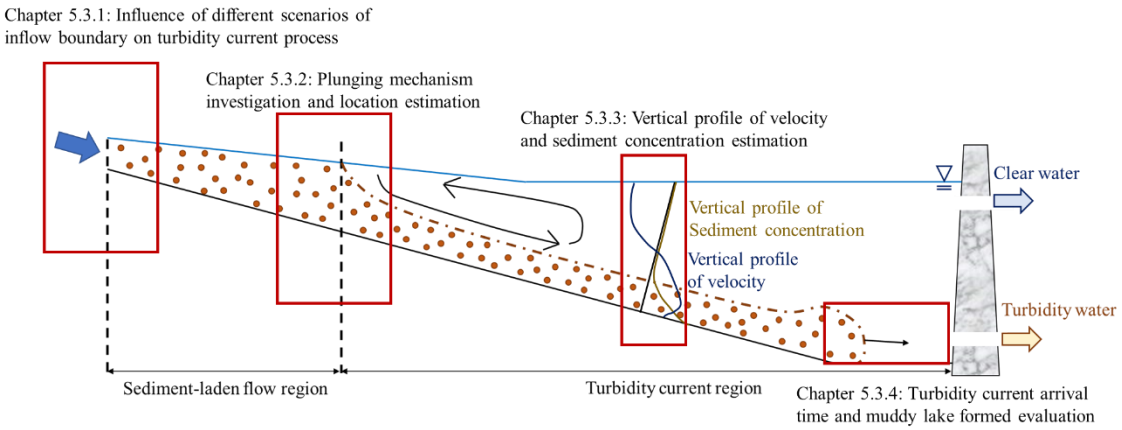

Figure 5.7 The configuration of the turbidity current process.

5.3.1 Influence of different scenarios of inflow boundary on turbidity current process

The generated hydrographs are based on the Soudelor Typhoon's observation (Figure 5.8). The nine scenarios were generated based on different inflow discharge and sediment concentration amounts. The threshold of each cluster could be expressed:

Small amount:

$1800\ m^3/s \leq$ peak inflow discharge $< 3000\ m^3/s$ (named Q_S)

$18000\ ppm \leq$ peak inflow sediment concentration $< 30000\ ppm$ (named S_S)

Middle amount:

$3000\ m^3/s \leq$ peak inflow discharge $< 5600\ m^3/s$ (named Q_M)

$30000\ ppm \leq$ peak inflow sediment concentration $< 56000\ ppm$ (named S_M)

Large amount:

$5600\ m^3/s \leq$ peak inflow discharge $< 8300\ m^3/s$ (named Q_L)

$56000\ ppm \leq$ peak inflow sediment concentration $< 83000\ ppm$ (named S_L)

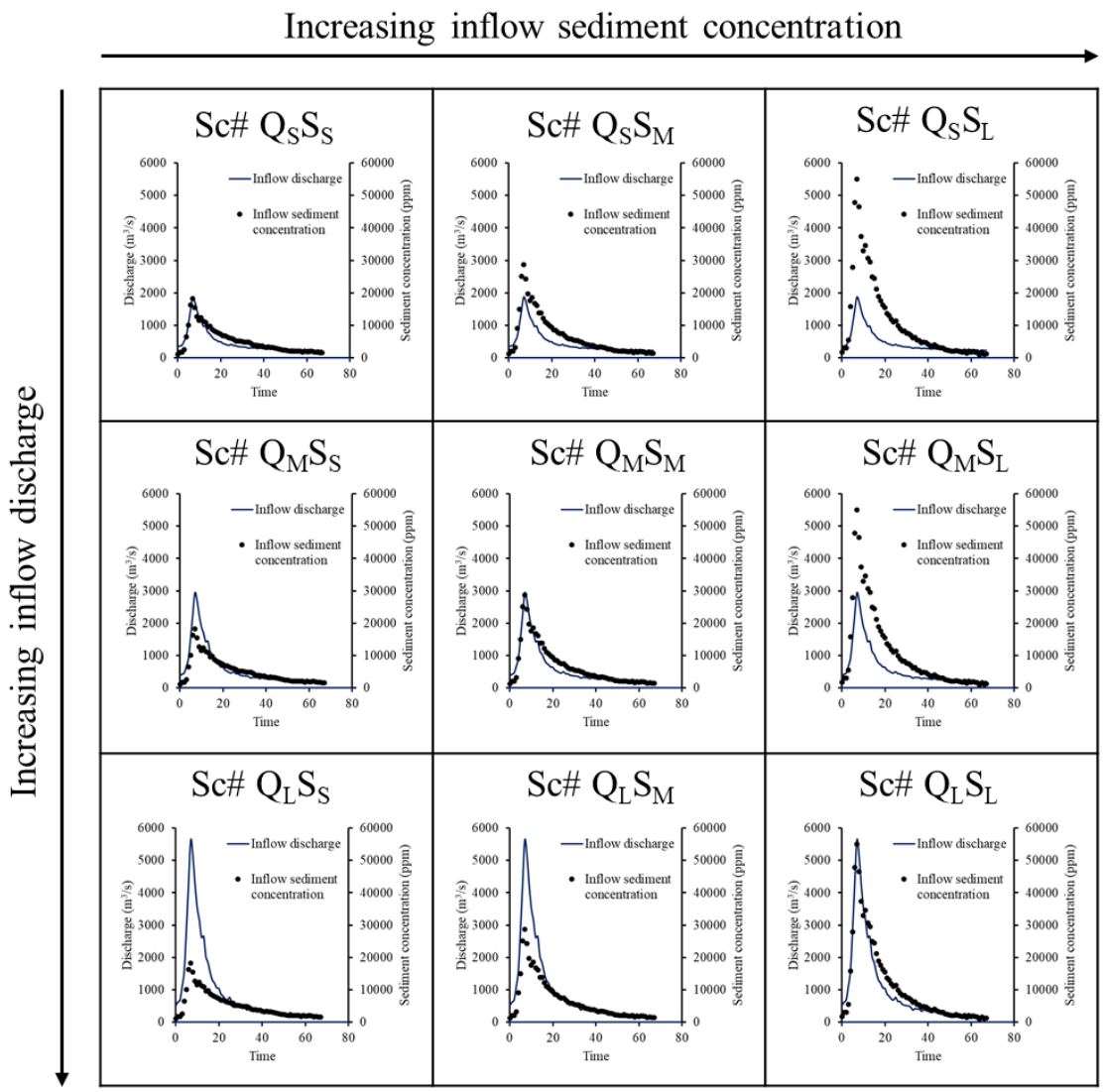

Figure 5.8 Generated inflow boundaries based on different amounts of inflow discharge and sediment concentration

Based on the aforementioned classify method, the typhoon events could be classified into the corresponding cluster (Table 5.1). In this section, the turbidity current process of each scenario is assessed, and the understanding of governing terms for turbidity current evolution and transportation is investigated. After that, the corresponding historical event could be used to evaluate the feasibility of turbidity current estimation.

Table 5.1 Classification of each typhoon event

	Peak inflow discharge (m^3/s)	Peak inflow sediment concentration (ppm)	Cluster
Fungwong	2040	28235	Sc# Q_SS_S
Sinlaku	3447	33270	Sc# Q_MS_M
Jangmi	3292	33195	Sc# Q_MS_M
Morakot	1838	23864	Sc# Q_SS_S
Saola	5385	39100	Sc# Q_LS_L
Soulik	5458	94900	Sc# Q_MS_L
Trami	2413	72594	Sc# Q_SS_L
Soudelor	5634	18287	Sc# Q_LS_S
Dujuan	3803	16177	Sc# Q_MS_S
Megi	4268	23221	Sc# Q_MS_S

As illustrated in Figure 5.9, Figure 5.10, and Figure 5.11, we found that the plunging location, turbidity current thickness, and velocity are similar with the same amount of inflow discharge. Moreover, it significantly reveals that the sediment concentration of turbidity current body has a high correlation to inflow sediment concentration. To investigate the governing terms for turbidity current thickness and velocity, the comparison between turbidity current simulation with same inflow discharge and with same inflow sediment concentration was shown in Figure 5.12. It significantly reveals that the turbidity current thickness is thicker with increasing inflow discharge. Meanwhile, according to the turbidity current head location, the turbidity current velocity is higher in more significant inflow discharge. Also, we found that the plunging location moves downstream with inflow discharge increasing. Based on the aforementioned results, the inflow discharge could be considered the governing term for turbidity current plunging, thickness, and velocity. On the contrary, the inflow sediment concentration is essential for the sediment concentration of the turbidity current body. The turbidity current processes from different inflow scenarios are shown in **Appendix B**.

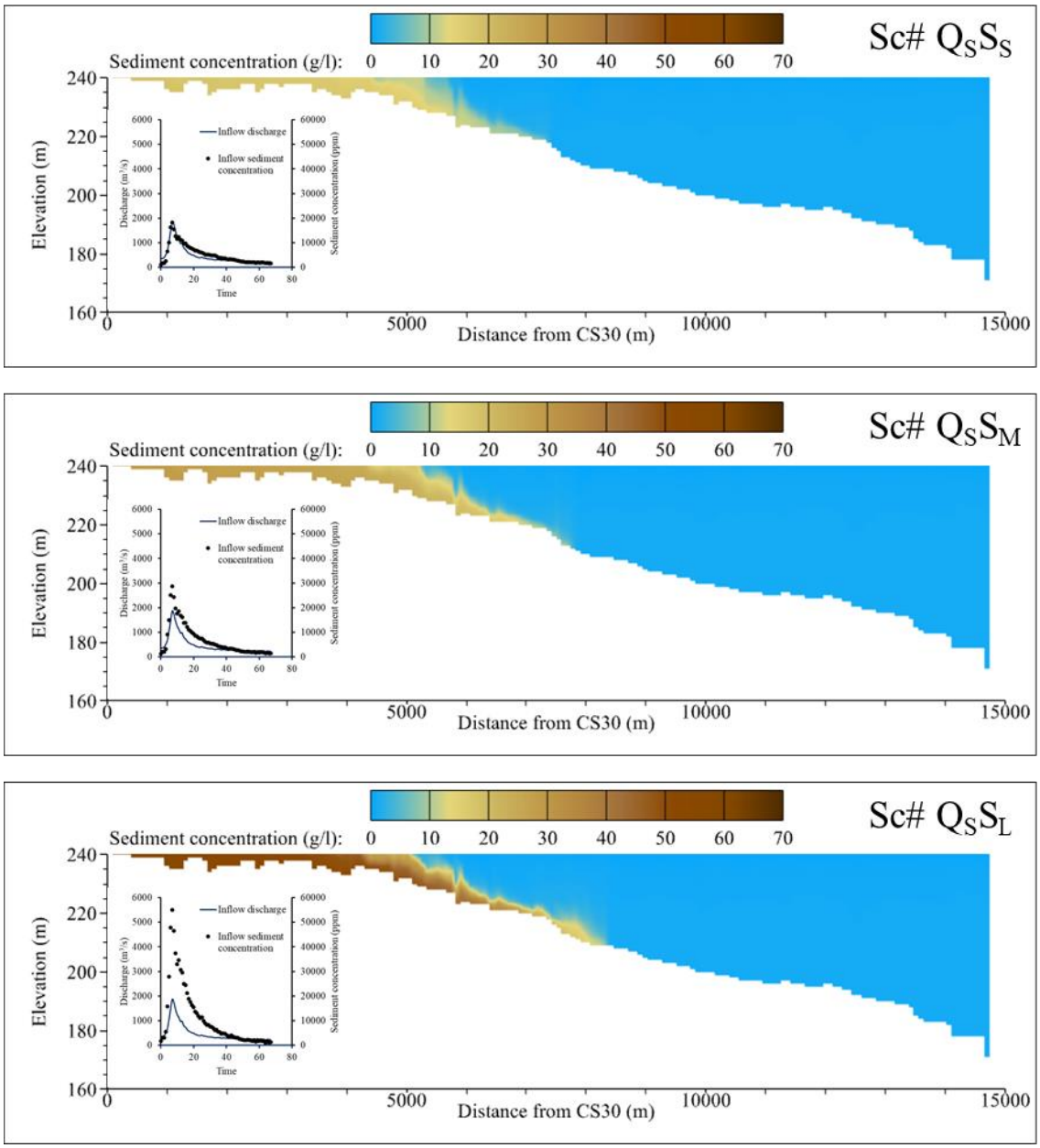

Figure 5.9 The turbidity current simulation with a small amount of inflow discharge and different amounts of inflow sediment concentration.

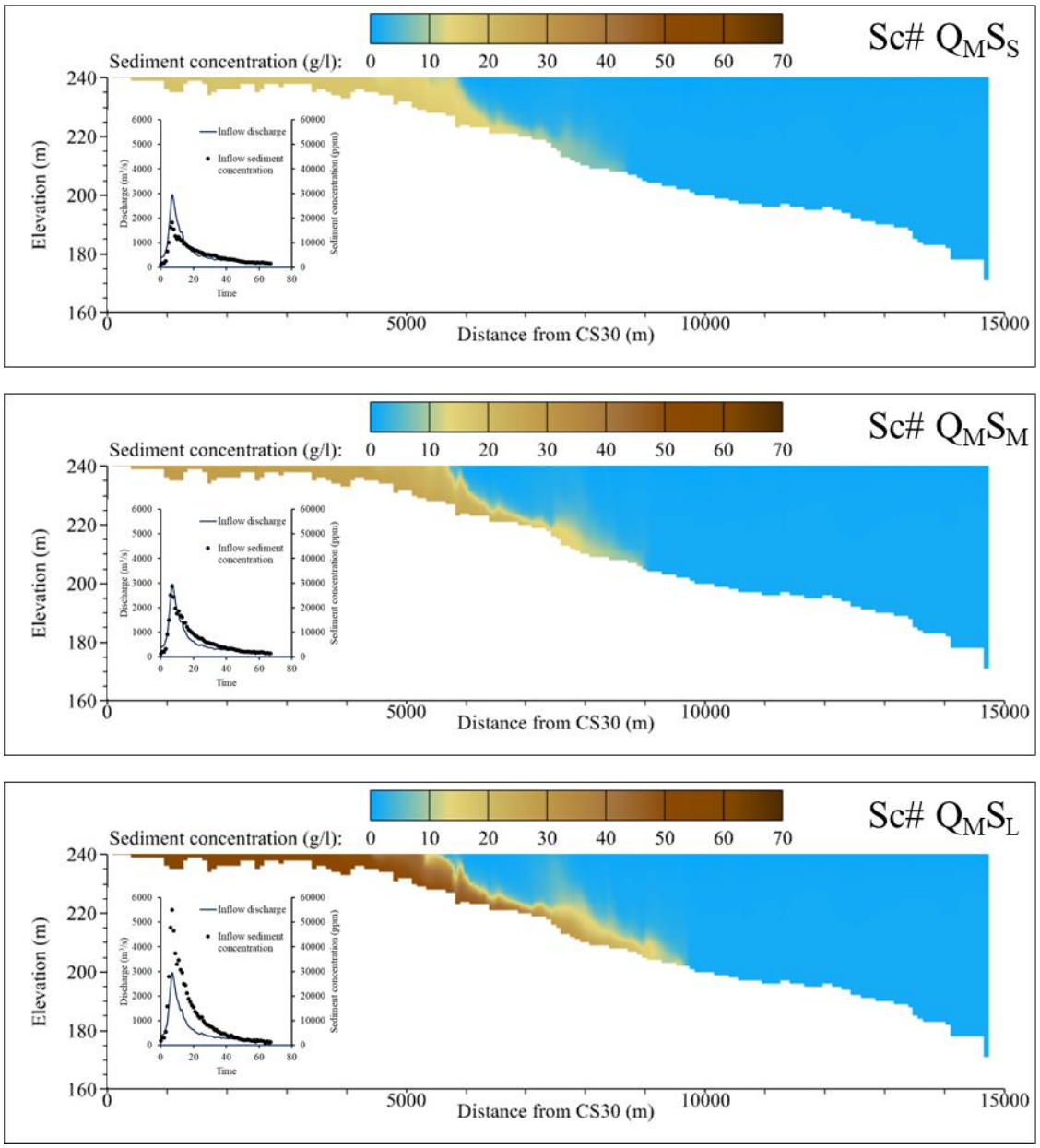

Figure 5.10 The turbidity current simulation with the middle amount of inflow discharge and different amounts of inflow sediment concentration.

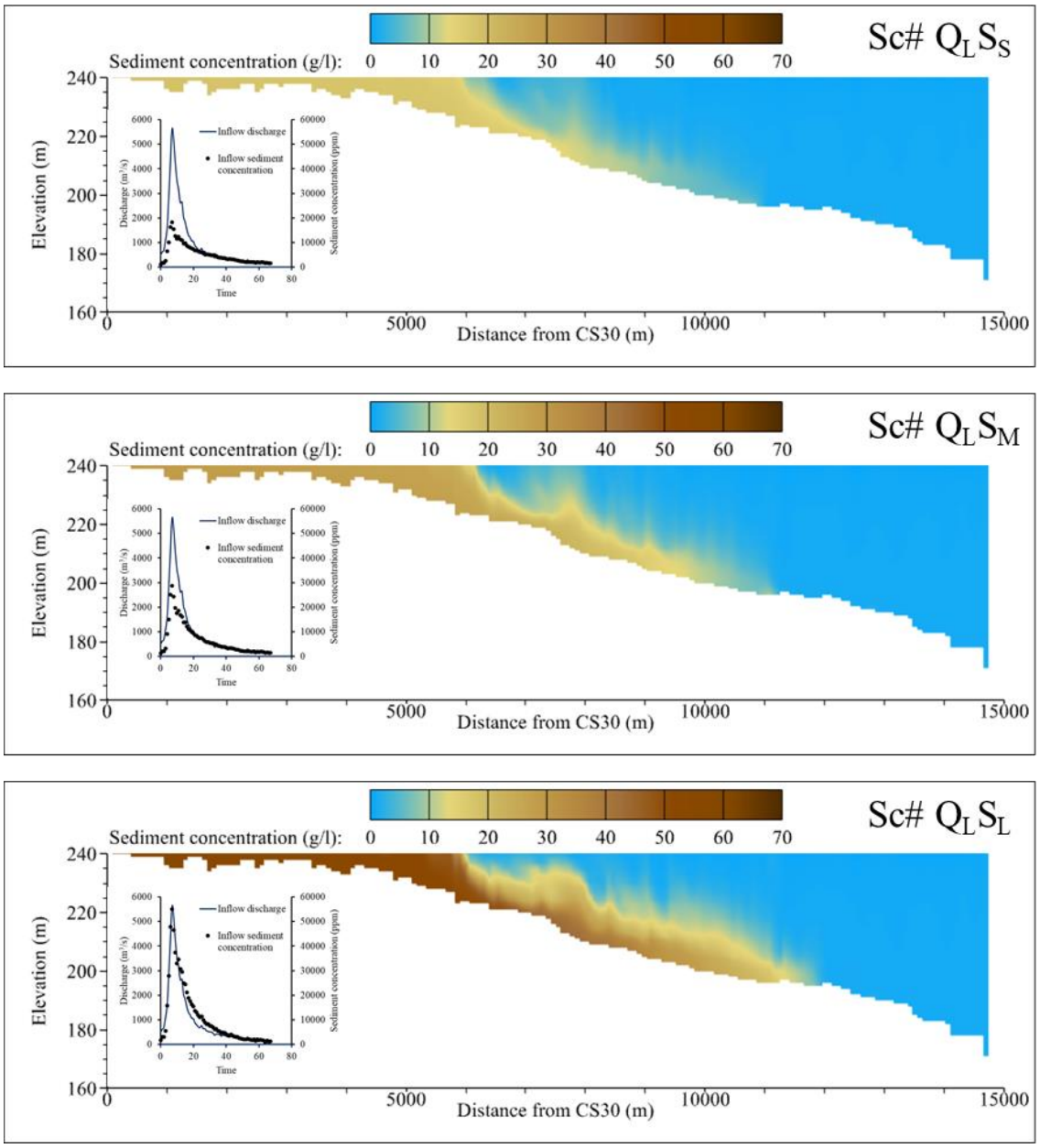

Figure 5.11 The turbidity current simulation with a large amount of inflow discharge and different amounts of inflow sediment concentration.

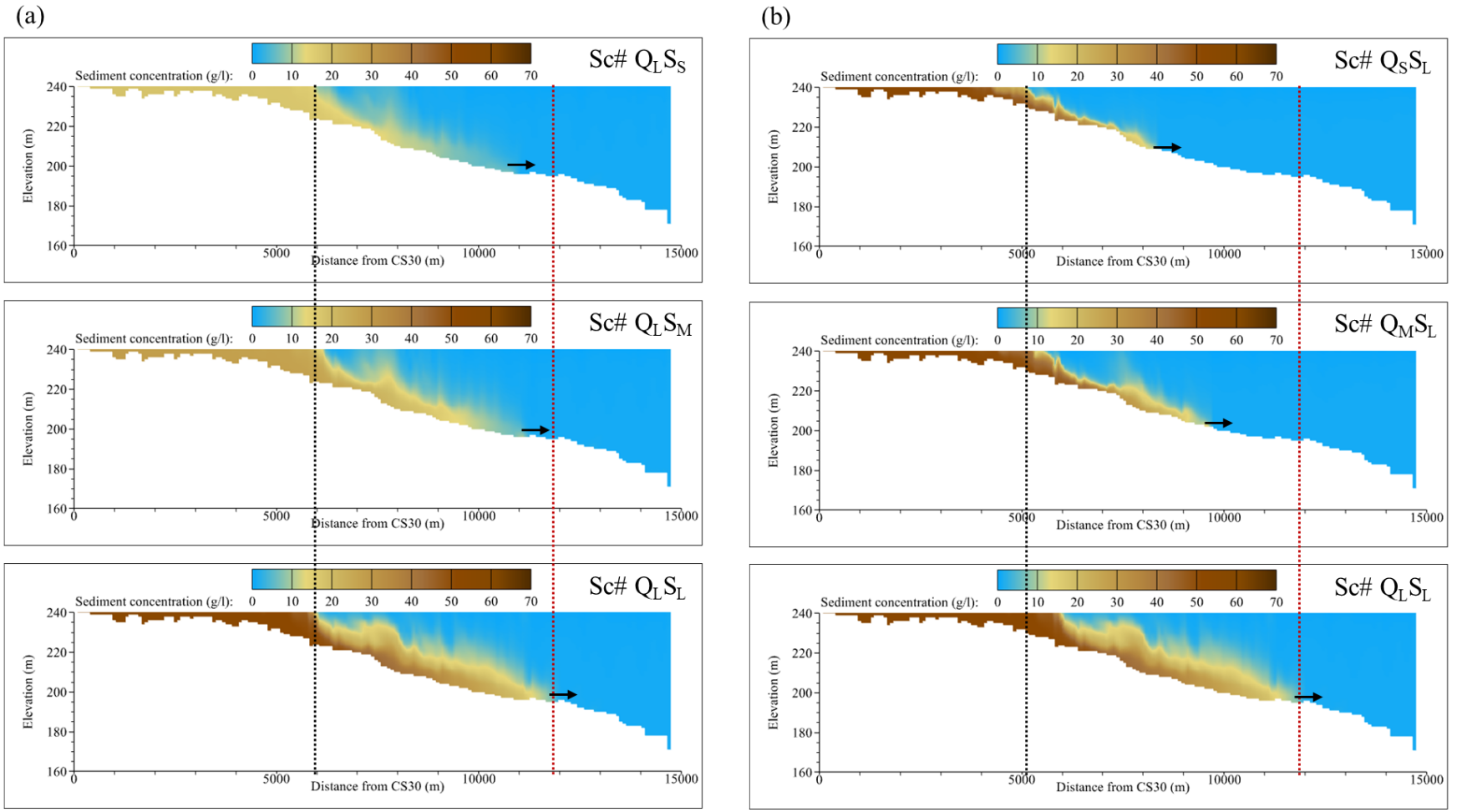

Figure 5.12 The comparison between turbidity current simulation with the (a) same amount of inflow discharge and (b) same amount of inflow sediment concentration (black and red line point out the plunging location and turbidity current head, respectively).

5.3.2 Plunging mechanism investigation and location estimation

Figure 5.7 showed that the turbidity current plunging force causes the vortex near the plunging location. Figure 5.13 significantly represented that the interface of positive and negative velocity is regarded as the plunging location. Several papers and researches about turbidity current plunging location have been presented. The densimetric Froude number (Fr_d) is considered to be the critical characteristic for plunging location evaluation:

$$\mathrm{Fr_d} = \frac{U_d}{\sqrt{\frac{\rho_t - \rho_a}{\rho_a} gD}} \qquad (5\text{-}1)$$

where U_d is depth-averaged velocity, ρ_t is the density of the turbidity flow, ρ_a is the density of the ambient water, g means gravity, and D is the water depth. Several papers have investigated the critical Fr_d for evaluating the turbidity current plunging. As listed inTable 2.2, the vast varying of Fr_d for turbidity current plunging (Fr_p) under different hydrologic and geometry conditions. It is difficult to determine the fixed range of Fr_p for assessing the turbidity current plunging, especially under the time-varying inflow discharge and sediment concentration conditions.

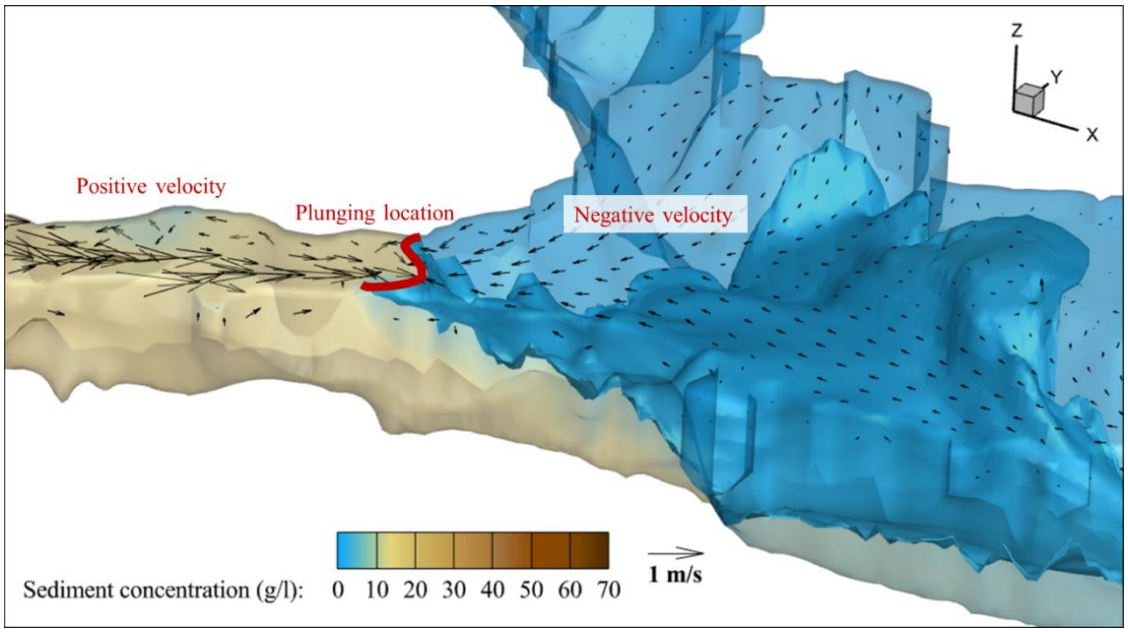

Figure 5.13 The flow regime near the plunging location.

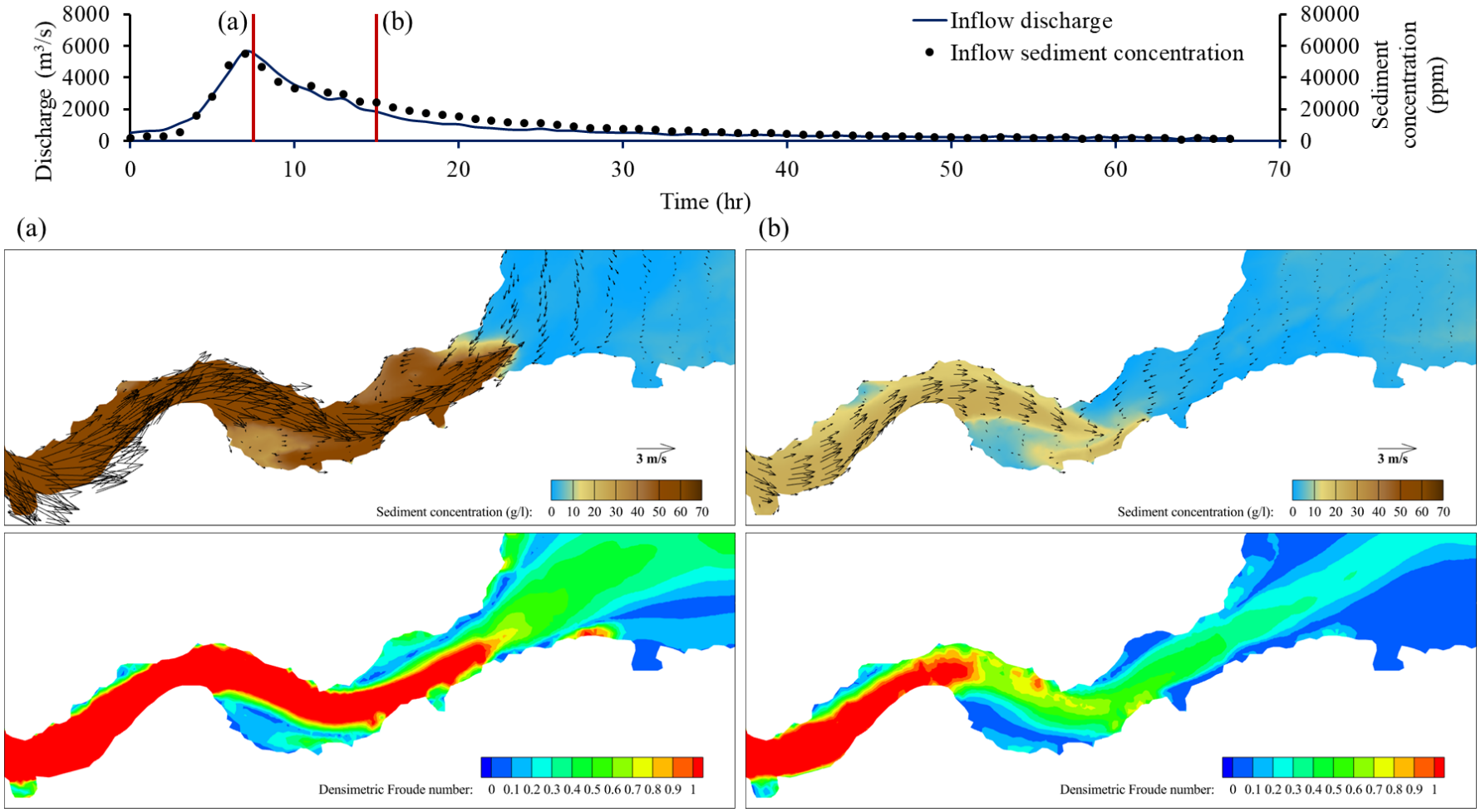

Figure 5.14 The plunging location and corresponding Fr_d with different inflow conditions at (a) 7.5 and (b) 15 hours.

As illustrated in Figure 5.14, it clearly showed that with different inflow conditions, the plunging location and the corresponding Fr_p are different. When inflow conditions are peak values, the Fr_p is around 0.8. When the flooding event is about to end, the Fr_p for reduces to approximately 0.6. Based on the aforementioned results, the inflow conditions are the critical factors for determining the turbidity current plunging location. To consider the influence of inflow conditions on turbidity current plunging, the general equation for calculating the modified Fr_p (Fr_p') is proposed (Figure 5.15):

$$Fr_p' = \alpha SIR^{\beta} \quad (5\text{-}2)$$

$$SIR = \frac{SSC_r}{Q_r} \quad (5\text{-}3)$$

$$SSC_r = \frac{SSC_{in}}{\text{Annual mean } SSC_{in}} \quad (5\text{-}4)$$

$$Q_r = \frac{Q_{in}}{\text{Annual mean } Q_{in}} \quad (5\text{-}5)$$

where, SIR is the sediment-inflow ratio; the α (= 0.61-0.86) and β (= 0.16-0.192) are the parameters; SSC_r and Q_r are the relative sediment concentration and relative inflow discharge; SSC_{in} is inflow sediment concentration; Q_{in} is inflow discharge.

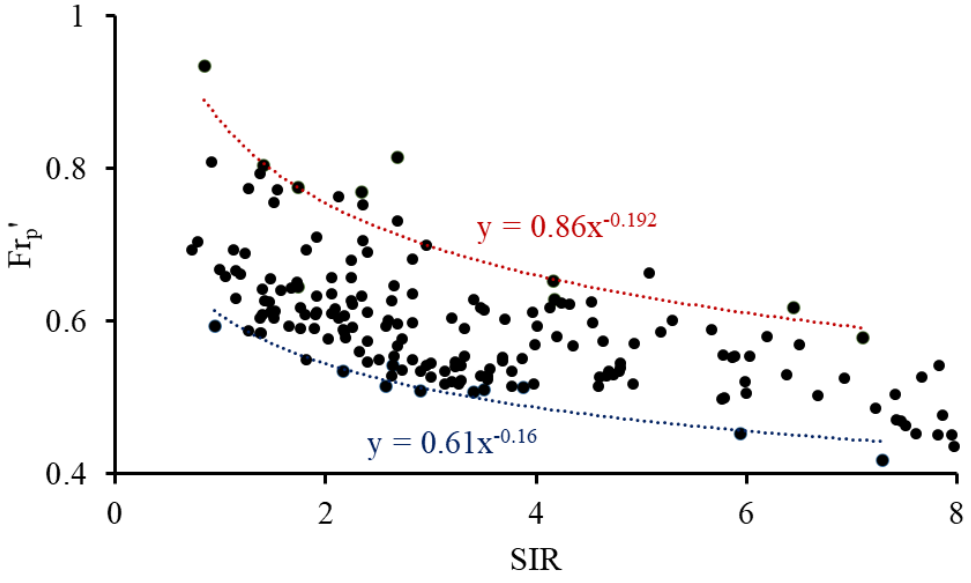

Figure 5.15 The relationship between inflow conditions and Fr_p'.

The Fr_p' is regarded as the critical factor for evaluating the turbidity current plunging location. Thus, based on the statistic from different scenarios results, the relative distance of turbidity current plunging location (D_r = distance of turbidity current plunging location from upstream boundary/full length of reservoir) could be briefly estimated by the calculated Fr_p' (Figure 5.16):

$$D_r = 0.38 Fr_p{}'^{1.18} \quad (5\text{-}6)$$

As illustrated in Figure 5.13 and Figure 5.14, they represent that the plunging location is irregular shape instead of a cross section. Thus, the Fr_p' is more appropriate for investigating the accurate turbidity current plunging location. However, equation (5-6) also can provide a brief plunging location estimation in a specific reservoir.

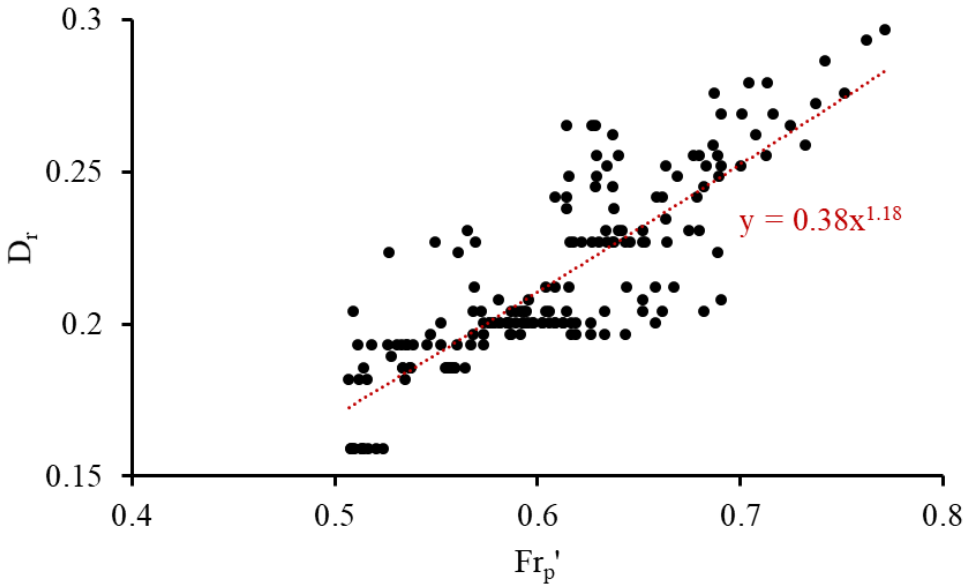

Figure 5.16 Turbidity current plunging location estimation in Shihmen Reservoir with inflow sediment concentration and discharge ratio.

Based on the aforementioned results, we found that the inflow sediment concentration and inflow discharge have a high correlation to the turbidity current plunging location. As illustrated in Figure 5.17, it significantly showed that with increasing inflow sediment concentration, the turbidity current plunging location move to upstream. On the contrary, the turbidity current plunging location moves downstream with increasing inflow discharge. The results revealed that the plunging location is between CS27 (in Sc# $Q_S S_L$) and CS24 (in Sc# $Q_L S_S$). Overall, the turbidity current plunging location could be estimated by using equations(5-2), and (5-6), and if it is necessary, the plunging location can be controlled by inflow sediment concentration and discharge.

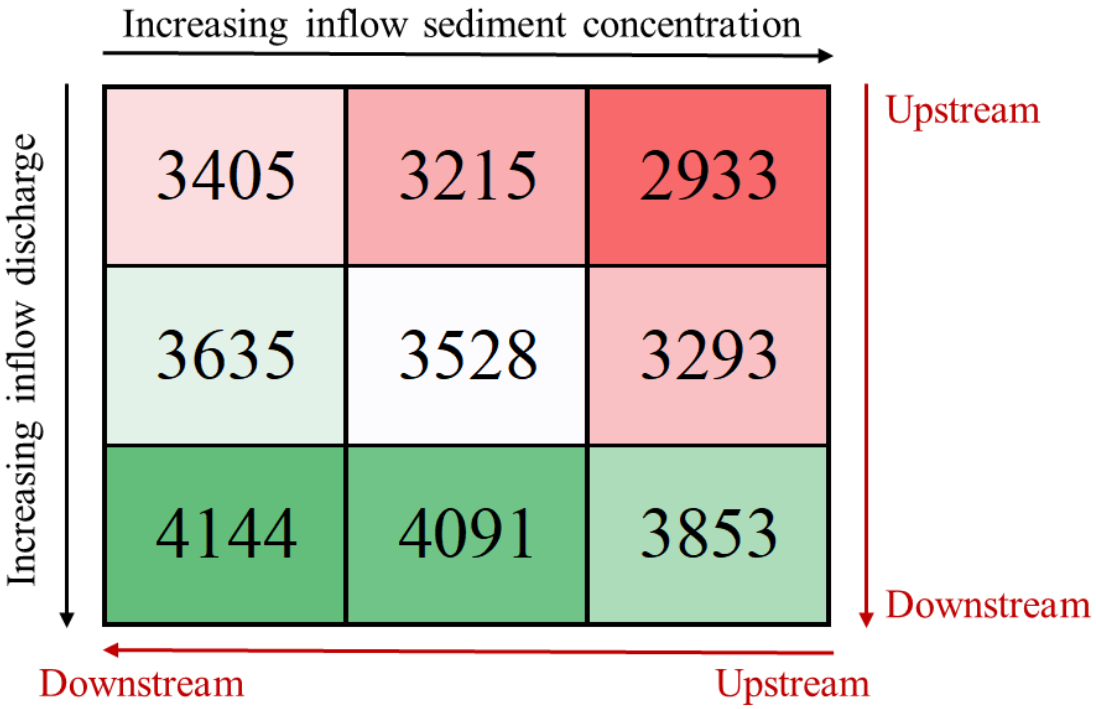

Figure 5.17 The averaged turbidity current plunging location from different inflow sediment concentrations and inflow discharge (unit: distance from CS30 (m)).

5.3.3 Vertical profile of velocity and sediment concentration estimation

As illustrated in Figure 5.12 (b), the inflow discharge is governing term for turbidity current thickness. Meanwhile, as shown in Figure 5.18, the turbidity current thickness from different inflow sediment concentrations and discharge could be divided into three groups based on the inflow discharge. It presented that the inflow discharge is the governing factor for the turbidity current body profile. As illustrated in Figure 5.19, there is TDR equipment in Shihmen Reservoir for detecting the vertical profile of sediment concentration. However, the continuous profile is difficult to achieve by only a few points and without the sensors close to the bottom leads to the critical data is missing. Moreover, the TDR equipment is used for sediment concentration measurement, but no equipment is applied for middle stream velocity detection in the Shihmen Reservoir. This study evaluated the estimated vertical profile of sediment concentration and velocity for different inflow discharges to solve these problems.

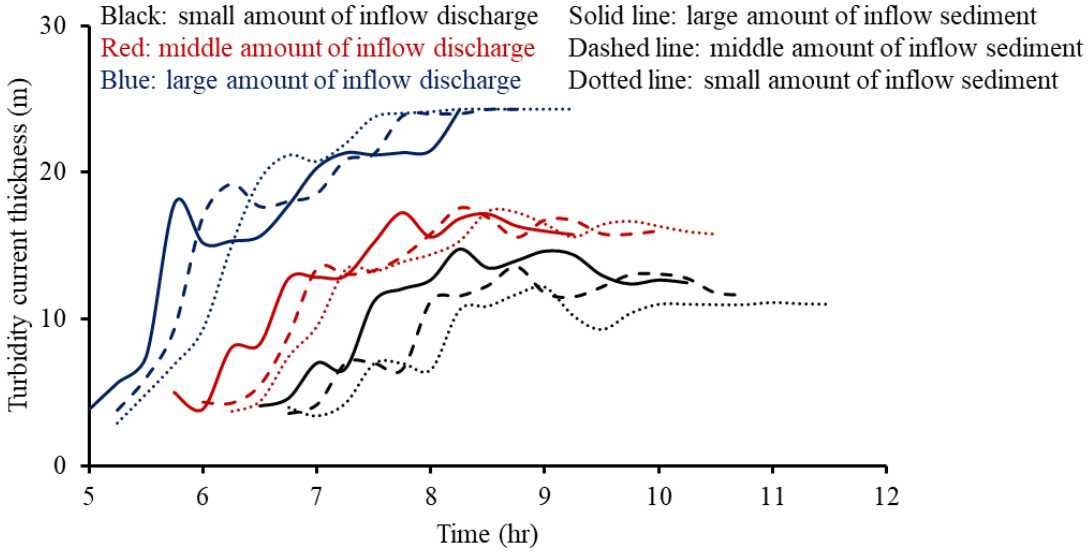

Figure 5.18 The turbidity current thickness at CS20 from different inflow sediment concentrations and discharges.

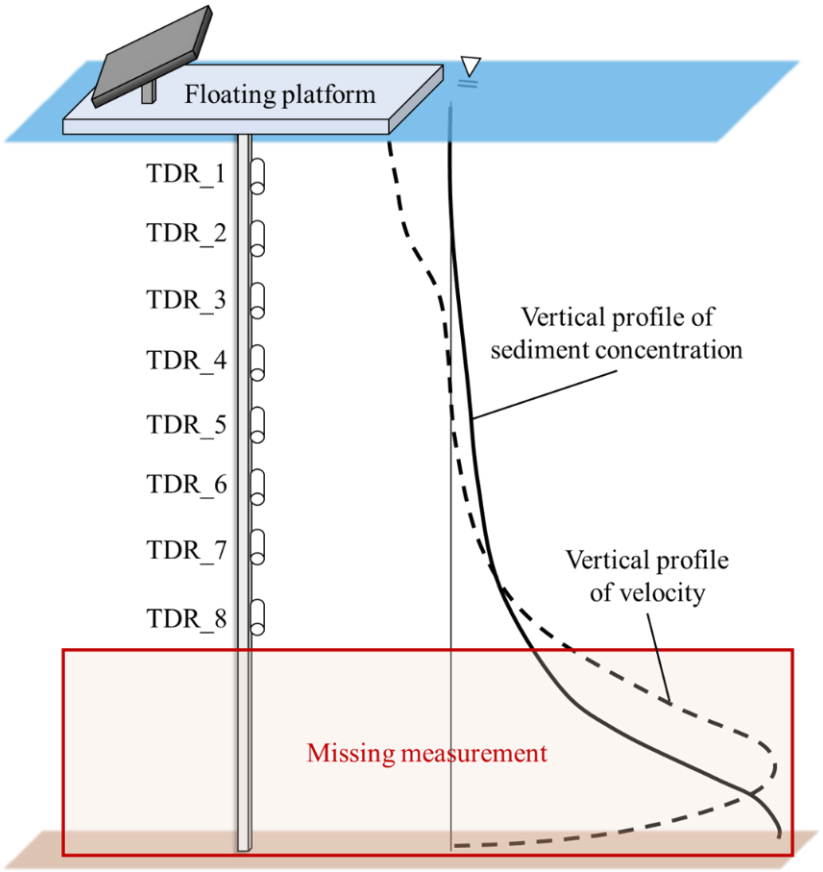

Figure 5.19 The sketch of TDR equipment and vertical profile of sediment concentration and velocity.

The typical vertical profiles and critical factors for turbidity current body and flow regime are shown in Figure 5.20 (a). The height of the backflow zone (H_b) is essential for understanding the vortex range. The velocity above H_b is negative due to the backflow effect. In the realistic, the velocity profile is drawn by velocity magnitude, calculated by x-, y- and z-directional velocity. It is impossible to show the negative values. However, according to the gradient changes from negative to positive, the H_b still could be evaluated. The height of the maximum velocity (H_m), maximum velocity (U_m), and the sediment concentration at H_m (C_m) were used to obtain the dimensionless sediment concentration and velocity profiles. As illustrated in Figure 5.20, the dimensionless sediment concentration and velocity profiles revealed the huge difference between different inflow

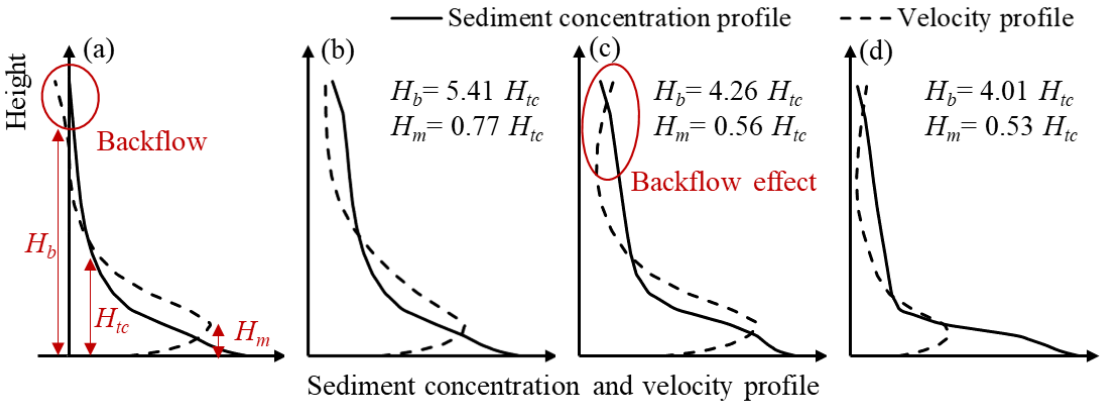

Figure 5.20 The sediment concentration and velocity profile in (a) concept and under (b) large, (c) middle, (c) small amount of inflow discharge.

discharge. Meanwhile, the characteristic factors (H_b and H_m) could be calculated by turbidity current thickness (H_{tc}):

$$H_b = \begin{cases} 5.41 & ; \text{ large amount of inflow discharge} \\ 4.26\,H_{tc} & ; \text{ middle amount of inflow discharge} \\ 4.01 & ; \text{ small amount of inflow discharge} \end{cases} \quad (5\text{-}7)$$

$$H_m = \begin{cases} 0.77 & ; \text{ large amount of inflow discharge} \\ 0.56\,H_{tc} & ; \text{ middle amount of inflow discharge} \\ 0.53 & ; \text{ small amount of inflow discharge} \end{cases} \quad (5\text{-}8)$$

Hosseini et al. (2006) established the equations for the sediment concentration and velocity profiles by near-Gaussian and empirical power relation:

$$\begin{cases} \dfrac{c(z)}{C_m} = \exp\left[-\alpha_c\left(\dfrac{z}{H_m} - 1\right)^{\beta_c}\right] & ; z > H_m \\ \dfrac{c(z)}{C_m} = \left(\dfrac{z}{H_m}\right)^{\gamma_c} & ; z \le H_m \end{cases} \quad (5\text{-}9)$$

$$\begin{cases} \dfrac{u(z)}{U_m} = \exp\left[-\alpha_u\left(\dfrac{z}{H_m} - 1\right)^{\beta_u}\right] & ; z > H_m \\ \dfrac{u(z)}{U_m} = \left(\dfrac{z}{H_m}\right)^{\gamma_u} & ; z \le H_m \end{cases} \quad (5\text{-}10)$$

where $c(z)$ and $u(z)$ are the velocity and sediment concentration at distance z above the bed, respectively. α_c, β_c and γ_c are coefficients for sediment concentration profile and values in 2, 1.3, and -0.7, respectively. α_u, β_u and γ_u are coefficients for velocity

profile and values in 0.5, 2.2 and $\frac{1}{3}$, respectively.

However, the equations (5-9) and (5-10) were proposed from the experiment and without considering the plunging phenomenon. Therefore, in this study, the sediment concentration and velocity profile equation are modified by equations (5-9) and (5-10):

Large amount of inflow discharge:

$$\begin{cases} \frac{c(z)}{C_m} = \exp\left[-0.67\left(\frac{z}{H_m}-1\right)^{0.43}\right] & ; z > H_m \\ \frac{c(z)}{C_m} = 1.3 - 0.5\frac{z}{H_m} & ; z \le H_m \end{cases} \quad (5\text{-}11)$$

$$\begin{cases} \frac{u(z)}{U_m} = \exp\left[-0.37\left(\frac{z}{H_m}-1\right)^{1}\right] & ; z > H_m \\ \frac{u(z)}{U_m} = \left(\frac{z}{H_m}\right)^{0.186} & ; z \le H_m \end{cases} \quad (5\text{-}12)$$

Middle amount of inflow discharge:

$$\begin{cases} \frac{c(z)}{C_m} = \exp\left[-0.83\left(\frac{z}{H_m}-1\right)^{0.41}\right] & ; z > H_m \\ \frac{c(z)}{C_m} = 1.2 - 0.32\frac{z}{H_m} & ; z \le H_m \end{cases} \quad (5\text{-}13)$$

$$\begin{cases} \frac{u(z)}{U_m} = \exp\left[-0.54\left(\frac{z}{H_m}-1\right)^{0.9}\right] & ; z > H_m \\ \frac{u(z)}{U_m} = \left(\frac{z}{H_m}\right)^{0.194} & ; z \le H_m \end{cases} \quad (5\text{-}14)$$

Small amount of inflow discharge:

$$\begin{cases} \frac{c(z)}{C_m} = \exp\left[-0.45\left(\frac{z}{H_m}-1\right)^{0.65}\right] & ; z > H_m \\ \frac{c(z)}{C_m} = 2.27 - 0.68\frac{z}{H_m} & ; z \le H_m \end{cases} \quad (5\text{-}15)$$

$$\begin{cases} \frac{u(z)}{U_m} = \exp\left[-0.47\left(\frac{z}{H_m}-1\right)^{0.89}\right] & ; z > H_m \\ \frac{u(z)}{U_m} = \left(\frac{z}{H_m}\right)^{0.21} & ; z \le H_m \end{cases} \quad (5\text{-}16)$$

As shown in Figure 5.20, the sediment concentration distribution below H_m is close

to linear relation instead of empirical power relation. Thus, linear regression is used for estimating the sediment concentration distribution below H_m. By adopting the proposed equations, the estimated sediment concentration and discharge profile have good agreements with three-dimensional simulation (Figure 5.21). Overall, the proposed equations help understand the turbidity current body and head velocity.

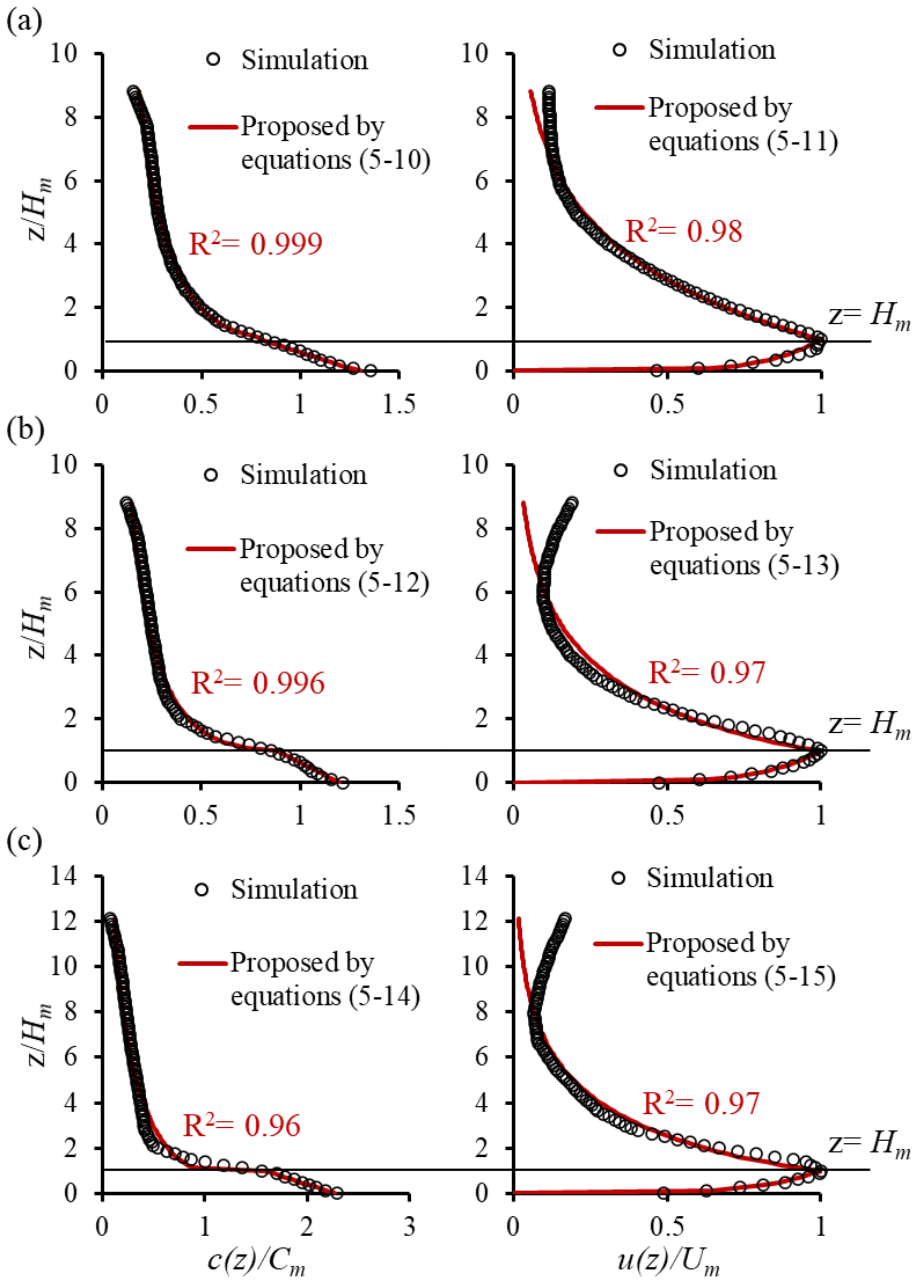

Figure 5.21 The dimensionless sediment concentration and velocity profile from proposed equations for (a) large, (b) middle, and (c) small amount of inflow discharge.

There are no velocity measuring facilities within Shihmen Reservoir. Also, it is difficult to measure the velocity profile during the flooding events due to the extremely high discharge. Therefore, the turbidity current velocity was estimated by arrival time at TDR stations and dam. To obtain the turbidity current head velocity (U_f), Turner (1979) proposed the turbidity current head velocity equation under quasi-uniform width flume and without considering the effects of bottom friction and mixing process:

$$U_f = \sqrt{2\frac{\rho_t - \rho_a}{\rho_a} g H_{tc}} \quad ; \rho_t = \rho_a \left(1 - \frac{C_{tc}}{\rho_s}\right) + C_{tc} \qquad (5\text{-}17)$$

where C_{tc} is averaged sediment concentration of turbidity current. Due to the equation (5-17) was established from the experiment, the modified turbidity current head velocity equation for the field is proposed by using the data from different inflow conditions (Figure 5.22) and expressed as:

$$U_f = \sqrt{3.72\frac{\rho_t - \rho_a}{\rho_a} g H_{tc}} \qquad (5\text{-}18)$$

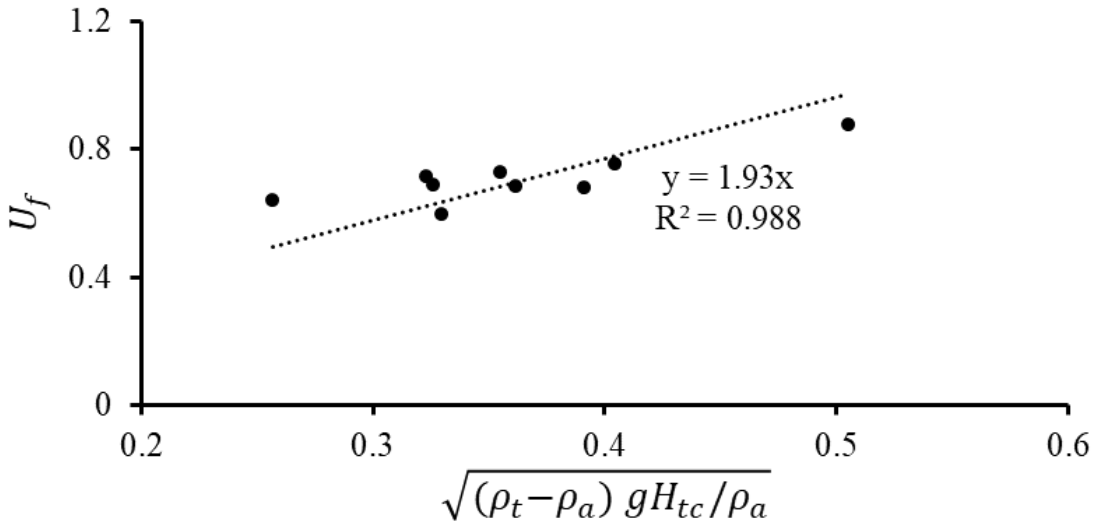

Figure 5.22 Assessment of the parameter of turbidity current head velocity.

According to the above equation, we found that the sediment concentration and thickness of turbidity current are the governing factors for turbidity current head velocity. As illustrated in Figure 5.23, the turbidity current head velocity is the maximum value of the velocity profile. After calculating the turbidity current head velocity by equation (5-18), it could be used for calculating the velocity distribution. Based on the aforementioned results, the structure of the turbidity current body could be obtained by the measurement from TDR and proposed equations.

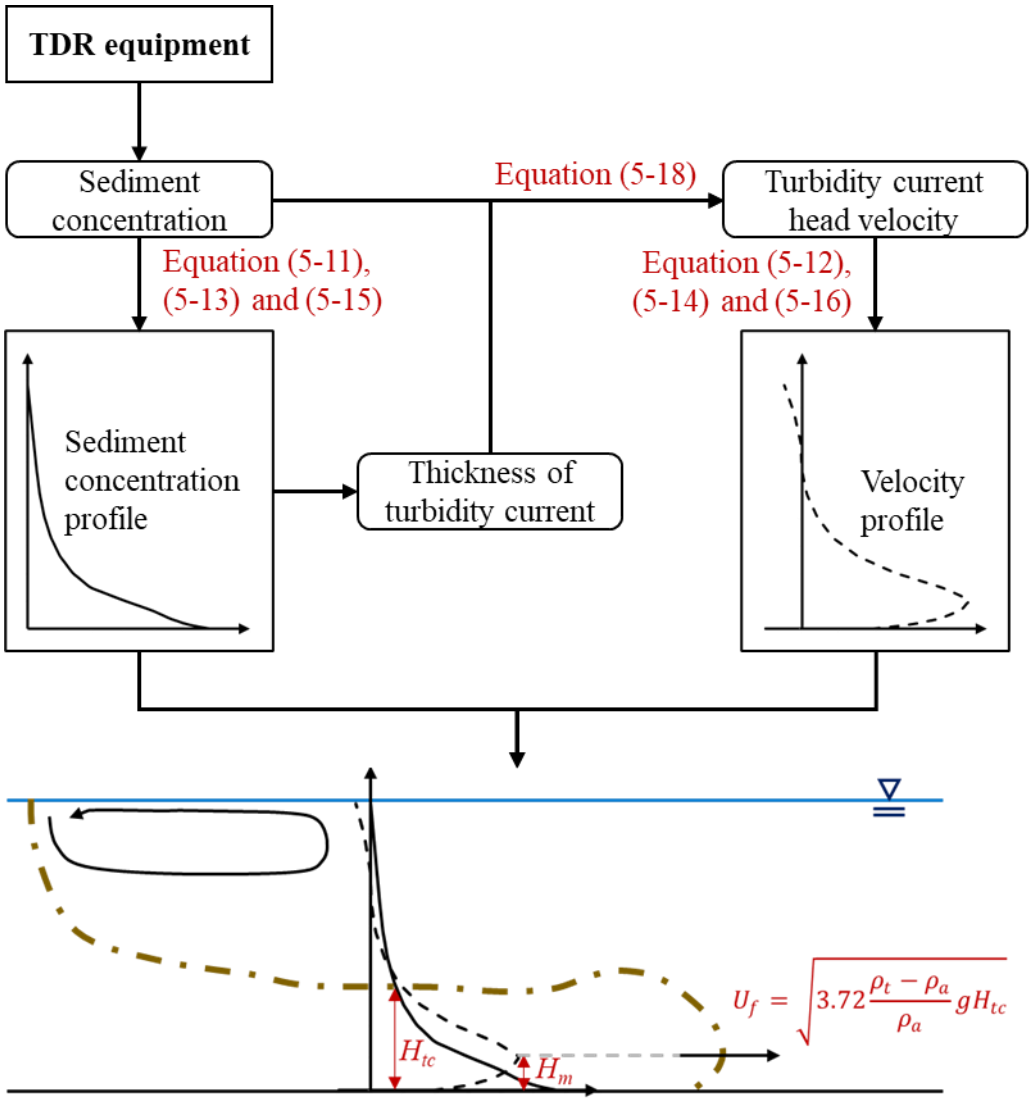

Figure 5.23 The flowchart for obtaining the pattern of turbidity current transportation.

5.3.4 Turbidity current arrival time and the muddy lake formed evaluation

This section investigates the turbidity current transportation (including velocity, travel time, and arrival time) and muddy lake evolution (Figure 5.24). With different inflow sediment concentrations and discharges, the turbidity current travel time and arrival time at the dam from different scenarios were shown in Figure 5.25. The results indicated less turbidity current travel time to arrive at the dam with increasing inflow sediment concentration and discharge. As Figure 5.25 (b) showed that turbidity current arrival time is between 8.25 (Sc# Q_LS_L) and 11.5 (Sc# Q_SS_S) hours. The turbidity current arrival time is crucial for real-time turbidity current venting outlets' operation. Therefore, the obtained results could give a rough estimation of turbidity current arrival time with different inflow conditions and provide a reference for the outlets' operation.

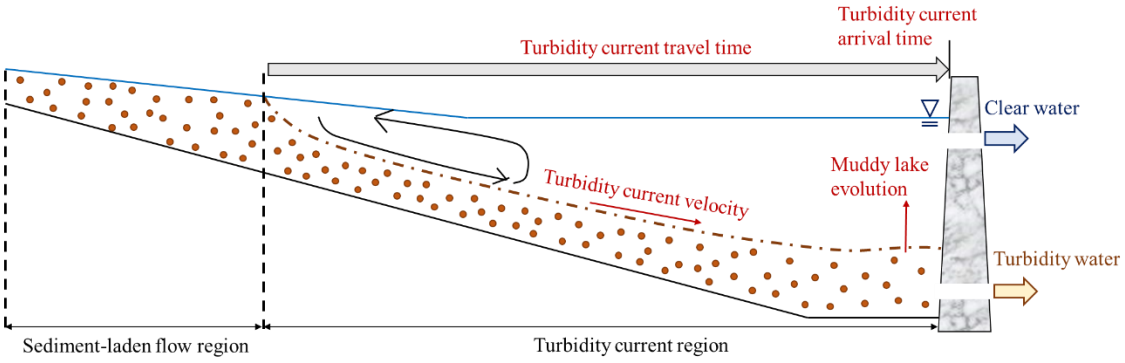

Figure 5.24 The turbidity current transportation (including velocity, travel time, and arrival time) and muddy lake evolution investigation in this section.

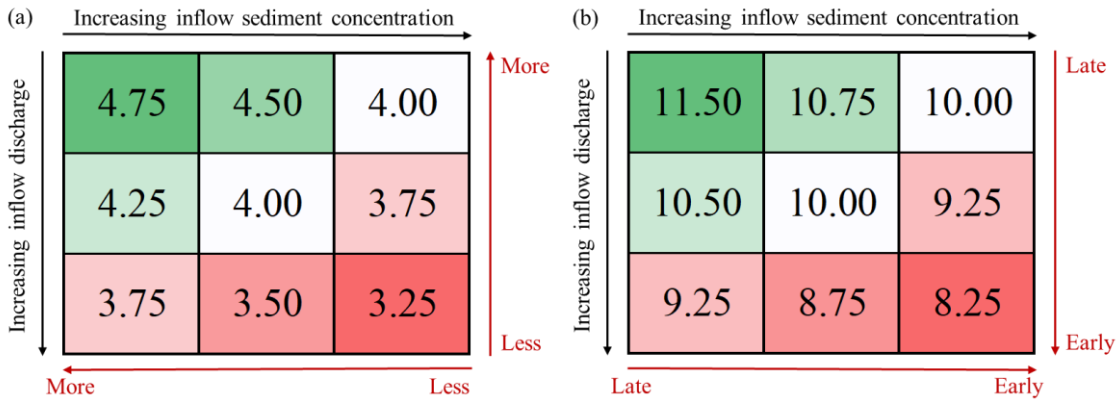

Figure 5.25 The turbidity current (a) travel time and (b) arrival time at the dam from different inflow sediment concentrations and discharges (unit: hours).

Based on the simplified velocity calculation (i.e., distance/travel time), the averaged velocity (Figure 5.26) is obtained by using average plunging location (Figure 5.17) and travel time (Figure 5.25 (a)). The results clearly showed that the turbidity current velocity increases with increasing inflow sediment concentration and discharge. According to the previous conclusion, the turbidity current velocity is highly related to inflow discharge. Thus, the same amount of inflow discharge could be divided into the same group and received the relationship between inflow sediment concentration and discharge and turbidity current velocity (Figure 5.27):

Small amount of inflow discharge:

$$U_{tc} = 0.08\text{SIR} + 0.49 \quad (5\text{-}19)$$

Middle amount of inflow discharge:

$$U_{tc} = 0.09\text{SIR} + 0.55 \quad (5\text{-}20)$$

Large amount of inflow discharge:

$$U_{tc} = 0.17\text{SIR} + 0.53 \quad (5\text{-}21)$$

where U_{tc} is averaged turbidity current velocity. Overall, the turbidity current averaged velocity could be calculated by linear regression.

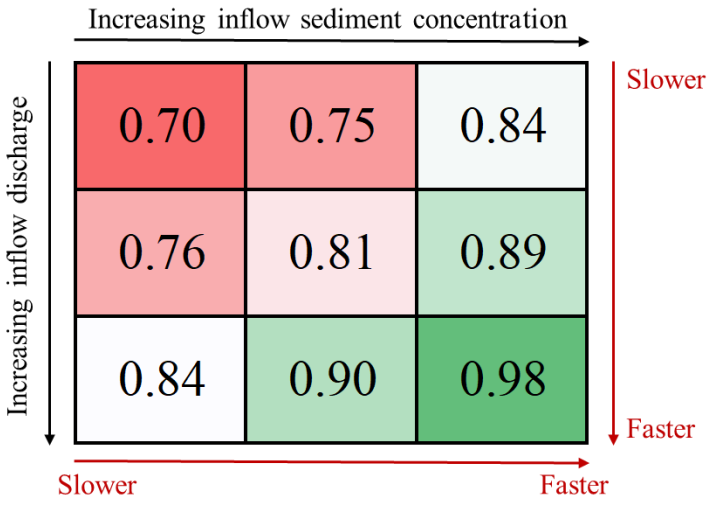

Figure 5.26 The averaged turbidity current velocity from different inflow sediment concentrations and inflow discharges (unit: m/s)

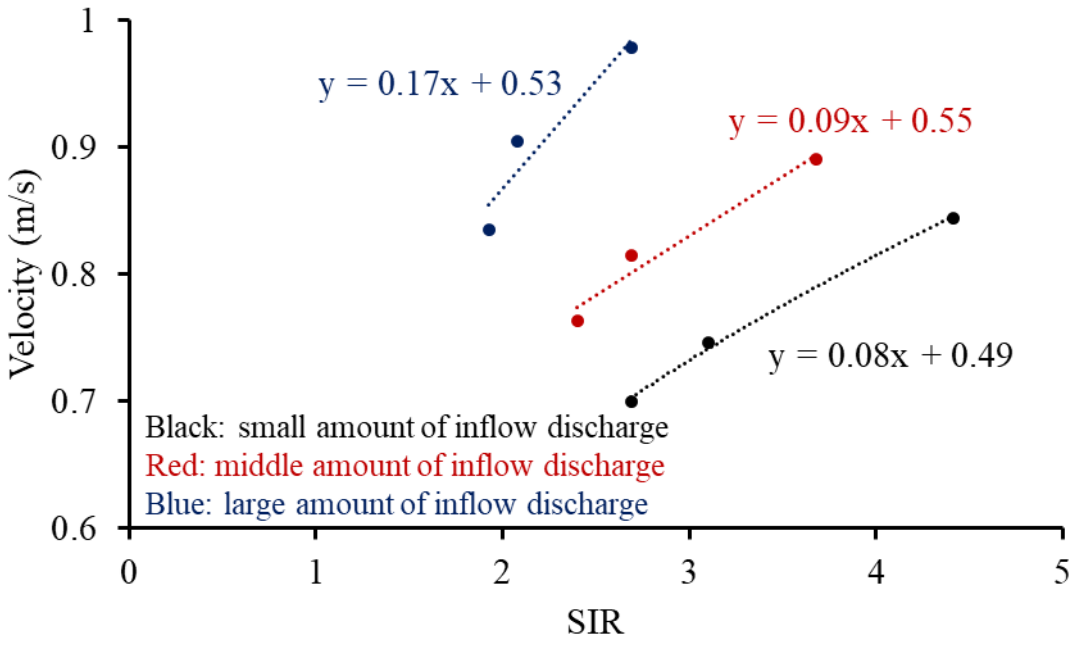

Figure 5.27 The relationship between inflow conditions and turbidity current velocity.

After the turbidity current arrives at the dam, the muddy lake starts to form in front of the dam. With increasing inflow sediment discharge ($Q_{s,in} = SSC_{in} \times Q_{in}$), the more serious muddy lake is formed in the reservoir (Figure 5.28, Figure 5.29, and Figure 5.30). With increasing time, the height of the muddy lake increases (Figure 5.31). When a muddy lake reaches the water supply intake, the turbidity water withdrawal harms the water purification plant and affects the people's livelihood water supply.

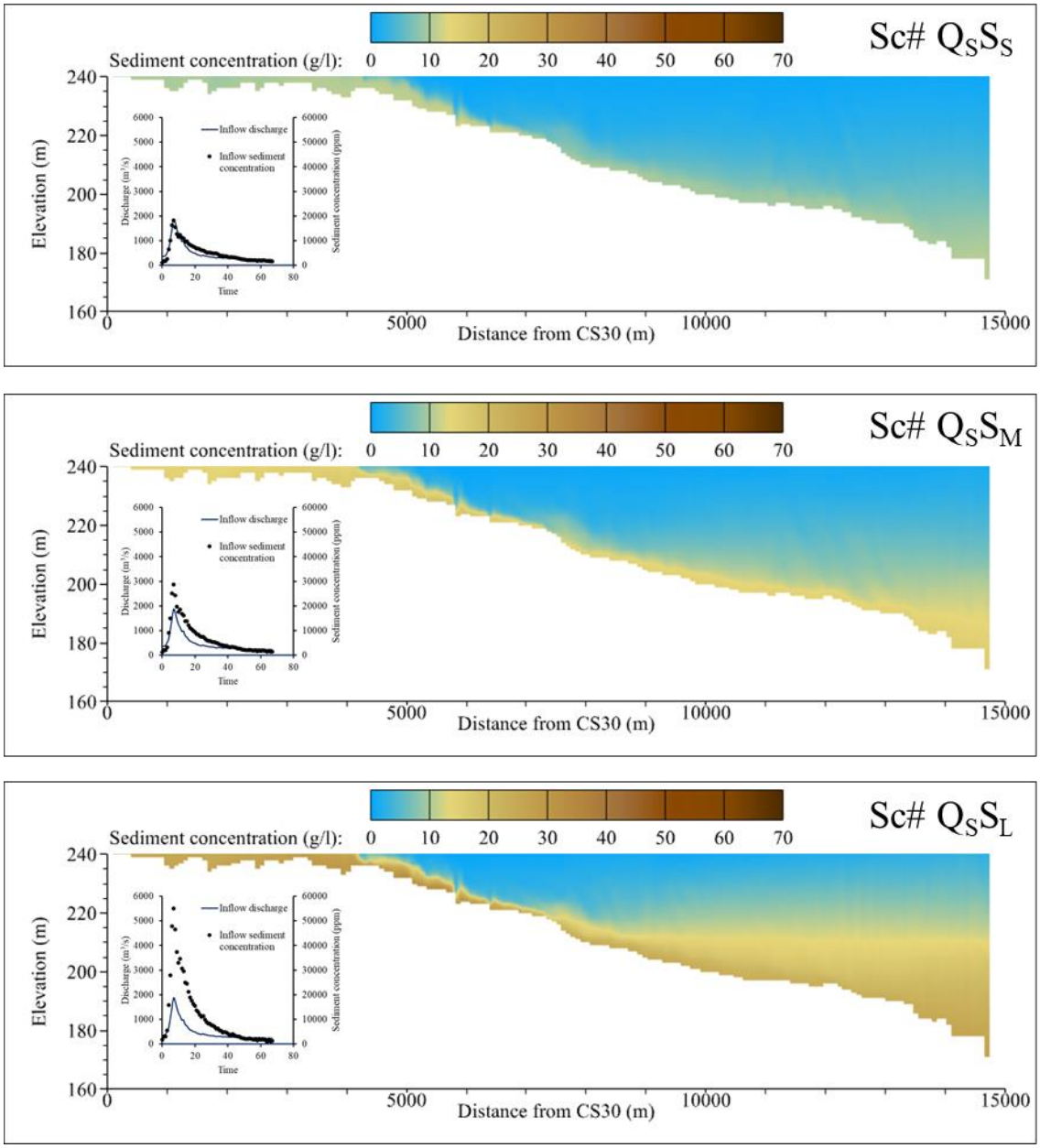

Figure 5.28 The muddy lake formed with a small amount of inflow discharge and different amounts of inflow sediment concentration.

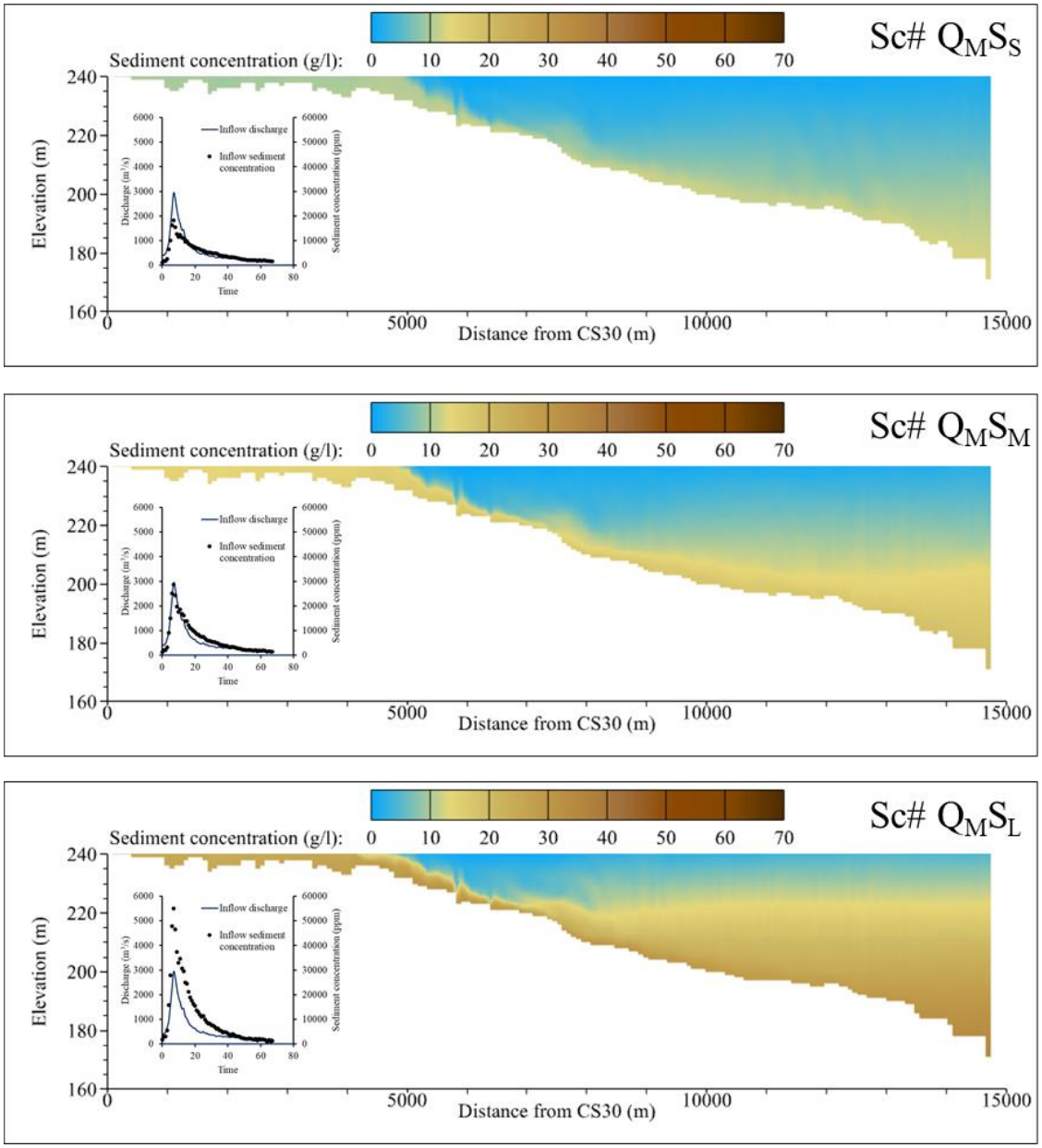

Figure 5.29 The muddy lake formed with a middle amount of inflow discharge and different amounts of inflow sediment concentration.

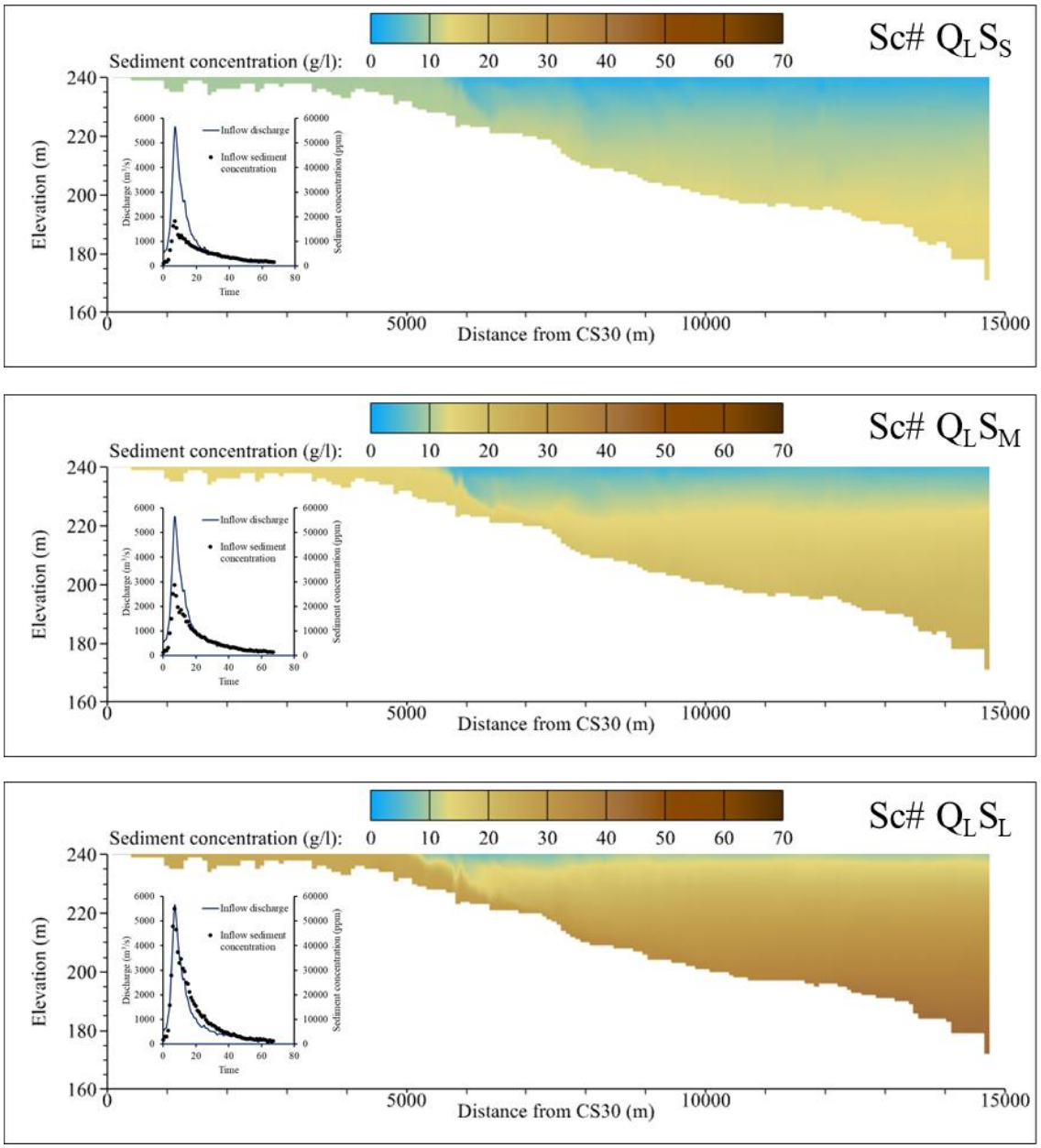

Figure 5.30 The muddy lake formed with a large amount of inflow discharge and different amounts of inflow sediment concentration.

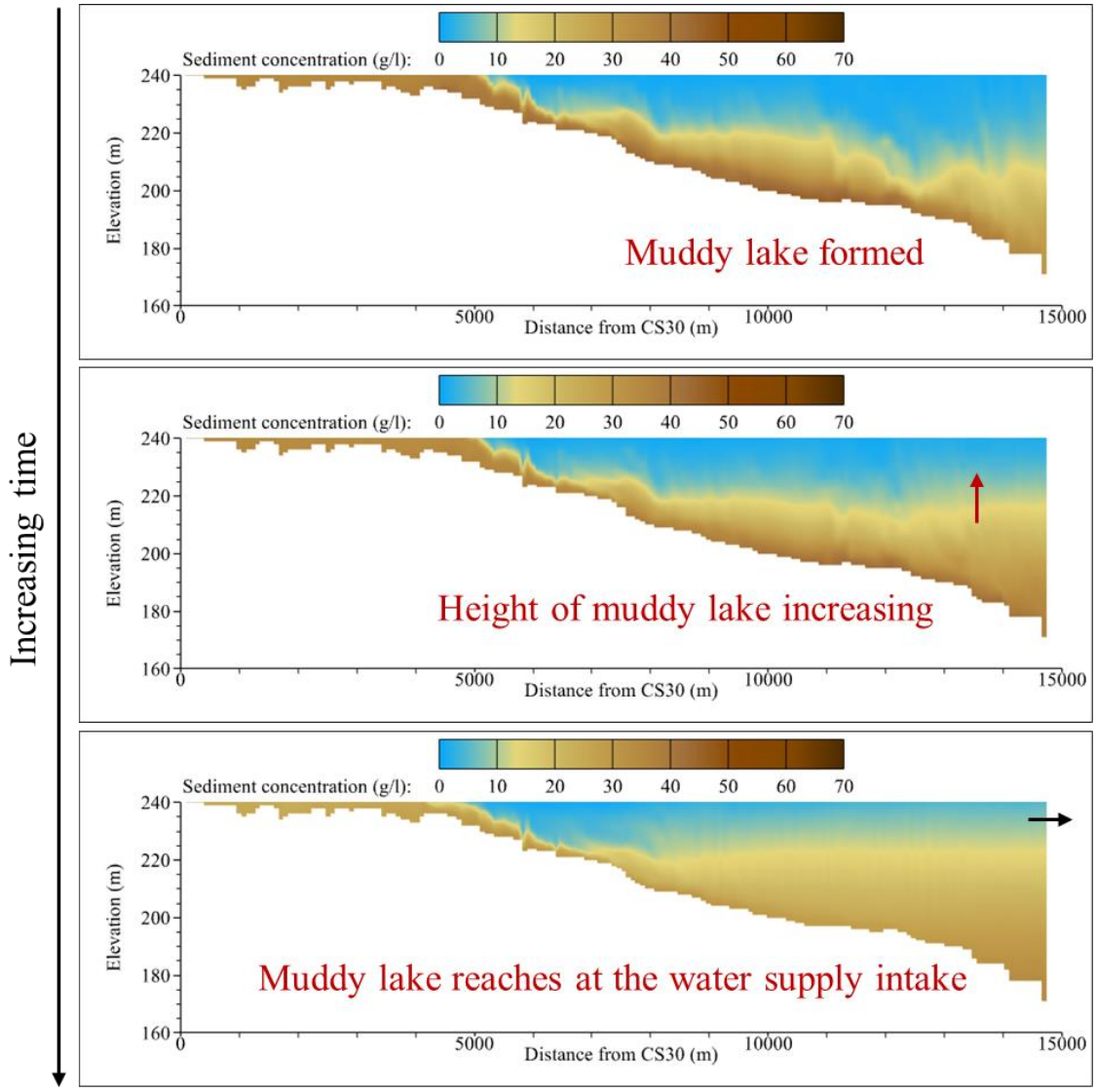

Figure 5.31 The configuration of muddy lake evolution and the influence of water supply intake.

As illustrated in Figure 5.32, with increasing inflow sediment concentration and discharge, the muddy lake reaches the water supply intake faster. It means a shorter water supply duration within the flooding events. The results revealed that no influence of muddy lake on water supply facilities with small amount of inflow conditions and one small and one middle of inflow condition. It gives a valuable reference for the water purification plant manager to operate the water withdrawal facilities. Overall, based on the comprehension of the turbidity current process and the muddy lake formed from different inflow conditions, the accurate turbidity current venting and clear water withdrawal operation could be evaluated according to the hydrologic situation.

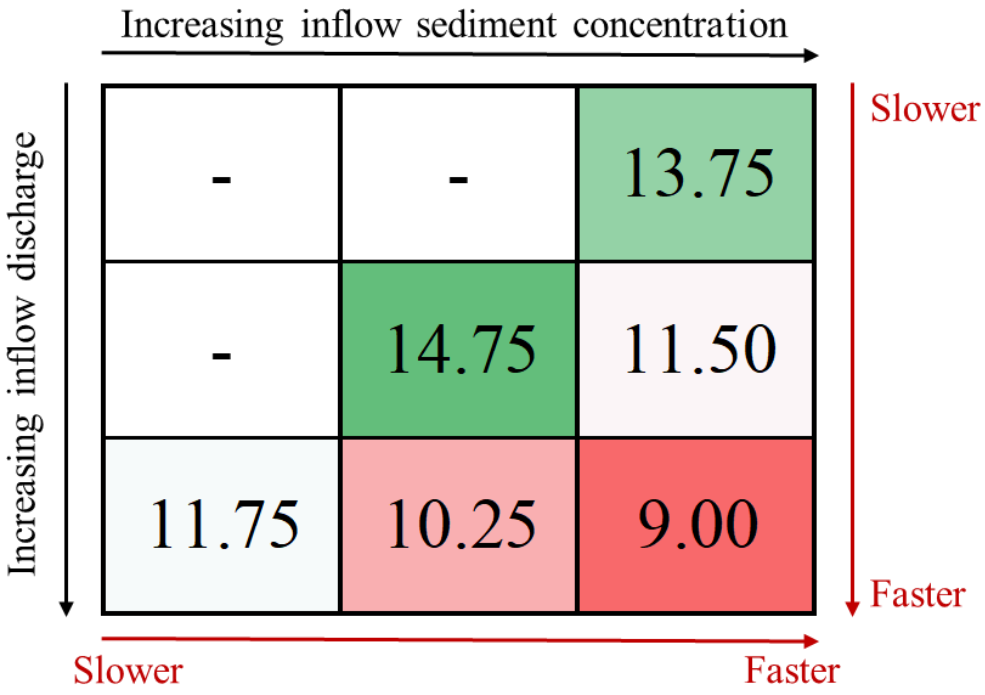

Figure 5.32 The muddy lake reach time at the water supply intake from different inflow sediment concentrations and inflow discharges (unit: hours). (Note: - means the muddy lake does not affect the water supply facilities.)

5.4 Evaluation of the potential improving methods for solving the shortcomings of the existing venting methods

Based on the aforementioned results, the turbidity current processes and characteristics were understood. The proposed empirical formulas from **Chapter 5.3** were considered helpful for the turbidity current arrival time estimation. According to the literature review, the venting outlets' location is essential for increasing the turbidity current venting efficiency. Figure 5.1 Figure 5.2 illustrate the divided flow of turbidity current into the mainstream and tributaries. With those understandings, the potential improving methods for improving the turbidity current venting efficiency were discussed in this study.

5.4.1 Estimation of turbidity current arrival time with the empirical formula

It is difficult to measure the turbidity current processes during flooding events. Understanding the flow regime and turbidity current transportation within Shihmen Reservoir was useful for operating the venting outlets at the correct timing. As illustrated in Figure 5.33, the proposed empirical formulas could be helpful for the turbidity current arrival time estimation.

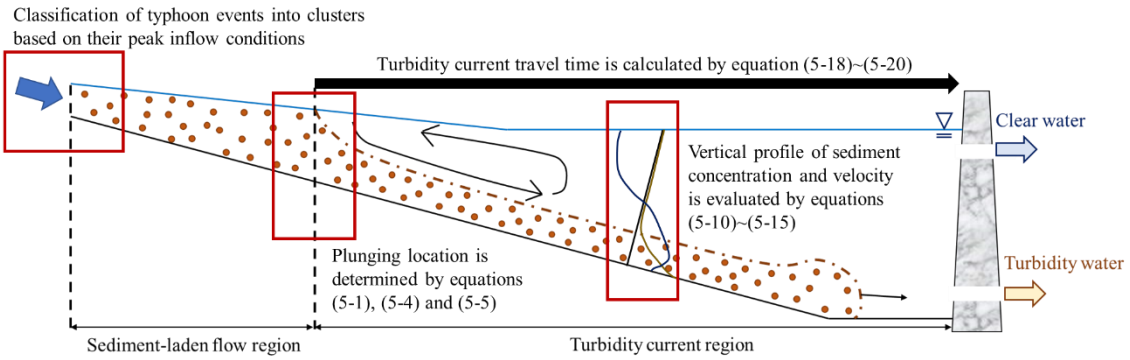

Figure 5.33 The turbidity current arrival time estimation by using the proposed empirical formulas.

The procedure of arrival time estimation was divided into four steps: (1) Classify the typhoon events into clusters based on their peak inflow conditions; (2) Determine the turbidity current plunging location by using the densimetric Froude number (equations (5-1) and (5-2)) and the empirical equation for Shihmen Reservoir (equation (5-6)); (3) As shown in Figure 5.33, the turbidity current body thickness, velocity, and sediment concentration profiles were evaluated by using equations (5-11) to (5-16). The turbidity current head velocity was calculated by equation (5-18). That information gives references for determining the operation of the midstream and different elevation outlets; (4) According to the different clusters of inflow discharge, the turbidity current arrival time could be assessed by equations (5-19), (5-20), and (5-21).

Overall, the proposed empirical formulas could estimate the turbidity current processes, structures, movement, and arrival time. The turbidity current transportation estimation provides a solution to solve the difficulty of the field measurements and gives a good reference for correctly turbidity current venting operation.

5.4.2 Investigation of the turbidity current venting ability of each outlet from different locations

As Figure 2.11 showed, the outlets' elevation is critical for the turbidity current venting efficiency. The bottom outlets have a better ability to vent through the turbidity current. In contrast, the upper outlets only release the ambient water. According to the previous understanding, the multiple outlets' function could be divided into flooding control and sediment venting outlets. Moreover, the proposed modification of the outlets' location is discussed in this study.

The multiple outlets' location within Shihmen Reservoir is shown in Figure 5.34. The SCI, PPI, VT, PRO, and ELEP are regarded as the sediment venting function. Furthermore, the SP, ST, water supply intakes, Amu_SBT, and Daw_SBT are the flooding

control functional outlets. As the laboratory results showed, the extended pipes from the upper SBT could effectively increase the turbidity current venting efficiency (Table 3.4). The additional extended pipe from Amu_SBT was proposed in this study for improving the turbidity current venting efficiency of Amu_SBT.

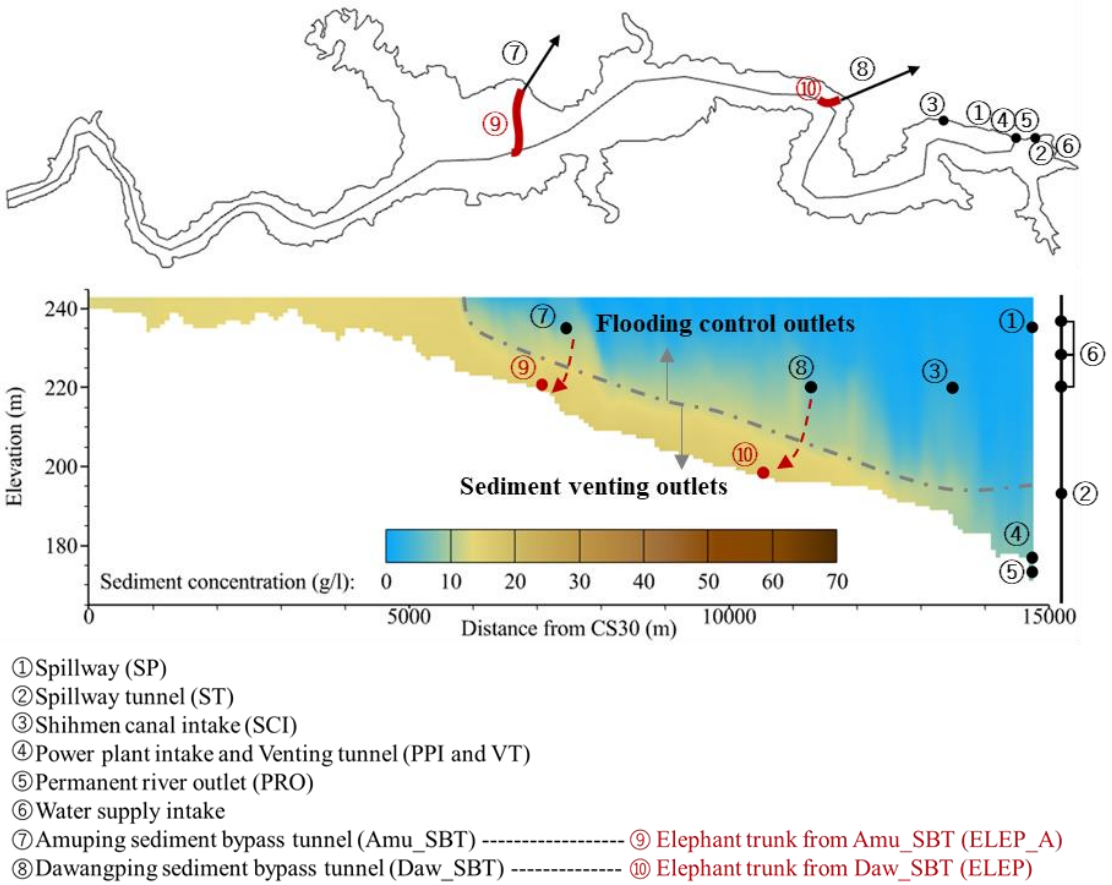

Figure 5.34 The location of each outlet within Shihmen Reservoir.

5.4.3 Influence of the tributaries on turbidity current transportation

As illustrated in Figure 5.1 and Figure 5.2, we found that the turbidity current transportation is divided into mainstream and tributary directions. Due to the turbidity flow spreading into the tributaries, the continuous turbidity current transportation was affected. It leads to the turbidity current thickness and sediment concentration decrease downstream of tributaries. Based on the reasons above, the turbidity current venting

efficiency could be increased by the application of the avoiding spread flow strategies. To achieve this goal, the improving engineering methods were proposed in this study: (1) the blockade structures were proposed to avoid the turbidity current spread flow into the tributaries (Figure 5.35 (a)); (2) The dredging channel was proposed to guide turbidity current effectively vent through the bottom outlets (Figure 5.35 (b)).

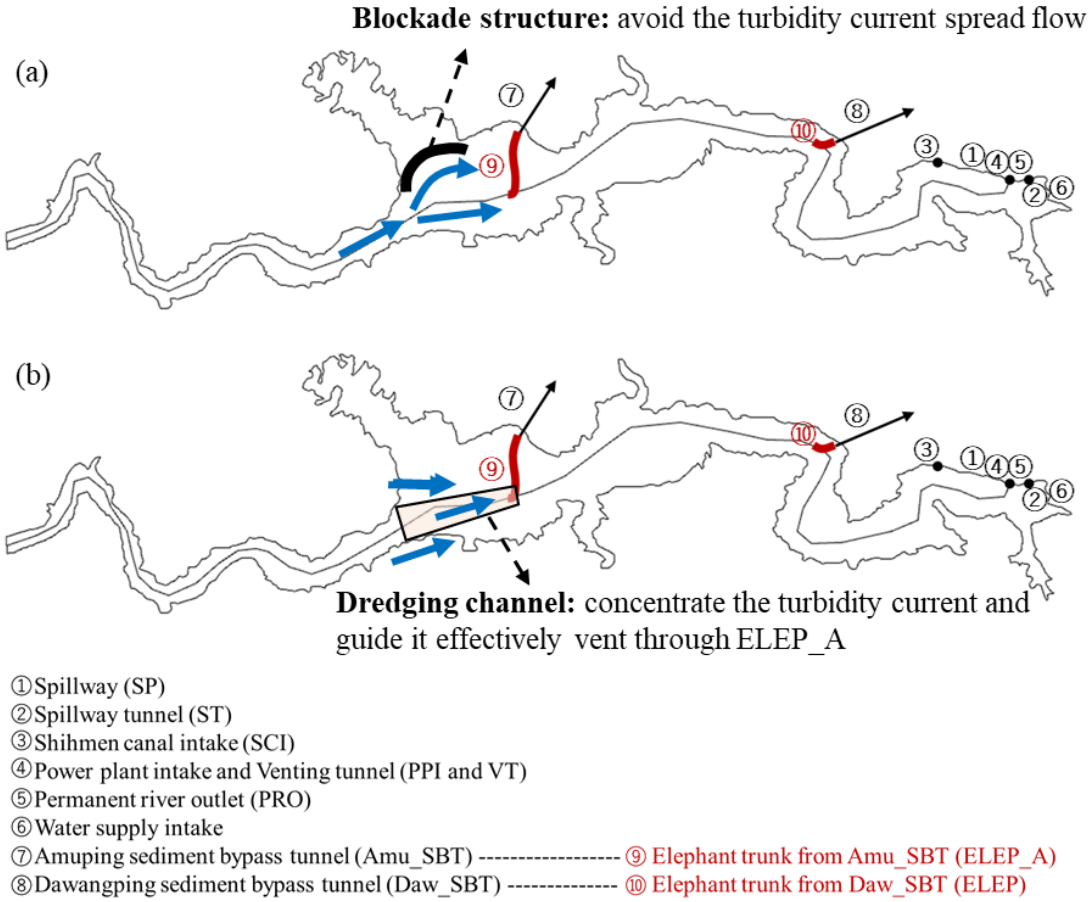

Figure 5.35 The concept diagram of (a) blockade structure and (b) dredging channel.

5.5 Assessment of the necessity of additional measurements to monitor the deficiencies for turbidity current simulation

5.5.1 Impact of the deficient observations from the tributary

As illustrated in Figure 3.1, we found three tributaries within the Shihmen Reservoir. However, most of the researches ignores the inflow from the tributaries. They only used the hydrologic data from the mainstream as the inflow boundary condition. The sediment concentration measurements from mainstream could be obtained by observation pipe (Figure 3.2 (b)), but the inflow discharge was calculated by continuity equation:

$$Q_{in} - Q_{out} = \frac{\partial S}{\partial t} \quad (5\text{-}22)$$

where, Q_{in} is inflow discharge (m^3/s); Q_{out} is outflow discharge (m^3/s); S means reservoir storage (m^3). Due to the inflow discharge being related to outflow discharge and reservoir storage, the ignorance of tributaries' inflow discharge causes the overestimated inflow discharge from the mainstream. Compared to the mainstream basin, the tributaries' basins are much smaller. We consider that the inflow from tributaries still has an influence on the flow regime and turbidity current transportation.

To investigate the inflow from tributaries impacts, the hypothesis of inflow discharge ratio for mainstream and tributaries was used for generating the new boundary condition (Figure 5.36 (a)). Moreover, the adjusted rating curve of inflow discharge and sediment was obtained by the modified mainstream inflow discharge (Figure 5.36 (b) and (c)), and then the inflow sediment concentration from tributaries could be estimated.

Adjusted rating curves with modified mainstream discharge in Soudelor Typhoon:

$$Q_{s,in} = 0.09{Q_{in}}^{1.65} \quad (5\text{-}23)$$

Overall, the boundary conditions of simulation, with and without considering the tributaries' inflow, were shown in (Figure 5.37).

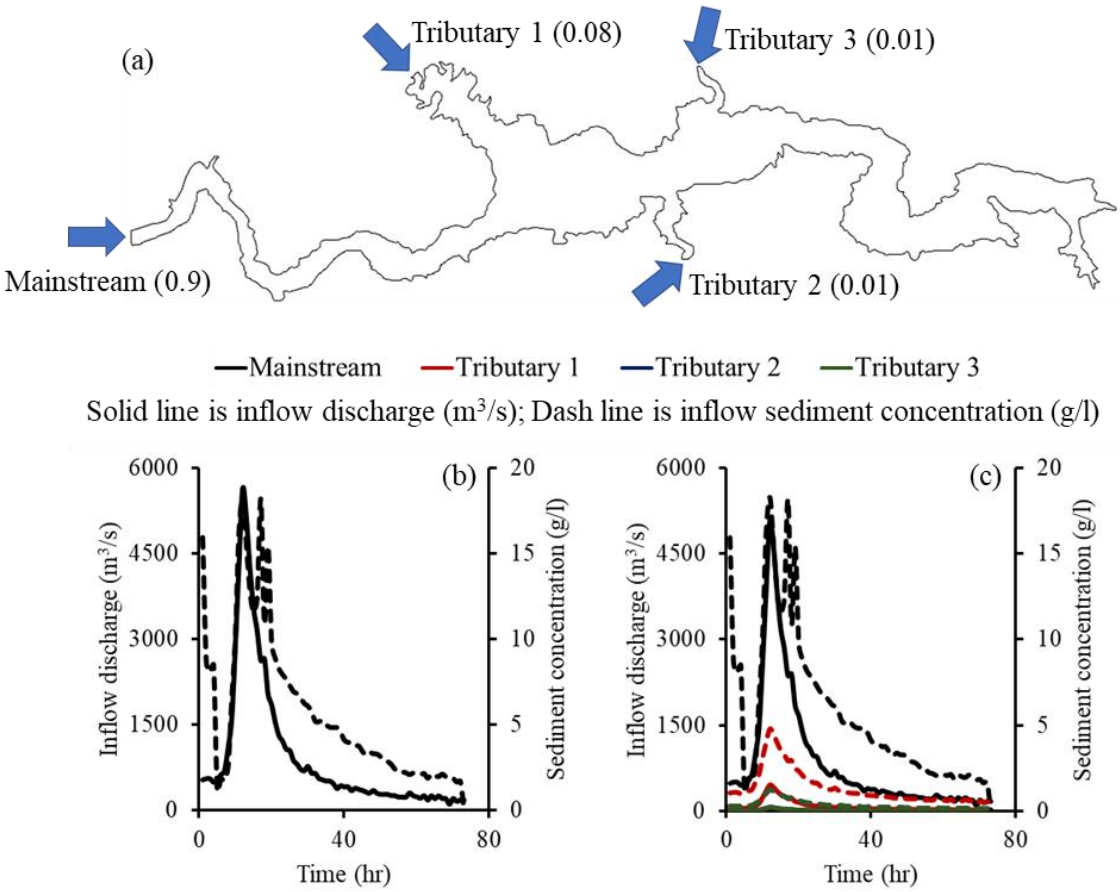

Figure 5.36 The (a) hypothesis of inflow discharge ratio for mainstream and tributaries (numbers in brackets represent proportions), and the upstream boundary conditions (b) without, and (c) with considering the tributaries' inflow.

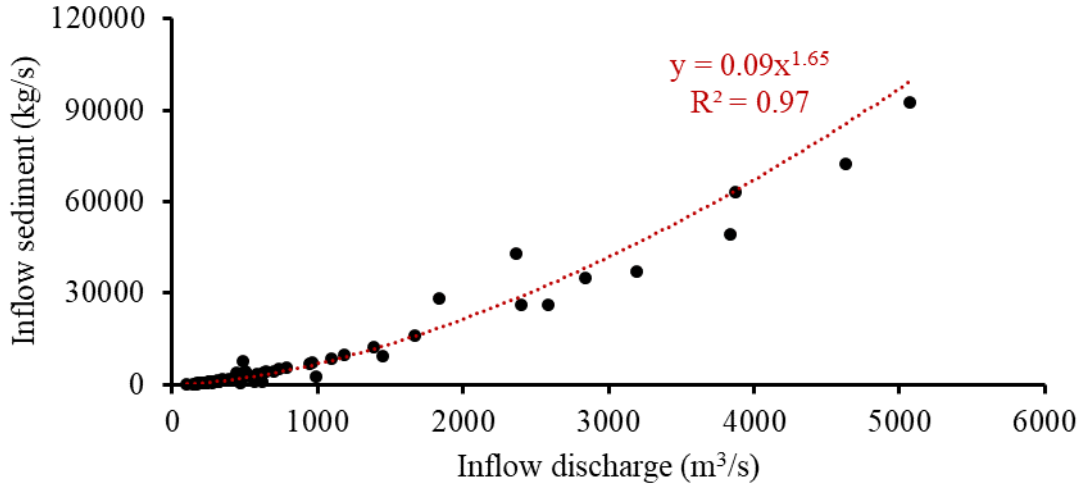

Figure 5.37 The relationship between inflow discharge and sediment with modified mainstream inflow discharge.

As illustrated in Figure 5.38, the tributaries' inflow could effectively avoid the turbidity current spread flow into tributaries. Meanwhile, the results revealed that the turbidity current velocity is faster without considering the inflow from the tributaries. Figure 5.26 showed that the turbidity current velocity was slower with smaller inflow discharge. It significantly indicated that the governing term for turbidity current transportation is the inflow discharge from the mainstream. Moreover, as shown in Figure 5.39, the turbidity current transportation in the mainstream from without and with considering the inflow from tributaries are similar. We found that only the turbidity current thickness slightly decreased due to the smaller inflow discharge. However, Figure 5.38 revealed that the turbidity current spread flows into tributary 1 was reduced due to the tributaries' inflow. Though the inflow amount of tributaries is limited, it still impacts turbidity current processes.

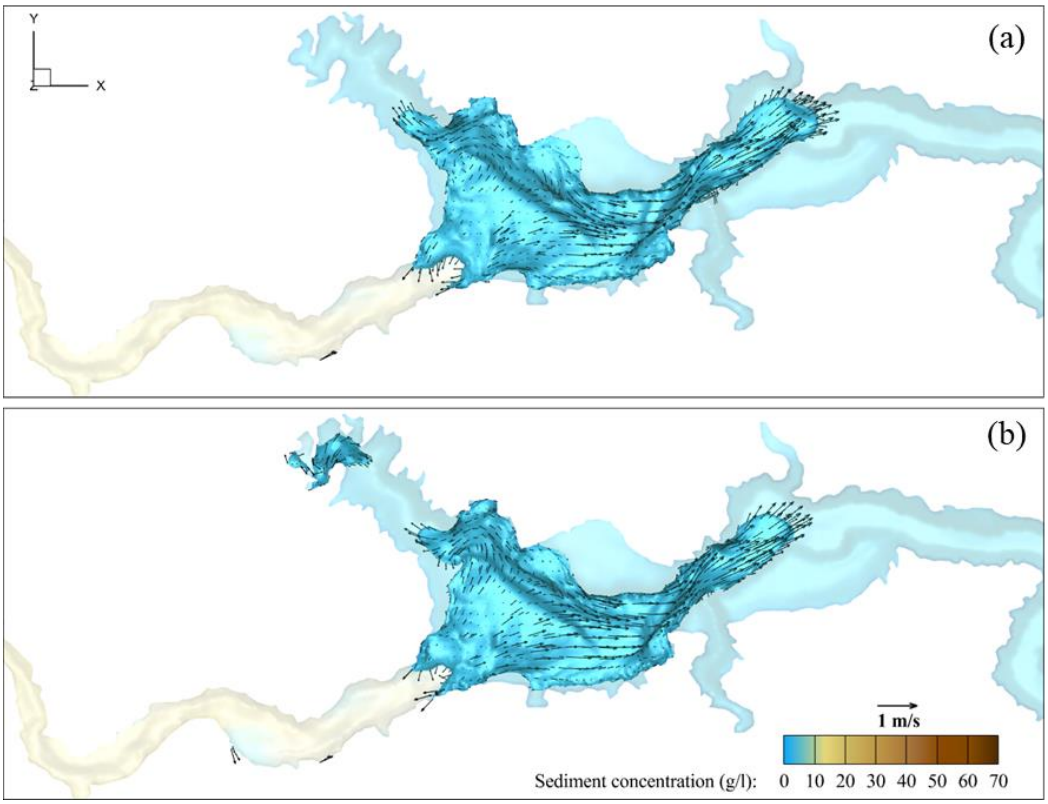

Figure 5.38 The turbidity current flow regime (a) without and (b) with inflow from the tributaries.

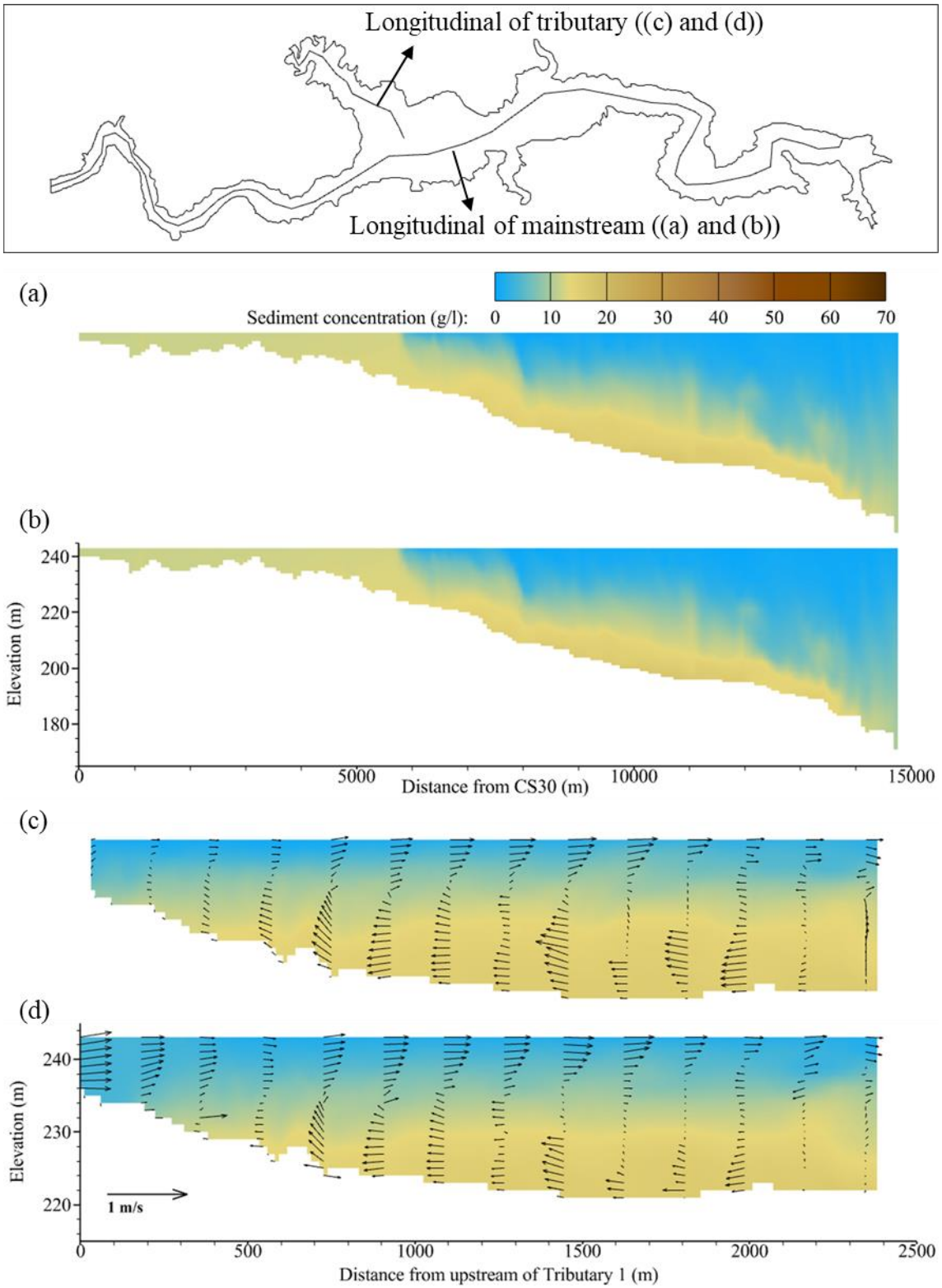

Figure 5.39 The longitudinal view of sediment concentration without ((a) and (c)) and with ((b) and (d)) tributaries' inflow at mainstream and tributaries.

5.5.2 Influence of the deficient observations of the active deposition layer

As illustrated in Figure 4.12, the released sediment concentration at bottom outlets (i.e., PPI, PRO, and VT) are underestimated but have good agreements at upper outlets. It might be caused by the lack of accumulated deposition layer setting in front of the dam. To investigate the impact of the deposition layer on the improvement of bottom outlets' simulation, the deposition layer setting used the same sediment material to inflow sediment with 1 m thick and 150 g/l sediment concentration. As illustrated in Figure 5.40, the released sediment concentration at turbidity current arrival increased due to the eroded deposition transport downstream. However, we found that the peak values were still underestimated, and the peak time was incorrect.

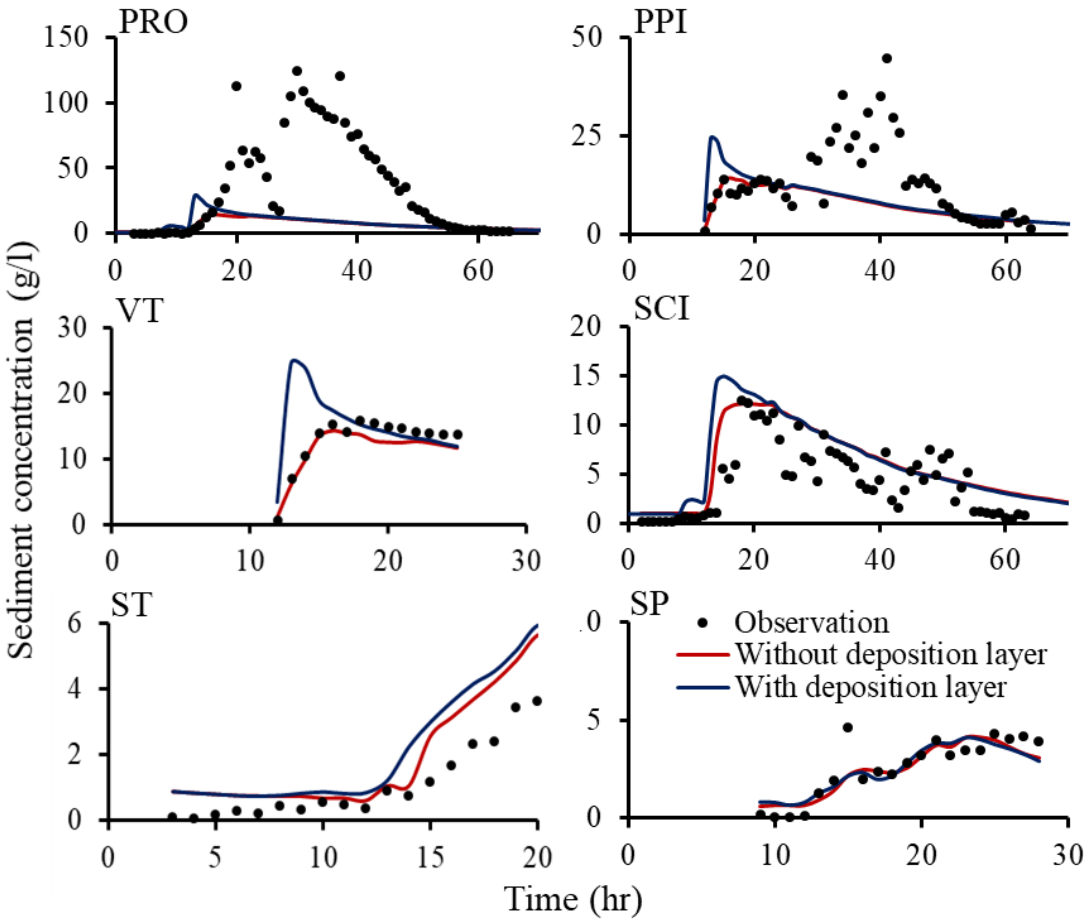

Figure 5.40 Comparison between the simulations, with and without deposition layer, and the observation of each venting outlet.

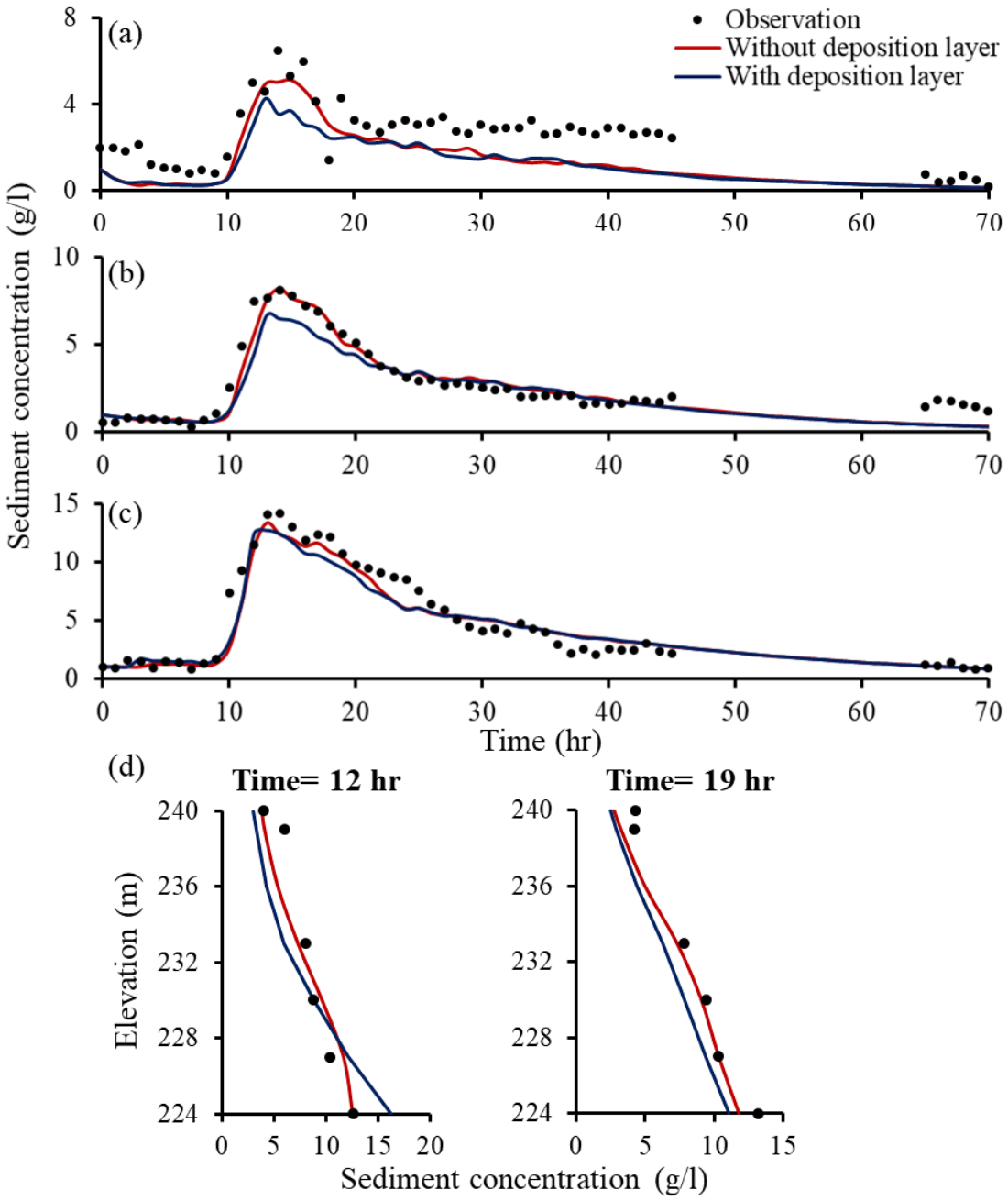

Figure 5.41 Cross-sectional performance comparison between the simulation with and without deposition layer and the TDR 20-1 observation of (a) top, (b) middle, (c) bottom reach, and (d) vertical profile

As the above shortcomings, the deposition layer material setting was inappropriate. The sediment concentration should be increased, eroded time of deposition should be later, and traffic time of eroded deposition should be slower. Moreover, Figure 5.41 showed the

sediment concentration was underestimated after the turbidity arrival. The erosion of the deposition layer leads to the water depth increases and sediment concentration distribution changes. Due to the turbidity current bringing enormous shear stress, the deposition layer starts to be eroded after the turbidity current arrives (Figure 5.42). Based on the aforementioned results, the hypothesis of the deposition layer setting was inappropriate. However, the correct deposition layer setting is difficult to determine without any deposition measurements and several unknown factors.

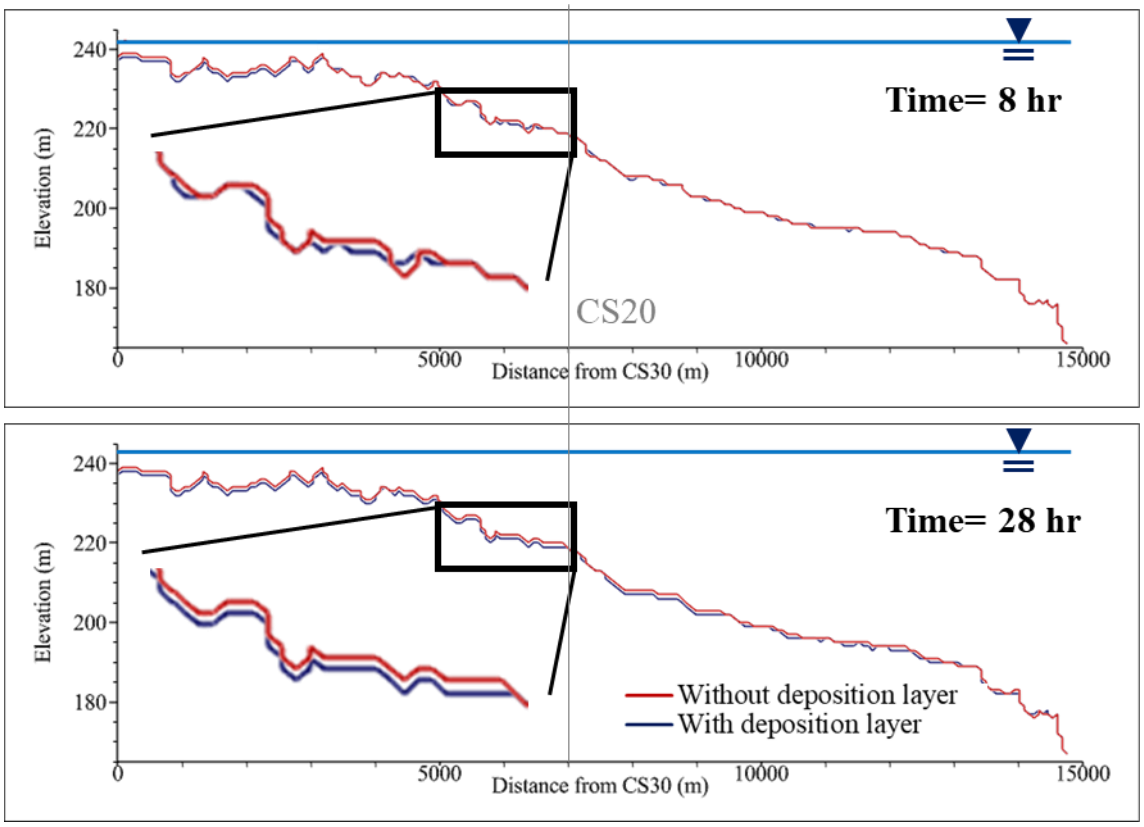

Figure 5.42 The bed elevation of simulation with and without deposition layer between before and after the turbidity current arrival.

5.5.3 Solution for solving the deficient observations within the reservoir to increase the simulation accuracy

Based on the aforementioned results, the deficient observations of tributaries and deposition layers impact the turbidity current movement. However, the lack of monitoring facilities and field sampling was challenging to fill these gaps. To solve the missing points, the solutions for solving the deficient observations are proposed in this section:

A. Build the monitoring facilities within tributaries

The same facilities (TDR equipment) in the mainstream could be applied to measure inflow sediment concentration in the tributaries. Moreover, the inflow discharge from mainstream and tributaries could be calculated by the velocity (measured by the pitometer) and cross section bathymetries. Thus, the inflow measurements from mainstream and tributaries could be obtained according to the additional hydraulic stations.

In addition, underwater terrain monitoring (using Acoustic Doppler Current Profiler), Large-Scale Particle Image Velocimetry (LSPIV), and watercolor analysis are helpful to obtain the inflow discharge and sediment concentration of mainstream and tributaries. Integrated with the underwater terrain monitoring data and image data, the LSPIV is adopted to calculate the surface flow pattern. Meanwhile, the sediment concentration could be evaluated by the watercolor, and turbidity current plunge location was judged by the woody debris gathering location. To achieve this proposal, the camera installation and underwater terrain measurements should be implemented in the future (Figure 5.43).

B. Apply the Soil drilling for investigating the sediment materials

As mentioned in **Chapter 5.5.3**, the deposition layer material is essential to the erosion, caused by turbidity current, within the reservoir. The grain size accounts for determining the cohesive or non-cohesive sediment, which has a high relationship with the sediment incipient motion and transportation mechanism. Also, the critical shear

stress of erosion is vital for determining the erosion site and time. Furthermore, the active deposition layer thickness, number, and sediment characteristic of each layer are crucial to deciding on the erodable deposition amount for the simulation. Overall, the soil drilling within the Shihmen Reservoir could provide critical information to the sediment exchange simulation at the interface of water and deposition.

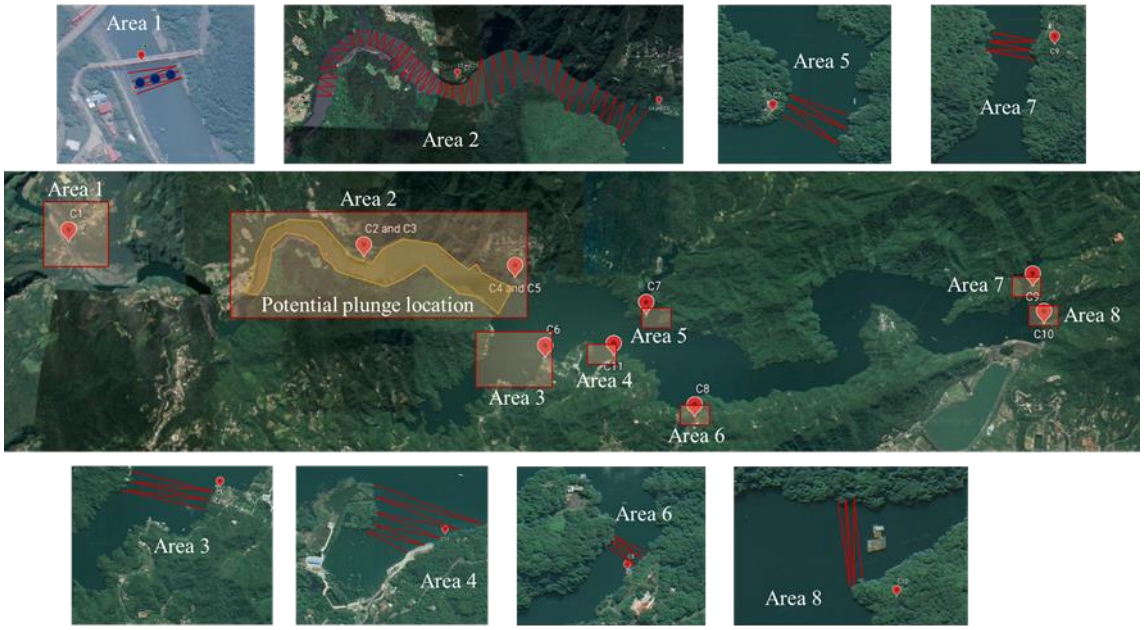

*Note: Red line means ship track for underwater terrain measurement
Location icon means the camera install location

Figure 5.43 The planned underwater terrain measurement area and camera install sites.

5.6 Conclusion

Using the fully three-dimensional numerical model, the turbidity flow converted from sediment-laden flow to turbidity current could be clearly understood. The flow regime and turbidity current transportation within Shihmen Reservoir under the flooding events could be divided into five parts: (1) the sediment-laden flow region; (2) the turbidity current plunging phenomenon; (3) the turbidity current transportation is divided into mainstream and tributary direction; (4) the circulation in the tributary due to the turbidity current spread flow; (5) the turbidity current region. Based on the comprehensive assessment of turbidity current characteristics and processes, the findings were expressed:

1. The vertical profiles of sediment-laden flow reveal that the flow regime and sediment distribution are similar to the open-channel flow. Meanwhile, the velocity of sediment-laden flow is higher due to the shallow water upstream of the reservoir.
2. According to the various generated hydrological conditions, the inflow discharge could be considered as the governing term for turbidity current plunging, thickness, and velocity. On the contrary, the inflow sediment concentration is crucial for controlling the sediment concentration of the turbidity current body.
3. Under certain hydraulic conditions, the high sediment concentration flow plunges and concentrates to turbidity current. The densimetric Froude number is the critical characteristic for evaluating the plunging location. The inflow discharge and sediment concentration were the critical factors for determining the plunging densimetric Froude number.
4. The structure of the turbidity current body and head velocity was evaluated by the measurement from TDR and proposed equations.
5. According to the new findings and literature, the potential improving methods were proposed in this section.

6. The influence of the deficient observations of tributaries and deposition layer showed the necessity of the additional monitoring facilities and field survey.

Based on the previous understanding, the shortcomings of the existing venting methods were found, and potential improving methods were proposed in **Chapter 6**. Moreover, additional measurements to monitor the deficiencies were crucial to obtain comprehensive assessments of turbidity current interaction at tributaries and beds.

Chapter 6: Investigating the impacts of sediment management options on efficiency of turbidity current venting

6.1 Introduction

The holistic understanding of the turbidity current process in the reservoir was analyzed in **Chapter 5** using the validated 3D numerical model proposed in **Chapter 4**. Based on the comprehension of the turbidity current transportation from the plunging location to each sediment venting outlet, the effective improvement scenarios are discussed in this chapter. As mentioned in **Chapter 5**, the field-scale simulation is more complicated due to the sediment exchange at the water-bed interface. To simplify the procedure of the improvement scenarios discussion, the experiment-scale numerical model is adopted to investigate the optimal strategies. This chapter aims to evaluate the feasibilities of the proposed improvement scenarios for increasing turbidity current venting efficiency and prolonging the water supply during flooding events. To achieve this goal, the soft and engineering methods are considered in this study (Figure 6.1).

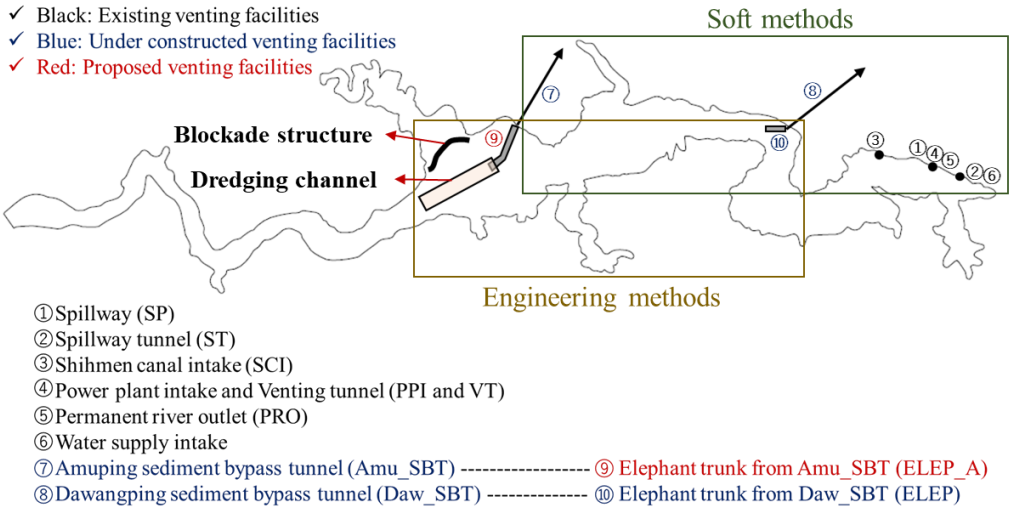

Figure 6.1 The proposed soft and engineering methods for investigating the optimal improvement scenario.

As illustrated in Figure 6.2, two significant parts were discussed for investigating the optimal soft methods: (1) Determine the optimal turbidity current venting operation from multiple outlets. The sediment venting ability of each operating facility is evaluated by released sediment concentration. After that, the operation sequence of each outlet could be determined. Meanwhile, the appropriate multiple outlets' operation was obtained by following the operating order in the sequence. (2) Assess the operating timing impact on turbidity current venting efficiency. Comparison of the performance from different operating timing, including from beginning, early, in-time, and later, for the outlets at the dam site and middle of reservoir is essential for determining the appropriate operating timing. Overall, the turbidity current venting operation improvement by appropriate operating timing could be regarded as a reference to enhance the importance of turbidity current transportation understanding and real-time outlets' operation.

According to the findings from numerical simulations and the physical model results, the feasibility of the additional structures for guiding the turbidity current movement, increasing venting outlets, and concentrating the turbidity current are investigated. As illustrated in Figure 6.3, the feasibilities of the proposed structures are assessed in this study: (1) The blockade structures are proposed to avoid the turbidity current spread flow into the tributaries. (2) The importance of the moveable inlet of the extended pipe from SBTs. (3) As the known effective improvement of application of the extended pipe from Daw_SBT, the feasibility of the additional extended pipe from Amu_SBT is assessed. (4) Application of dredging channel for guiding turbidity current effectively vent through the extended pipe from SBTs.

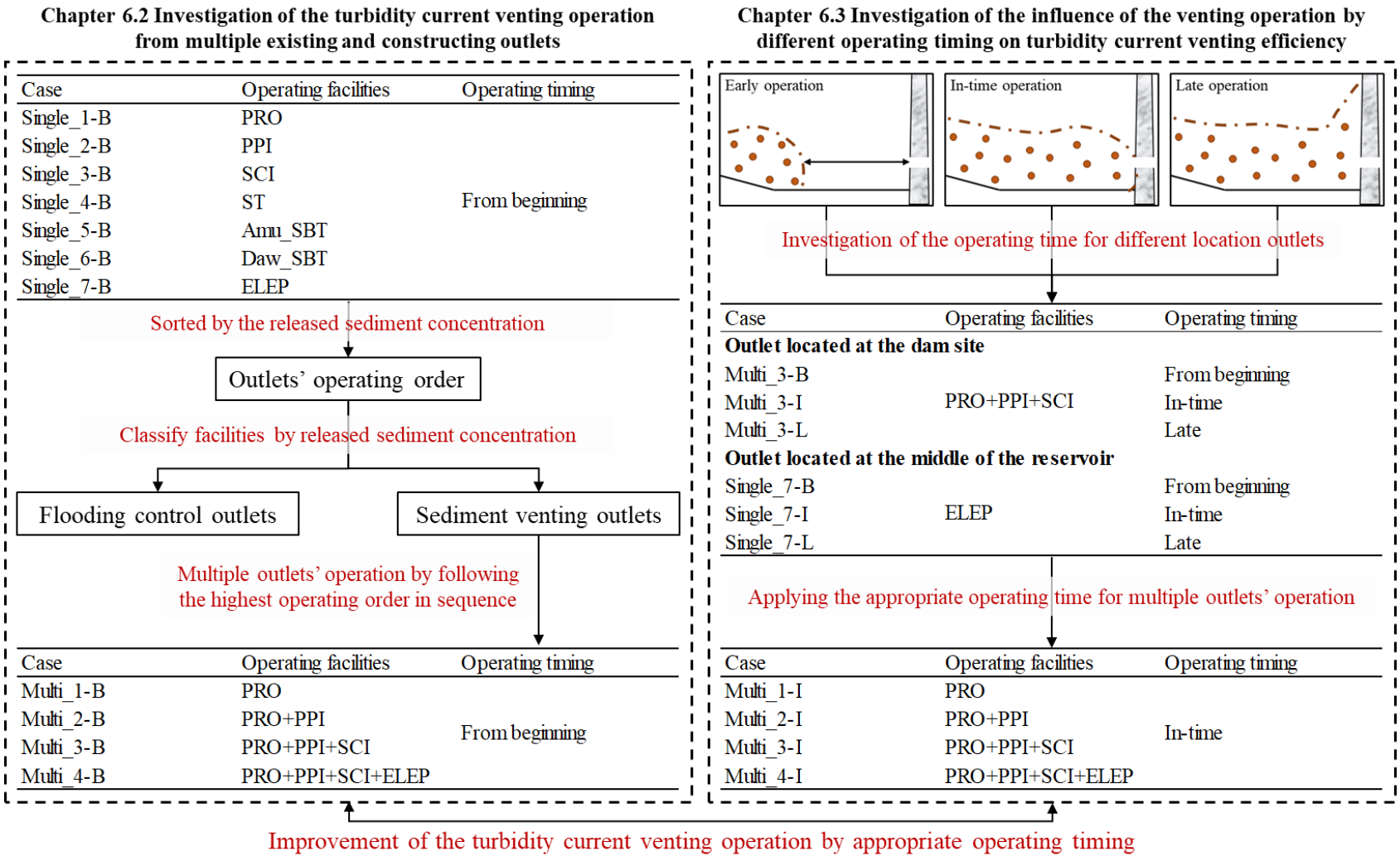

Figure 6.2 The proposed scenarios for investigating the optimal soft methods.

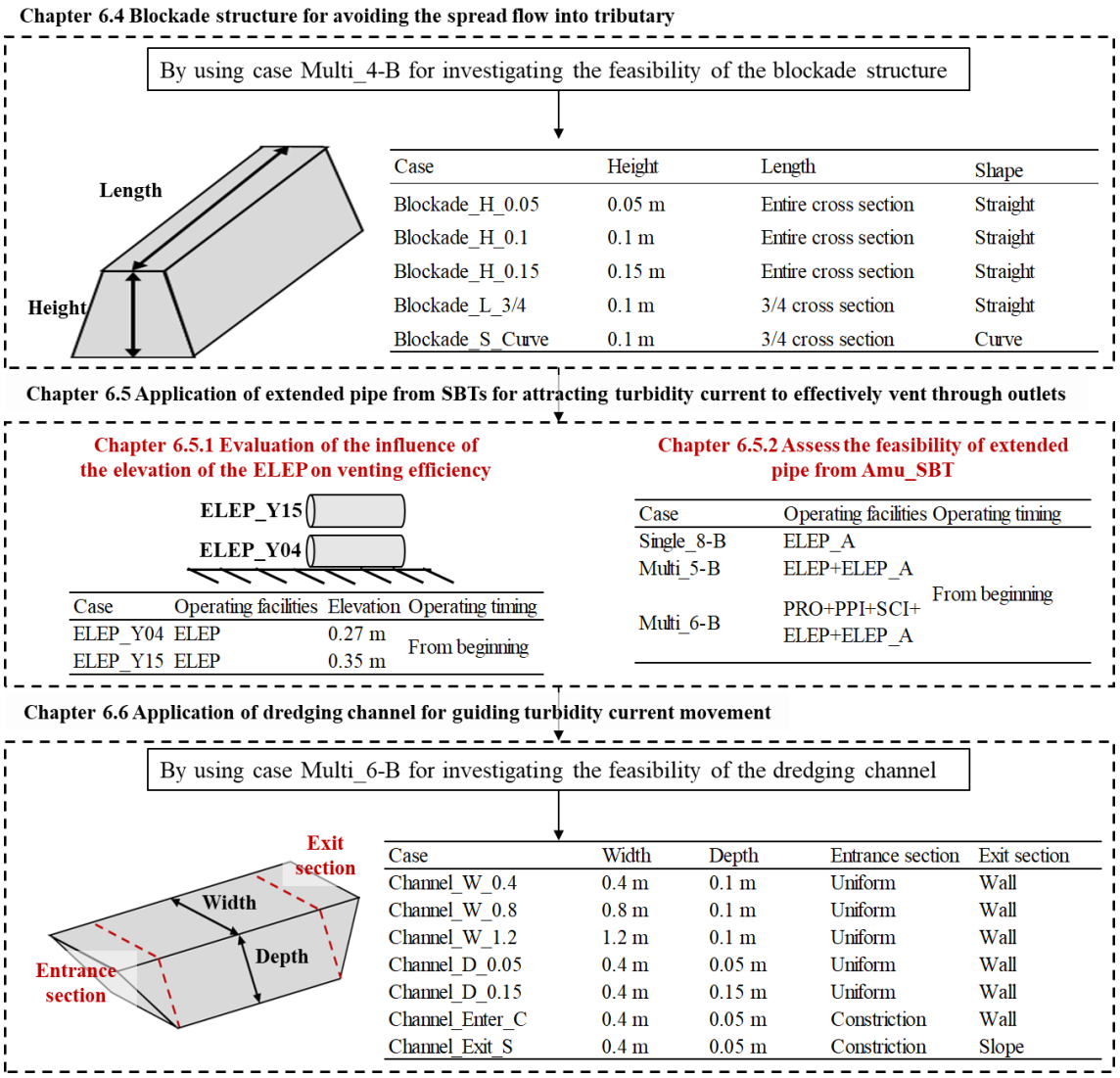

Figure 6.3 The proposed structures for determining the optimal engineering methods.

Overall, this chapter analyzes the improvement of the application of optimal venting operation from multiple outlets, gate operating timing, and additional venting facilities and constructures. The application of the proposed method in future flooding events and the extended usage life of reservoirs is concluded in **Chapter 7**. With the proposed turbidity current venting strategies, the main objectives of this study, maximum the turbidity current venting efficiency without trapping in the reservoir, is achieved and summarized in **Chapter 8**.

6.2 Investigation of the turbidity current venting operation from multiple existing and constructing outlets

As illustrated in (Figure 6.4), it significantly shows that the height of the turbidity current covers the outlets close to the bottom, including PPI, PRO, SCI, and ELEP. Still, it is lower than the upper outlets, including Amu_SBT, Daw_SBT, and ST. Due to their height of aspiration, using the higher outlets are not appropriate for a turbidity current venting (Chamoun et al., 2016). Nevertheless, with high designed outflow discharge, the Amu_SBT, Daw_SBT, and ST are essential for flood control under flooding events. Therefore, the outlets within Shihmen Reservoir could be divided into two clusters, sediment venting and flooding control outlets. For evaluating the sediment releasing ability, the venting efficiency (V_e) is used:

$$V_e = \frac{\int_{i=t_o}^{t_c} C_{out,i} Q_{out,i}}{\int_{i=0}^{t_c} C_{in,i}\, Q_{in,i}} \times 100\% \qquad (6\text{-}1)$$

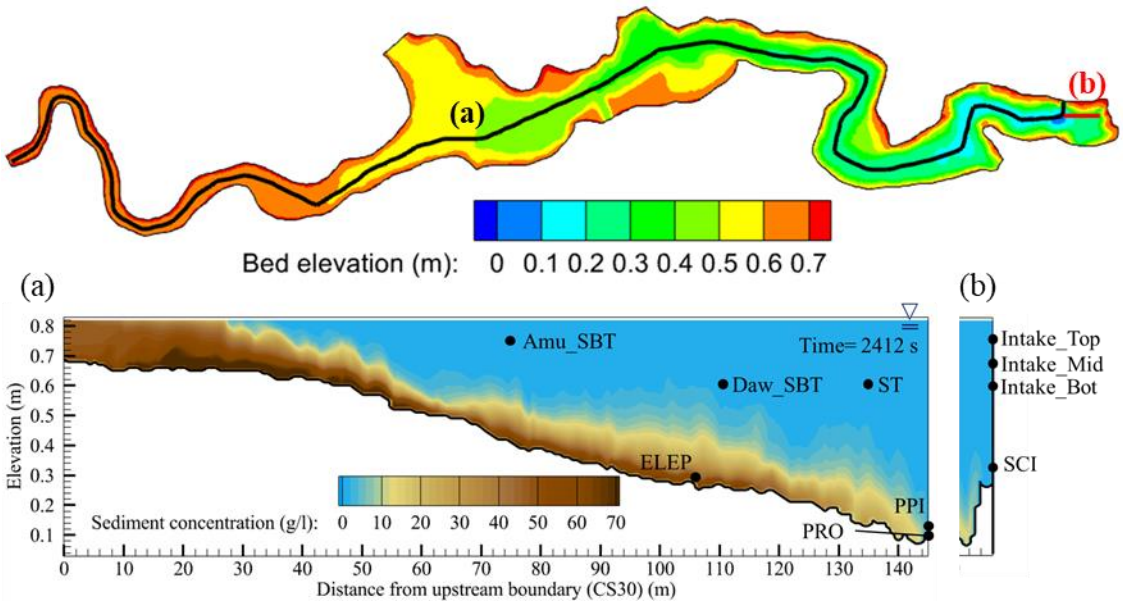

Figure 6.4 The location of venting facilities and the vertical profile of turbidity current body along longitudinal from upstream to (a) dam and (b) intake facility.

where, $C_{in,i}$ and $Q_{in,i}$ are inflow concentration and discharge at time i, respectively; $C_{out,i}$ and $Q_{out,i}$ are outflow concentration and discharge at time *i*, respectively; and the times corresponding to the outlet opening and closing time are called t_o and t_c, respectively. To investigate the impact of multiple outlets' operation without considering the effect of operating timing, the scenario with outlets' gate opening from the event beginning to the end was analyzed.

6.2.1 Operation sequence of each outlet for multiple outlets' operation

To make an appropriate venting operation for releasing turbidity currents and maintaining clear water, it is essential to determine the operation sequence of various outlets. As illustrated in Figure 6.5, the released sediment and water from each single outlet operation are obtained and helpful in determining the operation sequence. Due to the outflow discharge having a great influence on the released sediment, the high outflow discharge and low released sediment concentration also bring high released sediment. It is significantly observed in ST, Amu_SBT, Daw_SBT, and ELEP. Although these outlets release huge amounts of sediment, they also have to consume a lot of water resources. To increase the venting efficiency and avoid clear water wasting, the released sediment concentration is regarded as the critical factor for determining the operation sequence. The outlets with higher released sediment concentration mean that more released sediment with the same water releasing and it has higher operating order (Table 6.1). Meanwhile, based on the averaged released sediment concentration, the outlets could be divided into sediment venting outlets (i.e., PRO, PPI, SCI, and ELEP) and flooding control outlets (i.e., ST, Amu_SBT, and Daw_SBT). Based on the aforementioned results, the operation of sediment venting outlets following the operation sequence is considered a valuable reference for turbidity current venting operation management.

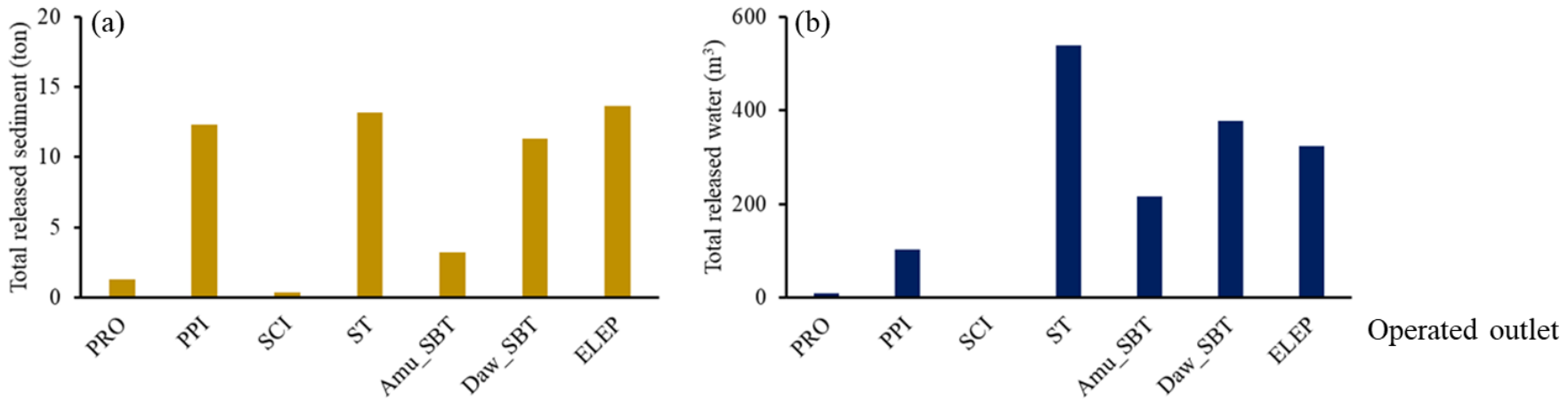

Figure 6.5 The comparison of (a) released sediment concentration and (b) accumulated released sediment from each single outlet operation.

Table 6.1 The sediment venting and water releasing performance of each outlet operation for determining the operating order.

Operated outlet	Operated outlet	V_e (%)	Total released sediment (ton)	Total released water (m^3)	Averaged released sediment concentration (kg/m^3)	Operating order	*Type
Single_1-B	PRO	4.78	1.30	8.1	159.88	1	S
Single_2-B	PPI	45.44	12.32	102.6	120.12	2	S
Single_3-B	SCI	1.28	0.35	3.51	99.28	3	S
Single_4-B	ST	48.51	13.16	540	24.36	6	F
Single_5-B	Amu_SBT	11.92	3.23	216	14.96	7	F
Single_6-B	Daw_SBT	41.71	11.31	378	29.93	5	F
Single_7-B	ELEP	50.23	13.62	324	42.04	4	S

*Note: S and F mean sediment venting and flooding control outlets, respectively.

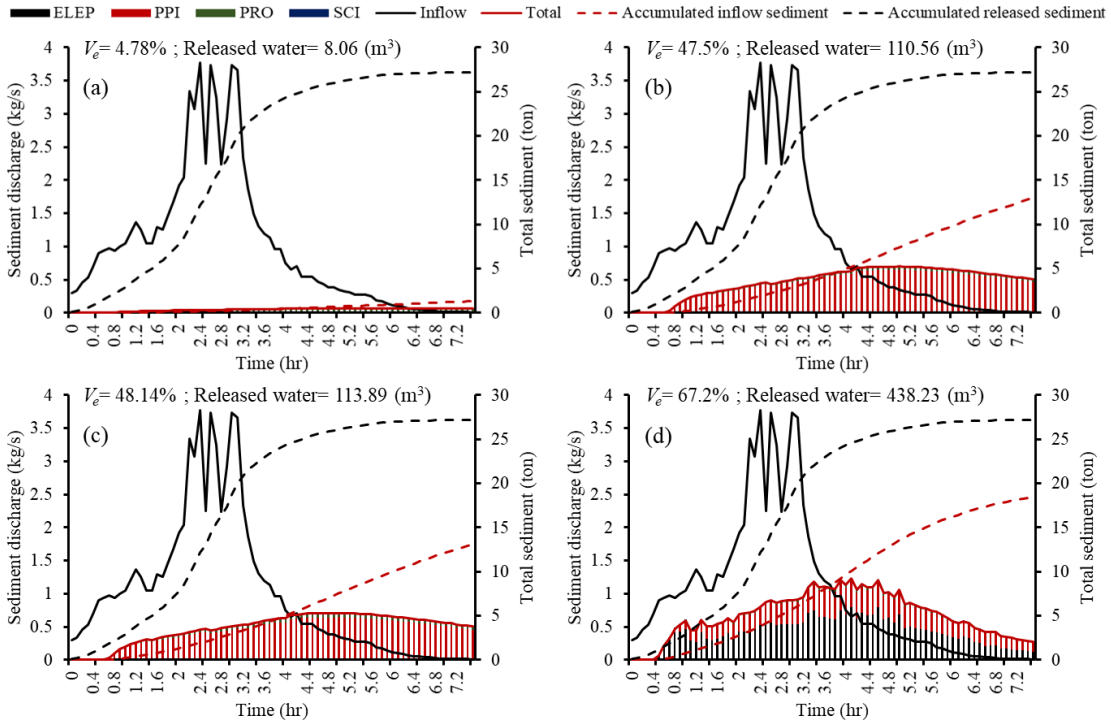

Figure 6.6 Comparison of each outlet's released sediment performance from (a) Multi_1-B, (b) Multi_2-B, (c) Multi_3-B, (d) Multi_4-B.

To investigate the multiple outlets' operation for turbidity current venting, the sediment venting outlets, following the highest operating order in sequence, are proposed and named in Multi_1-B, Multi_2-B, Multi_3-B, and Multi_4-B. The results indicate that more outlet operation leads to higher V_e values, but more water is released (Figure 6.6). Meanwhile, it reveals that the PPI and ELEP have higher contributions for the sediment release. Overall, a suitable venting operation can be chosen depending on the balance between water storage and sediment desiltation regarding the overall water resource conditions. For instance, Multi_1-B, which releases more turbidity flow but limits clear water is appropriate under the 2021 drought event. On the contrary, under the abundant water storage and significant flooding event, the Multi_4-B is suggested to be adopted for avoiding severe sedimentation and prolonging the reservoir usage.

6.2.2 Upstream outlet operation influence on turbidity current transportation and the muddy lake formed

As mentioned in **Chapter 5.2**, the velocity of turbidity current has a high relationship with sediment concentration of turbidity current. By adopting the bypassing facilities, the part of turbidity current could be vented through upstream outlets and lead to the sediment concentration decrease at downstream of outlets. It means that the arrival time of turbidity current will be delayed due to the diversion flow and decreased body sediment concentration. Figure 6.7 reveals that the operation of the ELEP reduces the thickness and sediment concentration downstream of the outlet. Moreover, the lag time of turbidity current arrival from operating ELEP due to the head velocity decrease. As illustrated in Figure 6.7 (a), due to the aspiration force of ELEP, the flow field around ELEP was affected, and the turbidity flow was effectively sucked into the outlet. Compared to upstream (i.e., CS14) cross sectional vertical profile, the thickness and averaged sediment concentration of turbidity current at downstream (i.e., CS8) cross section decreased 36.5% and 30.5%, respectively (Figure 6.7 (c)).

Meanwhile, the influence of aspiration force and released sediment from operating ELEP on head velocity is significantly shown in Figure 6.7 (d). The 12% slower head velocity leads to the turbidity current delay of 108 s (i.e., 18 minutes in field-scale). Overall, based on the information mentioned above, the precise outlets' operating timing at the dam site should consider the operation of upstream outlets.

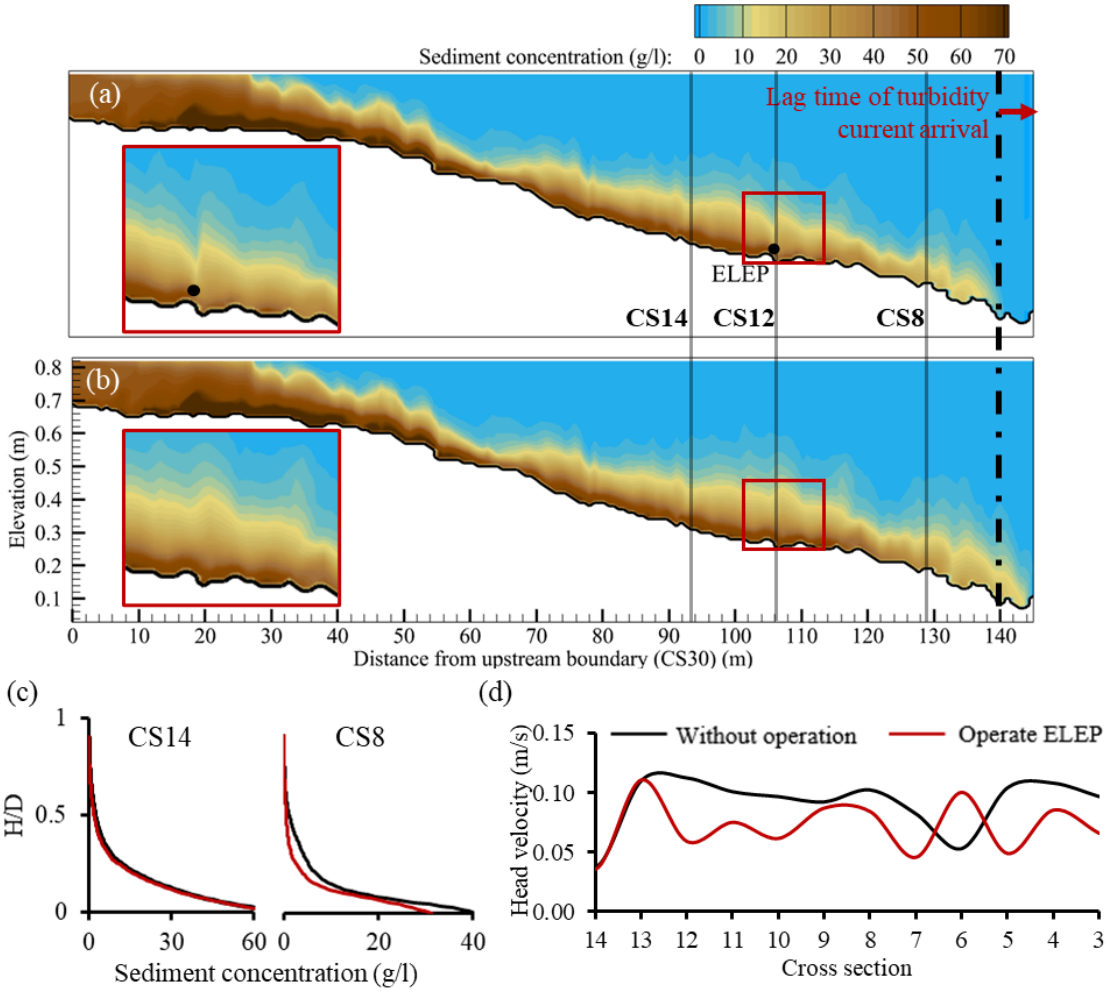

Figure 6.7 Comparison of simulation (a) with ELEP operation and (b) without any outlets operation: (c) difference of sediment concentration and turbidity current thickness from upstream (CS14) and downstream (CS8) of ELEP and (d) the ELEP operation causes head velocity decrease.

6.2.3 Impact of muddy lake evolution on clear water supply

It seemed impossible to release all of the turbidity currents through the outlets within the Shihmen Reservoir. The muddy lake is formed as the remaining turbidity flow is trapped in the reservoir. Predicting the high turbidity muddy lake reaching water supply facilities is essential to manage the withdrawal of clear water. The results reveal that appropriate withdrawal of sediments mitigates the muddy lake evolution and extends the clear water supply duration (Figure 6.8). We found that Multi_1-B has no positive effect on mitigating the muddy lake formed because the releasing amount of sediment from PRO is too small to affect the formation of a muddy lake. Also, since the muddy lake is immediately formed when the turbidity current reaches the dam, it is difficult to promptly mitigate the formation from dam outlets. Thus, as illustrated in Figure 6.9, the operation of additional PPI, with high V_e, in Multi_2-B still has only a limited impact on extended reach time. Compared to the dam outlets' operation, the additional operation of ELEP (Multi_4-B) could effectively prolong the clear water supply duration. As shown in Table 6.2, the dam outlets' operation only extends 2.08% to 5.04% of the water withdrawal period, but adopting Multi_4-B prolongs 15.97% to 22.78% water withdrawal period. It significantly indicates that the proper venting operation benefits from extending the clear water supply duration.

Table 6.2 The improvement percentage of the muddy lake reach time at water supply intake from each multiple outlets' operation instead of without operation.

	Multi_1-B	Multi_2-B	Multi_3-B	Multi_4-B
Intake_Bot	0	2.53	2.53	22.78
Intake_Mid	0	2.08	2.08	19.79
Intake_Top	0	4.20	5.04	15.97

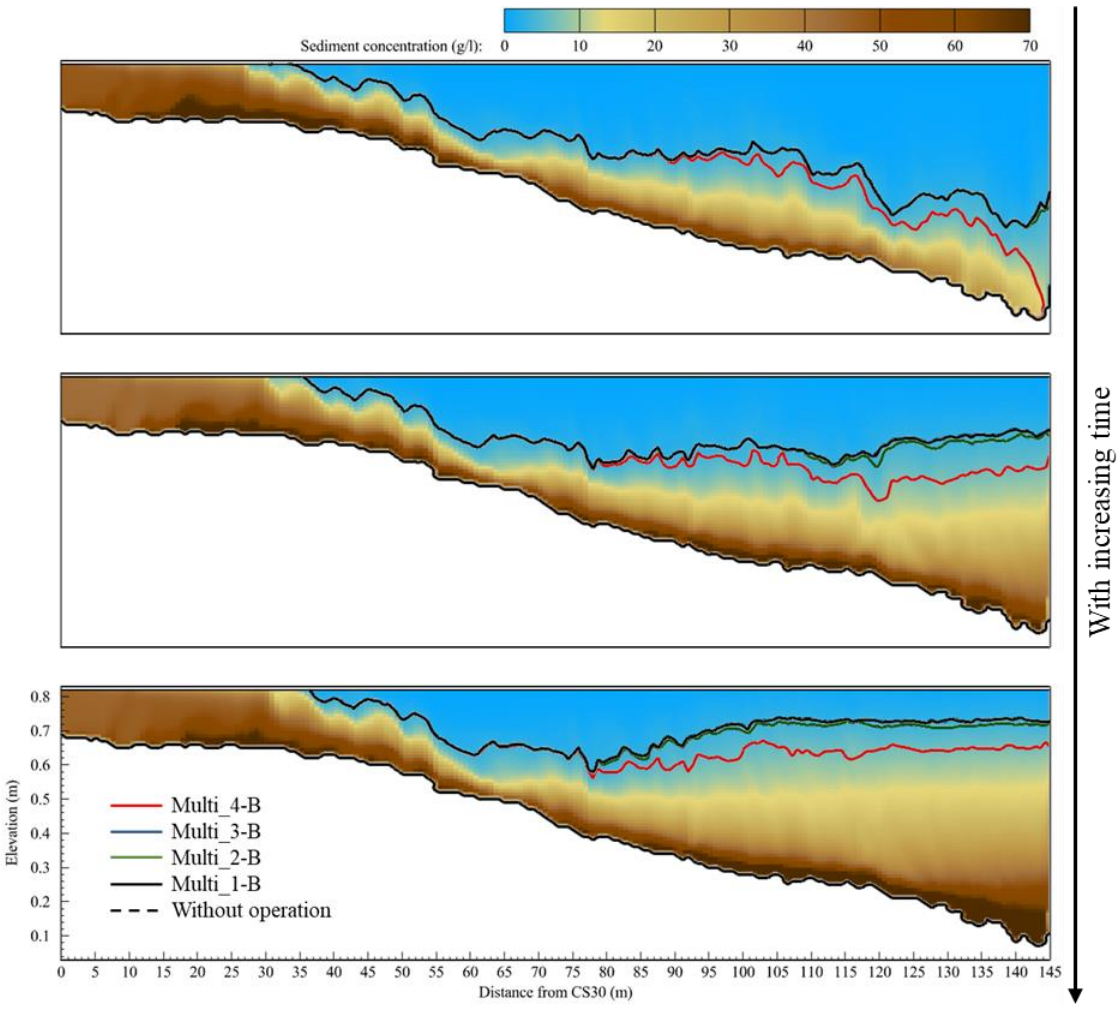

Figure 6.8 The muddy lake evolution from different multiple outlets' operations.

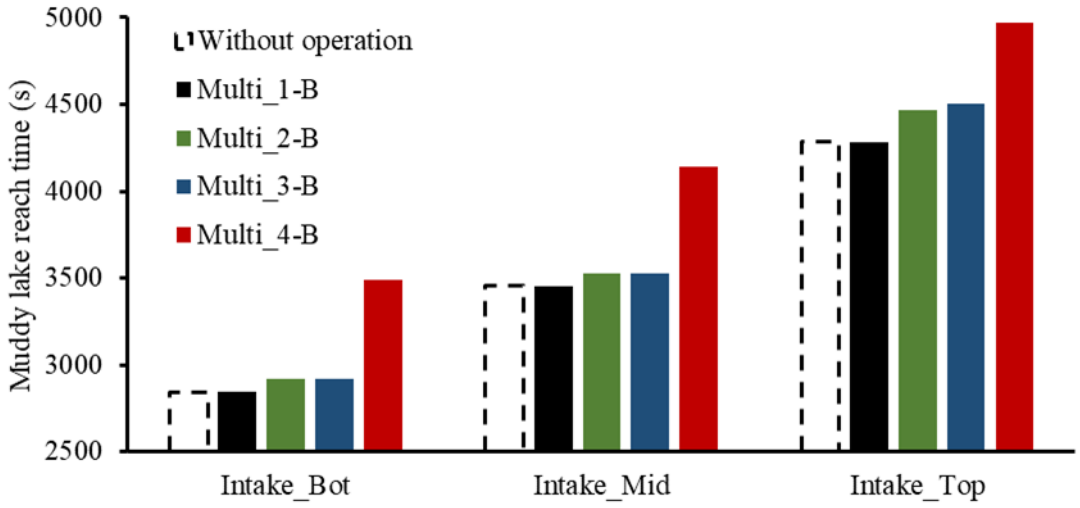

Figure 6.9 The muddy lake reach time at water supply facilities from multiple outlets' operation.

6.3 Investigation of the influence of the optimal outlets' operating timing on turbidity current venting

Chamoun et al. (2018) proposed that the in-time operation of outlets could provide better V_e. Most of the literature studies the operating timing of dam outlets. The SBTs' gates opening time for turbidity current venting is a research gap, and it was investigated in this study. For discussing the impact of outlets' operating timing, the operating timing of dam outlets from the beginning (named Multi_3-B), in-time (named Multi_3-I), and 360 seconds late (i.e., 1 hour late in the field) (named Multi_3-L) were analyzed (Figure 6.10). The results show a similar conclusion to Chamoun et al. (2018), the in-time operation was considered the appropriate timing for dam outlets. As illustrated in Figure 6.11, a small amount of sediment could be released before the turbidity arrives in early operation due to the aspiration force. However, the increasing released sediment is insufficient compared to the wasted clear water. Because the muddy lake starts to form after the turbidity current bumps into the dam, the late operation cannot smoothly vent turbidity current through the outlets and trap the sediment in the reservoir. Furthermore, as illustrated in Figure 6.10 (b), the in-time operation is also suitable for ELEP.

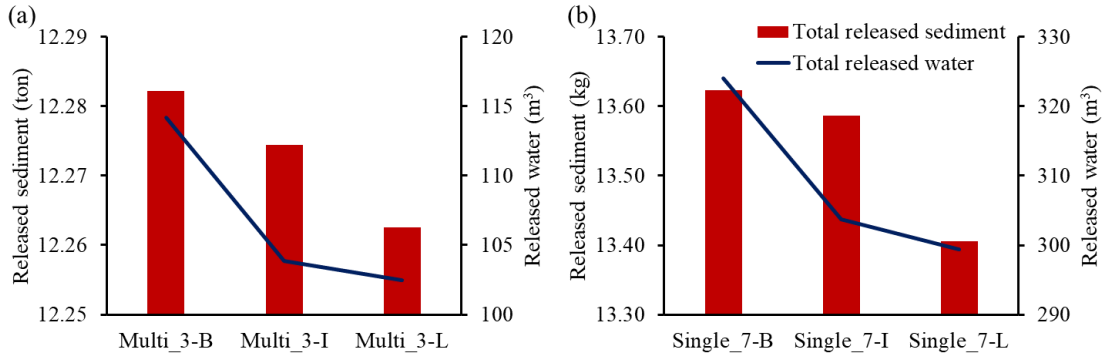

Figure 6.10 The comparison of released sediment and water at (a) dam outlets and (b) ELEP from different operating timing.

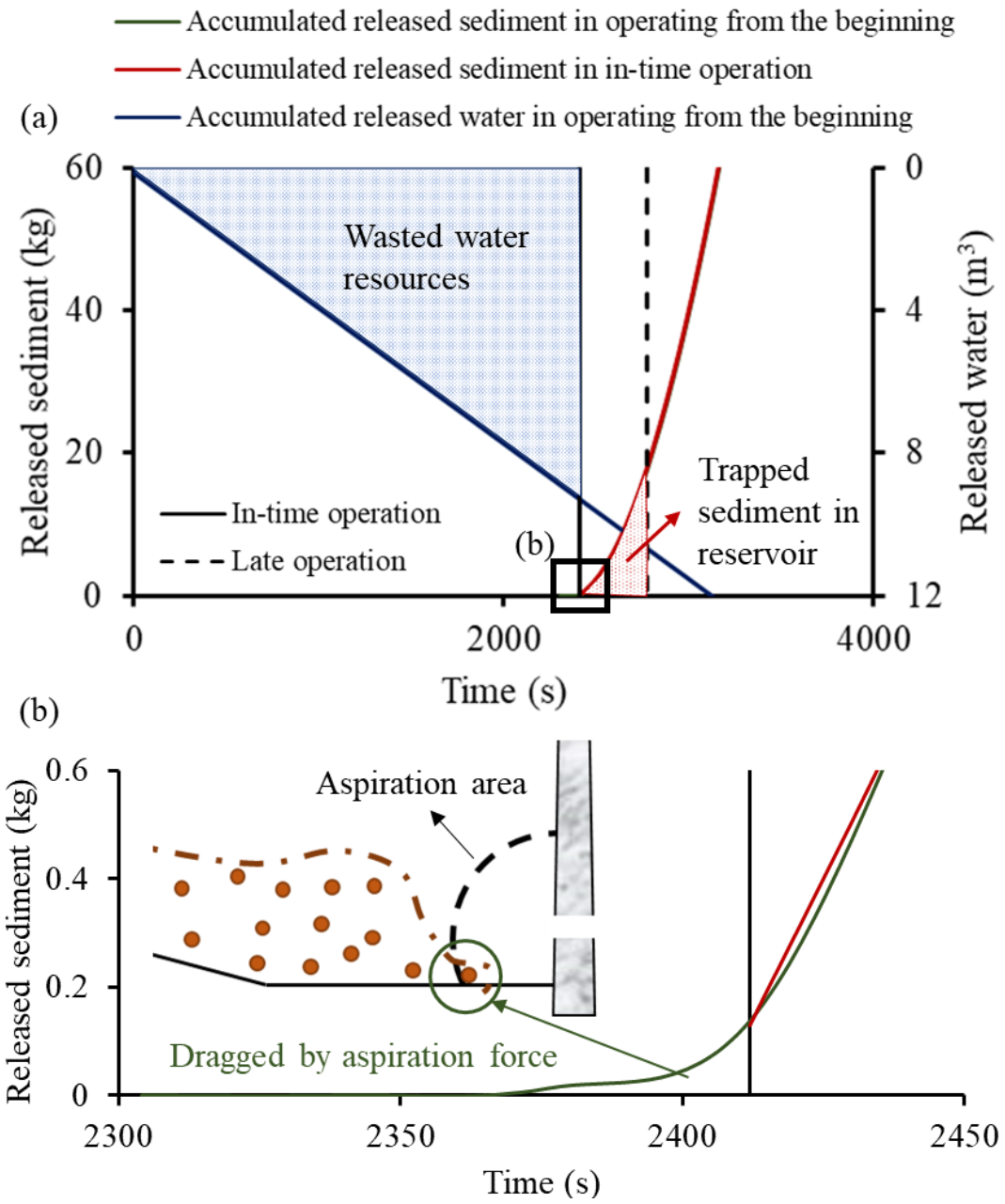

Figure 6.11 The (a) influence of the different operating timing on the accumulated released sediment and water and (b) concept of the dragged released sediment by aspiration force in early operation.

Based on the aforementioned results, the in-time operation is regarded as the appropriate operating timing for turbidity current venting. The improvement of the in-time operation instead of operating outlets from the beginning was shown in Table 6.3. The results showed that the released sediment only decreases by 0.12%, while 7.07% water resource is saved under Multi-4-I. To consider the balance between water storage and sediment desiltation under water resource availability, the in-time operation is regarded as the appropriate operating timing for turbidity current venting.

Table 6.3 The improvement percentage of total released sediment and water from multiple outlets' operation in in-time operation instead of operating from beginning.

	Multi_1-I	Multi_2-I	Multi_3-I	Multi_4-I
Total released sediment	-0.05%	-3.22%	-0.06%	-0.12%
Total released water	9.07%	9.07%	9.07%	7.07%

6.4 Blockade structure for avoiding the spread flow into tributary

To avoid the turbidity current flow into the tributaries, the feasibility of blockade structure, located at the confluence (between CS24 and CS19), was analyzed. For investigating the efficient blockade structure, the height, length, and shape of the blockade structure were discussed below:

6.4.1 Height of blockade structure

According to the simulations, we knew that the thickness of turbidity current is around 0.1 m at CS24. Thus, the 0.1 m height and parallel to the mainstream blockade structure was considered to be suitable for guiding the turbidity current flow direction (Figure 6.12). As illustrated in Figure 6.13, we found that the blockade structure could effectively avoid the diversion before the turbidity current arrived dam. However, with the muddy lake forming, the thickness of turbidity current increases, and high sediment concentration flow enters the tributary from the blockade structure overflow. It significantly indicated that when a muddy lake formed, the function of blockage structure converts from guiding and concentrating turbidity current to trapping the sediment within tributary (Figure 6.13(c)).

As shown in Figure 6.14 (a), due to the height of turbidity current being close to the top of the blockade structure, the small amount of turbidity current still can overflow from 0.1 m blockade structure during turbidity current transporting. To avoid the above problem, the 0.2 m blockade structure was built and worked pretty well (Figure 6.14 (b)). Compared to the 0.1 m blockade structure, the higher structure leads to the vortex near the obstacle at the entrance side (Figure 6.14 (c and d)). Moreover, the 0.2 m blockade structure interrupts sediment transport continuity from the tributary to venting outlets, which caused the other muddy lake to form at the tributary (Figure 6.15 (a and b)). As

illustrated in Figure 6.15 (c), a massive amount of sediment was trapped in the tributary due to the inappropriate obstacle. Based on the aforementioned results, the high blockade structure led to turbulence near the structure and sedimentation within the tributary. Thus, contrary to the expected result, less 0.5% and 1.2% of V_e were yielded from applying 0.1 and 0.2 m blockade structure, respectively.

In contrast, the results indicated that the application of a lower blockade structure, which elevation is 0.05 m, can slightly avoid the diversion of turbidity current and prevent the sediment trap due to the high structure. As shown in Figure 6.16, we knew that the V_e could be increased for both before and after the turbidity current arrival by adopting the 0.05 m blockade structure. Despite this, it still does not have a remarkable effect on the improvement of the turbidity current venting (Table 6.4).

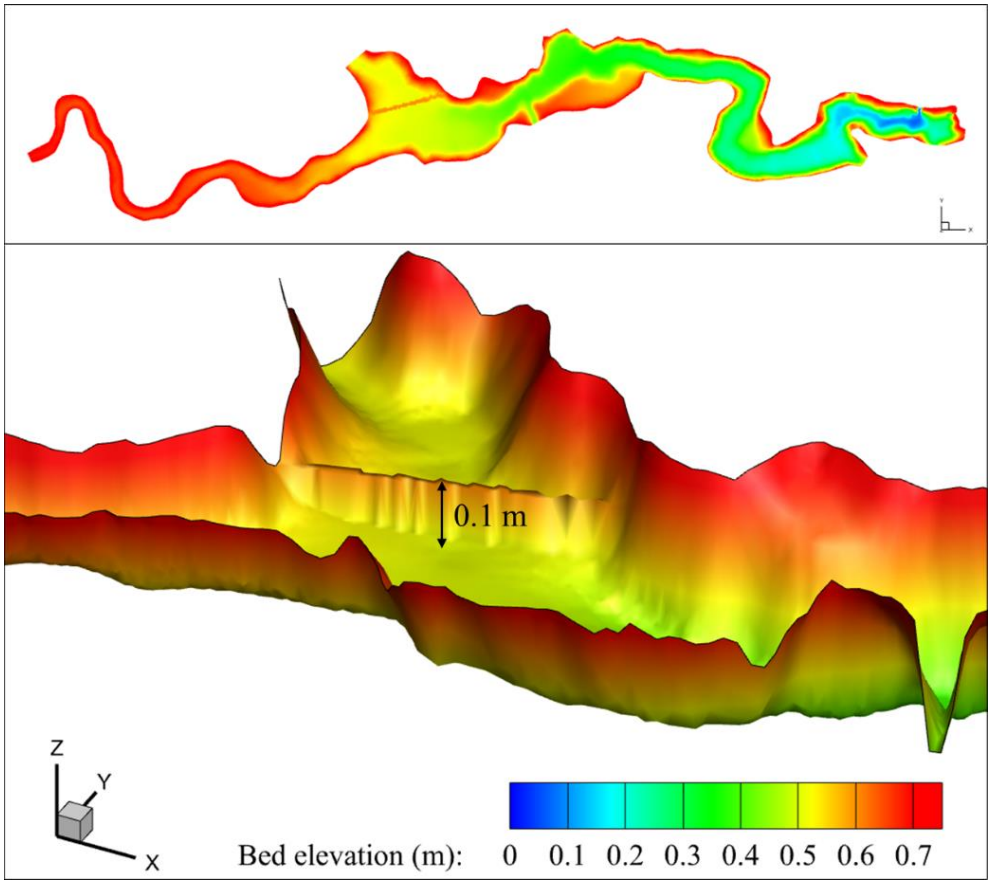

Figure 6.12 The configuration of the blockade structure within the reservoir.

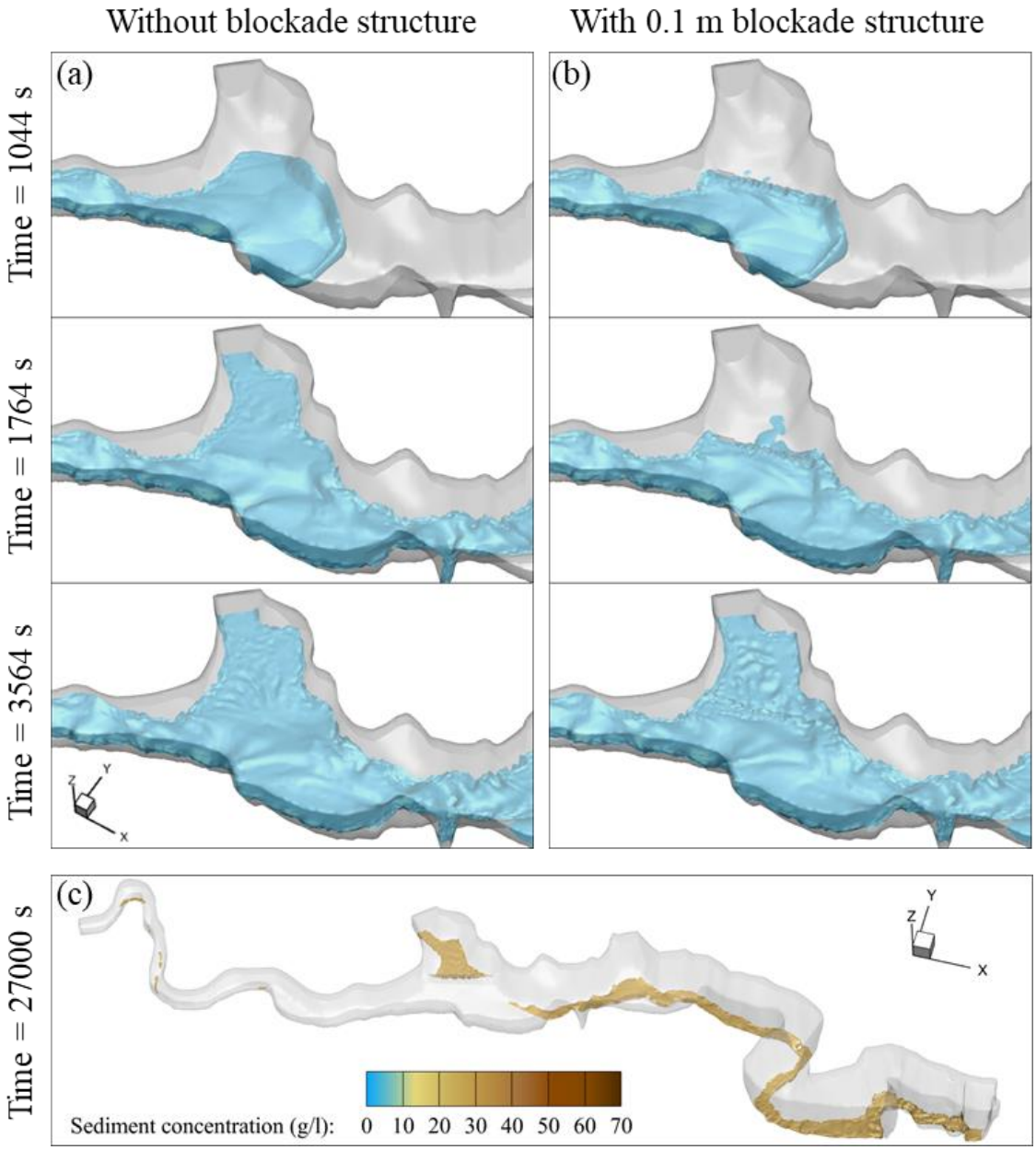

Figure 6.13 The turbidity current (shown in 3 g/l) transportation around the tributary area under (a) without and (b) with 0.1 m blockade structure; (c) the high sediment concentration turbidity flow (shown in 30 g/l) is trapped by blockage structure.

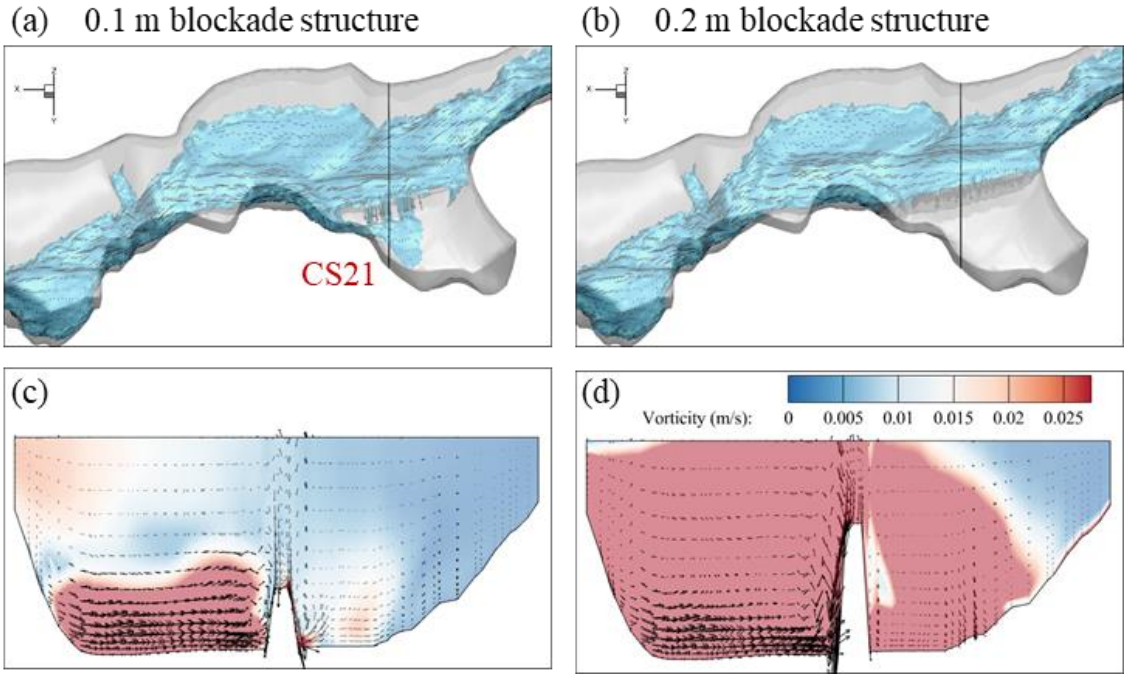

Figure 6.14 The blockade effect from (a) 0.1 m and (b) 0.2 m blockade structure and the flow field around (c) 0.1 m and (s) 0.2 m blockade structure.

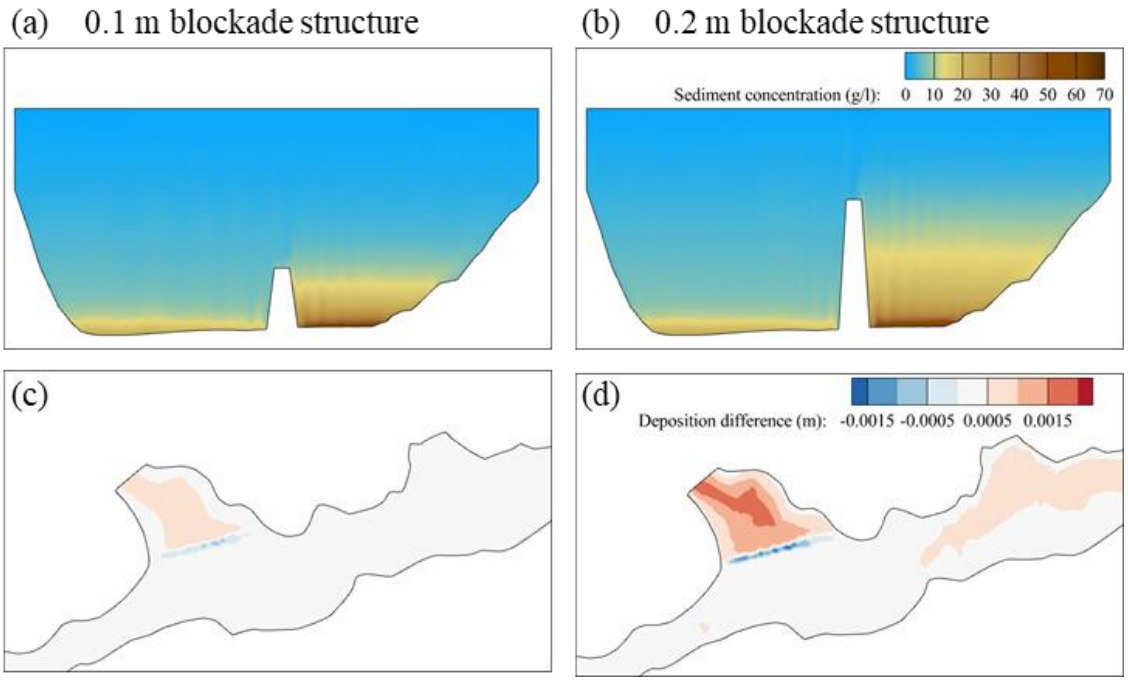

Figure 6.15 The other muddy lake formed at tributary due to the (a) 0.1 m and (b) 0.2 m blockade structure; the sediment deposition difference between without blockade structure and (c) 0.1 m, and (d) 0.2 m blockade structure.

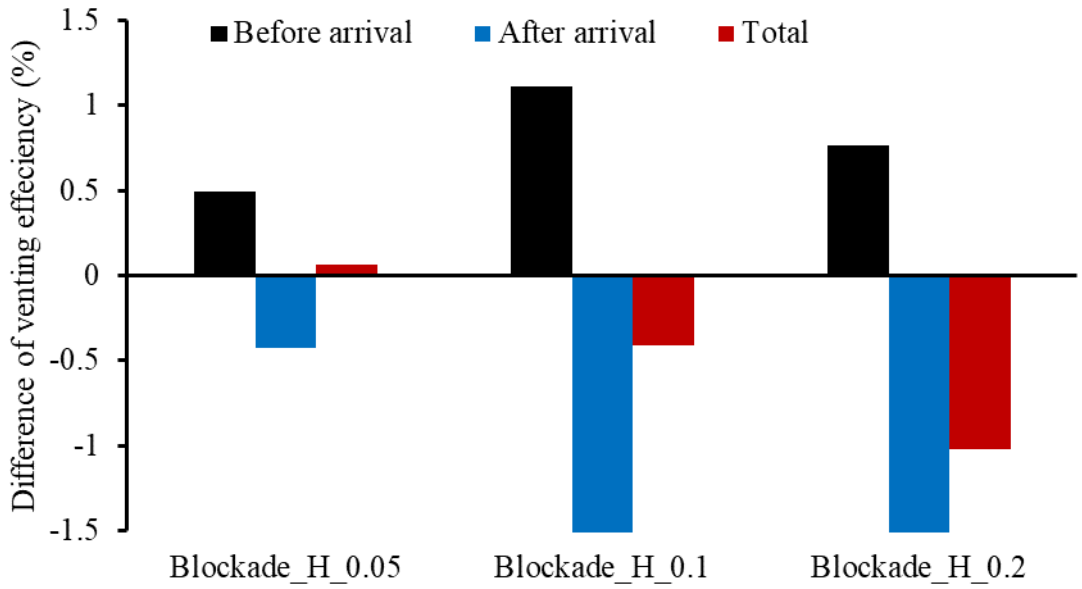

Figure 6.16 The difference of the V_e between without blockade structure and with 0.05, 0.1, and 0.2 m blockade structure from before and after turbidity current arrival.

Table 6.4 Comparison of the V_e from different height of the blockade structure.

Outlets	Multi_4-B	Blockade_H_0.05	Blockade_H_0.1	Blockade_H_0.2
ELEP	40.73	40.80	40.32	39.72
PPI	23.98	24.12	23.89	23.83
PRO	2.02	2.02	2.02	2.00
SCI	0.49	0.49	0.49	0.49
Total	**67.23**	**67.43**	**66.72**	**66.03**

6.4.2 Length of blockade structure

According to the results, a 0.1 m blockade structure blocking the entire tributary lead to severe sedimentation within the tributary. To solve this problem, the three quarters length blockade structure was built (Figure 6.17). As illustrated in Figure 6.18, the short blockade structure can avoid the turbidity current directly flowing into the tributary, but it still enters through the open gap. However, when the outlets release the muddy lake, the high turbidity flow could move through the opening to downstream and release from outlets (Figure 6.18 (c)). Table 6.5 shows that compared to the Blockade_H_0.1, the Blockade_L_3/4 just reduces a little V_e before the turbidity current arrives at the dam but increases 0.4 % of *Ve* after the turbidity current arrival the dam. Although the Blockade_L_3/4 slightly improves the performance, the overall performance still has no significant improvement and is even worse than that without any structures.

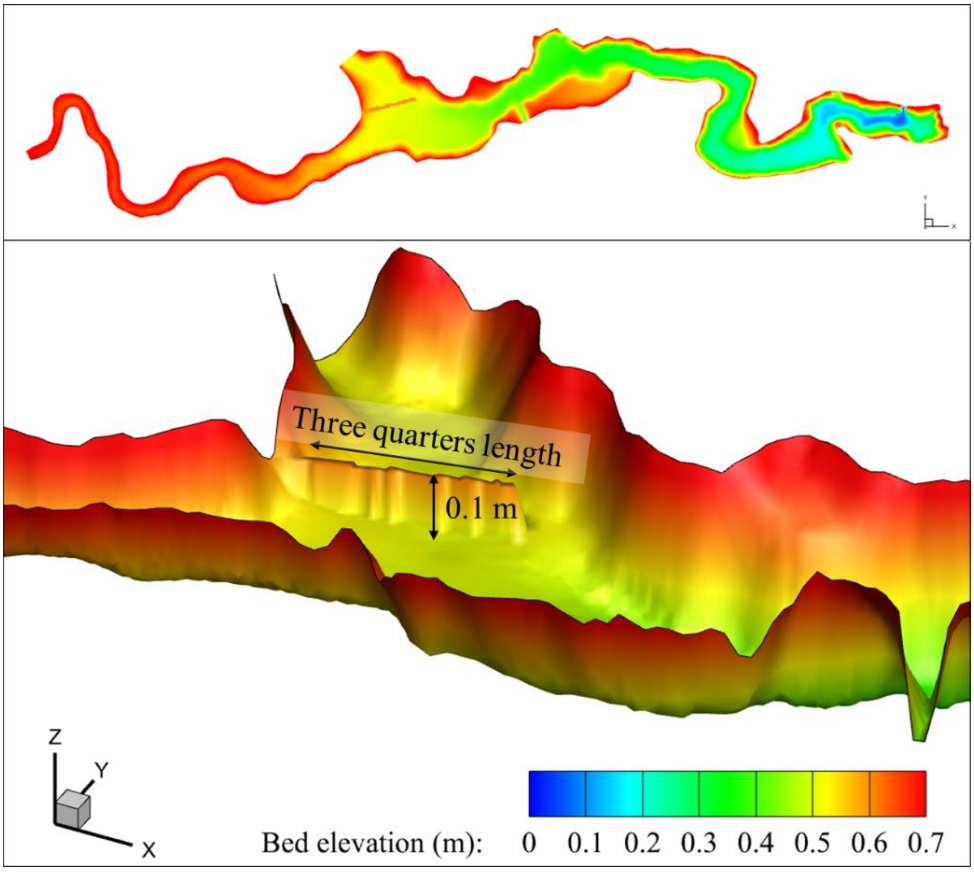

Figure 6.17 The configuration of the three quarters length blockade structure.

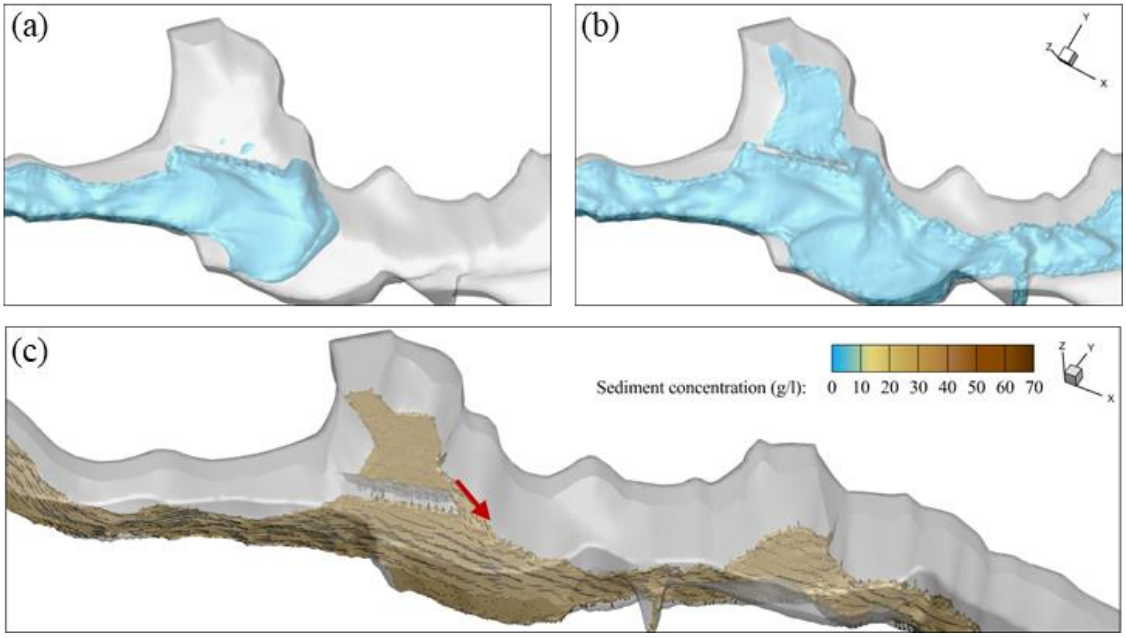

Figure 6.18 The turbidity current (shown in 3 g/l) transportation around the tributary area under Blockade_L_3/4 at (a) 1044 s and (b) 1764 s; (c) the flow regime of high sediment concentration turbidity flow (shown in 30 g/l) around blockade structure.

Table 6.5 Comparison of the V_e from different lengths of the blockade structure.

Outlets		Multi_4-B	Blockade_H_0.1	Blockade_L_3/4
	Before arrival	10.06	11.17	10.92
ELEP	After arrival	30.67	29.15	29.54
	Total	40.73	40.32	40.46
PPI		23.98	23.89	23.92
PRO		2.02	2.02	2.02
SCI		0.49	0.49	0.49
Total		**67.23**	**66.72**	**66.88**

6.4.3 Shape of blockade structure

Based on Figure 6.14, we notice that turbulence occurs due to the blockade structure interrupting the continuity of water flow. To gradually guide the flow direction to the mainstream, the curve shape of the blockade structure was built (Figure 6.19). The results revealed that compared to straight shapes, the curve shape could smoothly change the flow direction (Figure 6.20). Meanwhile, the direction of the blockade structure tail, parallel to the tributary, could guide the trapped turbidity flow effectively downstream. As Table 6.6 showed, compared to Blockade_L_3/4, the Blockade_S_C yields a higher V_e of ELEP both before and after turbidity current arrival. It significantly revealed that the curve shape blockade structure was beneficial to guide the turbidity current transportation and release the muddy lake at a tributary.

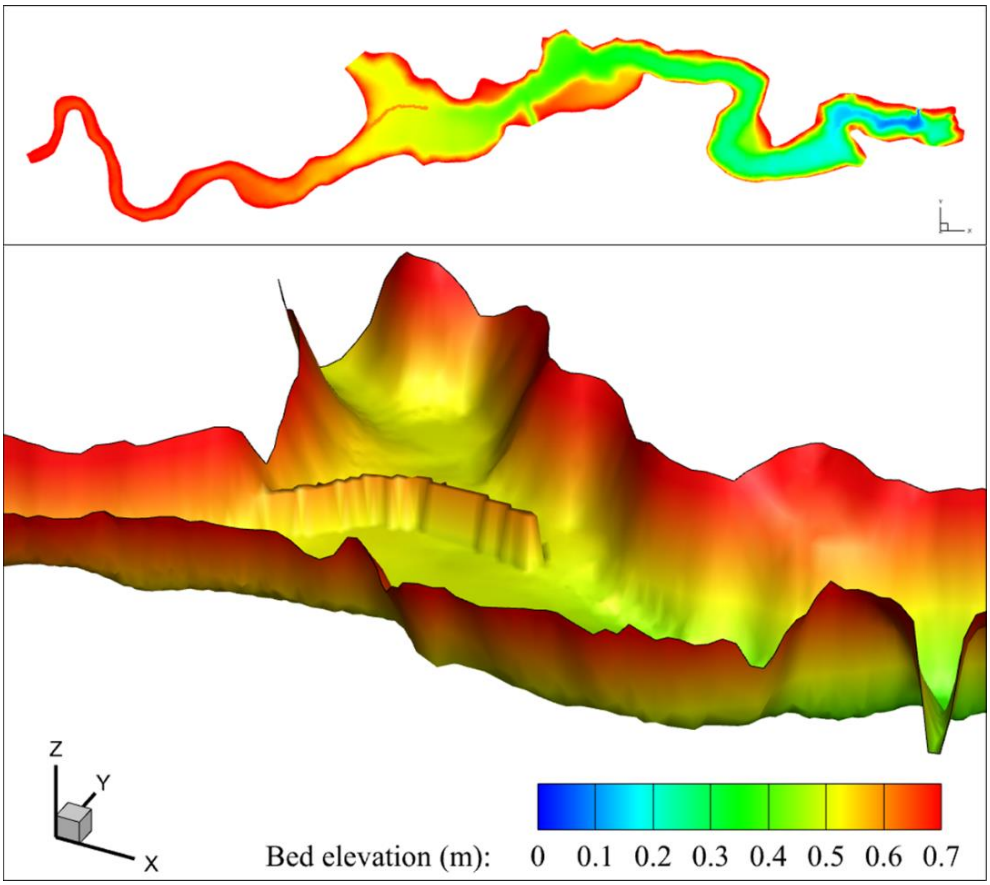

Figure 6.19 The configuration of the curve shape blockade structure.

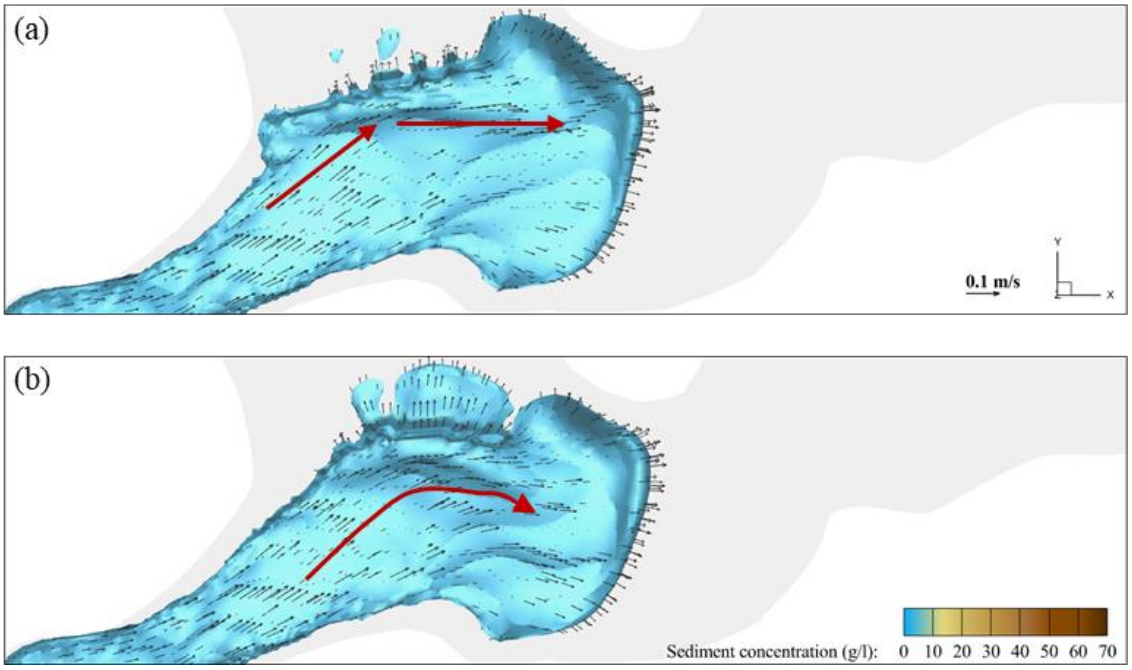

Figure 6.20 The influence of the (a) straight and (b) curve shape of the blockade structure on flow direction change.

Table 6.6 Comparison of the V_e from different shapes of the blockade structure.

Outlets		Multi_4-B	Blockade_L_3/4	Blockade_S_Curve
	Before arrival	10.06	10.92	10.93
ELEP	After arrival	30.67	29.54	29.72
	Total	40.73	40.46	40.65
PPI		23.98	23.92	23.95
PRO		2.02	2.02	2.02
SCI		0.49	0.49	0.49
Total		**67.23**	**66.88**	**67.11**

Based on the aforementioned results, the effect of blockade structure is very little. The application of blockade structure could effectively avoid the turbidity current flow into tributary and increase the venting efficiency before the muddy lake formed. Moreover, it still beneficial for trapping the sediment within tributary instead of depositing near to the dam. It could prevent the outlets blocked by sedimentation, and the concentrated siltation at tributary is easier for dredging and mechanical removal.

6.5 Application of extended pipe from SBTs for attracting turbidity current to vent through outlets effectively

Based on the aforementioned results, we understood that the extended pipe could effectively increase the V_e. The feasibility of additional extended pipes from Amu_SBT was investigated in this study. Moreover, the importance of the adjustable elevation of extended pipes was analyzed. To simplify the conditions, the operated outlets open the gates from beginning to end.

6.5.1 Evaluation of the influence of the elevation of the ELEP on venting efficiency

Based on the aforementioned results, the extended pipes from SBT were essential for increasing the V_e and prolonging the clear water supply period. The elevation of outlets is the critical factor for efficient turbidity current venting through the outlets. Due to the erosion, deposition, and desilting operation, the geometry change should be considered for the extended pipes' site location. To investigate the impact of outlets' location, the elevation of ELEP was 0.27 and 0.35 m according to 2004 and 2015 geometry (Figure 6.21). As illustrated in Table 6.7, the results show that the appropriate location of ELEP, which is set on the bed, increases 3.88% V_e. Moreover, we found that due to the inappropriate elevation of ELEP, the turbidity current was transported to the dam site and vent through dam outlets instead of ELEP (Table 6.8). It caused more turbidity flow transport downstream, and the earlier muddy lake formed. According to the above results, the adjustable extended pipes, based on geometry, were essential for effectively vent turbidity current through extended pipes.

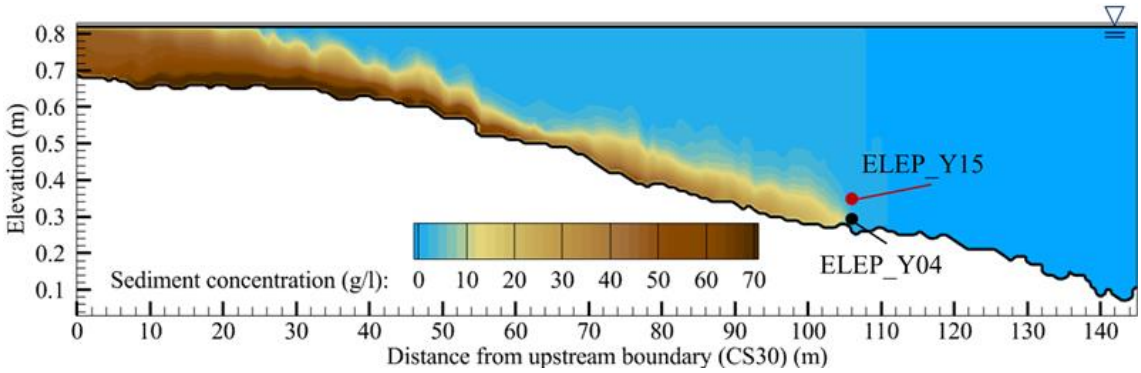

Figure 6.21 The location of the ELEP_Y04 and ELEP_Y15.

Table 6.7 Comparison of V_e and released sediment and water from ELEP_Y04 and ELEP_Y15.

	ELEP_Y04	ELEP_Y15
Elevation of ELEP (m)	0.27	0.35
Venting effeciency (%)	50.23	46.35
Total released sediment (ton)	13.62	12.57
Total released water (m^3)	324	324

Table 6.8 Comparison of V_e and muddy lake reach time at water supply intake from Multi_4-B with different elevations of ELEP

	Multi_4-B with ELEP_Y04	Multi_4-B with ELEP_Y15
Venting effeciency (%)		
ELEP	40.73	34.00
PPI	23.98	27.99
PRO	2.02	2.34
SCI	0.49	0.55
Total	**67.23**	**64.87**
The muddy lake reaches time (s)		
Intake_Bot	3492	3456
Intake_Mid	4140	4104
Intake_Top	4968	4932

6.5.2 Assess the feasibility of extended pipe from Amu_SBT

The additional extended pipe from Amu_SBT (named ELEP_A) was set, and the location was shown in Figure 6.22. As illustrated in Table 6.9, the comparison with sediment venting outlets revealed that the ELEP and ELEP_A have similar venting abilities. However, the higher V_e was obtained from ELEP due to the higher designed outflow discharge. Based on the previous results, we understood that the application of extended pipe from SBTs could effectively extend the clear water supply period. The results indicated that compared to Multi_4-B, the Multi_5-B provided worse $V_{e,}$ and more water was released, but the muddy lake reach time was significantly extended (Table 6.10). It means that the application of extended pipe from SBTs could effectively mitigate the muddy lake formed. Moreover, the operation of all sediment venting outlets, including ELEP_A (Multi_6-B), yields 75.82% V_e, releasing around 50% more water. With additional ELEP_A operation, the water supply facilities could prolong 1548 s (i.e., 4.3 hours in field-scale) for clear water supply. However, it is difficult to operate all of the sediment venting outlets due to the massive amount of released water that is not conducive to water resources storage.

Based on the aforementioned results, the more flexible turbidity current venting operation between each sediment venting outlet could increase V_e and prolong the water supply period. Multi_4-B is suitable for avoiding severe sedimentation by releasing related little water. In contrast, in the case of abundant water resources, Multi_6-B could provide better sediment releasing performance and more clear water supply. Furthermore, the operation of extended pipes (Multi_5-B) is beneficial when more clear water supply is needed. Overall, the additional extended pipe from Amu_SBT could provide more flexibility for turbidity current venting operation decisions.

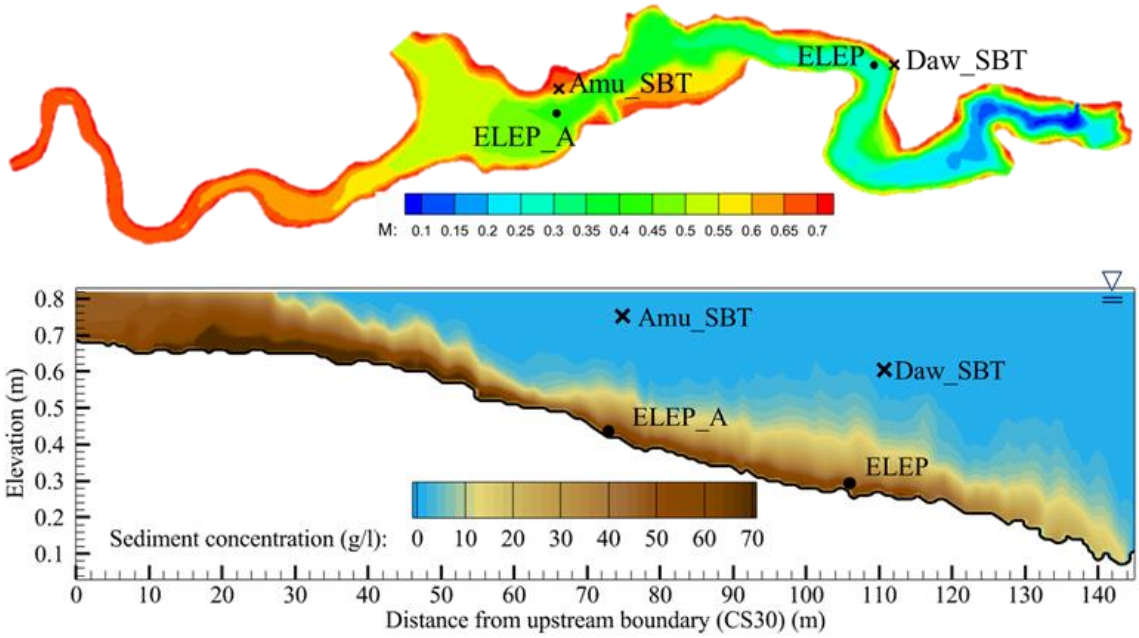

Figure 6.22 The locations of Amu_SBT and Daw_SBT and their extended pipes in a horizontal and vertical perspective.

Table 6.9 Comparison of the venting ability between Single_7-B and Single_8-B.

	Single_7-B	Single_8-B
Venting effeciency (%)	50.23	33.05
Total released sediment (ton)	13.62	8.96
Total released water (m^3)	324	216.11
Averaged released sediment concentration (kg/m^3)	42.04	41.46

Table 6.10 The venting abilities from adopting ELEP_A.

	Multi_4-B	Multi_5-B	Multi_6-B
Venting effeciency (%)	67.23	58.77	75.82
Total released water (m^3)	438.23	540.11	654.34
Muddy lake reach time at Intake_Top (s)	4968	5544	6516

6.6 Application of dredging channel for guiding turbidity current movement

The previous results reveal that the application of ELEP_A is essential for increasing the V_e. However, the limited effect of blockade structure still cannot avoid the turbidity current flow into tributaries. To solve this problem and increase the efficiency of ELEP_A, the dredging channel from CS24 to the location of ELEP_A was investigated:

6.6.1 Width of dredging channel

As illustrated in Table 6.11, applying a 1.2 m width dredging channel could slightly increase the V_e from a 0.8 m width dredging channel. Also, it can effectively extend the reach time muddy lake at water supply facilities due to the enormous storing space at midstream could avoid the turbidity flow arrives dam. However, the adoption of the narrow dredging (i.e., 0.4 m channel) channel has better V_e than the broad channel (i.e., 0.8 and 1.2 m channel).

Table 6.11 Comparison of the V_e from different width of the dredging channel.

Outlets	Channel_W_1.2	Channel_W_0.8	Channel_W_0.4
ELEP_A	34.58	33.8	39.08
ELEP	29.53	29.69	30.27
PPI	19.47	19.63	19.99
PRO	1.63	1.64	1.67
SCI	0.39	0.39	0.40
Total	**85.60**	**85.19**	**91.42**

The main reasons are that (1) the narrow channel was easier for concentrating the turbidity flow. In contrast, the sediment is more accessible to store within the dredging channel instead of venting through outlets. Figure 6.23 significantly indicated that the higher sediment concentration could vent through ELEP_A using a 0.4 m dredging channel. (2) as Table 6.13 showed, the 0.4 m width dredging channel is rugged because the 0.2 m triangle mesh is difficult to build the 0.4 m straight channel. But the rugged channel causes the velocity of turbidity current within the channel to slow down. It could effectively reduce the channel's turbidity flow overflow, and more sediment could be released through the ELEP_A (Figure 6.25). Overall, the narrow and rugged dredging channel is suitable for increasing the V_e.

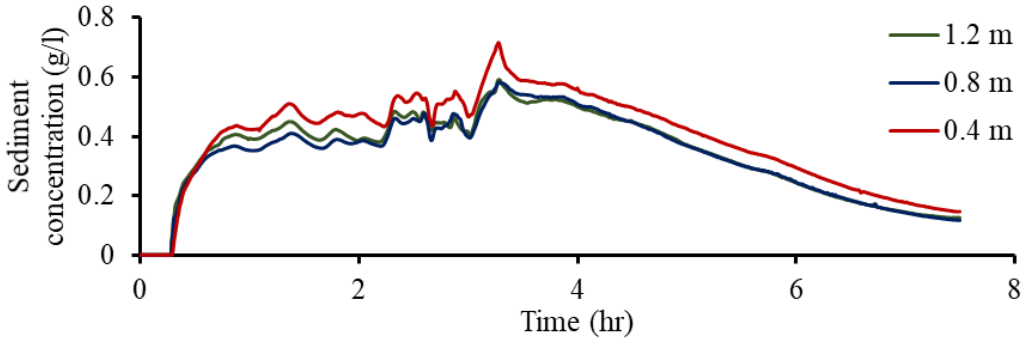

Figure 6.23 The released sediment concentration from ELEP_A with different widths of the dredging channel.

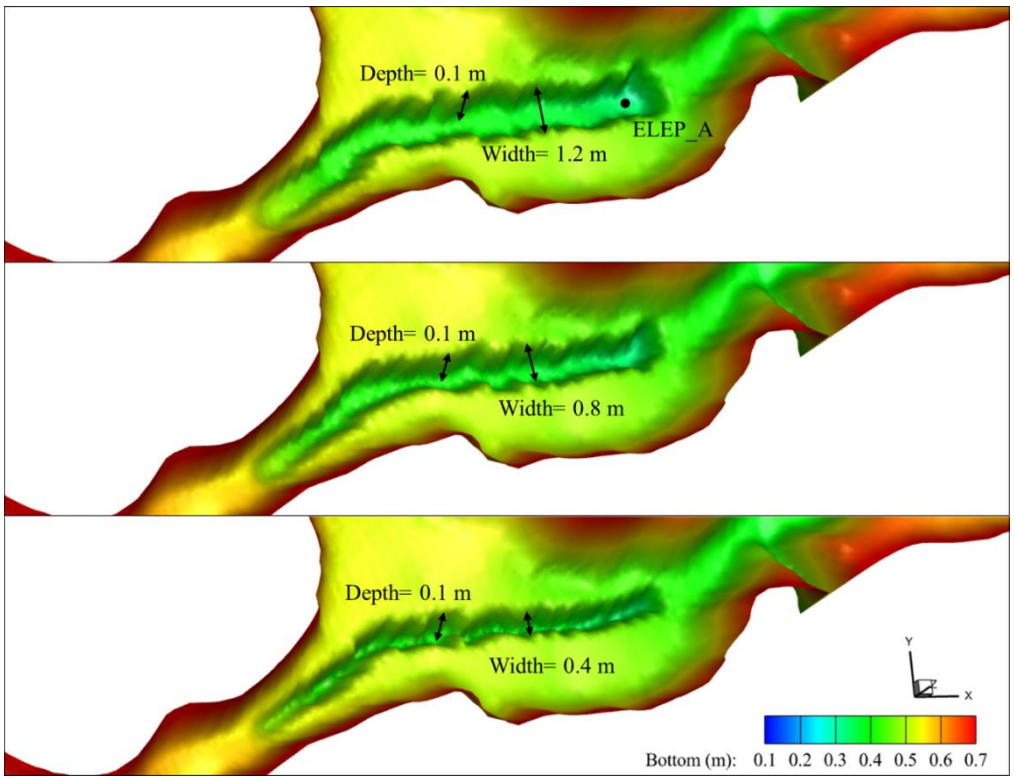

Figure 6.24 The configuration of the different widths of the dredging channel.

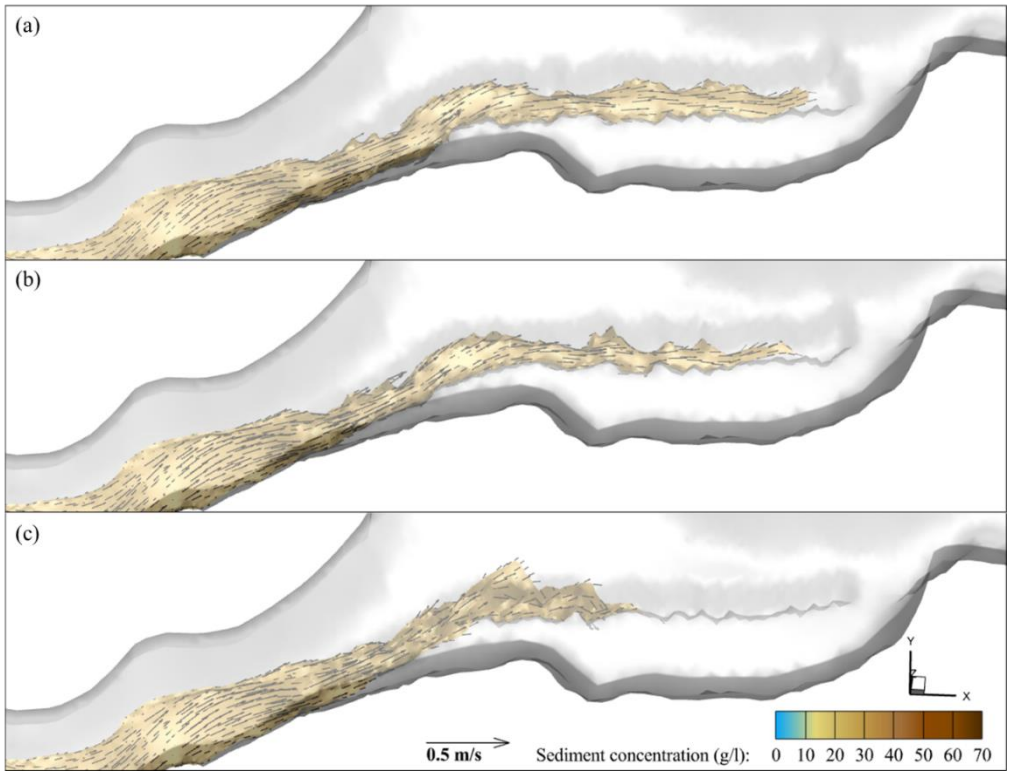

Figure 6.25 The turbidity current transportation (shown in 30 g/l) under (a) 1.2 m, (b) 0.8 m and (c) 0.4 m width of dredging channel.

6.6.2 Depth of dredging channel

The dredging channel's depth is considered the critical characteristic for attracting the turbidity current. Contrary to the expected results, the application of the deeper channel cannot store more sediment within the channel then bring more sediment releasing from ELEP_A (Table 6.12). As shown in Figure 6.26, the sediment concentration of turbidity current is lower with a deeper dredging channel. The higher water depth leads to easier turbidity current dissipation due to the deceleration and decrease of momentum for turbidity current transport to the dam. Therefore, the 0.05 m depth dredging channel is considered the suitable structure for attracting the turbidity flow and avoiding the turbidity current ceases.

Table 6.12 Comparison of the V_e from different depths of the dredging channel.

Outlets	Channel_D_0.15	Channel_W_0.4	Channel_D_0.05
ELEP_A	34.59	39.08	41.40
ELEP	30.43	30.27	30.29
PPI	20.07	19.99	20.11
PRO	1.67	1.67	1.68
SCI	0.40	0.40	0.40
Total	**87.16**	**91.42**	**93.88**

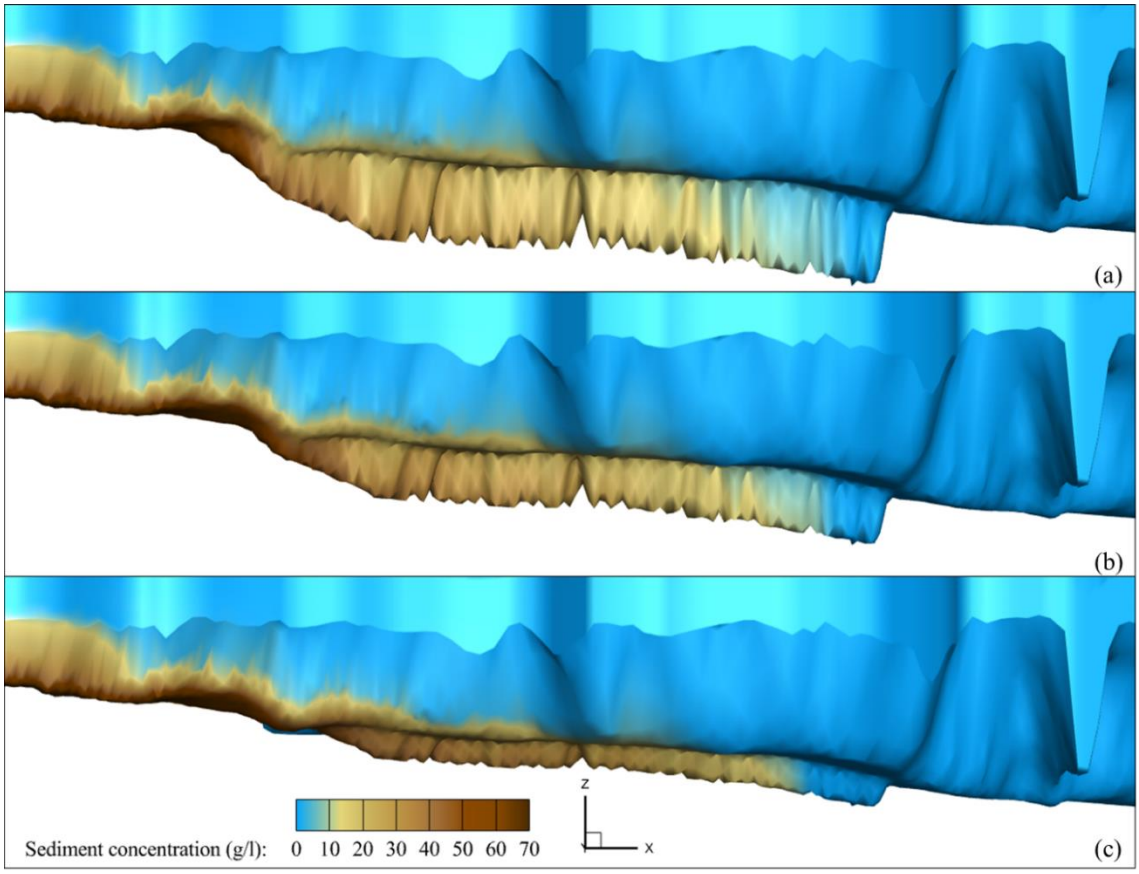

Figure 6.26 The turbidity current transportation under (a) 0.15 m, (b) 0.1 m and (c) 0.05 m depth of dredging channel.

6.6.3 Entrance and exit section of dredging channel

The appropriate entrance and exit of the dredging channel are considered as the critical factors for keeping the continuity of turbidity current transportation. For effectively concentrating the turbidity current to flow into the channel, the constriction format entrance section (Channel_Enter_C), the entry side of the entrance section is cross over the whole river cross section, and the tail of the entrance section is the same width as the dredging channel, was applied (Figure 6.27). As illustrated in Figure 6.28, the constriction format entrance section could productively concentrate the turbidity current flow into the channel. As shown in Table 6.13, compared to the uniform size of the entrance section (Channel_D_0.05), the slightly higher V_e is obtained by applying the

Channel_Enter_C. Due to the practical concentration effect, more sediment could be released through ELEP_A and less turbidity flow transport to downstream outlets of the ELEP_A (Table 6.13).

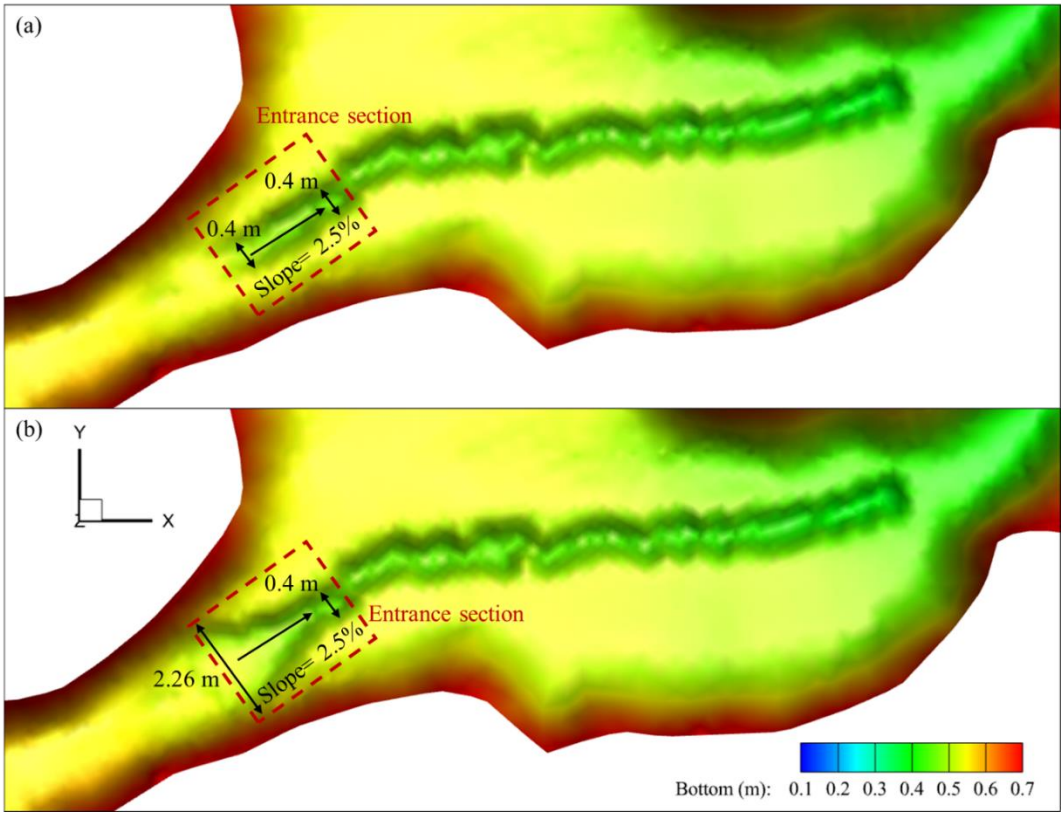

Figure 6.27 The configuration of the entrance section for (a) Channel_D_0.05 and (b) Channel_Enter_C.

Table 6.13 Improvement of the modified entrance and exit section of the dredging channel.

Outlets	Channel_D_0.05	Channel_Enter_C	Channel_Exit_S
ELEP_A	41.40	41.66	42.64
ELEP	30.29	30.23	30.34
PPI	20.11	20.09	20.14
PRO	1.68	1.68	1.68
SCI	0.40	0.40	0.40
Total	**93.88**	**94.06**	**95.20**

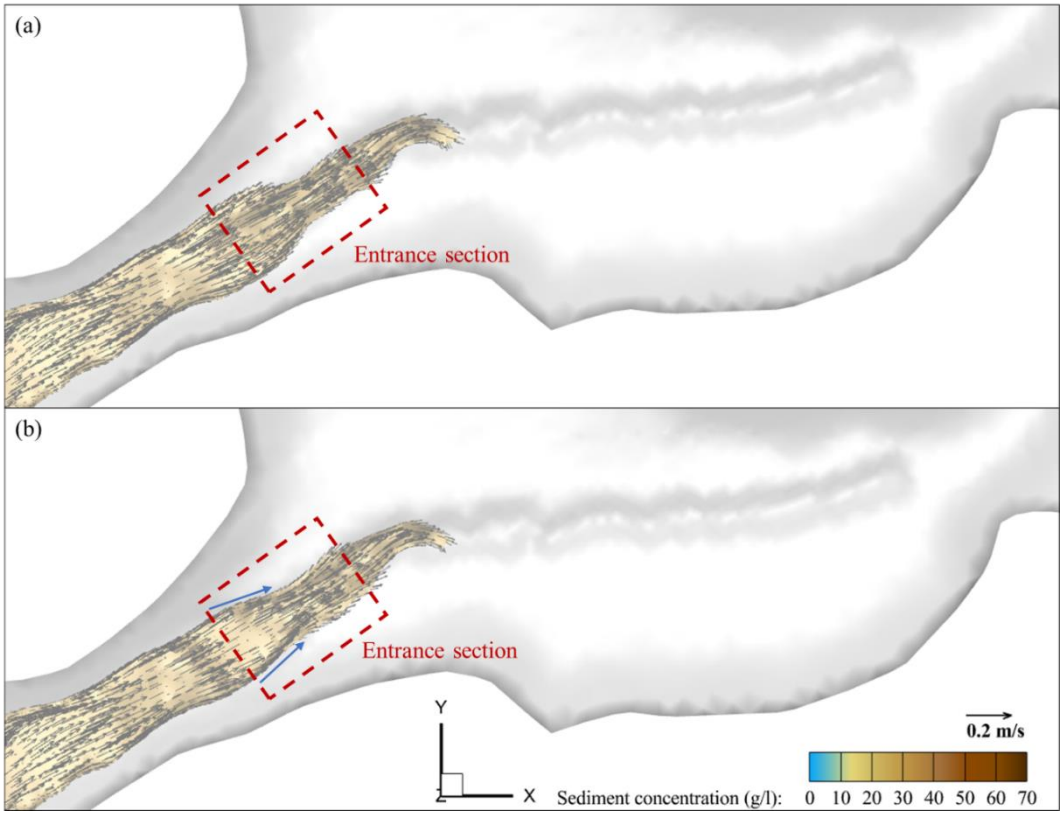

Figure 6.28 The flow regime of turbidity current at the entrance section in (a) Channel_D_0.05 and (b) Channel_Enter_C.

Based on the previous results, the continuity of turbidity current transportation is essential for avoiding the vortex near the blockade and inefficient turbidity current venting. Thus, the gradual slope at the exit section (Channel_Exit_S) was built to replace the vertical wall at the end of the channel (Figure 6.29). As shown in Table 6.13, compared to the Channel_Enter_C, the higher *Ve* of outlets downstream of the dredging channel could be obtained from Channel_Exit_S. It clearly showed that the turbidity current could flow smoothly from the dredging channel to downstream. Overall, adopting the suitably modified entrance and exit section can significantly increase the turbidity current venting efficiency.

Due to the dredging channel concentrating the turbidity current, the higher sediment concentration turbidity flows through ELEP_A. The operation sequence of sediment

venting outlets was changed. As shown in Table 6.14, the operating order of ELEP_A is higher than ELEP when the dredging channel is adopted. Therefore, the operation sequence should be updated with the proposed engineering methods.

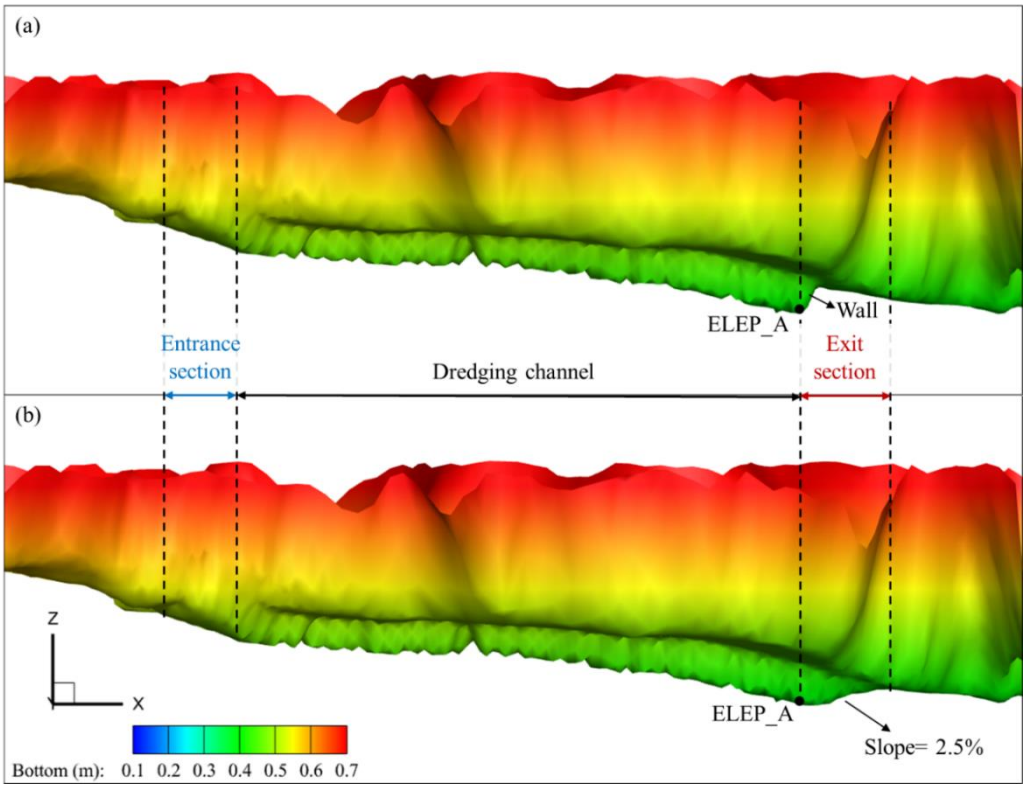

Figure 6.29 The configuration of the entrance section, dredging channel and exit section from (a) Channel_Enter_C and (b) Channel_Exit_S.

Table 6.14 The updated operating order of each outlet using the dredging channel.

Operated single outlet	Averaged released sediment concentration (kg/m^3)		Operating order	
	Without dredging channel	With dredging channel	Without dredging channel	With dredging channel
PRO	159.84	158.4	1	1
PPI	120.24	118.08	2	2
SCI	99.36	98.28	3	3
ELEP	42.12	42.12	4	5
ELEP_A	41.4	81	5	4

6.7 Conclusion

Based on understanding the turbidity current characteristics and shortcomings of the existing method from Chapter 5, the improving methods, including soft and engineering methods, were proposed in this chapter. The main findings of pros and cons of proposed scenarios are:

1. The various outlets within Shihmen Reservoir were classified into sediment venting and flood control function, based on the averaged released sediment concentration.
2. Higher averaged released sediment concentration means more sediment release with the same releasing water and higher operating priority. Thus, the proposed operation sequence of each outlet was determined.
3. As the remaining turbidity flow is trapped in the reservoir during the flooding events, the muddy lake was formed, impacting the clear water withdrawal through water supply facilities. The appropriate sediment venting method mitigates the muddy lake evolution and extends the clear water supply duration.
4. To consider the balance between water storage and sediment desiltation under water resource availability, the in-time operation is regarded as the appropriate operating timing for turbidity current venting.
5. The blockade structure was considered to avoid the turbidity current spread flow into the tributary. However, the results showed that blockade structure effects were very limited. Although the blockade structures cannot work well for the initially expected purposes, they could prevent the outlets blocked by sedimentation, and the concentrated siltation at tributary is easier for dredging and mechanical removal.
6. The feasibility of additional extended pipes from Amu_SBT the importance of the adjustable elevation of extended pipes was analyzed in this chapter. The flexible extended pipes, based on geometry, were essential for effectively vent turbidity

current through extended pipes. Meanwhile, the additional extended pipe from Amu_SBT could provide more flexibility for turbidity current venting operation decisions.

7. The dredging channel guided and concentrated the turbidity current vent through the ELEP_A. The results revealed that the application of the dredging channel significantly increases the venting efficiency of ELEP_A. Due to the sediment venting ability of ELEP_A increase, the operating priority of ELEP_A moves forward.

Based on the aforementioned results and findings, reservoir managers can evaluate the feasibility of applying engineering methods. Also, the appropriate operation sequence and timing were valid for reservoir operators. Overall, Figure 6.30 and Figure 6.31 provide good references for determining multiple outlets' operation and sediment management options.

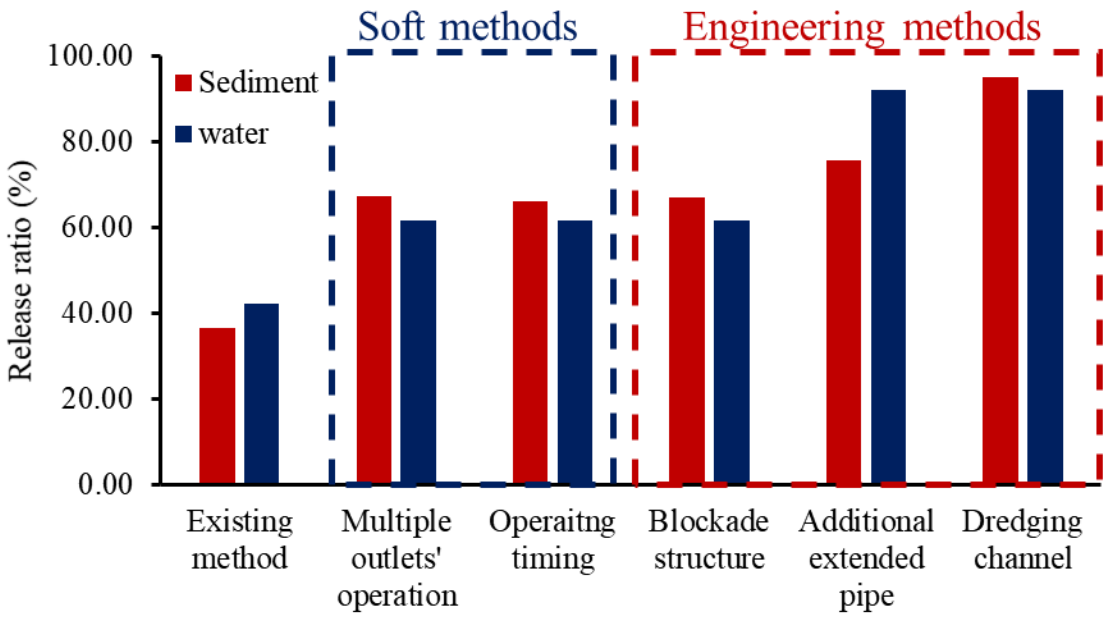

Figure 6.30 The released sediment and water ratios of existing, soft, and engineering methods.

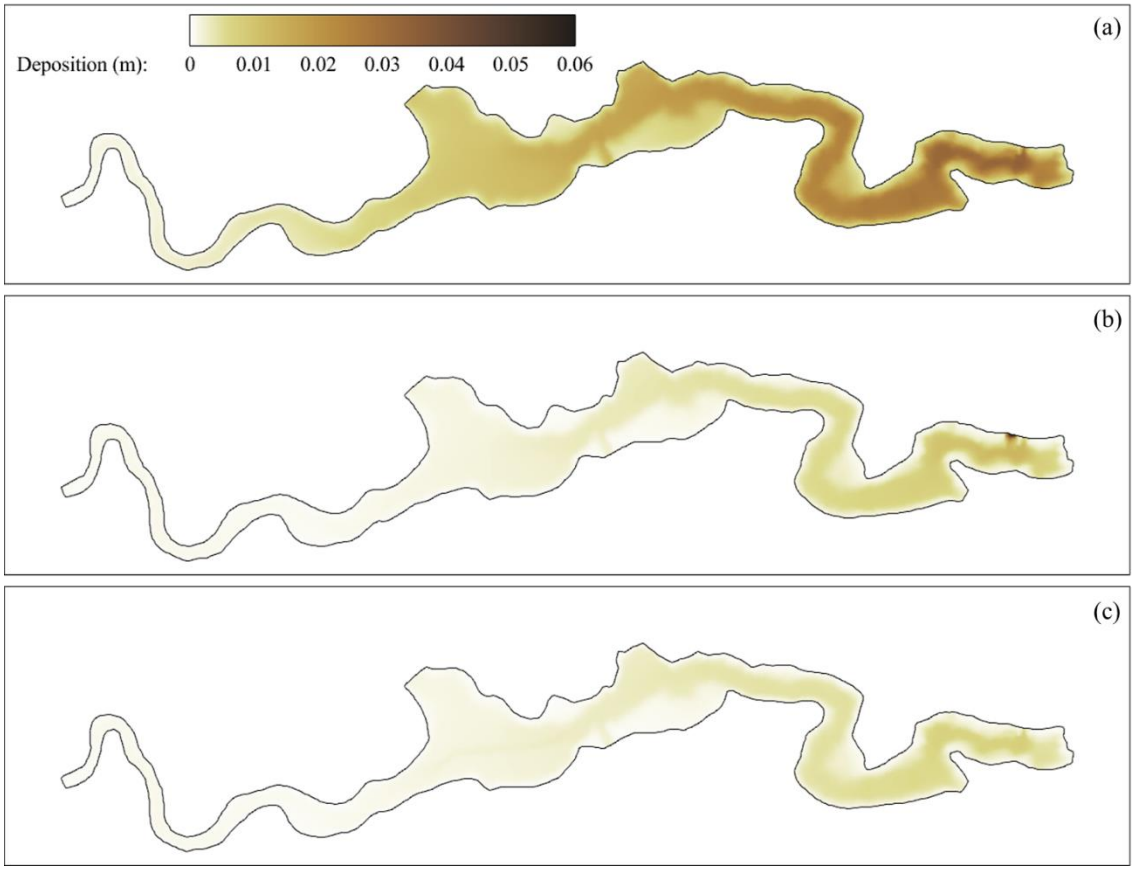

Figure 6.31 The deposition within Shihmen Reservoir by using (a) existing, (b) soft, and (c) engineering methods.

Chapter 7: Assessing the turbidity current venting and reservoir storage in future

7.1 Introduction

The appropriate improving methods for increasing turbidity current venting efficiency and prolonging the clear water supply duration were discussed in **Chapter 6**. Meanwhile, the experiment-scale numerical model is used to investigate the optimal strategies for simplifying the procedure of the discussion of the improving methods and reducing the computational time. However, the hydrological conditions and geological are more complicated in realistic situations. In real situations, both inflow sediment concentration and discharge are time serious. But, in the experiment, the fixed high sediment concentration is used. Moreover, the outlet's closing time must be considered in realistic situations due to the remaining water resources and inadequate inflow. The feasibility of proposed improving methods under the field hydrological and geological conditions was assessed based on the difference mentioned above.

To predict the reservoir usage life extension by adopting the proposed improving methods, the performance of improving methods under different inflow hydrological events should be evaluated. The improvement of proposed methods for different inflow hydrological events is essential to assess the necessities and efficiency, especially for making decisions about costly additional structures. The historical flooding events were classified into three clusters based on inflow discharge, which is the critical characteristic of turbidity current venting. According to each cluster's events probabilities and sedimentation mitigation ratio, the reservoir usage life extension by adopting the proposed improving methods could be predicted.

7.2 Assessment of the feasibility of proposed improving methods

7.2.1 Evaluate the proposed improving methods under the realistic situations

To simplify the designed outlets' operation procedure, the reservoir water level is controlled, kept at 243 m. Also, the sizeable hydrological event (i.e., Sc# Q_LS_L) was adopted to investigate the performance of turbidity current venting with different improving methods. According to the proposed operation sequence of each outlet, the details of operated outlets from the existing method and proposed improving methods are shown in Figure 7.1 to Figure 7.4. The results significantly indicate that the SP is not appropriate to turbidity current venting. In the existing method case, the SP provides 72% water release, but only 25% sediment is released from SP. After applying the improving methods, the released flow from SP is nearly ambient water due to the extremely low averaged released sediment concentration. Moreover, we found that extended pipes effectively increase the released sediment. The results revealed that more than half released sediment vent through the extended pipes in both soft and engineering methods.

To simplify the procedure and reduce the computational time, the 1/100 scale model is used to evaluate the proposed improving methods. The biggest difference between experiment and field is the inflow condition and bathymetry. The intensive inflow leads to the abundant water resources. Thus, the outlets' closing time could be ignored in experiment. In contrast, the outlets' closing order should be considered and followed the proposed operating sequence in real case. Due to the event strength is smaller and outlets' operating duration is shorter, the overall venting efficiency is lower in field (Figure 7.5). However, the improving trends of proposed methods application are similar. Meanwhile, we found that the application of the dredging channel seems useless in the real case.

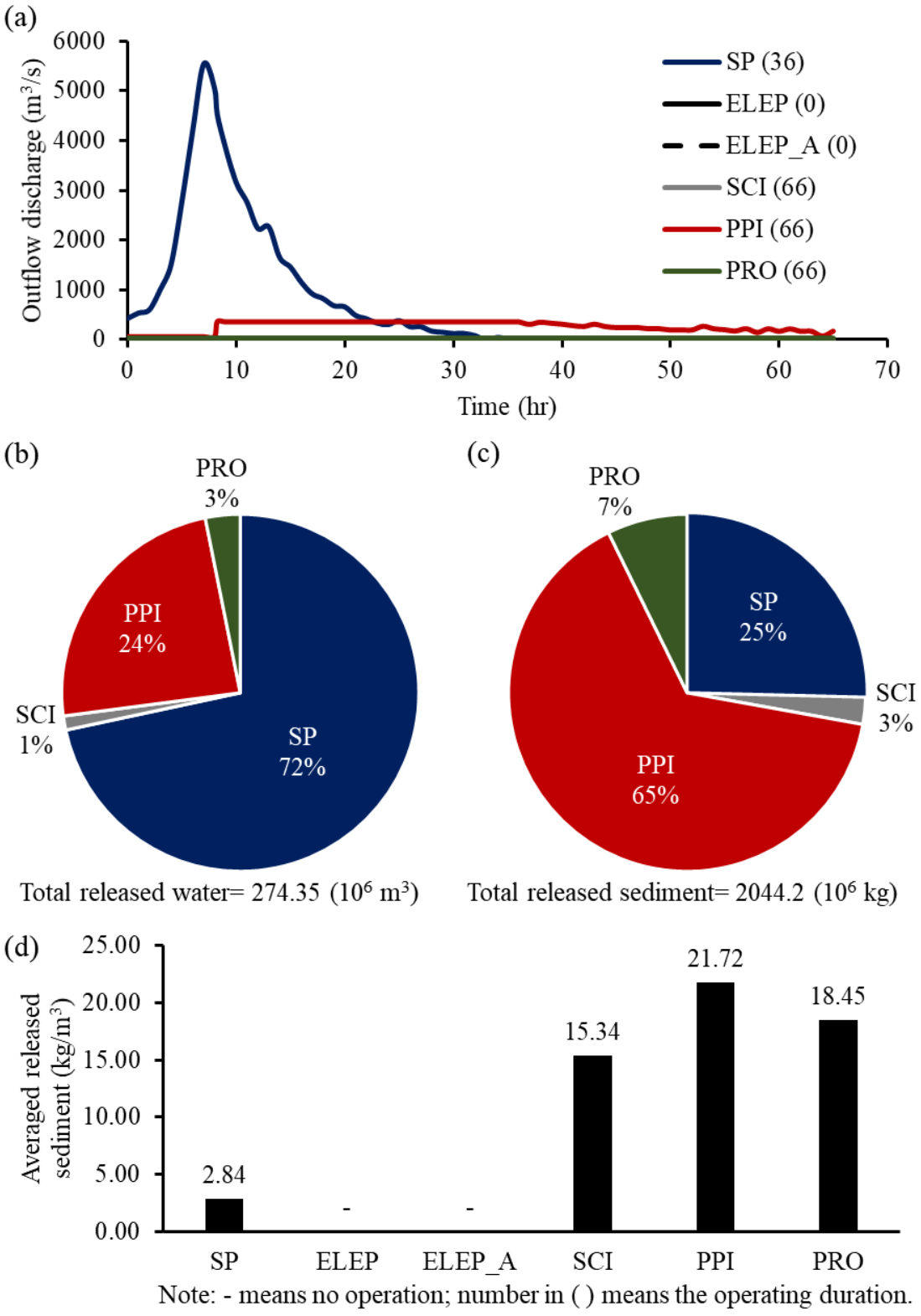

Figure 7.1 The details of (a) operating duration, (b) released water percentage, (c) released sediment percentage and (b) averaged released sediment concentration of each operated outlet under the existing method.

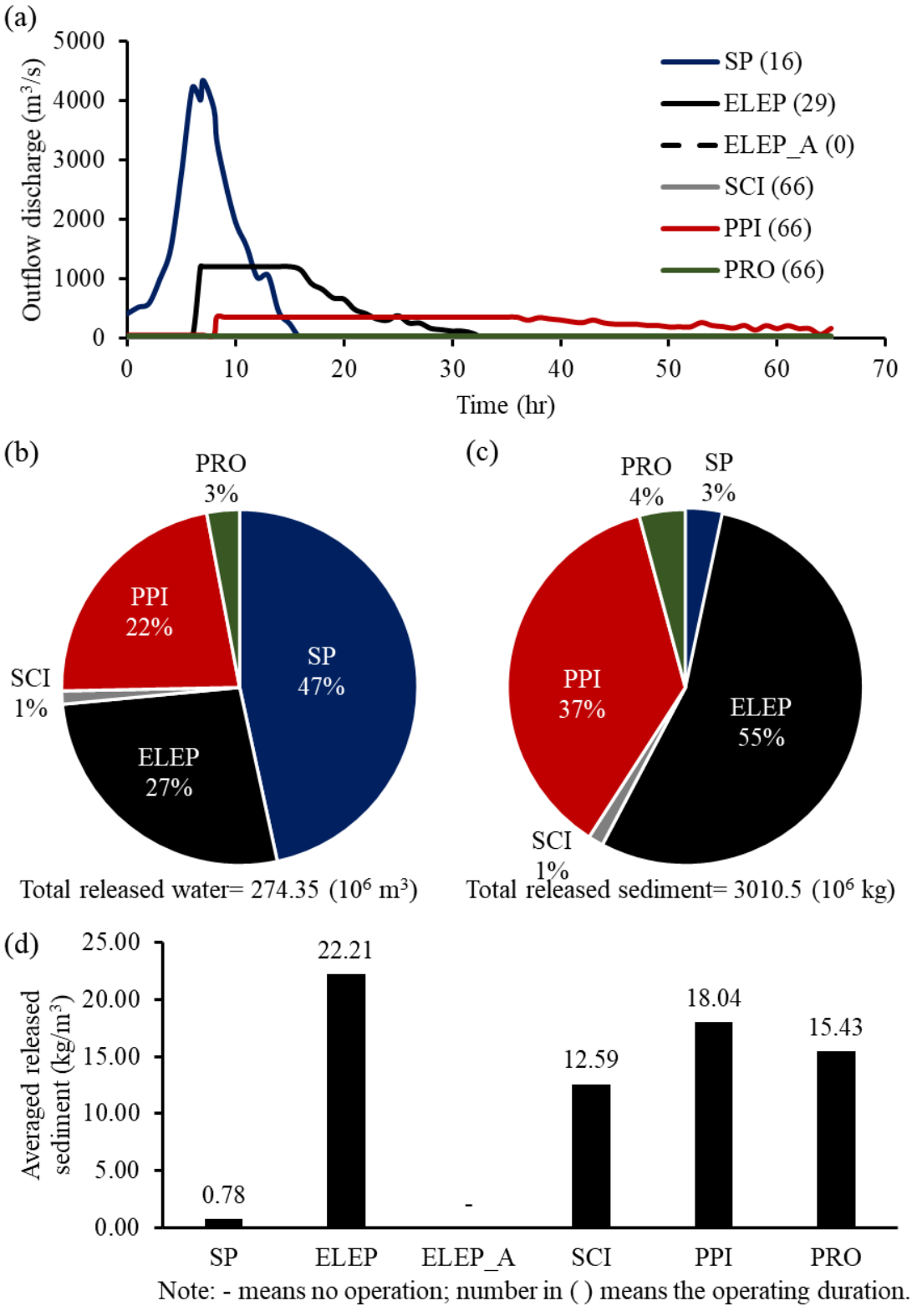

Figure 7.2 The details of (a) operating duration, (b) released water percentage, (c) released sediment percentage and (b) averaged released sediment concentration of each operated outlet under the soft methods.

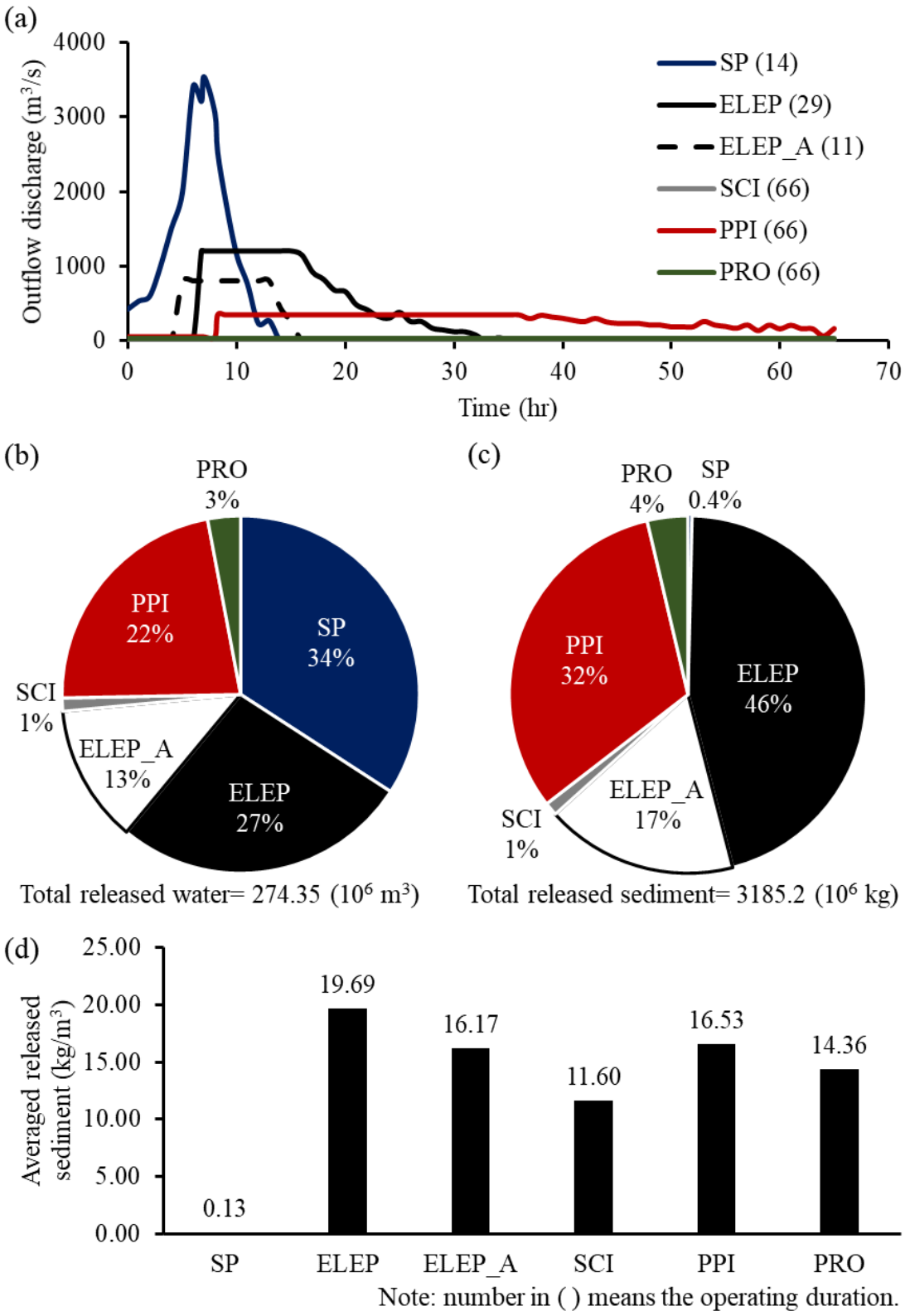

Figure 7.3 The details of (a) operating duration, (b) released water percentage, (c) released sediment percentage and (b) averaged released sediment concentration of each operated outlet under the engineering methods (with additional extended pipe).

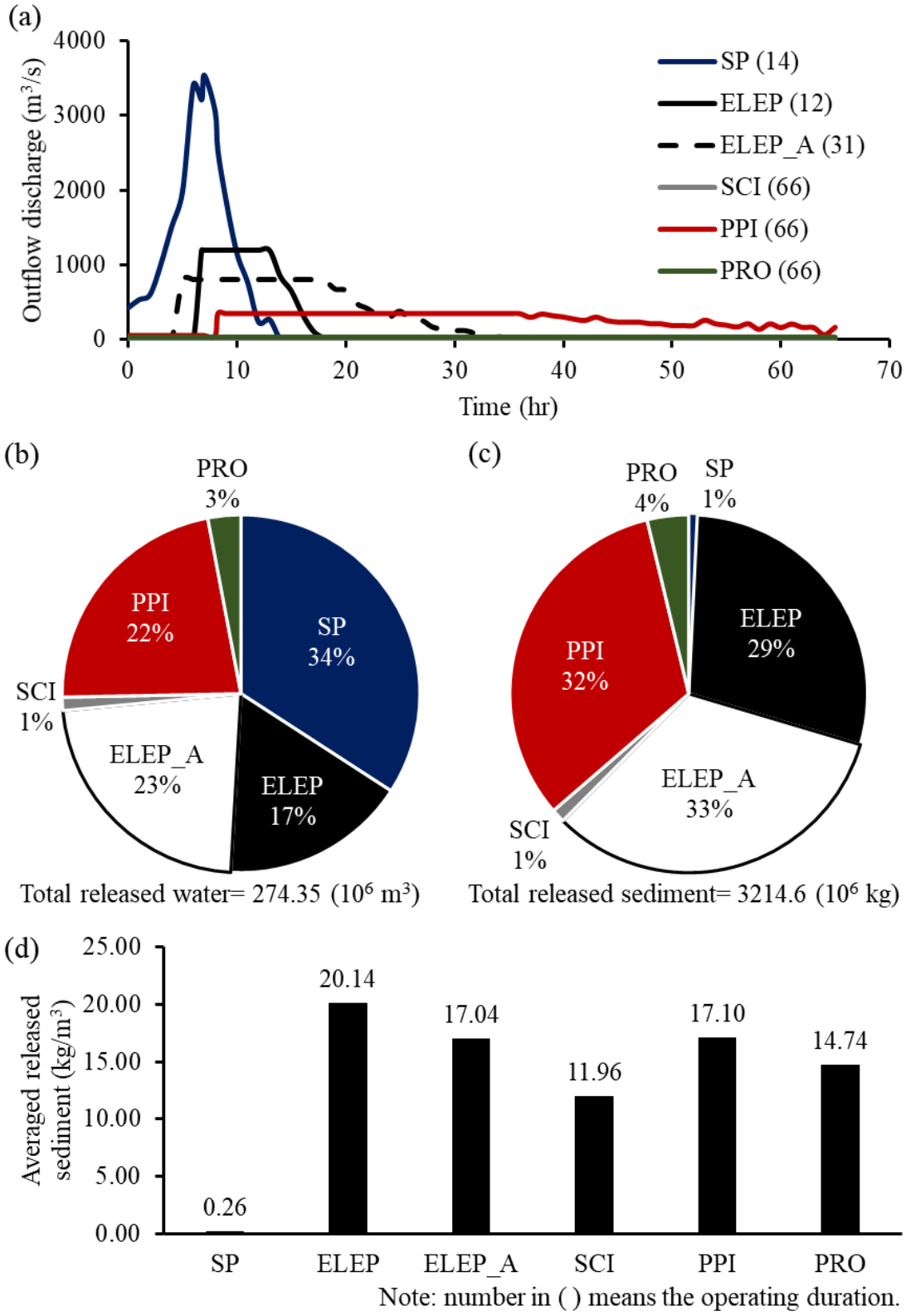

Figure 7.4 The details of (a) operating duration, (b) released water percentage, (c) released sediment percentage and (b) averaged released sediment concentration of each operated outlet under the engineering methods (with dredging channel).

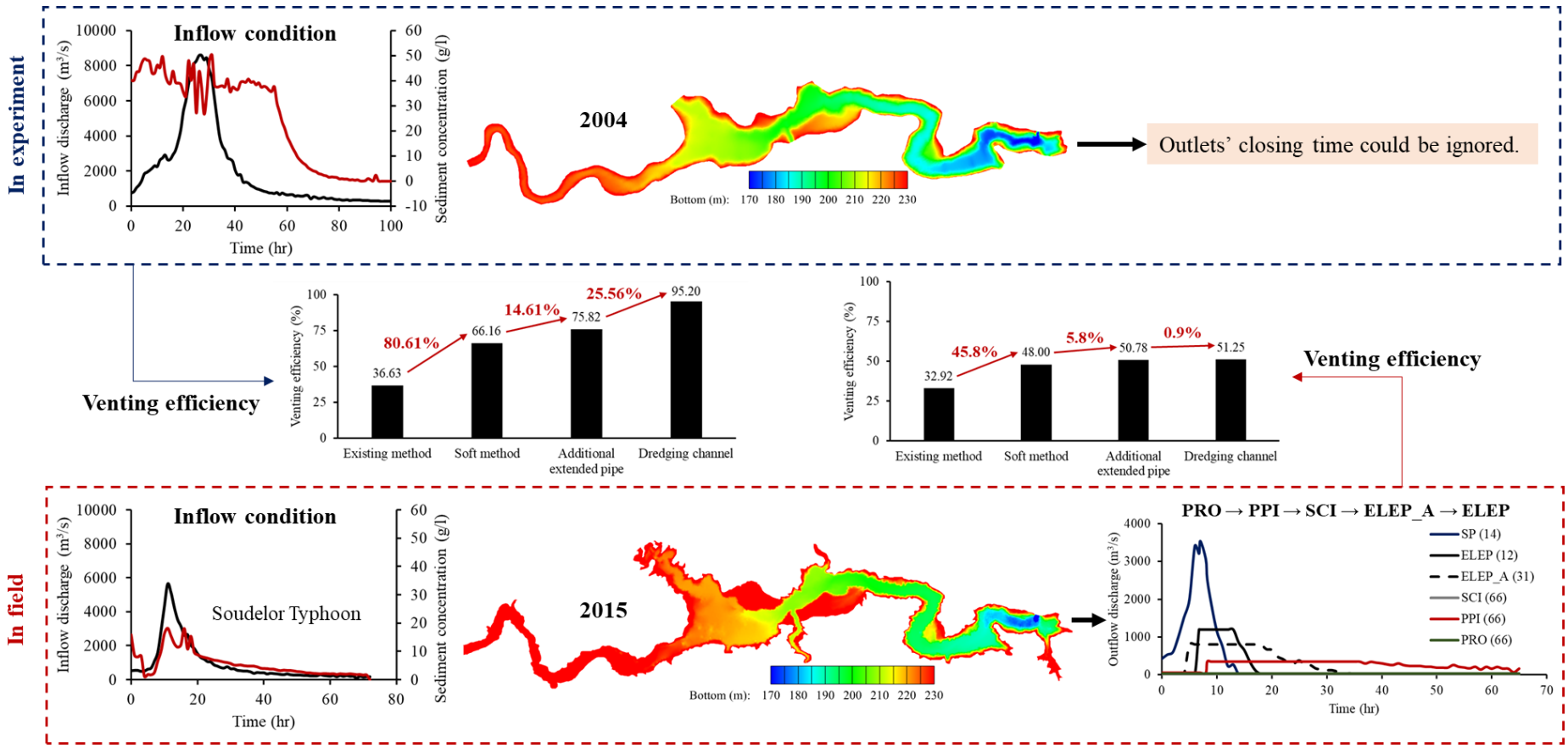

Figure 7.5 Comparison of proposed improving method under experimental-scale and field-scale.

As illustrated in Figure 7.3,Figure 7.4Figure 7.5, the application of dredging channel only provides a limited improvement, which is different from the conclusion in Chapter 6. Figure 7.6 showed that the ELEP_A has higher venting performance before turbidity current arrival, but the ELEP works better when the muddy lake is formed. The main reason for different conclusions from experimental and field-scale is that the constant inflow sediment concentration leads to the continuous sediment supply for turbidity current. The ELEP_A with dredging channel has better performance for keeping venting turbidity current and gets higher operation priority. However, in real cases, the effectiveness of turbidity current venting is reduced after the peak values of inflow. Then, the function of ELEP and ELEP_A convert from turbidity current venting to muddy lake releasing.

Due to the muddy lake formed near the dam, the ELEP_A is difficult to release muddy lake. Therefore, the well functional ELEP for turbidity current venting and muddy lake releasing should have higher operation priority. Based on the aforementioned results, the optimal operation sequence for Shihmen Reservoir's sediment venting outlets is: PRO> PPI> SCI> ELEP> ELEPA. As illustrated in Figure 7.7, the modified operation sequence could provide a good improvement for sediment release.

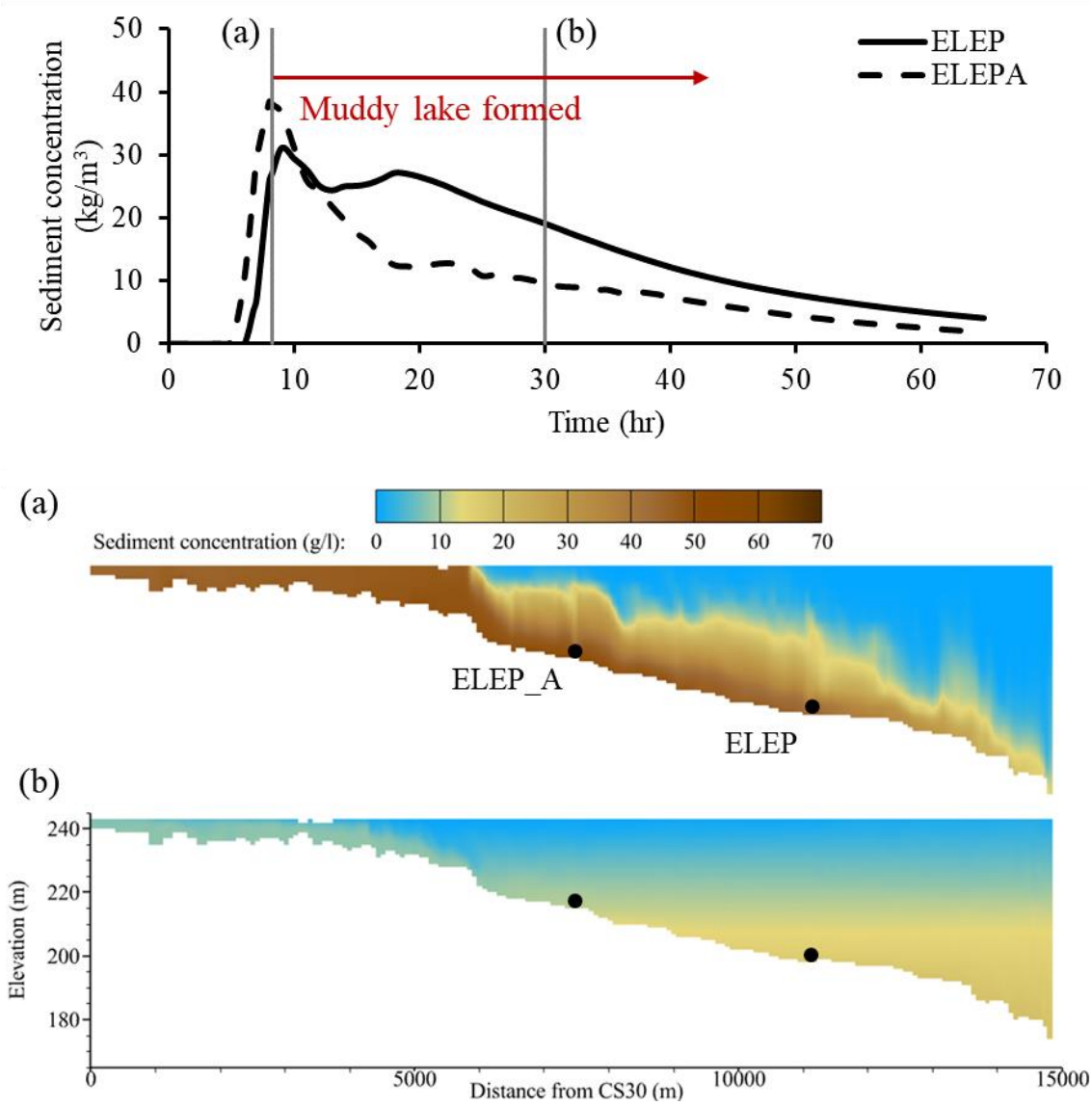

Figure 7.6 The released sediment concentration from ELEP and ELEP_A and the longitudinal view of (a) turbidity current arrival and (b) muddy lake.

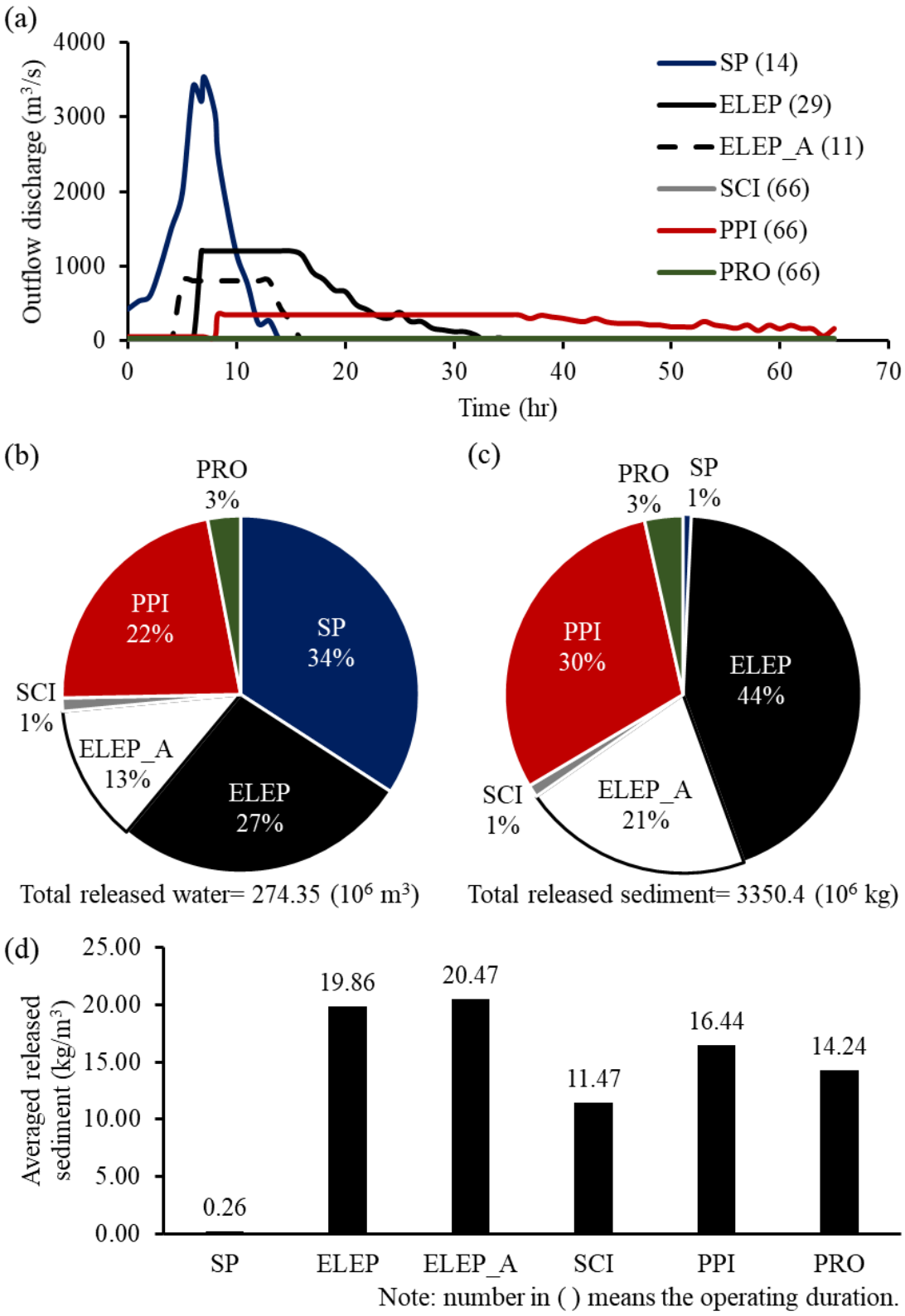

Figure 7.7 The details of (a) operating duration, (b) released water percentage, (c) released sediment percentage and (b) averaged released sediment concentration of each operated outlet under the engineering methods (modified operating sequence).

Based on the previous assessment and modification, the results showed that the proposed improving methods could effectively increase the turbidity current venting efficiency. As illustrated in Figure 7.8, the increased turbidity current venting efficiency by adopting the improving methods. The improvement percentage clearly showed that 47.3% and 63.9% more released sediment was obtained by adopting soft and engineering methods, respectively (Table 7.1). Although the application of dredging channel only provides 4.2% improvement, it still mitigates 165200 tons deposition in the reservoir.

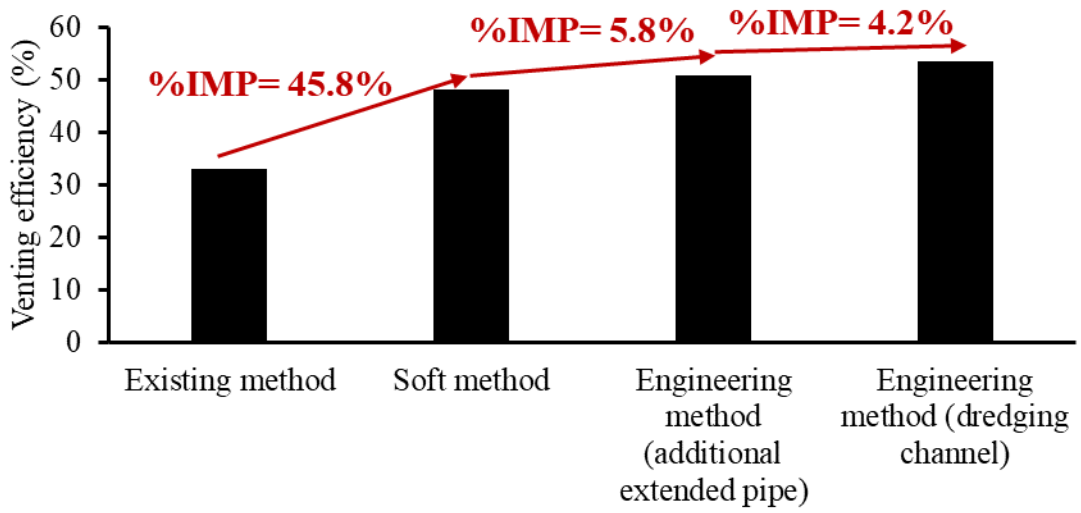

Figure 7.8 The turbidity current venting performance from existing method and improving methods.

Table 7.1 The performance of existing, soft, and engineering methods and improvement percentage of improving methods instead of the existing method.

	Total released sediment (10^6 kg)	Water supply duration (hr)	Improvement percentage (%)	
			Total released sediment	Water supply duration
Existing method	2044.2	9.5	-	-
Soft method	3010.5	10	47.3	5.3
Engineering method	3350.4	10.25	63.9	7.9

7.2.2 Investigate the sediment deposition after events under using improving methods

Based on the aforementioned results, the proposed improving methods could provide a higher turbidity current venting efficiency. It mitigates the deposition in the Shihmen Reservoir (Figure 7.9 and Figure 7.10). Due to the high flow velocity at upstream (i.e., sediment-laden region), it is difficult to deposit upstream of CS24 (Figure 5.2 and Figure 7.9). Comparison of the deposition at mainstream and tributary showed that applying engineering methods could significantly mitigate the deposition close to the dam, around one meter less deposit. Overall, the proposed engineering method is considered appropriate for avoiding severe sedimentation within the reservoir.

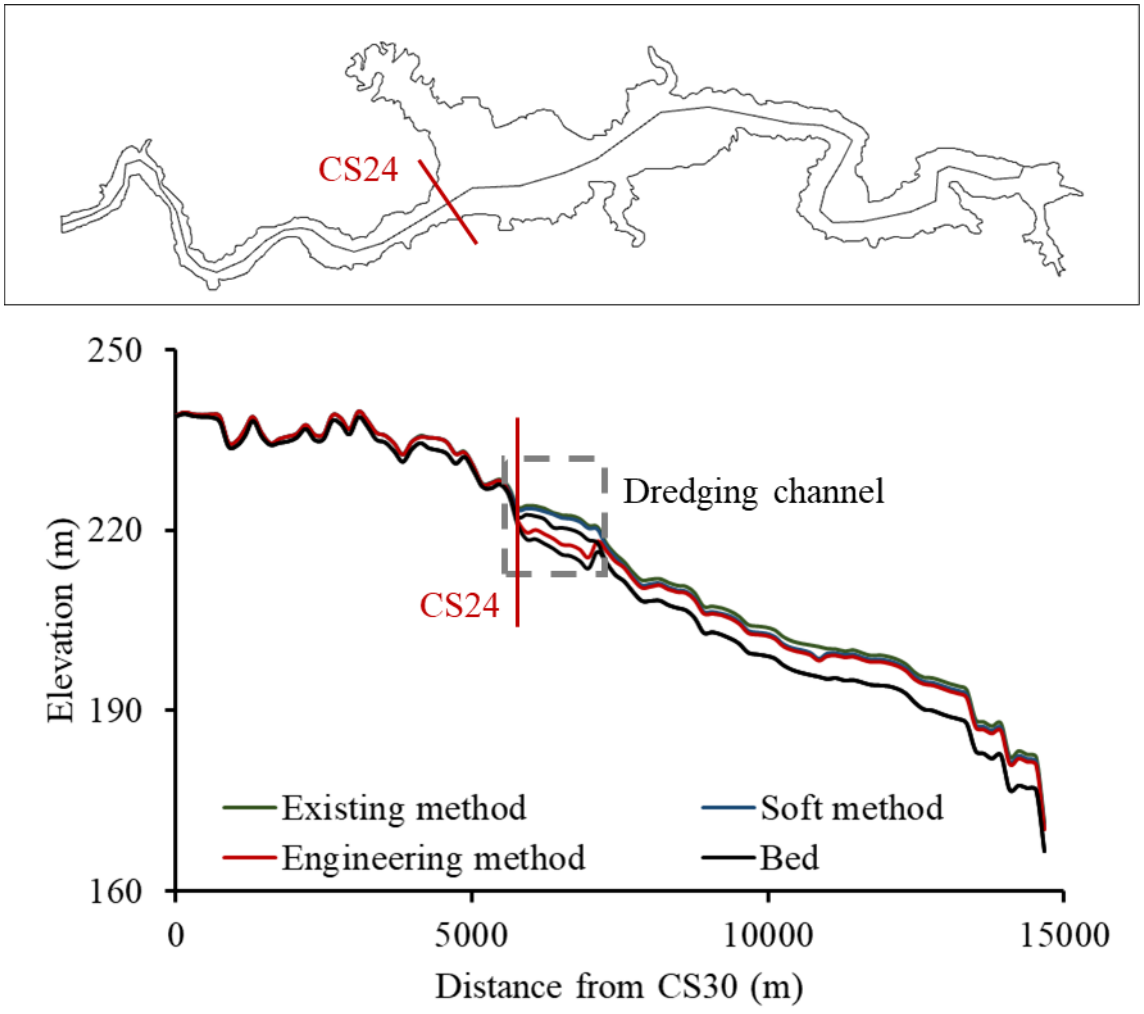

Figure 7.9 The longitudinal view of the bed elevation change after the flooding event.

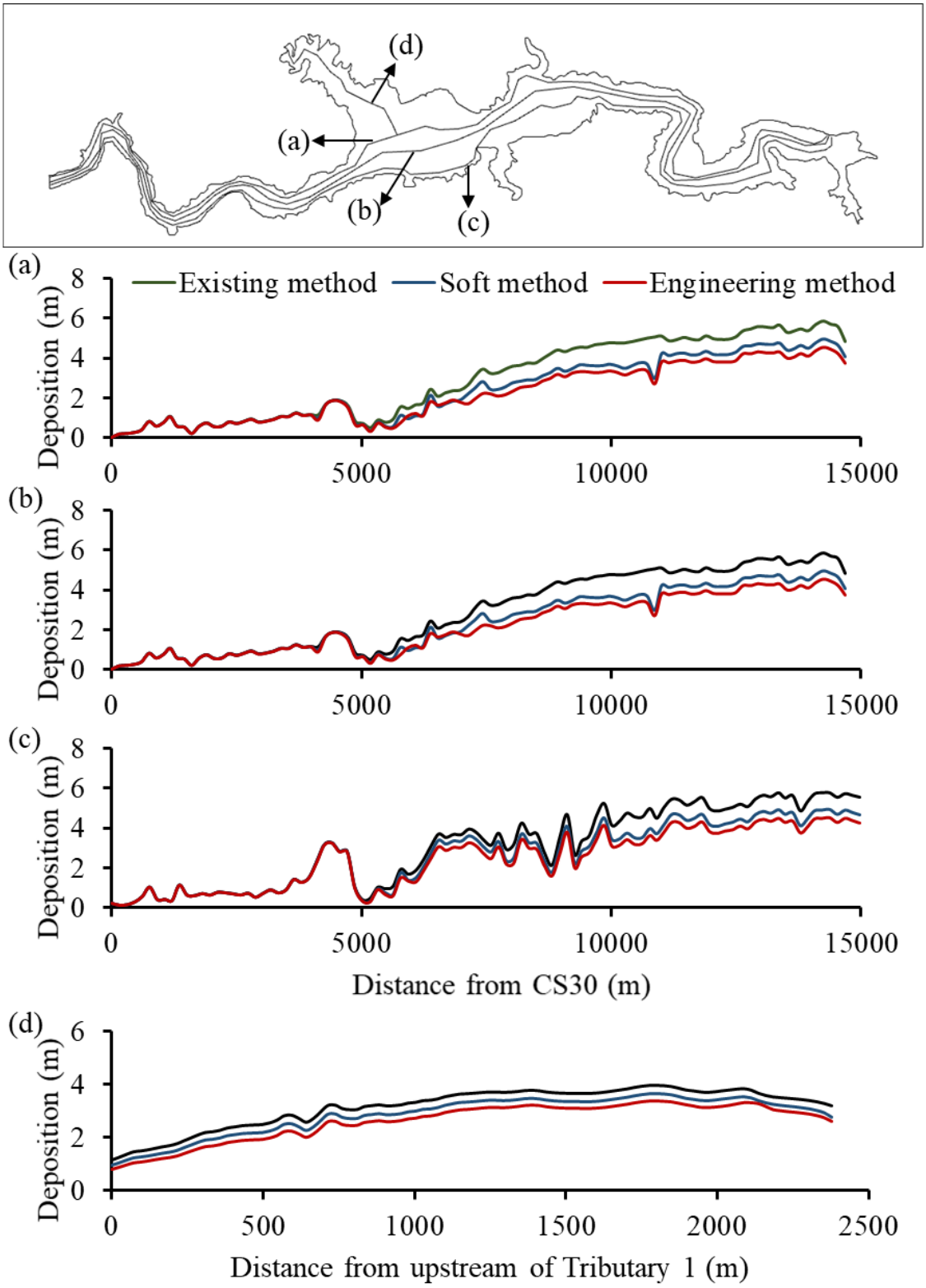

Figure 7.10 The deposition at (a) left, (b) middle and (c) right side of mainstream, and (d) tributary under existing, soft, and engineering methods.

7.2.3 Application of proposed improving methods under different inflow hydrological events

Based on the previous results, it indicated that the improving methods could yield more sediment releasing. Then, the improvement of proposed improving methods application for different inflow hydrological conditions (Figure 5.8) is evaluated in this section. As illustrated in Figure 7.11, we found that the inflow discharge and venting efficiency have a high relationship due to the longer outlets' operation duration. Therefore, the flooding events could be divided into three clusters: (1) small, (2) middle, and (3) large inflow discharge amount. Figure 7.11 showed the proposed soft and engineering methods bring 35.1% and 50.59% improvement percentages instead of existing method.

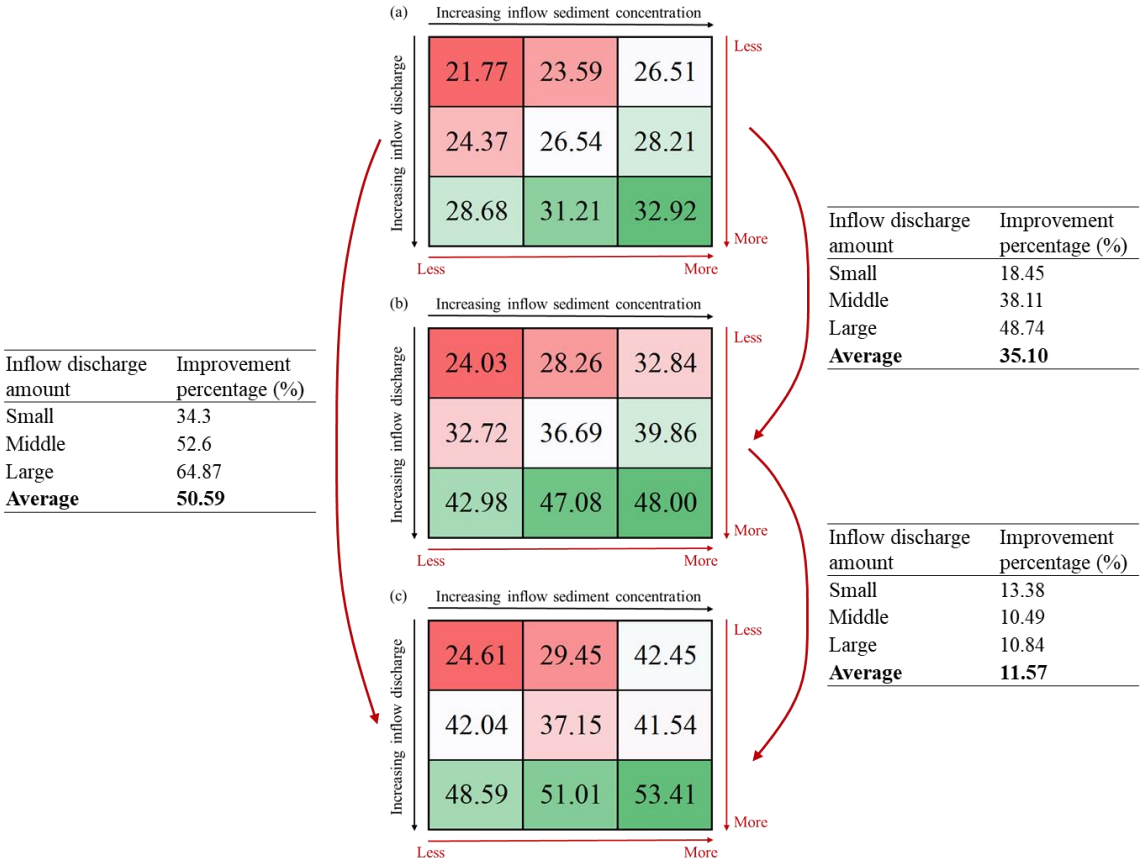

Inflow discharge amount	Improvement percentage (%)
Small	34.3
Middle	52.6
Large	64.87
Average	**50.59**

Inflow discharge amount	Improvement percentage (%)
Small	18.45
Middle	38.11
Large	48.74
Average	**35.10**

Inflow discharge amount	Improvement percentage (%)
Small	13.38
Middle	10.49
Large	10.84
Average	**11.57**

Figure 7.11 The turbidity current venting efficiency by using (a) existing, (b) soft, and (c) engineering methods from different inflow hydrological conditions (unit: %) and improvement percentage by adopting improving methods.

The results of the turbidity current processes and deposition in the reservoir under different venting strategies are shown in **Appendix C**. As the previous conclusions, increasing venting efficiency and operation of extended pipes mitigates the influence of muddy lakes on water supply facilities. As illustrated in Figure 7.12, using the improving methods, the muddy lake reach time at water supply facilities effectively extends, and more types of events are not necessary to consider the muddy lake impacts.

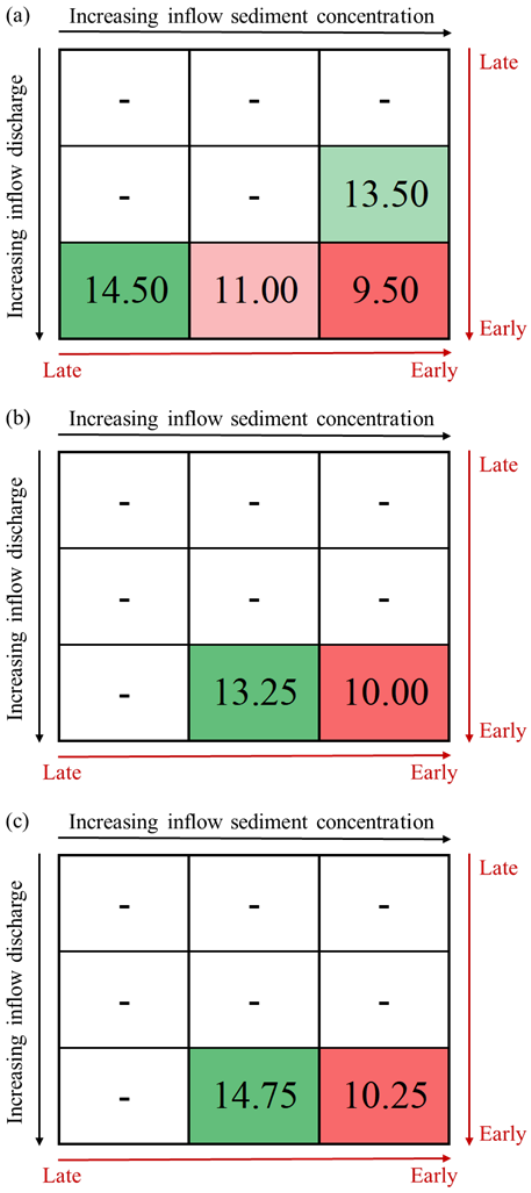

*Note: - means no impact of the muddy lake

Figure 7.12 The muddy lake reach time by using (a) existing, (b) soft, and (c) engineering methods from different inflow hydrological conditions (unit: hours)

7.3 Prediction of the reservoir usage life extension by adopting the proposed improving methods

The historical major flood typhoon events for Shihmen Reservoir since 1963 are classified into three clusters based on the threshold proposed in **Chapter 5.3.1** (Table 7.2). As listed in Table 7.3, the 15, 18, and 7 events are related to small, middle, and large inflow discharge clusters. Thus, the probability of the events is obtained and essential for future events prediction. Based on each cluster's obtained probability times improvement percentage, the prediction of averaged improvement for future events could be calculated. The results showed that the average desilting improvement for future events is 32.6% and 47.9% by adopting soft and engineering methods instead of the existing method.

Table 7.2 The historical major flood typhoon events since 1963 and clusters.

Typhoon	Year	Peak inflow discharge (m^3/s)	Cluster
Gloria	1963	10141	Large
Cora	1966	2176	Small
Elsie	1969	5703	Large
Fran	1970	6888	Large
Betty	1972	5665	Large
Irving	1979	2006	Small
Holly	1984	2166	Small
Nelson	1985	4906	Middle
Abby	1986	2129	Small
Sarah	1989	2959	Small
Yancy	1990	4343	Middle
Abe	1990	3764	Middle
Dot	1990	2593	Small
Polly	1992	2243	Small
Doug	1994	3065	Middle
Fred	1994	2440	Small
Seth	1994	3138	Middle
Herb	1996	6362	Large

Typhoon	Year	Peak inflow discharge (m^3/s)	Cluster
Winnie	1997	3411	Middle
Zeb	1998	4643	Middle
Bilis	2000	2230	Small
Nari	2001	4123	Middle
Rammasun	2002	2536	Small
Aere	2004	8594	Large
Haitang	2005	3199	Middle
Matsa	2005	5322	Middle
Talim	2005	3689	Middle
Sepat	2007	1844	Small
Wipha	2007	2788	Small
Krosa	2007	5300	Middle
Fungwong	2008	2040	Small
Sinlaku	2008	3447	Middle
Jangmi	2008	3292	Middle
Morakot	2009	1838	Small
Saola	2012	5385	Middle
Soulik	2013	5458	Middle
Trami	2013	2413	Small
Soudelor	2015	5634	Large
Dujuan	2015	3803	Middle
Megi	2016	4268	Middle

Table 7.3 The events' probability and improvement percentage for each cluster and prediction for future events.

Cluster	Number	Events' probability (%)	Improvement percentage (%)	
			Soft method	Engineering method
Small	15	37.5	18.45	34.3
Middle	18	45	38.11	52.6
Large	7	17.5	48.74	64.87
Prediction of averaged improvement for future events			**32.60**	**47.88**

As illustrated in Figure 7.13, the average Shihmen Reservoir storage capacity loss since 1962 is 1.91 (10^6 m^3/year). Without any improvement, the remaining storage capacity is 47.5% and 16.6% in 2050 and 2100, respectively. Based on the calculated prediction of averaged improvement for future events, the predicted storage loss decreases from 1.91 to 1.29 and 0.99 (10^6 m^3/year) using the soft and engineering methods. The results showed that if without any improvement, the Shihmen Reservoir will lose most of its function due to the severe sedimentation. However, the application of the proposed soft and engineering methods can remain 32.7% and 40.4% storage capacity in 2100. It means that with proposed improving methods, the Shihmen Reservoir usage life is significantly extended.

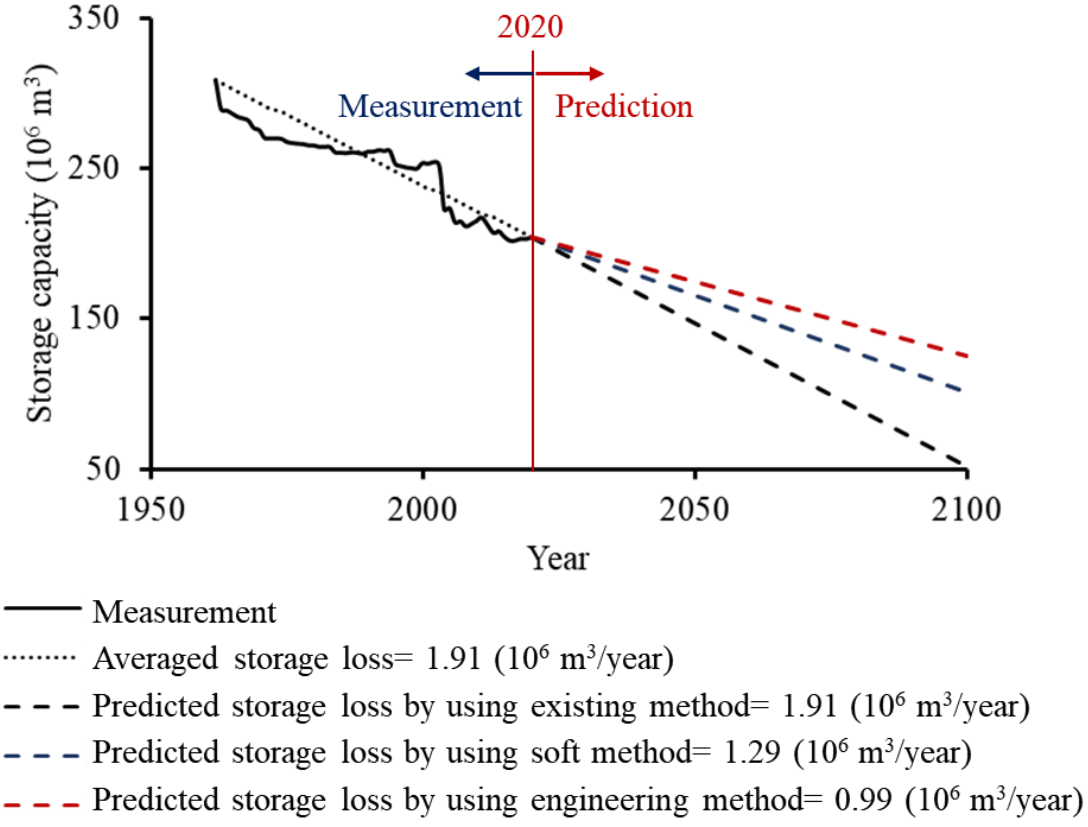

Figure 7.13 Prediction of remaining storage capacity by using existing, soft, and engineering methods.

7.4 Conclusion

This chapter assessed the feasibility of the proposed improving methods for realistic situations and future flooding events. To simplify the designed outlets' operation procedure, the reservoir water level is controlled, kept at 243 m. It means that the operation of multiple outlets and additional sediment management options were the critical characteristic to assess in this chapter. Based on the aforementioned results, the main findings of this chapter are:

1. The proposed outlets' operation sequence provides a good guideline for determining the multiple outlets' gate open and close. It effectively simplifies the decision-maker to determine the multiple outlets' operation, especially under complicated hydrological conditions.
2. The effectiveness of turbidity current venting is reduced after peak inflow sediment concentration, and then it converts to release muddy lake instead of a turbidity current. It is rare for the continuous sediment supply to turbidity current in realistic situations. Thus, the outlets' operation sequence under the dredging channel should be modified from the experiment's one because the inflow sediment concentration is hydrograph instead of fixed values.
3. The prediction of deposition rate was obtained by the probability of the events and improvement percentage from each cluster, which was classified by inflow discharge. Due to the outlets' operation duration having a high relationship to venting efficiency, the inflow discharge was regarded as the critical characteristic.
4. By adopting the proposed improving methods, in 2100, the Shihmen Reservoir could keep in acceptable status with at least 32.7% storage remaining.

Chapter 8: Conclusions and Recommendations

8.1 Conclusions

To mitigate the sediment deposition and prolong the reservoir life, the efficient turbidity current venting operation is gaining more importance for low-cost sediment desilting. The fully three-dimensional numerical model (Telemac-3D) was considered the appropriate tool for profoundly understanding the turbidity current characteristics and venting operation. Through comprehensive sensitivity analysis, which considers the computational time and accuracy simultaneously, the applicable scope of the dimensionless numerical model setting, including domain discretization, turbulence scheme, and morphodynamic aspect, was determined. According to the efficient and accurate turbidity current simulation in both experimental- and field-scale, the reliable three-dimensional numerical modelling setup could provide a reference for different scale numerical building.

Using the fully three-dimensional numerical model, the flow regime and turbidity current transportation within Shihmen Reservoir under the flooding events were investigated: (1) In the sediment-laden flow region, the flow regime and sediment distribution are similar to the open-channel flow. Also, the sediment-laden flow was faster than turbidity current due to the shallow water upstream of the reservoir; (2) For investigating the turbidity current plunging location, the inflow discharge, and sediment concentration were the critical factors for determining the plunging densimetric Froude number, which is the critical characteristic for plunging location evaluation; (3) In the turbidity current region, the measurement from TDR and proposed equations was crucial to obtain the structure of the turbidity current body and head velocity. (4) The additional measurements to monitor the deficiencies were crucial to obtain comprehensive

assessments of turbidity current interaction at tributaries. Based on the previous understanding, the shortcomings of the existing venting methods were found, and potential improving methods were proposed in this study.

For increasing the turbidity current venting efficiency, the improving methods, including soft and engineering methods, were proposed in this study. The operation sequence of each outlet sorted by sediment venting ability gave an excellent reference for reservoir operators. To consider the balance between water storage and sediment desiltation under water resource availability, the in-time operation is regarded as the appropriate operating timing. The blockade structures cannot work well for the initially expected purposes. Still, it could prevent the outlets blocked by sedimentation, and the concentrated siltation at tributary is easier for dredging and mechanical removal. The additional extended pipe from Amu_SBT with dredging channel provides more flexibility for turbidity current venting operation decisions and significantly increases the turbidity current venting efficiency.

The feasibility of the proposed improving methods for realistic situations was essential to predict the desilting performance for future flooding events. The proposed outlets' operation sequence provides a good guideline for the decision-maker to determine the multiple outlets' operation, especially under complicated hydrological conditions. The effectiveness of turbidity current venting is reduced after peak inflow sediment concentration, and then it converts to release muddy lake instead of a turbidity current. Thus, the outlets' operation sequence under application of the dredging channel should be confirmed in realistic situations. The prediction of deposition rate was obtained by the probability of the events and improvement percentage from each cluster, which was classified by inflow discharge. By adopting the proposed improving methods, in 2100, the Shihmen Reservoir could keep in acceptable status with at least 32.7% storage

remaining instead of losing most of its function due to the severe sedimentation (83.4% storage lost). Overall, the proposed multiple outlets' operation and sediment management options could be a reference for reservoir managers to increase the efficiency of turbidity current venting, clear water storage, and achieve the final goals of mitigating the sediment deposition in the reservoir and prolonging the reservoir usage life.

8.2 Recommendations

This study investigates the three-dimensional numerical modelling setup, turbidity current characteristics and processes understanding, improving methods for increasing turbidity current venting efficiency proposal, and the feasibility of proposed improving methods for future flooding events. This thesis gives a contribution for filling the research gaps and provides a good reference for turbidity current venting researcher and reservoir manager:

1. Through comprehensive sensitivity analysis, which considers the computational time and accuracy simultaneously, the applicable scope of the dimensionless numerical model setting. According to the proposed guideline of numerical aspects and equations setting, the efficient and accurate turbidity current simulation in any conditions was obtained.

2. Based on the comprehensive assessment of turbidity current plunging phenomenon, the woody debris gathering location could be estimated by plunging location due to the circulation near it. This information helps reservoir managers effectively remove the woody debris after the flooding events.

3. Because it is difficult to measure the turbidity current during flooding events, understanding the flow regime and turbidity current transportation within Shihmen Reservoir under the flooding events was helpful for making operating decisions.

4. The proposed improving methods provide reliable suggestions for multiple outlets' operation and sediment management options. It helps reservoir managers to make optimal policies based on considering the economic benefits and desilting efficiency.

5. The prediction of Shihmen Reservoir's remaining storage capacity emphasizes the importance of improving methods. This study recommends the reservoir manager should take some actions based on the conclusion from this study to avoid severe sedimentation within the Shihmen Reservoir.

Moreover, follow up the results, and of this research, some limitations still exist, and additional research should be addressed in future work:

1. The necessity of additional measurements to monitor the inflow from tributaries and the sediment material of the active deposition was essential to solve the limitation of field-scale simulation.

2. It is generating more types of hydrographs, including values and shapes, for the turbidity current simulation to cover the possibilities of future flooding events. Moreover, it should apply the machine learning techniques to classify the flooding events into clusters.

3. The influence of bathymetry change on turbidity current venting operation should be considered for future events prediction.

4. In this study, it mainly focuses on increasing sediment releasing. The impact of released high sediment concentration flow for biology at downstream should be investigated in the future.

References

Abdelhadi, M. (1995). Environmental and Socio-economic impacts of erosion and sedimentation in North African Countries. Proc. 6th International Symposium on River Sedimentation.

Akiyama, J., & Stefan, H. G. (1984). Plunging flow into a reservoir: Theory. *Journal of Hydraulic Engineering*, 110(4), 484–499.

Alemu, M. M. (2016). Integrated Watershed Management and Sedimentation. *Journal of Environmental Protection*, 07(04), 490–494.

Altinakar, M. S., Graf, W. H., & Hopfinger, E. J. (1996). Flow structure in turbidity currents. *Journal of Hydraulic Research*, 34(5), 713–718.

Amini, A., Heller, P., De Cesare, G., & Schleiss, A. (2014). Comprehensive numerical simulations of sediment transport and flushing of a Peruvian reservoir. In Proceedings of the River Flow 2014, Special Session on Reservoir Sedimentation, Iowa City, LA, USA 211–219.

Amini, A., Venuleo, S., Chamoun, S., De Cesare, G., Schleiss, A., & Takhtemina, F. (2017). Investigation of venting turbidity currents in the Rudbar-Lorestan reservoir in Iran. The 85th annual meeting of international commission on large dams, Prague, Czech Republic.

Annandale, G. W. (1987). *Reservoir sedimentation*. Elsevier.

Ashida K., & Egashira S. (1975). Basic study on turbidity currents. *Proceedings of the Japan Society of Civil Engineers*, 1975(237), 37–50.

Audouin, Y., Benson, T., Delinares, M., Fontaine, J., Glander, B., Huybrechts, N., Kopmann, R., Leroy, A., Pavan, S., Chi-Tuân Pham, Taccone, F., Tassi, P., & Walther, R. (2020). Introducing GAIA, the brand new sediment transport module of the TELEMAC-MASCARET system. The 15th TELEMAC-MASCARET User Conference, Toulouse, France.

Basson, G. (1997). Dealing with reservoir sedimentation. *Water Research Commission*

Report, 1–4.

Basson, G. (2009). Management of siltation in existing and new reservoirs. General Report. The 23rd Congress of the International Commission on Large Dams, Int. Com. on Large Dams, Brasilia.

Bournet, P., Dartus, D., Tassin, B., & Vincon-Leite, B. (1999). Numerical investigation of plunging density current. *Journal of Hydraulic Engineering*, 125(6), 584–594.

Chamoun, S., De Cesare, G., & Schleiss, A. J. (2016). Managing reservoir sedimentation by venting turbidity currents: A review. *International Journal of Sediment Research*, 31(3), 195–204.

Chamoun, S., De Cesare, G., & Schleiss, A. J. (2018). Influence of Operational Timing on the Efficiency of Venting Turbidity Currents. *Journal of Hydraulic Engineering*, 144(9), 04018062.

Chang, M. J., Lin, G. F., Chen, P. A., Lee, F. Z., & Lai, J. S. (2020). Development of a real-time forecasting model for turbidity current arrival time to improve reservoir desilting operation. *Hydrological Sciences Journal*, 65(6), 1022–1035.

Chen, P. A. (2017). Reservoir turbidity-current arrival-time and venting efficiency forecasting using machine learning. Master thesis, National Taiwan University (In Chinese).

Crowder, B. M. (1987). Economic costs of reservoir sedimentation: A regional approach to estimating cropland erosion damage. *Journal of Soil and Water Conservation*, 42(3), 194–197.

Dadson, S. J., Hovius, N., Chen, H., Dade, W. B., Hsieh, M. L., Willett, S. D., Hu, J. C., Horng, M. J., Chen, M. C., Stark, C. P., Lague, D., & Lin, J. C. (2003). Links between erosion, runoff variability and seismicity in the Taiwan orogen. *Nature*, 426(6967), 648–651.

Dai, A., & Garcia, M. H. (2009). Analysis of plunging phenomena. *Journal of Hydraulic Research*, 47(5), 638–642.

De Cesare, G., & Lafitte, R. (2007). Outline of the historical development regarding reservoir sedimentation. The 32nd IAHR Congress, Venice.

De Cesare, G., Boillat, J. L., & Schleiss, A. J. (2006). Circulation in Stratified Lakes due to Flood-Induced Turbidity Currents. *Journal of Environmental Engineering*, 132(11), 1508–1517.

De Cesare, G., Schleiss, A., & Hermann, F. (2001). Impact of Turbidity Currents on Reservoir Sedimentation. *Journal of Hydraulic Engineering*, 127(1), 6–16.

Ellison, T. H., & Turner, J. S. (1959). Turbulent entrainment in stratified flows. *Journal of Fluid Mechanics*, 6(03), 423.

Esmaeili, T., Sumi, T., Kantoush, S. A., Kubota, Y. (2018). Free-Flow Sediment Flushing: Insights from Prototype-Scale Studies. *Journal of Disaster Research*, 13(4), 677–690.

Esmaeili, T., Sumi, T., Kantoush, S., Kubota, Y., Haun, S., & Rüther, N. (2017). Three-Dimensional Numerical Study of Free-Flow Sediment Flushing to Increase the Flushing Efficiency: A Case-Study Reservoir in Japan. *Water*, 9(11), 900.

Fan, J. H. (1960). Experimental studies on density currents. *Water and Energy International*, 17(4), 706–729.

Farrell, G. J., & Stefan, H. G. (1986). Buoyancy induced plunging flow into reservoirs and costal regions. Tech. Rep. No. 241, At. Anthony Falls Hydr. Lab., Univ. of Minnesota, Minneapolis.

Ford, D. E., & Johnson, M. C. (1981). Field observations of density currents in impoundments. Proc., Symp. on Surface Water Impoundments, ASCE, New York, 2, 1239–1248.

Fukuoka, S., Fukushima, Y., & Nakamura, K. (1980). Study on the plunge depth and interface form of density currents in a two-dimensional reservoir. Proc. JSCE 302, 55–65 (In Japanese).

Garcia, M. H. (1994). Depositional Turbidity Currents Laden with Poorly Sorted

Sediment. *Journal of Hydraulic Engineering*, 120(11), 1240–1263.

Gogus, M., & Yalcinkaya, F. (1992). Reservoir sedimentation in Turkey. Proceedings of the 5th International Symposium on River Sedimentation, Karlsruhe, 909–918.

Graf, W. (1983). The behaviour of silt-laden current. *International Water Power & Dam Construction*, 35(9), 33–38.

Haun, S., Kjærås, H., Løvfall, S., & Olsen, N. R. B. (2013). Three-dimensional measurements and numerical modelling of suspended sediments in a hydropower reservoir. *Journal of Hydrology*, 479, 180–188.

Hebbert, B., Patterson, J., Loh, I., & Imberger, J. (1979). Collie river underflow into the Wellington reservoir. *Journal of the Hydraulics Division*, 105(5), 533–545.

Heimsund, S., Hansen, E. W. M., & Nemec, W. (2002). Computational 3-D fluid-dynamics model for sediment transport, erosion and deposition by turbidity currents. NGF Proceedings Geological Society of Norway, 18th Winter Conference, Nakrem, Norway.

Hosseini, S. A., Shamsai, A., & Ataie-Ashtiani, B. (2006). Synchronous measurements of the velocity and concentration in low density turbidity currents using an Acoustic Doppler Velocimeter. *Flow Measurement and Instrumentation*, 17(1), 59–68.

Huang, C. C., Chang, M. J., Lin, G. F., Wu, M. C., & Wang, P. H. (2021). Real-time forecasting of suspended sediment concentrations reservoirs by the optimal integration of multiple machine learning techniques. *Journal of Hydrology: Regional Studies*, 34, 100804.

Huang, C. C., Lai, Y. G., Lai, J. S., & Tan, Y. C. (2019). Field and Numerical Modeling Study of Turbidity Current in Shimen Reservoir during Typhoon Events. *Journal of Hydraulic Engineering*, 145(5), 05019003.

Hung, M., Hsieh, T., Wu, C., & Yang, J. (2009). Two-dimensional nonequilibrium noncohesive and cohesive sediment transport model. *Journal of Hydraulic Engineering*, 135(5), 369–382.

ICOLD. (2009). Sedimentation and Sustainable Use of Reservoirs and River Systems, International Commission on Large Dams (ICOLD), Paris.

Itakura, T., & Kishi, T. (1980). Open channel flow with suspended sediments. *Journal of the Hydraulics Division*, 106(8), 1325–1343.

Jain, S. C. (1981). Plunging phenomena in reservoirs. *American Society of Civil Engineers*, 1249–1257.

Janocko, M., Cartigny, M. B. J., Nemec, W., & Hansen, E. W. M. (2013). Turbidity current hydraulics and sediment deposition in erodible sinuous channels: Laboratory experiments and numerical simulations. *Marine and Petroleum Geology*, 41, 222–249.

Jodeau, M., Chamoun, S., Feng, J., De Cesare, G., & Schleiss, A. J. (2018). Numerical Modeling of turbidity currents with Ansys CFX and Telemac 3D. E3S Web of Conferences, 40, 03014.

Kneller, B. C., Bennett, S. J., & McCaffrey, W. D. (1999). Velocity structure, turbulence and fluid stresses in experimental gravity currents. *Journal of Geophysical Research: Oceans*, 104(C3), 5381–5391.

Kneller, B., & Buckee, C. (2000). The structure and fluid mechanics of turbidity currents: A review of some recent studies and their geological implications: Structure of turbidity currents. *Sedimentology*, 47, 62–94.

Kondolf, G. M., Gao, Y., Annandale, G. W., Morris, G. L., Jiang, E., Zhang, J., Cao, Y., Carling, P., Fu, K., Guo, Q., Hotchkiss, R., Peteuil, C., Sumi, T., Wang, H., Wang, Z., Wei, Z., Wu, B., Wu, C., & Yang, C. T. (2014). Sustainable sediment management in reservoirs and regulated rivers: Experiences from five continents. *Earth's Future*, 2(5), 256–280.

Kulis, P., & Hodges, B. R. (2006). Modeling gravity currents in shallow bays using a sigma coordinate model. The 7th international conference on hydroscience and engineering, Philadelphia.

Lai, J. S., & Shen, H. W. (1996). Flushing sediment through reservoirs. *Journal of Hydraulic Research*, 34(2), 237–255.

Lai, Y., & Wu, K. (2019). A Three-Dimensional Flow and Sediment Transport Model for Free-Surface Open Channel Flows on Unstructured Flexible Meshes. *Fluids*, 4(1), 18.

Lee, F. Z., Lai, J. S., Chen, P. A., Lin, G. F., Lee, H. Y., Wu, C. H., & Tan, Y. C. (2017). Investigation on plunge point location and turbidity current movement in the Shihmen Reservoir. Proc. of the 2nd Int. Workshop on Sediment Bypass Tunnels.

Lee, F. Z., Lai, J. S., Tan, Y. C., & Sung, C. C. (2014). Turbid density current venting through reservoir outlets. *KSCE Journal of Civil Engineering*, 18(2), 694–705.

Lee, H. Y. (2018). Research and development of operational desiltation techniques for reservoir sustainability. *Ministry of Science and Technology* (in Chinese).

Lee, H. Y., & Yu, W. S. (1997). Experimental study of reservoir turbidity current. *Journal of Hydraulic Engineering*, 123(6), 520–528.

Mahmood, K. (1987). Reservoir sedimentation: Impact, extent, and mitigation. Technical paper. International Bank for Reconstruction and Development, Washington, USA.

Maskey, D. L., & Ruther, N. (2019). Numerical modelling tools for sediment management in PROR reservoir of Kabeli A Hydroelectric Project (Nepal). Proceedings of the 3rd International Workshop on Sediment Bypass Tunnels, Taipei, Taiwan.

Morris, G. L., & Fan, J. H. (1998) *Reservoir Sedimentation Handbook: design and management of dams, reservoirs, and watersheds for sustainable use*. McGraw-Hill Book Co., New York, USA.

Mulder, T., Savoye, B., & Syvitski, J. (1997). Numerical modelling of a mid-sized gravity flow: The 1979 Nice turbidity current (dynamics, processes, sediment budget and seafloor impact). *Sedimentology*, 44(2), 305 – 326.

Oehy, C. D., & Schleiss, A. J. (2007). Control of Turbidity Currents in Reservoirs by Solid

and Permeable Obstacles. *Journal of Hydraulic Engineering*, 133(6), 637–648.

Ota, K., Sato, T., Nakagawa, H., & Kawaike, K. (2017). Three-Dimensional Simulation of Local Scour around a Weir-Type Structure: Hybrid Euler-Lagrange Model for Bed-Material Load. *Journal of Hydraulic Engineering*, 143(4), 04016096.

Pandey, A., Chaube, U. C., Mishra, S. K., & Kumar, D. (2016). Assessment of reservoir sedimentation using remote sensing and recommendations for desilting Patratu Reservoir, India. *Hydrological Sciences Journal*, 61(4), 711–718.

Parker, G., & Toniolo, H. (2007). Note on the analysis of plunging of density flows. *Journal of Hydraulic Engineering*, 133(6), 690–694.

Patra, B., Giri, S., & Narayan, P. (2019). Reservoir sedimentation in Indian dam: trend and challenges. International Dam Safety Conference, Bhubaneswar, Odisha, India.

Perez, S. (2010). CFD modeling of turbidity current deposition. *Journal of Marine Science and Application*, 9(1), 42–47.

Pérez-Díaz, B., Castanedo, S., Palomar, P., Henno, F., & Wood, M. (2019). Modeling Nonconfined Density Currents Using 3D Hydrodynamic Models. *Journal of Hydraulic Engineering*, 145(3), 04018088.

Peteuil, C., Jodeau, M., De Linares, M., Valette, E., Alliau, D., Wirz, C., Fretaud, T., Antoine, G., & Sécher, M. (2018). Toward an operational approach for the characterization and modelling of fine sediments dynamics in reservoirs. E3S Web of Conferences, 40, 03028.

Savage, S., & Brimberg, J. (1975). Analysis of plunging phenomena in water reservoirs. *Journal of Hydraulic Research*, 13(2), 187–205.

Schleiss, A. J., & De Cesare, G. (2010). Physical model experiments on reservoir sedimentation. 75th IAHR Hydrolink, 4, 54–57.

Schleiss, A. J., Franca, M. J., Juez, C., & De Cesare, G. (2016). Reservoir sedimentation. *Journal of Hydraulic Research*, 54(6), 595–614.

Shiklomanov, I. (1993). World fresh water resources. Water in Crisis: A Guide to the World's. Oxford University Press, Inc, Oxford.

Singh, B., & Shah, C. (1971). Plunging phenomenon of density currents in reservoirs. *La Houille Blanche*, 1, 59–64.

Sixth District Management Office. (2017). Integrated master plan for flood and siltation control of Nanhua Reservoir. *Taiwan water corporation* (In Chinese).

Sumi, T. (2015). Comprehensive reservoir sedimentation countermeasures in Japan. First International Workshop on Sediment Bypass Tunnels 1–20.

Turner, J. S. (1979). *Buoyancy effects in fluids*. Cambridge university press.

Van den Wall Bake, G. (1986). Siltation and soil erosion survey in Zimbabwe. IAHS-AISH Publication, 159, 69–80.

Vostruha, K., & Pelant, J. (2013). Perturbation Analysis of "k-ω" and "k-ε" Turbulent Models. Wall Functions. EPJ Web of Conferences, 45, 01097.

Wan, X. Y., Wang, G. Q., Yi, P., & Bao, W. M. (2010). Similarity-Based Optimal Operation of Water and Sediment in a Sediment-Laden Reservoir. *Water Resources Management*, 24(15), 4381–4402.

Wang, H. W., Kondolf, M., Tullos, D., & Kuo, W. C. (2018). Sediment Management in Taiwan's Reservoirs and Barriers to Implementation. *Water*, 10(8), 1034.

Water Resources Agency (WRA). (2018). Reservoir statistic data in April, 2018. Division of Water Resources, Taichung City, Taiwan.

White, R. (2001). *Evacuation of sediments from reservoirs*. Thomas Telford Publishing, London.

Wisser, D., Frolking, S., Hagen, S., & Bierkens, M. F. P. (2013). Beyond peak reservoir storage? A global estimate of declining water storage capacity in large reservoirs: Beyond Peak Reservoir Storage?. *Water Resources Research*, 49(9), 5732–5739.

Wunderlich, W. O., & Elder, R. A. (1973). Mechanics of flow through man-made lakes. Washington DC American Geophysical Union Geophysical Monograph Series, 17, 300–310.

Yu, W. S., Hsu, S. M., & Fan, K. L. (2004). Experiments on selective withdrawal of a codirectional two-layer flow through a line sink. *Journal of Hydraulic Engineering*, 130(12), 1156–1166.

Appendix A: Background of Telemac-3D and Gaia

A.1 Background of Telemac-3D

A.1.1 Governing equations

The Telemac-3D is solved by following the assumptions of three dimensional Navier-Stokes equation with a free surface in time, incompressible fluid, hydrostatic pressure hypothesis, and Boussinesq approximation for the momentum:

Continuity equation:

$$\frac{\partial U}{\partial x}+\frac{\partial V}{\partial y}+\frac{\partial W}{\partial z}=0 \qquad (A\text{-}1)$$

Momentum equation along x-direction:

$$\frac{\partial U}{\partial t}+\boldsymbol{u}\cdot\nabla U=-g\frac{\partial H}{\partial x}+v\Delta U+F_x \qquad (A\text{-}2)$$

Momentum equation along y-direction:

$$\frac{\partial V}{\partial t}+\boldsymbol{u}\cdot\nabla V=-g\frac{\partial H_s}{\partial y}+v\Delta V+F_y \qquad (A\text{-}3)$$

Hydrostatic pressure hypothesis:

$$P=P_{atm}+\rho_0 g(H-H_0)+\rho_0 g\int_{H_0}^{H}\frac{\Delta\rho}{\rho_0}dz' \qquad (A\text{-}4)$$

Tracer conservation:

$$\frac{\partial T}{\partial t}+\boldsymbol{u}\cdot\nabla T=Div(v\Delta V)+Q_t \qquad (A\text{-}5)$$

where, D is water depth (m); (U, V, W) is velocity component in x-, y-, and z-direction (m/s); T is tracer (g/l or °C); (F_x, F_y) are source terms denoting the wind, Coriolis force, and bottom friction (m/s^2); Q_t is tracer source of the sink (g/l or °C); P_s is water surface pressure; P_{atm} is atmospheric pressure and $\Delta\rho$ is a variation of density around the reference density.

A.1.2 The inputs and outputs

The Telemac-3D basic algorithm is solved in three computational steps: (1) Calculate the advected velocity component by solving the advection terms in the momentum equations. (2) The new velocity components, considering the advected velocities, diffusion terms, and the source terms in the momentum equations, are essential to obtain the intermediate velocity field. (3) The water depth could be obtained by solving the vertical integration of the continuity equation and the momentum equations, including the pressure-continuity terms.

The Telemac-3D code uses multiple mandatory and optional input and output files for computation. All keywords in the files are defined in the dictionary file. The default values are used if without giving the values for the keywords. The default values could be checked in the dictionary file. Meanwhile, we should caution that 72 characters are the maximum number for a line. The critical input and output files for Telemac-3D computation are introduced expressed:

The mandatory input files:

- The steering file, which contains all the computational options (physical, numerical aspect, etc.).
- The geometry file, which contains the mesh information, and a description of the type of boundaries.
- The liquid boundaries file, which provides the time-varying imposed values at liquid boundaries.

The optional input files:

- The Fortran file, which the user could modify the existing subroutines and announce the additional equations for the computation.
- The previous computation file, which provides the initial conditions from the

previous results for the restart calculation.

- The stage-discharge curves file, which gives an appropriate discharge-elevation law for determining the prescribed elevation.
- The sources file, which enables the user to set the time-dependent conditions, including discharge and tracers concentration, for the sources.

The output files:

- The 3D result file, which contains the results associated with three-dimensional simulation.
- The 2D result file, which contains the results associated with two-dimensional simulation.

A.2 Background of Gaia

The sediment transport simulation could be solved by Telemac-3D coupled with Gaia. In the computation procedure (Figure A.1), the sediment transport processes in the water column are dealt with Telemac-3D, and near the bed and bottom structure are solved by Gaia. Also, the Gaia could handle the sediment exchanges at the water-bed interface.

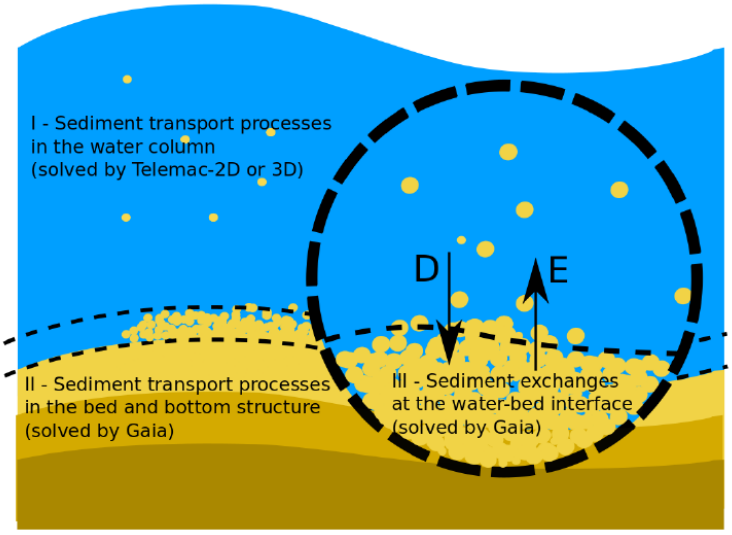

Figure A.1 Sketch of the sediment transport mechanisms. Above, D and E are deposition and erosion rates (Audouin et al., 2020).

Gaia solves the Exner equation for sediment mass:

$$(1-\lambda)\frac{\partial(\rho H_0)}{\partial t}+\nabla\cdot(Q_{mb}H_0)=0 \qquad \text{(A-6)}$$

where, Q_{mb} is the vector of the mass transport rate per unit width without pores (kg/m-s); λ is the bed porosity. The above equation could calculate the bed elevation by considering bedload and suspended sediment simultaneously.

A.2.1 Suspended sediment transport

The suspended sediment transport is solved via a two-dimensional advection-diffusion equation:

$$\frac{\partial hC}{\partial t}+\frac{\partial hUC}{\partial x}+\frac{\partial hVC}{\partial y}=\frac{\partial}{\partial x}\left(h\varepsilon\frac{\partial C}{\partial x}\right)+\frac{\partial}{\partial y}\left(h\varepsilon\frac{\partial C}{\partial y}\right)+E-D \qquad \text{(A-7)}$$

where, $C=C(x,y,z)$ is the depth-averaged concentration in % volume. Due to the different transport mechanisms, the sediment exchanges at the water-bed interface are separately discus into non-cohesive and cohesive sediment.

For non-cohesive sediment, the erosion (E) and deposition (D) rates are computed:

$$E=w_s C_{zref} \qquad \text{(A-8)}$$

$$D=w_s C_{eq} \qquad \text{(A-9)}$$

where, C_{zref} is the near-bed concentration, evaluated at the interface between bedload and suspended load. C_{eq} is the equilibrium near-bed concentration determined by using empirical formulas. The available equilibrium near-bed concentration formulas include Zyserman-Fredsoe, Bijker, van Rijn, and Soulsby & van Rijn.

For cohesive sediment, the erosion (E) and deposition (D) rates are computed:

$$E=\begin{cases}M[\left(\frac{\tau_b}{\tau_{ce}}\right)-1] & ;\tau_b>\tau_{ce}\\ 0 & ;otherwise\end{cases} \qquad \text{(A-10)}$$

$$D=w_s C[1-(\sqrt{\frac{\tau_b/\rho_a}{u_{*mud}^{cr}}})^2] \qquad \text{(A-11)}$$

where, M is Krone-Partheniades erosion constant (kg/m^2-s); τ_b is the bed shear stress; τ_{ce} is the critical bed shear stress (N/m^2); u_{*mud}^{cr} is the critical shear velocity for mud deposition (m/s).

A.2.2 Bedload transport

The dimensionless current-induced sediment transport rate (Φ_b) is expressed:

$$\Phi_b = \frac{Q_b}{\sqrt{g(s-1){D_{50}}^3}} \quad \text{(A-12)}$$

where, Q_b is the bedload transport rate per unit width (m^2/s); $s = \rho_s/\rho_a$ is the relative density; ρ_s and ρ_a is the density of sediment and clear ware (kg/m^3), respectively; D_{50} means sediment grain size (m). To obtain the sediment transport rate, the bedload transport formulas are commonly computed as the function of Shield number (θ):

$$\theta = \frac{\mu\tau_b}{(\rho_s - \rho_a)gd} \quad \text{(A-13)}$$

where, μ is the skin friction's correction factor.

Numerous empirical bedload transport formulas are available for computing the sediment transport rate of bedload, such as Meyer-Peter and Müller, Einstein-Brown, Engelund-Hansen modified by Chollet & Cunge, van Rijn's, Wilcock and Crowe, and Engelund-Hansen. The details of each formula can be found in the Gaia user manual.

Appendix B: Turbidity current processes from different inflow scenarios

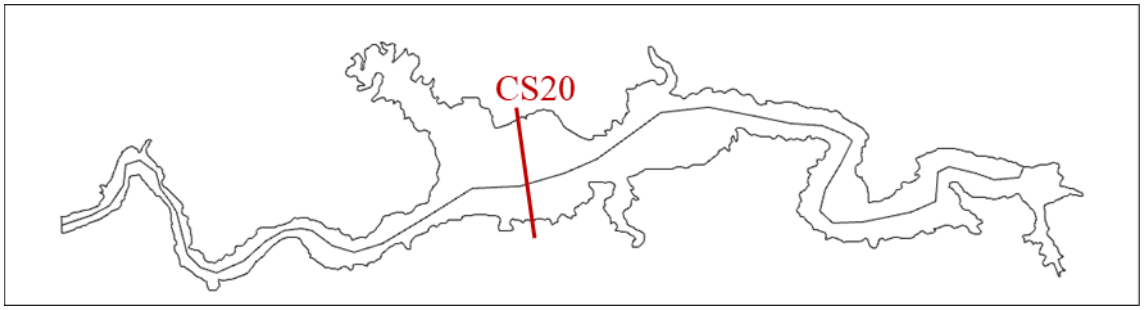

Figure B.1 The configuration of the Shihmen Reservoir and the longitudinal line.

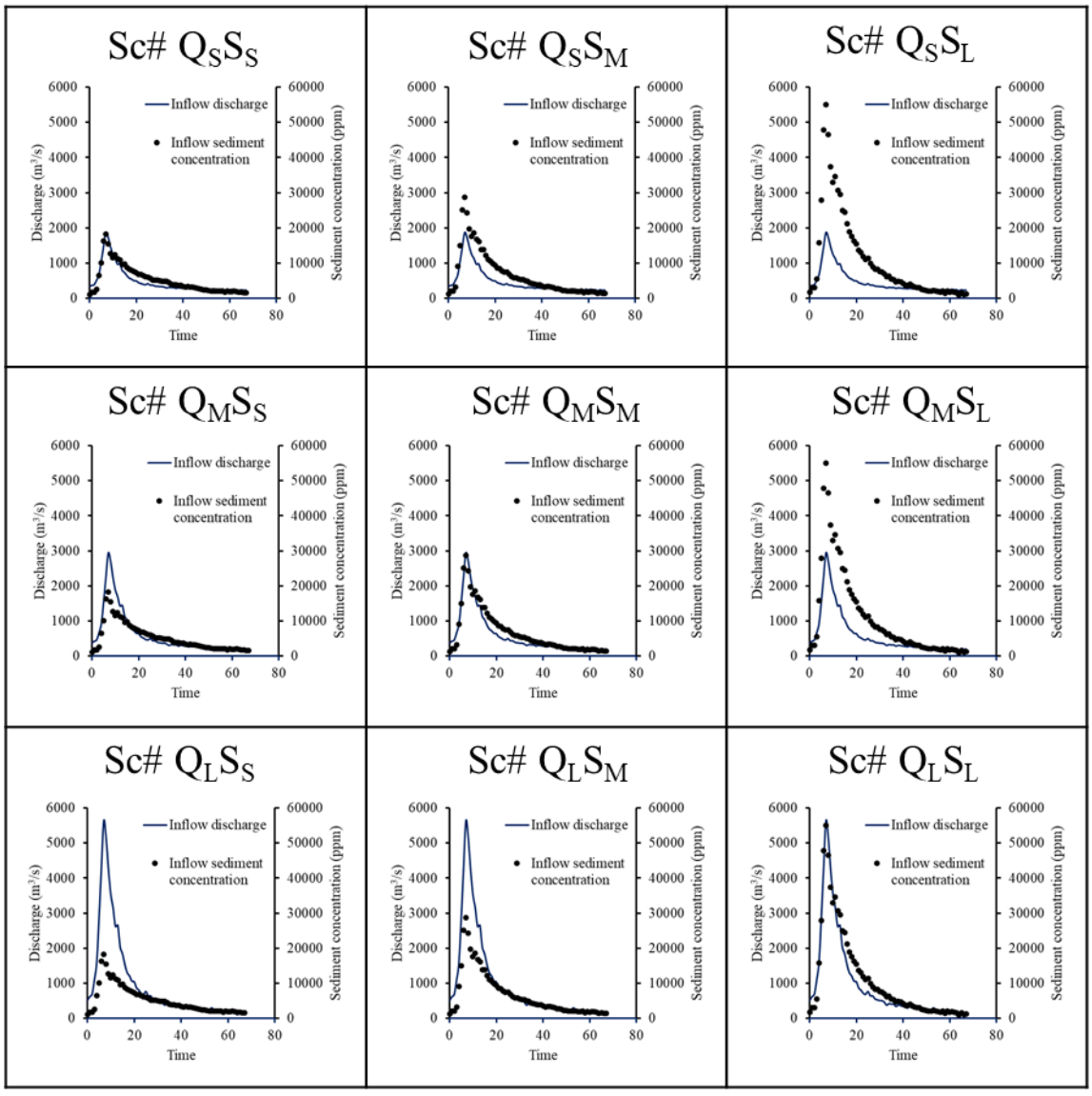

Figure B.2 Generated inflow discharge and sediment concentration.

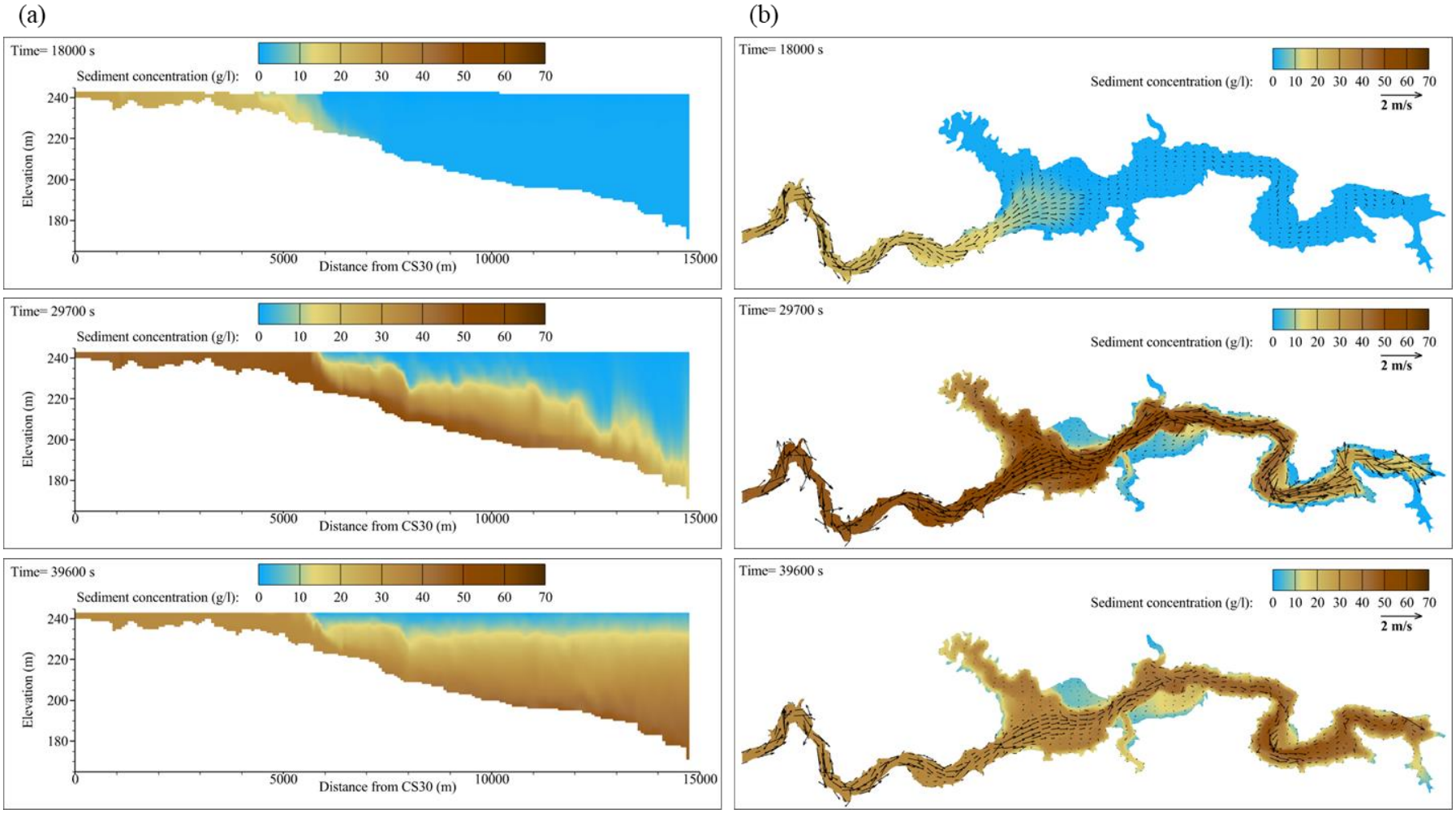

Figure B.3 The turbidity current processes from arrival at CS20, dam, and the muddy lake formed in (a) longitudinal and (b) plane view under Sc# $Q_L S_L$.

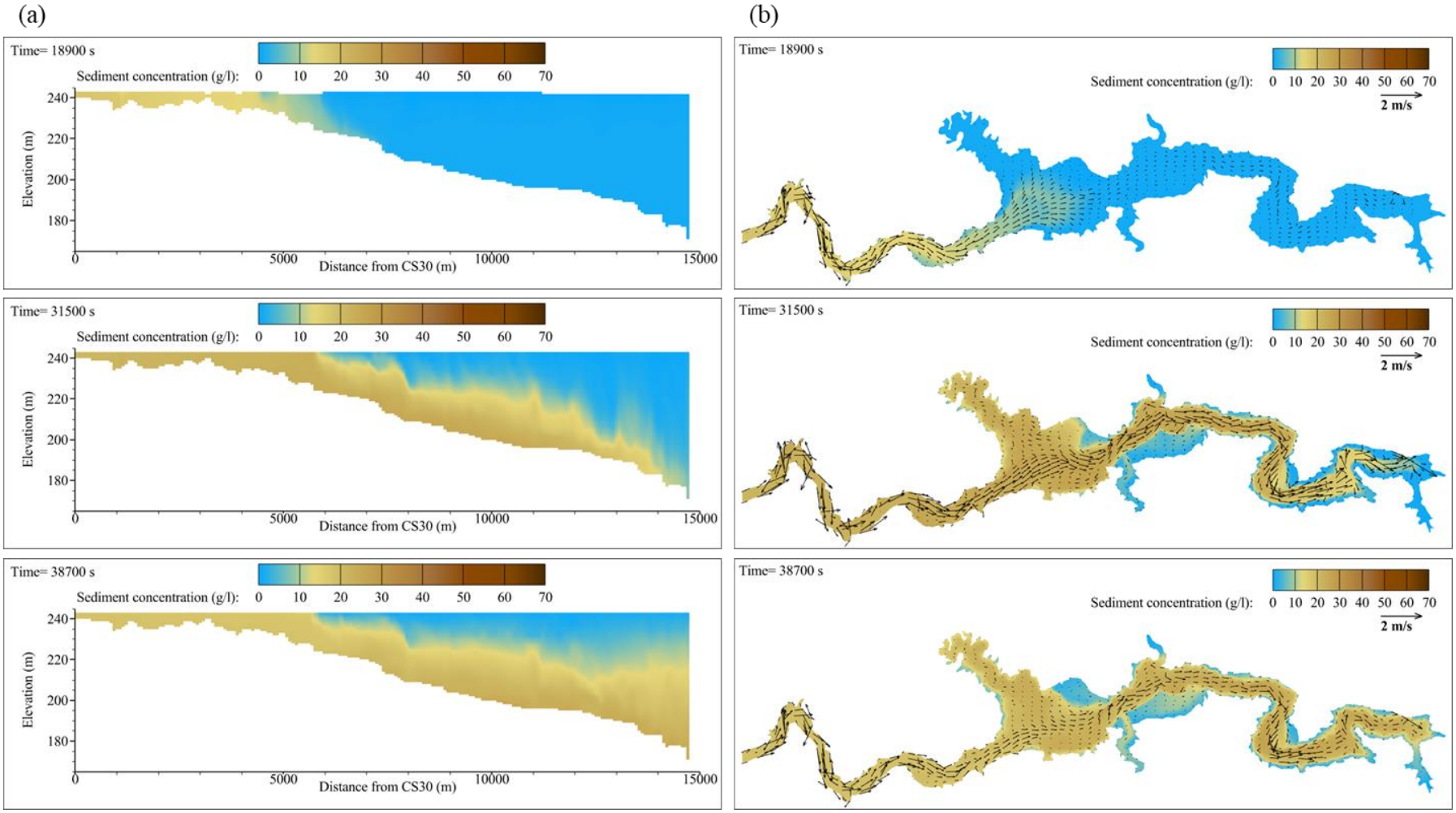

Figure B.4 The turbidity current processes from arrival at CS20, dam, and the muddy lake formed in (a) longitudinal and (b) plane view under Sc# $Q_L S_M$.

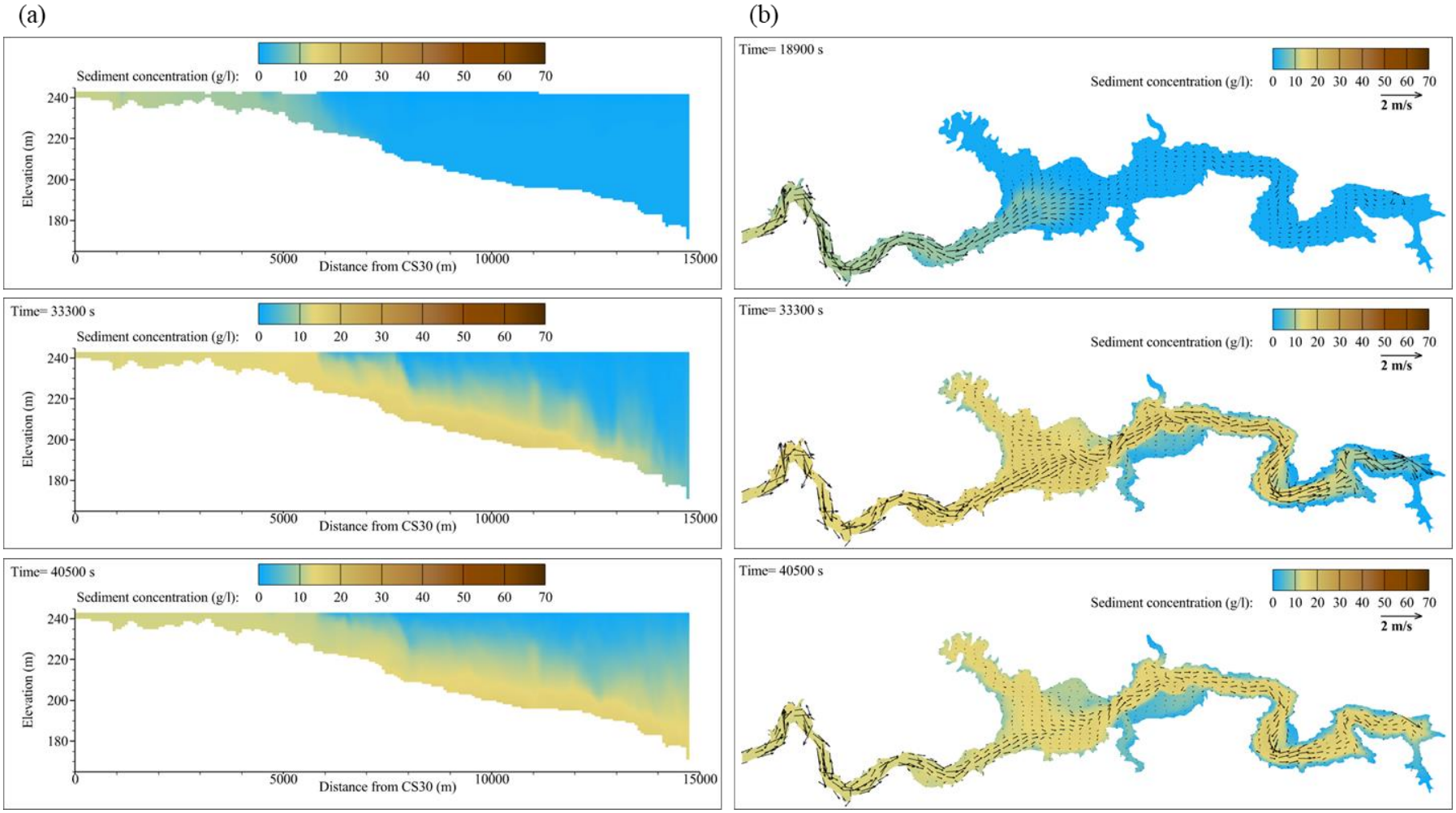

Figure B.5 The turbidity current processes from arrival at CS20, dam, and the muddy lake formed in (a) longitudinal and (b) plane view under Sc# $Q_L S_S$.

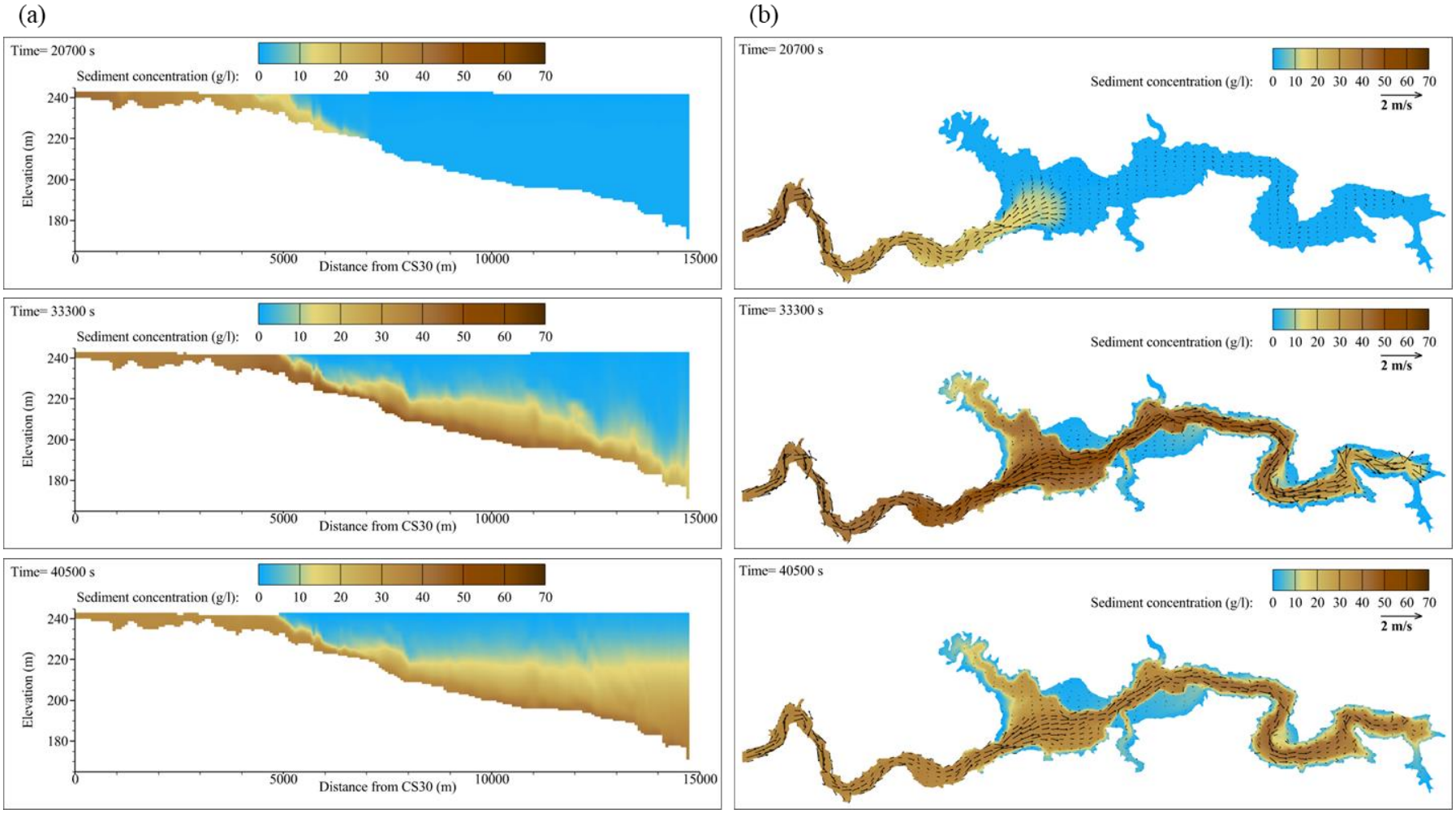

Figure B.6 The turbidity current processes from arrival at CS20, dam, and the muddy lake formed in (a) longitudinal and (b) plane view under Sc# $Q_M S_L$.

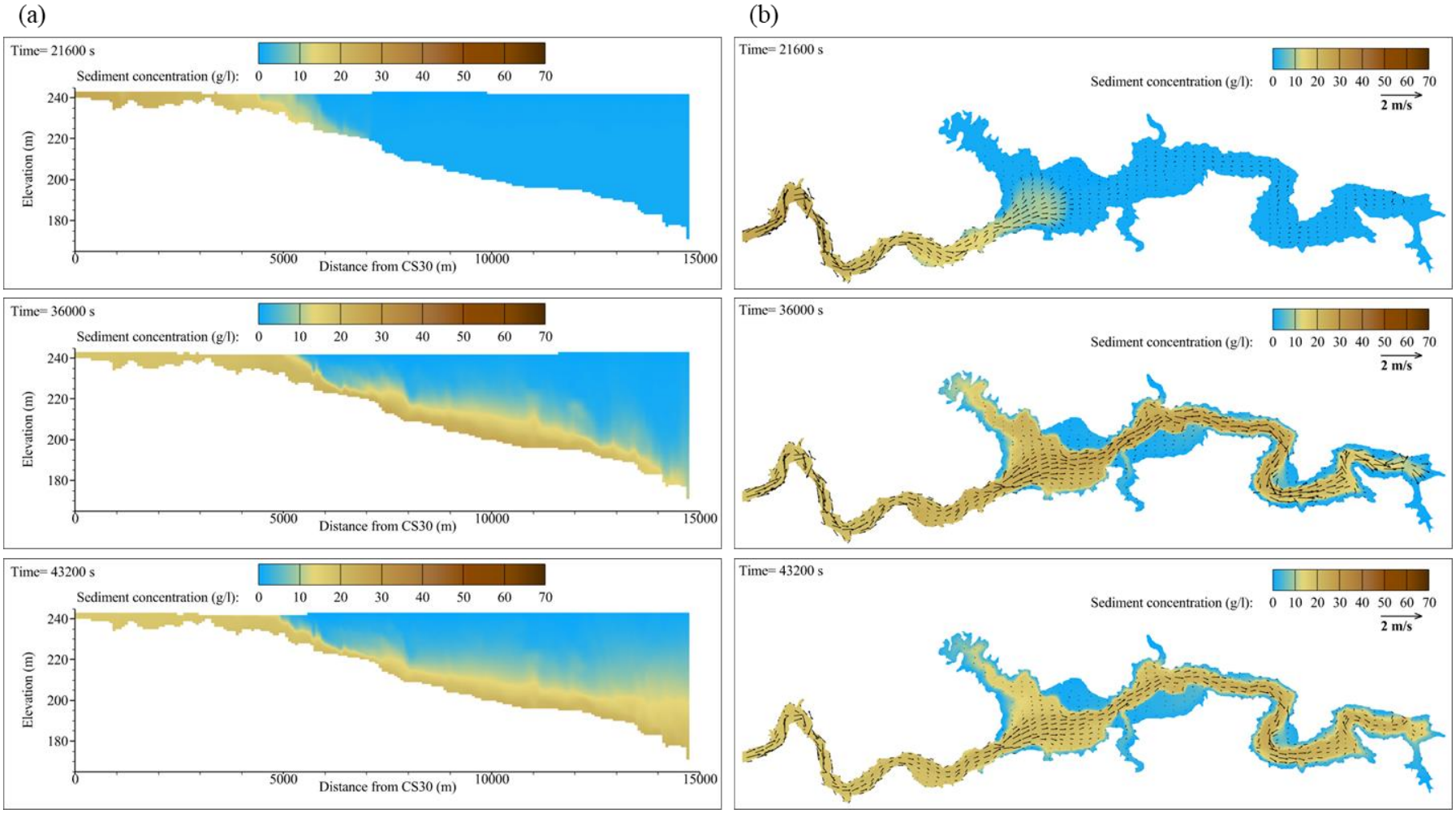

Figure B.7 The turbidity current processes from arrival at CS20, dam, and the muddy lake formed in (a) longitudinal and (b) plane view under Sc# $Q_M S_M$.

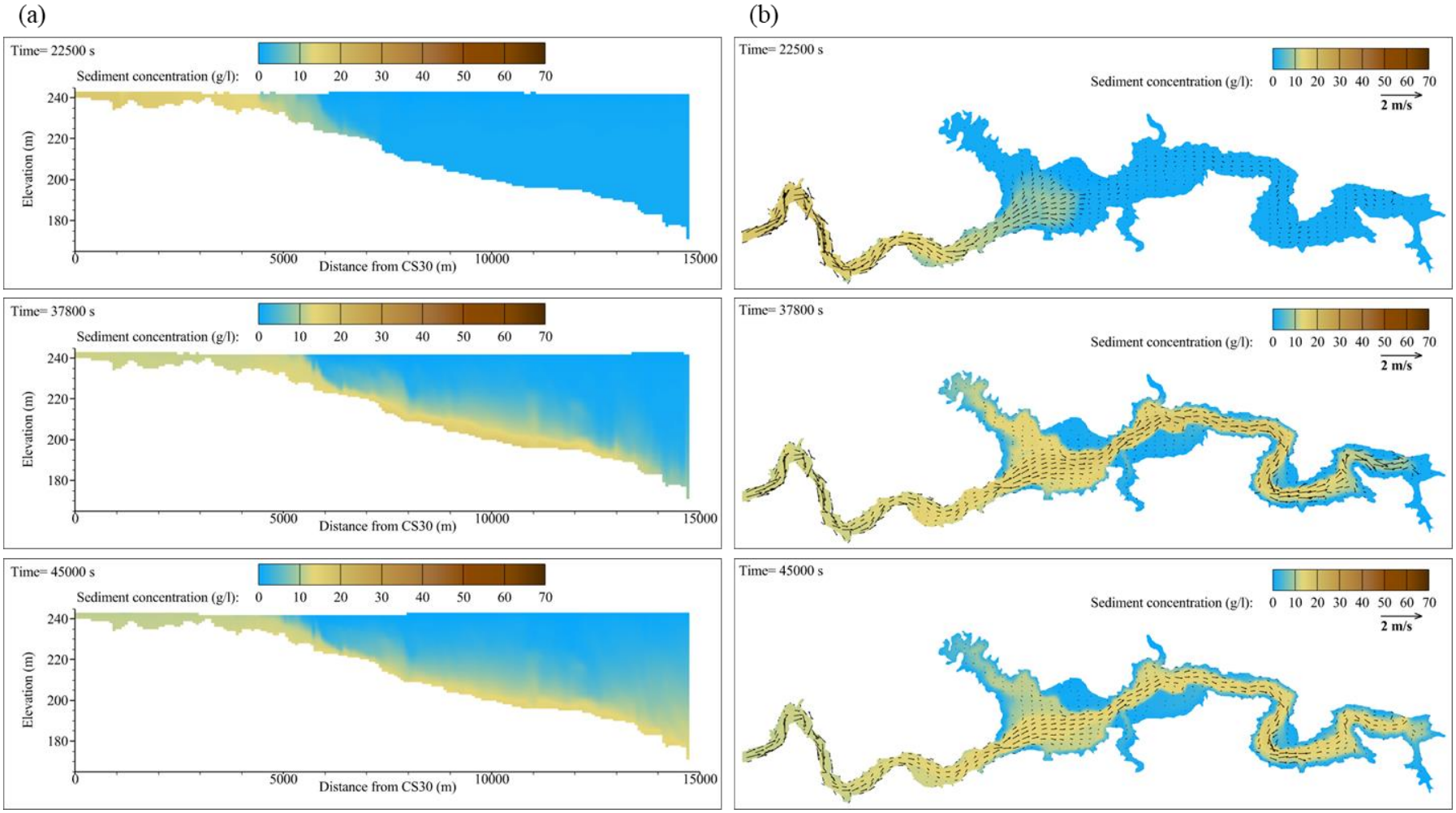

Figure B.8 The turbidity current processes from arrival at CS20, dam, and the muddy lake formed in (a) longitudinal and (b) plane view under Sc# $Q_M S_S$.

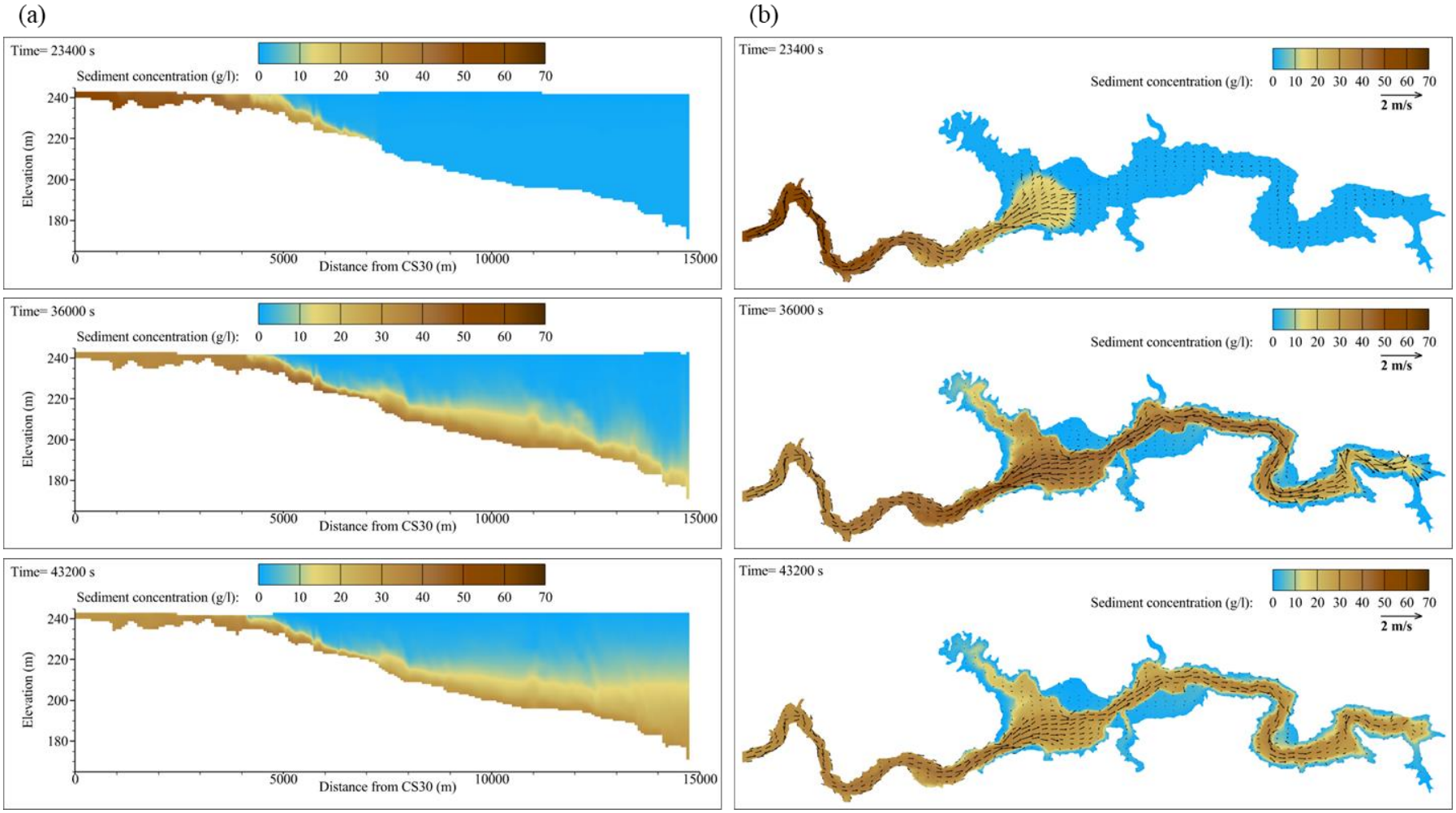

Figure B.9 The turbidity current processes from arrival at CS20, dam, and the muddy lake formed in (a) longitudinal and (b) plane view under Sc# $Q_S S_L$.

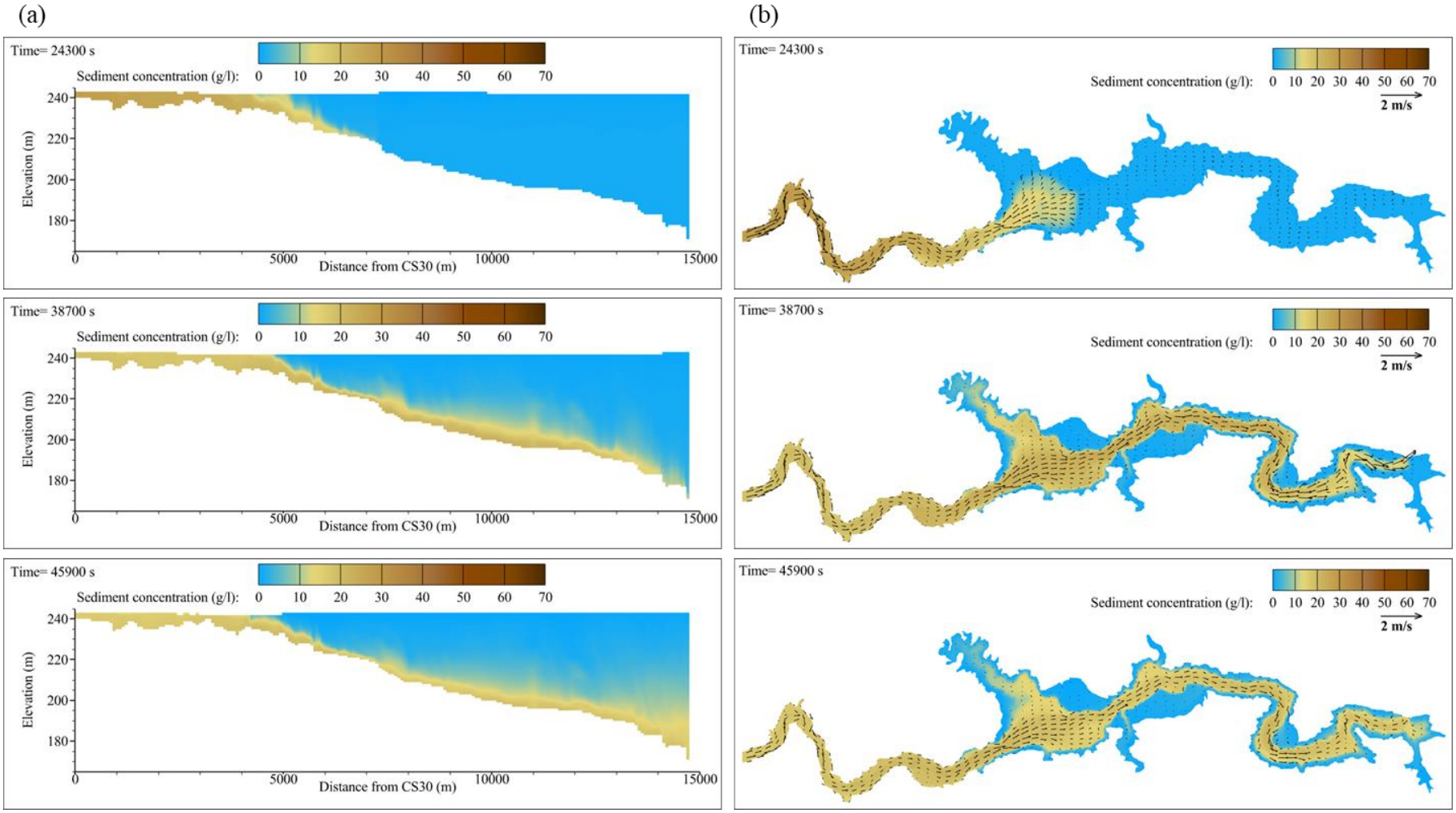

Figure B.10 The turbidity current processes from arrival at CS20, dam, and the muddy lake formed in (a) longitudinal and (b) plane view under Sc# $Q_S S_M$.

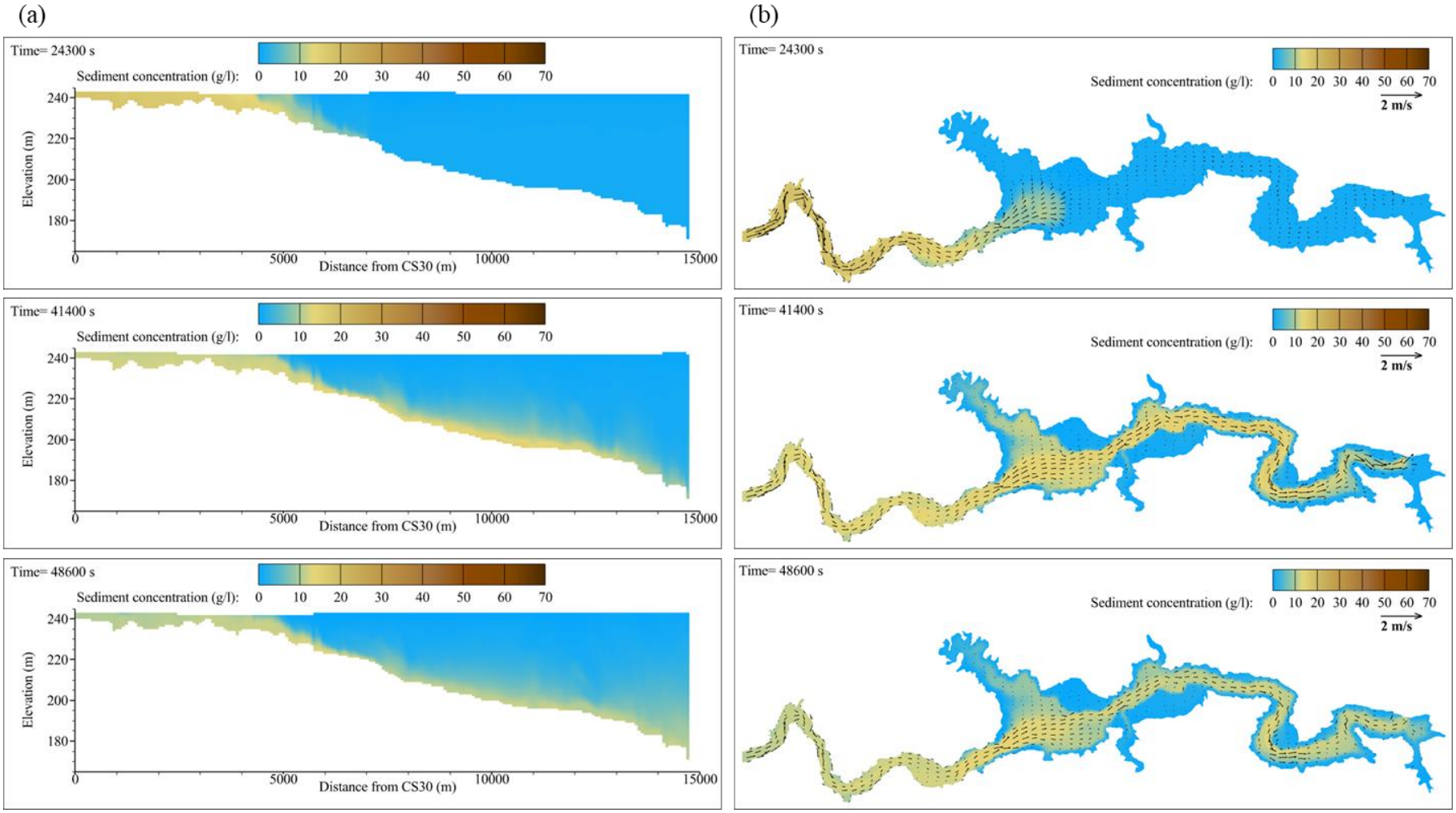

Figure B.11 The turbidity current processes from arrival at CS20, dam, and the muddy lake formed in (a) longitudinal and (b) plane view under Sc# $Q_S S_S$.

Appendix C: Turbidity current processes and deposition in the reservoir under different venting strategies

C.1 Existing method

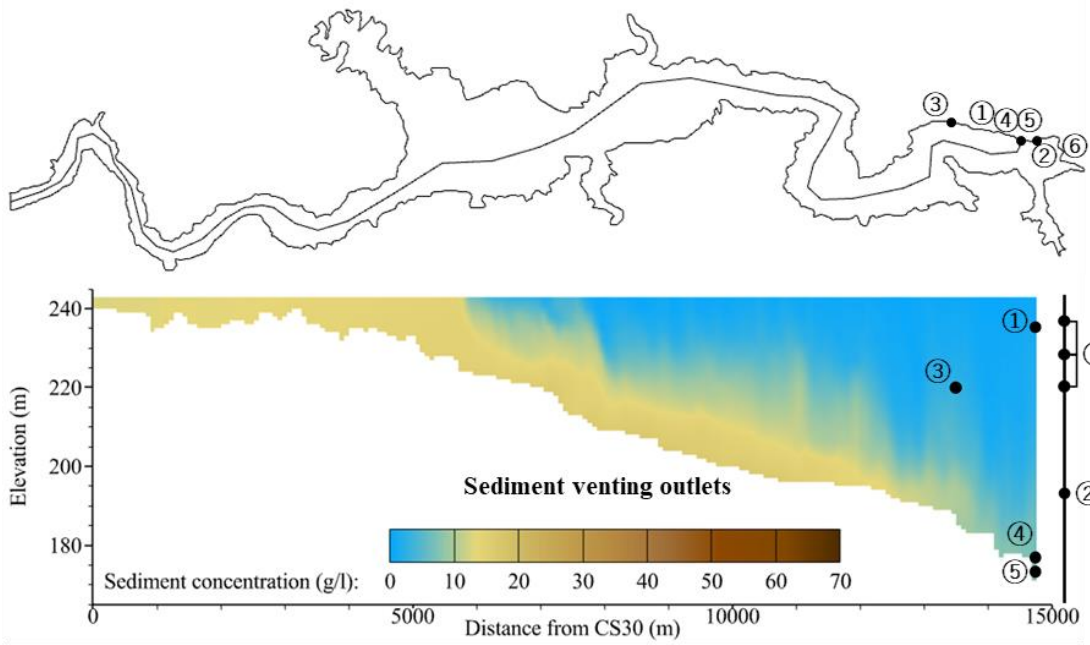

①Spillway (SP)
②Spillway tunnel (ST)
③Shihmen canal intake (SCI)
④Power plant intake and Venting tunnel (PPI and VT)
⑤Permanent river outlet (PRO)
⑥Water supply intake

Operating sequence: ⑤→④→③→②→①

Figure C.1 Operated outlets and the operating sequence under existing method.

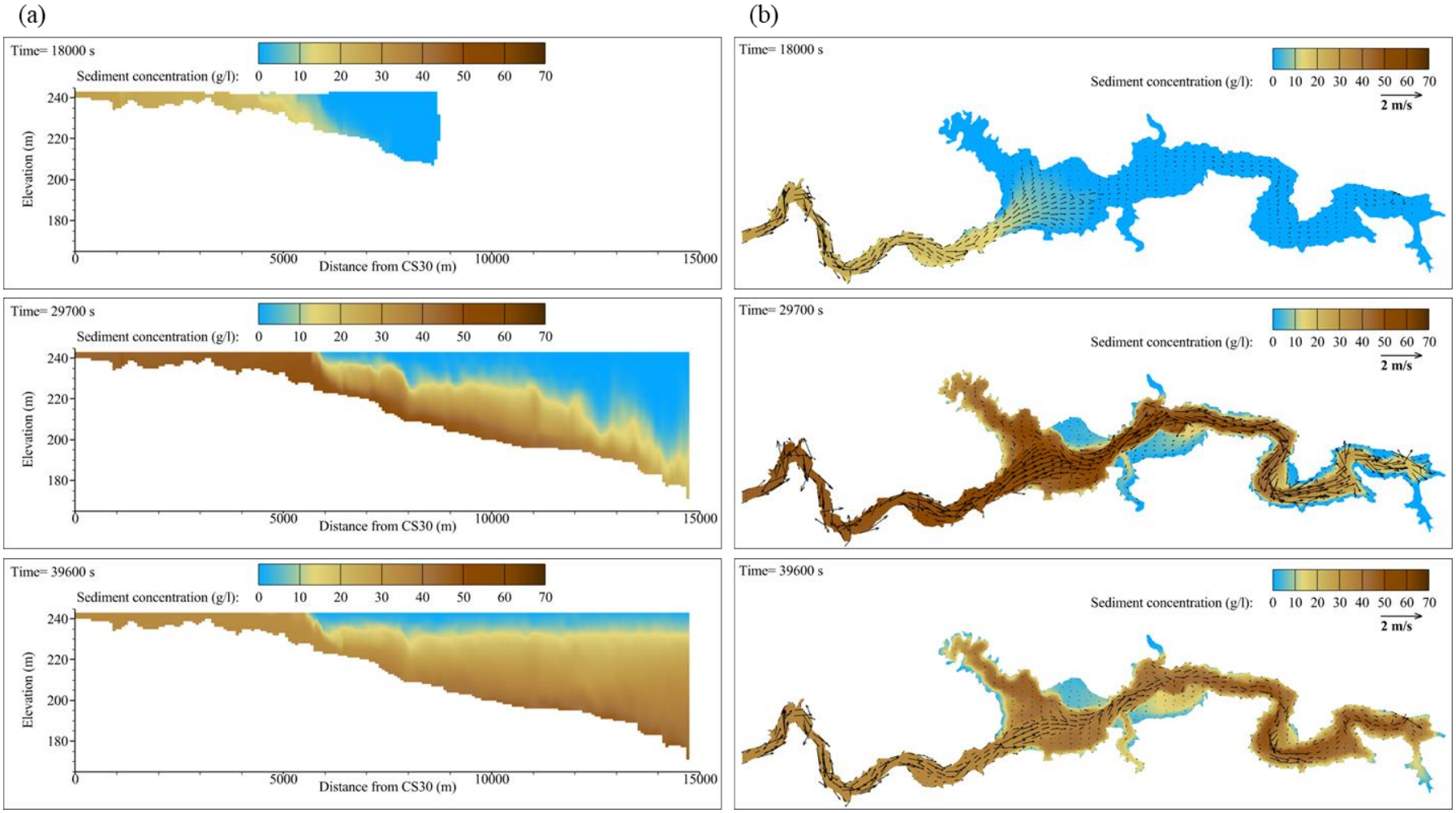

Figure C.2 The turbidity current processes from arrival at CS20, dam, and the muddy lake formed in (a) longitudinal and (b) plane view under Sc# $Q_L S_L$ with existing method.

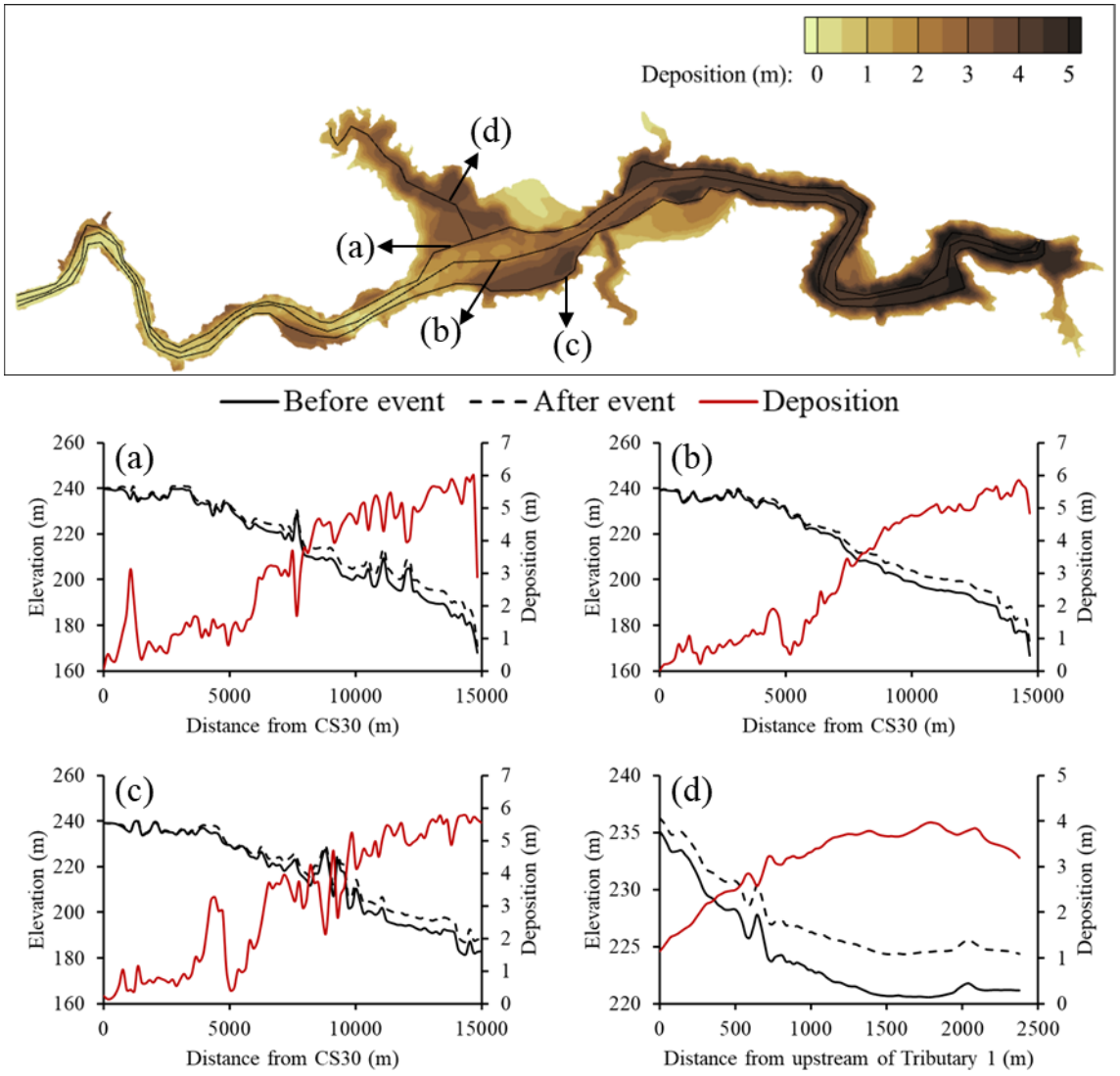

Figure C.3 The bed elevation before and after event, and deposition at (a) left, (b) middle and (c) right side of mainstream, and (d) tributary under Sc# Q_LS_L with existing method.

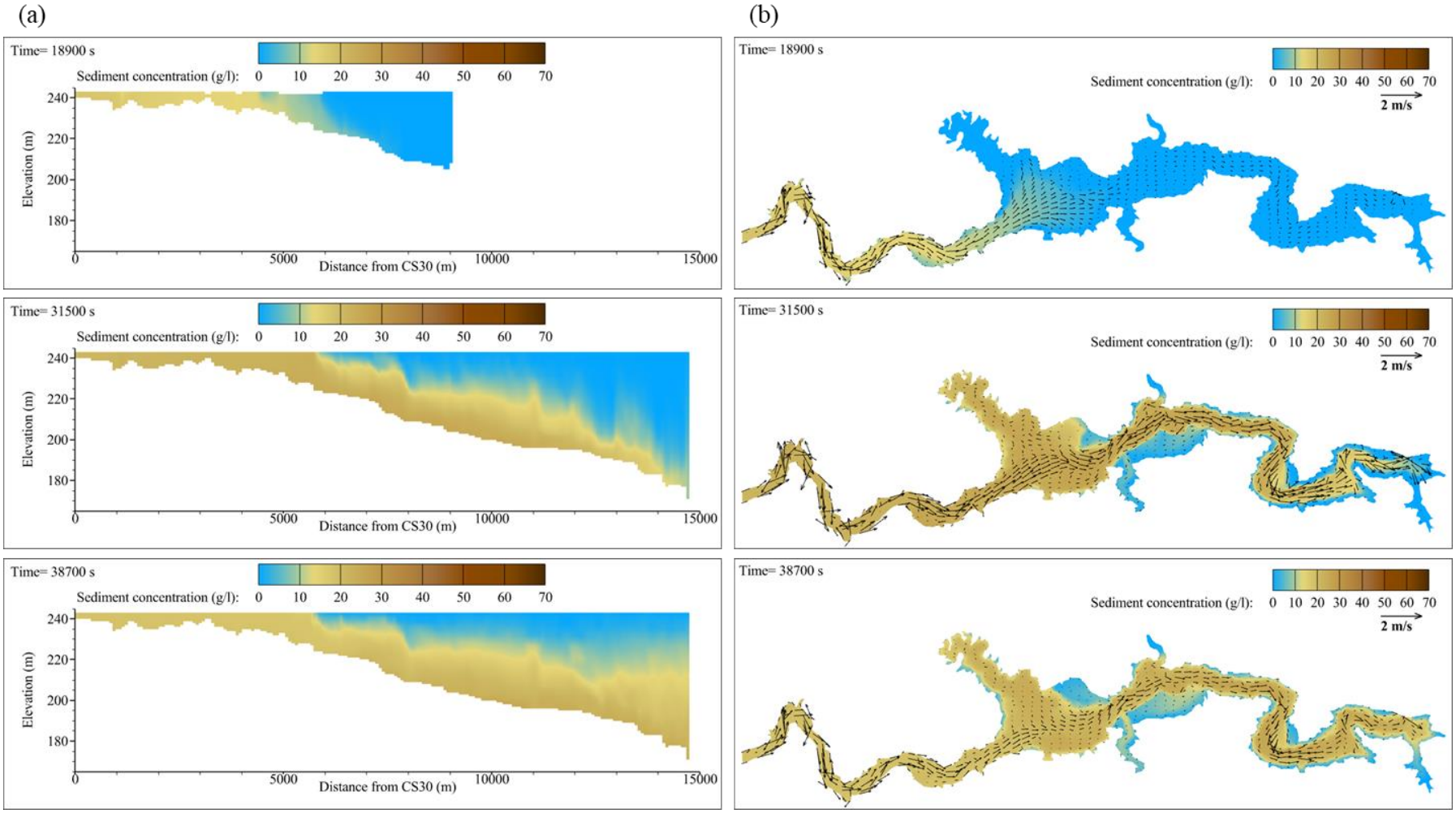

Figure C.4 The turbidity current processes from arrival at CS20, dam, and the muddy lake formed in (a) longitudinal and (b) plane view under Sc# $Q_L S_M$ with existing method.

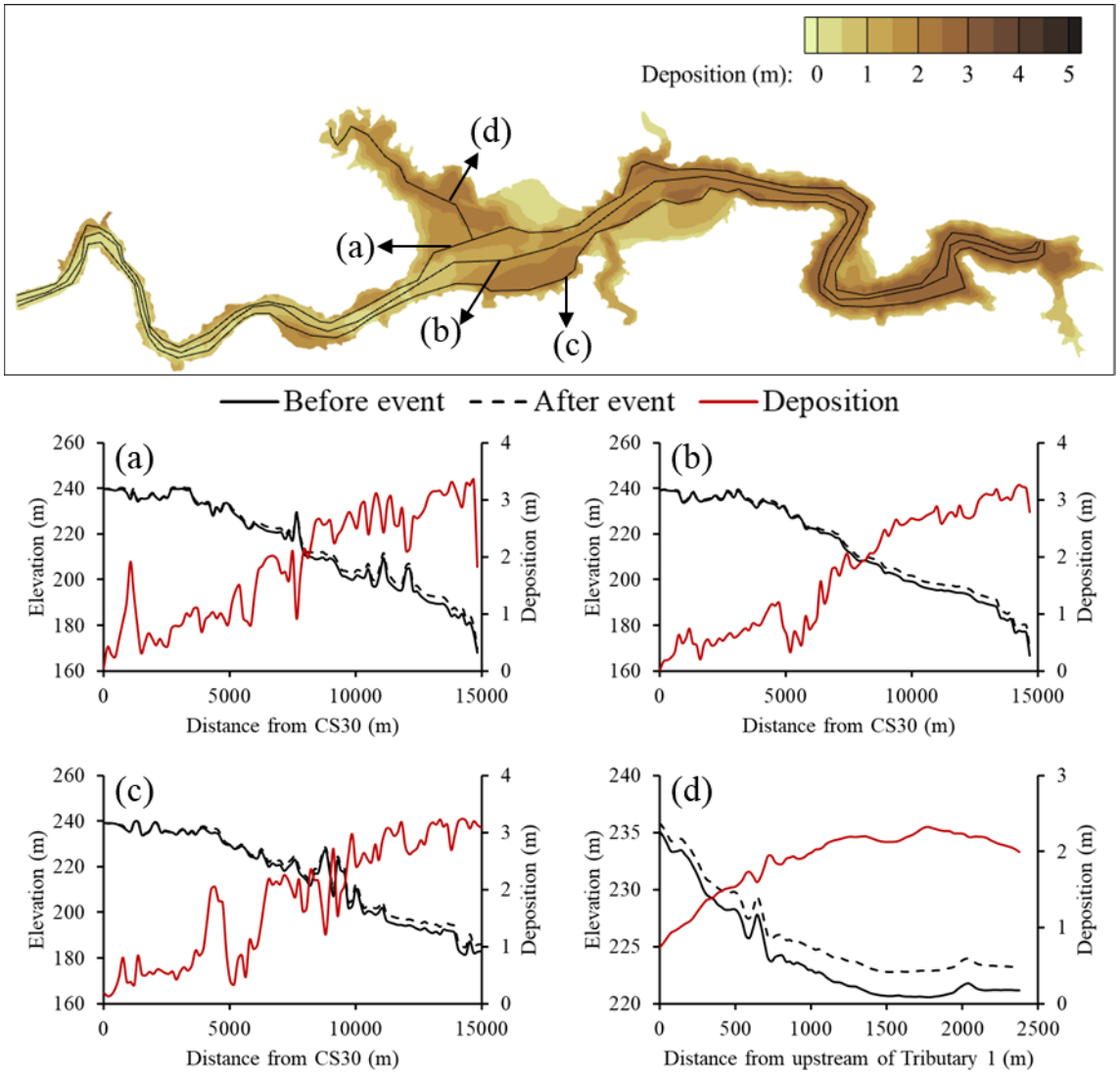

Figure C.5 The bed elevation before and after event, and deposition at (a) left, (b) middle and (c) right side of mainstream, and (d) tributary under Sc# $Q_L S_M$ with existing method.

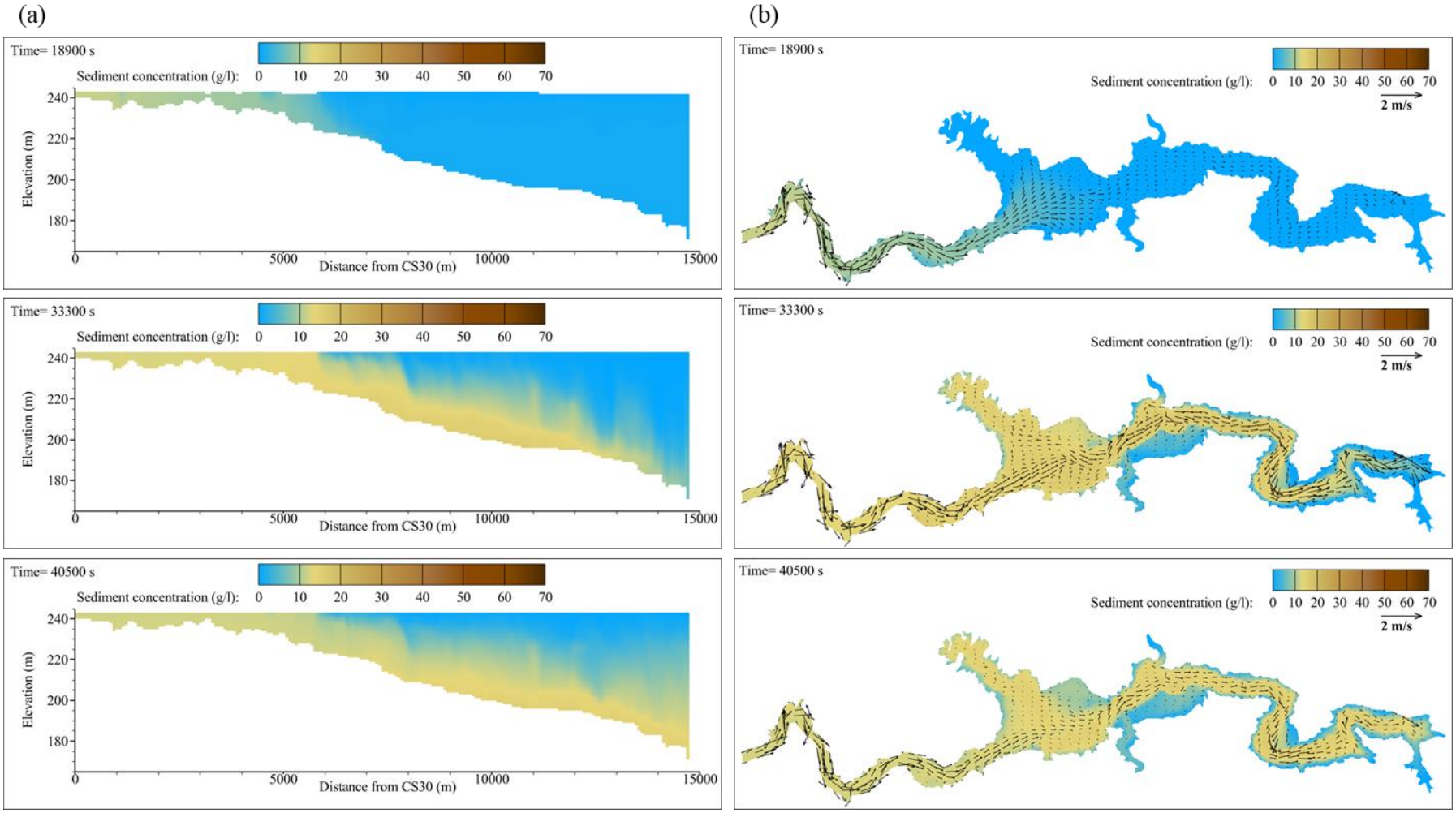

Figure C.6 The turbidity current processes from arrival at CS20, dam, and the muddy lake formed in (a) longitudinal and (b) plane view under Sc# $Q_L S_S$ with existing method.

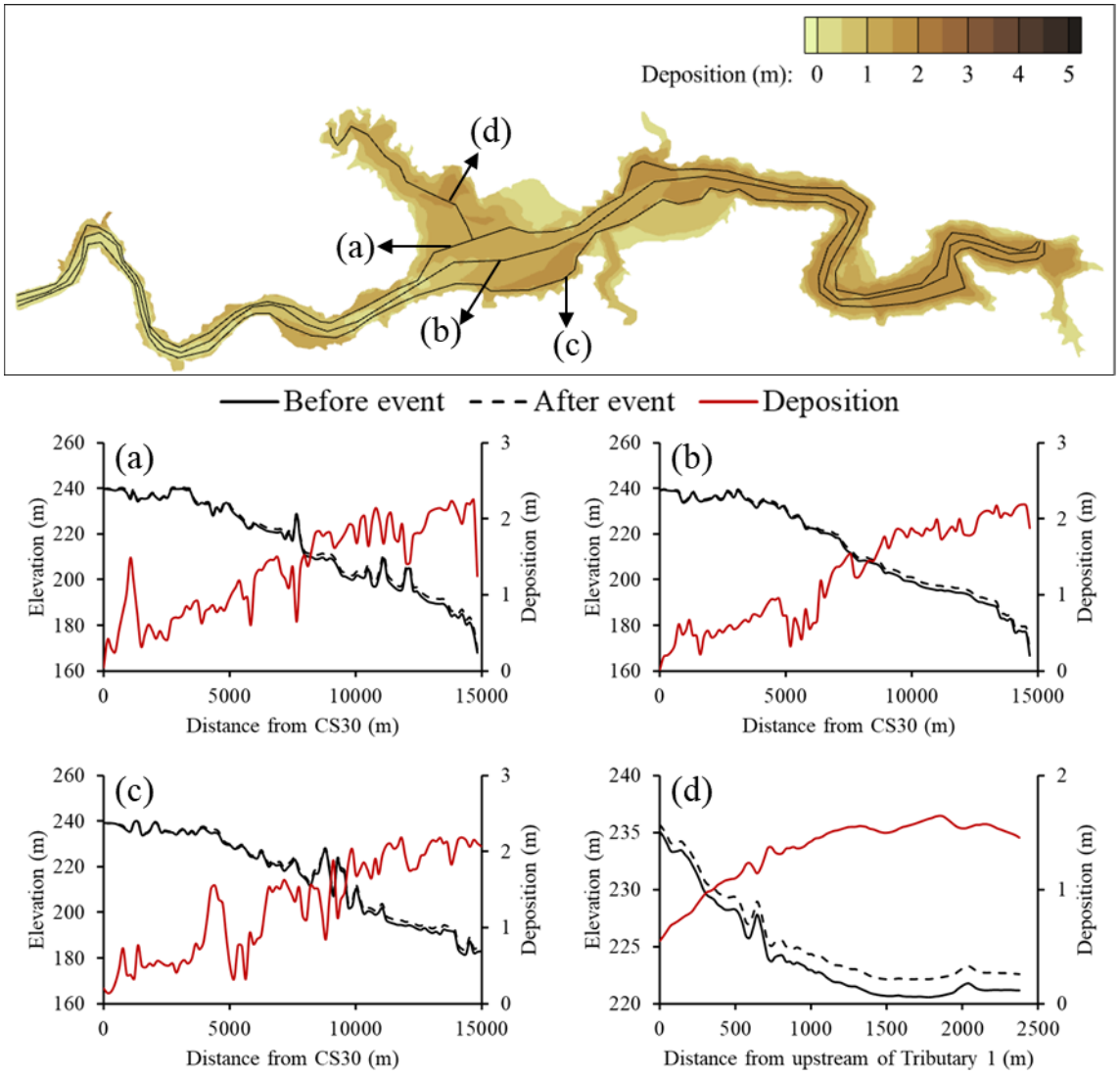

Figure C.7 The bed elevation before and after event, and deposition at (a) left, (b) middle and (c) right side of mainstream, and (d) tributary under Sc# $Q_L S_S$ with existing method.

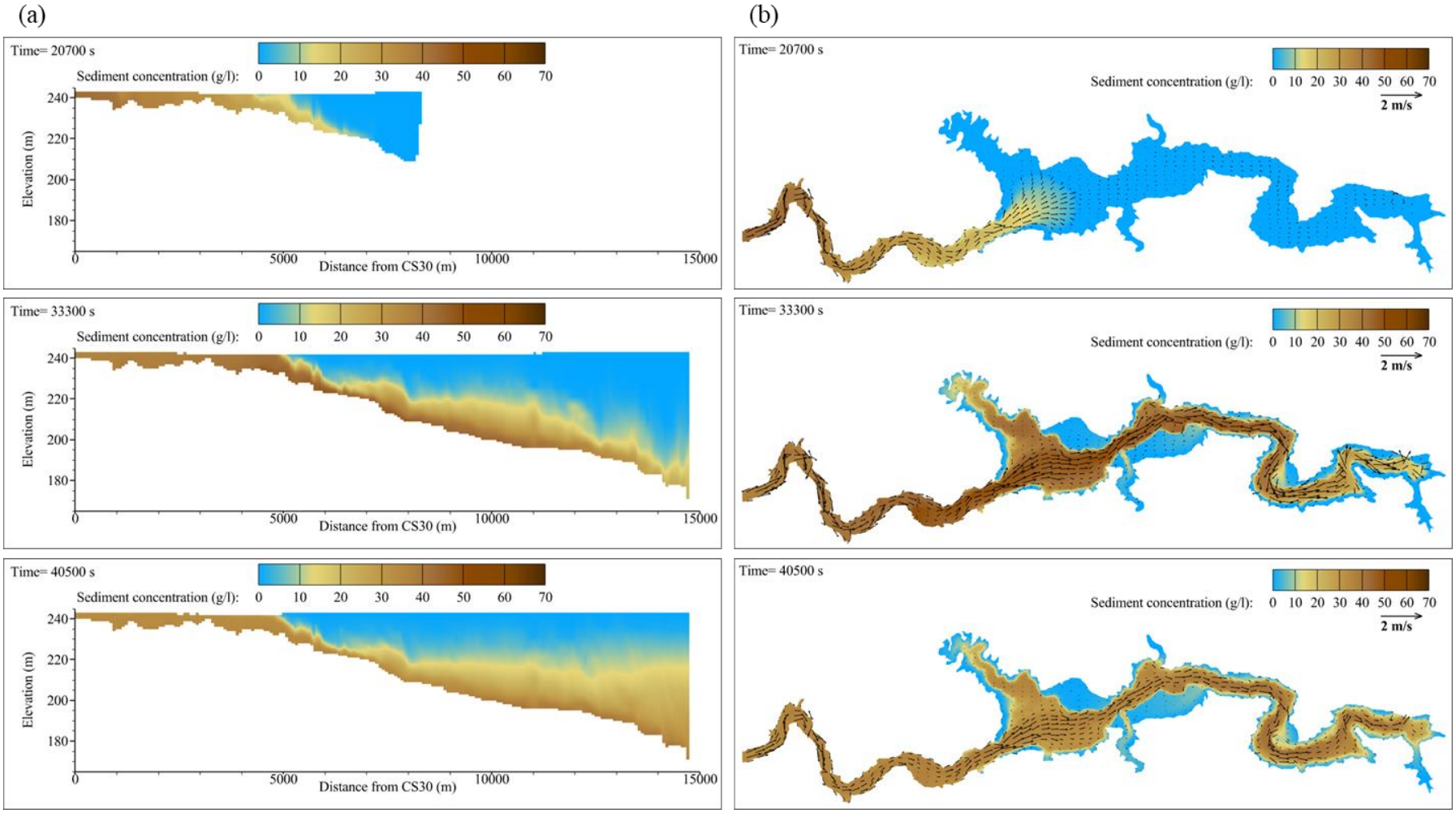

Figure C.8 The turbidity current processes from arrival at CS20, dam, and the muddy lake formed in (a) longitudinal and (b) plane view under Sc# $Q_M S_L$ with existing method.

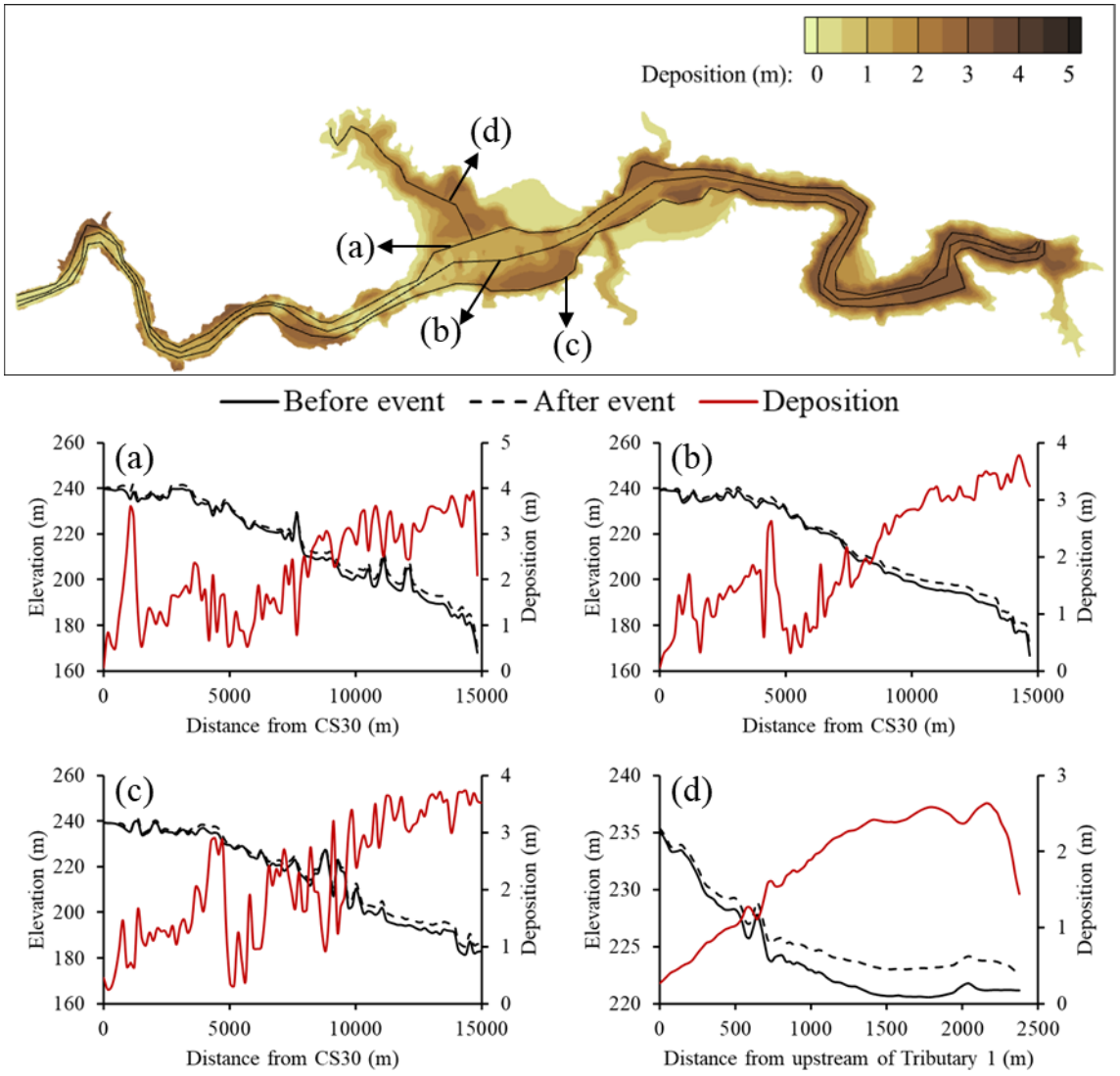

Figure C.9 The bed elevation before and after event, and deposition at (a) left, (b) middle and (c) right side of mainstream, and (d) tributary under Sc# $Q_M S_L$ with existing method.

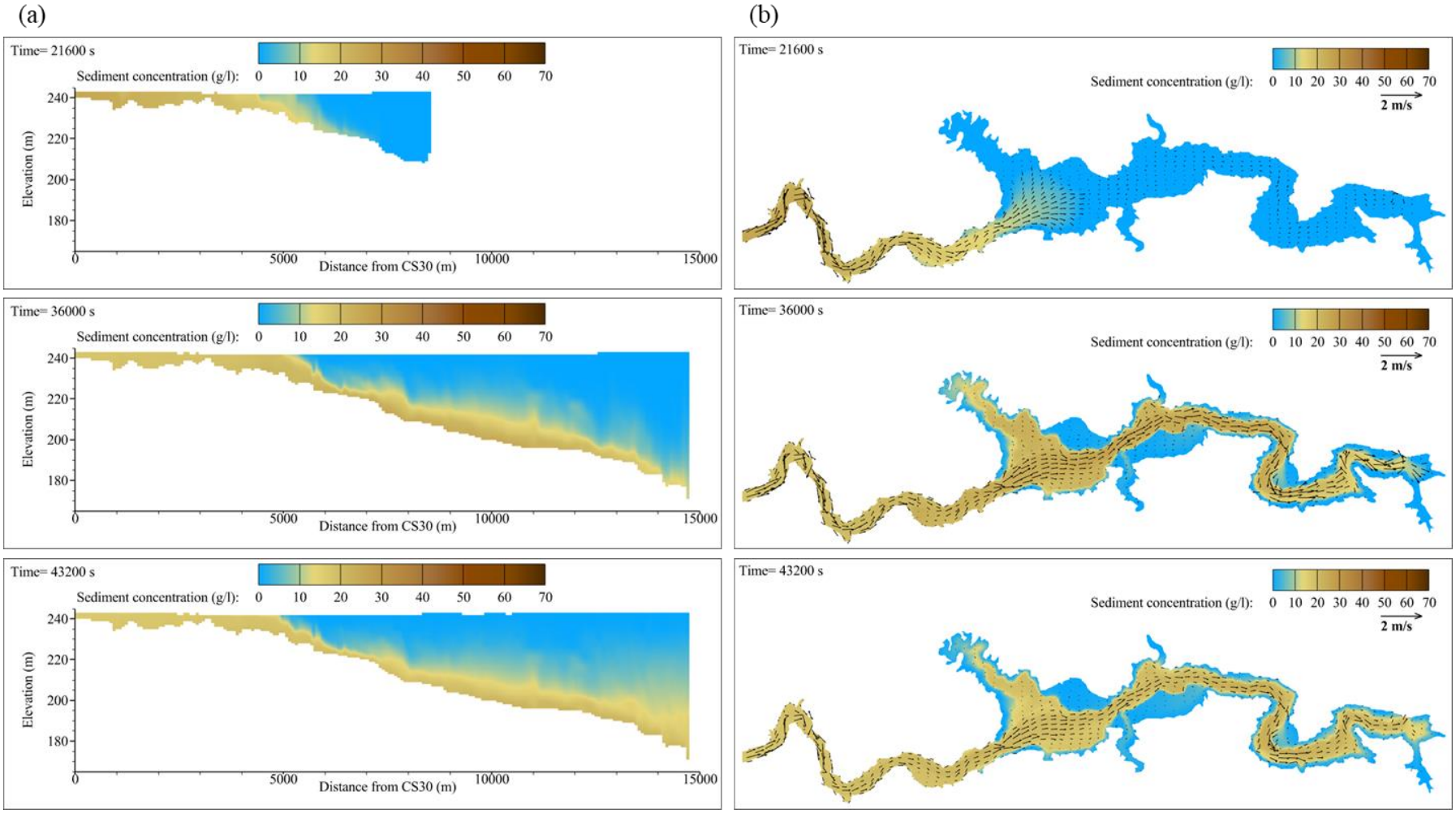

Figure C.10 The turbidity current processes from arrival at CS20, dam, and the muddy lake formed in (a) longitudinal and (b) plane view under Sc# $Q_M S_M$ with existing method.

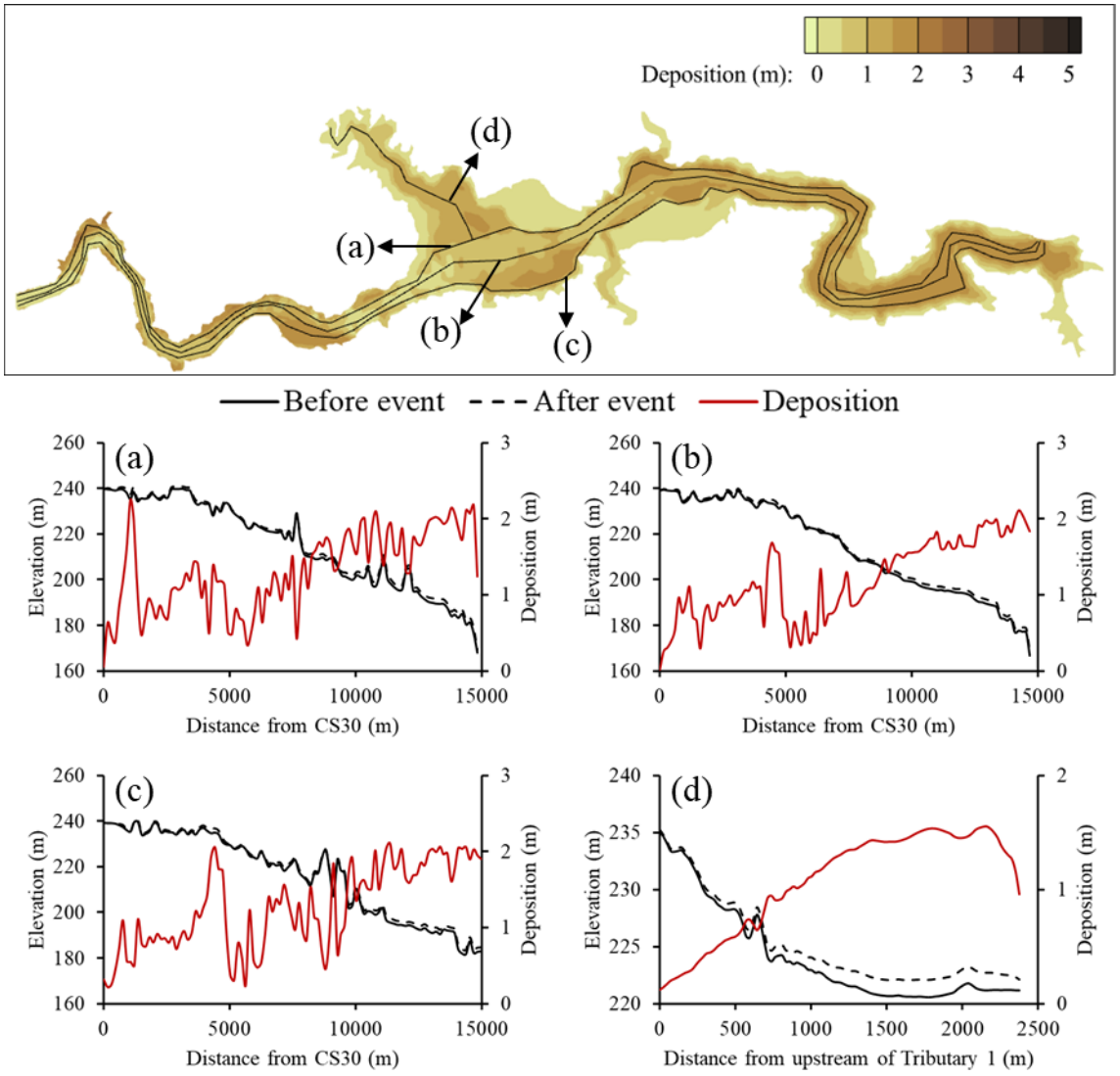

Figure C.11 The bed elevation before and after event, and deposition at (a) left, (b) middle and (c) right side of mainstream, and (d) tributary under Sc# Q_MS_M with existing method.

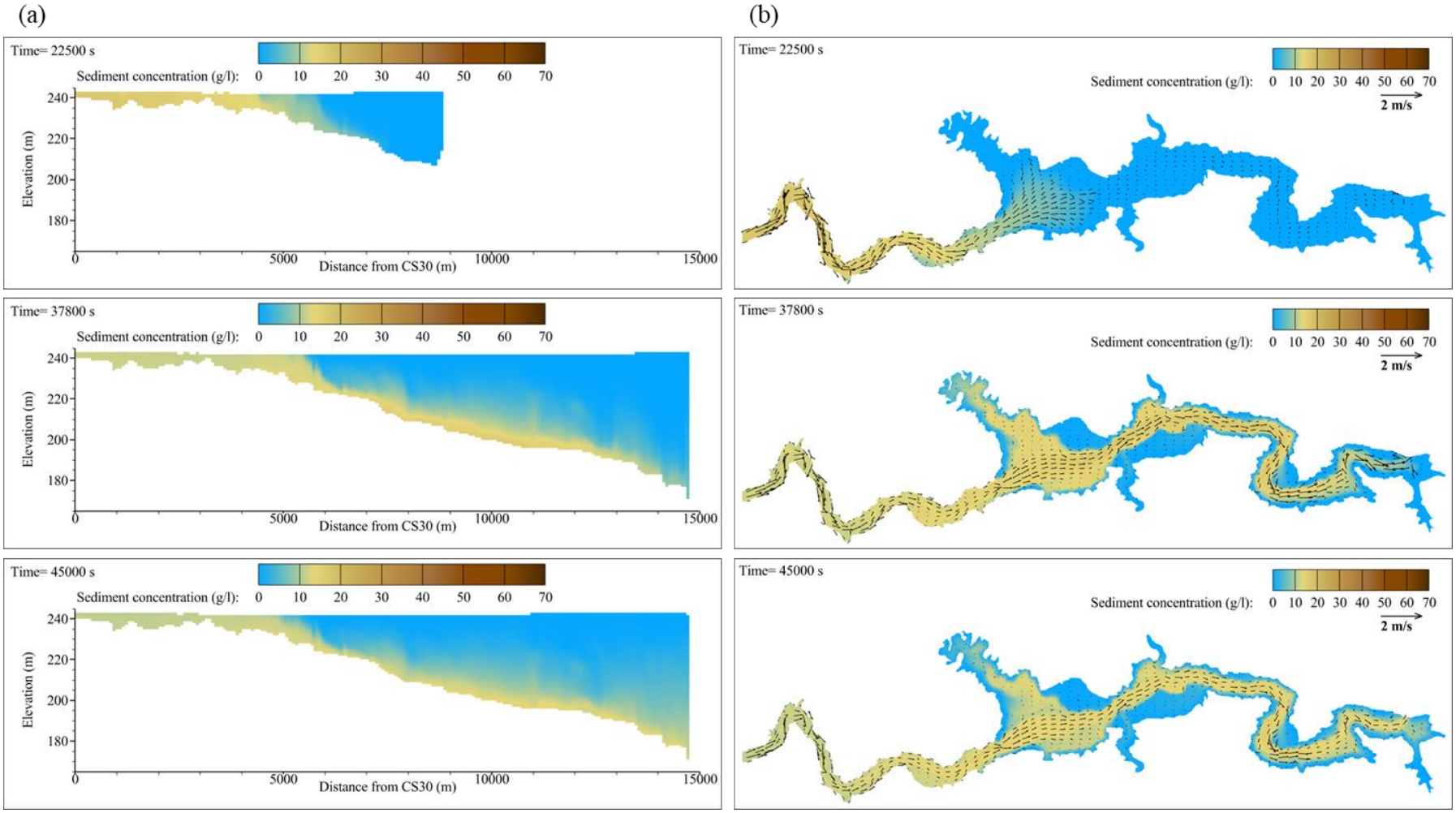

Figure C.12 The turbidity current processes from arrival at CS20, dam, and the muddy lake formed in (a) longitudinal and (b) plane view under Sc# $Q_M S_S$ with existing method.

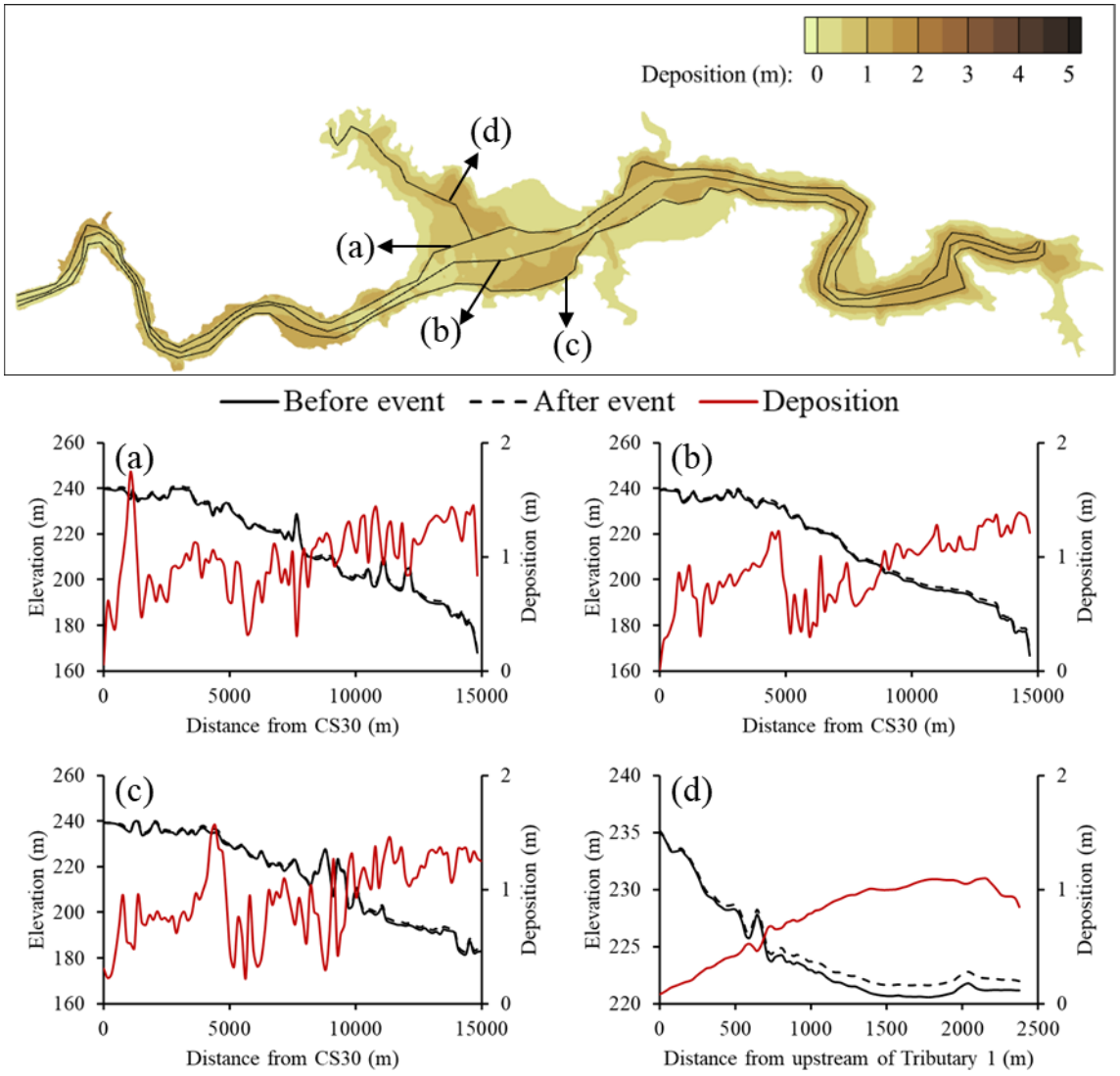

Figure C.13 The bed elevation before and after event, and deposition at (a) left, (b) middle and (c) right side of mainstream, and (d) tributary under Sc# $Q_M S_S$ with existing method.

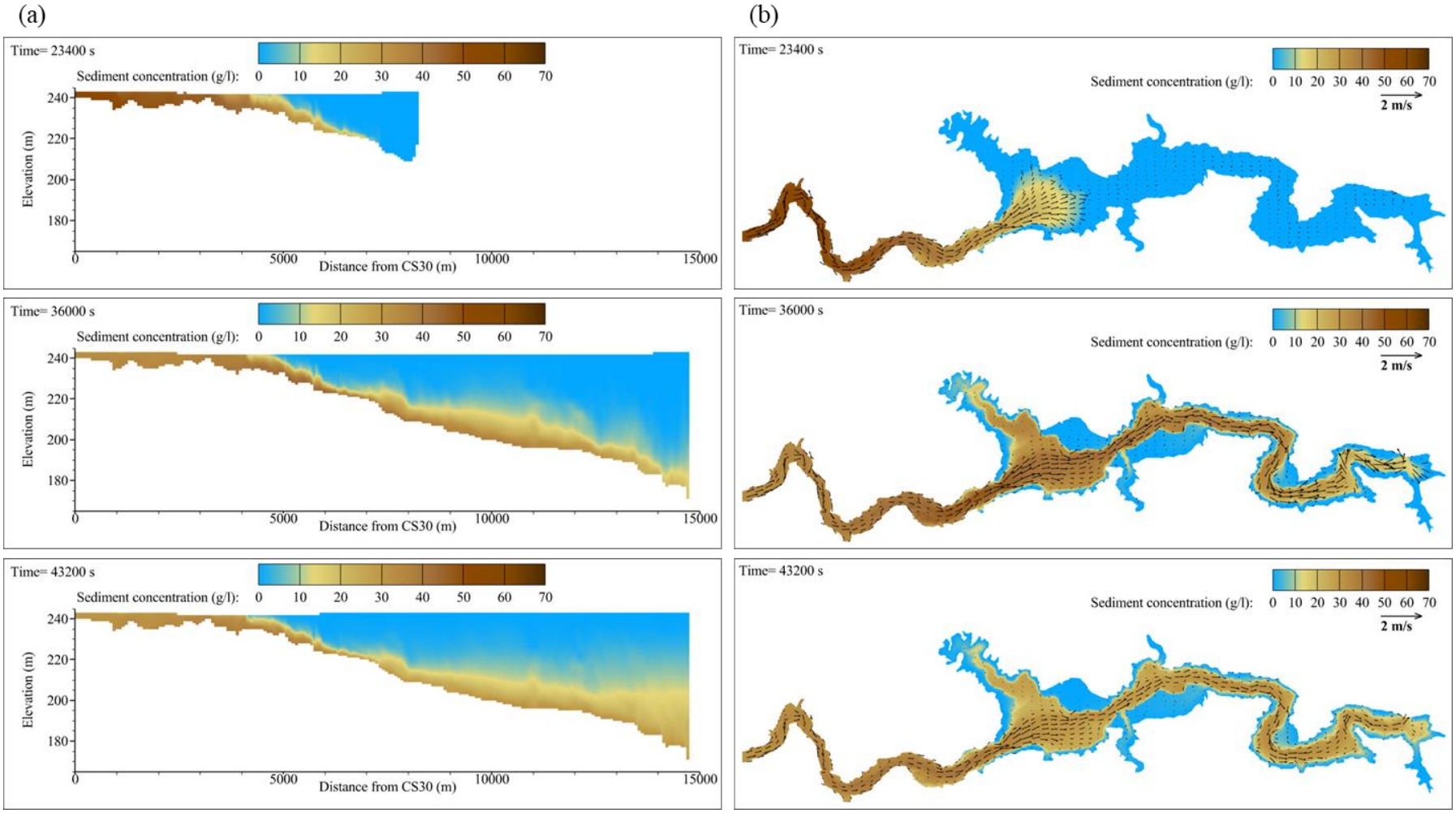

Figure C.14 The turbidity current processes from arrival at CS20, dam, and the muddy lake formed in (a) longitudinal and (b) plane view under Sc# $Q_S S_L$ with existing method.

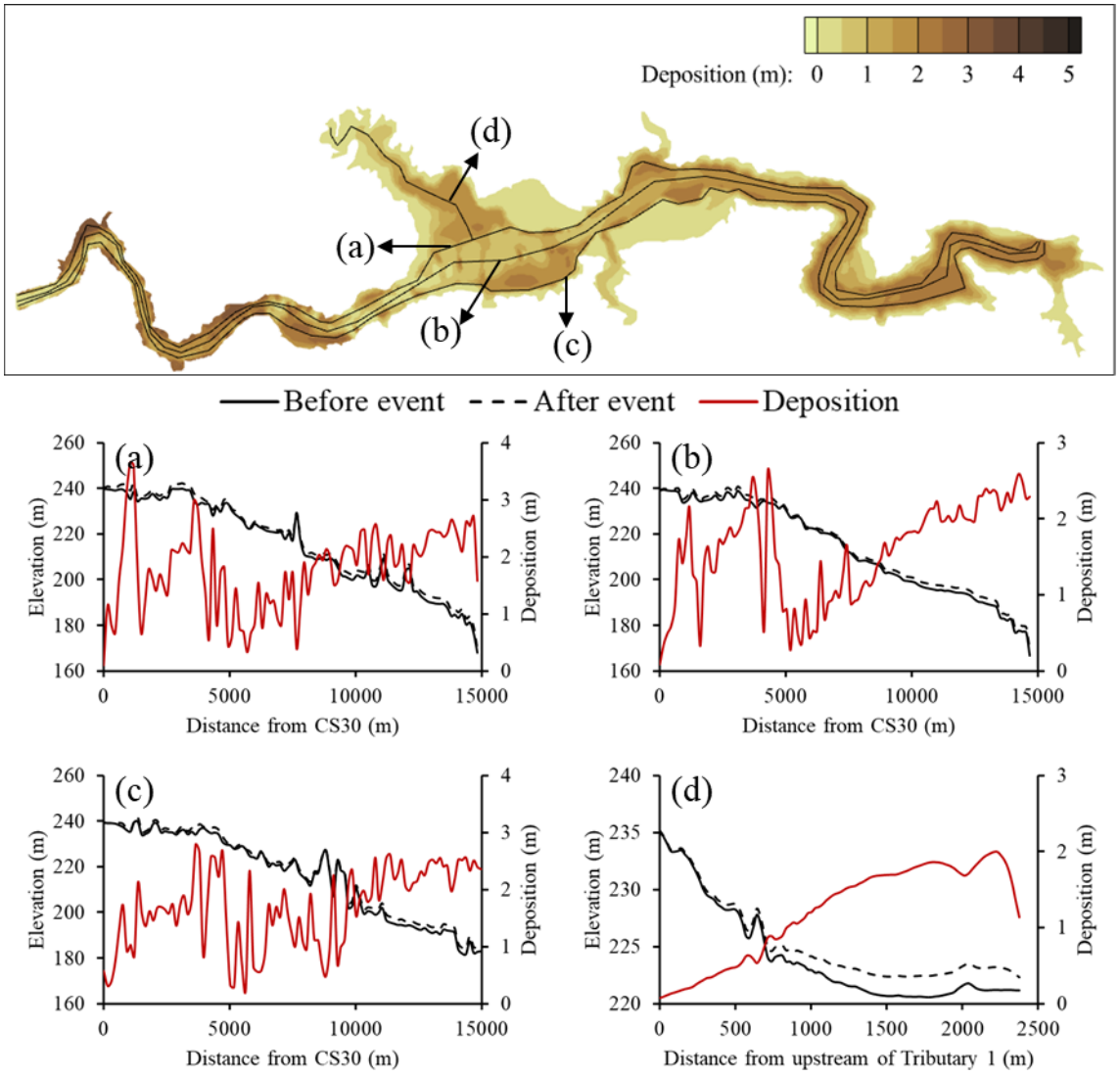

Figure C.15 The bed elevation before and after event, and deposition at (a) left, (b) middle and (c) right side of mainstream, and (d) tributary under Sc# $Q_S S_L$ with existing method.

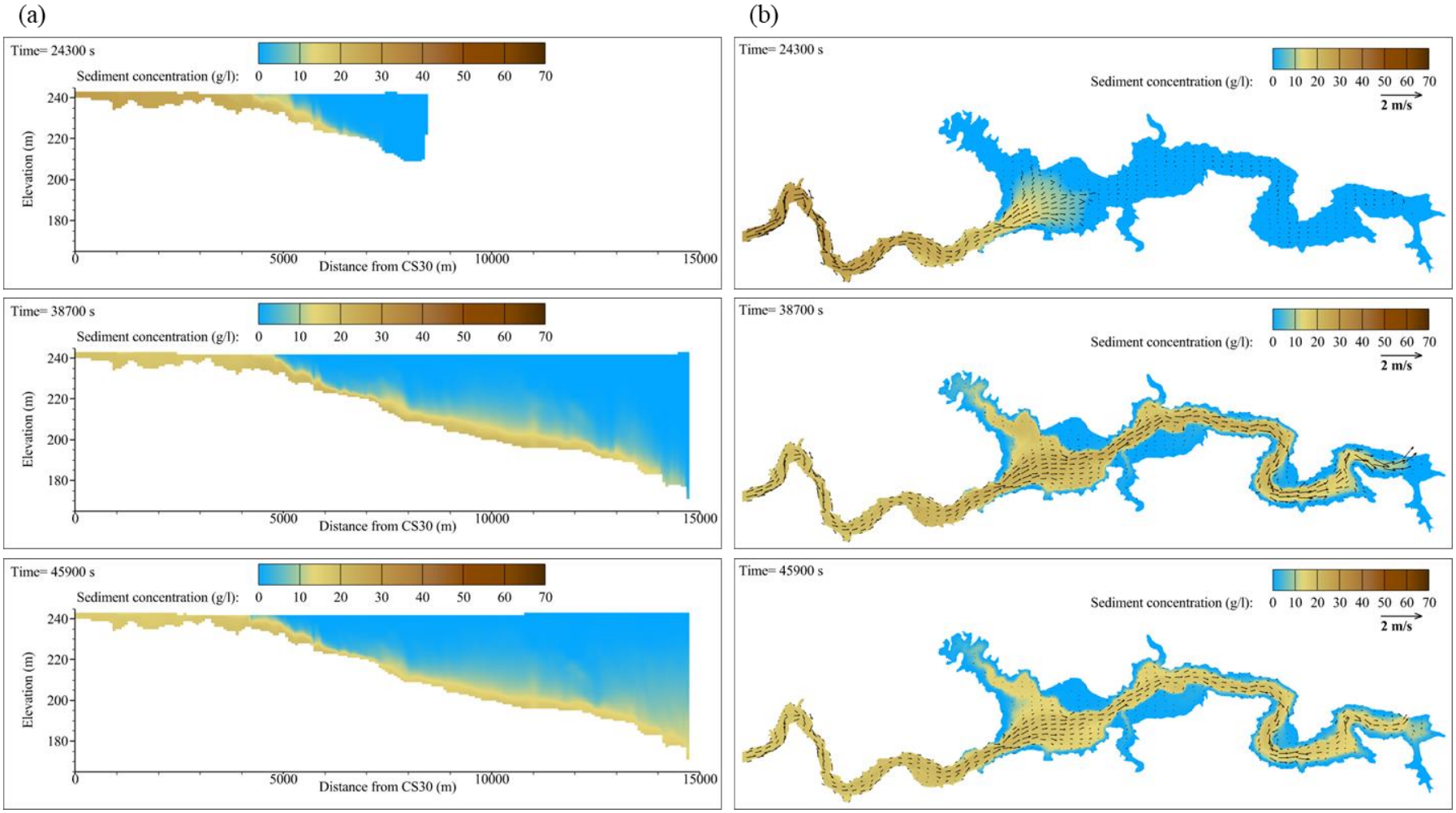

Figure C.16 The turbidity current processes from arrival at CS20, dam, and the muddy lake formed in (a) longitudinal and (b) plane view under Sc# $Q_S S_M$ with existing method.

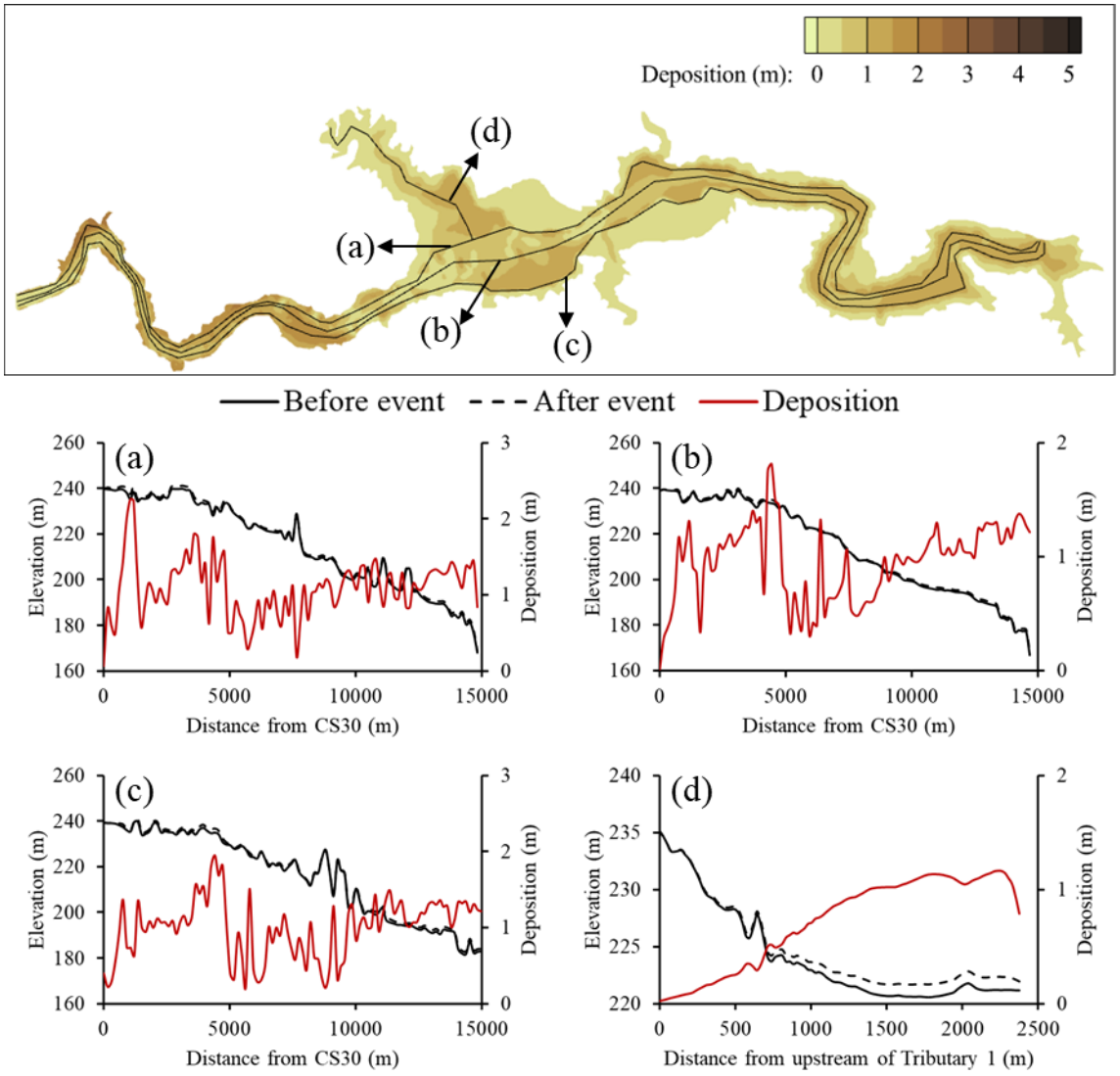

Figure C.17 The bed elevation before and after event, and deposition at (a) left, (b) middle and (c) right side of mainstream, and (d) tributary under Sc# $Q_S S_M$ with existing method.

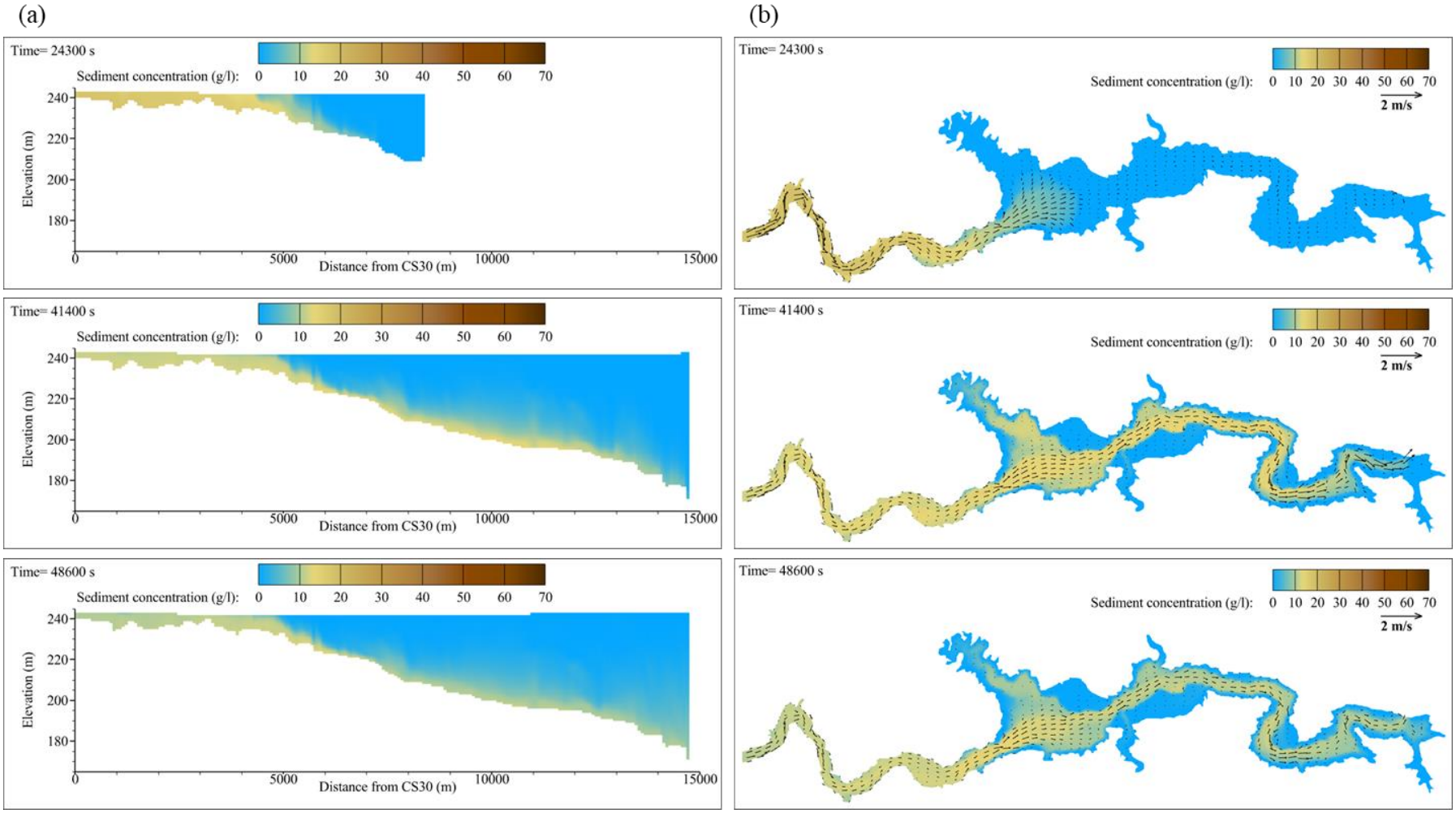

Figure C.18 The turbidity current processes from arrival at CS20, dam, and the muddy lake formed in (a) longitudinal and (b) plane view under Sc# $Q_S S_S$ with existing method.

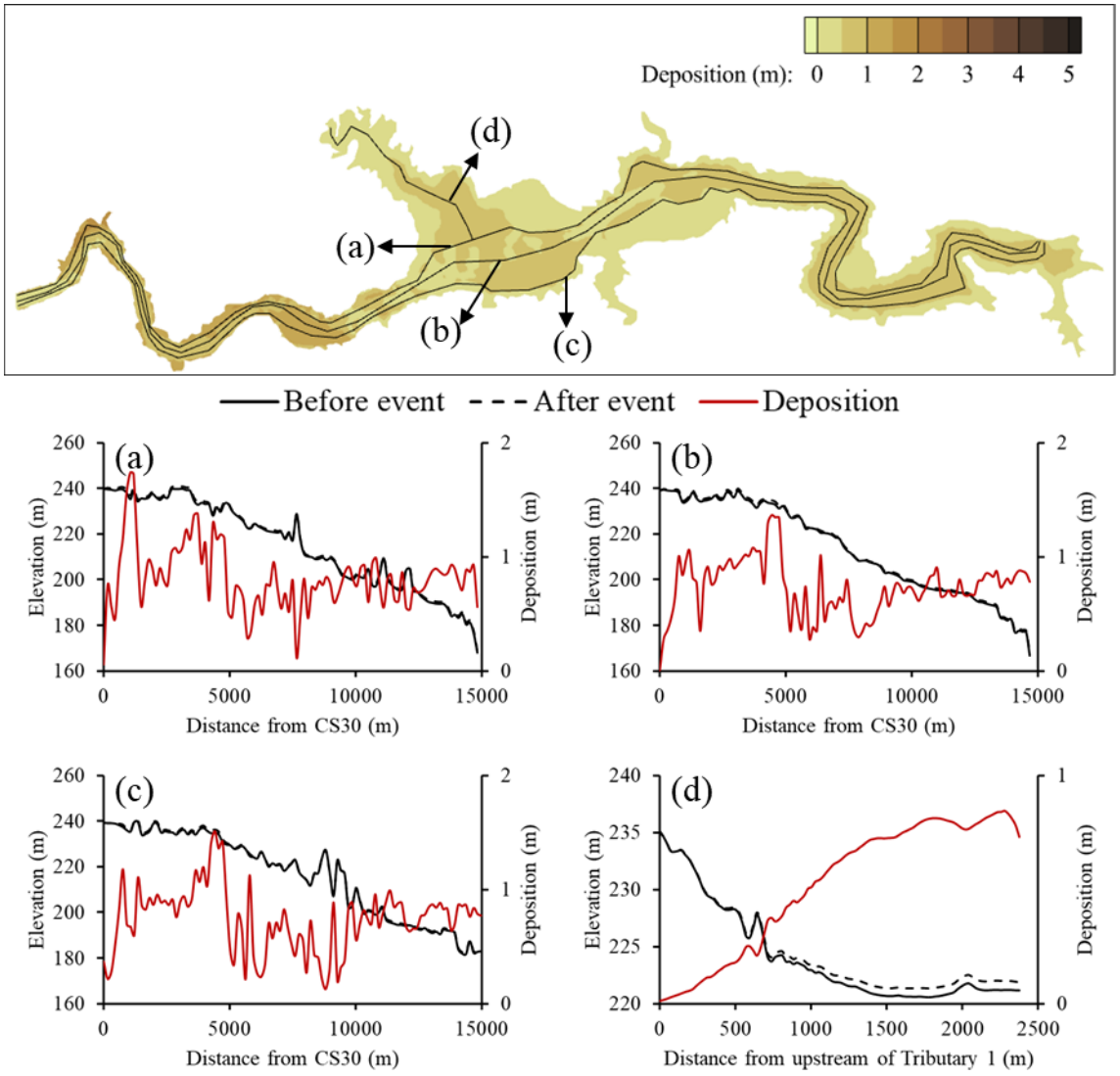

Figure C.19 The bed elevation before and after event, and deposition at (a) left, (b) middle and (c) right side of mainstream, and (d) tributary under Sc# $Q_S S_S$ with existing method.

C.2 Soft methods

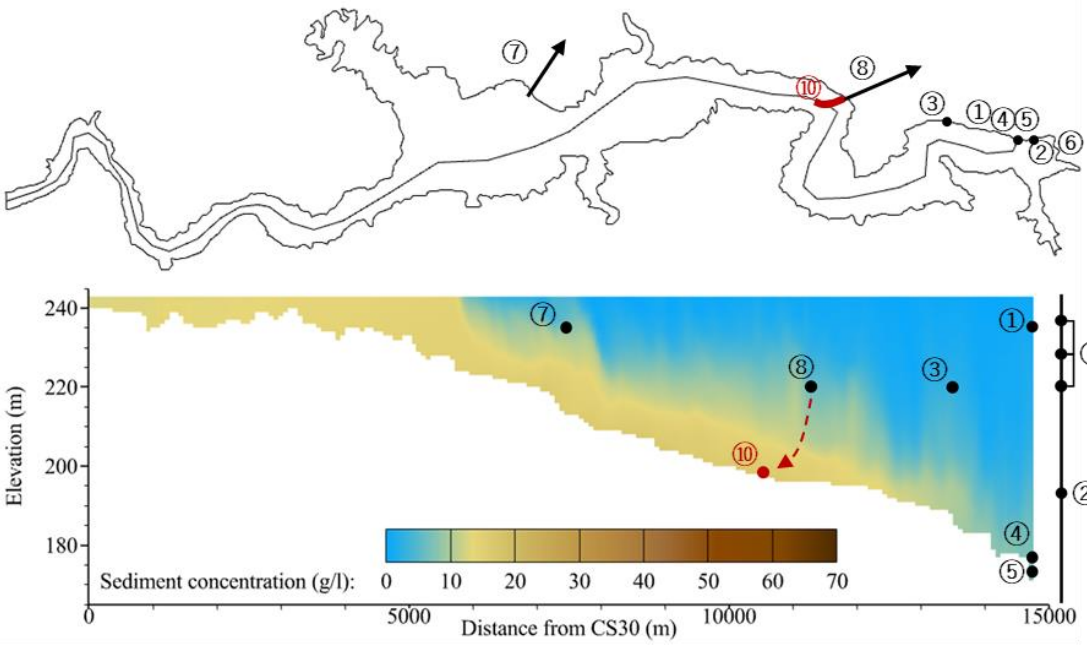

①Spillway (SP)
②Spillway tunnel (ST)
③Shihmen canal intake (SCI)
④Power plant intake and Venting tunnel (PPI and VT)
⑤Permanent river outlet (PRO)
⑥Water supply intake
⑦Amuping sediment bypass tunnel (Amu_SBT)
⑧Dawangping sediment bypass tunnel (Daw_SBT) ---------- ⑩ Elephant trunk from Daw_SBT (ELEP)

Operating sequence: ⑤→④→③→⑩→②→⑦→①

Figure C.20 Operated outlets and the operating sequence under soft methods.

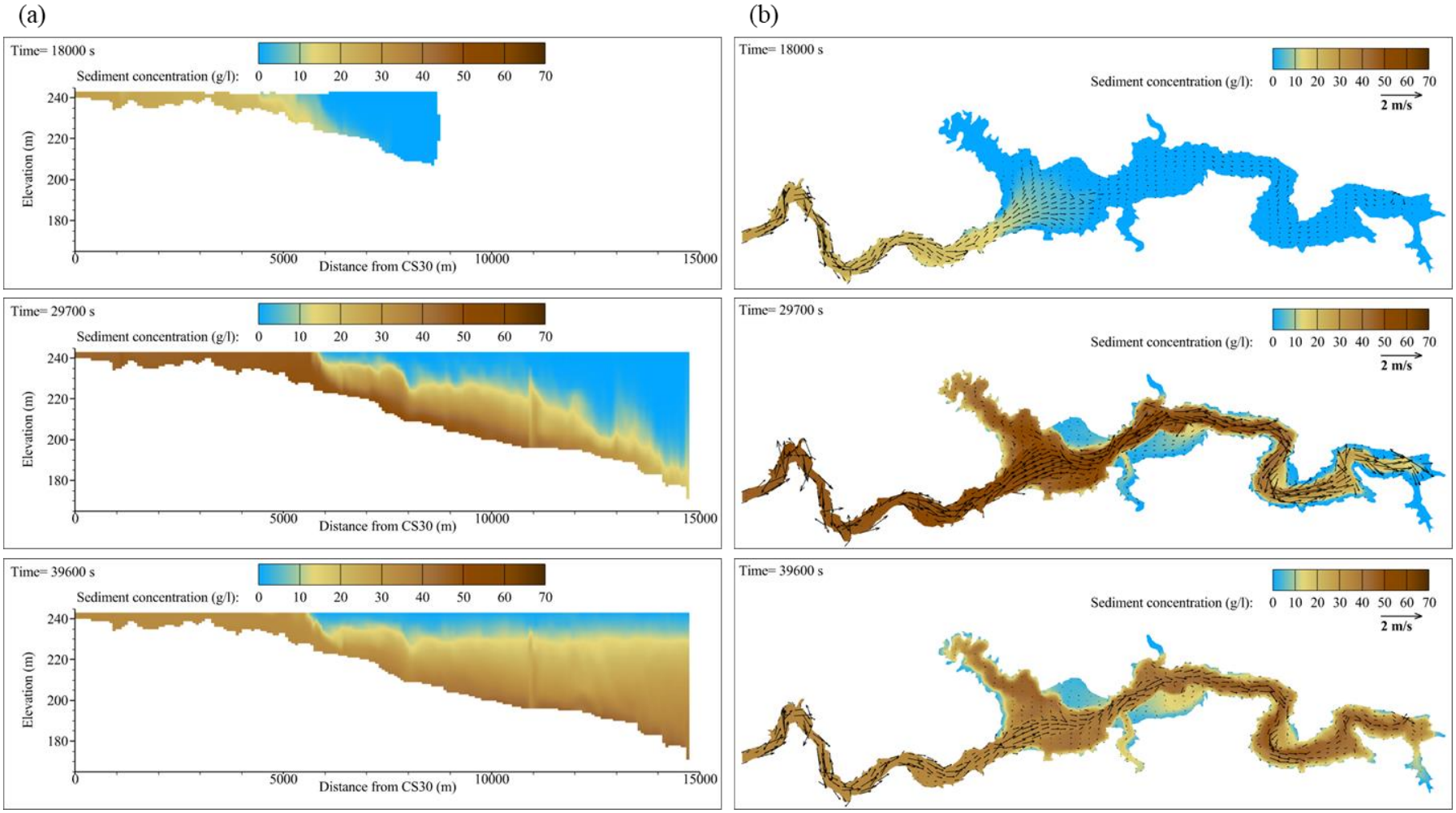

Figure C.21 The turbidity current processes from arrival at CS20, dam, and the muddy lake formed in (a) longitudinal and (b) plane view under Sc# Q_LS_L with soft methods.

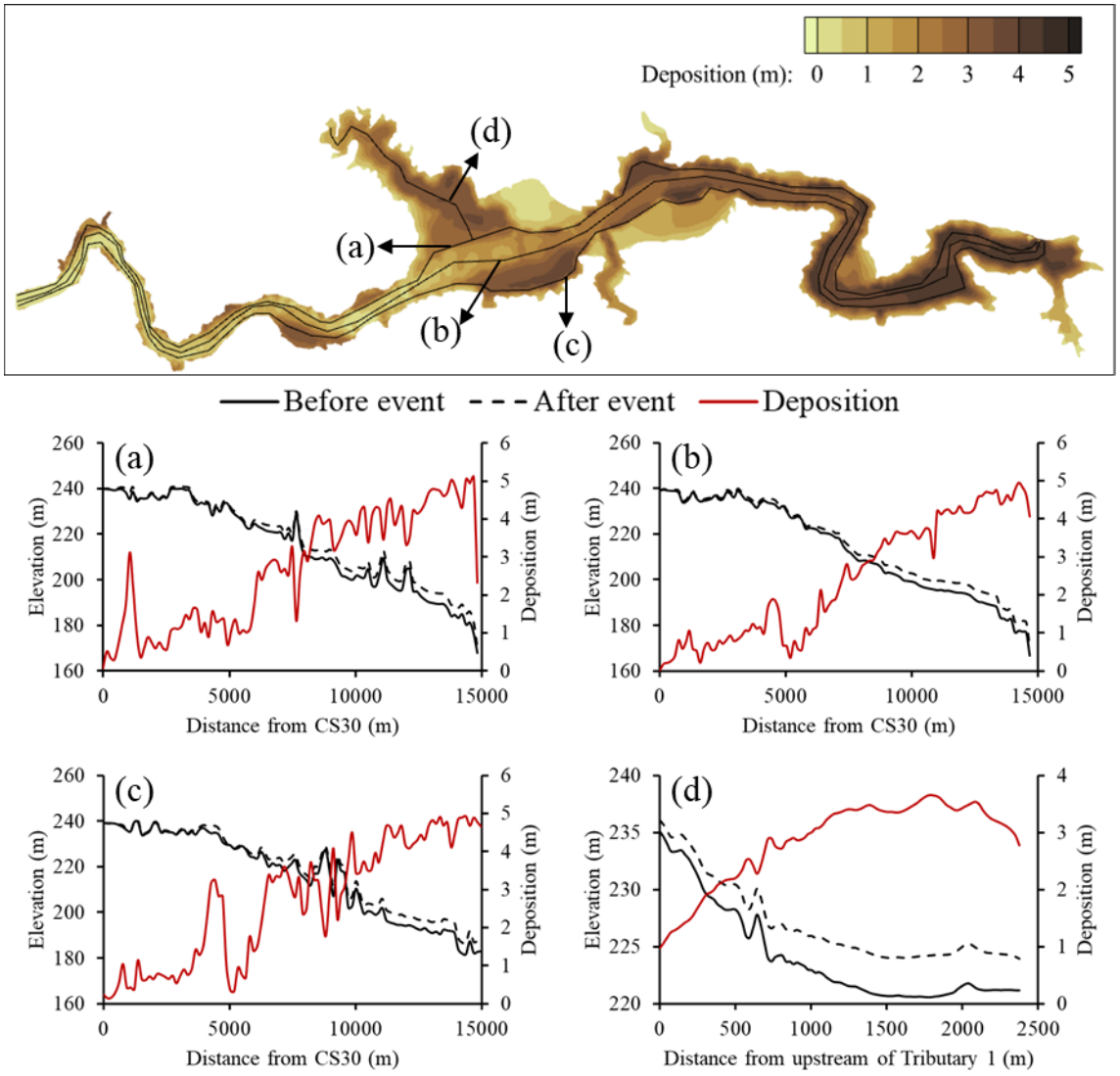

Figure C.22 The bed elevation before and after event, and deposition at (a) left, (b) middle and (c) right side of mainstream, and (d) tributary under Sc# Q_LS_L with soft methods.

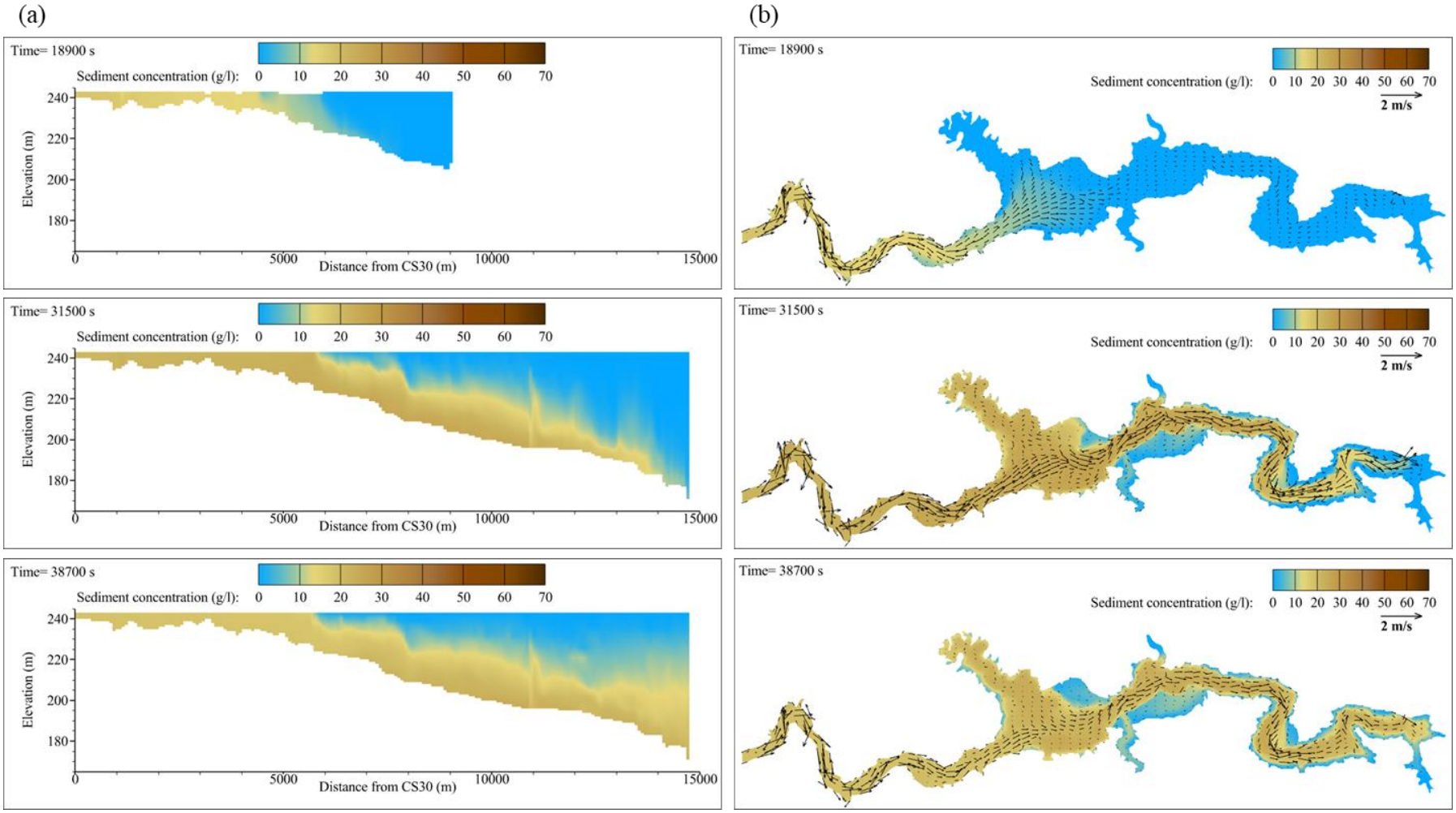

Figure C.23 The turbidity current processes from arrival at CS20, dam, and the muddy lake formed in (a) longitudinal and (b) plane view under Sc# $Q_L S_M$ with soft methods.

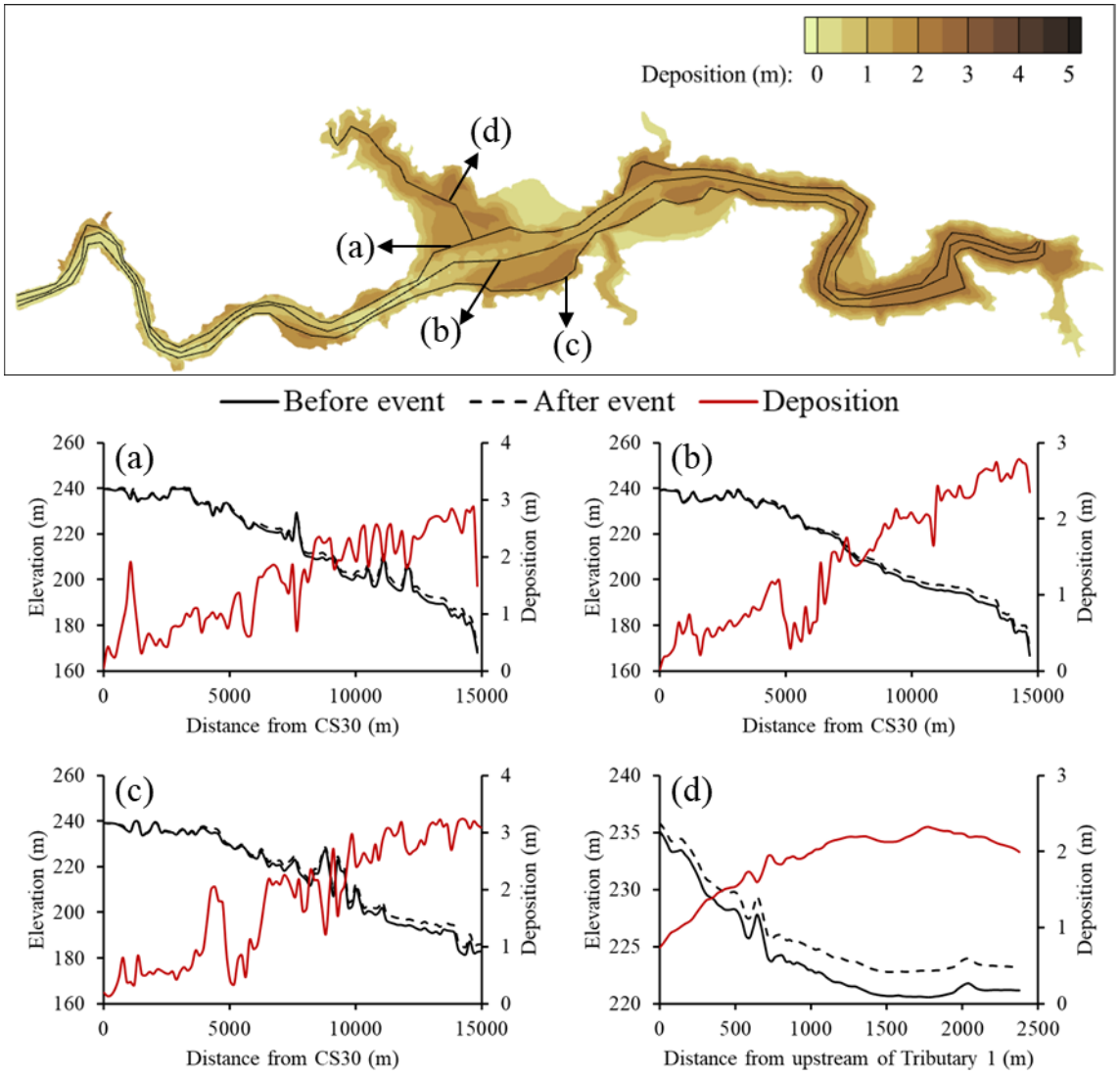

Figure C.24 The bed elevation before and after event, and deposition at (a) left, (b) middle and (c) right side of mainstream, and (d) tributary under Sc# $Q_L S_M$ with soft methods.

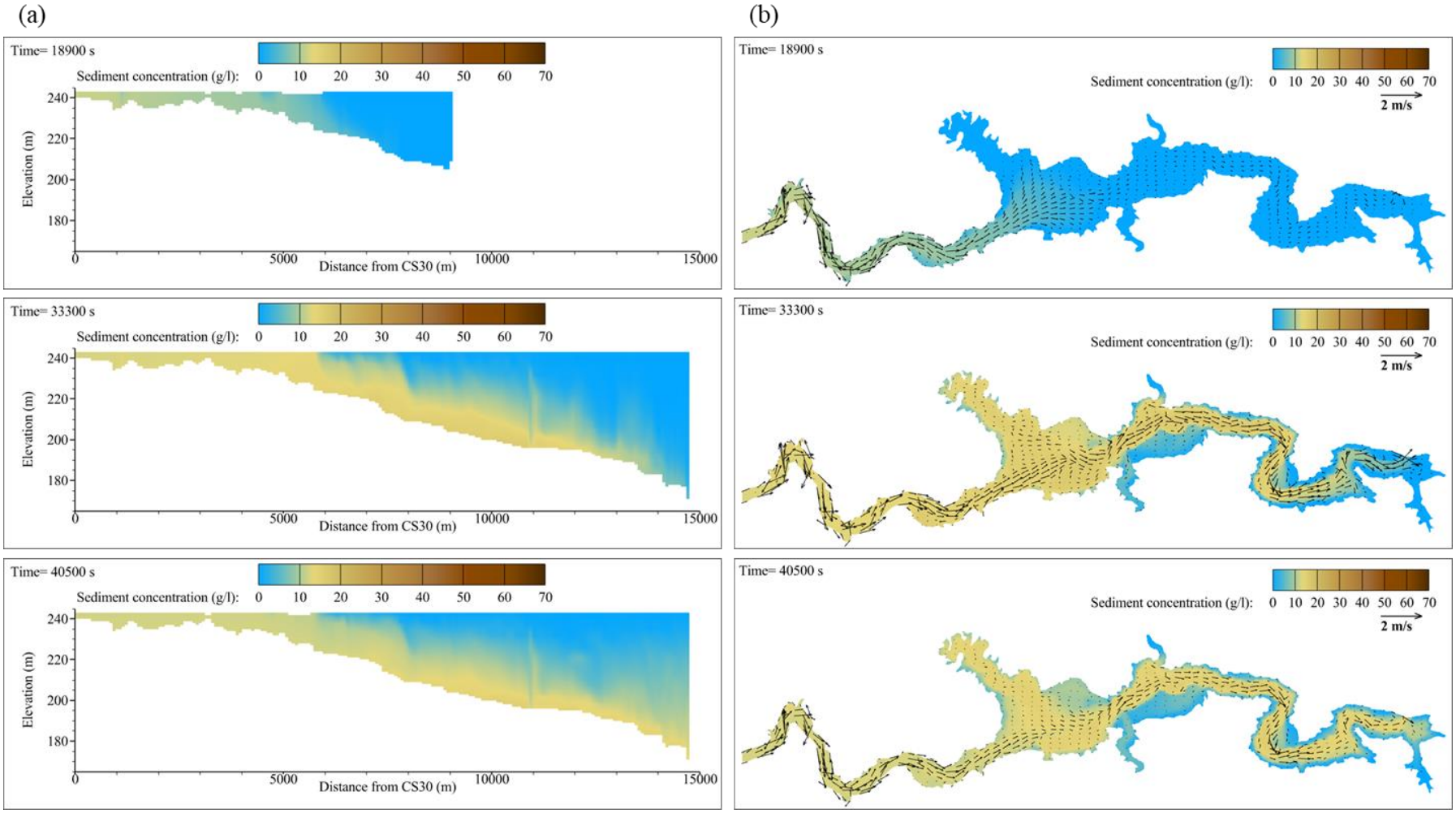

Figure C.25 The turbidity current processes from arrival at CS20, dam, and the muddy lake formed in (a) longitudinal and (b) plane view under Sc# $Q_L S_S$ with soft methods.

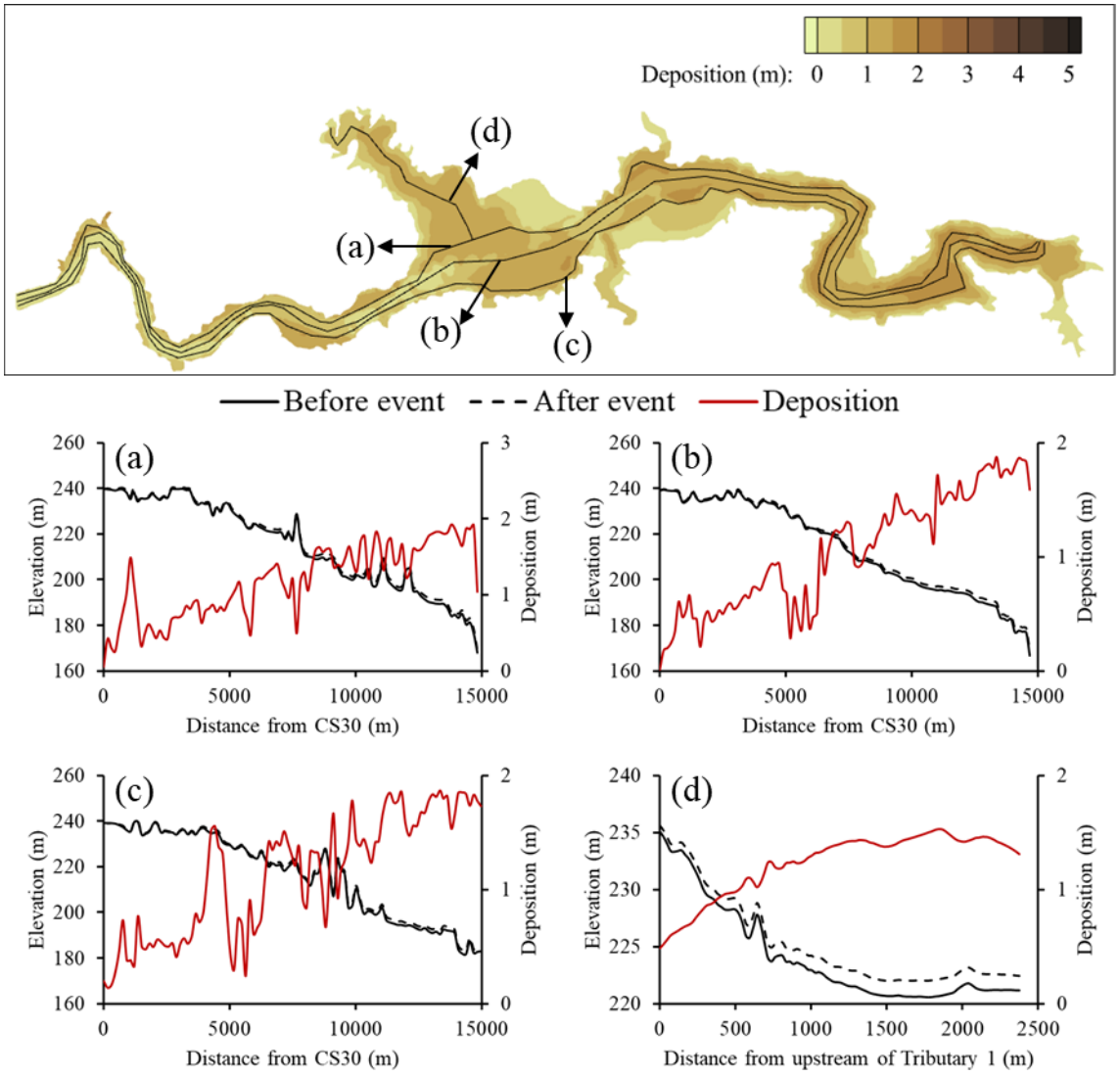

Figure C.26 The bed elevation before and after event, and deposition at (a) left, (b) middle and (c) right side of mainstream, and (d) tributary under Sc# $Q_L S_S$ with soft methods.

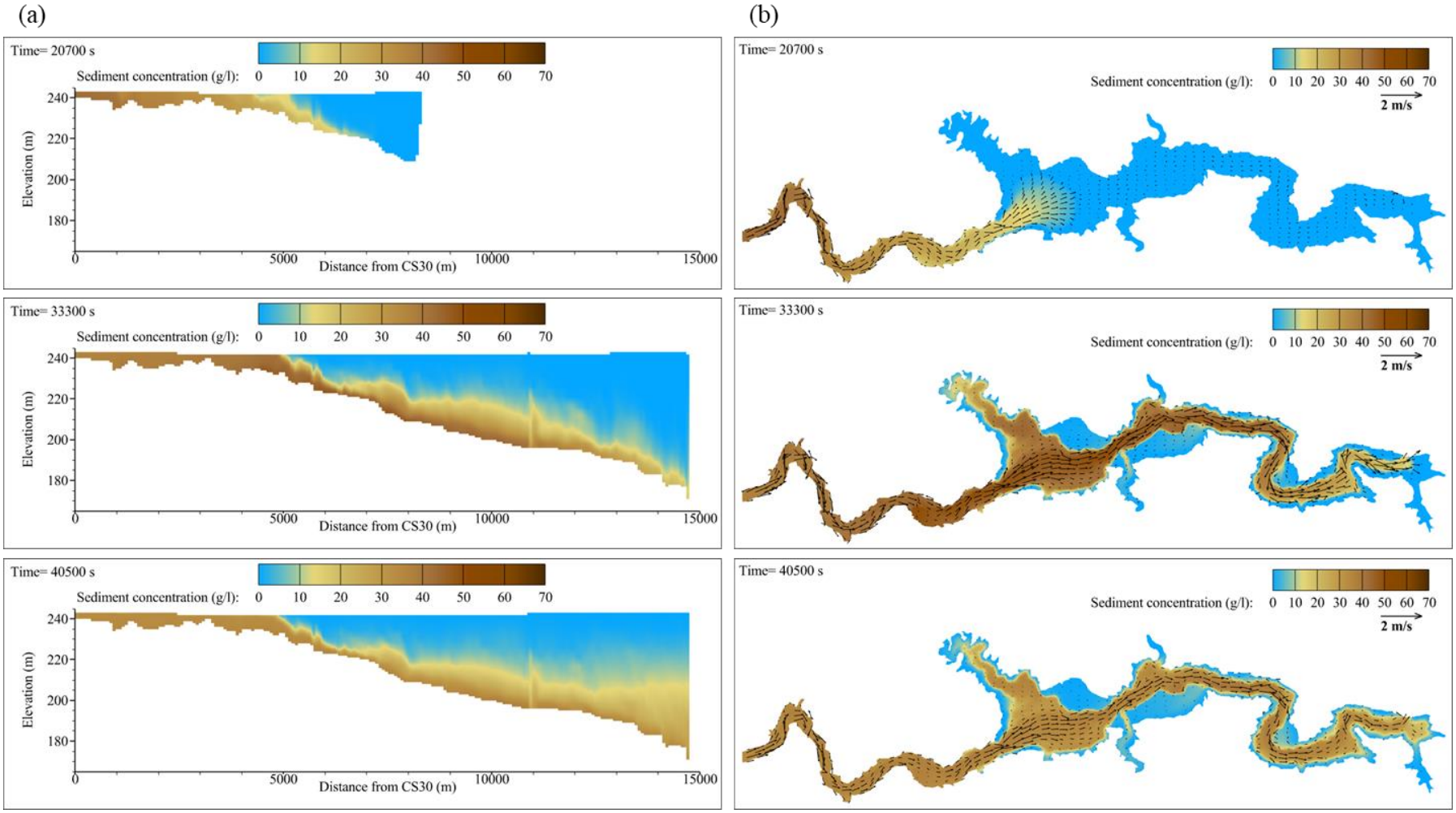

Figure C.27 The turbidity current processes from arrival at CS20, dam, and the muddy lake formed in (a) longitudinal and (b) plane view under Sc# $Q_M S_L$ with soft methods.

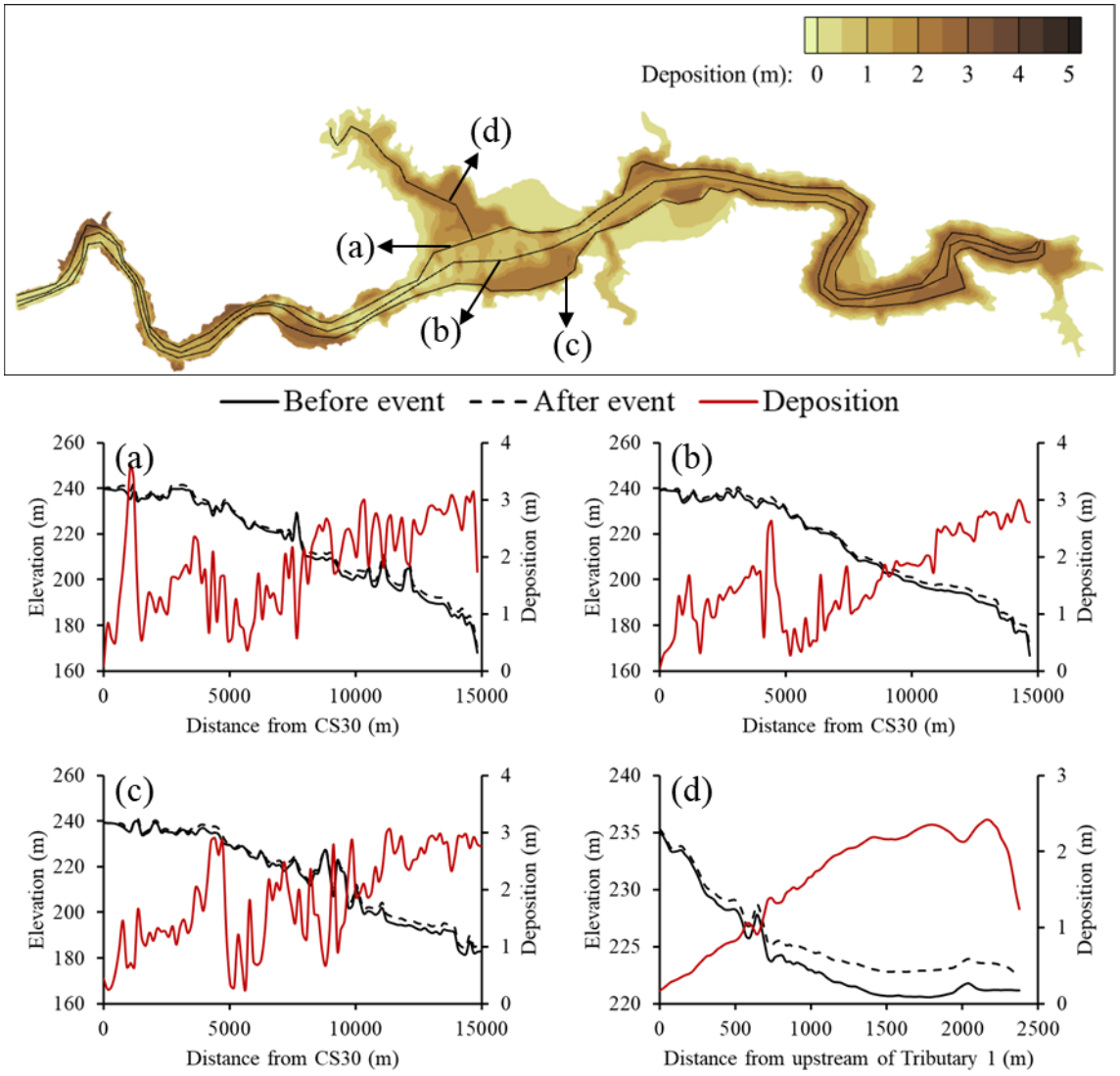

Figure C.28 The bed elevation before and after event, and deposition at (a) left, (b) middle and (c) right side of mainstream, and (d) tributary under Sc# Q_MS_L with soft methods.

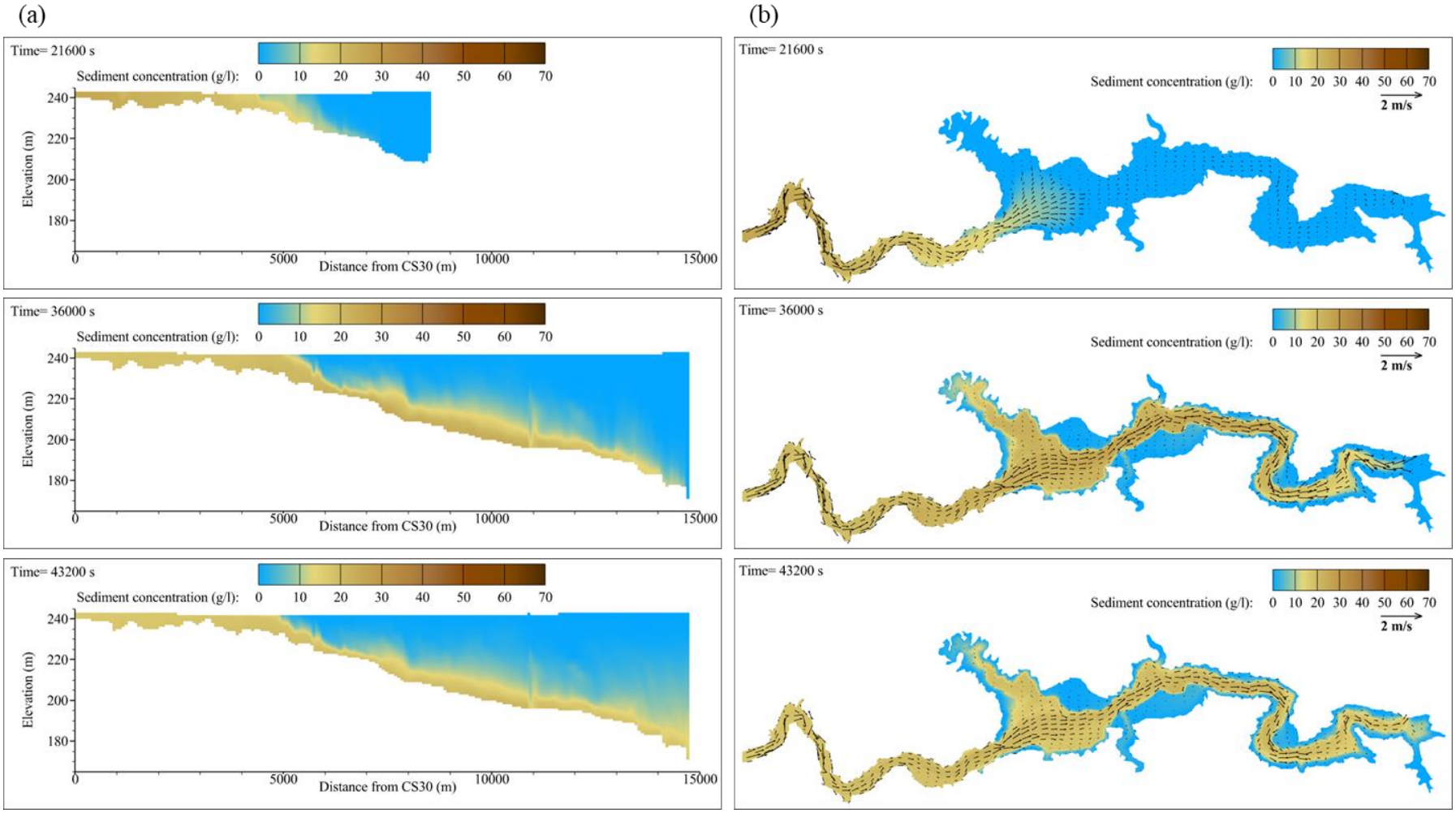

Figure C.29 The turbidity current processes from arrival at CS20, dam, and the muddy lake formed in (a) longitudinal and (b) plane view under Sc# $Q_M S_M$ with soft methods.

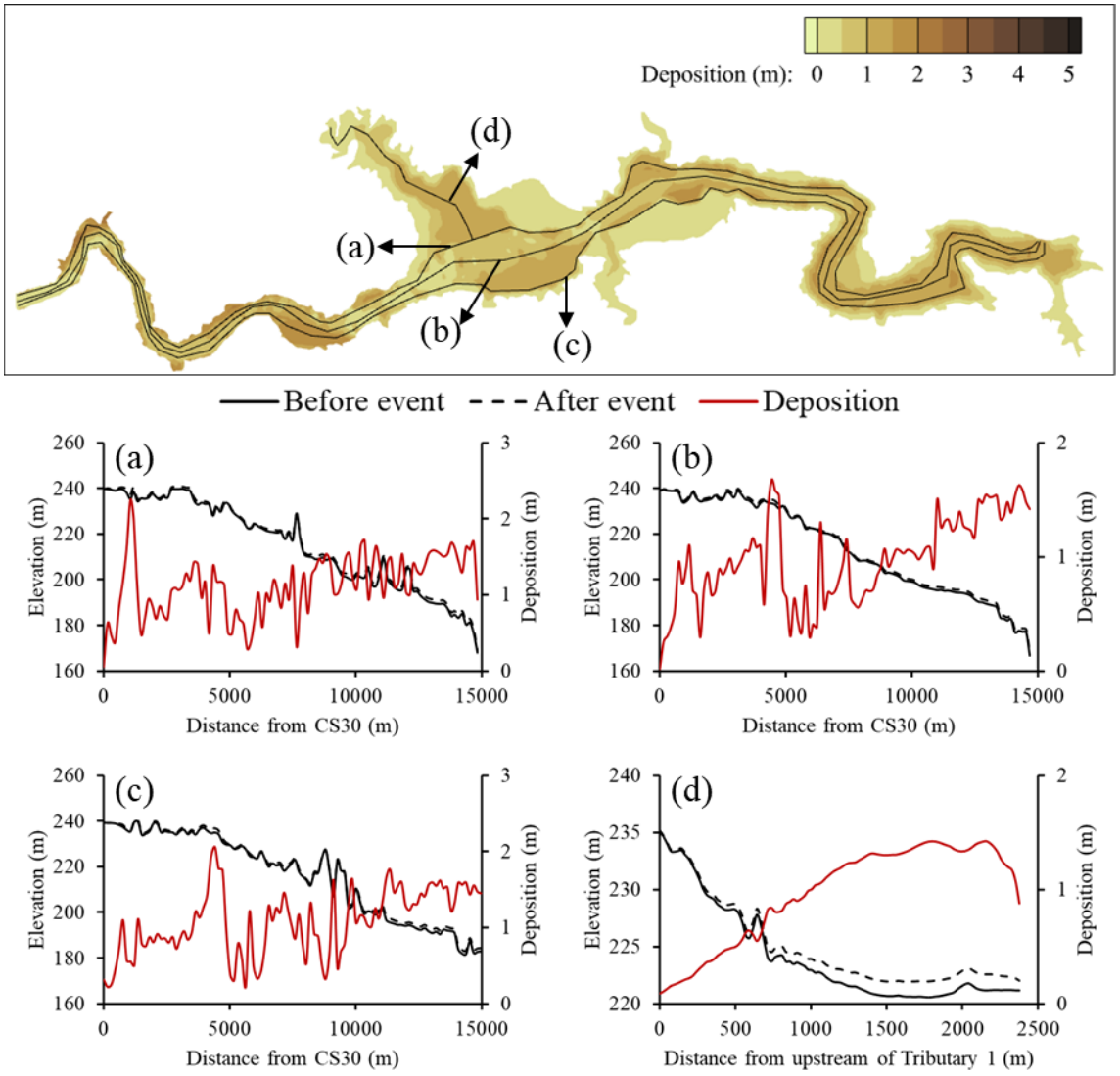

Figure C.30 The bed elevation before and after event, and deposition at (a) left, (b) middle and (c) right side of mainstream, and (d) tributary under Sc# Q_MS_M with soft methods.

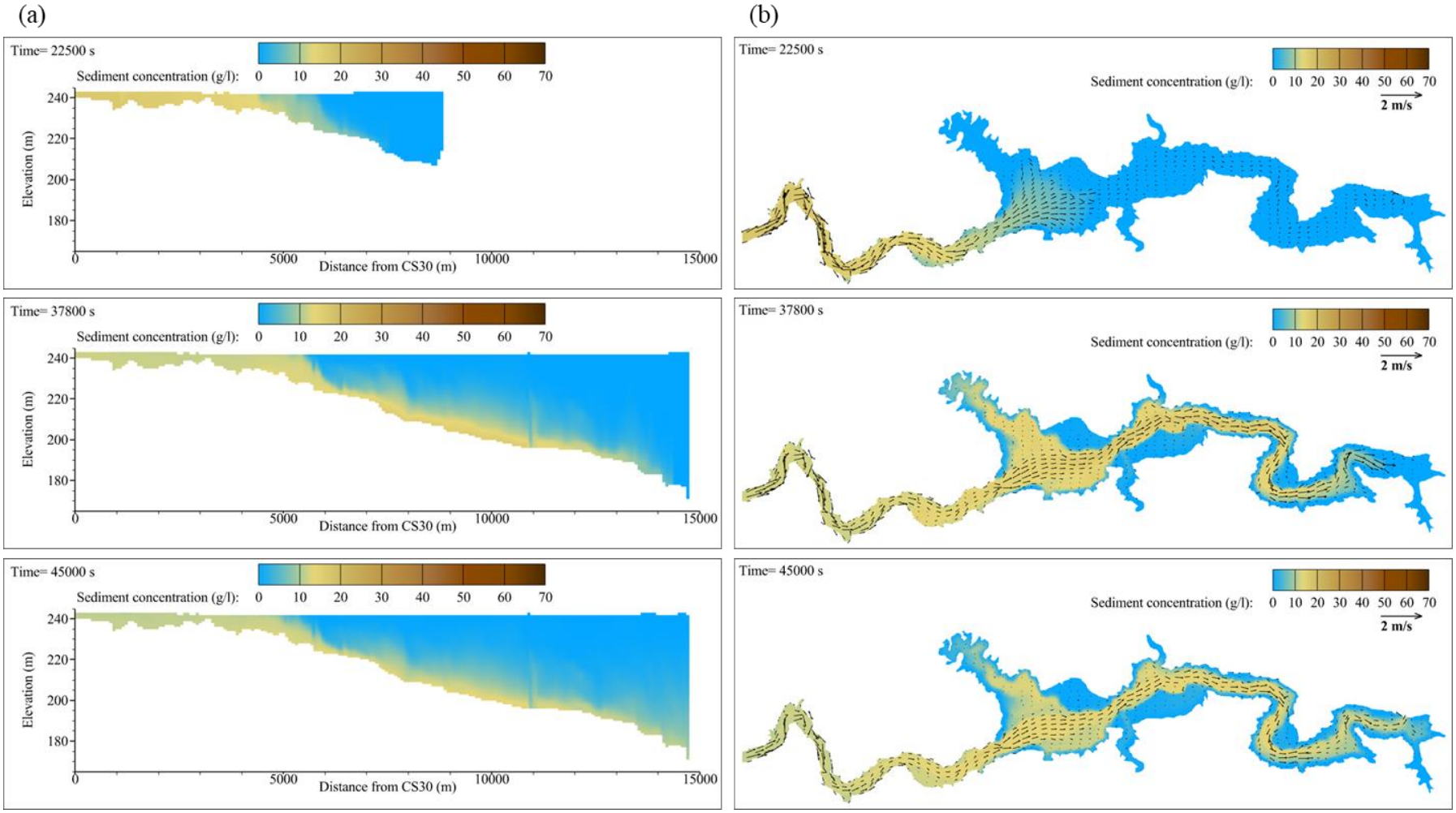

Figure C.31 The turbidity current processes from arrival at CS20, dam, and the muddy lake formed in (a) longitudinal and (b) plane view under Sc# $Q_M S_S$ with soft methods.

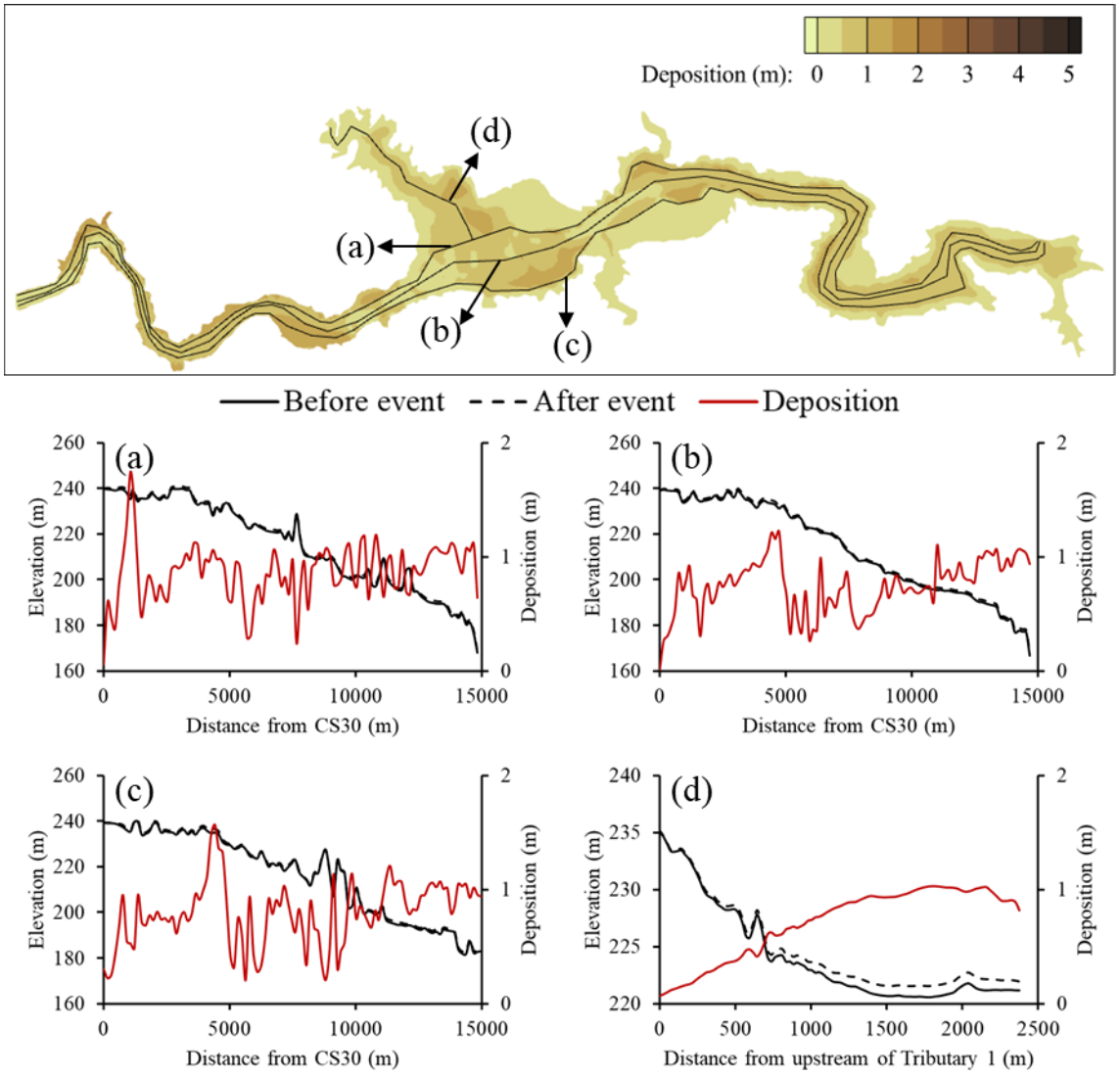

Figure C.32 The bed elevation before and after event, and deposition at (a) left, (b) middle and (c) right side of mainstream, and (d) tributary under Sc# $Q_M S_S$ with soft methods.

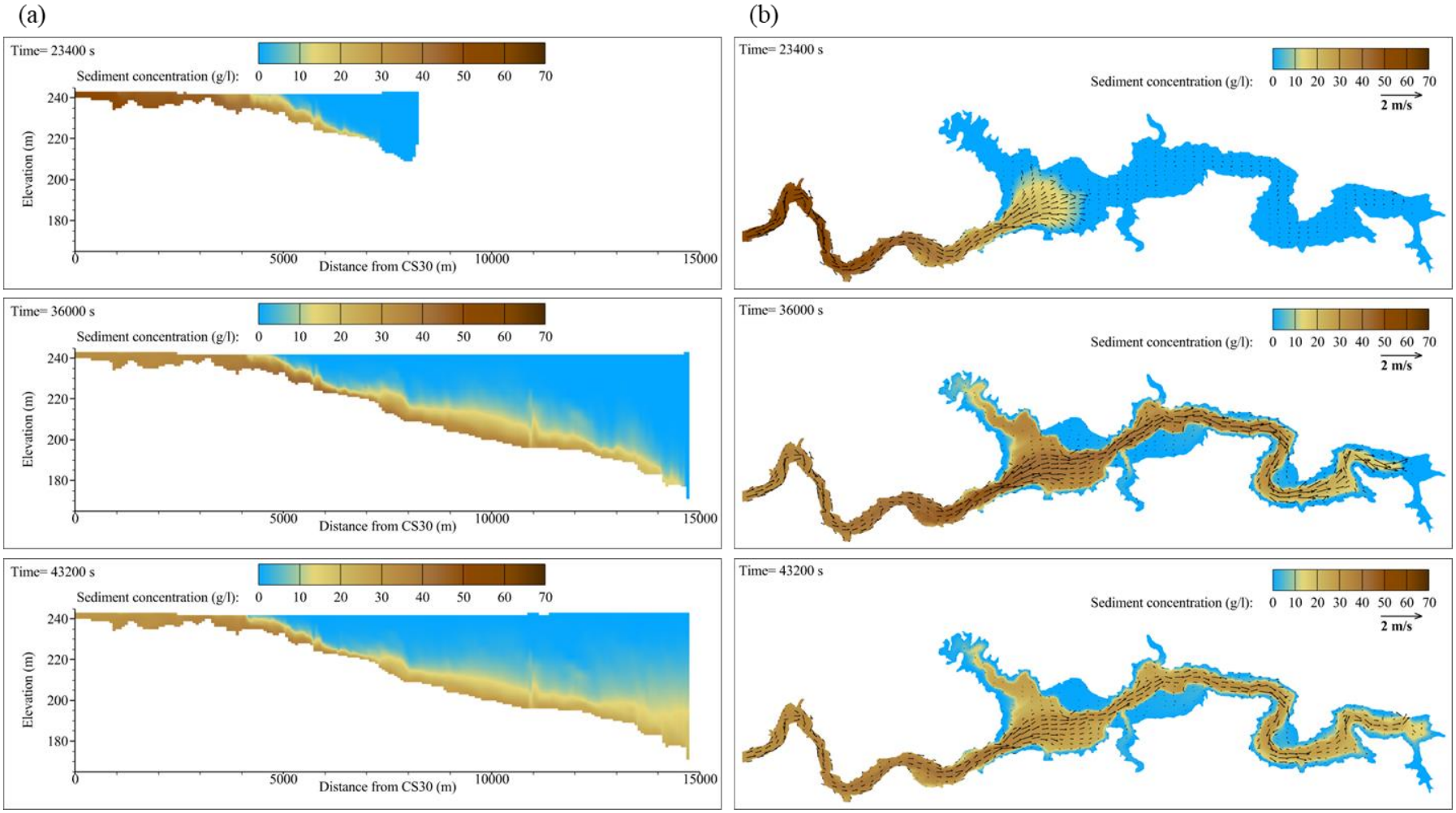

Figure C.33 The turbidity current processes from arrival at CS20, dam, and the muddy lake formed in (a) longitudinal and (b) plane view under Sc# $Q_S S_L$ with soft methods.

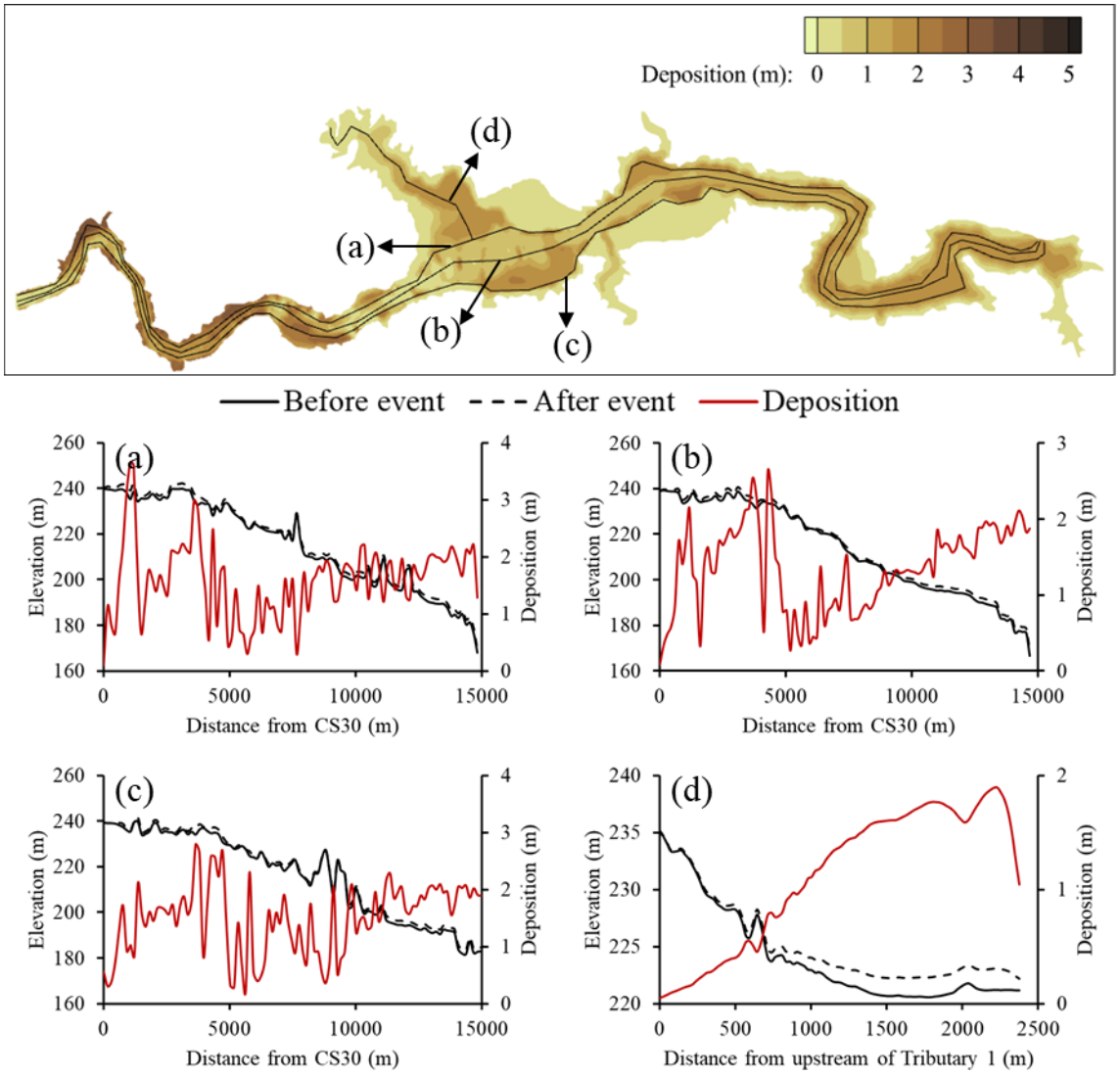

Figure C.34 The bed elevation before and after event, and deposition at (a) left, (b) middle and (c) right side of mainstream, and (d) tributary under Sc# $Q_S S_L$ with soft methods.

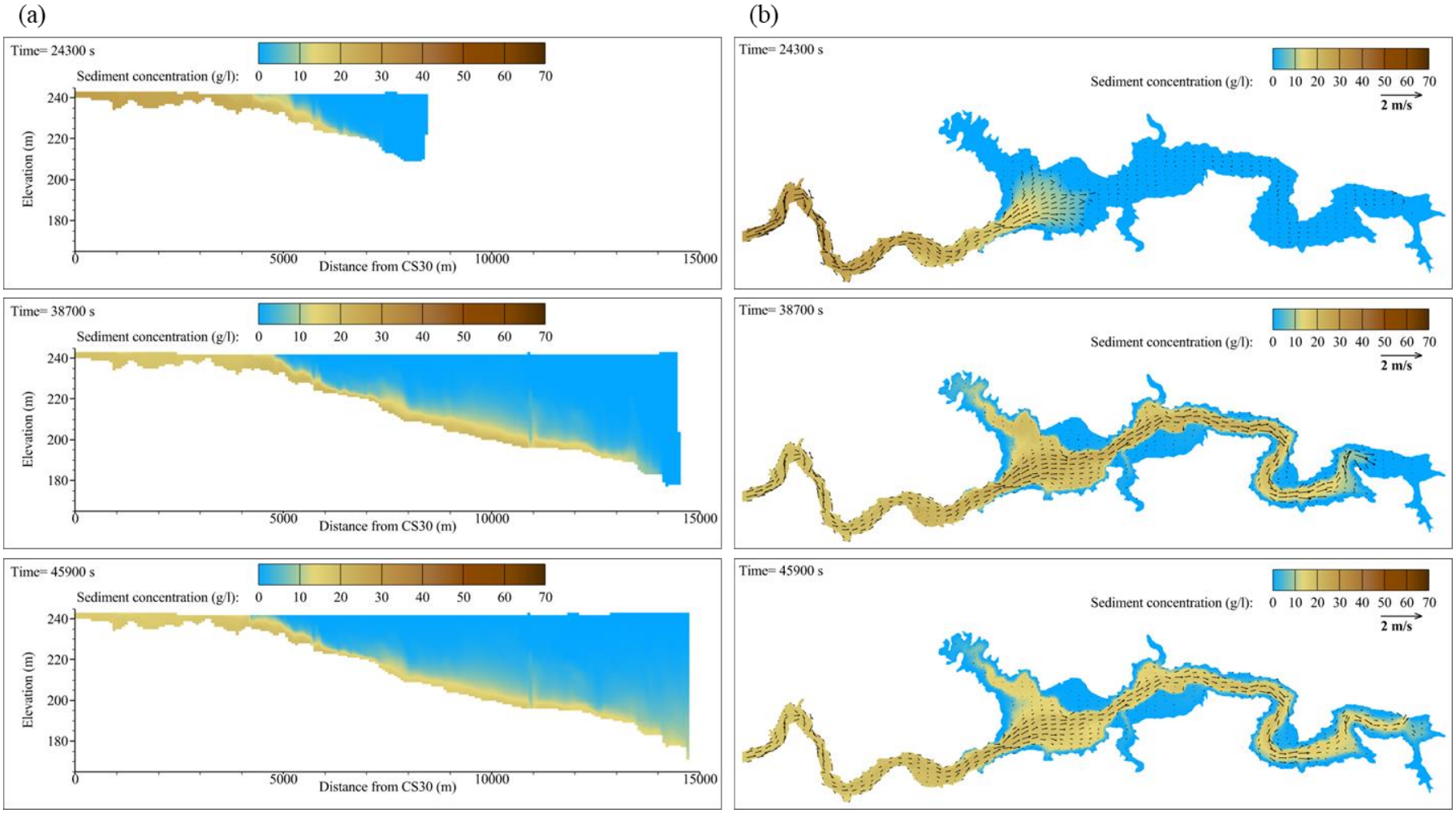

Figure C.35 The turbidity current processes from arrival at CS20, dam, and the muddy lake formed in (a) longitudinal and (b) plane view under Sc# $Q_S S_M$ with soft methods.

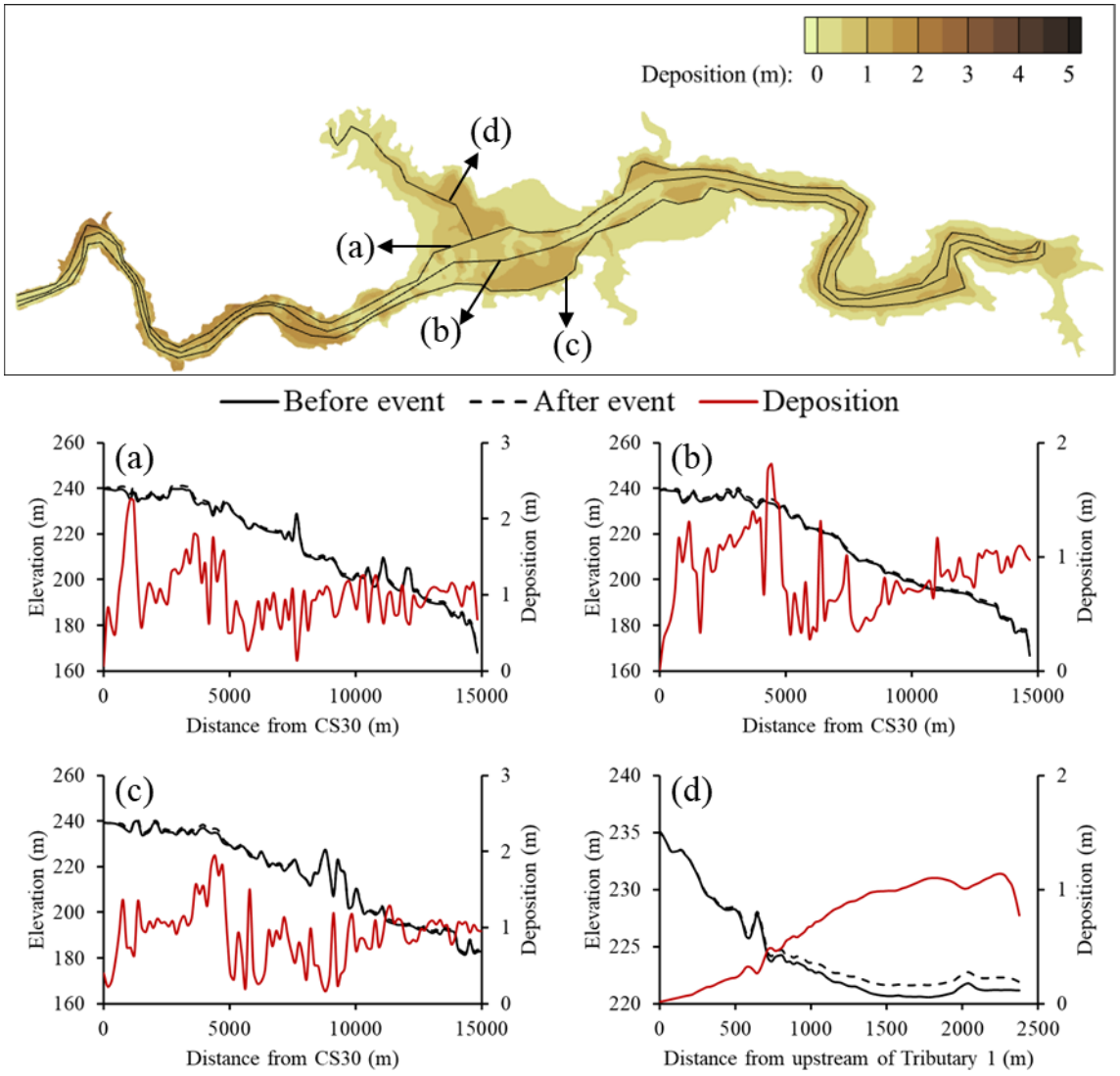

Figure C.36 The bed elevation before and after event, and deposition at (a) left, (b) middle and (c) right side of mainstream, and (d) tributary under Sc# $Q_S S_M$ with soft methods.

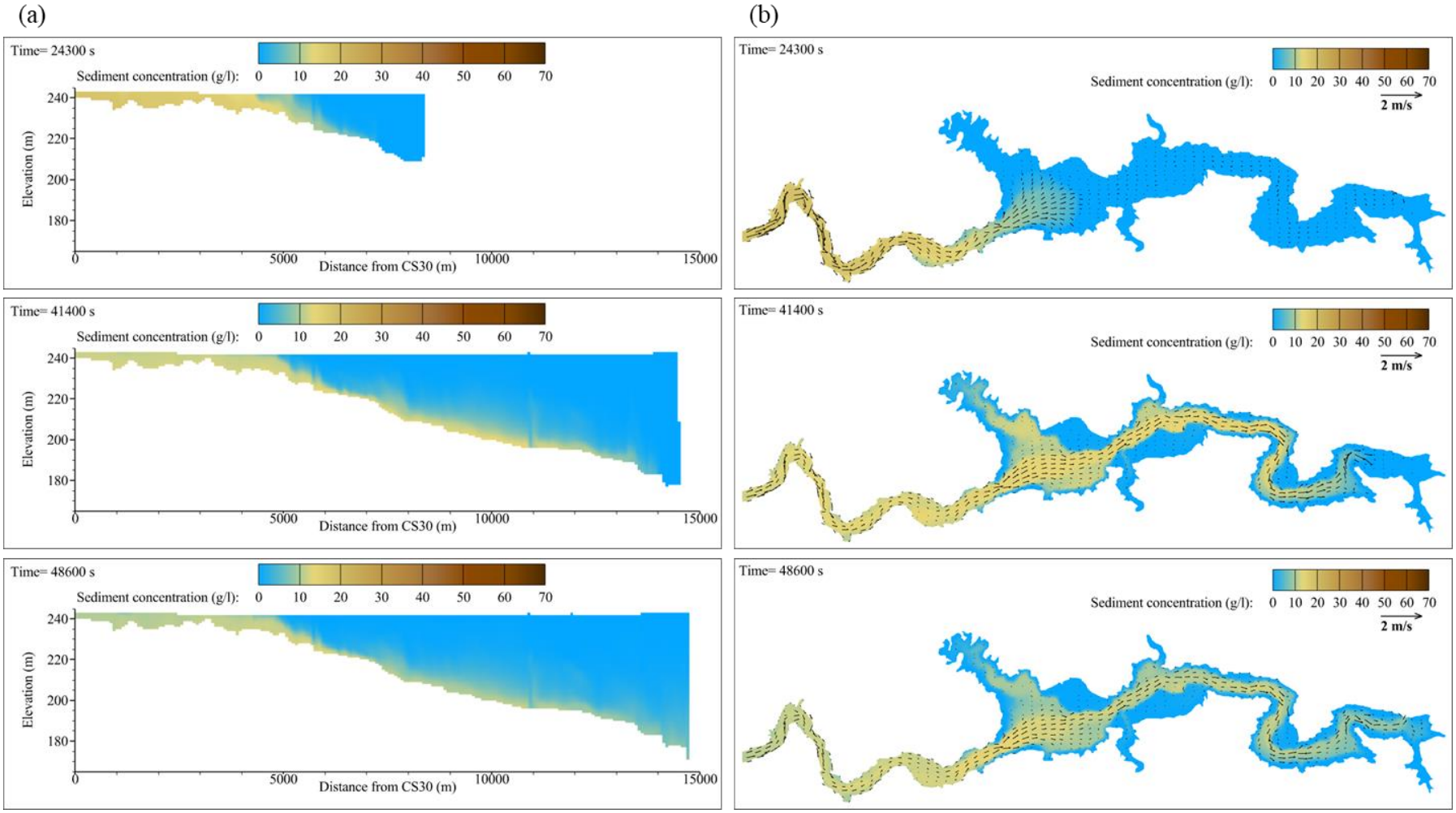

Figure C.37 The turbidity current processes from arrival at CS20, dam, and the muddy lake formed in (a) longitudinal and (b) plane view under Sc# $Q_S S_S$ with soft methods.

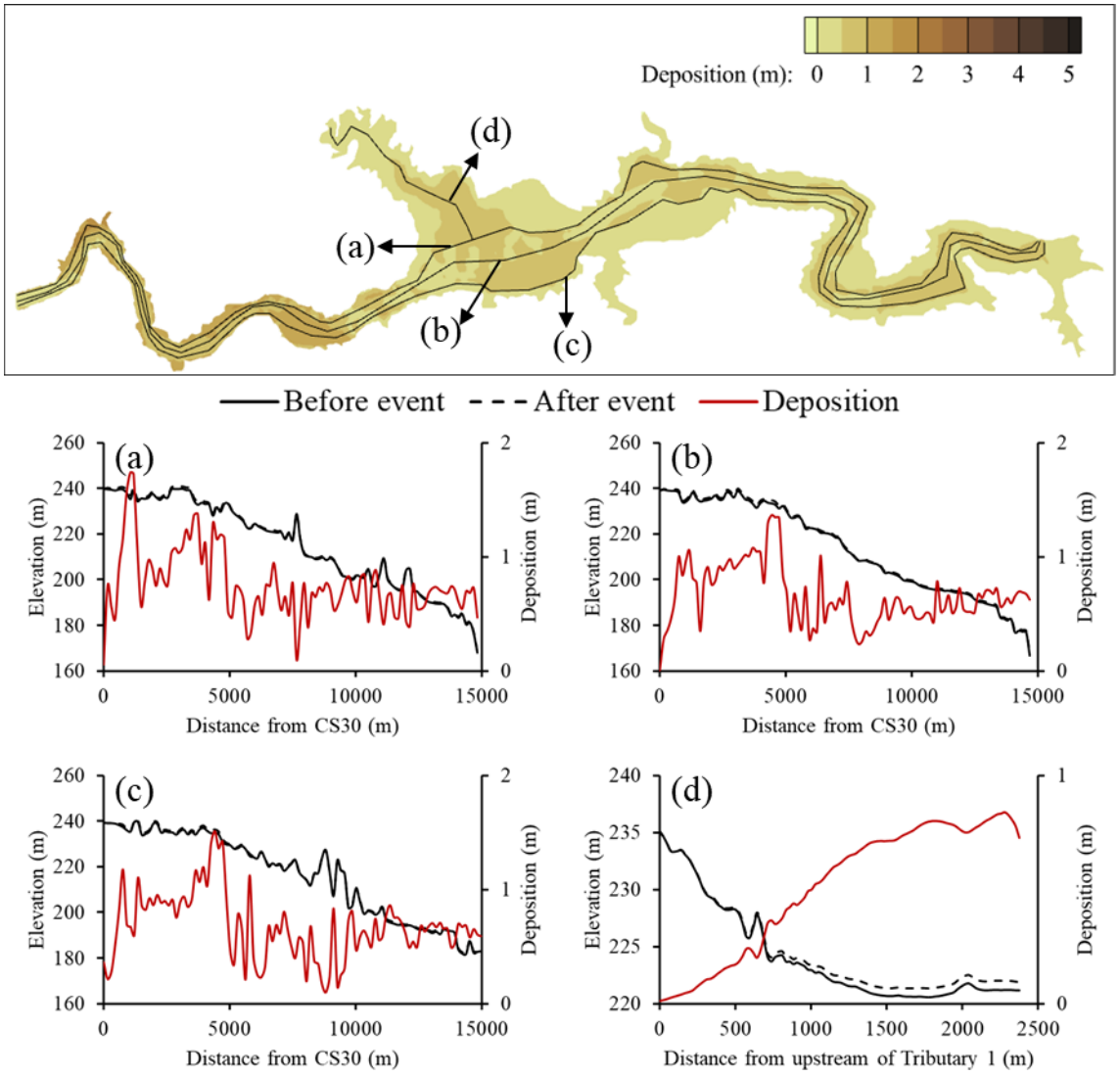

Figure C.38 The bed elevation before and after event, and deposition at (a) left, (b) middle and (c) right side of mainstream, and (d) tributary under Sc# $Q_S S_S$ with soft methods.

C.3 Engineering methods

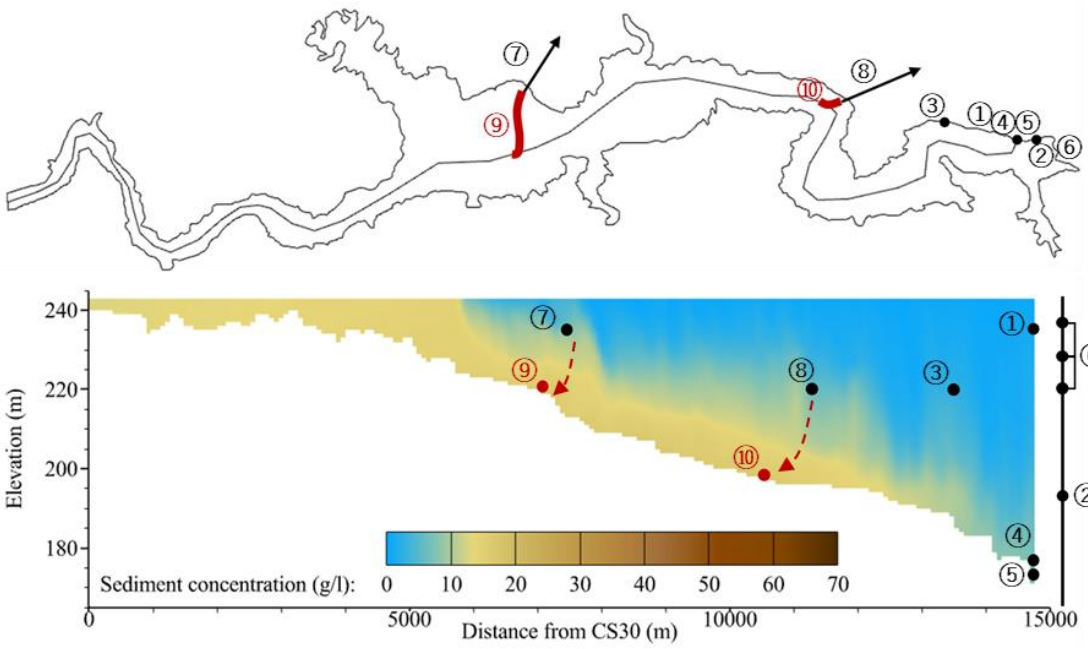

①Spillway (SP)
②Spillway tunnel (ST)
③Shihmen canal intake (SCI)
④Power plant intake and Venting tunnel (PPI and VT)
⑤Permanent river outlet (PRO)
⑥Water supply intake
⑦Amuping sediment bypass tunnel (Amu_SBT) ---------- ⑨ Elephant trunk from Amu_SBT (ELEP_A)
⑧Dawangping sediment bypass tunnel (Daw_SBT) ---------- ⑩ Elephant trunk from Daw_SBT (ELEP)

Operating sequence: ⑤→④→③→⑩→⑨→②→①

Figure C.39 Operated outlets and the operating sequence under engineering methods.

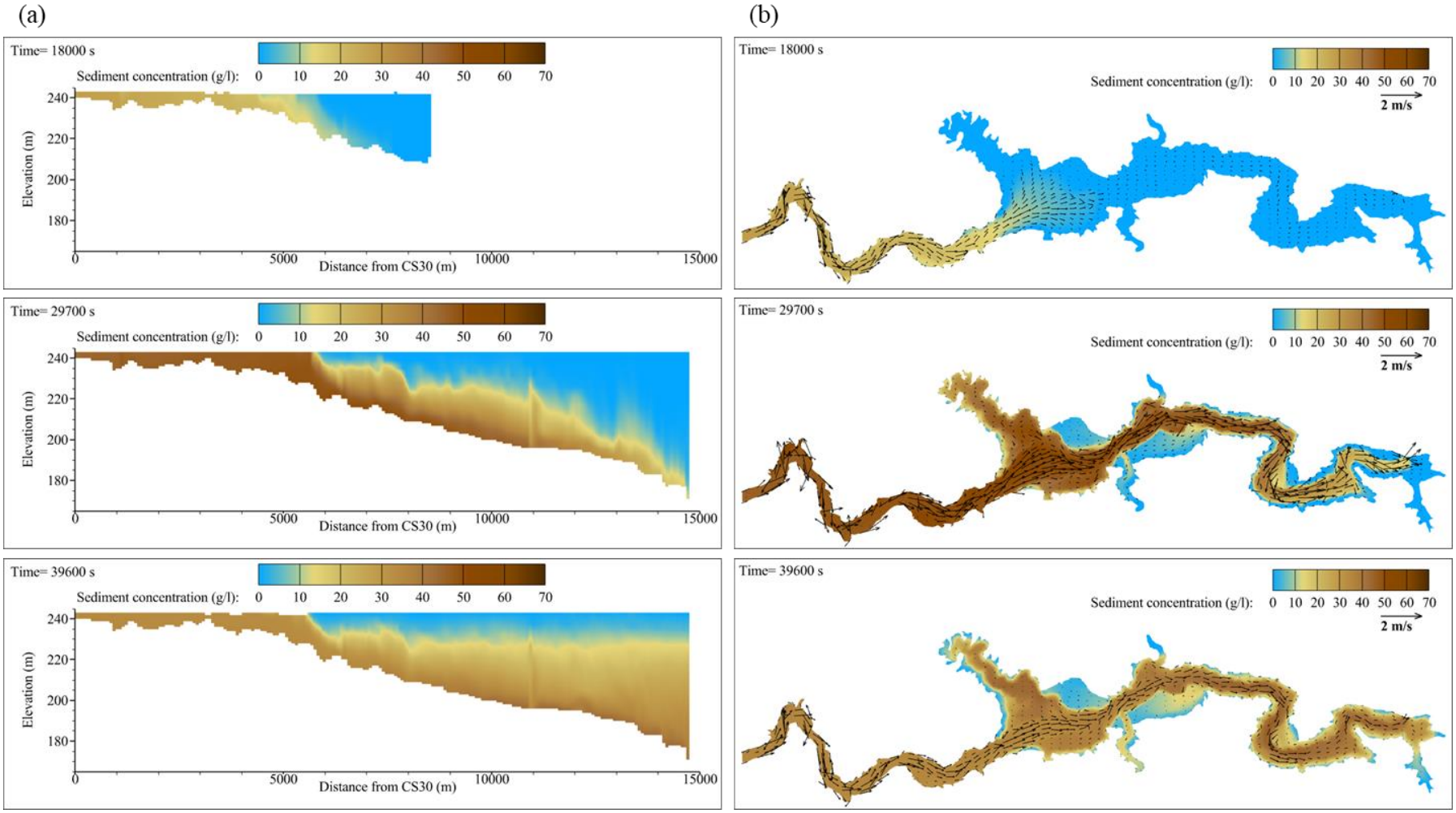

Figure C.40 The turbidity current processes from arrival at CS20, dam, and the muddy lake formed in (a) longitudinal and (b) plane view under Sc# $Q_L S_L$ with engineering methods.

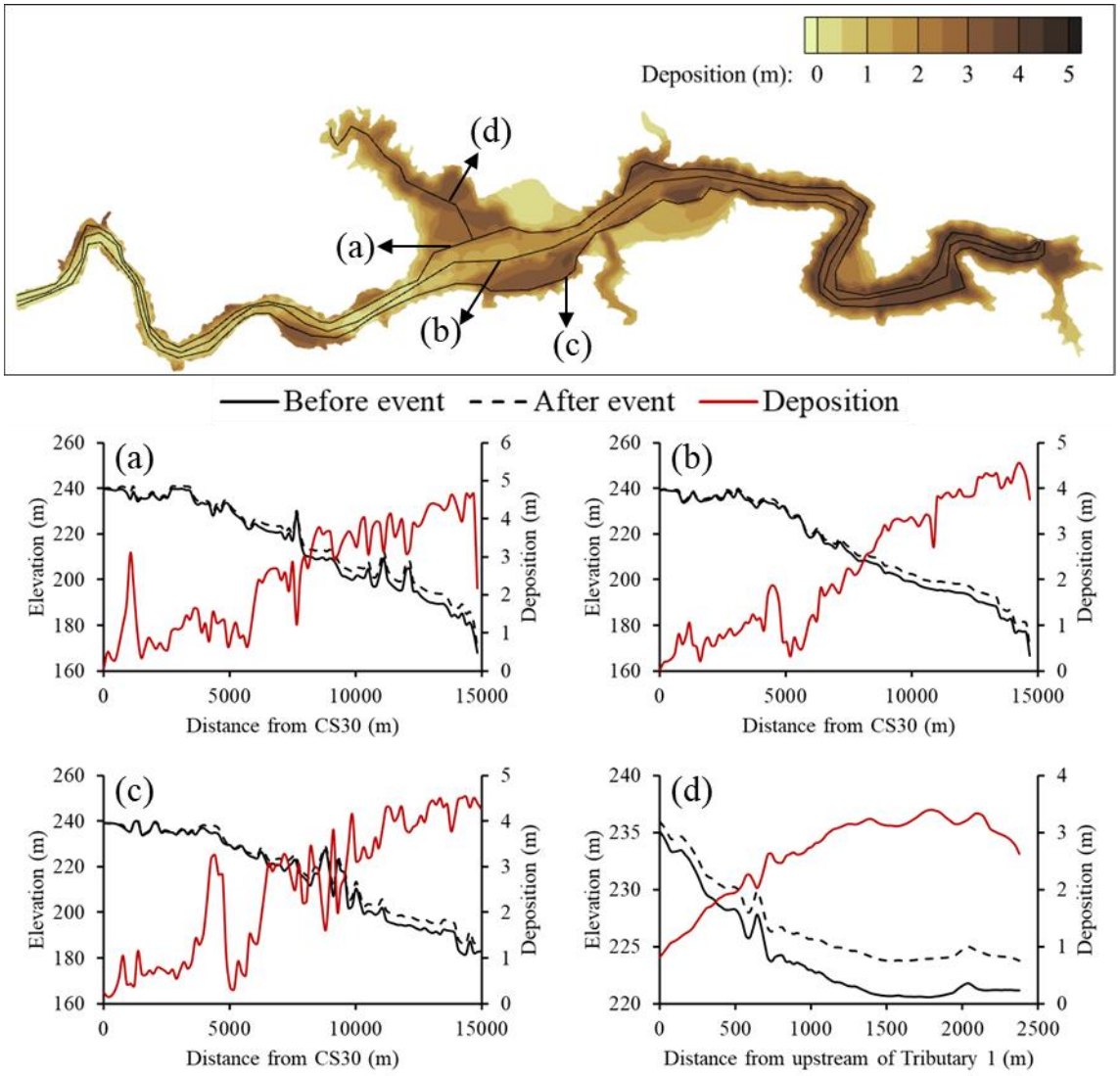

Figure C.41 The bed elevation before and after event, and deposition at (a) left, (b) middle and (c) right side of mainstream, and (d) tributary under Sc# Q_LS_L with engineering methods.

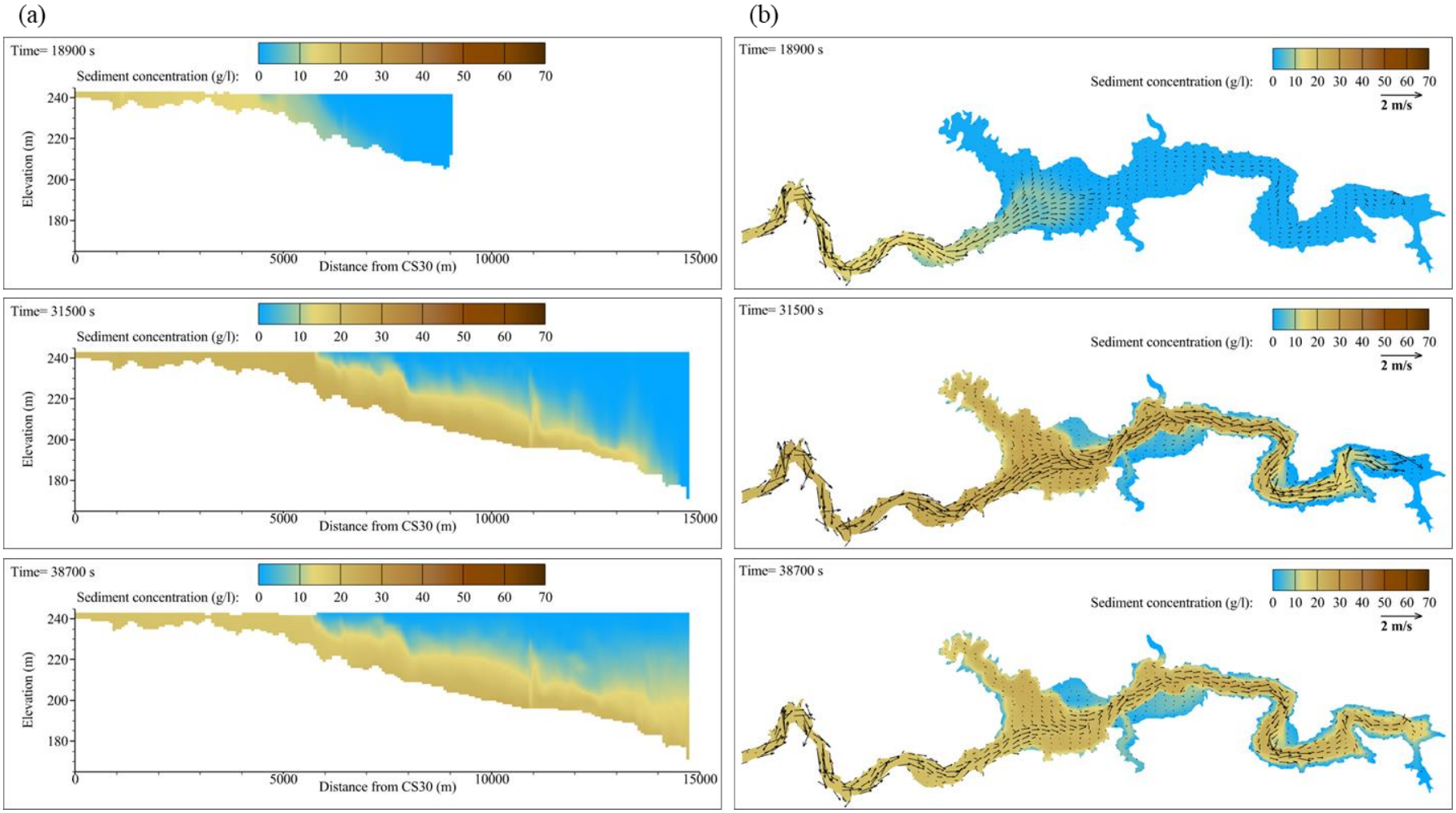

Figure C.42 The turbidity current processes from arrival at CS20, dam, and the muddy lake formed in (a) longitudinal and (b) plane view under Sc# $Q_L S_M$ with engineering methods.

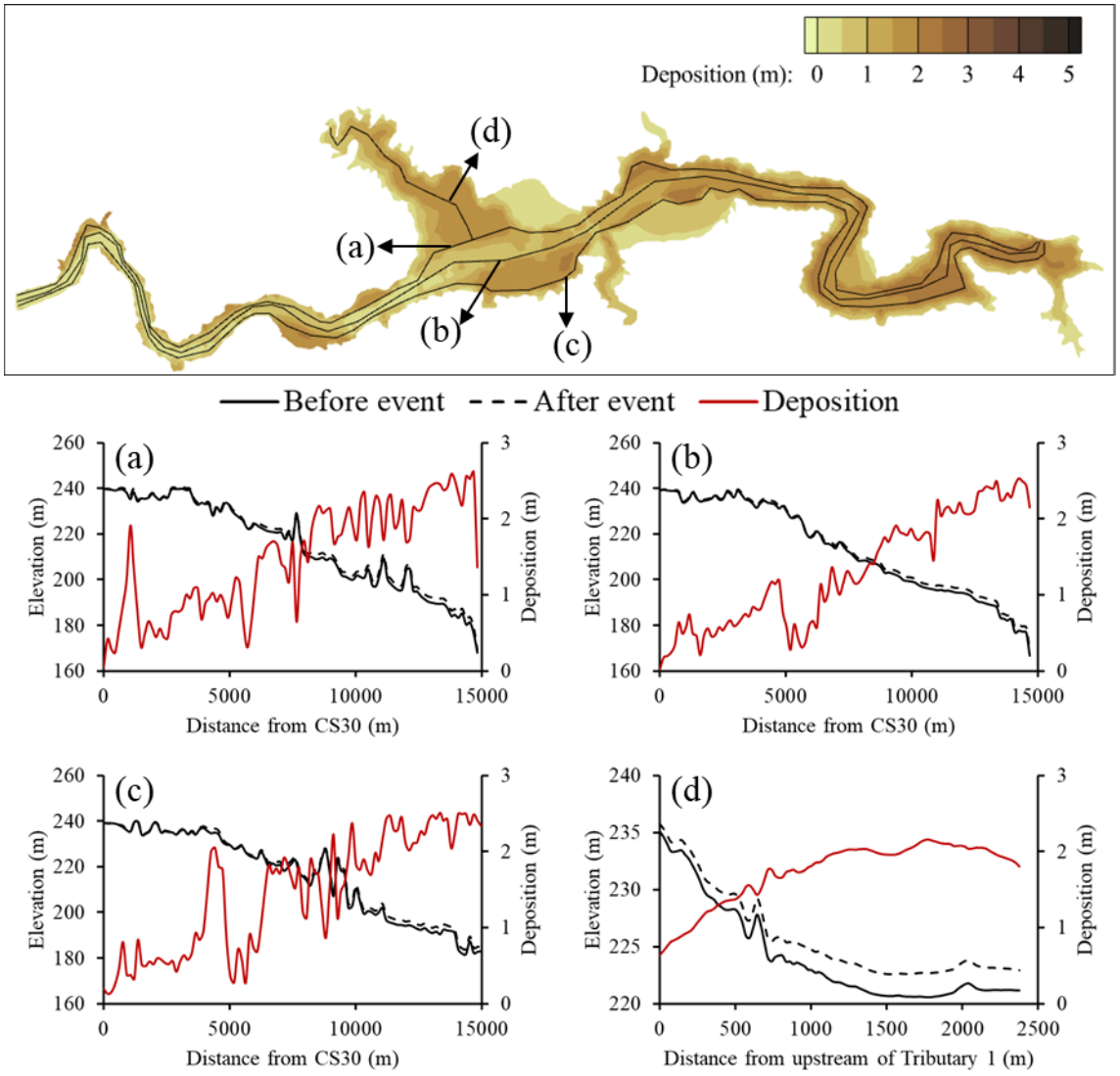

Figure C.43 The bed elevation before and after event, and deposition at (a) left, (b) middle and (c) right side of mainstream, and (d) tributary under Sc# $Q_L S_M$ with engineering methods.

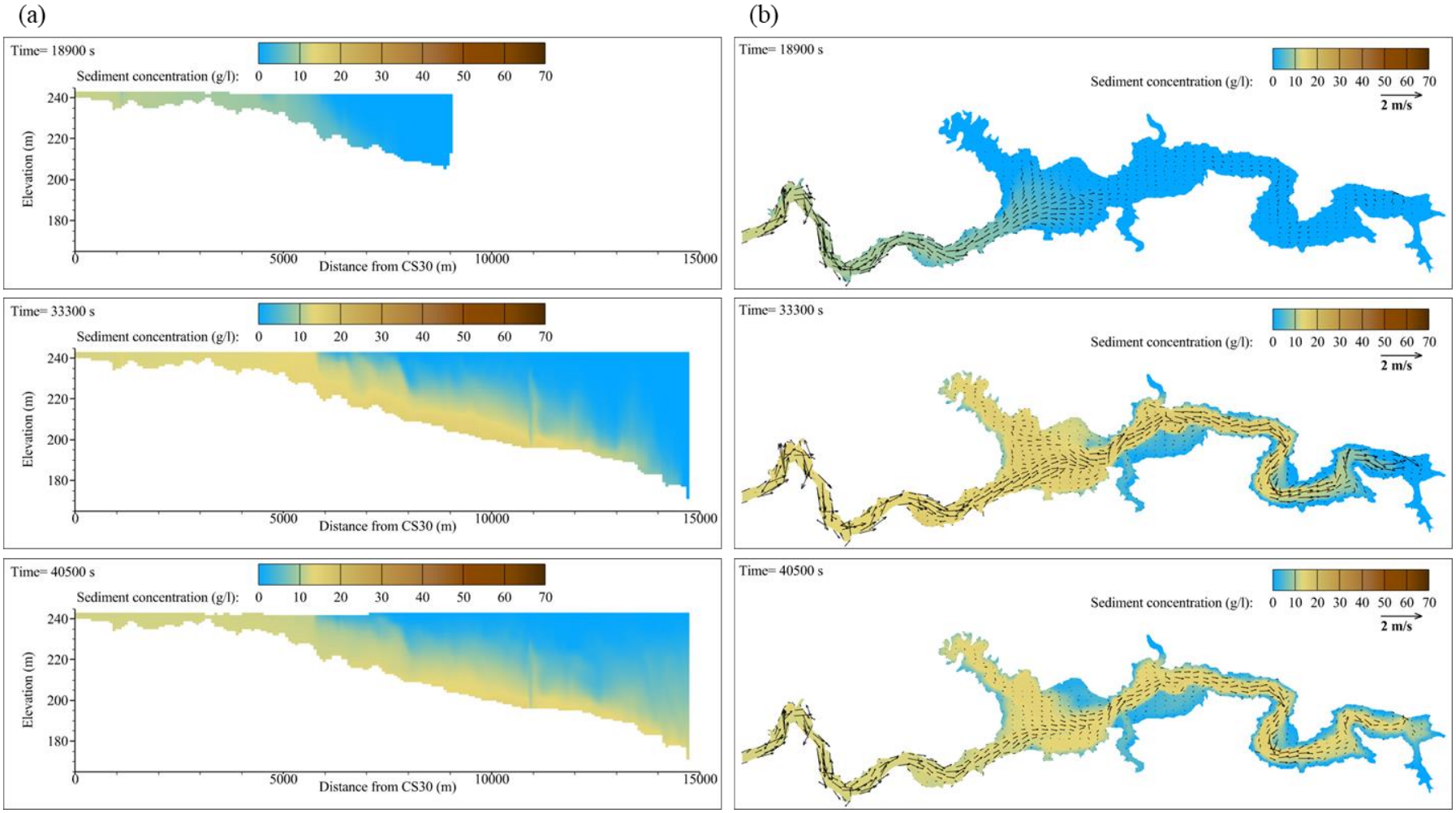

Figure C.44 The turbidity current processes from arrival at CS20, dam, and the muddy lake formed in (a) longitudinal and (b) plane view under Sc# $Q_L S_S$ with engineering methods.

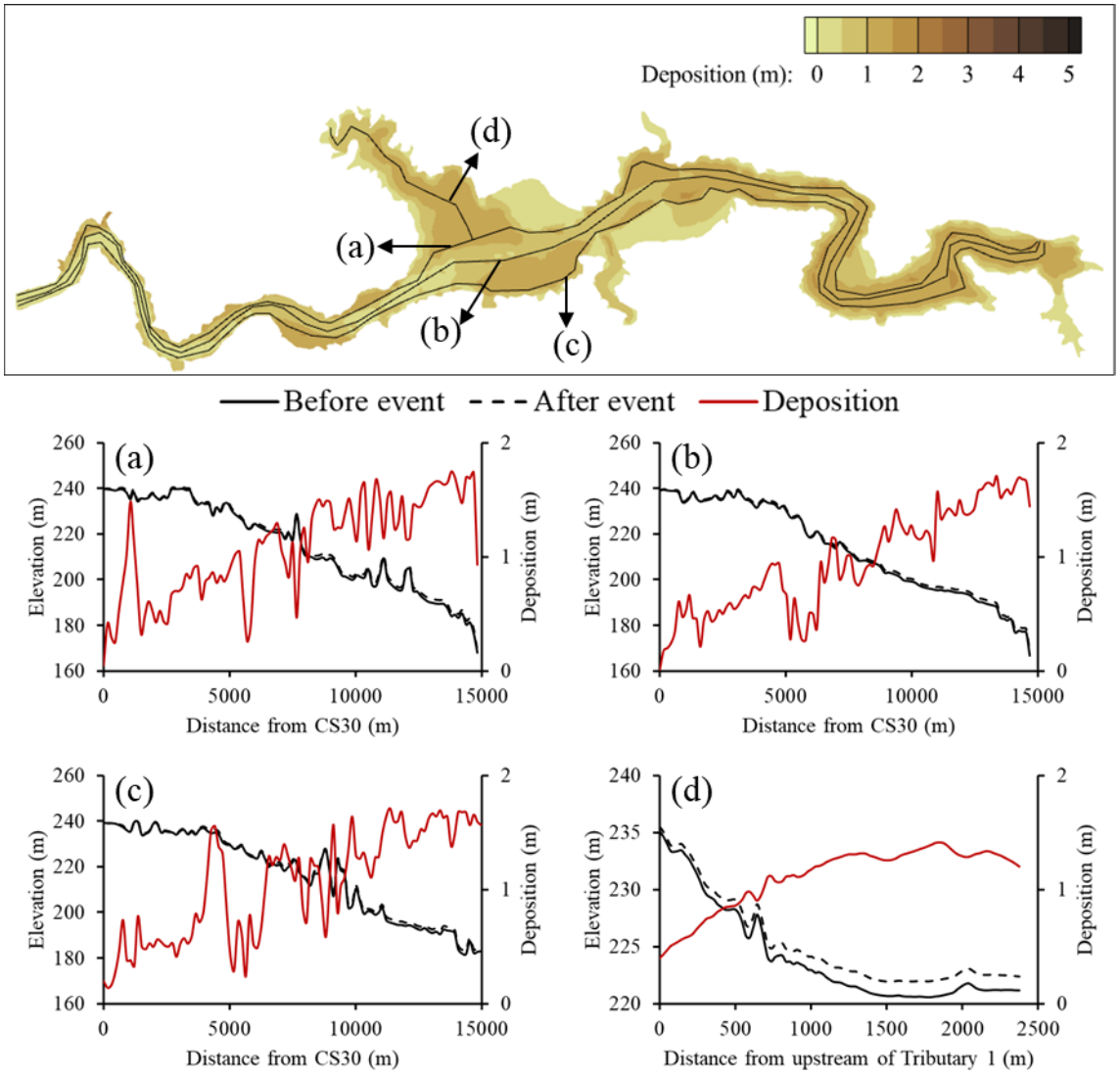

Figure C.45 The bed elevation before and after event, and deposition at (a) left, (b) middle and (c) right side of mainstream, and (d) tributary under Sc# $Q_L S_S$ with engineering methods.

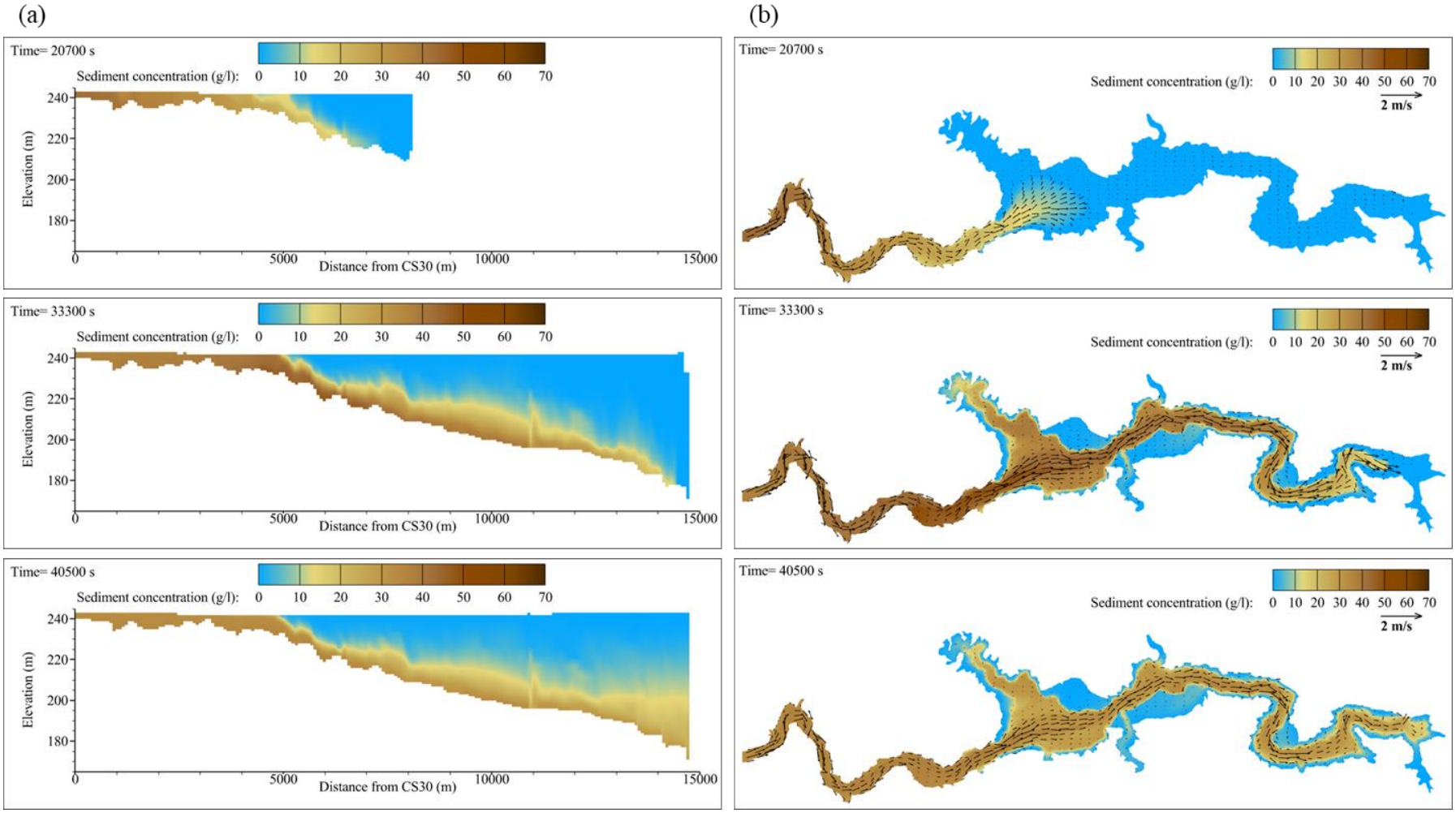

Figure C.46 The turbidity current processes from arrival at CS20, dam, and the muddy lake formed in (a) longitudinal and (b) plane view under Sc# $Q_M S_L$ with engineering methods.

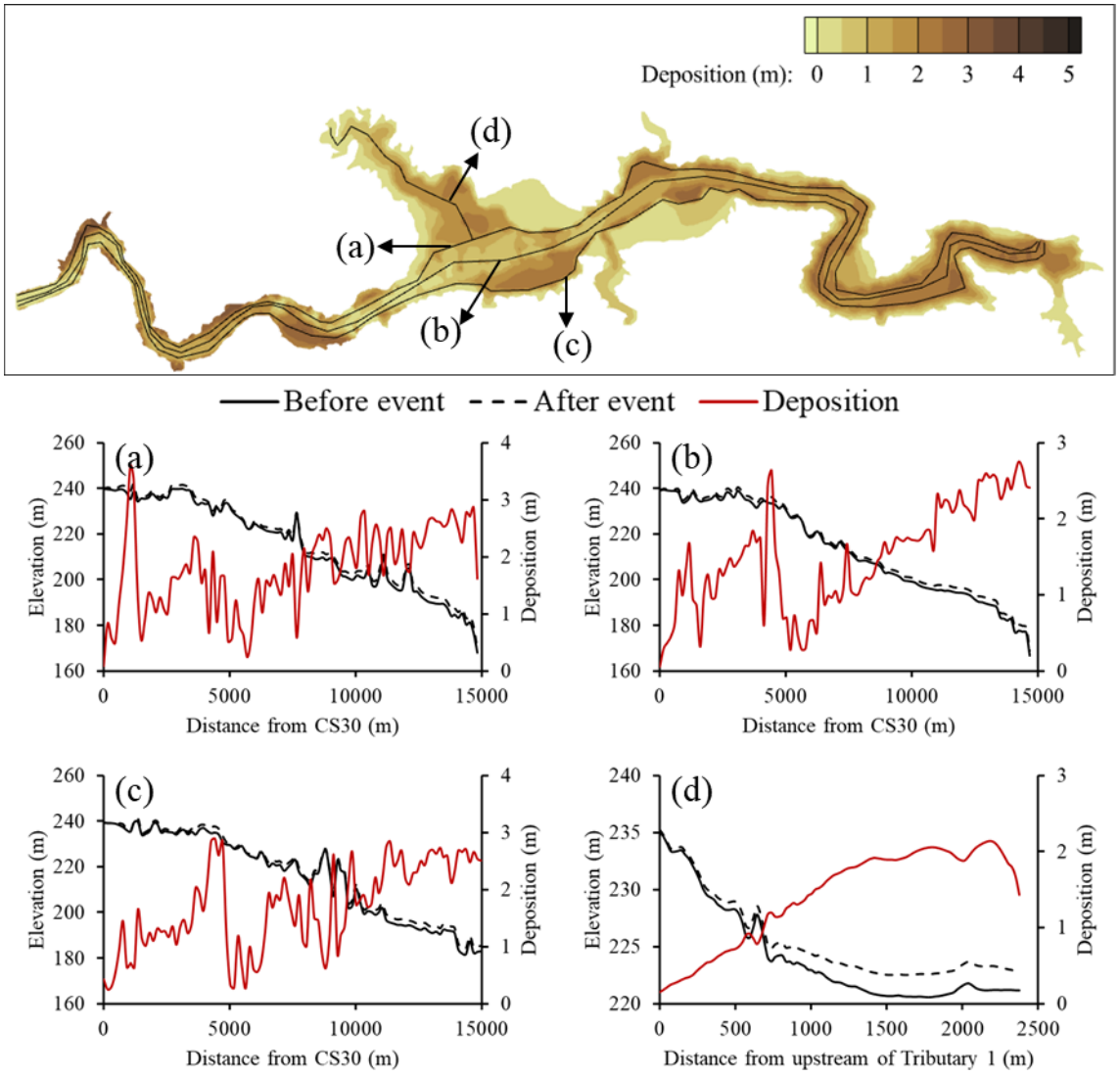

Figure C.47 The bed elevation before and after event, and deposition at (a) left, (b) middle and (c) right side of mainstream, and (d) tributary under Sc# Q_MS_L with engineering methods.

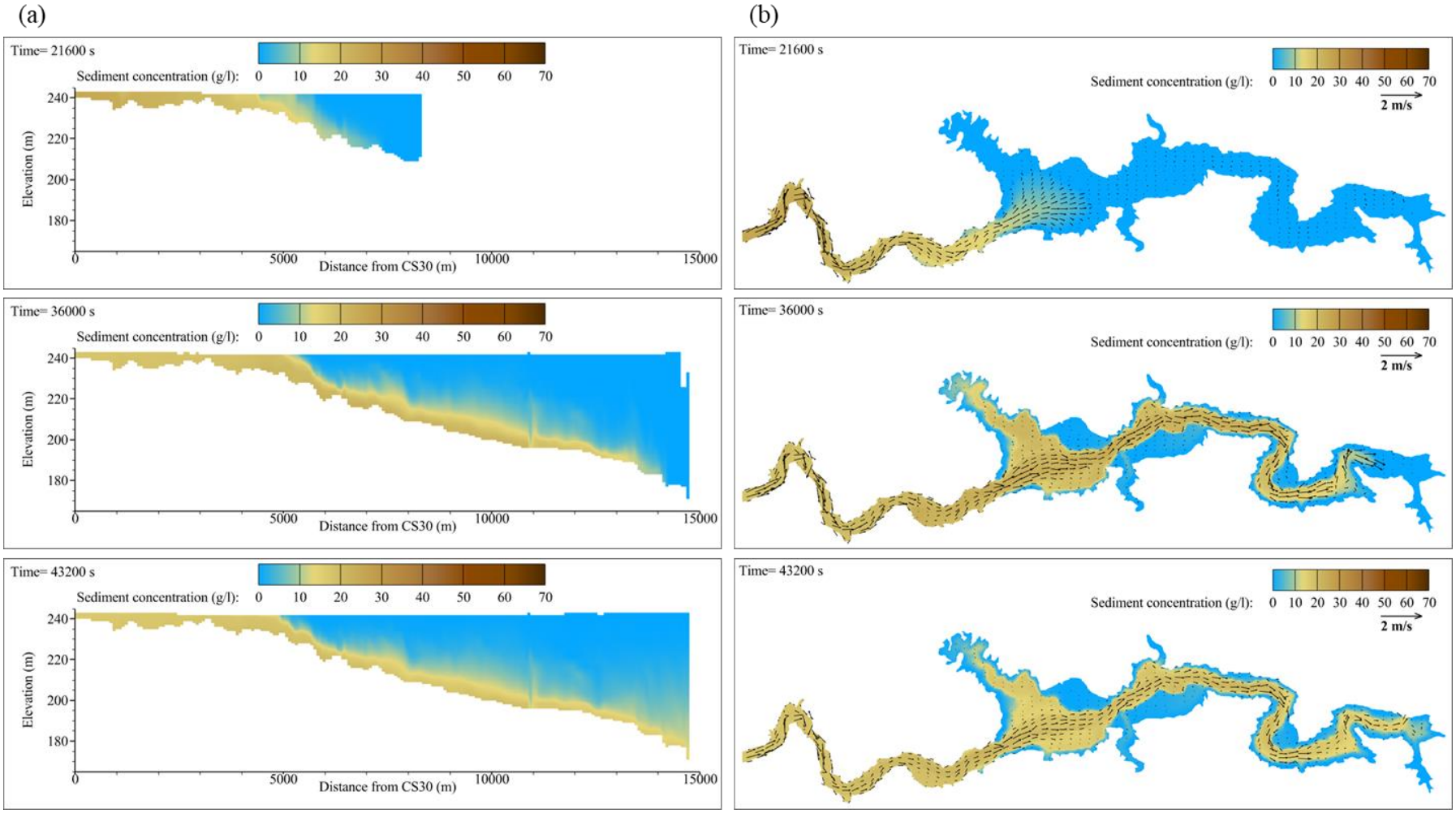

Figure C.48 The turbidity current processes from arrival at CS20, dam, and the muddy lake formed in (a) longitudinal and (b) plane view under Sc# $Q_M S_M$ with engineering methods.

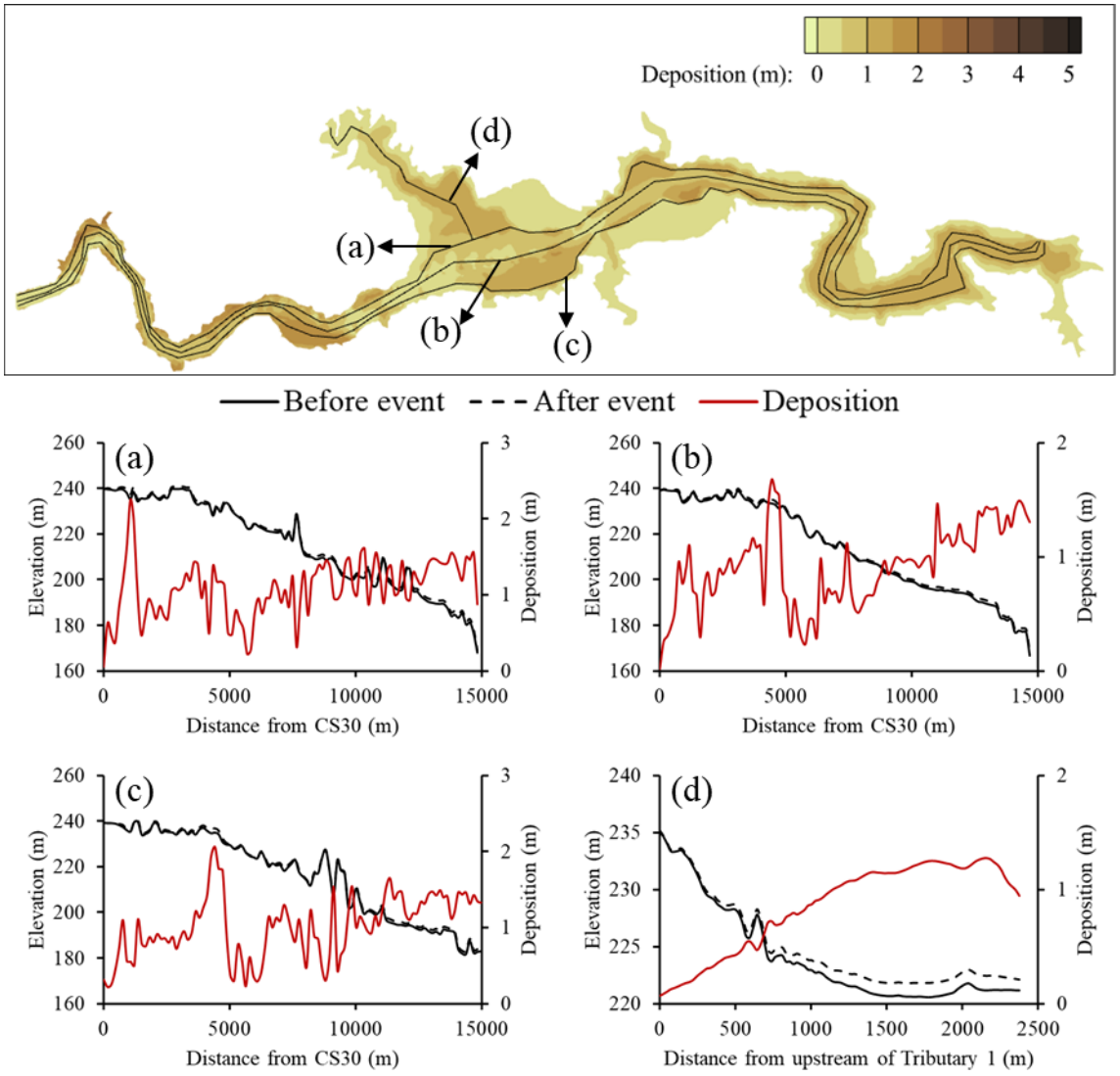

Figure C.49 The bed elevation before and after event, and deposition at (a) left, (b) middle and (c) right side of mainstream, and (d) tributary under Sc# Q_MS_M with engineering methods.

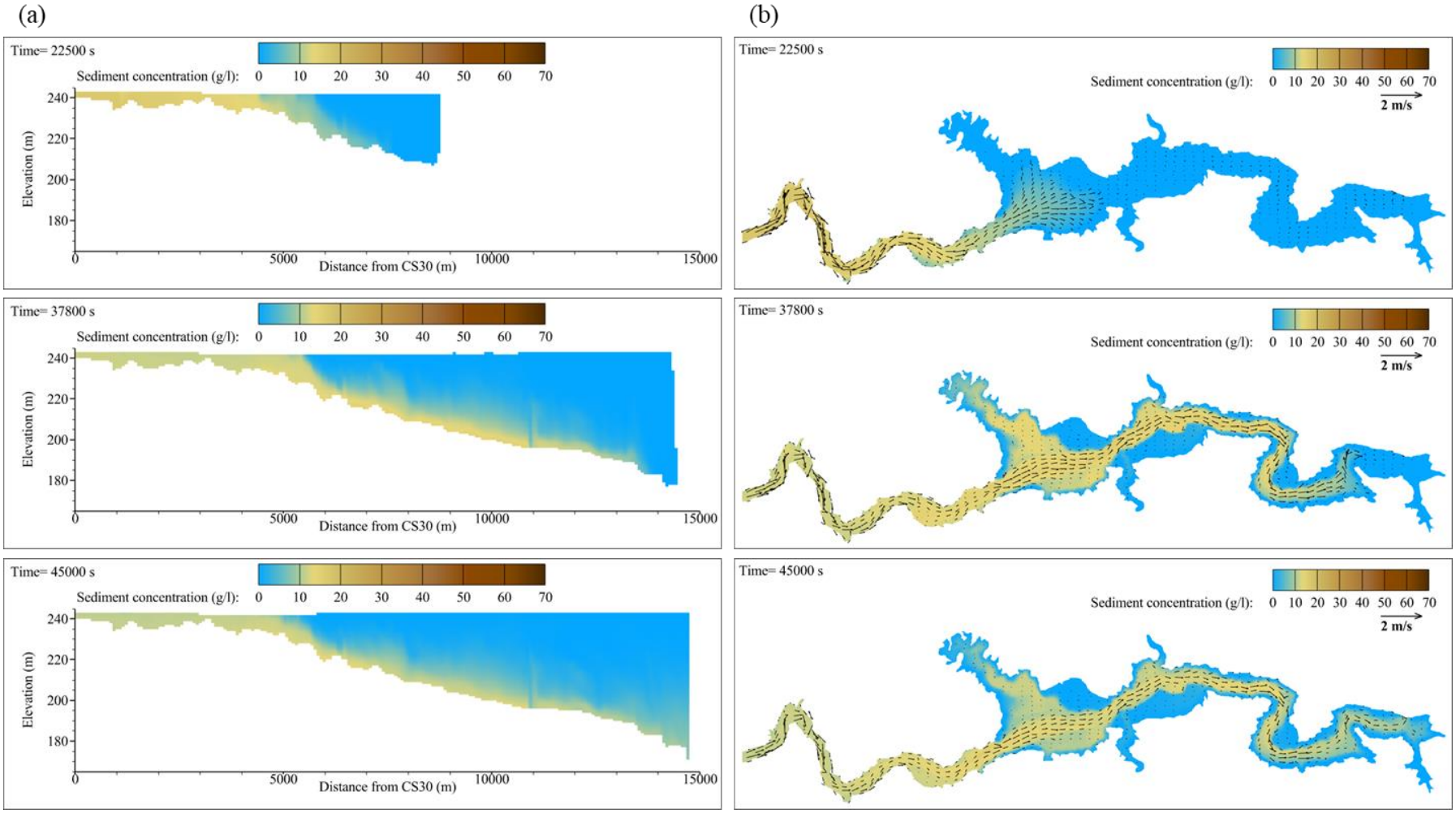

Figure C.50 The turbidity current processes from arrival at CS20, dam, and the muddy lake formed in (a) longitudinal and (b) plane view under Sc# $Q_M S_S$ with engineering methods.

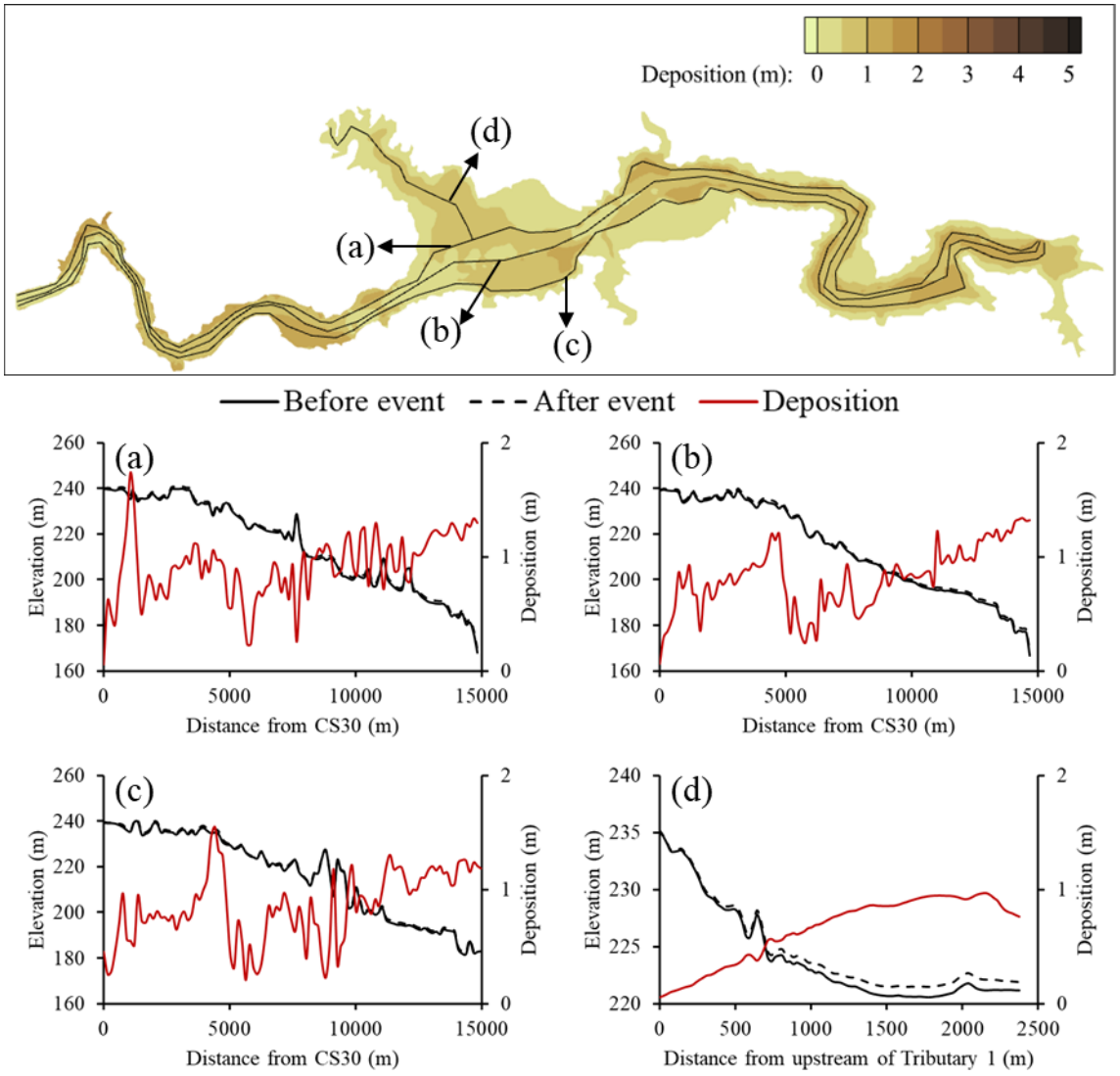

Figure C.51 The bed elevation before and after event, and deposition at (a) left, (b) middle and (c) right side of mainstream, and (d) tributary under Sc# $Q_M S_S$ with engineering methods.

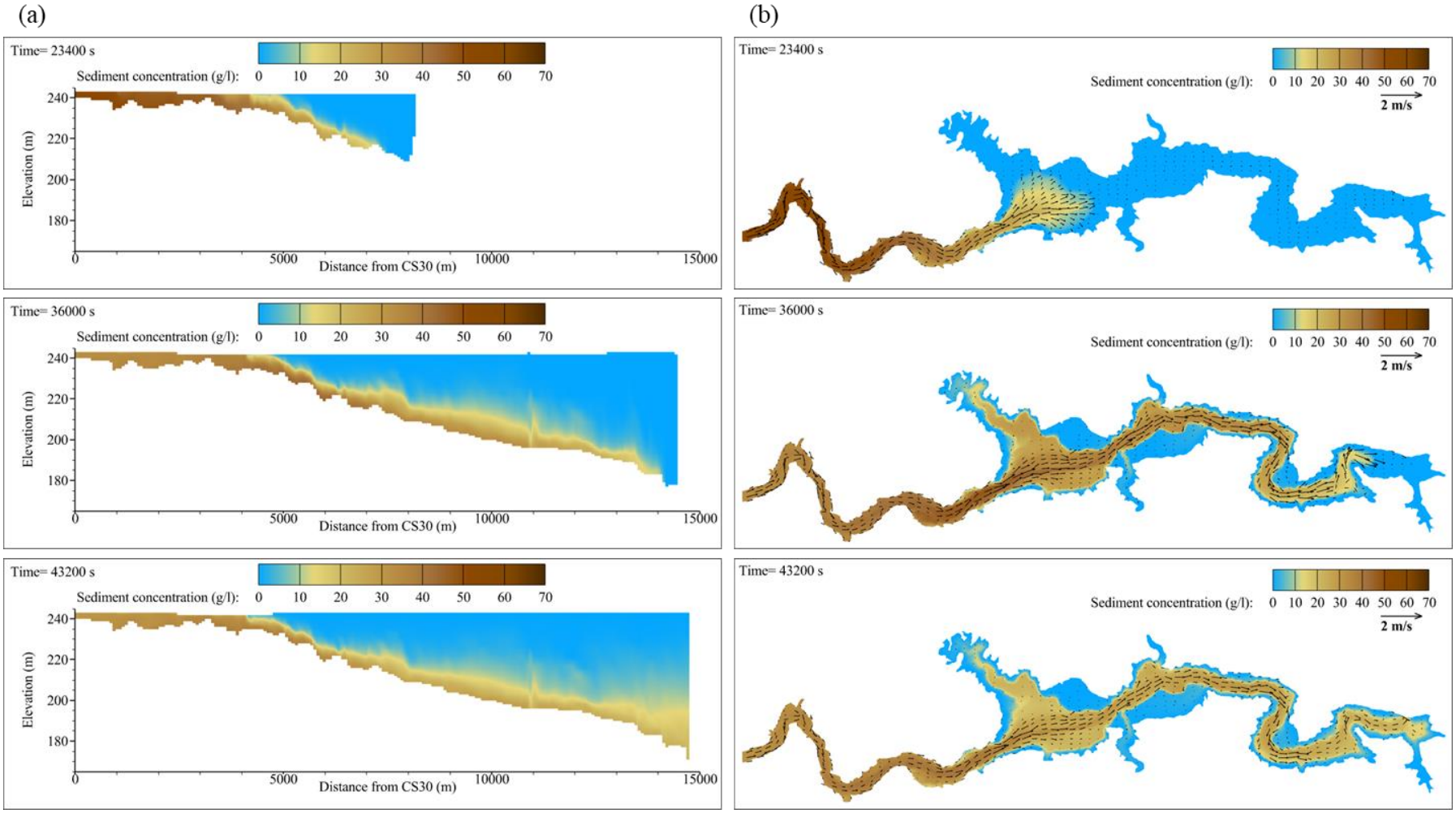

Figure C.52 The turbidity current processes from arrival at CS20, dam, and the muddy lake formed in (a) longitudinal and (b) plane view under Sc# $Q_S S_L$ with engineering methods.

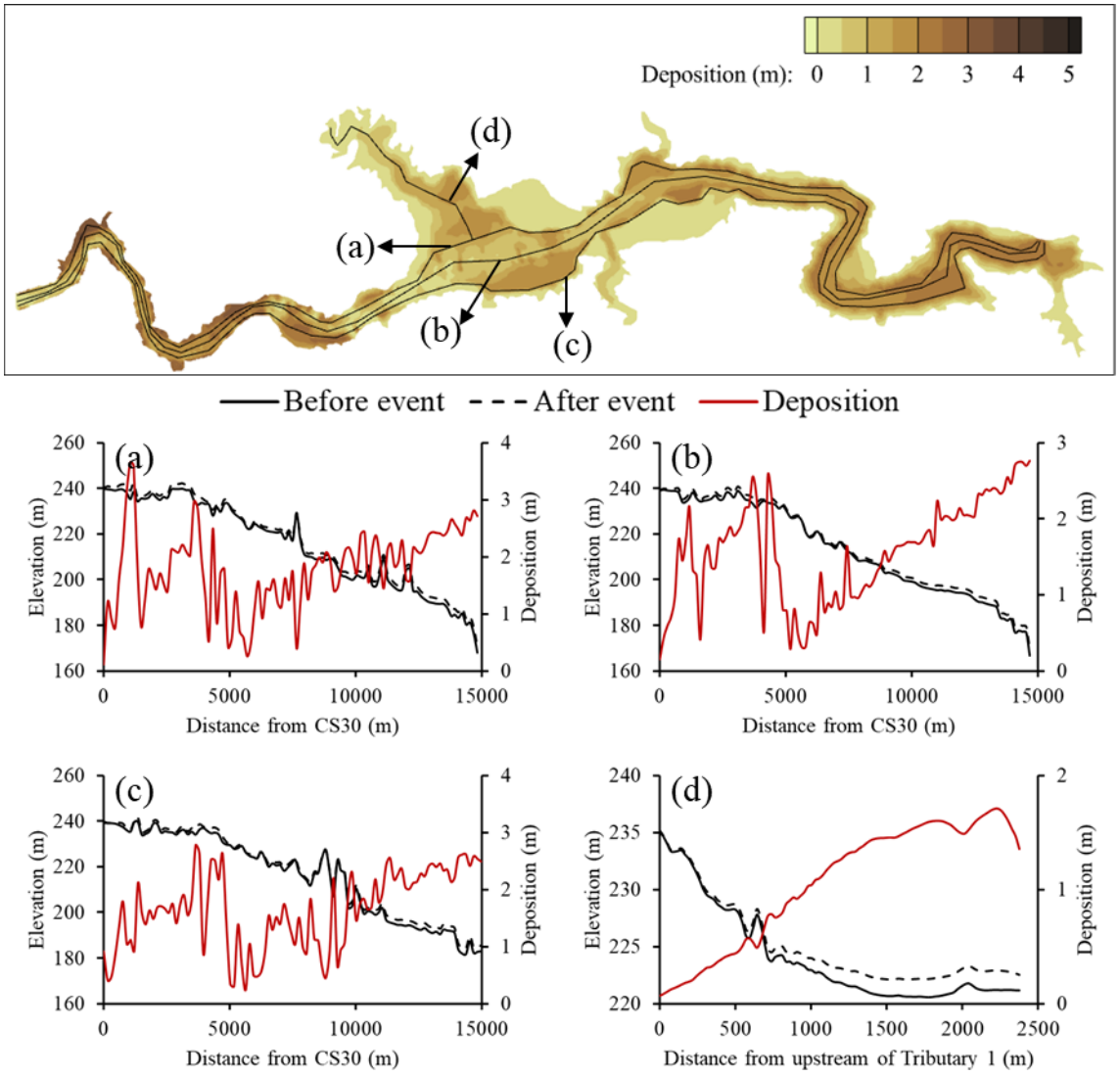

Figure C.53 The bed elevation before and after event, and deposition at (a) left, (b) middle and (c) right side of mainstream, and (d) tributary under Sc# $Q_S S_L$ with engineering methods.

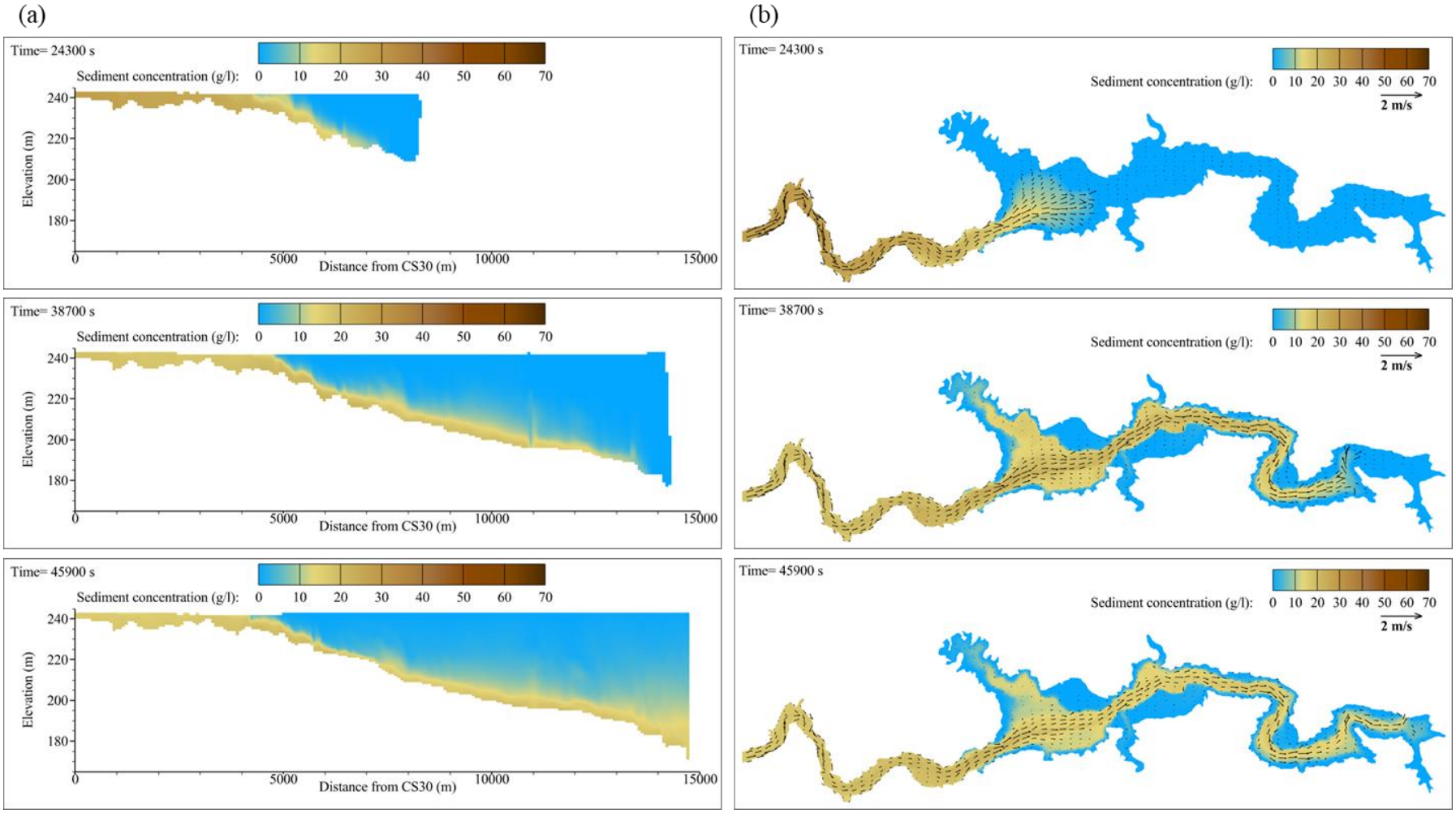

Figure C.54 The turbidity current processes from arrival at CS20, dam, and the muddy lake formed in (a) longitudinal and (b) plane view under Sc# $Q_S S_M$ with engineering methods.

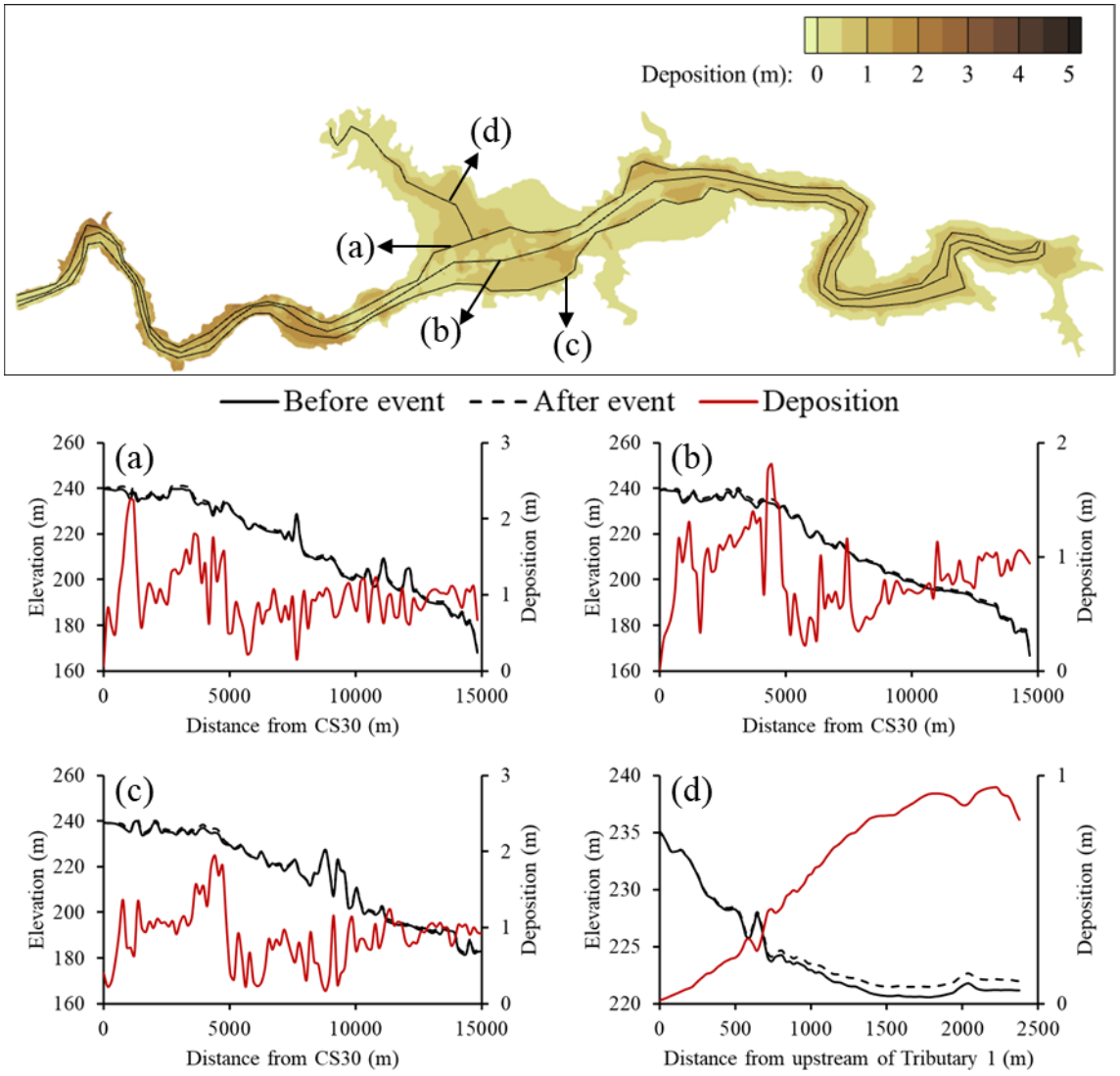

Figure C.55 The bed elevation before and after event, and deposition at (a) left, (b) middle and (c) right side of mainstream, and (d) tributary under Sc# $Q_S S_M$ with engineering methods.

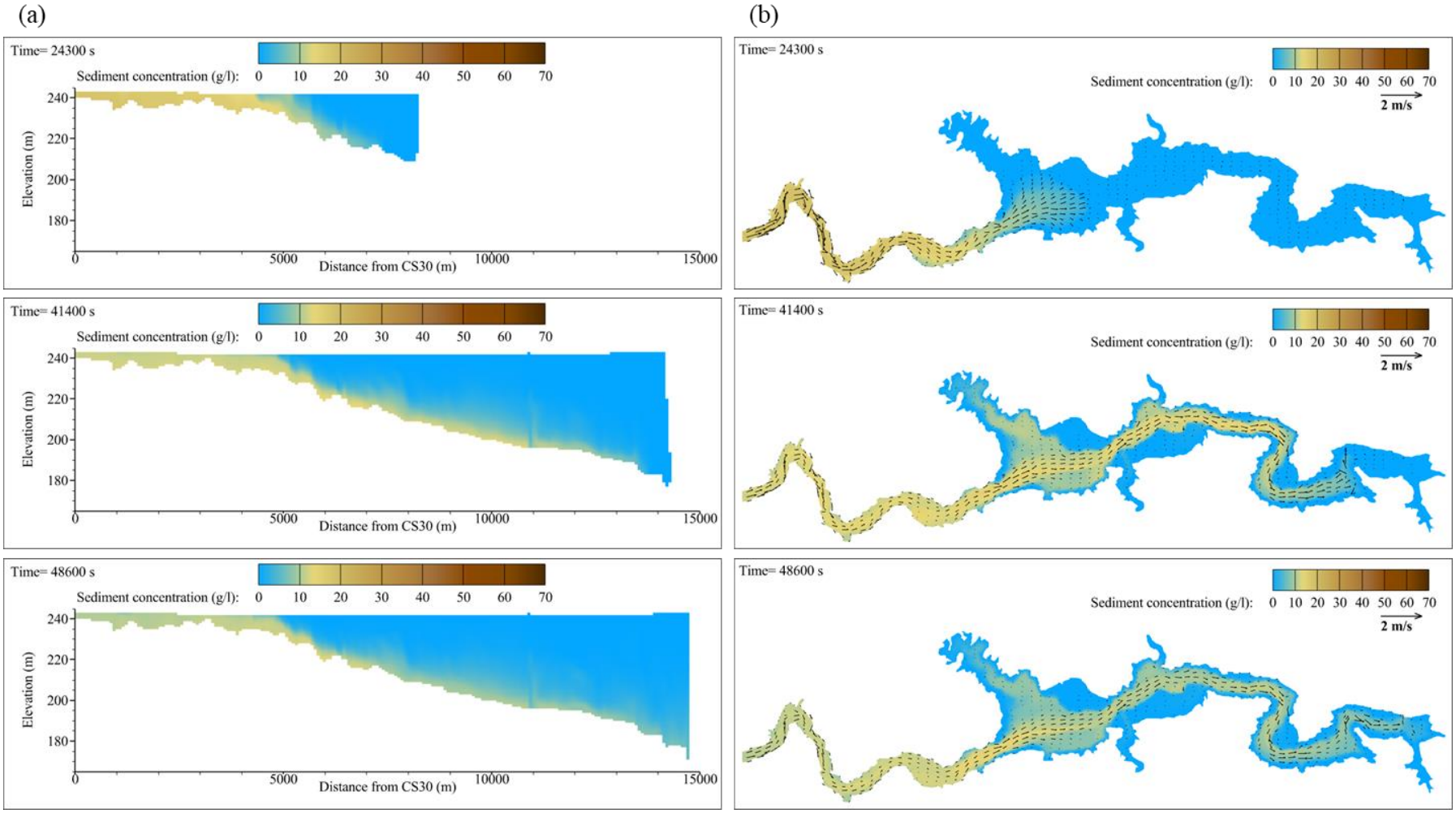

Figure C.56 The turbidity current processes from arrival at CS20, dam, and the muddy lake formed in (a) longitudinal and (b) plane view under Sc# $Q_S S_S$ with engineering methods.

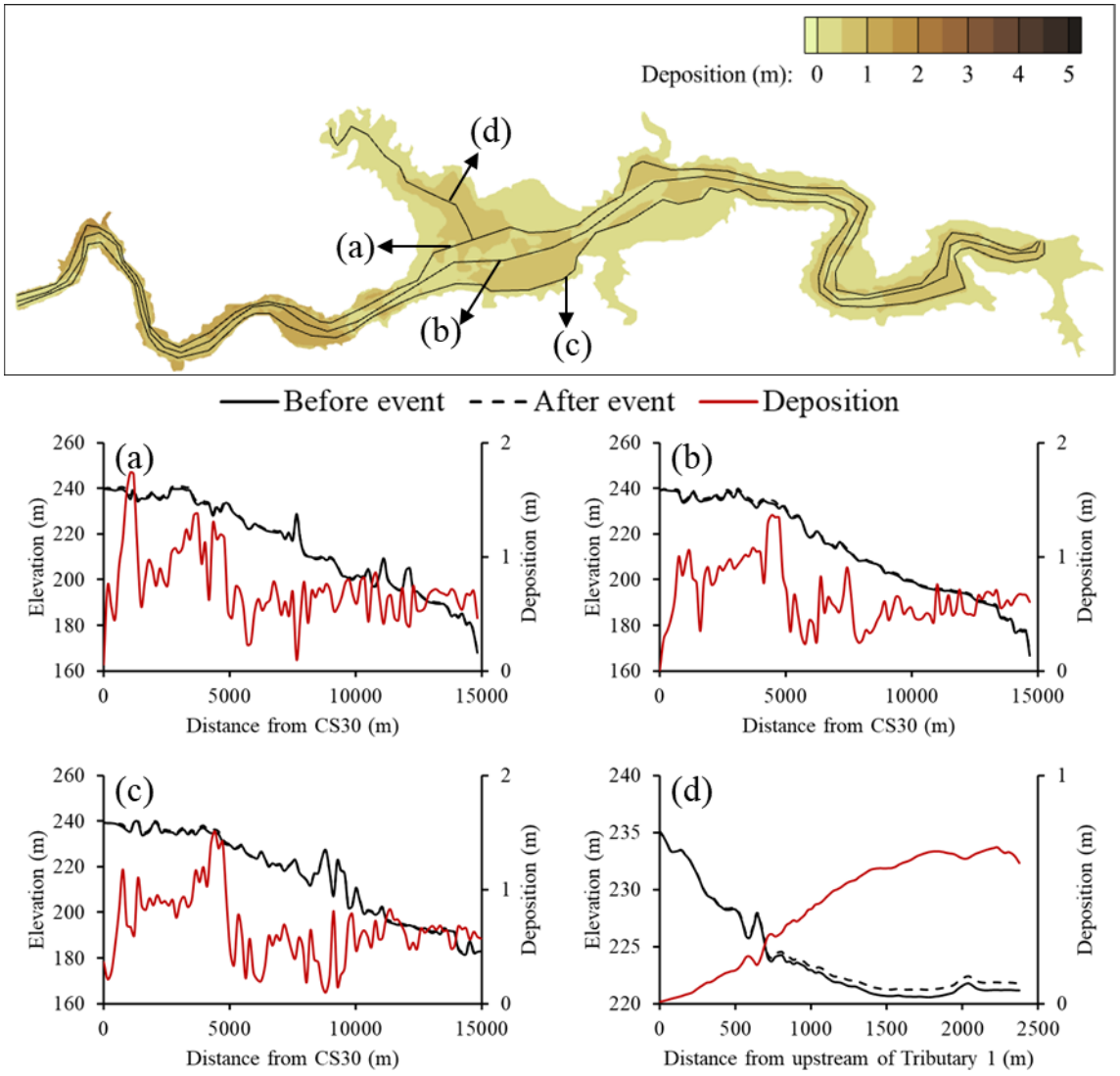

Figure C.57 The bed elevation before and after event, and deposition at (a) left, (b) middle and (c) right side of mainstream, and (d) tributary under Sc# $Q_S S_S$ with engineering methods.